20 September 2013 | $10

Science

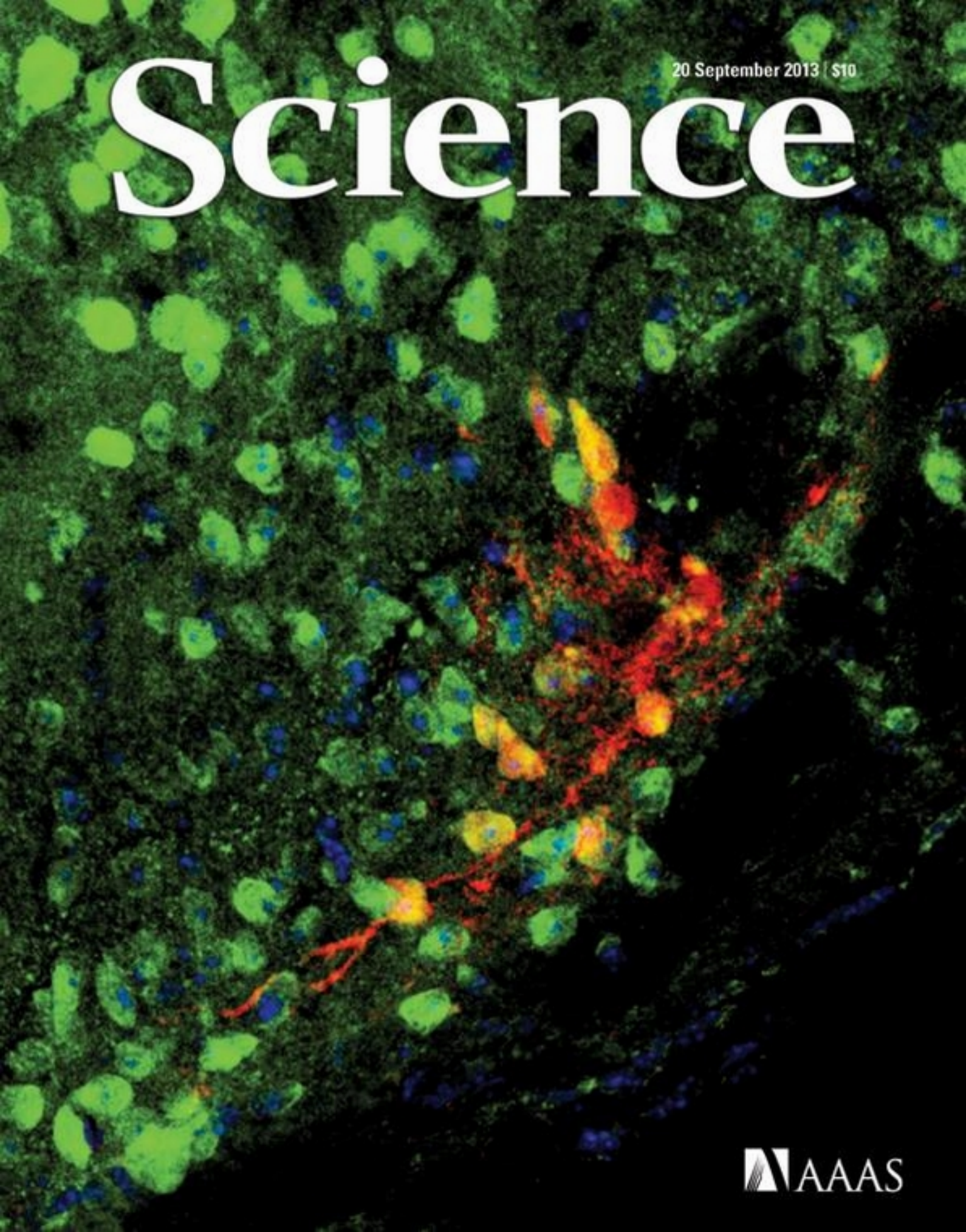

AAAS

CONTENTS continued >>

page 1332

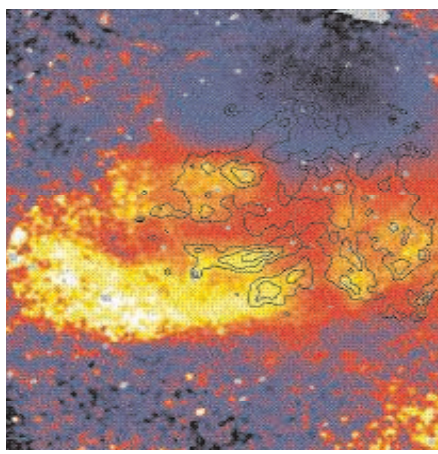

page 1365

ON THE WEB THIS WEEK

>> *Science* Podcast
Listen to stories on the deep history of animals on the planet, coexisting with carnivores, Earth's atmosphere more than 3 billion years ago, and more.

>> Find More Online
Check out *Science* Express, our podcast, videos, daily news, our research journals, and *Science* Careers at **www.sciencemag.org**.

COVER

Immunostained fluorescence microscopy image of a biomarker of endogenous withdrawal (phosphorylated extracellular regulated kinase, red) that increases in mouse spinal cord neurons (green) during opioid receptor blockade (image width: 250 micrometers). Inflammation or injury to the skin causes μ-opioid receptors to become constitutively active, which leads to long-term relief from chronic pain, but at the expense of endogenous opioid dependence. See page 1394.

Image: Suzanne Doolen, Greg Corder, and Brad Taylor/University of Kentucky

DEPARTMENTS

Published by AAAS

RESEARCH ARTICLES

REPORTS

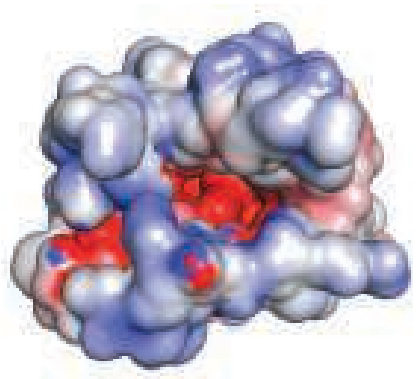

pages 1347 & 1387

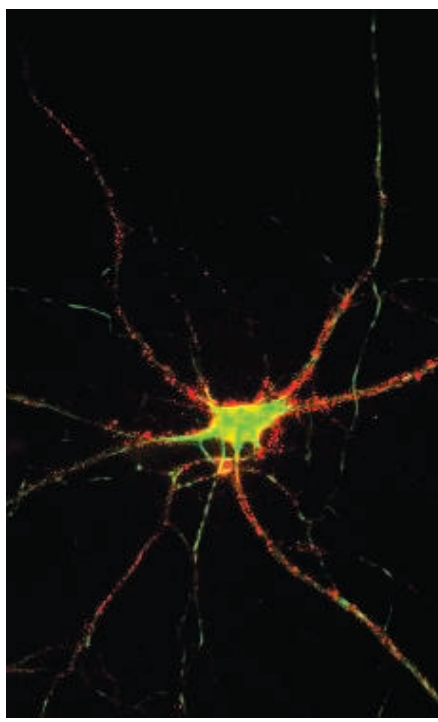

pages 1354 & 1399

CREDIT: (BOTTOM) JOSH SYKEN, CARLA SHATZ, AND TAEHO KIM

SCIENCE (ISSN 0036-8075) is published weekly on Friday, except the last week in December, by the American Association for the Advancement of Science, 1200 New York Avenue, NW, Washington, DC 20005. Periodicals Mail postage (publication No. 484460) paid at Washington, DC, and additional mailing offices. Domestic individual membership and subscription (51 issues): $149 ($74 allocated to subscription). Domestic institutional subscription (51 issues): $990; Foreign postage extra: Mexico, Caribbean (surface mail) $55; other countries (air assist delivery) $85. First class, airmail, student, and emeritus rates on request. Canadian rates with GST available upon request, GST #1254 88122. Publications Mail Agreement Number 1069624. **Printed in the U.S.A.**

Change of address: Allow 4 weeks, giving old and new addresses and 8-digit account number. **Postmaster:** Send change of address to AAAS, P.O. Box 96178, Washington, DC 20090–6178. **Single-copy sales:** $10.00 current issue, $15.00 back issue prepaid includes surface postage; bulk rates on request. **Authorization to photocopy** material for internal or personal use under circumstances not falling within the fair use provisions of the Copyright Act is granted by AAAS to libraries and other users registered with the Copyright Clearance Center (CCC) Transactional Reporting Service, provided that $30.00 per article is paid directly to CCC, 222 Rosewood Drive, Danvers, MA 01923. The identification code for *Science* is 0036-8075. *Science* is indexed in the *Reader's Guide to Periodical Literature* and in several specialized indexes.

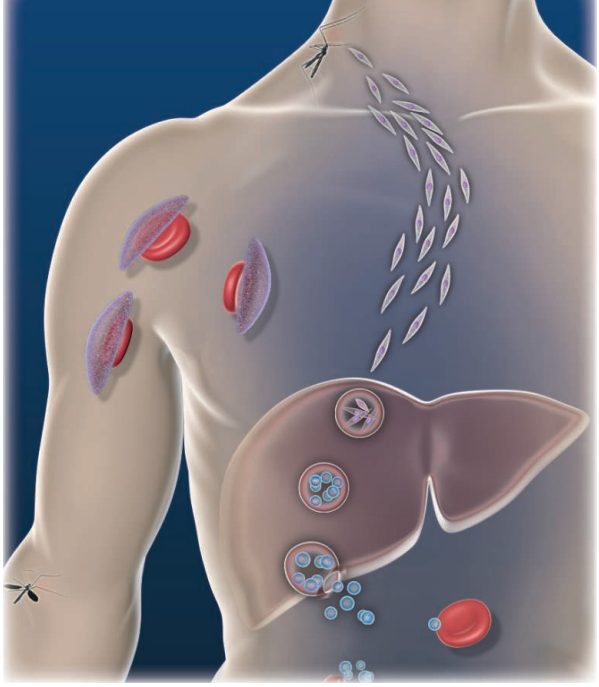

<< Malaria Sporozoite Vaccine

Each year, hundreds of millions of people are infected with *Plasmodium falciparum*, the mosquito-borne parasite that causes malaria. A preventative vaccine is greatly needed. **Seder *et al.*** (p. 1359, published online 8 August; see the Perspective by **Good**) now report the results from a phase I clinical trial where subjects were immunized intravenously with a whole, attenuated sporozoite vaccine. Three of 9 subjects who received four doses and zero of 6 subjects who received five doses of the vaccine went on to develop malaria after controlled malaria infection. Both antibody titers and cellular immune responses correlated positively with the dose of vaccine received, suggesting that both arms of the adaptive immune response may have participated in the observed protection.

Merging Coma

Galaxy clusters grow through mergers and accretion of matter to become the largest gravitationally bound structures in the universe. **Sanders *et al.*** (p. 1365) report long, high-resolution observations with NASA's Chandra X-ray Observatory that probe hot, ionized gas at the core of the Coma cluster—one of the nearest and best-studied galaxy clusters. The data reveal several large-scale, filament-shaped x-ray brightness enhancements, which provide insight into the cluster's merging history.

Polymer Dynamics

While free surfaces should allow polymer chains to move faster than in the bulk, the presence of a substrate might slow down the motion if there is an attraction between the two. **Tress *et al.*** (p. 1371; see the Perspective by **Russell**) used dielectric spectroscopy to study "polymer islands" deposited on a substrate from dilute solution, where some islands contained just a few or only one polymer chain. The confinement of the polymer chain to small-surface geometries had virtually no influence on the dynamics of the polymers, aside from the segments in direct contact with the substrate.

The Pull of Phosphorus

Lewis acidity is primarily associated with compounds like boranes that lack a full complement of electrons in their coordination sphere and therefore attract electron donors (Lewis bases) to fill the gap. **Caputo *et al.*** (p. 1374; see the Perspective by **Gabbaï**) now show that a class of 4-coordinate phosphonium salts can act as surprisingly potent Lewis acids, despite their electronic saturation. The phosphorus cations, bearing fluorine and fluorinated aromatic substituents, can sever an alkyl carbon-fluorine bond by pulling away its fluoride—a process rendered catalytic through the use of a silane acceptor.

Alarm Bells

The presence of DNA in the cytosol of mammalian cells is a danger signal, indicating, for example, that a DNA-containing virus has infected the cell. This signal triggers an innate immune response, which involves the expression of type I interferons, and is critical for antiviral immunity and responses to DNA vaccines. Cyclic GMP-AMP synthase (cGAS) was recently identified as a sensor of cytosolic DNA. **Li *et al.*** (p. 1390, published online 29 August) now use knockout mice to provide genetic evidence that, in multiple cell types, cGAS is the primary DNA sensor required for the type I interferon response in vivo.

Stealth Nod Factor Recognition

Legumes' symbiotic interaction with nitrogen fixing bacteria supplies the plant with nitrogen. Many important crop plants, however, cannot establish these symbioses and, thus, agriculture depends on externally applied fertilizers. Surprisingly, **Liang *et al.*** (p. 1384, published online 5 September) found that several nonleguminous plants, including *Arabidopsis*, tomato, and corn, were able to respond to the same Nod factors that initiate the microbial symbiosis in soybean.

Pain and Dependence

The properties and functions of μ-opioid receptors have been studied intensively with respect to the binding of endogenous or exogenous ligands. However, much less is known about the constitutive, ligand-independent, activation of opioid receptors. Working in mice, **Corder *et al.*** (p. 1394) observed the prolonged constitutive activation of μ-opioid receptors in the spinal dorsal horn after transient peripheral inflammation. The results suggest that constitutive activation of μ-opioid receptors depresses nociception—the perception of pain—for long periods of time and induces cellular and physical dependence on endogenous opioid signaling.

Delineating Deep Faults

Most large, damaging earthquakes initiate in Earth's crust where friction and brittle fracture control the release of energy. Strong earthquakes can occur in the mantle too, but their rupture dynamics are difficult to determine because higher temperatures and pressures play a more important role. **Ye *et al.*** (p. 1380) analyzed seismic *P* waves generated by the 2013 M_w 8.3 Sea of Okhotsk earthquake—the largest deep earthquake recorded to date—and its associated aftershocks. The earthquake ruptured along a fault over 180-kilometer-long and structural heterogeneity resulted in a massive release of stress from the subducting slab. In a set of complementary laboratory deformation experiments, **Schubnel *et al.*** (p. 1377) simulated the nucleation of acoustic emission events that resemble deep earthquakes. These events are caused by an instantaneous phase transition from olivine to spinel, which would occur at the same depth and result in large stress releases observed for other deep earthquakes.

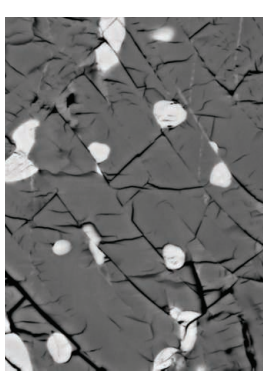

CREDITS (TOP TO BOTTOM): C. BICKEL/*SCIENCE*; ALEXANDRE SCHUBNEL, LABORATOIRE DE GÉOLOGIE, ENS/CNRS

Additional summaries

Pushing Metathesis Forward

It has been 8 years since the Nobel Prize in chemistry recognized the pioneers of olefin metathesis catalysis. Essentially, a means of shuffling the four carbons in a pair of double bonds, the transformation has enabled efficient synthesis of numerous complex organic compounds—particularly those incorporating large rings—and also underlies the ROMP (ring-opening metathesis polymerization) process for the preparation of specialty polymers. Analogous metathesis of (triple-bonded) alkynes has been applied as well. **Fürstner** (p. 1357) reviews recent developments in the continuing optimization of this extraordinarily versatile reaction class. A long-standing deficiency has been the lack of stereoselectivity by the standard catalysts, precluding deliberate placement of substituents on the same (*Z*) or opposite (*E*) sides of the double-bond axis in the product, but recently introduced catalysts have shown promise in achieving high *Z* selectivity.

Toward Synthetic Biology

The detection of an appropriate point to intervene in a cellular pathway and minimize off-target effects on other cellular processes present problems for the design of circuits that control cellular signaling pathways and thus direct cell function. **Galloway *et al.*** (p. 1358, published online 15 August; see the Perspective by **Sarkar**) report progress on these challenges in the yeast *Saccharomyces cerevisiae*. A molecular control system was developed to direct the yeast cells to one of three cell fates. To avoid disruption of other cellular controls, exogenous ribozyme-based controllers that interfaced with the endogenous control circuits were used, which avoided genetic alteration to the cells. After enhancing the control circuits with feedback loops to make their behavior more reliable, the circuits were used to modulate the abundance of particular components that acted as critical regulators of yeast cell-fate decisions. This allowed direction of cell fate in response to a chosen chemical stimulus. These strategies may be adaptable to allow similar direction of the physiological state of mammalian cells, for example, to allow therapeutic applications of synthetic biology.

Dissipating Static

The accumulation of a static charge on polymers and other insulators often causes little more than a slight annoyance but it can lead to the destruction of sensitive electrical equipment. Thus, approaches are required that prevent and dissipate static electricity through improved electrical conductivity, or that ensure complete discharge before a contact with a key piece of equipment. **Baytekin *et al.*** (p. 1368) show that surface charges will colocalize with radicals on the surface of a polymer, and that the addition of free radical scavengers causes a discharge of the surface as the charges are removed. The approach was used successfully to produce coatings that protected electronic circuits from damage caused by electrostatic discharge.

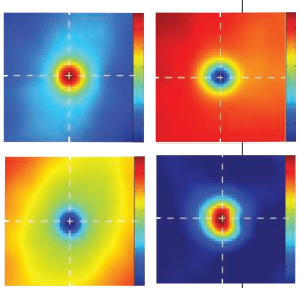

CREDIT (TOP TO BOTTOM): BAYTEKIN *ET AL.*

CCR5-Maraviroc Structure

The chemokine receptor CCR5, a G protein–coupled receptor best known as a co-receptor during HIV-1 infection, is important in a variety of physiological processes. **Tan *et al.*** (p. 1387, published online 12 September; see the Perspective by **Klasse**) now report the high-resolution crystal structure of CCR5 bound to the HIV-1 entry inhibitor, Maraviroc. The structure suggests that Maraviroc acts as a noncompetitive inhibitor by binding to a region of CCR5 that is distinct from the binding site of HIV-1 and chemokines. Comparison of the structure of CCR5 with the other HIV-1 co-receptor, the chemokine receptor CXCR4, provides insight into the co-receptor selectivity of the virus.

Amyloid Binding Partners

Amyloid-β (Aβ) is critical to the pathology of Alzheimer's disease (AD), but its role in normal physiology remains unclear. **Kim *et al.*** (p. 1399; see the Perspective by **Benilova and De Strooper**) found that murine-paired immunoglobulin-like receptor B (PirB) and its human ortholog, leukocyte immunoglobulin-like receptor B2 (LilrB2) both bound to oligomerized Aβ. Early in mouse development, ocular dominance plasticity was affected by interactions between oligomeric Aβ and PirB. In hippocampal brain slices from a mouse model of AD, reductions in long-term potentiation induced by Aβ required PirB. Furthermore, the memory defects characteristic of a mouse model of AD were dependent on function of PirB. Many binding partners for Aβ have been identified, and so the extent to which these findings can be exploited therapeutically remains unclear.

Extracellular Regulation

During *Caenorhabditis elegans* development, the hermaphrodite-specific neurons (HSNs) migrate and then extend axons toward their functional targets. Posttranslational modification of heparan sulfate proteoglycans are important for HSN development, and so **Pedersen *et al.*** (p. 1404) tested the effect of disrupting or reducing chondroitin and heparan sulfate synthesis during *C. elegans* development. The results suggest that proteoglycan biosynthesis is tightly regulated by a microRNA pathway to shape the cell surface glycosylation architecture required to direct neuronal migration.

Standing Up for GMOs

ON 8 AUGUST 2013, VANDALS DESTROYED A PHILIPPINE "GOLDEN RICE" FIELD TRIAL. OFFICIALS AND staff of the Philippine Department of Agriculture that conduct rice tests for the International Rice Research Institute (IRRI) and the Philippine Rice Research Institute (PhilRice) had gathered for a peaceful dialogue. They were taken by surprise when protesters invaded the compound, overwhelmed police and village security, and trampled the rice. Billed as an uprising of farmers, the destruction was actually carried out by protesters trucked in overnight in a dozen jeepneys.

The global scientific community has condemned the wanton destruction of these field trials, gathering thousands of supporting signatures in a matter of days.* If ever there was a clear-cut cause for outrage, it is the concerted campaign by Greenpeace and other nongovernmental organizations, as well as by individuals, against Golden Rice. Golden Rice is a strain that is genetically modified by molecular techniques (and therefore labeled a genetically modified organism or GMO) to produce β-carotene, a precursor of vitamin A. Vitamin A is an essential component of the light-absorbing molecule rhodopsin in the eye. Severe vitamin A deficiency results in blindness, and half of the roughly half-million children who are blinded by it die within a year. Vitamin A deficiency also compromises immune system function, exacerbating many kinds of illnesses. It is a disease of poverty and poor diet, responsible for 1.9 to 2.8 million preventable deaths annually, mostly of children under 5 years old and women.†

CREDIT: IRRI

Rice is the major dietary staple for almost half of humanity, but white rice grains lack vitamin A. Research scientists Ingo Potrykus and Peter Beyer and their teams developed a rice variety whose grains accumulate β-carotene. It took them, in collaboration with IRRI, 25 years to develop and test varieties that express sufficient quantities of the precursor that a few ounces of cooked rice can provide enough β-carotene to eliminate the morbidity and mortality of vitamin A deficiency.‡ It took time, as well, to obtain the right to distribute Golden Rice seeds, which contain patented molecular constructs, free of charge to resource-poor farmers.

The rice has been ready for farmers to use since the turn of the 21st century, yet it is still not available to them. Escalating requirements for testing have stalled its release for more than a decade. IRRI and PhilRice continue to patiently conduct the required field tests with Golden Rice, despite the fact that these tests are driven by fears of "potential" hazards, with no evidence of actual hazards. Introduced into commercial production over 17 years ago, GM crops have had an exemplary safety record. And precisely because they benefit farmers, the environment, and consumers, GM crops have been adopted faster than any other agricultural advance in the history of humanity.

New technologies often evoke rumors of hazard. These generally fade with time when, as in this case, no real hazards emerge. But the anti-GMO fever still burns brightly, fanned by electronic gossip and well-organized fear-mongering that profits some individuals and organizations. We, and the thousands of other scientists who have signed the statement of protest, stand together in staunch opposition to the violent destruction of required tests on valuable advances such as Golden Rice that have the potential to save millions of impoverished fellow humans from needless suffering and death.

– Bruce Alberts, Roger Beachy, David Baulcombe, Gunter Blobel, Swapan Datta, Nina Fedoroff, Donald Kennedy, Gurdev S. Khush, Jim Peacock, Martin Rees, Phillip Sharp

*B. Chassy *et al.*, "Global scientific community condemns the recent destruction of field trials of Golden Rice in the Philippines"; http://chn.ge/143PyHo (2013). †E. Mayo-Wilson *et al., Br. Med. J.* **343**, d5094 (2011). ‡G. Tang *et al.*, *Am. J. Clin. Nutr*. **96**, 658 (2012).

10.1126/science.1245017

Bruce Alberts is President Emeritus of the U.S. National Academy of Sciences and former Editor-in-Chief of *Science*.

Roger Beachy is a Wolf Prize laureate; President Emeritus of the Donald Danforth Plant Science Center, St. Louis, MO, USA; and former director of the U.S. National Institute of Food and Agriculture.

David Baulcombe is a Wolf Prize laureate and Royal Society Professor in the Department of Plant Sciences of the University of Cambridge, Cambridge, UK. He receives research funding from Syngenta and is a consultant for Syngenta.

Gunter Blobel is a Nobel laureate and the John D. Rockefeller Jr. Professor at the Rockefeller University, New York, NY, USA.

Swapan Datta is Deputy Director General (Crop Science) of the Indian Council of Agricultural Research, New Delhi, India; the Rash Behari Ghosh Chair Professor at Calcutta University, India; and a former scientist at ETH-Zurich, Switzerland, and at IRRI, Philippines.

Nina Fedoroff is a National Medal of Science laureate; a Distinguished Professor at the King Abdullah University of Science and Technology, Thuwal, Saudi Arabia; an Evan Pugh Professor at Pennylvania State University, University Park, PA, USA; and former President of AAAS.

Donald Kennedy is President Emeritus of Stanford University, Stanford, CA, USA, and former Editor-in-Chief of *Science*.

Gurdev S. Khush is a World Food Prize laureate, Japan Prize laureate, and former scientist at IRRI, Los Baños, Philippines.

Jim Peacock is a former Chief Scientist of Australia and former Chief of the Division of Plant Industry at the Commonwealth Scientific and Industrial Research Organization, Canberra, Australia.

Martin Rees is President Emeritus of the Royal Society, Fellow of Trinity College, and Emeritus Professor of Cosmology and Astrophysics at the University of Cambridge, Cambridge, UK.

Phillip Sharp is a Nobel laureate; an Institute Professor at the Massachusetts Institute of Technology, Cambridge, MA, USA; and President of AAAS.

EDITED BY MARIA CRUZ AND SACHA VIGNIERI

ECOLOGY

Be Honest

Sexual signals, such as plumage color, are thought to reflect an individual's condition and thus to be a relatively honest indicator of quality to those seeking a mate. The condition of individuals, however, can change over time, leaving one to wonder if such traits only provide honest information about condition at a specific point in the past. Vitousek *et al.* tested whether signals themselves may influence an individual's condition and thus provide a more accurate indicator of current quality. Specifically, they experimentally darkened the underside of female North American barn swallows and measured indicators of physiological state, such as reactive oxidative metabolites and circulating testosterone. Manipulated birds had consistently lower levels than controls. Naturally darker birds have greater resistance to oxidative stress and reproductively dominate lighter birds. The authors suggest that darkening the birds led to altered social interactions, including fewer challenges and greater mating success. Further, they suggest that the reduced stress experienced by darkened birds left them in better condition, one more reflective of the high-quality trait they displayed. These results suggest that feedback between a signal, its bearer, and recipients may help keep both the signal, and the signaler, honest. — SNV

Biol. Lett. **9**, 10.1098/rsbl.2013.0539 (2013).

GEOPHYSICS

Reconstructing Plate Tectonics

The modern-day distribution of Earth's tectonic plates is just a snapshot of an ever-changing process. Reconstructions of previous plate arrangements have resulted in the identification of the ancient supercontinents Pangea and Rodinia, but does this cycle follow any sort of predictable law or pattern? Morra *et al.* statistically analyzed the organization of large and small plates across Earth's surface over the past 200 million years, based on models of plate reconstructions. Small plates do not show much statistical variation in their distribution over time, because they are largely unstable and form from unrelated events. Large plates, however, tend to organize either into heterogeneous or homogenous states based on plate size distributions over ~100-million-year time scales. The rapid rate at which heterogeneous distribution states are stabilized suggests that these may be excited states, whereas homogeneous distribution states tend more toward equilibrium. In this case, the underlying driving force for the transition from one state to another depends on cycling between top-down and bottom-up mantle convection as a control on plate motion. — NW

Earth Planet. Sci. Lett. **373**, 93 (2013).

ENVIRONMENTAL SCIENCE

Historic Hg Legacy

Industrial operations such as metal smelters and coal-burning power plants release mercury (Hg) into the atmosphere, where it can remain for up to 2 years before it is deposited. Recent efforts to regulate these emissions have led to the Minamata Convention, an international treaty due to be signed in October 2013, which aims to address the toxic effects of mercury in the environment. Yet many aspects of the emission and dispersal of mercury remain unclear. Eckley *et al.* have undertaken a detailed study of local

ground-level air mercury concentrations near the Flin Flon, Manitoba, copper smelter. Until its closure in 2010, this was Canada's largest point source of mercury emissions. The closure provided the opportunity to study atmospheric mercury concentrations before and after the shutdown of a large point source. Although atmospheric mercury concentrations fell after the closure, they remained higher than at other Canadian monitoring stations, both in the atmosphere and in precipitation. Surface-to-air flux from local polluted soils is thus the most likely source of the elevated atmospheric mercury concentrations after closure. — JFU

Environ. Sci. Technol. 10.1021/es401352n (2013).

DEVELOPMENT

Growing Pains

Humans, unlike most other mammalian species, have an extended slow childhood growth period between the relatively rapid growth stages of infancy and puberty. Examining gene transcripts in lymphoid tissue in humans spanning infancy, childhood, puberty, and adulthood, Stevens *et al.* identified gene expression networks of age, of which a subset were growth-specific, and related them to a human protein and genetic interaction networks. The highest levels of predicted gene interactions were in infancy, showing decreasing connectivity with increasing age. Examination of different age-associated networks identified conserved pathways related to growth, which were also identified in the transcriptomes of other tissues. Furthermore, interactions between genes and glucocorticoid receptor–mediated transcription implicated age/stage-specific networks. Of the genes with age-specific expression, several had previously been identified as associated with height and, surprisingly, diabetes. This study suggests that gene interaction networks change, and are rewired, in a predicable manner throughout human development and growth. — LMZ

BMC Genom. **14**, 10.1186/1471-2164-14-547 (2013).

CREDITS (TOP TO BOTTOM): CEPHAS/WIKIMEDIA COMMONS; CHRIS ECKLEY

Published by AAAS

AROUND THE WORLD

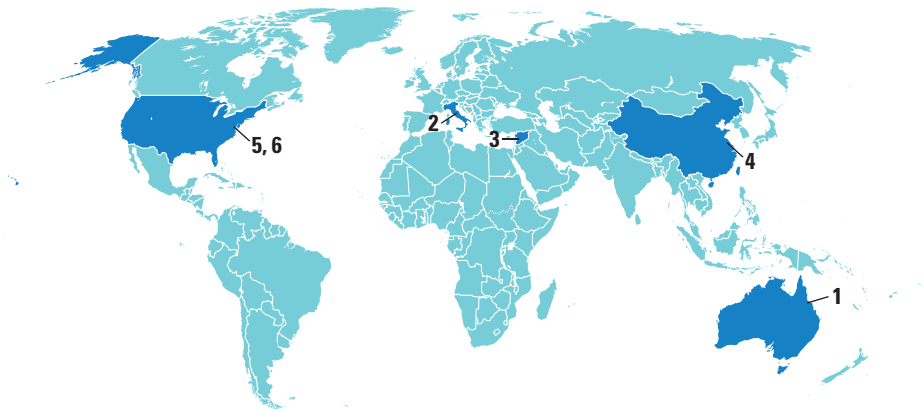

Canberra **1**

PM-Elect Goes Science-Lite

Australia's scientific community and incoming Prime Minister Tony Abbott are off to a rocky start. Unveiling his picks for Cabinet posts this week, Abbott left science out in the cold.

"Scientists around the nation are asking, 'Where's the science minister?' " said Catriona Jackson, CEO of Science and Technology Australia, an organization representing 68,000 scientists and technologists. This will be the first time that an Australian government has not had a science minister since the science portfolio was created in 1931. Pressed by journalists, Abbott revealed that Australia's national research agency, CSIRO, would report to industry minister Ian Macfarlane.

The omission comes on the heels of the incoming government's threat to micromanage grant selection at the Australian Research Council, with awards in philosophy, religious history, and the intersection of art and climate change singled out. Climate science and environmental protection may well need to brace for tough times. In 2009, Abbott dismissed climate change as "absolute crap," and this week reiterated a campaign pledge to scrap the outgoing government's carbon tax.

http://scim.ag/AbbottScience

Rome **2**

Italian Panel Assails Stem Cell Treatment

An expert panel that the Italian government asked to come up with a trial design for a controversial Italian stem cell therapy has thrown in the towel. In a report to Italian Minister of Health Beatrice Lorenzin last week, the group concluded that the treatment, designed by the Stamina Foundation, has no scientific basis.


Lorenzin

Facing strong pressure from patients who want to undergo Stamina's therapy for a range of diseases, the Italian government has allocated €3 million to studying the therapy, but the panel argued that there is no point in going forward.

In response, Stamina President Davide Vannoni questioned the impartiality of the panel's members and said they did not ask for medical records of patients responding well to treatment at the hospital in Brescia where Stamina operates. The foundation is also under investigation for allegedly treating patients with unapproved therapies in exchange for money.

Vannoni said last week that he was in Africa to negotiate a trial with government officials of a country he declined to identify.

http://scim.ag/stempanel

Damascus **3**

U.N. Team Confirms Sarin Attack in Syria

U.N. inspectors have found "clear and convincing evidence" that a chemical weapons attack using the nerve agent sarin killed a large number of civilians near Damascus on 21 August.

The U.N. team, led by Swedish scientist Åke Sellström, visited the Ghouta suburb of Damascus between 26 August and 29 August. Their 38-page report describes evidence such as soil samples, wipes from rockets, and blood and urine samples from survivors. Lab tests finding sarin or its degradation products in the samples, along with interviews of survivors and medical staff members, led the team to conclude: "Chemical weapons have been used in the ongoing [Syrian] conflict … on a relatively large scale."


Sellström and Ban

U.N. Secretary-General Ban Ki-moon called the findings "beyond doubt and beyond the pale." Although the report does not assign blame for the attack, it includes details on the rockets used to deliver the sarin, information that some countries said implicates the Syrian government. Russia and the United States have already agreed to a plan to allow U.N. inspectors to secure and destroy Syria's chemical arsenal.

http://scim.ag/syriasarin

Beijing **4**

Fraudulent Chinese Academy Bid Exposed

Zhang Shuguang, called the "father" of China's high-speed rail system, stood trial in Beijing last week on corruption charges, where he admitted to paying 23 million yuan (about $3.8 million) to burnish his credentials for membership in the Chinese Academy of Sciences (CAS). His attempts failed twice.

In 2007, as deputy chief engineer of the now-defunct railway ministry, Zhang used a slush fund provided by businessmen seeking contracts to cloister 30 experts in a hotel for 2 months while they produced three books on high-speed rail technology credited to Zhang, according to reporting in *Century Weekly*. His bid failed by seven votes.

Two years later, he again hired ghostwriters to produce more volumes on his behalf and allegedly bribed voting CAS members, but again fell one vote shy of election.

CAS academicians, or *yuanshi*, help set the nation's science policy and can keep their jobs as long they wish. Zhang's testimony has touched off a firestorm in China, where many commentators are questioning CAS members' integrity and calling for curbs on *yuanshi* perks. **http://scim.ag/corruptacademy**

CREDITS (TOP TO BOTTOM): UN PHOTO/PAULO FILGUEIRAS; ITALIAN MINISTRY OF HEALTH

Published by AAAS

Boston **5**

Reviews Find Fault in Transgenic Rice Study

A U.S.-led study in which Chinese children were fed genetically modified rice in 2008 didn't comply fully with regulations for studies in humans, Tufts University announced earlier this week after internal and external reviews. The university has barred the study's principal investigator, Guangwen Tang of the university's Jean Mayer USDA Human Nutrition Research Center on Aging, from doing human studies for 2 years. The study of "golden rice," modified to deliver vitamin A, triggered a firestorm in China. Greenpeace alleged ethical misconduct and called it a "scandal of international proportions" shortly after a paper reporting its results was published last year (*Science*, 14 September 2012, p. 1281); following an official Chinese investigation, three Chinese researchers were removed from their positions in December.

In a brief statement issued on 17 September, Tufts said there was "insufficient evidence of appropriate reviews and approvals in China," and that Tang—who did not respond to requests for comment—made changes to the study protocol without approval from Tufts University's Institutional Review Board. The reviews did not identify health or safety concerns and the study's results are not in dispute, the university says. **http://scim.ag/ricereviews**

Washington, D.C. **6**

BRAIN Initiative Gets (a Little) More Detailed

This week, the U.S. National Institutes of Health (NIH) made a first stab at fleshing out its plans for the roughly $40 million that it hopes to spend on the Brain Research through Advancing Innovative Neurotechnologies (BRAIN) Initiative in fiscal year 2014. A report compiled by 15 scientists over the course of four public meetings lists nine research priorities, including classifying brain cells, studying how they connect, and identifying how patterns of activity among them produce behavior. It's clear that achieving the report's ambitious goals will require far more than NIH has allotted, says Gerald Rubin, executive director of the Janelia Farm Research Campus in Ashburn, Virginia. "The plan is bigger than the money," he says.
http://scim.ag/BRAINdetails

PHOTO CREDIT: STOCKPHOTO/THINKSTOCK; BAR GRAPH SOURCE: ©2013 GALLUP INC.

FINDINGS

Wine Contaminant Puts a Cork In Olfactory Receptors

Have you ever ordered a bottle of wine in a nice restaurant only to reluctantly send it back because the wine seemed "corked"—it had a musty odor and didn't taste quite right?

There's a good chance that the wine was contaminated with 2,4,6-trichloroanisole (TCA), a molecule well known as the main cause of cork taint. A new study by Japanese researchers published online in the *Proceedings of the National Academy of Sciences* this week concludes that you don't actually smell TCA directly; rather, TCA blocks the action of olfactory cells in your nose, distorting your ability to detect odors. The findings, the result of experiments with extra-large newt olfactory cells and human wine tasting volunteers, could help the food and beverage industry improve its products and lead to less embarrassment for both you and your waiter.
http://scim.ag/corktaint

THEY SAID IT

"I think that we've stopped evolving."

—87-year-old British naturalist and broadcaster David Attenborough, in an interview with *Radio Times*, adding that, with so many babies now surviving childhood, natural selection cannot act on humans anymore. The comments drew heat from scientists, who note that his view doesn't reflect scientific consensus.
http://scim.ag/Attenevo

Full-Speed Reprogramming

By removing a molecular brake, scientists can turn mature cells into embryolike ones with almost 100% efficiency. In a process called cellular reprogramming, researchers switch on four genes in skin, blood, or other mature cells to transform them into induced pluripotent stem cells (iPSCs), which can become any of the body's cell types. >>

Top-Rated Subjects

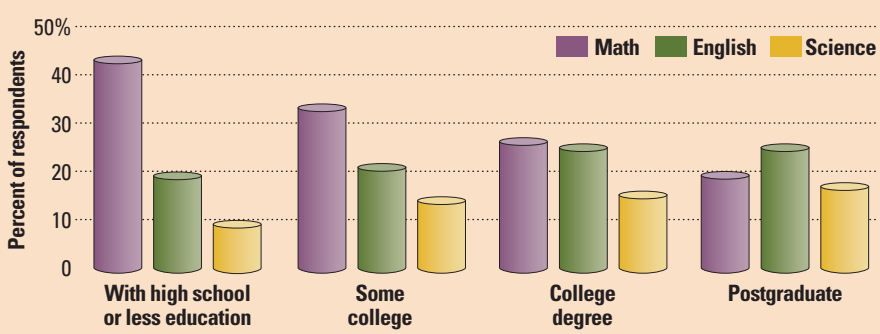

What I Learned in School

Science is moving up the ranks on a list of the most important courses Americans take in school. A Gallup poll of 2059 U.S. adults, released earlier this month, found that 12% think science was "the most valuable" subject in their academic careers. That's up from 4% in 2002, the last time Gallup asked the question.

The perceived value of studying science also rises with level of education. Those with no more than a high school diploma chose math over science by a whopping margin of 43% to 9%. But those with postgraduate training ranked science third, at 17%, only slightly behind math at 19%. English topped their list of most valuable subject, at 25%. Overall, math and English still claimed the top two spots in this year's survey, at 34% and 21%.

Published by AAAS

>>FINDINGS

The procedure is usually hit-and-miss, though: The most efficient methods reprogram only around 10% of the mature cells into iPSCs.

Now, Jacob Hanna and his colleagues at the Weizmann Institute of Science in Rehovot, Israel, have identified a protein that acts as a brake on the process. When the protein, called Mbd3, is removed by mutating its gene or interfering with its expression, the four reprogramming factors can turn nearly 100% of cells into iPSCs, Hanna and his colleagues report online in *Nature* this week. The reprogramming genes in fact recruit Mbd3 to the cell's chromosomes, where it inhibits their further expression. The find not only makes it easier to make iPSCs, it should also help researchers better understand how reprogramming works.
http://scim.ag/brakeprotein

Early Cichlids Traversed the World's Oceans

More than 1600 species of cichlids swim in fresh water around the world, spanning a rainbow of colors and shapes. New research casts doubt on an old hypothesis:

that cichlids reached multiple continents by swimming in place while the ancient supercontinent Gondwana broke up about 135 million years ago. The oldest known cichlid fossils are only about 45 million years old. To estimate just how likely it was that there are more ancient ones out there, paleobiologist Matt Friedman of the University of Oxford in the United Kingdom and colleagues compared a database of known cichlid fossils to a list of sedimentary rocks that might plausibly contain them and counted mutations in genes shared by cichlids and their relatives to estimate when they diverged. Their findings, published this week in the *Proceedings of the Royal Society B*, suggest a cichlid origin 65 million to 57 million years ago, long after Gondwana separated. The researchers say the little fish must have undertaken death-defying dispersals by paddling across the ocean.
http://scim.ag/cichlidorigins

BY THE NUMBERS

6.6 million Children worldwide who died in 2012 before reaching age 5—50% fewer than in 1990, according to a U.N. report.

9 Papers still not retracted by journals, 2 years after editors pledged to withdraw a record 88 papers associated with German anesthesiologist Joachim Boldt, who was found guilty of scientific misconduct. http://scim.ag/PapersTrail

Science LIVE

Join us on Thursday, 26 September, at 3 p.m. EDT for a live chat with experts on **the workings of the teen brain**.
http://scim.ag/science-live

Random Sample

Ig Nobels Honor Dung Rolling and Shrew Swallowing

"Some people say our science is crap," declared Marie Dacke, a biologist at Lund University in Sweden, while accepting the 2013 Ig Nobel joint prize in biology and astronomy for the discovery that African dung beetles use the Milky Way to navigate.

The annual ceremony honoring research that "first makes people laugh, and then makes them think" was hosted last week by Marc Abrahams, editor of the *Annals of Improbable Research*, in a packed theater at Harvard University in Cambridge, Massachusetts.

In their prizewinning work, Dacke and her colleagues observed that beetles rolling dung across the floor of a planetarium changed their direction in response to the Milky Way's orientation.

Brian Crandall, a science educator based in Hudson, New York, dedicated his archaeology prize to the people who ate whole parboiled shrews for his undergraduate study at the University of Victoria in Canada. He was studying the effect of human digestion on tiny mammal skeletons.

A team led by Masateru Uchiyama, a biologist at Teikyo University in Tokyo, won the medicine prize for its study of the effect of music on mice that had received heart transplants. Control mice died after a week; those exposed to opera recordings survived as much as three times as long. The researchers arrived on stage in head-to-toe mouse outfits.

The prize consisted of a hammer sealed within a glass case with instructions to "use hammer to break glass in case of emergency" and $10 trillion … in Zimbabwean dollars. **http://scim.ag/IgNobel2013**

CREDITS (TOP TO BOTTOM): ISTOCKPHOTO/THINKSTOCK; *ANNALS OF IMPROBABLE RESEARCH*

Published by AAAS

WATER RESOURCES

Kenyan Find Heralds New Era in Water Prospecting

Dozens of meters below the parched, treeless landscape of northwestern Kenya lies a hidden treasure: vast supplies of water. Last week, the leaders of a new hydrogeological survey, part of a U.N. program aimed at quenching the thirst of drought-stricken countries, announced that they have discovered five deep aquifer systems. They hold enough water to boost Kenya's known water reserves by 17%.

Properly managed, the find could be a game-changer for Kenyans, who have suffered through a series of severe droughts in recent decades. But it also marks a triumph for prospectors who are melding traditional geology and cutting-edge digital tools to reveal hidden water supplies in seemingly unpromising places. Such approaches represent "a revolution" in groundwater detection, says geologist Alain Gachet, head of Radar Technologies International (RTI), a French company that assisted with the work in Kenya. "We've just started to initiate the discovery of these deep aquifers."

The hunt for Kenya's water began last year, after seasonal rains failed in the Horn of Africa. Crops and livestock died, prompting a food crisis that affected millions in Kenya, Somalia, South Sudan, and Ethiopia. In response, the United Nations Educational, Scientific and Cultural Organization (UNESCO) launched the Groundwater Resources Investigation for Drought Mitigation in Africa Programme to find groundwater supplies that could offer solutions.

In the past, such searches have been somewhat haphazard affairs—a dash of savvy science mixed with educated guesses and brute force exploratory drilling. But RTI and other groups are now using powerful computer programs to merge refined geological knowledge with a flood of data from ground- and space-based sensors. In recent years, they've found signs of groundwater reserves in Sudan's Darfur region and elsewhere.

In Kenya, UNESCO hired RTI to apply the new tools to a survey of Turkana County, which covers 36,000 square kilometers in the country's arid northwestern corner. The county is bordered to the east by Lake Turkana, a water-filled depression that is part of the East African Rift, a region of stretched and fractured crust. Between the fractures, sunken blocks of land called grabens can form sediment-filled troughs as much as 4 kilometers deep.

The troughs were a prime target, Gachet says, because they are potential traps for ground water. To identify them, RTI collected traditional geologic maps, hydrological data, satellite images, and gravity and seismic survey data. Then they added commercial satellite radar images that can detect soil moisture. However, surface objects—such as rocks and villages—can obscure the images. So RTI developed its proprietary image-processing technology, WATEX, which "erases" the obstacles, revealing the hints of moisture that can betray a hidden aquifer. "Like a radio tuner, you can fine-tune the final result into a WATEX map," Gachet says.

The data suggested "that there was plenty of water under the desert," Gachet says. In the end, WATEX helped identify five likely aquifer systems, each more than 100 meters below the surface, containing water reserves totaling at least 250 billion cubic meters. So far, drilling has confirmed two of the aquifers, known as the Lotikipi and Lodwar basins. Lotikipi, the largest, is roughly the size of Rhode Island.

The discoveries are a "critical scientific breakthrough," Judi Wakhungu, Kenya's Cabinet secretary of the Ministry of Environment, Water and Natural Resources, said at a UNESCO meeting in Nairobi on 11 September. "This newly found wealth … opens a door to a more prosperous future for the people of Turkana and the nation as a whole."

The Kenyan find demonstrates the value of maintaining a diverse fleet of Earth-sensing satellites, which often face funding challenges, says hydroclimatologist Benjamin Zaitchik of Johns Hopkins University in Baltimore, Maryland. It is also "a powerful example of a private company making use of government-supported satellite capabilities to support U.N. humanitarian goals."

Tapping the water is the next hurdle. "Drilling equipment, to drill water below 80 meters, is a problem in Kenya," Gachet says. It will probably fall to foreign governments and aid organizations to fund the needed infrastructure.

Another looming challenge is managing the resource. Studies suggest the aquifers are replenished by rainfall in the highlands of Kenya and Uganda. But the recharge rates are slow, meaning the two nations may need to cooperate to avoid overuse.

Deep groundwater resources may exist in many other regions with similar geology, Gachet says. "I have great certainty we'll find a deep buried aquifer in South Sudan," he says, where surface waters are often contaminated with parasites. "We can create change all along the rift system, from Syria down to Mozambique. Our playground is very big."

–CAROLYN GRAMLING

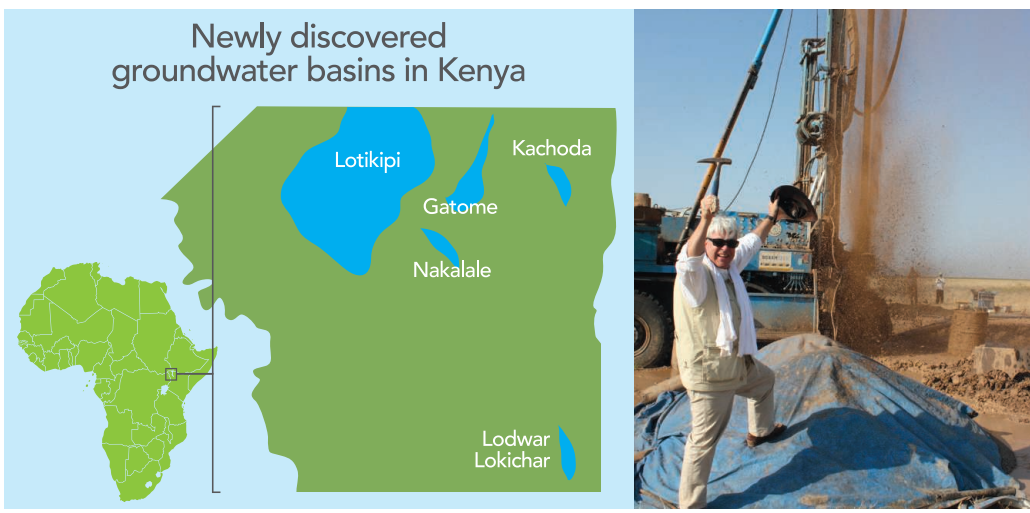

Bull's-eye! Geologist Alain Gachet (*right*) celebrates striking water in Kenya's Lotikipi Basin Aquifer, one of the five deep aquifers he helped discover.

CREDIT: RTI

Published by AAAS

ISRO's inner sanctum. Mangalyaan unveiled.

SPACE EXPLORATION

India Aims a Probe at Mars—And At Earthly Prestige

BANGALORE, INDIA—In August 2012, on India's Independence Day, Prime Minister Manmohan Singh made a Kennedy-esque announcement: India would send a probe to Mars, he vowed, calling it "a huge step for us" in science. Just over a year later, India is about to launch its first interplanetary mission. At its ultrahigh security satellite facility here last week, the Indian Space Research Organisation (ISRO) unveiled Mangalyaan, Hindi for "Mars craft," an unmanned orbiter slated to launch as early as 21 October.

Mangalyaan, covered in gold-colored reflective foil and about the size of a full-sized refrigerator, will carry four research instruments and a camera. Highest hopes for a scientific jackpot lie with a spectrometer designed to sniff out methane, a gas that would hint that Mars once hosted life, or may still. But science is not the $100 million mission's primary objective. ISRO calls it a "technology demonstrator" that aims to build on its Chandrayaan-1 lunar mission, which in 2009 found the first convincing evidence of water on the moon. "Looking for signatures of life on Mars is a natural progression," ISRO Chair K. Radhakrishnan tells *Science*.

Another agenda may be at work as well. ISRO built Mangalyaan in a mere 15 months. Some observers see the lightning-fast mission as the latest move in a game of one-upmanship as India, China, and Japan vie for preeminence in Asia in planetary exploration. "We are not racing with any country," insists S. K. Shivakumar, director of the ISRO Satellite Centre. Mangalyaan was "fast tracked," he says, to take advantage of a favorable launch window.

Successfully putting a spacecraft in orbit around Mars would be a triumph in its own right. Over the past 5 decades, about one-third of the 45 missions to the Red Planet have failed. The most recent debacle happened in 2011, when Russia's Phobos-Grunt mission and a tagalong Chinese probe failed after takeoff. NASA has had better luck of late: The Mars Reconnaissance Orbiter is taking data 3 years after its mission officially ended, and Curiosity rover has been perambulating Gale crater for more than a year, searching for favorable conditions for microbial life and evidence of past life. Next up for NASA, launching late this year, is the orbiting Mars Atmosphere and Volatile Evolution mission, or MAVEN, which will attempt to unravel the processes that stripped away much of Mars's early atmosphere.

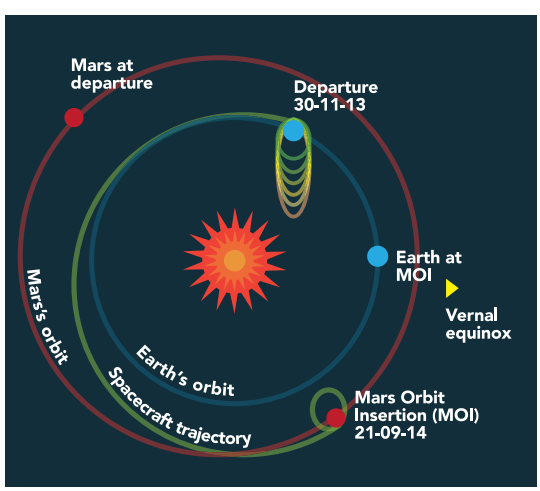

To Mars or bust. Assuming it leaves Earth's orbit on 30 November and sails smoothly, Mangalyaan will reach Mars 295 days later.

India's maiden Mars mission will get an unconventional start. ISRO's Polar Satellite Launch Vehicle can't generate enough thrust to set Mangalyaan on a straight shot to Mars. So after launch from Sriharikota spaceport, the spacecraft will swing around Earth on ever-widening orbits until it gains enough velocity to slingshot onto a trajectory that will reach Mars in late September 2014.

The white-knuckle moment for ISRO's 500-strong Mangalyaan team will be slowing the probe for insertion into Mars orbit, a maneuver that requires a precisely timed rocket firing. "We are jittery," says Mangalyaan's project director, Subbiah Arunan. The mechanical engineer says that he has slept at the satellite center almost every day since the project began 15 months ago, returning home briefly to perform religious duties.

If Mangalyaan arrives safely in Mars orbit, it will turn to science, notably whether the atmosphere has methane. This week, Curiosity's scientists reported that the rover's spectrometer has failed to detect traces of the gas, a signature byproduct of carbon-based life. But the finding, from Gale crater, can't rule out pockets of methane elsewhere on Mars—leaving an opening for Mangalyaan. "I will be excited to see the first credible measurements of methane made from Mars orbit," says MAVEN principal investigator Bruce Jakosky, a geophysicist at University of Colorado, Boulder, who hopes to discuss with Indian counterparts "the potential synergies" of combining data from both missions. Mangalyaan's photometer will measure the atmosphere's deuterium-hydrogen ratio, complementing MAVEN's efforts. And a mass spectrometer will confirm atmospheric constituents, while an infrared spectrometer will map hot spots and icy areas on the surface.

Mangalyaan could also witness a rare celestial event: the collision of a comet with a planet. In late 2014, comet 2013 A1 is expected to barrel into Mars, the kind of spectacle last witnessed when comet Shoemaker-Levy 9 bombarded Jupiter in 1994. That comet was lost in Jupiter's roiling atmosphere, but comet 2013 A1 should kick up a massive dust cloud for Mangalyaan and MAVEN to feast their sensors on. The impact may churn up something surprising—and one spacecraft, or both, could be in the right place at the right time for a revelation. **–PALLAVA BAGLA**

CREDITS: (TOP TO BOTTOM) PALLAVA BAGLA; ADAPTED FROM ISRO/(ILLUSTRATION) G. GRULLÓN/*SCIENCE*

Published by AAAS

AGRICULTURE

What Happens When Weed Killers Stop Killing?

INDIANAPOLIS—"U.S. farmers are heading for a crisis," says Stephen Powles of the University of Western Australia, Crawley. Powles is an expert on herbicide resistance, a worsening problem in U.S. fields. Weeds resistant to glyphosate—the world's most popular herbicide—are now present in the vast majority of soybean, cotton, and corn farms in some U.S. states. Perhaps even worse, weeds that can shrug off multiple other herbicides are on the rise. Although the problem was highlighted here last week at an American Chemical Society (ACS) meeting symposium, chemists have little to offer: Few new weed killers are near commercialization, and none with a novel molecular mode of action for which there is no resistance.

Herbicide resistance has ebbed and flowed for decades. But because most herbicides could not kill all weeds, farmers had to continually rotate their crops and rotate herbicides to prevent resistant weeds from taking over their fields. That picture changed in the 1990s with the commercialization of transgenic crops resistant to glyphosate, marketed as Roundup by Monsanto. Glyphosate disrupts the ability of growing plants to construct new proteins. Because the transgenic crops didn't suffer this fate, their use—and glyphosate's—soared.

"Glyphosate used to control everything easily," says Bryan Young, a plant biologist at Southern Illinois University, Carbondale. Some experts referred to it as agricultural heroin because it was so effective and easy to use that farmers quickly became hooked. "We trained a generation of farmers that weed control was very easy," says Thomas Mueller, a weed management scientist at the University of Tennessee, Knoxville. But the overuse had a cost, selecting for resistant weeds.

Among the biggest concerns is a family of weeds that includes waterhemp (*Amaranthus rudis*). At the ACS meeting, Kevin Bradley, a weed management scientist with the University of Missouri, Columbia, reported that a 2008 to 2009 survey of 144 populations of waterhemp in 41 Missouri counties revealed glyphosate resistance in 69%. "It's way higher than that now," Bradley says. "It just blew up dramatically." The problem extends far beyond Missouri. Micheal Owen of Iowa State University in Ames reported that surveys of weeds from some 500 sites throughout Iowa in 2011 and 2012 revealed glyphosate resistance in approximately 64% of waterhemp samples.

In response to the rise in glyphosate resistance, farmers have turned to other herbicides—often applying several in a single growing season—to protect their crops. In the United States, most midwestern and southern farmers continue to use glyphosate because it still kills most weed species. But they've had to add additional herbicides, known as residuals, to deal with resistant weeds. "We've seen the use of more residuals in the last couple of years than the previous 10 years combined," says Bob Scott, an agricultural extension scientist with the University of Arkansas in Lonoke.

The need to apply more herbicides, more often, is affecting farmers' bottom line. For cotton grown in the South, the cost of using herbicides has climbed from between $50 and $75 per hectare a few years ago to about $370 per hectare today, Scott says. For soybeans in Illinois, Young says the jump has been from about $25 to $160 per hectare. "It changes how profitable it is to grow the crops," Scott says. And in the South it is contributing to a massive shift away from growing cotton; over the past few years, the area planted with cotton has declined by 70% in Arkansas and by 60% in Tennessee, says Larry Steckel, a weed management scientist at the University of Tennessee's West Tennessee Research and Education Center in Jackson.

Survivors. Glyphosate-resistant horseweed plants stand bright green amid dead stalks of their vulnerable kin in a soybean field in Illinois.

CREDIT: BRYAN YOUNG

Perhaps because of the use of multiple herbicides, the spread of glyphosate resistance appears to have slowed. According to data at WeedScience.org, an international database of herbicide resistance in weeds, from 2005 through 2010 researchers discovered 13 different weed species that had developed resistance to glyphosate. But since then only two more have been discovered.

The alternatives could meet the same fate as glyphosate, however. A survey that Bradley and colleagues conducted last year in Missouri shows that weeds resistant to multiple herbicides with completely different biological modes of action are also on the rise. Of weed populations they sampled in Missouri, 43% are now resistant to two different herbicides; 6% are resistant to three herbicides; and 0.5% are resistant to four separate herbicides. In Iowa, Owen also found a rise in multiherbicide resistance, with 89% of waterhemp populations he sampled now resistant to two or more herbicides, 25% resistant to three, and 10% resistant to five separate herbicide classes. "We are looking at control that is not working," Owen says.

Dow, Bayer CropScience, Syngenta, and Monsanto are all developing new seed varieties resistant to herbicides other than glyphosate, which will make it easier for farmers to use alternative weed killers. Even though weeds have already evolved some resistance to those herbicides, Powles says the new seed-and-herbicide combos should work well if used with proper crop and herbicide rotation. However, he adds, "if there is an over-reliance on them, they will fail and fail rapidly."

If that happens, farmers may have little to fall back on. Although herbicide companies say research is going full tilt, no new herbicide with a novel mode of action has hit the market in 20 years. And researchers at the meeting say they know of no new herbicides on the way that have proven to be effective, short-lived, and nontoxic to other life forms. "Growers think there will be something over the horizon that will bail them out," Steckel says. "But there isn't."

–ROBERT F. SERVICE

Published by AAAS

BIOMEDICAL PUBLISHING

Secretive and Subjective, Peer Review Proves Resistant to Study

CHICAGO, ILLINOIS—Drummond Rennie was a youngish editor at *The New England Journal of Medicine* in 1978 when his boss instructed him to take his place on the Australian lecture circuit, discussing issues in scientific publishing. A few days before departure, Rennie sent his administrative assistant to the library, asking her to pick 30 medical journals at random and photocopy one research article from each. He hoped to critique them during the long flight from New York to Sydney.

On the plane, he came to the conclusion that "we as a community had a colossal problem," as he recalled to an audience of several hundred assembled here last week for the International Congress on Peer Review and Biomedical Publication. The papers were "perfect" for the planned lectures because they were "perfectly awful," he recalls—filled with biased reporting and basic errors. Peer review was not working as promised, it seemed.

That flight set Rennie, now a nearly retired editor at the *Journal of the American Medical Association* with a deep voice and a shock of white hair, on an uphill climb to improve the state of the medical literature. He and a small group of journal editors and academic researchers began analyzing publication bias, data sharing, citation patterns, authorship, and other issues. Each in its own way has proven difficult to tackle.

But while many pieces of the publications puzzle are yielding to scrutiny, the peer-review process itself is not. "Nothing much has changed in 25 years," says Ana Marušić of the University of Split in Croatia, who studies research methodologies. "It's always the same story." Interventions to improve peer review fail again and again. Mentorship to train reviewers doesn't make a difference in their ability to spot problems in papers. And there is still scant evidence that peer review makes published papers any stronger.

One challenge in studying peer review is simply getting the data: closely guarded peer-review reports submitted to biomedical journals, and the conversations that take place inside a journal's offices. "Often what happens is the peer-review process is hidden within the journal," says Sally Hopewell, who studies clinical trial reporting at the University of Oxford in the United Kingdom.

Hopewell and her colleagues did catch a glimpse of how peer review works thanks to an unusual set of journals. They sifted through reports from reviewers on 93 clinical trials submitted to BioMed Central medical series journals, an umbrella group of several dozen open-access journals that publish all versions of a manuscript submitted along with peer-review comments and responses from authors. They wanted to learn exactly what peer review was contributing. What sorts of changes did reviewers suggest? Did authors comply?

Hopewell's team was pleasantly surprised to see that reviewers frequently picked up overinflated conclusions ("authors often got overexcited," she says) and got them toned down. But they missed cases where authors left out a treatment's side effects, the goals of the study, or how volunteers were randomized to one therapy or another. The reviewers also sometimes requested additional analyses that the study wasn't designed to tackle. Hopewell would love to know whether her findings apply to higher impact journals, but she concedes that because reviews are normally confidential, she's unlikely to find out.

The study conducted by Hopewell and her colleagues is a rarity. Like most in the peer-review world, it had no dedicated funding, but her group had sufficient resources to pursue it. "To actually get any funding for this sort of research is very difficult because it encompasses all diseases," she says. Most funding agencies divvy up their money one ailment at a time. Marušić says the research is unlikely to move forward "unless you open the field to everybody" with competitive funding.

Beyond the practical hurdles to studying peer review is its deeply subjective nature, which hampers rigorous study. "There is a whole area of cognitive psychology [of] how people read scientific papers," Marušić says. "It's not where you make an equation and calculate an outcome," she adds, although some organizations have tried to develop checklists for peer reviewers in areas such as clinical trials. "It should be looked at as more of a process, a social activity."

Journals are in many ways best placed to study what peer review contributes, because they have access to their own internal workings. Catharine Stack, statistical deputy editor of the *Annals of Internal Medicine*, sought authors' reactions to the *Annals*' extensive statistical review of manuscripts, which occurs late in the vetting process. Most authors appreciated it, she reported at last week's meeting—but then, Stack admits, the journal surveyed only those whose papers had been accepted and whose authors were already happy.

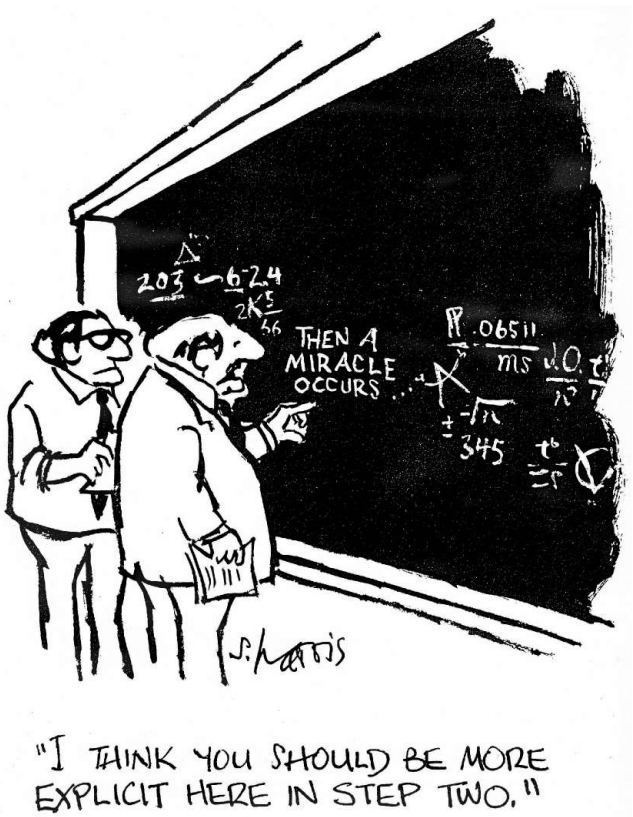

CREDIT: SCIENCECARTOONSPLUS.COM

At the first Peer Review Congress, in 1989, half the talks were on peer review, Rennie says; this time there were a relative handful, suggesting the field itself has been supplanted by more systematic studies of bias and errors in published work—an acknowledgment that the love-hate relationship with peer review will likely endure.

–JENNIFER COUZIN-FRANKEL

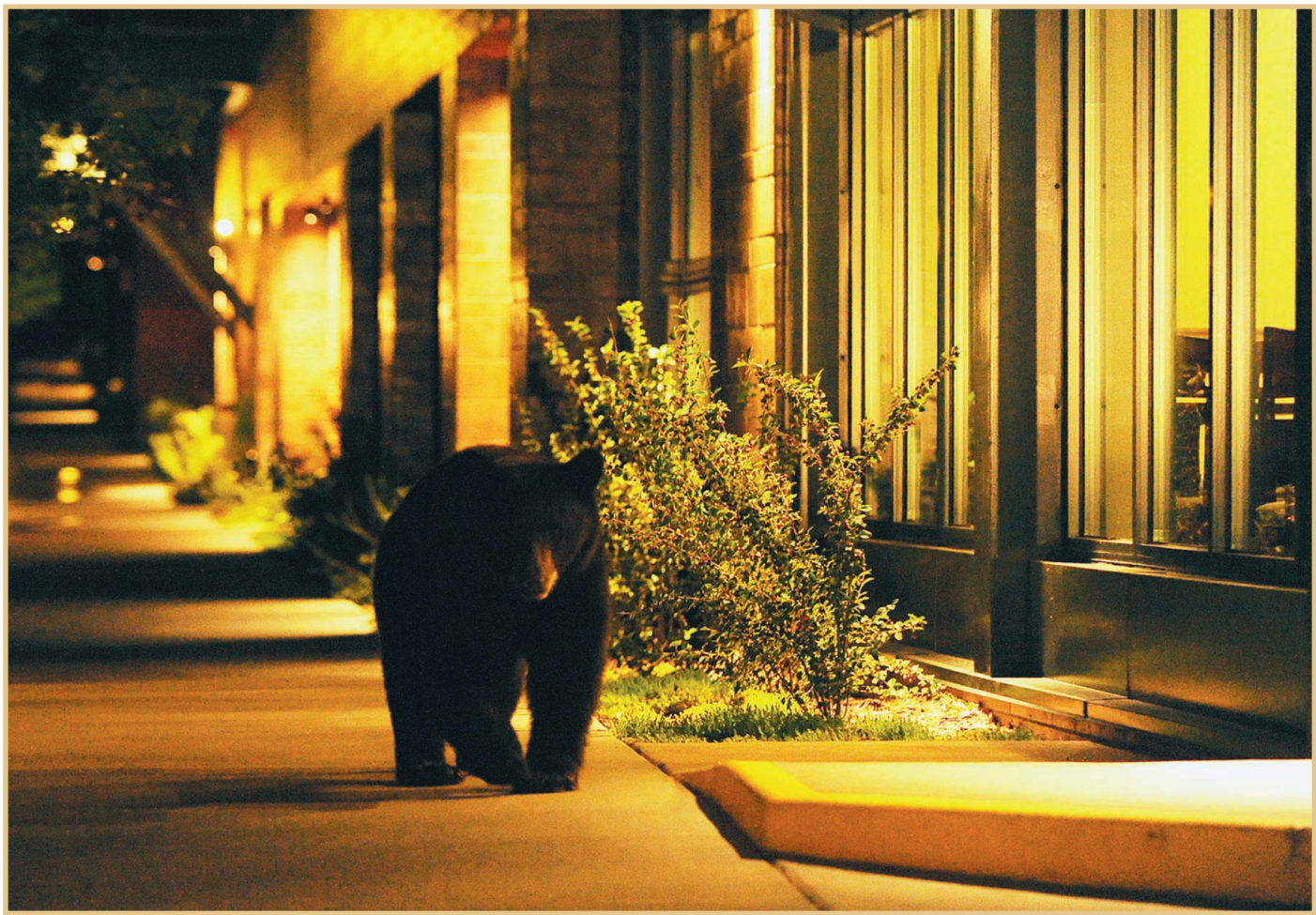

At home. An American black bear roamed downtown Aspen, Colorado, on a summer night.

CREDIT: RJ SANGOSTI/THE DENVER POST/GETTY IMAGES

Predators in the 'Hood

As cougars, coyotes, and bears spread into backyards and downtowns, science is helping to show how people and predators can coexist

TWO YEARS AGO, IN JUNE 2011, A COUGAR wandered through backyards and peered into homes in Milford, Connecticut, the first mountain lion in that state in more than 100 years. Later that same year, a gray wolf crossed the Oregon border into California, the first wolf in that state in more than 80 years. Black bears now lumber through subdivisions in Ohio and Missouri, states that were bearless until recently. And coyotes, once restricted to the prairie states, now live from Panama to Alaska, including a booming population in downtown Chicago. The only chunk of North America that coyotes have not colonized is Long Island. "But it's only a matter of time before they do," says Mark Weckel, a conservation biologist at the American Museum of Natural History in New York City who is happily following coyotes' spread into his city.

Once hunted nearly to extinction in the lower 48, America's biggest predators are making a remarkable comeback. Their return has sparked a range of emotions, from surprise and joy to demands that the animals be harshly controlled, if not shot outright. Europe is experiencing a similar resurgence, and similar reactions (*Science*, 3 November 2006, p. 746). Recently, the Dutch were astonished to learn that a wolf had made its way to the Netherlands from Eastern Europe—the first since 1897—while French shepherds complain that wolves slaughter sheep and endanger their way of life.

Yet ecologists agree that the animals benefit ecosystems, and many citizens, especially in cities of the western United States, seem willing to have them back, says Stanley Gehrt, a wildlife biologist at Ohio State University, Columbus, who tracks Chicago's coyotes. That leaves scientists, conservationists, and wildlife managers all scrambling to figure out how to best manage animals that literally live next door and are capable of killing humans. "If you're interested in large carnivores, it's a very exciting time," Gehrt says. "There are more people than ever and yet we're seeing a resurgence and acceptance of these predators. Thirty years ago, no one would have predicted this would happen."

Online
sciencemag.org
Podcast interview with author Virginia Morell (http://scim.ag/pod_6152).

On the move

Several factors are spurring the predators' expansion. First, the landscape is getting greener: Forest land has expanded by 28% across 20 of the northern states, even as the human population has jumped by 130%, according to a 2012 U.S. Forest Ser-

American Black Bear

Ursus americanus, 57–250 kg

Omnivore: Eats nuts, berries, insects, salmon, fawns

Populations growing; 15,000 live in Pennsylvania alone

vice report. Cities contain more tree cover, plus bountiful white-tailed deer and cottontails. "Maybe having coyotes living next to us isn't what we were going for when we talked about 'greening' our cities," Weckel says. "But this is the result—and it's a positive thing. If they're successful here, it means we've succeeded."

Predators bring ecological benefits: Coyotes help control Canada geese; black bears spread seeds; mountain lions and wolves eat deer. Wolves have helped restore Yellowstone National Park, for example, although managers face criticism from all sides (see sidebar, p. 1334).

In addition, most of North America's surviving predators have traits that make coexistence at least possible, says David Mattson, a wildlife biologist with the U.S. Geological Survey in Flagstaff, Arizona. "They're the last of the large Pleistocene carnivores and they've survived because they're the shyest and least aggressive," he says. "Most of them try to avoid [confronting] us."

Take the black bears of Durango, Colorado, a community of 20,000 people that abuts the 1.8 million–acre San Juan National Forest. At a recent meeting,* Heather Johnson, a wildlife researcher with Colorado Parks and Wildlife in Durango, told of her informal survey of the city's school kids. "If you ask them if they've seen a bear in the wild, one or two will raise their hands. But if you ask, 'Have you seen a bear in your backyard?' every hand goes up."

During the dry summer of 2012, a black bear broke into someone's home or car in Durango most every night. Johnson and her team trap and count bears within 10 kilometers of the city to try to understand why. One reason is obvious: Bears need 20,000 calories per day in the late summer and can eat the same kinds of foods we do. Plus their huge home ranges, up to 260 square kilometers or more, inevitably overlap with some neighborhoods, where they find bounty in fruit trees and dumpsters. "It's a perfect storm for bear-human conflicts," Johnson says, adding that the same pattern afflicts many cities in the mountain west.

Although bears increasingly encounter humans, the interactions are rarely violent. Since 1900, black bears have killed only 14 people in the lower 48 states. As a result, we've reduced "the mindset that we should get rid of every bear we run into," says Brian Scheick of the Florida Fish and Wildlife Conservation Commission in Gainesville.

In Durango, for example, despite 431 complaints in the summer of 2012—about bears interrupting barbecues, ripping off siding, and eating trash—residents are surprisingly tolerant. In a formal survey, Johnson's agency found an almost 100% approval rating for bears. "People love the bears," Johnson says.

Occasionally bears may scratch someone, if a person acts foolishly by feeding it. Or they may break into someone's home, as a few have done in Durango. "People don't see their behavior as endangering themselves and the bear," Johnson says. But after such incidents, the animal may be identified as a "problem bear," requiring managers to try to capture or kill it.

Lethal force?

When a bear—or a cougar or coyote—becomes a nuisance, officers typically reach for a gun. It "is the easiest thing to do," Johnson says. "But there's no evidence that this is effective on a large scale." A growing number of wildlife researchers say that shooting a predator often doesn't solve the problem, because it merely opens territory to another animal. "It isn't a simple numbers game," says Robert Wielgus, a wildlife ecologist at Washington State University in Pullman.

For the last 30 years, Wielgus and his colleagues have studied what happens when cougars and grizzly bears are heavily hunted. In 1996, Washington state passed a law banning hunting cougars with dogs—the best method for finding the elusive animals. Some livestock owners feared that the population of mountain lions, as cougars are also called, would soar, leading to more stock losses. In response, state agencies extended the hunting season, increased the number of lions a hunter could take, and dropped the cost of a hunting tag. More than 66,000 tags were sold in 2007 (up from 1000 in 1996), although the cougar population was then estimated at fewer than 4000 animals. Cougar deaths skyrocketed—but so did complaints about problem animals.

State wildlife officials had made the common mistake of modeling the lions' response to hunting as if the carnivores were white-tailed deer, Wielgus says. Managers hadn't considered what happens to cougar society with such a high mortality rate. "A stable cougar society has senior, adult males," who patrol large territories and father and protect the kittens of several females, Wielgus explains. When a male dies, incoming younger males will fight over his territory, and kill kittens in order to bring the females into estrus again, as his team will report in *Biological Conservation* in November.

When the researchers looked at the cougar population of the Selkirk Mountains in eastern Washington, where lion complaints had increased, they discovered that most of the older male cats had been replaced by adolescent males. Because of the threat from these

CREDIT: NATIONAL PARK SERVICE

Cougar

Puma concolor, 42–62 kg

Prey: Deer, elk, bighorn sheep

Seldom seen, but found across the West, including in Los Angeles

*Conservation Behavior Workshop, Merging Science and Application, sponsored by the Animal Behavior Society in Boulder, Colorado, 28 July 2013.

Man in the Middle

MAMMOTH HOT SPRINGS, YELLOWSTONE NATIONAL PARK—In February 2012, wildlife biologist Douglas Smith fired a tranquilizing dart at a Rocky Mountain gray wolf, a member of a pack living here in Yellowstone, as part of his ongoing project to tag wolves and study their movements. As he knelt next to the drugged wolf, Smith realized he'd mistakenly darted the pack's alpha or breeding female, named '06 for the year of her birth by the park's wolf-watchers. Darting the wolf wouldn't hurt her, Smith knew, as he took her measurements, checked her teeth, and fastened a GPS collar around her neck. But this wolf was hugely popular with park visitors, and the collar would trigger complaints that she no longer looked wild. The GPS unit, shaped like a tin can, jutted out slightly beneath the wolf's neck. Henceforth, she'd be known as 832F for the number on her collar.

Less than a year later, 832F was dead—felled by a hunter's bullet 15 miles outside of Yellowstone's border in Wyoming (http://scim.ag/832Fdeath). Smith's phone began to ring, and angry messages poured into his e-mail inbox. "People from the wolf-watching community blame me," Smith said. "They think that if 832 hadn't been wearing a collar, the

Gray Wolf

Canis lupus, 36–45 kg

Prey: Elk, bison, moose, deer, rodents

Found in eight states; dispersal slowed by hunters

CREDIT: NPS PHOTO

infanticidal young males, many of the female lions there had also moved to higher elevations with their cubs, Wielgus's team discovered. "The females moved to areas they would normally never use, where they eat prey they normally wouldn't eat, including the highly endangered mountain caribou," Wielgus says. The younger males also attacked livestock. "They're the ones that haven't learned to avoid people and so get into trouble."

Wielgus and his colleagues have worked with Washington's Department of Fish and Wildlife to overhaul cougar hunting rules to help restore the cat's society. Cougars in the state are no longer regarded as a single population. Instead, the state recommends that no more than 14% of the lions in any of 49 management units be killed annually. "It should lessen this massive social disruption they've experienced in the past," Wielgus says. He points out that California, which bans sport hunting of cougars, has one of the largest mountain lion populations (about 4000) and the lowest rate of livestock depredations. In contrast, other western states with lion hunts also have high depredation rates.

California's citizens seem as willing to accommodate cougars as Durango's inhabitants do bears—even though the big cats occasionally kill people. Since 1986 in California, cougars have attacked a dozen people and killed three, probably because of the growing human population. Yet Governor Jerry Brown signed a bill earlier this month that prevents managers from killing lions unless they pose an urgent threat to public safety. Wildlife wardens are to help capture and relocate the animals instead. "I'm amazed that Californians still want to protect them," says Gehrt, the coyote watcher.

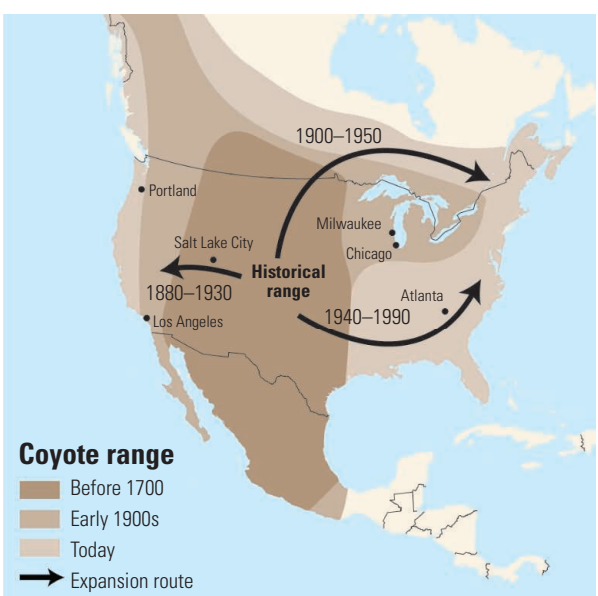

The coyotes are coming

No predator has faced more lethal force than the coyote, which has never been protected. Several states still pay bounties for killing coyotes, and the U.S. Department of Agriculture (USDA) killed nearly 80,000 in 2012. Yet they have thrived anyway, Gehrt says.

In part, that's thanks to humans: We removed coyotes' top competitor and killer, the gray wolf, in the early 20th century. With wolves out of the way, coyotes began spreading across the country, and they're still on the move (see map). They arrived on the outskirts of Chicago in the 1990s, most likely by following railroad tracks, where fences and walls offer cover and make hunting easy. By 2000, they were in the city proper, and over the next decade their numbers rocketed by 3000%, to about 2000, for reasons that Gehrt is still trying to understand. "They've flexed their adaptive muscle and crept into openings in the urban landscape," he says. "Any small natural area in the city now has coyotes."

Over the past 13 years, he has published a string of studies analyzing coyote numbers, prey, and social structure using radio collars and camera traps. He's found that Chicago's coyotes eat the same prey that rural ones do: voles, shrews, rabbits, and fawns. To avoid people, city coyotes have switched to a nocturnal lifestyle, hunting at dawn and dusk. But they are clearly at home in the city. They cross lanes of traffic with aplomb, trot down the center of roads, duck into subways, and seek shelter in culverts and underpasses. And it's not just Chicago. Coyotes are moving east into every major U.S. city, including Milwaukee, Atlanta, and Dallas. They'll eventually meet up with those already in New York City, which migrated in via Canada.

Coyotes have some ecological benefits: They devour the eggs of Canada geese, and in Chicago have pushed the geese's

Published by AAAS

Diplomat. Wolf expert Douglas Smith faces scrutiny from all sides in Yellowstone.

hunter wouldn't have targeted her."

Smith is in the crossfire of the wolf wars. On one side are the wolf-watchers who thrill at the sight of the animals; on the other are the ranchers and hunters who blame wolves for a plunge in Yellowstone's elk population and for livestock losses, and who eagerly shoot as many wolves as legally allowed once the animals stray outside the park. It is an occupational hazard, says Smith, who recalls another researcher saying that "the landscape is littered with the carcasses of wolf biologists," who couldn't handle the constant attacks and quit or were fired. "Every year my main goal has been to survive to the next [year] and keep the study going," Smith says. "You always hear from people when you're working with wolves."

Tall and fit, with a ranch hand's lanky build and straightforward manner, Smith, 53, has been working with wolves—and hearing from people—since he was 18. He decided to become a wolf biologist after reading a cover story about the animals in *National Geographic* in 1977. Fresh out of high school, he landed a plum job as a field assistant with the wolf-moose project at Isle Royale National Park in Lake Superior (*Science*, 24 May, p. 919). Project leader Rolf Peterson of Michigan Technological University in Houghton recalls how the then–assistant secretary of the interior, no fan of wolves, cut off the team's permits and funding that winter. "But we were already on the island, so we just persevered. It was good training for Doug—he saw at a very early age how wolf research gets co-opted by various agendas."

Since arriving in Yellowstone in 1994 to help reintroduce gray wolves to the park, Smith has had many occasions to put that training to use. Scientifically, the project has been a huge success (*Science*, 23 October 2009, p. 506), as the newly arrived wolves reduced an out-of-control elk population and allowed the park's ecosystem to recover. "For a long time, Yellowstone wasn't natural," Smith says. "Now it's as pristine as it's ever been.

But politically the project is a hot potato. "I'm criticized for not being more outraged about the hunting of the park's wolves; I'm criticized for calling them 'the park's wolves,' and for asking the states to put a protective buffer-zone outside the park," Smith says. He's been called a liar and some ranchers and state officials have lobbied for his removal.

With nine of the park's collared wolves lost to hunters since 2009, Smith is steeling himself for the coming months. Wolf hunting season just opened. **–V. M.**

annual population growth down from 10% or 20% per year around 1990 to 1% to 2% now. They may also be welcomed by suburban gardeners, because they eat fawns. The coyotes found in the Northeast, which have some wolf ancestry, can even take down adult deer.

People will need to adjust to their new neighbors, Gehrt says. Coyotes may bite—especially if they are accustomed to people feeding them—and they hunt pet cats and dogs. At first, many Chicagoans demanded the animals' removal, Gehrt says, in "a typical response to a new carnivore." However, as 2 centuries of hunting shows, a coyote killed will simply be replaced by another—so it's important that people know how to deal with them, says Valerie Matheson, the urban wildlife conservation coordinator for Boulder, Colorado. "People need to know that coyotes do pose a threat and they need to learn what to do when they see one," she says. Or what not to do: Coyotes chased and bit five people over 2 years on Boulder's bike path, probably because someone had first fed them.

Once coyotes are accepted, they may boost tolerance to other predators. "They crack open the door for other large carnivores to live next door to us," Gehrt says.

However, one large carnivore is not likely to set up shop near U.S. cities anytime soon: the wolf. Once found across most of the country, wolves became the most hated of predators once European settlers arrived. When sentiment changed in the 1970s, gray wolves were one of the first species to be protected by the federal Endangered Species Act, and the federal government actively helped restore them to the wilds of Montana, Wyoming, and Idaho. Other wolves independently loped in from Canada. Now, the federal government is seeking to remove their protected status, and they are hunted fiercely in several states.

Although many welcome the return of the wolf, others, particularly livestock owners, think that wolves and ranches cannot coexist—and that the only good wolf is a dead wolf. Wolves rarely kill people, but they do at times attack unprotected livestock. In 2010, USDA fingered them for the deaths of about 8100 cattle. But conservationists like to put that number in context: The same figures show that domestic dogs killed 21,800 cattle, and coyotes 116,700. "About 80% of wolf packs don't do this," says Wielgus, who's just launched a new study in conjunction with federal and Washington state agencies and livestock operators to find ways to alter the behavior of the other 20%.

CREDIT: © RYAN STAVELY

Coyote

Canis latrans (the barking dog), 6.8–21 kg

Prey: Voles, shrews, cottontails, invertebrates, fawns, and more

Urban Chicago population: 2000

Even so, wolves aren't expected near a city anytime soon, says Douglas Smith, the head of the National Park Service's wolf project in Yellowstone National Park. Given the space they need and the feelings against them, "they'll always be restricted to places with a few people and no agriculture," he predicts. But if the wolf remains a creature of wilderness, North America's other predators have, like so many of its human inhabitants, opted for the suburbs.

–VIRGINIA MORELL

Published by AAAS

NEUROSCIENCE

Concentrating on Kindness

Tania Singer helped found the field of social neuroscience. Now she wants to apply what has been learned—by training the world to be more compassionate through meditation

Empathy made Antoinette Tuff a minor celebrity. On 20 August, a young man armed with an AK-47 and 500 rounds of ammunition burst into the school in Decatur, Georgia, where Tuff works as a bookkeeper. It might have ended in yet another senseless mass killing if it hadn't been for Tuff's compassionate response to the gunman, recorded in its entirety because she had dialed 911.

As the man loads his weapon, Tuff seeks a human connection with him. She talks of her own struggles, her disabled son, her divorce, her thoughts of committing suicide. Finally, she persuades him to lay down his weapon, lie down on the ground, and surrender to the police. "I love you," she says near the end of the call. "You're gonna be OK, sweetheart." (Only after the man is arrested does she break down, crying "Woo, Jesus!")

Tuff's heroic conversation, posted on the Internet, was hailed by many commentators as evidence of the power of empathy and the value of compassion. If more people were like Tuff, there would be less violence and suffering, they say.

For neuroscientist Tania Singer, that sentiment has become an ambitious research program. Singer, a director at the Max Planck Institute for Human Cognitive and Brain Sciences in Leipzig, wants to find out if people can be trained to be more compassionate. Her program combines rigorous neuroscience with a practice some scientists dismiss as subjective and spiritual: meditation. The effort, called the ReSource Project, involves dozens of scientists and heavy use of magnetic resonance imaging (MRI). It also includes 17 meditation teachers and 160 participants in Leipzig and Berlin who meditate at least 6 days a week for 9 months. Singer hopes to find a "signature of compassion" emerging in her subjects' brains: evidence that the instinct to be kind to others can be nurtured through meditation. Singer is candid about her ultimate goal: She wants to make the world a better place.

For Singer, two interests converge in the study, which she spent 5 years developing. She has been a pioneer in brain studies of empathy, making her "one of the most influential social neuroscientists in the world today," says Richard Davidson, a psychologist who studies emotions at the Univer-

CREDIT: SVEN DÖRING FOR MAX PLANCK SOCIETY

Empress of empathy. Tania Singer has long practiced meditation herself. Now she is leading a large study to find out how meditation can mold the mind.

sity of Wisconsin, Madison. She also has a long-running interest in meditation. She tries to meditate every day, has met the Dalai Lama several times, and has been to spiritual retreats lasting months. Although compassion is the study's main focus, she also aims to discover if meditation can make people better at regulating their emotions, help them concentrate, or reduce stress.

Singer knows all of this makes some people cringe. During most of her career, she kept her interest in meditation to herself. "When I was younger, it was unthinkable for meditation research to be taken seriously," she says. "I had my life as a researcher and then I had my private life, where I could follow these interests." Even her father, Wolf Singer—a neuroscientist who until 2011 headed the Department of Neurophysiology at the Max Planck Institute for Brain Research in Frankfurt—was skeptical. "We certainly didn't practice meditation at home," Tania Singer says.

Ouch, that hurt

Empathy is the bridge that allows us to cross into the territory of someone else's feelings. It establishes a connection between two people, and it's the reason we enjoy reading novels and watching movies. But empathy has long been outside the scope of neuroscience. Scientists studied what happens in the brain when someone thinks or feels, but not how we can know and feel what someone else experiences.

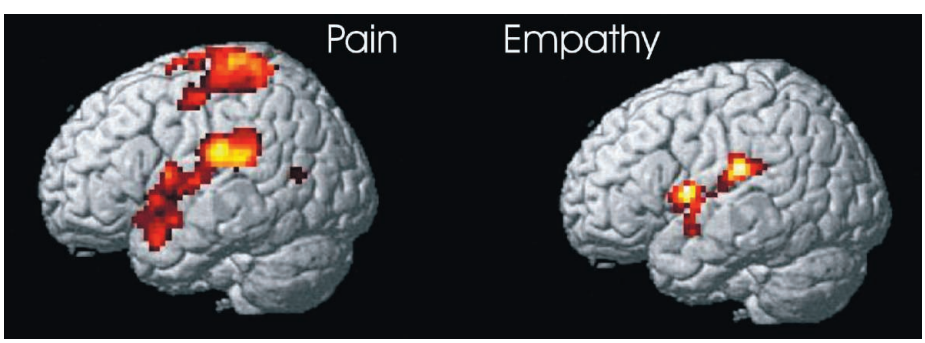

I feel your pain. In a 2004 paper, Singer showed that watching someone suffer activates some of the same brain areas as experiencing pain. The overlap is the root of empathy, she says.

But in 2004, while at University College London (UCL), Singer published a landmark paper in *Science* exploring what happens in our heads when we see a loved one suffer (20 February, p. 1157). For the study, she brought couples into her lab; the woman was lying in an MRI machine, and either she or her partner, who was sitting next to the scanner, received an electric shock to the hand.

The jolts themselves activated multiple areas involved in sensing and experiencing pain, such as the sensorimotor cortex and the insula; surprisingly, observing the partner in pain engaged some of the same brain areas. Not the ones that tell you you're feeling a searing pain in your left hand, Singer says, but the "end note" of pain, that feeling of "ouch, that hurt." This overlap is the root of empathy, she argues.

The experiment changed how people did neuroscience, says Chris Frith, then Singer's group leader. "People hadn't thought before that you could study empathy in this very reductionist way," he says. Involving more than one person at a time in an MRI study was a daring move, Frith adds. "Tania is incredibly enthusiastic and she is prepared to deal with problems and design experiments which other people would feel are too difficult."

Other scientists are studying the importance of empathy as well. Christian Keysers, a brain researcher at the University of Groningen in the Netherlands, is approaching the topic from a different, darker angle: He is studying imprisoned psychopaths to find out what happens when the connection between people breaks down.

In a recent paper in *Brain*, Keysers reported that there was little overlap between the brain regions active when psychopaths felt pain themselves and those lighting up when they watched videos of someone else experiencing pain. But when Keysers asked them specifically to try to empathize with the actors in the videos, the psychopaths showed the same pattern that Singer saw in her romantic couples. "The capacity to empathize seems to be preserved in psychopaths," Keysers says. "They just don't use it automatically."

Embracing empathy

Such studies have helped to bring new attention to an age-old idea: that the world needs more love, or at least empathy. In his recent book *The Empathic Civilization*, author Jeremy Rifkin argues that humanity needs to develop a "global empathic consciousness" to avoid disaster. U.S. President Barack Obama has called for a more empathic society as well; as he put it in a 2011 commencement address at Xavier University, "When you choose to broaden your ambit of concern and empathize with the plight of others, whether they are close friends or distant strangers—it becomes harder not to act; harder not to help." There's a more cynical way to make that case: You help someone not because you want to reduce their pain, but your own. Feel their suffering more strongly, and you are more likely to act.

For Singer, who moved from UCL to the University of Zurich in 2006 and took her current job in 2010, the interest in empathy came naturally. She has an identical twin sister, and likes to say that she was "born as a we" and that people "constantly resonate with each other." What she is trying to train in the ReSource Project, however, is a slightly different capacity that she calls compassion. In daily life, the two words have overlapping meanings and they're often used interchangeably, but Singer suspects that they are two different phenomena associated with different brain activity patterns.

That insight came from her work with Matthieu Ricard, a French Buddhist monk with a background in molecular biology who lives in Nepal and practices meditation. When Singer asked Ricard to "do his thing," focusing on compassion, in the MRI scanner, she got a surprise. The brain regions she saw light up were not the ones that she had seen time and again when subjects tuned into the suffering of another person. Instead, areas associated with romantic love or reward, such as the nucleus accumbens and ventral striatum, were activated.

Confused, Singer asked Ricard what he had been doing. He explained that he had put himself into a state of compassion, a warm feeling of well-wishing toward the world. When Ricard went back into the scanner and concentrated on the plight of children in a Romanian orphanage he had seen in a documentary, his brain showed the typical signature of empathy. But Ricard later said that the pain quickly became unbearable. "I felt emotionally exhausted, very similar to being burned out."

Doctors and nurses have also reported being worn out by too much secondhand suf-

CREDIT: SCIENCESOURCE

fering. And empathy has other drawbacks, Harvard University psychologist Steven Pinker writes in an e-mail. Corruption, for instance, is basically a result of our natural tendency to empathize more with our friends and relatives than with strangers, and to favor them at the expense of others. "No amount of training is going to erase this difference," Pinker writes.

Indeed, studies have shown that people are more likely to empathize with others of their own race or supporters of their favorite football team; even rats show a stronger signature of empathy toward cagemates than to other rats. The world needs justifiable policies and a robust commitment to human rights rather than more empathy, Pinker argues. "Frankly, I don't feel empathy for every one of the two billion Indians and Chinese—who has the time or energy? But I also feel very strongly that they should not be harmed, exploited, or killed. These aren't the same thing."

Singer, too, acknowledges the limits of empathy. After her experience with Ricard she changed tack and concentrated on compassion, Ricard's state of general warmth—which she also calls "empathic concern," as opposed to "empathic distress." "I thought we should all be more empathic and the world would be a better place," Singer says. "But Ricard taught me that compassion is something completely different from empathy." Now, she's convinced it is this "caring system" that needs to be used more. The general warm feelings from compassion would not be limited to friends or relatives, and they are less stressful for caregivers than empathy.

Helping each other. Singer and economist Dennis Snower (*right*) received a grant to develop their ideas for a compassion-based economy.

Love generation

Numerous studies have shown that people can be "primed" to think more socially in various ways—from reading simple instructions to holding a warm cup of coffee. In one test, participants who listened to Bob Sinclar's hit song "Love Generation" were more likely to come up with words like "help" than those who listened to Sinclar's less uplifting song "Rock This Party." But Singer isn't interested in words; she wants to train people to act more socially in everyday life. And from personal experience, she believes meditation may be the way to do it.

> ***"We are researching a system that … allows us to go in peace, to trust ourselves and others more, that breeds tolerance."***
>
> **—TANIA SINGER**

At its most basic, the technique simply involves focusing on a feeling. In one meditation exercise in her study, participants are told to imagine a person they love and to concentrate on positive feelings toward them. "May you be happy. May you be safe and sheltered. May you be healthy. May you live with a light heart," the teacher intones. Like bodybuilders increasing the weights they lift, meditators can intensify their compassionate feelings over time. Expert meditators can go very far, Singer says; rape victims may meditate on feeling compassion for their rapist, for instance.

To measure meditation's effects, researchers in the ReSource Project determine the level of the stress hormone cortisol in participants' saliva, test their reaction times, have them fill out questionnaires, and shepherd them through virtual reality worlds while monitoring their heart rate. Each participant's brain is scanned for several hours five times over the course of the study.

Participants also play computer games designed to evaluate their compassion level. In one of them, developed with Swiss economist Ernst Fehr, they have to guide a smiley along a winding path that leads to a treasure chest; they have blue or red keys to open gates of the same color. But another smiley is also wandering the screen, on its own quest to another treasure, and players have to decide whether to open gates for it, too. In a preliminary study in 2011, Singer showed that just one day of compassion meditation made people more likely to help the other smiley, whereas 1 day of memory training did not.

Singer is also trying to better understand what goes on in the brain when it is feeling compassion. The activation patterns seen in the scanner leave open two possibilities: The feeling could be linked to the neurotransmitter dopamine and the brain's reward circuits (which, among many other things, makes you crave chocolate) or it could be linked to what she calls the affiliation network, which is activated for example when you view a picture of your partner or your own child, and is mediated by the neurotransmitters oxytocin or opioids.

Singer admits that pinning down the neurobiology of compassion is difficult because the mental state it corresponds to remains fuzzy. A French Buddhist monk may have a very different concept of compassion than an African doctor or a British businessman, and there's friction between the classic third-person perspective of science and subjective experiences. "But we need the first-person experience as well as the third-person science," she says.

Wet noodle

On an evening in early September, Singer is sitting barefoot on the floor of the Berlin apartment that she rents from Danish-Icelandic artist Ólafur Elíasson, known for his mood-altering installations of water, air, and light. Beautiful globes made of wood, glass, and metal hang from the ceiling, like huge glowing molecules, as Singer talks about what compassion training, practiced on a large scale, could help achieve. At the World Economic Forum in Davos, she has spoken about "caring economics," based on cooperation and compassion instead of just competition. A new grant from the George Soros–backed Institute for New Economic Thinking will allow her and economist Dennis Snower of the Kiel Institute for the World Economy to outline how a compassion-based economy could work.

She has also produced a free 900-page e-book, entitled *Compassion. Bridging Practice and Science*, scheduled to go online on 18 September. Based on a 2011

CREDIT: MAX PLANCK SOCIETY

Published by AAAS

Berlin workshop, it covers everything from the neuroscience of compassion and empathy to specific training schedules. Bringing together texts from Singer and others, sound collages from her twin sister, and Elíasson's photos, it shows "that science and art are actually capable of producing things together," Elíasson says.

Singer hopes the book will help spread her message. People think compassion makes you vulnerable for exploitation, that it is weak, that it is a "wet noodle," she says. "In fact compassion is courageous, compassion is tough." But she's aware that many of her colleagues are skeptical of her sweeping vistas—and even more about getting there through meditation.

One problem is that historically, meditation is intertwined with religion. Scientists like Singer and Davidson take care not to include religious references in their study designs; meditation practices "offer a kind of training technology" that even strident atheists can use, Davidson says. But many meditation studies, including Davidson's, for Complementary and Alternative Medicine sifted through more than 800 studies looking at meditation's health effects. They were not impressed. The research "does not appear to have a common theoretical perspective and is characterized by poor methodological quality," they wrote.

The most important problem has been that scientists fail to use adequate control groups. Many studies compare participants in a meditation program to people who applied for the study but did not take part. That leaves many factors unaccounted for, from being part of a group experience and having a devoted teacher to the fresh air at a retreat. In a 2012 paper, Davidson showed that many reported effects of "mindfulness" meditation disappear when the control group takes part in a similar program without the specific meditation techniques.

Singer hopes her own study design is rigorous enough to withstand criticism. During the first 3 months, both groups are trained in meditation focused on attention; then one group gets 3 months of compassion training, while the other focuses on "perspective-taking"—a way of viewing their own thoughts and feelings from a distance. If Singer sees differences between the groups after that, it will be due to the different meditation techniques, she says. "I've had people tell me I'm crazy to use such a conservative measurement, and that I will never find anything this way," she says. Meditation training and follow-up studies will run until 2015, but Singer expects the first results next year.

Starting early. Buddhist monks are trained in meditation from a young age.

Seasoned by skeptical responses, Singer has learned not to bring up her own meditation with fellow scientists, and she is reluctant to discuss it with *Science*. But she's encouraged that many scientists have recently become more interested. Christof Koch, chief scientific officer at the Allen Institute for Brain Sciences in Seattle, Washington, for instance, says that he used to doubt the value of studying meditation. But at a meeting between Western scientists and Buddhist monks, he was impressed by the Dalai Lama and by researchers like Singer and Davidson, "very serious basic scientists who knew their stuff." The meeting convinced him that meditation research is worthwhile, Koch says.

Singer's father, too, changed his position, after attending a 2-week meditation retreat in the Black Forest a few years ago where speaking, or even making eye contact, was forbidden. "There is no question that meditation can lead to altered states of consciousness while you are doing it," Wolf Singer says. He has become friends with Ricard, and a conversation between the two about meditation and brain sciences was just published as a book.

For Tania Singer, compassion research is a logical next step in neuroscience—but one that offers more hope for humanity than most other lines of research. "Why do other people study the amygdala and research how fear works? It's basic science," she says. "We are researching a system that is the opposite of fear, that allows us to go in peace, to trust ourselves and others more, that breeds tolerance."

–KAI KUPFERSCHMIDT

A mind for science. Postdocs prepare a Tibetan monk for an MRI study at Stanford University, where researchers are also studying compassion.

CREDITS (TOP TO BOTTOM): THIERRY FALISE/GETTY IMAGES; BRYCE E. JOHNSON/SCIENCE FOR MONKS

are funded by the John Templeton Foundation, a philanthropic organization that has frequently been criticized for trying to blur the boundaries between science and religion. (Davidson says that the foundation is "doing a great service" and that the money comes with no strings attached.)

Another problem is that meditation research is not known for rigor. In 2007, scientists working for the U.S. National Center

Published by AAAS

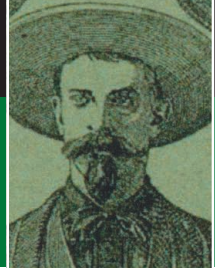

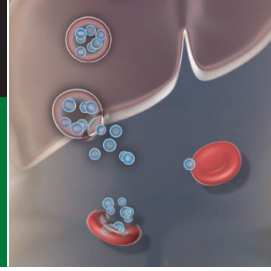

LETTERS

edited by Jennifer Sills

Putting GenBank Data on the Map

IN AN EARLY PAPER, ALFRED RUSSEL WALLACE (*1*) LAMENTED THE LACK of geographical precision of naturalists when describing where their specimens were collected: "In the various works on natural history and in our museums, we have generally but the vaguest statements of locality…. [O]n [the] accurate determination of an animal's range many interesting questions depend." No modern biologist would disagree, and substantial efforts have established the well-known Darwin Core Standard for biological specimen data (*2*). Nevertheless, deficiencies in the most basic information associated with biological materials persist, particularly in our modern museum of genetic sequences, GenBank. Researchers deposit sequences in GenBank, either routinely or by journal rules, but an extremely high proportion fail to include the precious information of latitude and longitude at which the specimens sequenced (just 4% of 5000+ for the animals we know best, medusozoan cnidarians) were found (*3*).

Readers who recall a relatively recent call for minimal information to be associated with genetic markers (*4*) might think that the situation has improved. However, even for markers whose variation is commonly used to examine species boundaries and geographic structuring—mitochondrial cytochrome oxidase I gene (COI) and 16S rRNA gene—only 7% of 1000+ deposited since mid-2011 have latitude and longitude (18% list a museum catalog number associated with the original specimen) (*3*).

There is no excuse for omitting this most basic and valuable information, easily obtainable by GPS or Google Earth. This deficiency wastes money, effort, and opportunities, and hinders scientific precision. Because geographic information and date of collection—easily derived from any device with a clock—are fundamental for biodiversity inferences, GenBank should adopt a mandatory, so-called "Wallace Core" of data necessary for submission: latitude, longitude, and date.

ANTONIO C. MARQUES,[1]* MAXIMILIANO M. MARONNA,[1] ALLEN G. COLLINS[2]

[1]Institute of Biosciences, University of São Paulo, São Paulo, SP, 05508-090, Brazil. [2]National Systematics Laboratory of NOAA's National Marine Fisheries Service and the National Museum of Natural History, Smithsonian Institution, Washington, DC 20013–7012, USA.

*Corresponding author. E-mail: marques@ib.usp.br

References

1. A. R. Wallace, *Proc. Zool. Soc. London* **20**, 107 (1852).
2. Biodiversity Information Standards (TDWG) (www.tdwg.org/about-tdwg/).
3. GenBank (www.ncbi.nlm.nih.gov/genbank/) [data as of 15 June 2013].
4. P. Yilmaz, *Nat. Biotechnol.* **29**, 415 (2011).

Beware Side Effects of Research Ethics Revision

THE WORLD MEDICAL ASSOCIATION'S Declaration of Helsinki is one of the most important ethical guidelines pertaining to biomedical research. It was originally adopted in 1964 as a statement of ethical principles in research involving human subjects, addressed primarily to physicians. The Declaration's roots are in the Nuremberg code, which grew out of the trials against Nazi doctors. Since the first revision of the document in 1975, it has explicitly stated that the interests of the research subject should prevail over those of science and society. It has been modified six times, most recently in 2008 (*1*). Although it is not legally binding, it has influenced legislation in many countries and become a cornerstone in research ethics. In October 2011, the General Assembly of the World Medical Association decided to initiate a new revision of the Declaration (*2*). In the current version, the Declaration states that consent should be required for all research that uses identifiable tissue samples and data. It then adds, "There may be situations where consent would be impossible or impractical to obtain for such research or would pose a threat to the validity of the research." The proposed revision would strike the phrase "or would pose a threat to the validity of the research" (*3*). We question this change and believe that further discussion on the issue is needed.

In medical research, the risks must always be weighed against the benefits. When the risks are significant, the interests of the individual should obviously prevail over the interests of society. It is uncontroversial that one person should not be sacrificed for the benefit of the many, a principle reflected in the declaration since 1975. But when the risks are minimal, it is not clear that the individual's interest in having a say should automatically outweigh the good that can result from robust research. For example, many countries have cancer registries that collect data without consent, because universal inclusion is deemed more important than respecting the preferences of each individual. The proposed change suggests that no research on samples and data is important enough to be conducted

without consent, if it is practically possible to ask for it. From such a perspective, not even major challenges to people's health (e.g., cancer) would be sufficient to outweigh the right of individuals to decide whether their material can be used. Although we acknowledge the value of self-determination, this is a narrow interpretation of research ethics that can affect a wide range of research activities using public health data and sample collections.

JOANNA STJERNSCHANTZ FORSBERG[1]* AND YUSUKE INOUE[1,2]

[1]Centre for Research Ethics and Bioethics, Uppsala University, SE-761 22 Uppsalar Sweden. [2]The Institute of Medical Science, The University of Tokyo, Tokyo 108–8639, Japan.

*Corresponding author. E-mail: joanna.forsberg@crb.uu.se

References

1. R. V. Carlson, K. M. Boyd, D. J. Webb, *Br. J. Clin. Pharmacol.* **57**, 695 (2004).
2. World Medical Association, DoH Public Consultation 2013 (www.wma.net/en/20activities/10ethics/10helsinki/15publicconsult/index.html).
3. World Medical Association Declaration of Helsinki (www.wma.net/en/20activities/10ethics/10helsinki/15publicconsult/DoH-draft-for-public-consultation_annotated.pdf).

Protecting Privacy for Dual-Use Researchers

WITH THE RECENT REVELATION THAT U.S. intelligence agencies have been broadly tracking electronic communications for years (*1*, *2*), a public discussion regarding the appropriate balance between privacy and security is overdue. The science community, especially those involved in dual-use research, should pay particular attention to how this conversation proceeds.

Historically, dual-use research (such as the nuclear sciences) has been controlled by limiting access, primarily through security clearances and classifying research. However, more recent dual-use research, particularly in the biological sciences, is more difficult to regulate because the knowledge and materials involved are already widely available (*3*). Thus, self-regulation in the form of educational outreach, professional codes of conduct, and internal review boards is often advocated as the appropriate governance method. These self-governance measures can appear to be grossly insufficient considering the public perception of potential catastrophe if biological dual-use research were to start a pandemic.

In the absence of more active and reassuring oversight, I believe that it is increasingly possible that state intelligence agencies will add monitoring of dual-use research to their counterterrorist activities. The history of dual-use research oversight in the nuclear sciences suggests that policy-makers do not trust scientific self-governance (*4*). However, instead of a small group of scientists voluntarily giving up their privacy and some autonomy in order to work in their chosen field, modern surveillance technologies may facilitate the involuntary and unwitting loss of privacy for many scientists working in dual-use research fields.

The U.S. Privacy and Civil Liberties Oversight Board, the primary mission of which is reviewing executive branch counterterrorism activities, has received renewed attention after languishing since its inception in 2004 (*5*). However, given that none of the board's five members has a connection to the sciences (*6*), the science community should proactively discuss the effectiveness and desirability of dual-use research surveillance. This important topic should not be left out of the policy debate about acceptable methods of ensuring public safety and privacy.

DANIEL J. ROZELL

Department of Technology and Society, Stony Brook University, Stony Brook, NY 11790, USA. E-mail: daniel.rozell@stonybrook.edu

References

1. G. Greenwald, E. MacAskill, S. Ackerman, "NSA collecting phone records of millions of Verizon customers daily" *The Guardian* (6 June 2013); www.guardian.co.uk/world/2013/jun/06/nsa-phone-records-verizon-court-order.
2. B. Gellman, L. Poitras, "U.S., British intelligence mining data from nine U.S. Internet companies in broad secret program," *The Washington Post* (6 June 2013); www.washingtonpost.com/investigations/us-intelligence-mining-data-from-nine-us-internet-companies-in-broad-secret-program/2013/06/06/3a0c0da8-cebf-11e2-8845-d970ccb04497_story.html).
3. J. B. Tucker, R. Danzig, *Innovation, Dual Use, and Security: Managing the Risks of Emerging Biological and Chemical Technologies* (MIT Press, Cambridge, MA, 2012), p. 356.
4. N. G. Evans, *Dual-Use Bioethics: The Nuclear Connection, Research Report for the Wellcome Trust Project on "Building a Sustainable Capacity in Dual-Use Bioethics"* (Univ. of Bradford, Bradford, UK, 2010), p. 51.
5. R. Weiner, "Never heard of the Privacy and Civil Liberties Oversight Board? You should," *The Washington Post* (10 June 2013); www.washingtonpost.com/blogs/the-fix/wp/2013/06/10/never-heard-of-the-privacy-and-civil-liberties-oversight-board-you-should/.
6. J. Epstein, "Obama to meet Friday with privacy and civil liberties oversight board," *Politico* (21 June 2013); www.politico.com/politico44/2013/06/obama-to-meet-friday-with-privacy-and-civil-liberties-166740.html).

TECHNICAL COMMENT ABSTRACTS

Comment on "Invasive Harlequin Ladybird Carries Biological Weapons Against Native Competitors"

Peter W. de Jong, Joop C. van Lenteren, C. Lidwien Raak-van den Berg

We comment on the implications that Vilcinskas *et al*. (Reports, 17 May 2013, p. 862) attach to the finding that the exotic, invasive ladybird *Harmonia axyridis* carries microsporidia to which this species is insensitive but that is lethal to species that are native to the invaded areas. The authors suggest that these microsporidia might serve as "biological weapons" against the native competitors, but we cast doubt on the importance of this suggestion in the field.

Full text at http://dx.doi.org/10.1126/science.1241745

Comment on "Invasive Harlequin Ladybird Carries Biological Weapons Against Native Competitors"

Leellen F. Solter, George K. Kyei-Poku, Shajahan Johny

Conclusions about the nontarget effects of putatively invasive pathogens should be based on biologically relevant data. We disagree that the research experiments on a microsporidium isolated from *Harmonia axyridis* conducted by Vilcinskas *et al*. (Reports, 17 May 2013, p. 862) can explain the decline of native coccinellid species in the absence of such data.

Full text at http://dx.doi.org/10.1126/science.1241600

Comment on "Invasive Harlequin Ladybird Carries Biological Weapons Against Native Competitors"

John J. Sloggett

Vilcinskas *et al*. (Reports, 17 May 2013, p. 862) proposed that infectious microsporidia of the invasive ladybird *Harmonia axyridis* act against intraguild predators rather than ladybird alkaloid defenses. However, as both microsporidia and the harmonine defense alkaloid were administered to predators by microinjection rather than into the gut, such a conclusion is premature. Alkaloids also provide defense when predation occurs, whereas microsporidia act much later.

Full text at http://dx.doi.org/10.1126/science.1241827

Response to Comments on "Invasive Harlequin Ladybird Carries Biological Weapons Against Native Competitors"

Andreas Vilcinskas, Kilian Stoecker, Henrike Schmidtberg, Christian R. Röhrich, Heiko Vogel

Comments by de Jong *et al*., Solter *et al*., and Sloggett question the ecological relevance of the abundant microsporidia found in the invasive ladybird *Harmonia axyridis*. We contend that there is abundant evidence that native ladybirds feed on *H. axyridis* eggs and that interspecific microsporidial transfer is a common phenomenon, supporting the proposed role of these parasites as biological weapons.

Full text at http://dx.doi.org/10.1126/science.1242484

Comment on "Invasive Harlequin Ladybird Carries Biological Weapons Against Native Competitors"

Peter W. de Jong,* Joop C. van Lenteren, C. Lidwien Raak-van den Berg

We comment on the implications that Vilcinskas *et al*. (Reports, 17 May 2013, p. 862) attach to the finding that the exotic, invasive ladybird *Harmonia axyridis* carries microsporidia to which this species is insensitive but that is lethal to species that are native to the invaded areas. The authors suggest that these microsporidia might serve as "biological weapons" against the native competitors, but we cast doubt on the importance of this suggestion in the field.

The invasive ladybird, *Harmonia axyridis*, has a negative impact on comembers of the aphidophagous guild in the invaded areas (*1*). One of the main reasons that have been suggested is its voracious character, making this invader dominant in competition for food and a strong intraguild predator as well (*2*). Vilcinskas *et al*. (*3*) propose another factor contributing to *Harmonia*'s negative effect: *Harmonia* carries spores of parasitic microsporidia, which, when experimentally injected into the indigenous *Coccinella septempunctata*, cause a strong reduction in survival. *Harmonia* itself seems to be insensitive to the microsporidia. The authors suggest that these microsporidia act as biological weapons: They spread from *Harmonia* to native ladybird species by intraguild predation and kill them. Although we do not cast any doubt on these experimental results, we question their importance in the field.

The proposed mechanism for transfer of microsporidia from *Harmonia* to native ladybirds is that heterospecifics prey on *Harmonia*. This is most likely to happen at the immature stages (*2*). Two problems arise: (i) Vilcinskas' experimental work (*3*) focuses on microsporidia isolated from the hemolymph of *Harmonia*; microsporidial abundance is neither quantified nor differentiated between adult and larval hemolymph. Moreover, for the eggs—the stage most vulnerable to intraguild predation (*2*)—only microsporidial presence, rather than abundance, is reported. (ii) More important, published evidence shows that *Harmonia* usually is the intraguild predator instead of the intraguild prey (*2*, *4*), also under field conditions (*5*). Even *Harmonia* eggs deter heterospecifics (*2*, *6*). This makes us wonder whether *Harmonia*'s "biological weapons" are deployed to a sufficient extent to contribute substantially to the negative impact on native ladybird communities, above the already demonstrated impact of the highly asymmetric intraguild predation. Another mechanism, co-hibernation, may lead to conspecific transmission of microsporidia (*7*), but because hibernating ladybird beetles usually form monospecific clusters (*8*), which is also likely the case for *H. axyridis* (*9*), this mechanism is unlikely to play a role in the transfer of microsporidia to native ladybirds. Therefore, we argue that, at present, there is no proof for the conclusion in Reynolds' accompanying Perspective that "the almost worldwide invasive triumph of the harlequin ladybird *Harmonia axyridis* depends on the presence of a coexisting pathogen within the invading insect...." (*7*).

Laboratory of Entomology, Wageningen University, P.O. Box 8031, 6700 EH Wageningen, Netherlands.

*Corresponding author. E-mail: Peter.deJong@wur.nl

References

1. H. E. Roy *et al*., *Divers. Distrib.* **18**, 717–725 (2012).
2. J. K. Pell, J. Baverstock, H. E. Roy, R. L. Ware, M. E. N. Majerus, *BioControl* **53**, 147–168 (2008).
3. A. Vilcinskas, K. Stoecker, H. Schmidtberg, C. R. Röhrich, H. Vogel, *Science* **340**, 862–863 (2013).
4. H. Yasuda, T. Kikuchi, P. Kindlmann, S. Sato, *J. Insect Behav.* **14**, 373–384 (2001).
5. C. L. Raak-van den Berg, H. J. De Lange, J. C. Van Lenteren, *PLoS ONE* **7**, e40681 (2012).
6. T. E. Cottrell, *Environ. Entomol.* **36**, 390–401 (2007).
7. S. E. Reynolds, *Science* **340**, 816–817 (2013).
8. I. Hodek, in *Ecology and Behaviour of the Ladybird Beetles (Coccinellidae)*, I. Hodek, H. F. van Emden, A. Honek, Eds. (Wiley-Blackwell, Oxford, 2012), pp. 275–342.
9. D. Durieux *et al*., *J. Insect Physiol.* **58**, 801–807 (2012).

7 June 2013; accepted 14 August 2013
10.1126/science.1241745

Comment on "Invasive Harlequin Ladybird Carries Biological Weapons Against Native Competitors"

Leellen F. Solter,[1]*† George K. Kyei-Poku,[2]† Shajahan Johny[2]†

Conclusions about the nontarget effects of putatively invasive pathogens should be based on biologically relevant data. We disagree that the research experiments on a microsporidium isolated from *Harmonia axyridis* conducted by Vilcinskas *et al*. (Reports, 17 May 2013, p. 862) can explain the decline of native coccinellid species in the absence of such data.

We respectfully disagree that conclusions about invasiveness and population impacts can be drawn from the published study concerning the decline of the seven-spotted ladybeetle, *Coccinella septempunctata*, as a result of consuming microsporidian-infected eggs of the introduced Asian harlequin lady beetle, *Harmonia axyridis* (*1*). The conclusions were based on the results of several laboratory tests. First, *C. septempunctata* develops infections from injected *H. axyridis* microsporidia but not from heat-treated spores; second, *H. axyridis* is not deleteriously affected by infection of the microsporidian pathogen, a conclusion based on observation of adult beetles and on transcriptome data from adult beetles and eggs containing spores; and third, injection of synthetic harmonine does not kill the beetles. These tests were not validated with field collections or feeding bioassays, yet the authors invoke the microsporidium as a "biological weapon" against *C. septempunctata* and other native ladybird beetles.

Our first concern is that injection of partially purified microsporidian spores bypasses the natural barriers to infection—e.g., the midgut milieu that may or may not stimulate spore germination to initiate infection (*2*) and immune response in midgut cells (*3*). *C. septempunctata* will readily imbibe sugar water (*4*); therefore, a test of natural response to the microsporidium alone would be to feed isolated spores in a sugar-water suspension, answering the following questions: Is *C. septempunctata* naturally susceptible to this microsporidium and, if so, how does it respond to infection? Likewise, purified or synthetic harmonine should be fed to the beetles to determine whether ingested harmonine can kill *C. septempunctata* larvae.

C. septempunctata is Palearctic in distribution (*5*), and *H. axyridis* and *C. septempunctata* are naturally sympatric in Asia (*6*). It is counterintuitive that a naturally occurring pathogen of *H. axyridis* only severely affects *C. septempunctata* in other geographic areas. It is not known whether the *Nosema* sp. found in *H. axyridis* has a broad natural host range within the Coccinellidae that might include *C. septempunctata* and other European species.

In a major study cited by the researchers, Kajita *et al*. (*7*) showed mortality of *C. septempunctata* within 3 days of feeding on *H. axyridis* eggs. The generation time of microsporidia in the *Nosema*/*Vairimorpha* complex is typically 4 to 7+ days (*8*), with increased spore production occurring after the first sporulation. Indeed, in this study by Vilcinskas *et al*. (*1*), which bypassed the normal infection process, the microsporidium performed typically, and mortality occurred at about 2 weeks after inoculation, not within the 3-day period previously reported for egg-feeding. Over many collective years of working with microsporidian species from a variety of insect hosts, including coccinellids, and of evaluating infections in nontarget species in the laboratory and in the field (*9*–*11*), we have observed only one case of early fatal response to microsporidia in a nontarget species, that of the lepidopteran *Hemileuca maia*, fed *Nosema lymantriae*. No spores were produced in these larvae, suggesting a massive immune response and a "dead-end" infection (*10*). It is possible that early mortality of *C. septempunctata* fed *H. axyridis* eggs is a result of naturally produced harmonine (rather than the synthetic harmonine used in the reported experiments), another constituent in the eggs, or a combination of harmonine and another constituent.

Although *C. septempunctata* will occasionally feed on other arthropods, this species is primarily aphidophagous and fungivorous (*12*, *13*), and the enzootic and epizootic prevalence of *Nosema* sp. in *H. axyridis* is unknown. Microsporidia are typically density-dependent pathogens, and some species may, indeed, attain high prevalence in insect populations, but many species are maintained at very low enzootic levels in the host population. Low natural prevalence in *H. axyridis* would suggest that even if the pathogen has a broad host range, the chance that it might be a major factor in the serious decline of a nontarget species that does not feed primarily on coccinellid eggs is low. It is not reasonable to assert that this microsporidium precipitated the severe decline of several coccinellid species without consideration of the dynamics of the pathogen and the natural feeding behavior of the declining coccinellids in the presence of *H. axyridis* eggs. *H. axyridis* is known to be a generalist predator, and the literature contains several reports of high-density populations and unidirectional predation by *H. axyridis* on native lady beetles (*14*), with *C. septempunctata* being particularly susceptible (*15*). This suggests that direct predation and possibly competition are more likely causes for the decline.

The authors state that *H. axyridis* is not harmed by the microsporidium. Many adult insects and late larval instars exhibit low mortality and few obvious effects of infection with their naturally occurring microsporidia, and, like the fungi to which they are related, microsporidia can "hide" from the host immune system (*3*). If, however, as the authors suggest, this species is transmitted transovarially, it is likely that the mortality rate is high in newly hatched infected larvae and/or that egg production is low or hatch rate is reduced (*8*), effectively removing intensely infected insects from the population.

Microsporidia are of importance as primary pathogens of insects and have the potential to be invasive with the global invasions of their natural hosts. Our studies have shown, however, that the physiological (laboratory) host range of microsporidia is rarely equivalent to the ecological (field) host range (*10*), and we believe that appropriate and ecologically relevant research is needed before drawing conclusions about the dynamics of any particular host-pathogen system.

[1]Illinois Natural History Survey, Prairie Research Institute, University of Illinois, Champaign, IL 61820, USA. [2]Canadian Forest Service, Great Lakes Forestry Centre, Sault Ste. Marie, ON P6A 2E5, Canada.

*Corresponding author. E-mail: lsolter@illinois.edu
†These authors contributed equally to this work.

References

1. A. Vilcinskas, K. Stoecker, H. Schmidtberg, C. R. Röhrich, H. Vogel, *Science* **340**, 862–863 (2013).
2. J. Vávra, J. Lukeš, in *Advances in Parasitology, Vol. 82*, D. Rollinson, Ed. (Academic Press, 2013), pp. 253–320.
3. E. R. Troemel *et al*., *PLoS Biol.* **6**, e60309 (2008).
4. E. W. Evans, A. T. Stevenson, D. R. Richards, *Oecologia* **121**, 107–112 (1999).
5. J. Marin, B. Crouau-Roy, J.-L. Hemptinne, E. Lecompte, A. Magro, *Zool. Scr.* **39**, 591–602 (2010).
6. J. P. Reider, T. A. S. Newbold, S. Sato, H. Yasuda, E. W. Evans, *Ecol. Entomol.* **33**, 53–58 (2008).
7. Y. Kajita, J. J. Obrycki, J. J. Sloggett, K. F. Haynes, *Oecologia* **163**, 313–322 (2010).
8. L. F. Solter, J. J. Becnel, D. H. Oi, in *Insect Pathology*, F. E. Vega, H. K. Kaya, Eds. (Elsevier, San Diego, CA, ed. 2, 2012), pp. 221–263.
9. L. F. Solter, J. V. Maddox, M. L. McManus, *J. Invertebr. Pathol.* **69**, 135–150 (1997).
10. L. F. Solter, J. V. Maddox, *J. Invertebr. Pathol.* **71**, 207–216 (1998).
11. L. F. Solter *et al*., *J. Invertebr. Pathol.* **105**, 1–10 (2010).
12. H. Triltsch, *Eur. J. Entomol.* **96**, 355–364 (1999).
13. L. N. Davidson, E. W. Evans, *Environ. Entomol.* **39**, 576–582 (2010).
14. R. L. Koch, T. L. Galvan, in *Biological Control to Invasion: The Ladybird* Harmonia axyridis *as a Model Species,* H. E. Roy, E. Wajnberg, Eds. (Springerlink, Berlin, 2008), pp. 23–35.
15. A. Katsanis, D. Babendreier, W. Nentwig, M. Kenis, *BioControl* **58**, 73–83 (2013).

7 June 2013; accepted 14 August 2013
10.1126/science.1241600

Comment on "Invasive Harlequin Ladybird Carries Biological Weapons Against Native Competitors"

John J. Sloggett

Vilcinskas *et al*. (Reports, 17 May 2013, p. 862) proposed that infectious microsporidia of the invasive ladybird *Harmonia axyridis* act against intraguild predators, rather than ladybird alkaloid defenses. However, as both microsporidia and the harmonine defense alkaloid were administered to predators by microinjection rather than into the gut, such a conclusion is premature. Alkaloids also provide defense when predation occurs, whereas microsporidia act much later.

Vilcinskas *et al*. (*1*) proposed that the invasive harlequin ladybird beetle *Harmonia axyridis* defends itself against intraguild predation (IGP) by other ladybirds using parasitic microsporidia to which it is immune but other ladybirds are not. They dismiss earlier hypotheses based around the defensive chemistry of ladybirds (*2*–*4*) because microinjection of the *H. axyridis* alkaloid harmonine into larvae of another ladybird, *Coccinella septempunctata*, was not lethal. The authors suggest that this microbial defense could explain an IGP-related decline in native ladybirds.

Their study is open to several criticisms. First, the use of microinjection does not mimic the putative natural transfer of the microbe, especially through IGP. The situation is comparable to ladybird endosymbiotic male-killing bacteria. Although cross-genus microinjection of such endosymbionts reduces recipient fitness or survival (*5*), male killers are apparently rarely, if ever, transferred from ladybird to ladybird by predation, even by intraspecific egg cannibalism (*6*). Microbial defense by *H. axyridis* thus remains speculative until an interspecific transfer mechanism is demonstrated.

Chemistry remains a likely mode of *H. axyridis* defense against IGP. Vilcinskas *et al*. administered harmonine using microinjection. However, many defensive chemicals act in the gut or are enzymatically rendered toxic there [e.g., (*7*–*9*)]. Work on IGP and harmonine by Kajita *et al*. (*3*), discussed by Vilcinskas *et al*., used *H. axyridis* eggs frozen at –80°C: thus, the *C. septempunctata* mortality resulting from consuming these eggs was unlikely to have come from infection by living microbes. The possibility exists that apart from harmonine, *H. axyridis* might contain other untested alkaloids or defensive chemicals that protect it against natural enemies, including intraguild predators (*4*, *10*).

The death of a *C. septempunctata* predator from microsporidian infection after several days confers very little benefit to the *H. axyridis* victim of the IGP. By contrast, the apparent toxicity of allospecific alkaloids can be near instantaneous and costly even when sublethal to ladybird intraguild predators (*11*). Furthermore, chemistry confers repellency as well as toxicity (*4*, *12*). Kajita *et al*. found that *H. axyridis* eggs containing more harmonine were consumed less by *C. septempunctata* larvae (*3*). Repellency, possibly combined with fast-acting toxicity, would immediately protect potential ladybird victims of intraguild predation. For the alkaloid-bearing egg clutches, consumption of one egg would deter further egg consumption, and larvae and adults can protect themselves with alkaloid-laden defensive secretions.

Finally, if declines of native ladybirds have resulted from IGP at all, it is from *H. axyridis* IGP of other ladybirds, not through IGP of *H. axyridis* or its avoidance. The ladybird is a voracious intraguild predator and possesses at least some metabolic resistance to other ladybirds' defensive alkaloids (*13*–*15*).

Maastricht Science Programme, Maastricht University, P.O. Box 616, 6200 MD Maastricht, Netherlands.

E-mail: j.sloggett@maastrichtuniversity.nl

References

1. A. Vilcinskas, K. Stoecker, H. Schmidtberg, C. R. Röhrich, H. Vogel, *Science* **340**, 862–863 (2013).
2. S. Sato, A. F. G. Dixon, *Agric. For. Entomol.* **6**, 21–24 (2004).
3. Y. Kajita, J. J. Obrycki, J. J. Sloggett, K. F. Haynes, *Oecologia* **163**, 313–322 (2010).
4. J. J. Sloggett *et al*., *BioControl* **56**, 643–661 (2011).
5. M. C. Tinsley, M. E. N. Majerus, *BMC Evol. Biol.* **7**, 238 (2007).
6. G. D. D. Hurst, thesis, University of Cambridge, UK (1994).
7. T. Hartmann, *Planta* **219**, 1–4 (2004).
8. S. Dobler, G. Petschenka, H. Pankoke, *Phytochemistry* **72**, 1593–1604 (2011).
9. S. K. Upadhyay, P. K. Singh, *Protein J.* **31**, 439–446 (2012).
10. P. M. Brakefield, *Biol. J. Linn. Soc. London* **26**, 243–267 (1985).
11. J. J. Sloggett, K. F. Haynes, J. J. Obrycki, *Oikos* **118**, 1396–1404 (2009).
12. J.-L. Hemptinne, G. Lognay, C. Gauthier, A. F. G. Dixon, *Chemoecology* **10**, 123–128 (2000).
13. Y. Hironori, S. Katsuhiro, *Entomophaga* **42**, 153–163 (1997).
14. R. L. Ware, M. E. N. Majerus, *BioControl* **53**, 169–188 (2008).
15. J. J. Sloggett, A. J. Davis, *J. Exp. Biol.* **213**, 237–241 (2010).

12 June 2013; accepted 14 August 2013
10.1126/science.1241827

Response to Comments on "Invasive Harlequin Ladybird Carries Biological Weapons Against Native Competitors"

Andreas Vilcinskas,[1,3]* Kilian Stoecker,[2,3] Henrike Schmidtberg,[3] Christian R. Röhrich,[3] Heiko Vogel[4]

Comments by de Jong *et al*., Solter *et al*., and Sloggett question the ecological relevance of the abundant microsporidia found in the invasive ladybird *Harmonia axyridis*. We contend that there is abundant evidence that native ladybirds feed on *H. axyridis* eggs and that interspecific microsporidial transfer is a common phenomenon, supporting the proposed role of these parasites as biological weapons.

We recently reported that the invasive harlequin ladybird *Harmonia axyridis* carries microsporidia that do not harm their host but can infect and kill native ladybirds such as *Coccinella septempunctata* (*1*). In their Comments on our article, de Jong *et al*. (*2*), Solter *et al*. (*3*), and Sloggett (*4*) cast doubt on the relevance of this phenomenon in the field (and thus its potential impact on the ecology of native ladybirds) based on three principal objections: (i) the behavior of native ladybirds suggests that they are unlikely to feed substantially on *H. axyridis* eggs; (ii) there is insufficient evidence for interspecific microsporidial transfer; and (iii) our injection-based laboratory assays are artificial and cannot predict the outcome of natural interactions between coexisting ladybird species. Solter *et al*. and Sloggett further suggest that our findings may instead be explained solely by the presence of harmonine in *H. axyridis* eggs.

Is there enough evidence for intraguild predation on *H. axyridis* eggs? de Jong *et al*. and Solter *et al*. each cite reports that describe intraguild predation upon *H. axyridis* eggs as a limited phenomenon—e.g., preferentially occurring at the larval stage with *H. axyridis* in the role of predator and rarely as prey or typically occurring only when preferred prey (aphids and fungi) are not available, thus making the consumption of *H. axyridis* eggs by adult coccinellid beetles rather uncommon and unlikely to explain the invasive success of the species. We agree that the heterospecific feeding behavior of ladybird larvae is well documented, but there is ample evidence that intraguild predation also includes the widespread consumption of heterospecific eggs by beetles (*5*–*8*). For example, Gagnon *et al*. (*5*) clearly demonstrated high levels of intraguild predation among four ladybird species in the field. They analyzed the alkaloid content of field-collected specimens (including *H. axyridis* and *C. septempunctata*) over 2 consecutive years and found that each of the four species fed on the eggs of the other three. Although the intraguild predator/prey relationship varied, both *H. axyridis* and *C. septempunctata* were found in both roles. Furthermore, intraguild predation among predaceous ladybird species is not restricted to conditions of limited prey availability (e.g., in autumn when aphid numbers decline) but also occurs when the preferred prey is abundant (*6*–*8*). de Jong *et al*. and Sloggett also argue that *H. axyridis* eggs deter heterospecifics (*9*), but the cited data show that the deterrence is not absolute, i.e., that coccinellid species prey on *H. axyridis* eggs, albeit to a lesser extent than the reciprocal process.

Is there enough evidence for interspecific microsporidial transfer? Solter *et al*. suggest that microsporidial transfer between species cannot explain the invasive success of *H. axyridis* because there is no evidence for the widespread presence of microsporidia in natural populations and that microsporidia could also be found in native species. This contrasts with our findings that all *H. axyridis* individuals we have studied, whether reared in the laboratory or sampled from native populations in different parts of the world, contain large numbers of microsporidia, whereas coccinellid individuals from European populations consistently lack microsporidia in their hemolymph. This observation also contradicts the claim by Solter *et al*. that *H. axyridis* individuals carrying large numbers of microsporidia may be selectively removed from natural populations due to a decline in fitness. Indeed, we have deliberately sought *H. axyridis* populations without microsporidia in order to test uninfected individuals exposed to microsporidia for the first time, but we have thus far failed to identify such populations in the field. de Jong *et al*. note correctly that our Report does not discuss the abundance of microsporidia in *H. axyridis* eggs (*1*). However, we have carried out a detailed investigation of microsporidial pathogenesis that confirms the presence of microsporidia at all developmental stages (extracellular spores and a full spectrum of intracellular stages), which indicates their viability and therefore the potential for transmission by intraguild predation.

All three Comments also express doubt that microsporidia, even if prevalent, are capable of being transferred between species in the field. Sloggett compares this situation with the male-killing endosymbiotic bacteria in some ladybird species that are rarely transferred between individuals in the field, even within the same species. However, several previous studies have already shown that horizontal transmission of microsporidia occurs among ladybird species through intraguild predation (*10*, *11*). Indeed, for this very reason, it is recommended that field-collected ladybirds should be controlled for the presence of microsporidia before being used for mass rearing and release in biological control programs (*10*). These data provide adequate evidence for horizontal transmission without considering more unlikely mechanisms such as cohibernation, which we would not advocate as a useful hypothesis for the reasons stated by de Jong *et al*. Similarly, we see no similarity between the microsporidia we identified and the male-killing bacteria discussed by Sloggett: There is no indication that the microsporidia are endosymbiotic, and they are clearly maintained in an inactive state as spores in the hemolymph.

All three Comments draw attention to the artificial nature of the injection-based assays we carried out and suggest that feeding assays and/or field studies are necessary before conclusions can be drawn. We agree fully that field studies are the only way to confirm the role of microsporidia in the invasive success of *H. axyridis*, although we note that the injection assays are sufficient to advance a hypothesis and that feeding studies—e.g., using sugar water (as suggested by Solter *et al*.)—would also be artificial in nature.

Both Slogget and Solter *et al*. claim that our results can be interpreted in terms of chemical defenses provided by the synthesis of harmonine and other alkaloids. We should first point out that we do not dismiss the importance of harmonine, as suggested by Slogget. Indeed, we actually set out initially to test the importance of this compound, which is why we injected it into adult *C. septempunctata* beetles. We should also state that synthetic harmonine is identical to natural harmonine, in contrast to the claim by Solter *et al*. We disagree that other untested alkaloids or unknown chemicals are responsible for the effects we observed, because we carried out several controlled experiments to rule out the contribution of impurities in the hemolymph. The hemolymph fractions used in our assays were not lethal unless

[1]Institute of Phytopathology and Applied Zoology, Heinrich-Buff-Ring 26-32, Justus-Liebig-University of Giessen, D-35392 Giessen, Germany. [2]Bundeswehr Institute of Microbiology, Neuherbergstrasse 11, D-80937 Munich, Germany. [3]Fraunhofer Institute of Molecular Biology and Applied Ecology, Winchesterstrasse 2, 35394 Giessen, Germany. [4]Max-Planck-Institute of Chemical Ecology, Hans-Knoell-Strasse 8, D-07745 Jena, Germany.

*Corresponding author. E-mail: andreas.vilcinskas@agrar.uni-giessen.de

they contained live microsporidia. Sloggett also claims that chemical defenses such as harmonine would be more beneficial than intraguild predation because the effects would be "near instantaneous," but this author's own published data shows that the toxicity peaks after 3 days, which is similar to the onset of effects caused by microsporidia. Sloggett states that if the decline in native ladybirds has resulted from intraguild predation at all, it is from *H. axyridis* preying on other ladybirds, not the intraguild predation of *H. axyridis* eggs, but this reads as an opinion and is not backed up by any supporting data. Finally, Sloggett claims that ladybirds are voracious intraguild predators and possess at least some metabolic resistance to heterospecific defensive alkaloids (*12*–*14*). However, harmonine is present at a lower concentration in *H. axyridis* eggs compared with larvae and adults, so the concentrations used in our experiments represent the upper level found during the developmental stages of this species. Furthermore, all ladybird species produce alkaloids, many of which display cell toxicity, so surely all species could evolve metabolic resistance against heterospecific alkaloids, and this would not explain the invasive success of *H. axyridis*.

de Jong *et al*. end their Comment stating "at present, there is no proof for the conclusion in Reynolds' accompanying Perspective that 'the almost worldwide invasive triumph of the harlequin ladybird *Harmonia axyridis* depends on the presence of a coexisting pathogen within the invading insect...'" (*2*, *15*). Although we feel that our data, combined with the literature cited above, provide enough evidence to support the role of microsporidia in the invasive success of *H. axyridis*, we should point out that we do not claim to have found proof, only to have developed a hypothesis that needs to be tested in the field. We also note that the microsporidia, should they prove to be used as "biological weapons" in the field, are only one component of the armory of this remarkable species, which also includes chemical defenses based on the production of harmonine (*16*) and an unusually diverse repertoire of antimicrobial peptides (*17*). It is likely that all these capabilities, as well as the behavioral traits mentioned in the Comment by de Jong *et al*., contribute to the invasive success of *H. axyridis*.

References

1. A. Vilcinskas, K. Stoecker, H. Schmidtberg, C. R. Röhrich, H. Vogel, *Science* **340**, 862–863 (2013).
2. P. W. de Jong, J. C. van Lenteren, C. L. Raak-van den Berg, *Science* **341**, 1342 (2013); www.sciencemag.org/content/341/6152/1342-b.
3. L. F. Solter, G. K. Kyei-Poku, S. Johny, *Science* **341**, 1342 (2013); www.sciencemag.org/content/341/6152/1342-c.
4. J. J. Sloggett, *Science* **341**, 1342 (2013); www.sciencemag.org/content/341/6152/1342-d.
5. A.-E. Gagnon, G. E. Heimpel, J. Brodeur, *PLoS ONE* **6**, e28061 (2011).
6. B. K. Agarwala, A. F. G. Dixon, *Ecol. Entomol.* **17**, 303–309 (1992).
7. A. K. Gupta, S. Srivastava, G. Mishra, K. Singh, *Insect Sci.* **13**, 119–126 (2006).
8. A. A. Pervez, A. K. Gupta, *Biol. Control* **38**, 307–313 (2006).
9. T. E. Cottrell, *Environ. Entomol.* **36**, 390–401 (2007).
10. T. Saito, S. Bjørnson, *Biol. Control* **39**, 427–433 (2006).
11. T. Saito, S. Bjørnson, *J. Invertebr. Pathol.* **99**, 294–301 (2008).
12. Y. Hironori, S. Katsuhiro, *Entomophaga* **42**, 153–163 (1997).
13. R. L. Ware, M. E. N. Majerus, *BioControl* **53**, 169–188 (2008).
14. J. J. Sloggett, A. J. Davis, *J. Exp. Biol.* **213**, 237–241 (2010).
15. S. E. Reynolds, *Science* **340**, 816–817 (2013).
16. C. R. Röhrich *et al*., *Biol. Lett.* **8**, 308–311 (2012).
17. A. Vilcinskas, K. Mukherjee, H. Vogel, *Proc. Biol. Sci.* **280**, 20122113 (2012).

26 June 2013; accepted 14 August 2013
10.1126/science.1242484

MEDICINE

Powerful Opinions, Capable of Harm

Donald M. Marcus

"Science is the father of knowledge, but opinion breeds ignorance."–Hippocrates

Paul Offit's lively *Do You Believe in Magic?* provides accounts of how uninformed opinions generate enterprises that bilk the public and cause needless suffering and deaths. Offit, an infectious disease specialist at the University of Pennsylvania, has written several books for the public on vaccines, including refutations of claims that they cause autism [e.g., (*1*–*3*)]. Here he examines various factors that motivate people to turn to alternative medicines.

Among these are the unfounded belief that "natural" remedies such as herbals are fundamentally different from synthetic drugs and the opinion that the government, pharmaceutical companies, and the medical establishment conspire to suppress information about inexpensive, effective remedies. In "Little Supplement Makers Versus Big Pharma," Offit describes how the supplement industry in the United States maneuvered to get Congress to pass legislation that renamed herbal medicines as "dietary supplements," effectively removing them from regulation by the Food and Drug Administration. He also devotes a pair of chapters to the cruel deceptions of cancer quackery. Although Offit provides short summaries of the hazards of alternative remedies and the lack of supporting evidence for therapies such as herbals and megavitamins, his emphasis is on analyzing how health frauds arise and prosper.

As Offit notes, the advocates for alternative remedies include alternative practitioners, distinguished scientists, physicians, nurses, pitchmen who lack medical or scientific training, movie stars, media personalities, other celebrities, and elected officials. Among the book's strong points are his detailed accounts of how such advocates sway public opinion. In particular, the section "When the Stars Shine on Alternative Medicine" recounts the impact of such advocates in the areas of menopause, autism, and chronic Lyme disease.

After actress Suzanne Somers received surgery and radiation for breast cancer, she rejected conventional treatment with tamoxifen in favor of a natural herbal remedy. The rise of her commercial health empire began with her promotion of "natural bioidentical hormones" as a safe alternative to conventional synthetic estrogen for treatment of menopause symptoms. In fact, conventional and bioidentical estrogens have the same potential benefits and risks, and there are no clinical trials of the efficacy or safety of bioidentical hormones. As Offit notes, the main difference between conventional and bioidentical hormones is that the latter are sold by compounding pharmacies, "an unsupervised industry." The recent outbreak of severe fungal infections caused by contaminated products sold by a compounding pharmacy demonstrates the need for concern about the lack of supervision. Through her appearances on television programs, endorsements by celebrity talk-show hosts such as Oprah Winfrey, and support from gynecologist Christiane Northrup, Somers's claims received widespread coverage. She later extended the purported power of bioidentical hormones to prevention of aging and subsequently embraced claims for antiaging effects of a remarkable number of herbals, vitamins, minerals, and other products. Such alternative remedies are available for sale through her website, which also offers food, cooking utensils, and weight loss and detoxification products.

Do You Believe in Magic? The Sense and Nonsense of Alternative Medicine

by Paul A. Offit
Harper, New York, 2013. 335 pp. $26.99.
ISBN 9780062222961.

Appearances on Winfrey's show also helped actress Jenny McCarthy publicize her belief that vaccines cause autism and fuel an antivaccine movement that caused outbreaks of infectious diseases in unvaccinated children.

Advocates of chronic Lyme disease, both lay people and "Lyme Literate doctors," claim that chronic infection by *Borrelia burgdorferi* causes a long list of problems, including autism, chronic fatigue syndrome, homicidal behavior, and multiple sclerosis. To treat the supposed infection and subsequent conditions, Lyme literate doctors recommend therapies such as vitamins, supplements, herbals, special diets, homeopathic remedies, machines that electrocute Lyme bacteria, and long-term, high-dose intravenous antibiotics. Scientists who speak out against these unfounded beliefs have received threats. Offit uses this example to spotlight "political shenanigans."

Many people, including some physicians, believe that although alternative remedies may not be effective, they are harmless. While there are no large systematic studies of the adverse effects of alternative remedies, evidence of their hazards has accumulated as their popularity has increased. For example, *Aristolochia* plants, a popular source of herbals worldwide, have been found to contain potent mutagens that cause renal failure and cancer of the upper urinary tract (*4*).

Do You Believe in Magic? achieves Offit's aim of taking "a critical look at the field of alternative medicine" and separating fact from myth. Informative and well-written, the book deserves a wide audience among the general public, scientists, and health care professionals. Many alternative remedies are self-prescribed, and the information provided by the extensive page-by-page references and bibliography will enable people with open minds to make more informed choices about their health care.

One-hundred and fifty years ago, physician and author Oliver Wendell Holmes Sr. commented, "Quackery and idolatry are all but immortal" (*5*). In this age of celebrity health gurus, quackery and idolatry have merged.

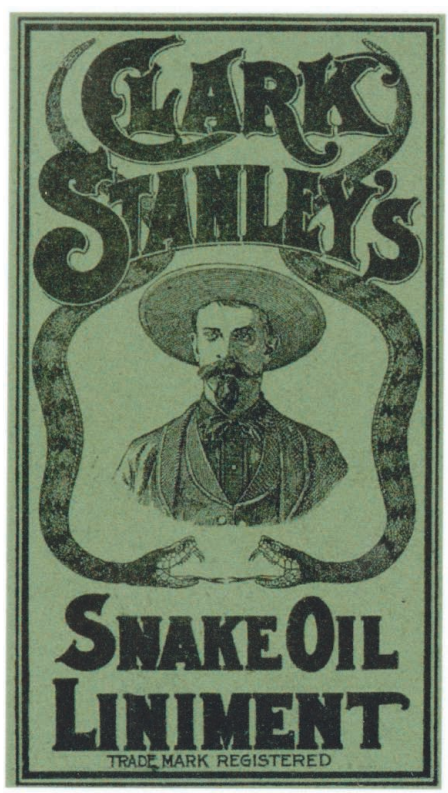

CREDIT: COURTESY WILLIAM H. HELFAND

The reviewer is at the Department of Medicine, Baylor College of Medicine, One Baylor Plaza, BCM 285, Houston, TX 77030, USA. E-mail: dmarcus.bcm.edu

Published by AAAS

References

1. P. A. Offit, *The Cutter Incident: How America's First Polio Vaccine Led to the Growing Vaccine Crisis* (Yale Univ. Press, New Haven, CT, 2005).
2. P. A. Offit, *Autism's False Prophets: Bad Science, Risky Medicine, and the Search for a Cure* (Columbia Univ. Press, New York, 2008).
3. P. A. Offit, *Deadly Choices: How the Anti-Vaccine Movement Threatens Us All* (Basic Books, New York, 2011).
4. A. P. Grollman, *Environ. Mol. Mutagen.* **54**, 1 (2013).
5. O. W. Holmes, *The Medical Profession in Massachusetts* (Wilson, Boston, 1869).

10.1126/science.1244006

SCIENCE AND RELIGION

When Prior Belief Trumps Scholarship

Charles R. Marshall

The power of scientific reasoning derives from the complex interplay between the desire to know, the ability to reason, and the ability to evaluate ideas with data. As scientists, we have learned how to make ideas dance with reality, and we expect them to be transformed in the process. We typically add to what we already know, often showing along the way that old ideas are incomplete or, occasionally, wrong. And so we collectively build an understanding of the world that is accurate, reliable, and useful.

In *Darwin's Doubt*, Stephen Meyer (who runs the Discovery Institute's Center for Science and Culture) also tries to build. He aims to construct the philosophical and scientific case for intelligent design. I am not a philosopher, so I will not attempt to evaluate his philosophical argument that in principle it might be possible to recognize the action of a designer in the history of life. But I am willing to evaluate his scientific case for the participation of such a designer. It centers on one of the most remarkable events in that history, the relatively rapid emergence of animal phyla in the Cambrian.

Meyer's scientific approach is negative. He argues that paleontologists are unable to explain the Cambrian explosion, thus opening the door to the possibility of a designer's intervention. This, despite his protest to the contrary, is a (sophisticated) "god of the gaps" approach, an approach that is problematic in part because future developments often provide solutions to once apparently difficult problems.

Darwin's Doubt
The Explosive Origin of Animal Life and the Case for Intelligent Design

by Stephen C. Meyer
HarperOne (HarperCollins), New York, 2013. 520 pp. $28.99. ISBN 9780062071477.

Darwin's Doubt begins with a very readable review of our knowledge of the Cambrian explosion. Despite its readability and a plethora of scholarly references, however, there are substantial omissions and misrepresentations. For example, Meyer completely omits mention of the Early Cambrian small shelly fossils and misunderstands the nuances of molecular phylogenetics, both of which cause him to exaggerate the apparent suddenness of the Cambrian explosion.

I like to read the arguments of those who hold fundamentally different views from my own in the hope of discovering weaknesses in my thinking. And so even after reading the flawed first part of his book, I dared hope that Meyer might point the way to fundamental problems in the way we paleontologists think about the Cambrian explosion.

However, my hope soon dissipated into disappointment. His case against current scientific explanations of the relatively rapid appearance of the animal phyla rests on the claim that the origin of new animal body plans requires vast amounts of novel genetic information coupled with the unsubstantiated assertion that this new genetic information must include many new protein folds. In fact, our present understanding of morphogenesis indicates that new phyla were not made by new genes but largely emerged through the rewiring of the gene regulatory networks (GRNs) of already existing genes (*1*). Now Meyer does touch on this: He notes that manipulation of such networks is typically lethal, thus dismissing their role in explaining the Cambrian explosion. But today's GRNs have been overlain with half a billion years of evolutionary innovation (which accounts for their resistance to modification), whereas GRNs at the time of the emergence of the phyla were not so encumbered. The reason for Meyer's idiosyncratic fixation with new protein folds is that one of his Discovery Institute colleagues has claimed that those are mathematically impossibly hard to evolve on the timescale of the Cambrian explosion.

Scree slope site. Walcott quarry in the Burgess Shale, which beautifully preserves soft-bodied animals from shortly after the Cambrian explosion.

CREDIT: MARK A. WILSON (DEPARTMENT OF GEOLOGY, WOOSTER COLLEGE)/WIKIMEDIA COMMONS

As Meyer points out, he is not a biologist; so perhaps he could be excused for basing his scientific arguments on an outdated understanding of morphogenesis. But my disappointment runs deeper than that. It stems from Meyer's systematic failure of scholarship. For instance, while I was flattered to find him quote one of my own review papers (*2*)—although the quote is actually a chimera drawn from two very different parts of my review—he fails to even mention the review's (and many other papers') central point: that new genes did not drive the Cambrian explosion. His scholarship, where it matters most, is highly selective.

Meyer's book ends with a heart-warming story of his normally fearless son losing his orientation on the impressive scree slopes that cradle the Burgess Shale, the iconic symbol of the Cambrian explosion, and his need to look back to his father for security. I was puzzled: why the parable in a book ostensibly about philosophy and science? Then I realized that the book's subtext is to provide solace to those who feel their faith undermined by secular society and by science in particular. If the reviews on Amazon.com are any indication, it is achieving that goal. But when it comes to explaining the Cambrian explosion, *Darwin's Doubt* is compromised by Meyer's lack of scientific knowledge, his "god of the gaps" approach, and selective scholarship that appears driven by his deep belief in an explicit role of an intelligent designer in the history of life.

References

1. D. H. Erwin, J. W. Valentine, *The Cambrian Explosion: The Construction of Animal Biodiversity* (Roberts and Company, Greenwood Village, CO, 2013); reviewed in (*3*).
2. C. R. Marshall, *Annu. Rev. Earth Planet. Sci.* **34**, 355 (2006).
3. C. J. Lowe, *Science* **340**, 1170 (2013).

10.1126/science.1244515

The reviewer is at the Department of Integrative Biology and Director of the Museum of Paleontology, University of California, Berkeley, CA 94720–4780, USA. E-mail: crmarshall@berkeley.edu

MEDICINE

Mitochondrial Replacement, Evolution, and the Clinic

Mitochondrial replacement therapy might bear health risks, especially for males.

Klaus Reinhardt,[1,2]* Damian K. Dowling,[3] Edward H. Morrow[4]

Mitochondrial diseases [often caused by mutations in mitochondrial DNA (mtDNA)] can manifest in a range of severe symptoms, for which there are currently no cures (*1*). The diseases are passed from mothers to offspring. Intense research efforts have recently focused on a germline therapeutic strategy to prevent the inheritance of disease-causing mitochondria. However, although there has been increased government interest, especially in the United Kingdom, for using this approach to treat patients, there are reasons to believe that it is premature to move this technology into the clinic at this stage.

Early experiments in mice produced disease-free oocytes by means of mitochondrial replacement (MR): the fertilized nucleus from an oocyte laden with mitochondria carrying mtDNA mutations was injected into the cytoplasm of an enucleated donor oocyte that carried mutation-free mitochondria (*2*). A breakthrough in primates came when four macaque babies were born after MR-assisted in vitro fertilization (IVF) (*3*) and when human embryos survived intact after MR to the blastocyst stage (*4*). Consequently, the British government commissioned the Human Fertilisation and Embryology Authority (HFEA) to collect evidence as to the suitability of MR as a therapeutic approach. The HFEA urged further experiments before clinical use of MR (*5*). The U.K. Nuffield Council on Bioethics initiated an ethical review of MR and concluded it was ethically acceptable (*6*). This view was supported by the Medical Research Council and Wellcome Trust of the United Kingdom, who suggested that MR will not affect characteristics normally associated with individual identity (*6*). MR was compared with replacing the batteries of a camera (*6*), an analogy picked up by the popular press.

Subsequently, the four macaques born after MR were shown to be healthy at 3 years of age (*7*), and technical difficulties have been reduced in human blastocysts (*7*, *8*). These results were used to urge the U.S. Food and Drug Administration to review its funding policy on gene therapy (*7*).

The HFEA then was asked to initiate a public consultation into the question of whether MR-assisted IVF "should be made available to couples at risk of having an affected child" (*9*). The results, published in March 2013, note general support within the United Kingdom for permitting MR; if applied under strict regulation, such as case-by-case approval of licensed hospitals, ethical concerns about the implementation of MR were considered to be outweighed by arguments in favor of MR (*10*). In June 2013, the British government announced they will produce draft regulations on therapeutic MR for further public consultation, to be debated in parliament in 2014 (*11*).

Much of the scientific debate has focused on genetic factors that are well known to affect mitochondrial disease, which typically develops only if the relative amount of mutated, relative to healthy, mtDNA in any given tissue surpasses a critical threshold (*1*, *10*). These frequencies can shift rapidly at embryogenesis. If any mutant mtDNA remains in an enucleated oocyte after MR, the children might be at risk of developing the disease or passing the pathogenic mutation on to their offspring. As a result, the HFEA considered whether only male embryos should be allowed to develop post-MR, to ensure that no mutations are inadvertently transmitted after the treatment. This body of research was carefully considered by the HFEA, and we do not review it here (*10*).

Rather, we draw attention to theory and experimental findings that appear to have been overlooked in the scientific and public forums of this debate. Studies on model organisms, ranging from mice to fruit flies, indicate that MR can profoundly change the expression profiles of nuclear genes and affect a range of important traits such as individual development, cognitive behavior, and key health parameters. These studies also suggest that males of reproductive age are particularly sensitive to MR-induced effects.

Natural genetic differences in the mtDNA sequence exist from one individual to another,

Health outcomes of intraspecies experimental MR in animals

Studies using invasive techniques

Human (*Homo sapiens*)
Development to blastocyst stage
Normal gene expression and metabolic profile in cell lines

Macaque (*Macaca mulatta*)
Normal embryo development and metabolic profile at juvenile age

Mouse (*Mus musculus*)
Altered respiration and growth in mouse hybrid cell line

Studies using genetic crossing techniques

Mouse (*Mus musculus*)
Normal survival to adulthood
Reduced growth, exercise ability, learning in adult ♂

Fruit fly (*Drosophila melanogaster*)
Altered juvenile viability
Altered nuclear gene expression in adult ♂
Altered, aging mostly in adult ♂
Altered, often reduced, fertility in adult ♂

Seed beetle (*Callosobruchus maculatus*)
Altered development time and metabolic rate
Altered fertility in adult ♂
Altered survival in adult ♀

Copepod (*Tigriopus californicus*)
Reduced juvenile viability
Reduced mitochondrial function and ATP production in adults

Health outcomes of intraspecies experimental MR in animals. Studies either invasively removed the nucleus by placing it into the enucleated donor oocyte (blue shading) or replaced mitochondria by repeatedly crossing foreign mitochondrial genotypes into nuclear backgrounds (green shading) (see table S1 for details). All species share the same 37 mitochondrial encoded genes. Studies of health effects of MR on vertebrates that have reached reproductive ages are lacking.

[1]Animal Evolutionary Ecology, University of Tuebingen, 72076 Tuebingen, Germany. [2]Department of Animal and Plant Sciences, University of Sheffield, Sheffield S10 2TN, UK. [3]School of Biological Sciences, Monash University, 3800 Victoria, Australia. [4]Evolution, Behaviour, and Environment Group, School of Life Sciences, University of Sussex Brighton BN1 9QG, UK.

*Corresponding author. k.reinhardt@uni-tuebingen.de

broadly denoted as mtDNA haplotypes. Putatively healthy mitochondrial haplotypes differ in their effect on the expression of key health and performance parameters. In particular, energy production critically hinges on extensive cross-talk between genes dispersed across the nucleus and the mitochondria (*12*). Because phenotypes with less-than-ideal cross-talk are disfavored by natural selection, coordinated mitochondrial-nuclear interactions become highly specific over evolutionary time. If MR disrupts such specific, highly coordinated mito-nuclear allelic interactions, adverse health outcomes might occur.

This prediction is supported by experimental studies reporting the expression of disease phenotypes when genetic backcrossing was used to replace mitochondria and to create intergenomic mismatches in mice. Altered respiratory metabolism and reduced performance, learning, and exploratory capacity in males were reported when mitochondrial-nuclear genomic interactions were experimentally mismatched (see the table and table S1). Females were not tested in those studies. The health effects were observed after mismatches between mitochondrial and nuclear genomes in mice of different inbred strains of the same species. Furthermore, experimental mismatches of putatively healthy mitochondrial and nuclear genomes from different populations within the same species in invertebrate models, suggest that the reduced performance reported in mice extends to a range of organisms [see the table and supplementary materials (SM) for additional information].

MR-assisted IVF immediately places the offspring's mtDNA (acquired from a donor) alongside a novel set of maternal and paternal nuclear alleles—a different situation from the case of sexual reproduction, in which the offspring's mitochondrial DNA is invariably inherited together with and exposed to a haploid maternal genome (see SM). Maternal inheritance of mitochondria means natural selection can only shape mitochondrial gene evolution directly through females. This facilitates the accumulation of mtDNA mutations that are harmful to males, if these mutations have favorable, benign, or only slightly deleterious, effects on females (*13*–*15*). Male-limited mitochondrial diseases such as Leber's disease, or forms of impaired fertility, might be clinical manifestations of this evolutionary hypothesis. This specific prediction has experimental backing: MR in fruit flies had little effect on nuclear gene expression in females but changed the expression of roughly 10% of genes in adult males (*14*). The mitochondrial haplotypes responsible for these male-specific effects were naturally occurring, putatively healthy variants. Hundreds of mitochondrial-sensitive nuclear genes identified in that study had a core role in male fertility. For example, one of the five combinations in which mitochondrial-nucleus interactions were disrupted by mismatching was completely male-sterile but female-fertile (*14*). In other fly studies, MR resulted in male-biased modifications to components of aging and affected the outcomes of in vivo male fertility (see the table). Together, these results suggest that core components of male health depend on fine-tuned coordination between mitochondrial and nuclear gene complexes, and thus the HFEA conclusion that "there is no evidence for any mismatch between the nucleus and any mtDNA haplogroup, at least within a species" [(*10*), 6.17 on p. 17] is incomplete and unsubstantiated.

Two points may deserve careful consideration prior to any change in legislation. First, studies in humans have only tracked health through to the blastocyst stage and in macaques to 3 years of age (see the table). The results from mice and invertebrates suggest that many deleterious effects of MR would not be revealed until adulthood. Without preclinical trials that take a longer-term approach, the current suggestion that families allow "very long term follow-up of their children and families in order to acquire further knowledge about the outcomes of these techniques" [(*6*), p. xvi] would place an experimental risk on families. It would seem fruitful to monitor fertility and health outcomes through to sexual maturity among the macaques born after MR-assisted IVF. Awaiting the macaques' health outcome upon sexual maturity in ~2 years seems a relatively low-cost endeavor. Equivalent studies assessing health post-MR in the mouse model [also recommended by (*10*)] would help to further quantify the potential costs and benefits of MR therapy.

Second, the possibility that MR outcomes may be improved by matching mtDNA haplotypes of donor and recipient (*10*) warrants experimental attention. The proof-of-principle MR study on macaques was based on oocytes of donors and recipients from the same troop (*3*, *7*). The resulting high genetic relatedness between donor and recipient at both the mtDNA and the nuclear level predicts low levels of mitochondrial-nuclear mismatch, probably to a degree that makes it unrepresentative for prospective donors and recipients from the targeted general human population. Comparing the genetic relatedness between recipients and donors for both successful and failed MR outcomes in the studies of macaques (*3*, *7*) should be relatively simple.

In conclusion, recent technical advances suggest that MR-assisted gene therapy could soon be available to help female sufferers of mitochondrial diseases have healthy children, and this is clearly an exciting prospect. Changing legislation that would facilitate this technique will require a debate over the extent to which the results and principles outlined here are ethically and clinically relevant to MR in humans. MtDNA diseases vary from mild symptoms and learning disabilities to severe disabilities and premature death. Assessing the costs and benefits of MR treatment requires that prospective patients are as fully informed as possible. The difference across patients in the severity of expected offspring symptoms in the event that MR treatment is not taken will shape the decision of choosing the treatment versus waiting for the outcomes of further research. Some families who are predicted to be, or who have previously conceived offspring that were, severely afflicted by mtDNA diseases are more likely to be prepared to take the risk. Others whose children are expected to suffer less detrimental symptoms, cognition problems or infertility, may wish to wait for further empirical clarification of the risks involved.

References and Notes

1. R. W. Taylor, D. M. Turnbull, *Nat. Rev. Genet.* **6**, 389–402 (2005).
2. A. Sato *et al.*, *Proc. Natl. Acad. Sci. U.S.A.* **102**, 16765–16770 (2005).
3. M. Tachibana *et al.*, *Nature* **461**, 367–372 (2009).
4. L. Craven *et al.*, *Nature* **465**, 82–85 (2010).
5. N. Haites, R. Lovell-Badge, "Scientific review of the safety and efficacy of methods to avoid mitochondrial disease through assisted conception" (HFEA, London, 2011); www.hfea.gov.uk/docs/2011-04-18_Mitochondria_review_-_final_report.PDF.
6. Nuffield Council on Bioethics, *Novel Techniques for the Prevention of Mitochondrial DNA Disorders* (Nuffield Council on Bioethics, London, 2012), www.nuffieldbioethics.org/mitochondrial-dna-disorders.
7. M. Tachibana *et al.*, *Nature* **493**, 627–631 (2013).
8. D. Paull *et al.*, *Nature* **493**, 632–637 (2013).
9. HFEA, HFEA launches public consultation, Medical Frontiers: Debating mitochondria replacement; www.hfea.gov.uk/7517.html.
10. HFEA, Mitochondria public consultation 2012; www.hfea.gov.uk/6896.html.
11. U.K. government, www.gov.uk/government/news/innovative-genetic-treatment-to-prevent-mitochondrial-disease.
12. J. D. Woodson, J. Chory, *Nat. Rev. Genet.* **9**, 383–395 (2008).
13. S. A. Frank, L. D. Hurst, *Nature* **383**, 224 (1996).
14. P. Innocenti *et al.*, *Science* **332**, 845–848 (2011).
15. N. J. Gemmell *et al.*, *Trends Ecol. Evol.* **19**, 238–244 (2004).

Acknowledgments: We thank J. Abbott and a reviewer for helpful discussion. K.R. was funded by the VolkswagenStiftung, D.K.D. by the Australian Research Council through fellowship and grants and by Monash University, and E.H.M. by a Royal Society University Research Fellowship and the European Research Council (grant 280632).

Supplementary Materials

www.sciencemag.org/cgi/content/full/341/6152/1345/DC1

10.1126/science.1237146

STRUCTURAL BIOLOGY

A New Bundle of Prospects for Blocking HIV-1 Entry

A crystal structure of the HIV-1 co-receptor CCR5 with a bound inhibitor may assist the rational improvement of small-molecule inhibitors.

P. J. Klasse

Undulating seven times across the cell surface, thus positioning its amino-terminal head and three humps outside and three other humps and its carboxy-terminal tail inside the cell, a G protein–coupled receptor (GPCR) may conjure up images of the Loch Ness monster. But unlike Nessie, GPCRs are ubiquitous, mediating physiological functions from vision and smell to fight-or-flight responses and inflammation. Only a few high-resolution structures of GPCRs are available (*1*, *2*). The main HIV-1 co-receptors, CXCR4 (C-X-C chemokine receptor type 4) and CCR5 (C-C chemokine receptor type 5) are GPCRs. Wu *et al*. previously solved the structure of CXCR4 (*1*). On page 1387 of this issue, Tan *et al*. (*3*) present a 2.7 Å–resolution crystal structure of CCR5, the co-receptor most frequently used by HIV-1 strains for entry into the cell.

The authors solved the structure for the complex between an inhibitor of HIV-1 entry, maraviroc (MVC), and a detergent-solubilized engineered form of CCR5 that is stabilized by several modifications. MVC is an allosteric inhibitor: Its binding site differs from those of the molecules it blocks; it acts indirectly by changing the overall shape of the receptor. Although the CXCR4 structure was solved for complexes containing more direct inhibitors of interactions with the HIV-1 envelope glycoprotein (Env) (*1*), its bundle of seven transmembrane helices resembles that in the newly solved CCR5 structure with the allosteric inhibitor (*3*).

But there are also important differences between the two structures. MVC penetrates deeply into a pocket lined by residues from six of the seven transmembrane helices; the CXCR4 inhibitor inserts itself less profoundly. The helices differ in tilt in the two structures, yielding domino effects through the network of connections among the amino-terminal segment and the extracellular loops (ECLs). The upshot is that ECL2 and the amino-terminal segment partly cover the ligand-binding pocket in CXCR4, whereas the binding pocket of CCR5 remains more open. The amino-terminal part and ECL2 are also crucial to Env and chemokine interactions, which will be affected by the differential bonding and positioning of these elements.

HIV-1 virions are studded with Env trimers of hetero-dimers, each consisting of an outer subunit (gp120) that is anchored by the transmembrane moiety (gp41) in the viral membrane (*4*). Binding of Env to the cell-surface receptor CD4 enables interactions with a co-receptor, CXCR4 or CCR5, triggering drastic changes in the whole Env complex. These changes drive the eventual fusion of the viral with the cellular membrane (see the figure, panel A) (*5*, *6*).

Gp120 contacts CCR5 at multiple points. The tip of the variable V3 region in gp120 interacts with ECL2, whereas the base of V3, together with a nearby minidomain, juxtaposes the amino-terminal segment of the receptor (see the figure) (*7*). In spite of the other contacts with gp120, residues in V3 determine the usage of CCR5 or CXCR4, designated, respectively, the R5 or X4 phenotype of the virus (*8*). Modeling the insertion of R5-V3 or X4-V3 sequences into either co-receptor structure elegantly explains co-receptor usage: Favorably located residues in X4-V3 and CXCR4 attract each other; R5-V3 bonds well only in CCR5; the mismatched combinations, in contrast, yield weak bonds and numerous steric clashes (*2*).

Part of this elegance is surprising. Tan *et al*.'s structure, although modeled without the allosteric inhibitor for the simulated V3 insertions, was solved in the inhibited conformation (see the figure, panel B). Therefore, it is not expected to interact productively even with the matching R5 Env; regular HIV-1 of the R5 phenotype cannot enter cells in the presence of MVC. But under selective pressure of the inhibitor the virus transcends this block, usually through mutations in V3, though sometimes in gp41 (*9*). Future research may elucidate whether R5-V3 fits better into an uninhibited form of CCR5 and whether V3 from inhibitor-resistant mutants can take advantage of the altered binding site in the allosterically shifted co-receptor conformation.

Viral escape from CCR5 inhibitors is convoluted and intriguing. Some HIV-1 mutants that partly overcome the inhibitor block of CCR5 usage display peculiar dome-

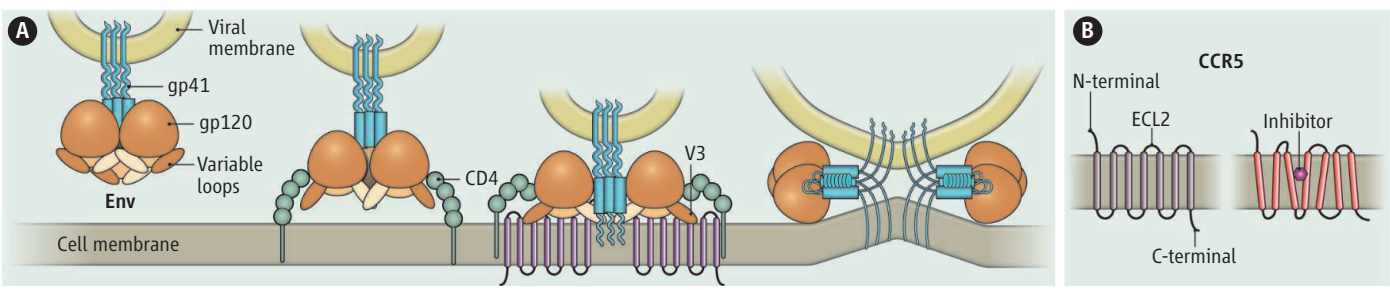

CREDIT: P. HUEY/*SCIENCE*

The role of CCR5 in HIV-1 entry. (**A**) An Env trimer, with its gp120 subunits anchored by gp41 in the viral membrane, contacts the CD4 receptor on the cell surface. A co-receptor binding site is induced involving the V3 loop of gp120. The co-receptor, here CCR5, triggers further conformational changes; gp41 inserts itself into the cell membrane and refolds into a bundle, driving the fusion. The number of trimers required for fusion is unknown (*6*); only two are shown. (**B**) CCR5 has seven transmembrane helices. The amino-terminal segment and the second extracellular loop (ECL2) interact with Env. To the right, CCR5 is shown with an allosteric inhibitor—such as MVC in the structure solved by Tan *et al*.—that has shifted the conformation of CCR5 and thereby blocks HIV-1 entry.

Department of Microbiology and Immunology, Weill Cornell Medical College, Cornell University, New York, NY 10065, USA. E-mail: pek2003@med.cornell.edu

Published by AAAS

shaped inhibition curves (*6*, *10*). This can be explained if cell-surface CCR5 exists in different forms with different affinities for the inhibitor, and if the mutant virus can use both the low-affinity form with the inhibitor bound and the high-affinity form without it (*6*, *10*). Indeed, diverse evidence suggests that CCR5 on the cell surface is highly heterogeneous (*11*). The heterogeneity might arise from differential posttranslational modification, conformational influences of the cell-membrane microenvironment, interactions with the endocytic machinery, and the degree of coupling to G proteins (*6*, *12*). Then the relative prevalence of the conformers could be shifted by the binding of inhibitors.

Like many other inhibitors, MVC is an inverse agonist, i.e., it reduces the spontaneous signaling by CCR5 [compare (*13*)]. Tan *et al.*'s CCR5 structure explains the mechanism for this inactivation. MVC prevents helix movements that normally relay the ligand-induced conformational change to the interior of the cell. There, the G protein is prevented from its normal mode of binding by the effects of MVC on the packing of the helices in the bundle (*3*, *12*). This effect may be enhanced in the stabilized CCR5 mutant for which the structure was solved, but it nevertheless suggests that high-affinity MVC binding favors the G protein–uncoupled form of CCR5. That would not, however, exclude the possibility of lower-affinity interactions by at least some small-molecule CCR5 inhibitors with G protein–coupled forms, yielding complexes that resistant virus can use as co-receptors (*10*).

The new CCR5 structure sheds mechanistic light not only on HIV-1 co-receptor selectivity, but also on the allosteric inhibition of Env and chemokine interactions, as well as on the inverse agonism of inhibitors. The new structural knowledge sets the stage for rational design of improved small-molecule CCR5 inhibitors of R5 HIV-1 entry. Ultimately, knowledge of how the entire Env trimer (*14*, *15*), after binding CD4, interacts with co-receptors may usher in the tailoring of receptor mimicry to inactivate Env irreversibly. Structural knowledge of these beasts will thus help us tame them and prevent their coupling.

References and Notes

1. B. Wu *et al.*, *Science* **330**, 1066 (2010).
2. T. M. Blois, J. U. Bowie, *Protein Sci.* **18**, 1335 (2009).
3. Q. Tan *et al.*, *Science* **341**, 1387 (2013) 10.1126/science.1241475.
4. M. A. Checkley *et al.*, *J. Mol. Biol.* **410**, 582 (2011).
5. R. A. Weiss, *BMC Biol.* **11**, 57 (2013).
6. P. J. Klasse, *Cell. Microbiol.* **14**, 1183 (2012).
7. C. C. Huang *et al.*, *Science* **317**, 1930 (2007).
8. O. Hartley, P. J. Klasse, Q. J. Sattentau, J. P. Moore, *AIDS Res. Hum. Retroviruses* **21**, 171 (2005).
9. J. P. Moore, D. R. Kuritzkes, *Curr. Opin. HIV AIDS* **4**, 118 (2009).
10. C. G. Anastassopoulou, T. J. Ketas, P. J. Klasse, J. P. Moore, *Proc. Natl. Acad. Sci. U.S.A.* **106**, 5318 (2009).
11. R. Berro *et al.*, *J. Virol.* **85**, 8227 (2011).
12. T. W. Schwartz, T. P. Sakmar, *Nature* **477**, 540 (2011).
13. M. M. Rosenkilde, T. W. Schwartz, *Mol. Pharmacol.* **3**, 602 (2000).
14. J. Liu *et al.*, *Nature* **455**, 109 (2008).
15. R. Pejchal, I. A. Wilson, *Curr. Pharm. Des.* **16**, 3744 (2010).

Acknowledgments: The author's work in this area is supported by NIH grants R01 AI41420 and P01 AI82362.

Published online 12 September 2012;
10.1126/science.1245384

CHEMISTRY

Lewis Acids with a Difference

A fluorinated phosphorus Lewis acid may find application in fluorocarbon remediation.

François P. Gabbaï

Lewis acids are electron-pair acceptors that readily bind electron-rich molecules and anions. Examples include fluorinated organoboranes such as **1** (see the first figure), which are widely used in synthesis, small-molecule activation, and catalysis (*1*–*4*), and silylium cations such as $\mathbf{2}^+$,which are powerful anion abstractors (*5*). Pentavalent group 15 fluorides such as PF_5 are another class of strong Lewis acids (*6*, *7*), but they react with water to release hydrogen fluoride, making them corrosive. In principle, these inconvenient properties could be tamed by introducing organic substituents, a strategy validated in the development of boron Lewis acids such as **1**. By analogy with silylium cation chemistry, the Lewis acidity of group 15 derivatives could be further enhanced if they were cations. Putting these ideas into practice, Caputo *et al*. report, on page 1374 of this issue, the synthesis and properties of the Lewis acid $[(C_6F_5)_3PF]^+$ [$\mathbf{3}^+$ (see the first figure)] (*8*).

Simple organophosphonium cations ($[R_4P]^+$) combine with fluoride in non-coordinating solvents or in the gas phase to give the corresponding fluorophosphoranes (R_4P-F) (*9*, *10*). When dissolved in polar solvents, these species readily dissociate, leading to the release of a fluoride anion and regeneration of the phosphonium ion. Hence, although coordination of a fluoride anion to the phosphorus center of a phosphonium ion is possible, the P-F bond is weak and easily perturbed by subtle changes in the environment. A similar conclusion is derived from the structure of molecules with adjacent fluoroborate and phosphonium units, for which the donation of a fluoride lone pair into a vacant phosphorus orbital has been observed (*11*).

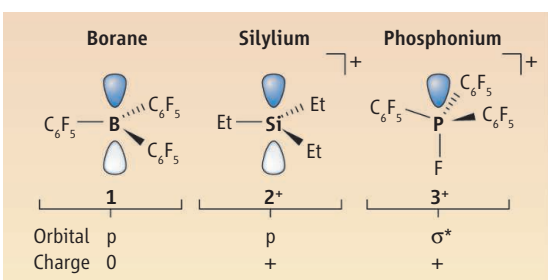

Lewis acids. In contrast to its borane (**1**) and silylium (**2**) predecessors, the organophosphorus Lewis acid $\mathbf{3}^+$ reported by Caputo *et al*. has an empty σ* orbital.

Caputo *et al*. alter this situation by introducing a set of electron-withdrawing ligands at the phosphorus center of $\mathbf{3}^+$. Three ligands are pentafluorophenyl groups, whose steric bulk helps to kinetically stabilize the compound. The fourth ligand is a fluorine atom, which forms a highly polar bond with the phosphorus center. Associated with this polar P-F bond is a phosphorus-centered coordination site defined by a σ*(P-F) orbital whose main lobe protrudes in a direction opposite from the fluorine atom (see the second figure). Electron-rich species (Lewis bases) are drawn to this site, where they donate a pair of electrons into the vacant σ* orbital (see the second figure).

Caputo *et al*. show that this process occurs with neutral Lewis bases such as dimethylformamide (DMF) and $Et_3P{=}O$, which can donate a lone pair from the terminal oxygen atom. The drive for coordination of Lewis bases to the phosphorus center is even stronger in the case of fluoride anions,

Department of Chemistry, Texas A&M University, College Station, TX 77843, USA. E-mail: francois@tamu.edu

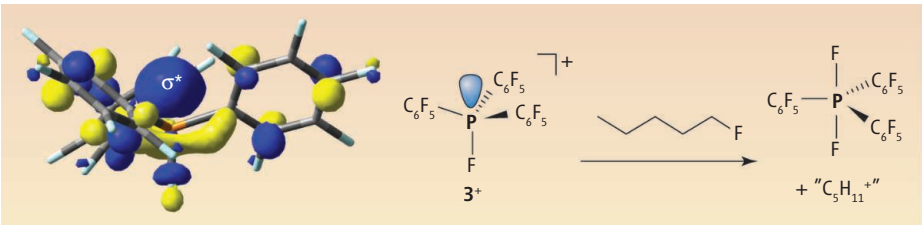

Lewis acidity at work. The fluorinated phosphonium cation 3^+ reported by Caputo *et al*. is a powerful Lewis acid that can cleave the C-F bonds of fluoroalkanes (**right**). This high Lewis acidity originates from the presence of a vacant coordination site defined by an empty σ* orbital whose main lobe is centered on the phosphorus atom (**left**).

which readily interact with 3^+ to form the difluorophosphorane $(C_6F_5)_3PF_2$. The thermodynamic drive for this reaction is so strong that 3^+ can abstract a fluoride anion from comparatively inert fluorocarbons (see the second figure), a class of molecules that, when volatile, contribute to the greenhouse effect. This fluoride abstraction reaction, which involves activation of a C-F bond, can be carried out in the presence of a hydride donor such as a trialkylsilane. Under these conditions, fluorocarbons are catalytically converted into alkanes through a process known as hydrodefluorination.

Cation 3^+ is not as effective as the silylium-based hydrodefluorination catalysts pioneered by Douvris and Ozerov (*12*), but it nonetheless has a number of unique features that could make this class of Lewis acids attractive as reagents and catalysts. One key point is that the phosphorus center of 3^+ has a full valence of eight electrons. As a result, salts of 3^+ are more stable and easier to handle than their silylium counterparts. The compound also contains ^{31}P and ^{19}F nuclei, making its chemistry easy to follow with nuclear magnetic resonance.

The results described by Caputo *et al*. go beyond the simple discovery of a new Lewis acid. They set the stage for broader developments in the chemistry of cationic Lewis acids containing phosphorus and other group 15 elements. For example, an antimony compound was recently used for the fluorescence sensing of fluoride in water at part-per-million concentrations (*13*). Such compounds may also find applications in asymmetric synthesis. The tetrahedral geometry of these cations should lead to increased steric interactions with incoming substrates—a phenomenon that could be exploited for asymmetric induction if chirality is present at the group 15 element.

References and Notes

1. E. Y.-X. Chen, T. J. Marks, *Chem. Rev.* **100**, 1391 (2000).
2. G. Erker, *Dalton Trans.* **2005**, 1883 (2005).
3. W. E. Piers, *Adv. Organomet. Chem.* **52**, 1 (2004).
4. D. W. Stephan, *Dalton Trans.* **2009**, 3129 (2009).
5. C. A. Reed, *Acc. Chem. Res.* **43**, 121 (2010).
6. G. A. Olah, *J. Org. Chem.* **70**, 2413 (2005).
7. I. Krossing, I. Raabe, *Chemistry* **10**, 5017 (2004).
8. C. B. Caputo, L. J. Hounjet, R. Dobrovetsky, D. W. Stephan, *Science* **341**, 1374 (2013).
9. H. Schmidbaur, K. H. Mitschke, J. Weidlein, *Angew. Chem. Int. Ed. Engl.* **11**, 144 (1972).
10. A. Kornath, F. Neumann, H. Oberhammer, *Inorg. Chem.* **42**, 2894 (2003).
11. T. W. Hudnall, Y.-M. Kim, M. W. P. Bebbington, D. Bourissou, F. P. Gabbaï, *J. Am. Chem. Soc.* **130**, 10890 (2008).
12. C. Douvris, O. V. Ozerov, *Science* **321**, 1188 (2008).
13. I.-S. Ke, M. Myahkostupov, F. N. Castellano, F. P. Gabbaï, *J. Am. Chem. Soc.* **134**, 15309 (2012).

Acknowledgments: Supported by NSF grant CHE-1300371 and Welch Foundation grant A-1423.

10.1126/science.1244423

CELL SIGNALING

Concentrating (on) Native Proteins to Control Cell Fate

Synthetic genetic controllers modulate endogenous signaling networks to route cells toward desired behaviors.

Casim A. Sarkar

Synthetic biology has ambitious goals—to engineer and repurpose cells for applications ranging from medicine to energy (*1*, *2*). Such achievements require robust designs for programming cell behavior. Signaling pathways within cells integrate information from the environment to drive specific gene expression programs, so from an engineering perspective, these pathways represent prime interventional targets for harnessing control of cellular decision-making (*3*). The output of a signaling pathway ultimately depends on the dynamics of its constituents, which, in turn, are determined by their concentrations and interactions. Given that these properties are hard-wired into the genome of the organism, how might cell fate be artificially regulated without manipulating the host's DNA? On page 1358 of this issue, Galloway *et al*. (*4*) demonstrate that this can be accomplished by introducing synthetic genetic controllers into the host to modulate the activity of a native signaling pathway. Cell fate "rerouting" in yeast was accomplished by using these genetic controllers to conditionally increase the concentrations of key endogenous proteins in a mitogen-activated protein kinase (MAPK) pathway, thereby reshaping the signaling dynamics and cellular response without introducing new proteins into the network.

MAPK pathways are attractive targets for cell engineering because they are ubiquitously expressed in eukaryotic organisms and are vital cogs in the decision-making machinery, regulating cellular processes such as differentiation, proliferation, motility, and death (*5*). The concentrations of the constituent proteins in the MAPK cascade can vary substantially across organisms (*6*), which in turn can alter the signal-processing characteristics of the network (*7*).

Galloway *et al*. focused on a yeast mating behavior that is governed by a pheromone called α-factor. This stimulus activates a MAPK pathway that stops cell division and promotes a mating response. To identify concentration-dependent control points in this pathway, the authors increased the expression of individual signaling proteins in the network. In the absence of pheromone, they identified Ste4 as a protein whose overexpression results in pathway activation. In the pres-

Department of Biomedical Engineering, University of Minnesota, Minneapolis, MN 55455, USA. E-mail: csarkar@umn.edu

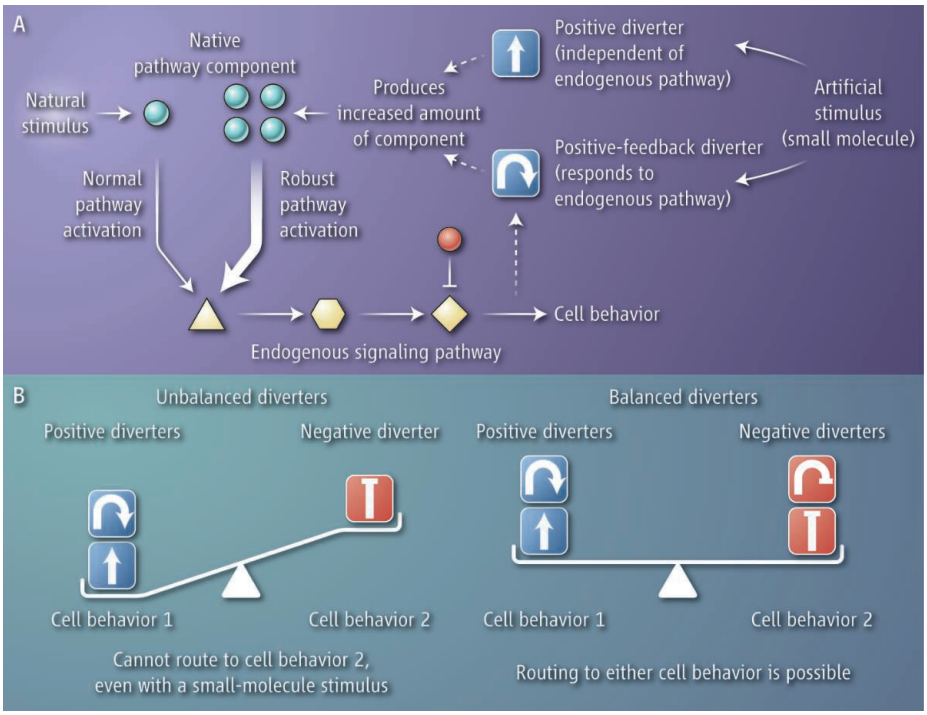

Controlling cell behavior with molecular network diverters. (**A**) A cell signaling pathway that is normally activated by a natural stimulus can be artificially controlled by increasing the expression of a key native pathway component. This can be accomplished by introducing "diverters" (synthetic genetic elements) into the cell that respond to an artificial stimulus. Positive diverters can increase pathway activity in the absence of a natural stimulus by increasing the concentration of a pathway activator (blue circle); negative diverters (not depicted) can decrease pathway activity in the presence of a natural stimulus by increasing the concentration of a pathway repressor (red circle). (**B**) A signaling network may be modulated by several diverters to enable conditional routing of a cell to multiple different fates, but this requires an appropriate balance of positive diverters (blue) and negative diverters (red) so that each small-molecule inducer has enough sway to redirect the cell toward the corresponding fate.

ence of α-factor, the authors identified Msg5 as a pathway constituent whose overexpression can override this pheromone and attenuate pathway activity.

To understand the effect of protein overexpression on signaling dynamics, it is also important to consider how the concentration is increased. One way to boost expression of a gene is to use a constitutive or pathway-independent genetic element called a promoter. With such a promoter, the concentration of the gene's corresponding protein can be increased without changing the topology of the signaling network. In synthetic MAPK cascades with the same network topology, varying the concentrations of pathway members can enable predictable tuning of the output response (*7*). Alternatively, gene expression can be enhanced using a pathway-responsive promoter. In this case, not only is the protein concentration increased, but the network structure is also changed by introducing a feedback loop. Endogenous MAPK pathways have been rewired using feedback-driven artificial protein interactions to rationally alter signaling dynamics (*8*).

To modulate protein concentrations, Galloway *et al*. constructed a series of molecular network "diverters." Each diverter consisted of three genetic elements: a pathway-independent or pathway-responsive promoter to control gene expression; a concentration-dependent pathway regulator (i.e., the gene encoding either the pathway activator Ste4 or the pathway repressor Msg5); and one or more transducers that enable small-molecule control of protein synthesis (*9*). These diverters were assembled in plasmids that were introduced into the yeast but remained separate from the host's native genetic material. The modular design of the diverters facilitates piecewise engineering of the component parts and their overall function enables conditional increase in expression of a key protein of interest, with or without network rewiring (see the figure).

Although Ste4 overexpression increases pathway activity, a diverter that drives constitutive expression of this protein with a small-molecule inducer only elicited weak routing to the mating fate (in the absence of the natural pheromone stimulus). However, by changing to a diverter in which expression of Ste4 was under control of a pathway-responsive promoter, a positive-feedback loop was created that robustly amplified the effects of Ste4 on the pathway. By contrast, for routing to the nonmating fate in the presence of both pheromone and a different small-molecule inducer, feedback-driven expression of Msg5 could not elicit the desired outcome, whereas constitutive expression of this protein could do so. Msg5 is a negative regulator of the MAPK pathway, so unlike Ste4, its effect is attenuated when its expression is driven by a pathway-responsive promoter.

What if a cell was engineered to harbor both of these diverters—that is, one for pathway-responsive expression of Ste4 and one for constitutive expression of Msg5? Could regulation of multiple cell behaviors be achieved? Galloway *et al*. tried this, but "background cross talk" got in the way—basal activity from the uninduced Msg5 diverter antagonized the ability of the Ste4 diverter to route the cell to the mating fate. Through computational modeling, the authors identified additional genetic elements that could enhance the function of the two original diverters while buffering against undesirable cross talk. Importantly, when combining diverters that act on the same signaling network to route cells toward different behavioral outcomes, their strengths must be appropriately balanced so that the small-molecule inducers can elicit the desired effects. For example, in the study by Galloway *et al*., a system with both constitutive and positive-feedback diverters for Ste4, but only the constitutive diverter for Msg5, was unbalanced. The mating phenotype could be induced with the appropriate small-molecule stimulus (in the absence of the natural pheromone stimulus), but the nonmating fate could not be induced in the presence of pheromone and the other small molecule. The final system design consisted of two genetic controllers for the expression of Ste4 and two for the expression of Msg5 (one constitutive and one pathway-responsive for each); this balanced structure enabled inducible cell fate routing in multiple directions.

To complement the promising strategy developed by Galloway *et al*., methods could be developed to further streamline its implementation. Identification of key control nodes in a signaling pathway of interest may be guided by computational modeling and sensitivity analyses (*10*). This can be useful when working with a network containing many proteins or a network whose activity may be largely insensitive to overexpression of individual proteins but sensitive to simultaneous perturbation of two or more proteins. Exper-

CREDIT: H. MACDONALD/*SCIENCE*

imentally, directed evolution is a powerful optimization tool (*11*) that may be useful in refining promoter and transducer sequences to achieve the desired balance among diverters.

Galloway *et al*. demonstrate that natural cell signaling pathways can be coaxed to elicit desired cell fate outcomes using molecular network diverters. The approach does not require new protein components to achieve this control, but instead relies on conditionally augmenting the concentrations of existing signaling proteins in the cell. Furthermore, this cellular reprogramming strategy can be implemented without manipulating the host's genome; rather, the native genetic material is supplemented with plasmids harboring the diverters. For synthetic biologists, these features should make the approach attractive for implementation in a variety of organisms, including higher eukaryotes.

References and Notes

1. P. E. M. Purnick, R. Weiss, *Nat. Rev. Mol. Cell Biol.* **10**, 410 (2009).
2. A. S. Khalil, J. J. Collins, *Nat. Rev. Genet.* **11**, 367 (2010).
3. E. C. O'Shaughnessy, C. A. Sarkar, *Curr. Opin. Biotechnol.* **23**, 785 (2012).
4. K. E. Galloway *et al*., *Science* **341**, 1235005 (2013); 10.1126/science.1235005.
5. J. Avruch, *Biochim. Biophys. Acta* **1773**, 1150 (2007).
6. J. E. Ferrell Jr., *Trends Biochem. Sci.* **21**, 460 (1996).
7. E. C. O'Shaughnessy *et al*., *Cell* **144**, 119 (2011).
8. C. J. Bashor *et al*., *Science* **319**, 1539 (2008).
9. M. N. Win, C. D. Smolke, *Proc. Natl. Acad. Sci. U.S.A.* **104**, 14283 (2007).
10. B. B. Aldridge *et al*., *Nat. Cell Biol.* **8**, 1195 (2006).
11. Y. Yokobayashi, R. Weiss, F. H. Arnold, *Proc. Natl. Acad. Sci. U.S.A.* **99**, 16587 (2002).

Acknowledgments: Supported by the NSF (MCB-1154509) and the University of Minnesota.

10.1126/science.1243994

MATERIALS SCIENCE

Polymers Find Plenty of Wiggle Room at the Bottom

The glassy dynamics of an isolated polymer chain is found to be identical to that of a bulk material.

Thomas P. Russell

In his 1959 lecture "There's Plenty of Room at the Bottom," Richard Feynman discussed the prospects of developing future nanoscale technologies (*1*). There, he stated that the homogeneous properties of amorphous plastics and glasses would render them the materials of choice for such applications. Today, polymeric materials—particularly glassy, noncrystalline polymers—do play a key role in the manufacturing sector, but these tend to be bulk materials. Realizing Feynman's vision of nanomachines based on polymers would require an understanding of the properties of polymeric materials as they are shrunk to comprise a few or even single polymer chains. But the characterization of such nanoscopic amounts of material, and how they may differ (or not) from the bulk, remains a challenging and controversial area. On page 1371 of this issue, Tress *et al*. (*2*) have developed a technique using a nanoelectrode and broadband dielectric spectroscopy (BDS) to characterize tiny volumes of polymers and isolated polymer chains. Their results lead to the remarkable conclusion that the glassy dynamics of an isolated polymer chain is identical to that seen in the bulk.

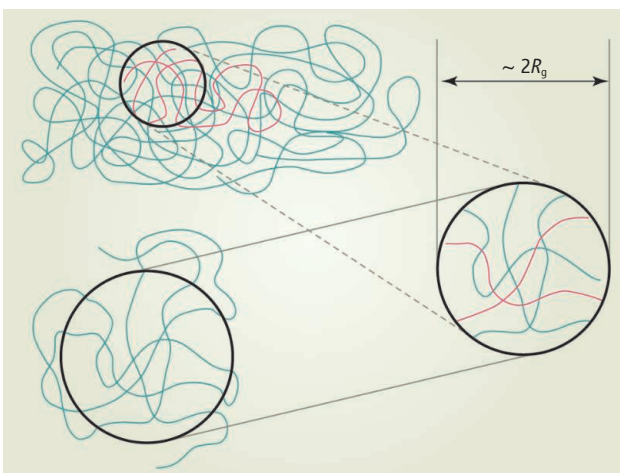

A close up view. The sphere shows a volume taken from bulk polymer defined by the dimension of a single chain. The ends of the segments can then be connected to get a single chain. Tress *et al*. (*2*) find that these behave in the same way.

Nanoimprint lithography, step-and-flash lithography, templating for bit-patterned media or low–dielectric constant materials, organic photovoltaics, and batteries are just a few examples where polymers can be molded into nanoscopic objects, or where the polymer self-assembles into a morphology with nanoscopic features, or where a morphology is kinetically trapped at nanoscopic length scales. As the size scale of the features decreases, we must remain cognizant that they are comparable to or even less than the radius of gyration of the polymer chain, R_g—a characteristic dimension that describes the volume pervaded by an unperturbed polymer chain in the bulk. Consequently, with decreasing size, there must be some compression or stretching of the polymer chain to accommodate the confining geometry. This deformation comes at the cost of an elastic retractive force, a very strong entropic force that we are all familiar with from stretched rubber bands. As objects get smaller, the surface-to-volume ratio increases and interfaces play an ever more important role. Because polymers are incompressible, we must understand how the change in density of the polymer at an interface is accommodated by the long-chain molecules, particularly those with a center of mass that is located within one radius of gyration (or less) from the interface. How does the presence of a surface or interface influence the configuration of the polymer chain and the dynamics of the polymer either in segments or as a full chain? Equally important is the fact that synthetic polymers, regardless of the method of synthesis, have a finite molecular weight distribution, which translates into a distribution of molecular sizes and therefore a distribution in the response of different chains to confinement.

The ability to assess the properties of nanoscopic elements (structural, electrical, magnetic, optical, etc.) has given rise to many exceptional developments in tools to probe isolated nanoscopic elements, as well as the creative use of existing tools to measure collections of nanoscopic elements. Synchrotron sources and free electron lasers provide suffi-

Polymer Science and Engineering Department, University of Massachusetts, Amherst, MA 01003, USA, and Advanced Institute of Materials Research, Tohoku University, 2-1-1 Katahira, Aoba, Sendai 980-8577, Japan. E-mail: russell@mail.pse.umass.edu

cient flux to characterize even the smallest of crystals, where the diffraction can be recorded before the sample is destroyed. By coupling the isotopic labeling of polymer chains with deuterium to sample geometries that place multiple samples in a neutron beam, small-angle neutron scattering—a technique normally used for the characterization of materials in the bulk or solution—has enabled the characterization of polymer chains in thin films in cylindrically confined geometries (*3*, *4*). In general, the polymer chains are found to minimize chain distortion while sacrificing a compression in one dimension. Dielectric spectroscopy, for example, has been used to probe the ferroelectric properties of 80 attograms (10^{-18} g) of a polymer, corresponding to ~480 polymer chains, confined within cylindrical pores 40 nm in diameter in an alumina membrane (*5*). The geometry of the measurement enabled the simultaneous measurement of ~4×10^9 independent samples, providing a statistically averaged property of the polymer within the membrane.

Tress *et al*. show that when the BDS dipolar fluctuations, which reflect segmental motions, are measured over a broad frequency and temperature range, they can provide insight into the molecular dynamics and phase transitions. The glassy dynamics of a condensed isolated polymer chain is found to be identical to that seen in the bulk.

The segmental and long-range motions markedly slow down as the calorimetric glass transition temperature T_g is approached. The dynamic glass transition (α-relaxation) is assigned to fluctuations of two or three segments (*6*) that reach a typical relaxation rate of 10^{-2} Hz at this temperature. If we look at a volume in the bulk (see the figure) with a diameter of $2R_g$, parts of many chains are included with this volume. Highlighting one in red, the motions of the red chain in a sea of blue chains depend on both intramolecular and intermolecular relaxations. If this volume is pulled out and the ends of all the chains linked, then we essentially have an isolated single chain. This is simple enough conceptually but requires a tour de force to realize. By spin-coating a polymer from a very dilute polymer solution, Tress *et al*. isolated polymer droplets with a volume that corresponds to the occupied volume of a single polymer chain. Under these conditions, the density of the droplet is equal to the bulk density, and the dynamic glass transition determined by BDS is essentially identical to the bulk. This can be understood, because the length scale on which the α-relaxation takes place (~0.5 nm) is small relative to the dimensions of the chain as a whole or the size of the droplet. The only observed difference is a broadening of the BDS relaxation on the low-frequency side, which arises from a slowing down in the dynamics of the polymer at the polymer-substrate interface. They argue that this constitutes ~25% of the total volume. Other than that, the α-relaxation remained the same as the bulk with no influence of the exposed free surface.

The findings reported by Tress *et al*. are important when considering the use of polymers in nanotechnology, but will be met with a degree of skepticism from those who hold that the free surface causes a reduction in T_g. The challenge now is to develop other, noninvasive methods to confirm these findings or, better yet, demonstrate the ramifications of these findings in an application.

References

1. R. P. Feynman, *Eng. Sci.* **23**, 22 (1960).
2. M. Tress *et al*., *Science* **341**, 1371 (2013).
3. A. Serghei *et al*., *Soft Matter* **6**, 1111 (2010).
4. K. Shin *et al*., *Nat. Mater.* **6**, 961 (2007).
5. A. Serghei *et al*., *Nano Lett.* **13**, 577 (2013).
6. I. Bahar *et al*., *Macromolecules* **25**, 816 (1992).

10.1126/science.1244110

IMMUNOLOGY

Pasteur Approach to a Malaria Vaccine May Take the Lead

A rationalized and reinvented approach to vaccinating against malaria shows impressive results.

Michael F. Good

Malaria is an infectious disease that is responsible for more loss of young lives than any other health condition. Eighty percent of the cases and nearly 1 million deaths from malaria occur in Africa each year. Although mortality has decreased in recent years, more must be done to improve and save the lives of sufferers. On page 1359 of this issue, Seder *et al.* (*1*) report that an attenuated form of the causative parasite can be administered intravenously and provide protection against malaria, taking us a step closer to achieving the goal of an effective vaccine.

Malaria is caused by parasitic protozoans of the genus *Plasmodium*. The disease is transmitted when the bite of an infected *Anopheles* mosquito transfers the microorganisms (in the form of sporozoites) from its saliva into a person's blood stream. Sporozoites infect liver cells and multiply into merozoites, which return to the circulation and infect red blood cells. There, they produce more merozoites or develop sexual forms that can be taken up by a mosquito and continue the life cycle (see the figure).

Since the first half of the 20th century, a vaccine has been heralded as the great hope for eradicating malaria. Initial attempts were inspired by the Pasteur approach of producing bacterial vaccines by inactivating the infectious agent, but formalin-inactivated malaria sporozoites failed to induce protection. At that time, it was not known that the parasite had a liver stage nor that sporozoites must be motile and present in large numbers to invade the liver cells and trigger immunity. Then, in the 1940s, lethal malaria in monkeys was prevented with inactivated merozoites and a potent immune-stimulating "adjuvant" as a vaccine (*2*). But the toxicity of the adjuvant and the inability to obtain sufficient parasites from human blood to make the vaccine rendered this approach untenable. However, in 1967, in a major advance, malaria sporozoites extracted from salivary glands of infected mosquitoes and then irradiated induced immunity in mice without the need for an adjuvant (*3*). Similar findings were demonstrated in human volunteers exposed to irradiated mosquitoes infected with human malaria parasites (*4*, *5*). Because the sporozoites and mosquitoes were irradiated, the mice and the volunteers did not acquire malaria, but their immune cells mounted a response that could protect them from subsequent infection.

Although highly promising, this approach to a human vaccine lay dormant for more than 30 years due largely to the difficulties of harvesting sufficient parasites and to

Institute for Glycomics, Griffith University, Gold Coast 4222, Australia. E-mail: michael.good@griffith.edu.au

the development of technology to clone *Plasmodium* antigens (*6*, *7*). The latter ushered in the "subunit" phase of malaria vaccine research. It was hoped that individual parasite proteins and modern, safe adjuvants would be effective—an approach that has been widely successful for vaccines against various infectious diseases.

Indeed, a subunit malaria vaccine candidate (called RTS,S and based on the coat protein of sporozoites of the major human parasite *Plasmodium falciparum*) aims to stimulate the production of antibodies to kill the parasite after it is inoculated by the mosquito and before it reaches the liver. This vaccine is in phase III clinical trials in various African countries (*8*, *9*). However, both the efficacy (30 to 50%) and the duration of protection (a few months) are limited. Nevertheless, it is the lead candidate of all the subunit vaccines that are currently under development. RTS,S and other single-antigen vaccine candidates suffer from insufficient immunogenicity and/or from the high polymorphism of the individual malaria proteins on which they are based, enabling the malaria parasite to easily evade immune surveillance.

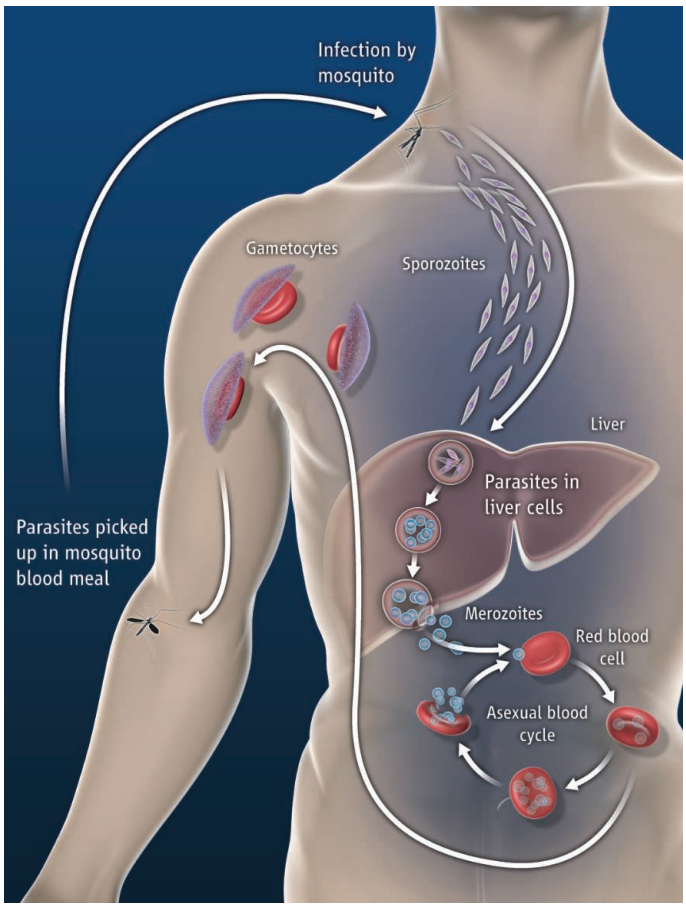

Attacking a very old problem. The malaria life cycle is shown. A high dose of irradiated sporozoites delivered intravenously shows promising results as a vaccine.

About 10 years ago, the irradiated sporozoite-and-mosquito approach to make a vaccine was revisited—but with a twist: The falciparum sporozoites were dissected manually from the salivary glands of mosquitoes, irradiated, and cryopreserved before inoculation (*10*). Dissected, irradiated sporozoites had never before been administered to humans. Initial experiments found the approach safe in humans but showed only modest immune responses after intradermal or subcutaneous inoculation and only a small percentage were protected from a challenge infection (*11*). However, in that study, rhesus macaques were also immunized but by the intravenous route as well as the subcutaneous route. *P. falciparum* sporozoites can invade hepatocytes of macaques (as in humans), but the merozoites that emerge from the monkey's liver cannot invade their red blood cells to continue the life cycle. Thus, although macaques cannot develop a blood infection, they can be used to study the immune responses that develop during a liver-stage infection. Surprisingly, intravenous inoculation resulted in far superior responses within the T cells taken from liver tissue of macaques compared to the subcutaneous route. T cells are believed responsible for generating immunity to the liver stages of the parasite (*12*, *13*).

With this knowledge, Seder *et al*. embarked on a human intravenous vaccination protocol. They found that high doses of irradiated sporozoites delivered intravenously protected six out of six volunteers, placing this vaccine in a most favorable position compared to all other vaccine candidates for advancing into further stages of development. At the next lower dose of sporozoites, six out of nine individuals were protected. Those who received the most sporozoites and who demonstrated the greatest levels of protection had higher antibody titers and more robust T cell (CD4 and CD8) responses. Although numbers were small, the strongest correlate with protection was the development of memory CD8 T cells that produced the cytokine interferon-γ, which is critical for immunity against many pathogen infections. This response to whole-parasite antigenic material underscores a major strength and the rationale behind a whole-parasite approach to malaria vaccines as all 1000+ protein antigens expressed in the sporozoite can potentially be targets of immunity.

Despite the very encouraging results, many challenges remain before this vaccine might be licensed for widespread use. Seder *et al*. required more than 600,000 sporozoites per subject to induce complete immunity. An infected mosquito might contain at most a couple of hundred thousand sporozoites. High-throughput mechanical dissection of mosquitoes may be possible, and viability of sporozoites may be increased by improved cryopreservation. Alternatively, other ways to render sporozoites nonreplicative and safe might lead to increased vaccine potency (*14*–*16*). The vaccine requires delivery by the intravenous route; how that will affect compliance has yet to be determined. Another major issue is whether this vaccine will protect against multiple strains of *P. falciparum*. From an antigenic view, parasites from no two patients are identical. But a distinct advantage of a "whole parasite" vaccine is that every protein of the parasite is represented, reducing the effect of polymorphism in any one protein. Another important issue is the duration of protection after immunization. In the study of Seder *et al*., volunteers received a challenge infection only 3 weeks after the final vaccination. These hurdles are not insurmountable, and further investigations could happen relatively quickly; if the results are promising, then a vaccine could be ready for limited use in a fairly short time frame.

References and Notes

1. R. A. Seder *et al*., *Science* **341**, 1359 (2013); 10.1126/science.1241800.
2. J. Freund *et al*., *Am. J. Trop. Med. Hyg.* **28**, 1 (1948).
3. R. S. Nussenzweig *et al*., *Nature* **216**, 160 (1967).
4. D. F. Clyde *et al*., *Am. J. Med. Sci.* **266**, 169 (1973).
5. K. H. Rieckmann *et al*., *Trans. R. Soc. Trop. Med. Hyg.* **68**, 258 (1974).
6. D. J. Kemp *et al*., *Proc. Natl. Acad. Sci. U.S.A.* **80**, 3787 (1983).
7. J. Ellis *et al*., *Nature* **302**, 536 (1983).
8. S. Casares *et al*., *Vaccine* **28**, 4880 (2010).
9. S. T. Agnandji *et al*., *N. Engl. J. Med.* **367**, 2284 (2012).
10. T. C. Luke, S. L. Hoffman, *J. Exp. Biol.* **206**, 3803 (2003).
11. J. E. Epstein *et al*., *Science* **334**, 475 (2011).
12. L. Schofield *et al*., *Nature* **330**, 664 (1987).
13. W. R. Weiss *et al*., *Proc. Natl. Acad. Sci. U.S.A.* **85**, 573 (1988).
14. A. K. Mueller *et al*., *Nature* **433**, 164 (2005).
15. M. R. van Dijk *et al*., *Proc. Natl. Acad. Sci. U.S.A.* **102**, 12194 (2005).
16. L. A. Purcell *et al*., *Infect. Immun.* **76**, 1193 (2008).

10.1126/science.1244157

NEUROSCIENCE

Promiscuous Alzheimer's Amyloid: Yet Another Partner

A neuroimmune receptor has high affinity for Alzheimer's β-amyloid aggregates and mediates a synaptotoxic cascade in neurons.

Iryna Benilova and Bart De Strooper

Although genetic evidence puts the amyloid peptide (β-amyloid or Aβ) center stage in Alzheimer's disease (AD), it remains far from clear how this 4-kD protein fragment compromises neuronal function (*1*). On page 1399 of this issue, Kim *et al*. identify two new receptors for aggregated Aβ: the mouse paired immunoglobulin-like receptor B (PirB) and its human ortholog, leukocyte immunoglobulin-like receptor LilrB2 (*2*). The binding interaction triggers a signaling cascade that compromises the actin cytoskeleton of neurons and ultimately causes synaptic loss in a mouse model of AD.

PirB (see the figure) and LilrB2 are noncanonical major histocompatibility complex class I (MHC I) immune receptors, best known in the context of antigen presentation and T lymphocyte–mediated reactions. Some MHC I receptors are also found in the brain, where they interact with MHC I and regulate synaptic plasticity (*3*–*5*). One example of synaptic plasticity is ocular dominance plasticity (ODP), which is measured as the expansion of the visual brain area where the immediate early gene Arc is expressed in response to visual stimuli provided to one eye when the other is occluded (*2*, *6*). Kim *et al*. observed that impaired ODP is one of the earliest Aβ-induced deficits in a mouse model of AD (*6*). Because PirB plays a central role in ODP (*3*), Kim *et al*. asked whether Aβ could exert its neuropathological effects through perturbation of the PirB receptor.

In a series of in vitro assays, Aβ oligomers were shown to bind PirB, specifically and with nanomolar affinity, through two N-terminal immunoglobulin-like domains in the receptor. To determine the importance of the Aβ-PirB receptor interaction, the authors investigated the effects of removing PirB in paradigms of neuronal plasticity in mice. ODP and hippocampal long-term potentiation in brain slices, as well as behavioral tests of learning and memory in adult mice, showed that PirB knockout mice were protected against the toxic effects of Aβ. Thus, PirB contributes to Aβ-induced memory deficits in a mouse model of AD.

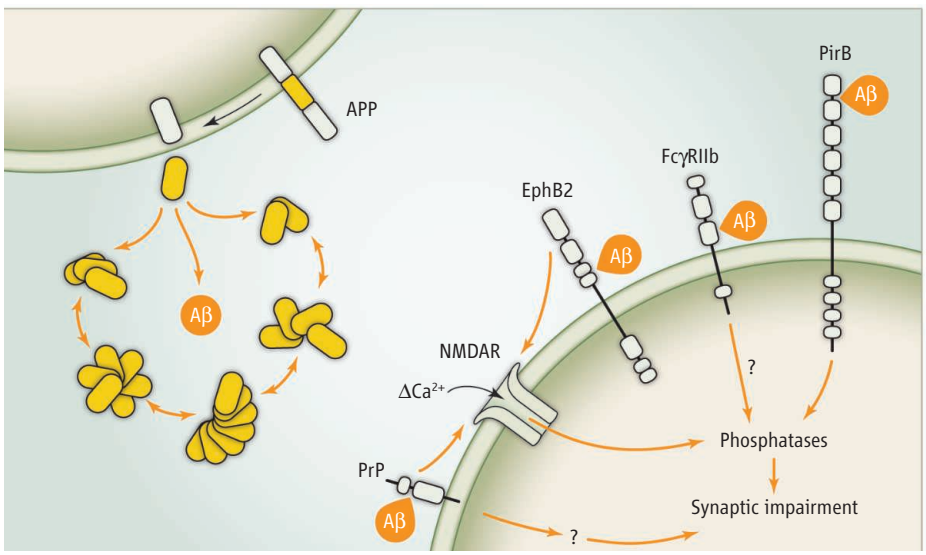

Receptor-mediated synaptotoxic pathways of the amyloid peptide, Aβ. Aβ monomers are cleaved from the amyloid precursor protein APP and form oligomers (of unknown composition) that engage with several candidate Aβ receptors (orange arrows indicate putative Aβ oligomer binding sites). Whereas Aβ signaling via PrP^C and EphB2 is thought to affect NMDA receptor function and Ca^{2+} influx, neuroimmune receptors FcγRIIB and PirB/LilrB2 are directly engaged in signaling cascades that lead to synaptic impairment. Note that NMDA receptor (NMDAR) is shown only as a Ca^{2+} channel for reasons of clarity.

Signaling through the PirB receptor in the immune system involves phosphorylation of immunoreceptor tyrosine-based inhibitory motifs (ITIMs) followed by recruitment of Src homology 2 (SH2) domains–containing tyrosine phosphatases SHP-1 and SHP-2 to the cytosolic domain of the receptor. This pathway of PirB signaling is conserved between the immune and the nervous system (*3*). However, tyrosine phosphorylation of PirB (and its association with SHP phosphatases) is apparently not involved in the signal transduction induced by Aβ engagement. Instead, the authors provide preliminary evidence that calcineurin, a PP2B serine/threonine phosphatase typically involved in synaptic depression and Aβ-mediated synaptotoxicity, is the mediator of the toxic effects.

The nature of the receptors that engage Aβ is not yet fully resolved and remains controversial in the Alzheimer's field (*7*). Among previously discovered Aβ receptors are ligand-gated ion channels [*N*-methyl-D-aspartate (NMDA) receptor, α7-acetylcholine receptor], receptor tyrosine kinases (insulin R, EphB2), cellular prion protein (PrP^C), the receptor for advanced glycation end products (RAGE) located at the blood-brain barrier, and another inhibitory neuroimmune receptor—the immunoglobulin G Fcγ receptor II-b (FcγRIIb) (*1*, *8*–*10*). For at least four of these (see the figure), experimental evidence shows that Aβ-impaired memory improves when the receptors are genetically deleted (PrP^C, FcγRIIb, PirB) or up-regulated (EphB2), providing credibility to the claim that modulation of these receptors could be beneficial for treatment of the disease.

If Aβ neurotoxicity is indeed caused by specific receptor-ligand interactions, then the neuroimmune receptor PirB is clearly a candidate for mediating at least some of the disease symptoms. The protein is expressed on the surface of neuronal cells, it has a high-affinity Aβ binding site, and it has well-characterized roles in signal transduction and synaptic inhibition. Furthermore, PirB and the Nogo receptor complex together repress

CREDIT: P. HUEY/*SCIENCE*

Vlaams Instituut voor Biotechnologie (VIB) Center for the Biology of Disease, 3000 Leuven, Belgium, and Center for Human Genetics and Leuven Institute for Neuroscience and Disease (LIND), University of Leuven (KU Leuven) and University Hospitals, 3000 Leuven, Belgium. E-mail: bart.destrooper@cme.vib-kuleuven.be

Published by AAAS

axonal outgrowth and neuronal regeneration via their interaction with myelin-associated inhibitors (*11*). That PirB appears to be responsible for only 50% of the binding of Aβ to neurons in culture echoes similar observations made with PrP^C (*12*) and suggests that other receptors also play a role in mediating Aβ neurotoxicity effects. Finally, engagement of this neuroimmune receptor might play a role in hypothetical immunological aspects of Aβ-mediated toxicity.

The plethora of Aβ receptors now identified has not yet resolved a nagging question in the field: What features characterize a canonical Aβ receptor? The crucial issue in this debate is the lack of definition of what is called "toxic" Aβ (*1*). Aβ preparations used for receptor discovery are typically generated by incubating monomeric Aβ peptides in buffer solutions. This results in heterogeneous mixes of monomers and various aggregates that are in dynamic equilibrium with each other. There is some evidence that more stable intermediates with specific conformations are formed, but it is unclear how these complex mixtures behave, and their standardization and fine structural characterization is lacking (*1*, *13*). Most of the identified Aβ receptors seem to prefer oligomeric forms of Aβ, but it is as yet unclear what these oligomeric species look like, or whether all identified receptors bind to the same oligomers. Finally, and perhaps most important, the structural basis of the Aβ oligomer–receptor interaction remains poorly characterized. Do the numerous "Aβ receptors" simply reflect the "sticky" nature of Aβ oligomeric species, or is there a particular "pathological conformation" in some of the putative oligomeric intermediates that promotes interaction with specific receptors? For instance, FcγRIIb has a preference for Aβ42 over Aβ40 oligomers, and the flexible N terminus in Aβ42 is important for its binding to FcγRIIb and for toxicity (*10*).

Even though PirB is a good candidate for pursuing the basis of Aβ neurotoxicity, the field must also get to grips with what is meant by "toxic" Aβ oligomers. Exchange of Aβ preparations and careful comparison of data across different laboratories is required (*1*, *13*). Of course, as has been noted elsewhere (*14*), the key question is not so much whether sticky Aβ oligomers bind a particular receptor, but whether such Aβ receptor–mediated pathways are functionally meaningful and can ultimately be used to create novel therapies.

References and Notes

1. I. Benilova et al., *Nat. Neurosci.* **15**, 349 (2012).
2. T. Kim *et al.*, *Science* **341**, 1399 (2013).
3. J. Syken, T. Grandpre, P. O. Kanold, C. J. Shatz, *Science* **313**, 1795 (2006).
4. T. Takai, *Immunology* **115**, 433 (2005).
5. G. S. Huh *et al.*, *Science* **290**, 2155 (2000).
6. C. M. William *et al.*, *J. Neurosci.* **32**, 8004 (2012).
7. I. Benilova, B. De Strooper, *Mol. Med.* **2**, 289 (2010).
8. Y. Verdier, M. Zarándi, B. Penke, *J. Pept. Sci.* **10**, 229 (2004).
9. M. Cissé *et al.*, *Nature* **469**, 47 (2011).
10. T. I. Kam *et al.*, *J. Clin. Invest.* **123**, 2791 (2013).
11. J. K. Atwal *et al.*, *Science* **322**, 967 (2008).
12. J. Laurén, D. A. Gimbel, H. B. Nygaard, J. W. Gilbert, S. M. Strittmatter, *Nature* **457**, 1128 (2009).
13. "State of aggregation" (editorial), *Nat. Neurosci.* **14**, 399 (2011).
14. R. Malinow, *Curr. Opin. Neurobiol.* **22**, 559 (2012).

Acknowledgments: B.D.S. is a consultant for Janssen Pharmaceutica, EnVivo Pharmaceuticals, and Remynd NV.

10.1126/science.1244166

EARTH SCIENCE

Causes of the Cambrian Explosion

The rapid diversification of animal species in the early Cambrian was the result of a range of interacting biotic and abiotic processes.

M. Paul Smith[1] and David A. T. Harper[2]

Many hypotheses have been invoked to explain the rapid diversification of animal species in the early Cambrian (541million to 515 million years ago), ranging from starbursts in the Milky Way to intrinsic genomic reorganization and developmental patterning. Recent hypotheses for the Cambrian explosion fall into three main categories: developmental/genetic, ecologic, and abiotic/environmental, with geochemical hypotheses forming an abundant and distinctive subset of the last (*1*). Most of these hypotheses have been posited as stand-alone processes that were the main cause of the explosion, yet many of them are tightly interlinked and codependent. The rapid diversification of animals in the early Cambrian is likely to have been the result of a complex interplay of biotic and abiotic processes (see the first figure).

One challenge relates to the precise definition of the explosion. Is it the first appearance of animal groups, their diversification, the emergence of marine ecosystems with "modern" trophic structures, or all of these? The timing of the diversification of animal groups is now fairly well known, allowing a clear distinction to be made between the first appearances of high-level animal crown groups in the Neoproterozoic (1000 million to 541 million years ago), followed by the main diversification of animal groups, a substantial increase in morphological disparity, and the emergence of complex food webs in the early Cambrian (*2*–*4*). Molecular clock estimates predict that the earliest members of many animal groups, including sponges, cnidarians, and bilaterians, lived 850 million to 635 million years ago. Yet molecular clocks and the fossil record together indicate that more than 100 extant animal phyla and classes first appeared in the Cambrian; only a handful predate the start of the Cambrian. Two events are thus distinguishable, with the origin of high-level animal groups temporally distant to the abrupt increase in diversity and disparity within the Cambrian—the Cambrian explosion in the strict sense (see the second figure).

One essential component of the Cambrian explosion is the advent of bilaterian developmental systems. Bilaterians are animals with a longitudinal plane of symmetry and specialized internal organ systems, and include most living animals with the notable exceptions of sponges, cnidarians, and some minor groups. It has been argued that the origin of the bilaterian gut and the ability to feed on large prey items (macrophagy) around 650 million years ago in turn enabled the evolution of large body sizes and skeletons in response to seabed predation pressures (*5*). This ignores, however, an apparent >100-million-year gap between the evolutionary innovation and its consequences. Developmental systems must have been in place to enable the macroevolutionary cascade, but the clues for the causes of the Cambrian diversification must lie closer to 540 million years. By then, stem bilaterians had already evolved the developmental tool kit to exploit the complex mosaic of opportunities that arose (*6*).

With macrophagy in place, the emergence of complex food webs was a crucial driver for diversity increase in the Cambrian

[1]Oxford University Museum of Natural History, Parks Road, Oxford OX1 3PW, UK. [2]Department of Earth Sciences, Durham University, Durham DH1 3LE, UK. E-mail: paul.smith@oum.ox.ac.uk

explosion (*1*, *7*), partly because of the tendency of burrowing organisms to modify the physicochemical properties of their substrates (ecosystem engineering) (*8*). In addition, it has been argued that the inherent "evolvability" of bilaterian animals and their tendency to induce escalatory arms races may account for much extant diversity (*7*). These types of feedback are manifest in the origins of planktic and free-swimming animals, burrowing, and biomineralization, which initially were new evolutionary products but rapidly became entrained in the diversification.

In the case of biomineralization, the presence of feedback loops is evidenced by the near-simultaneous appearance of both predatory and defensive hard tissues across a wide range of animal groups (*9*, *10*). These hard tissues mainly consist of two types of calcium biomineral, suggesting that the availability of calcium is an important aspect of the event. It has been argued that the emergence of complex food webs is the result of crossing a threshold or tipping point (*7*), but it may have been an end product of complex feedback loops (see the first figure).

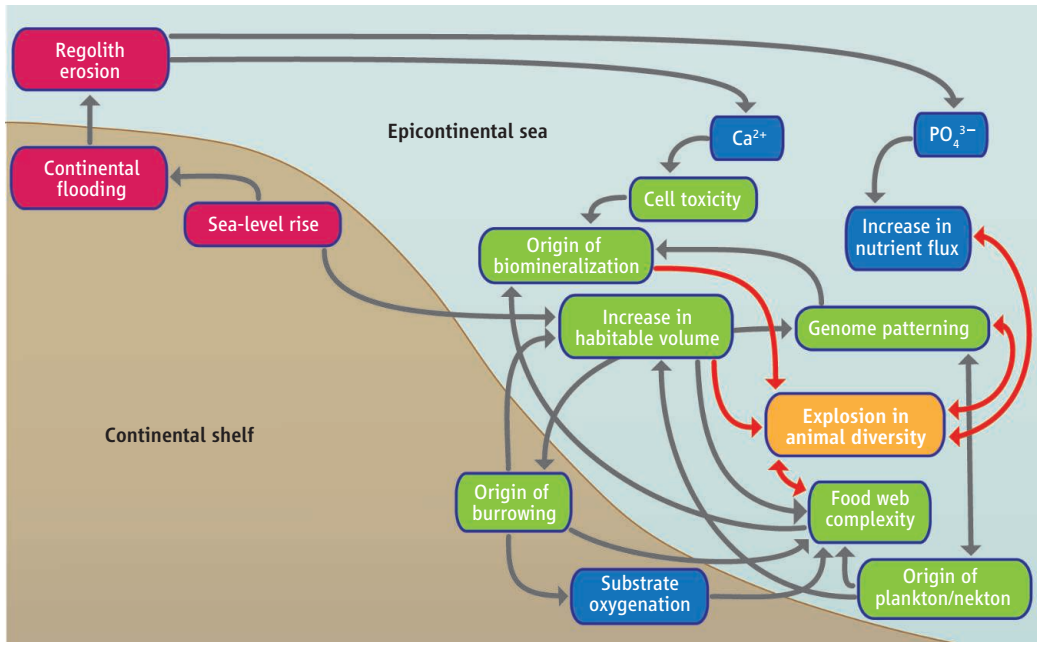

Interconnected causes. Earth system, developmental, and ecological processes have been hypothesized as isolated, singular causes of the major diversification of marine taxa early in the Cambrian. Instead, many of these processes sit within a series of cascading and nested feedback loops that together generated the Cambrian explosion. Each box corresponds broadly to a stand-alone hypothesis or suite of related hypotheses (red, geological; blue, geochemical; green, biological). The figure represents a narrow interval of time at the beginning of the Cambrian (541 million to 521 million years ago).

Recently, attention has returned to abiotic processes as a possible cause of the Cambrian explosion. A long period of Neoproterozoic erosion had resulted in very low-relief continental interiors with highly weathered crystalline basement rock at the surface, together with associated soils (regolith). Major sea-level rise in the early, but not earliest, Cambrian led to the flooding of these interiors and triggered a range of Earth system responses (*11*), including the extensive erosion and mobilization of weathered rock and regolith and the rapid input of calcium (*11*), phosphate (*12*, *13*), and other ions into the oceans. Calcium concentrations in seawater increased almost threefold in the early Cambrian, and this input may have directly facilitated the origin of biomineralization (*14*). The input of phosphate provided simultaneous nutrient flux to shallow-water areas (*12*, *13*).

Each hypothesis outlined here is a viable mechanism for increasing mean species diversity within habitat, differentiation between habitats, and/or total regional biodiversity. However, it is unlikely that any single casual mechanism can explain the Cambrian explosion, with many of the individual hypotheses instead acting as components of interacting feedback loops between Earth systems and biological processes.

Together, these interacting processes generated an evolutionary cascade that led to the rapid rise in diversity. The initiating event is likely to have been the early Cambrian sea-level rise that led to inundation of continental margins and interiors and the rapid input of erosional by-products (*11*). This sea-level rise would also have generated a very large increase in habitable area lying between the base of wave turbulence and the depth to which light penetrates, providing a further driver for large increases in diversity. These early events then segue into the complex interaction of abiotic and biotic processes shown in the first figure. It would be valuable, therefore, to model the diversification in a holistic and interdisciplinary way, rather than focusing on individual causal factors. A substantial challenge then lies in determining the relative position of each component process upstream or downstream in the cascade of events that produced the Cambrian explosion.

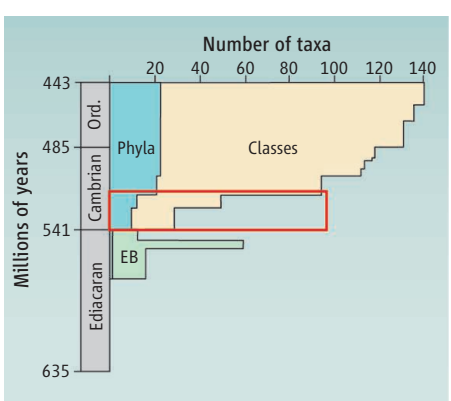

Times of change. The major diversification of marine taxa at high taxonomic levels between 635 and 443 million years ago [after (*2*)]. The red box indicates the time interval discussed in the text. EB, Ediacaran biota.

References

1. C. R. Marshall, *Annu. Rev. Earth Planet. Sci.* **34**, 355 (2006).
2. D. H. Erwin *et al.*, *Science* **334**, 1091 (2011).
3. D. H. Erwin, J. W. Valentine, *The Cambrian Explosion: The Construction of Animal Diversity* (Roberts, Greenwood Village, CO, 2013).
4. C. J. Lowe, *Science* **340**, 1170 (2013).
5. K. J. Peterson *et al.*, *Paleobiology* **31** (suppl.), 36 (2005).
6. D. H. Erwin, E. H. Davidson, *Development* **129**, 3021 (2002).
7. N. J. Butterfield, *Trends Ecol. Evol.* **26**, 81 (2011).
8. R. H. T. Callow, M. D. Brasier, *Earth Sci. Rev.* **96**, 207 (2009).
9. D. J. E. Murdock, P. C. J. Donoghue, *Cells Tiss. Organs* **194**, 98 (2011).
10. R. Wood, A. Y. Zhuravlev, *Earth Sci. Rev.* **115**, 249 (2012).
11. S. E. Peters, R. R. Gaines, *Nature* **484**, 363 (2012).
12. P. J. Cook, J. H. Shergold, *Nature* **308**, 231 (1984).
13. M. D. Brasier, R. H. T. Callow, *Mem. Ass. Austral. Palaeontol.* **34**, 377 (2007).
14. S. T. Brennan, T. K. Lowenstein, J. Horita, *Geology* **32**, 473 (2004).

10.1126/science.1239450

Teaching Metathesis "Simple" Stereochemistry

Alois Fürstner*

READ THE FULL ARTICLE ONLINE
http://dx.doi.org/10.1126/science.1229713

Cite this article as A. Fürstner, *Science* **341**, 1229713 (2013). DOI: 10.1126/science.1229713

Background: Transition metal–catalyzed alkene metathesis has revolutionized organic synthesis during the last two decades, even though the commonly used catalysts do not provide kinetic control over the stereochemistry of the newly formed double bonds. It is of utmost importance to fix this shortcoming, because the olefin geometry not only determines the physical and chemical properties of the alkene products but is also innately linked to any biological activities that the olefins may have.

Advances: Recent progress in catalyst design led to the development of a first set of metal alkylidene complexes of ruthenium, molybdenum, and tungsten that allow a host of inter- and intramolecular alkene metathesis reactions to be performed with good to excellent levels of *Z* selectivity (see the figure). This marks a considerable advancement over prior art, even though inherently *E*-selective catalysts remain elusive. In the case of disubstituted olefins, this gap in coverage can be filled by a sequence of alkyne metathesis followed by stereoselective semi-reduction of the resulting acetylene derivatives, which provides highly selective access to either geometrical series. Because the required alkylidyne catalysts have also been greatly improved in terms of activity, functional group tolerance, and user-friendliness, this method constitutes a valuable preparative complement.

Outlook: It is expected that the new catalysts will be rapidly embraced by the synthetic community. Because the as-yet limited number of published case studies is very encouraging, it is reasonable to believe that more sophisticated applications to polyfunctionalized and/or industrially relevant targets will follow shortly. Such investigations will allow the selectivity and performance of the stereoselective metathesis catalysts to be scrutinized in great detail. In parallel, growing mechanistic insights into their mode of action will almost certainly be forthcoming that can then be translated into refined ligand design. The resulting feedback loops will likely result in the evolution of ever more selective and practical catalysts, the long-term impact of which on organic synthesis and materials science will surely be profound and lasting.

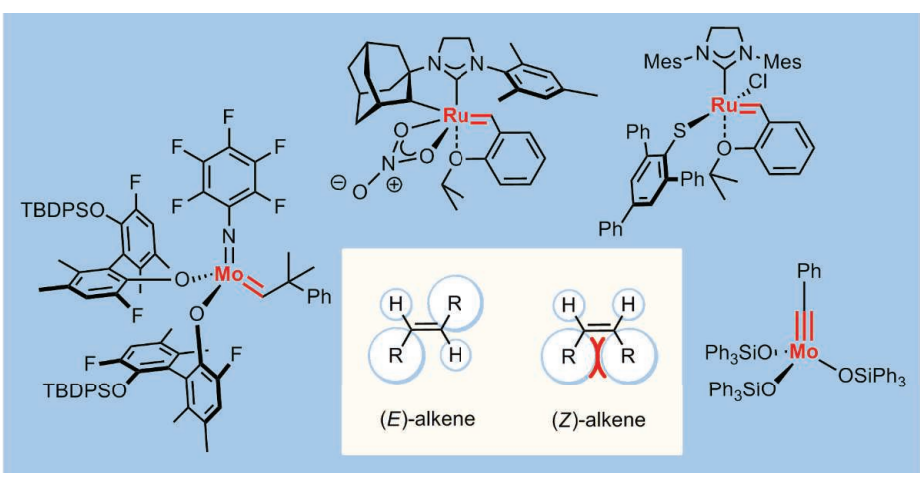

Advances in catalyst design solve a long-standing stereochemical issue. Alkene metathesis was tremendously successful in the past despite lacking catalyst control over the geometry (*E* versus *Z*) of the newly formed double bond. Recently introduced molybdenum (left), tungsten, and ruthenium (center) alkylidenes partly fix this problem as they allow preparation of *Z*-alkenes with high selectivity. Alternatively, either geometrical series can be accessed by alkyne metathesis followed by semi-reduction, which also benefits from new catalysts (right) of much improved performance. R, generic substituent; TBDPS, *tert*-butyldiphenylsilyl; Mes, mesityl; Ph, phenyl.

ARTICLE OUTLINE

BACKGROUND READING

A new generation of metal alkylidene catalysts for olefin metathesis provides levels of stereoselectivity that were inconceivable only a few years ago. A complementary approach is based on alkyne metathesis followed by stereoselective semi-reduction. These enabling methodologies are expected to profoundly affect organic synthesis and materials science.

M. Yu, C. Wang, A. F. Kyle, P. Jakubec, D. J. Dixon, R. R. Schrock, A. H. Hoveyda, Synthesis of macrocyclic natural products by catalyst-controlled stereoselective ring-closing metathesis. *Nature* **479**, 88–93 (2011).
Medline doi:10.1038/nature10563

L. E. Rosebrugh, M. B. Herbert, V. M. Marx, B. K. Keitz, R. H. Grubbs, Highly active ruthenium metathesis catalysts exhibiting unprecedented activity and Z-selectivity. *J. Am. Chem. Soc.* **135**, 1276–1279 (2013).
Medline doi:10.1021/ja311916m

G. Occhipinti, F. R. Hansen, K. W. Törnroos, V. R. Jensen, Simple and highly Z-selective ruthenium-based olefin metathesis catalyst. *J. Am. Chem. Soc.* **135**, 3331–3334 (2013).
Medline doi:10.1021/ja311505v

A. Fürstner, Alkyne metathesis on the rise. *Angew. Chem. Int. Ed.* **52**, 2794–2819 (2013).
doi:10.1002/anie.201204513

The list of author affiliations is available in the full article online.
*Corresponding author. E-mail: fuerstner@kofo.mpg.de

Published by AAAS

Teaching Metathesis "Simple" Stereochemistry

Alois Fürstner

Applications of metal-catalyzed olefin metathesis reactions manifested dramatic growth during the late 20th and early 21st centuries, culminating in the 2005 Nobel Prize awarded to three of the pioneers. The standard catalysts developed during that time frame and their descendants have profoundly changed the mindset of the synthetic community, even though they do not provide a handle to control selectivity issues as fundamental as the *E/Z* geometry of the newly formed double bond. With yet another generation of catalysts in the making that are far superior in this regard, a new wave seems to be building up that is expected to have enormous impact, too. The current state of the art is critically assessed, as are possible alternatives such as the metathesis of triple bonds followed by stereoselective semi-reduction.

Transition metal–catalyzed olefin metathesis had already been known for more than three decades before it started—in the early 1990s—to revolutionize organic synthesis (*1*). The long lag period stands in sharp contrast to the ensuing avalanche of interest in this seemingly unsensational transformation, which in its basic format does nothing else but equilibrate a pair of olefins. It was a triumph in catalyst design that had a profound and lasting impact on the practice of organic and bioorganic chemistry as well as material science. The now-classical catalysts **1** and **2** published by the groups of Schrock and Grubbs, respectively, can activate ordinary alkenes in the presence of polar functional groups with unparalleled levels of selectivity (Fig. 1A) (*2*, *3*). Olefins are fairly stable entities that are typically carried through multistep sequences without resorting to protection or any other precautionary measures. Complexes **1** and **2** and their later progeny, most notably the "second generation" ruthenium carbenes with an N-heterocyclic carbene (NHC) ligand such as **4** and **5**, allow formation and cleavage of C-C double bonds in the presence of almost any polar substituent, many of which were traditionally regarded as much more reactive. Only very few functionalities have been found to interfere with these marvelous tools.

This truly exquisite and—at that time—somewhat counterintuitive chemoselectivity profile translated into a complementary logic of synthesis (*4*): Whereas traditional planning largely follows polarity principles and therefore gravitates toward bond formation at or close to resident or temporary functional groups, metathesis is often particularly effective at distant sites. Consequently, bonds within a given target can gain strategic importance that would have never been seriously considered otherwise. At the same time, the superb functional-group tolerance reduces the necessity of protecting group chemistry to a minimum, unless other pre- or postmetathetic steps demand it. Many metathesis-based syntheses are therefore pleasingly short, concise, and productive (*4*–*7*). The ruthenium-based catalysts are even tolerant of oxygen and moisture and hence largely bench stable (*1*, *3*). This practicality is a major reason why ruthenium-based Grubbs-type catalysts gained tremendous popularity and were rapidly embraced even by practitioners who are unfamiliar with organometallic techniques. Prototype Schrock alkylidene complexes such as **1** comprising an inherently more oxophilic early transition metal center are more demanding in this regard. Recently, however, it has been demonstrated that they can also be rendered bench stable by reversible complexation to bipyridine (*8*).

Several other advantages of the standard catalysts are also worth mentioning. As it is not the purpose of this article, however, to reiterate in any great length what has become textbook knowledge, a few key words must suffice (*1*–*7*, *9*): A priori, the reaction works equally well in intermolecular and intramolecular settings; when applied to ring closures, it opens access to virtually all ring sizes and turned out to be one of the best methods for macrocyclization known to date. Because metathesis converts olefins into new olefins, it is predisposed for reaction cascades that can lead to a pronounced increase in molecular complexity. The scalability of metathesis—even to industrially relevant levels—was proven by a number of elegant case studies; another major advantage is the ready accessibility of substrate olefins, many of which are commercially manufactured at large scale or can be prepared by standard chemistry.

The modular design of the parent catalysts **1** and **2** is another asset. Systematic variations of the ligand sphere allowed the activity, stability, initiation rate, turnover number, and other relevant features to be tuned over a large range; moreover, the physical properties and chemical attributes of the catalysts can be adapted to the specific needs of a given transformation (*10*–*12*). This aspect will resurface in the following discussion.

Grounds for Improvement

In view of these overwhelming virtues, one may ask if there is any substantial shortcoming left that still needs to be addressed. Although a detailed discussion is beyond the scope of this article, a few important issues may stand out in view of the foregoing.

Consider alkenes, which themselves are highly polarized by adjacent substituents: Although the standard catalysts, in particular the more active recent variants, may accept such substrates, their transformations are not nearly as general as those of electronically "unbiased" olefins. Certain electron-deficient or electron-rich alkenes even fail to react completely; for example, successful metathesis reactions of nitroolefins, enol triflates, ketene acetals, and alkenyl stannanes are practically unknown to date. Likewise, alkenyl halides remain problematic, although a few successful applications were described (*13*). This particular deficiency in substrate scope is unfortunate, as it prevents metathesis from being more serviceable for follow-up cross-coupling chemistry. Moreover, high degrees of substitution on the alkenes to be metathesized and/or steric hindrance in their vicinity can prevent the reaction from occurring. It is reasonable to expect, however, that a further fine tuning of the catalysts will close many of these remaining gaps in coverage.

A more inherent problem surfaces when discriminating between various alkenes within a given substrate. As long as they exhibit different degrees of substitution, the necessary site selectivity can eventually be reached by meticulous choice of the catalyst and optimization of the conditions. This aspect is evident from a recent total synthesis of the potently cytotoxic macrolide iejimalide B, in which 2 out of 10 double bonds in the cyclization precursor could be selectively engaged in ring-closing metathesis (RCM) (Fig. 1B) (*14*, *15*). However, such applications are by no means routine, and many examples are known in which even starting materials with fewer unsaturation sites gave low yields or led to complex mixtures.

Conjugated di- or polyenes comprising olefinic subunits of similar character pose even larger problems. Several impressive successes notwithstanding, the preparation of such motifs by metathesis remains erratic (*16*). Even the "first generation" ruthenium carbene complex **2** does not rigorously discriminate between the two olefinic sites of a 1,3-diene, and its more recent and more active congeners are usually even less selective. As a result, ring contraction can interfere or even become the prevalent pathway. Because the standard catalysts do not work stereoselectively

Max-Planck-Institut für Kohlenforschung, D-45470 Mülheim/Ruhr, Germany.

E-mail: fuerstner@kofo.mpg.de

either (see below), complex mixtures frequently ensue. Ironically, the only rational approach to conjugated 1,3-diene products known to date takes recourse to protecting group chemistry—not for any polar functionality but to safeguard the alkene sites themselves (Fig. 1C) (*17*). Thus, a strategically placed C-silyl residue exerts a multitasking function, in that it protects the inner double bond from being attacked by the catalyst and hence suppresses undesirable ring contraction. At the same time, it serves as a stereodirecting substituent that favors the metallacyclic intermediate **6** over isomer **7** on steric grounds (Fig. 1D). A concerted cycloreversion delivers products of type **8**, which are readily protodesilylated to afford *E,Z*-configured 1,3-dienes with high fidelity or can be engaged in other postmetathetic transformations (*17*).

The Quest for Kinetic Stereocontrol

This example leads to what is arguably the biggest current deficit in synthetic terms: the general lack of kinetic stereocontrol. Because metathesis is inherently reversible, the product composition is time dependent (*18*) and the reaction ultimately leads to the thermodynamically most favorable product(s) (*1*–*7*). The difference in stability between a pair of olefin isomers, however, can be rather small and may not translate into a preparatively meaningful *E*/*Z* ratio. In many cases, the outcome is hard to predict, and the isomers are difficult to separate. Therefore, it was advisable (and in many cases, remains so) to apply metathesis at nonstereogenic sites, or to plan for postmetathetic steps that allow an inadequate outcome to be corrected.

Many metathesis reactions deliver olefinic products that are more highly substituted than the starting materials, which results in a kinetic handicap for the retro-reaction; a few well-pondered cases show how advantage can be taken of this situation (*19*). Although the development of ever more active catalysts gradually levels this barrier off and hence favors equilibration, it can be surprisingly difficult to harness thermodynamic

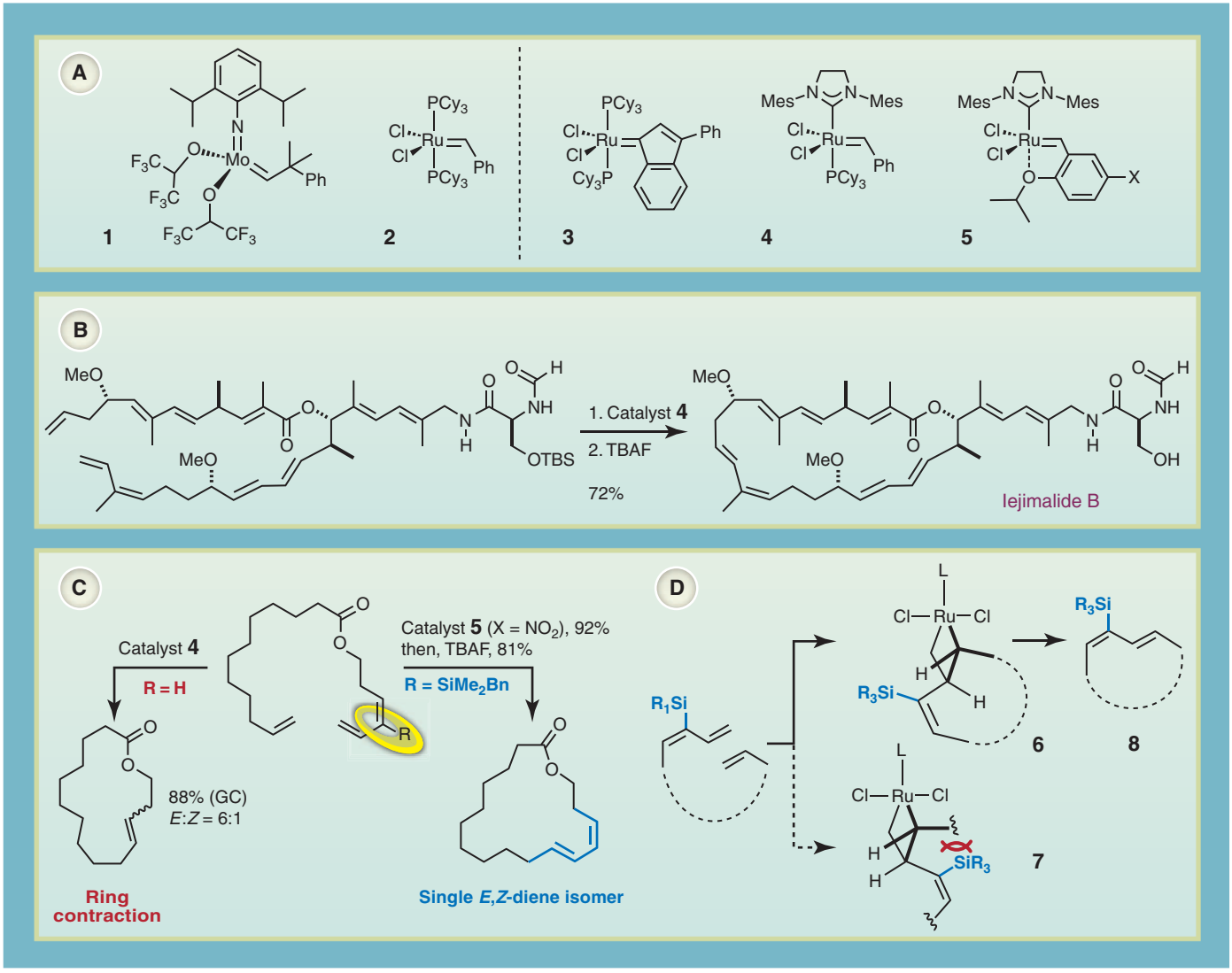

Fig. 1. Standard metathesis catalysts and applications to the synthesis of dienes (polyenes). In contrast to the outstanding ability of the standard olefin metathesis catalysts (**A**) to discriminate between C-C double bonds and polar functional groups (*1*–*12*), selecting among more than one olefinic site within a given target is inherently more difficult. This makes the preparation of polyunsaturated products rather challenging, although successful outcomes are known such as the total synthesis of the highly cytotoxic macrolide iejimalide (**B**) (*14*, *15*). Even the attempted formation of 1,3-dienes can result in disastrous outcomes because ring contraction may become prevalent [(**C**), left arrow]. This problem was partly fixed by introducing a multitasking silyl substituent on one of the double bonds [(C), right arrow] (*17*). In addition to protecting the inner alkene, this group exerts a strong stereodirecting effect by favoring one of the two isomeric metallacyclic intermediates on steric grounds (**D**). Unless stated otherwise, the yields in this and the following figures refer to isolated material. Abbreviations: Bn, benzyl; Cy, cyclohexyl; GC, gas chromatography; L, two-electron donor ligand; Mes, 2,4,6-trimethylphenyl (mesityl); Ph, phenyl; TBAF, tetra-*n*-butylammonium fluoride; TBS, *tert*-butyl-dimethylsilyl.

preferences. Thus, examples are known in which seemingly minor modifications of a peripheral protecting group or even the protonation state of a lateral basic site (*20*) engendered marked changes in the observed *E*/*Z* ratios, which cannot be accounted for purely on thermodynamic grounds. In another case, the stereochemical outcome of a macrocyclization was correlated with the preference of the catalyst in choosing one or the other olefin terminus of the substrate as the initiation site (*21*). Again, this observation implies that a kinetic caprice overrides the thermodynamic profile. Although such subtleties have been cleverly used for reaction optimization, it is also clear that they provide only case-specific solutions. As long as catalyst control over the newly formed double-bond geometry is missing, frustrations or even failures are inevitable. The kendomycin case serves as an instructive example, where RCM invariably delivered the incorrect isomer when performed at the trisubstituted olefin embedded into the macrocyclic framework of this natural product [for a review, see (*22*)]. Considerable efforts were necessary to later correct this unfavorable outcome; alternatively, a redesigned synthesis plan was pursued, invoking RCM at more forgiving sites. This example is only one of many to highlight the notion that rigorous kinetic control over the stereochemical course of a given metathesis reaction is essential from the organic synthesis viewpoint. Gratifyingly, recent forays into this strategic issue are about to bear important fruits.

Tuning Catalysts for *Z* Selectivity

In many cases, *Z* alkenes are thermodynamically less stable than the corresponding *E* isomers. A cerebral approach toward the catalyst-controlled formation of these intrinsically disfavored products was outlined by Schrock, Hoveyda, and co-workers (*23*–*26*). They translated the well-understood fluxional behavior of alkylidene complexes of molybdenum and tungsten into a creative catalyst design: Control over product stereochemistry is imposed by a sufficient size difference between the imido- and a freely rotating aryloxide ligand on the stereogenic metal center (Fig. 2A). Provided that this differential is sufficiently large, the substituents (R) of the metallacyclic intermediate formed in the crucial [2+2]-cycloaddition step are forced into the same more open sector; cycloreversion of the resulting all-cis–configured metallacyclobutadiene intermediate then delivers a *Z*-olefin product.

A priori, it does not matter which of the ligands is the large or the small partner; so far, however, the synthetically relevant incarnations of this design concept rely on the combination of a (relatively) small imido substituent and a bulky aryloxide. This choice may be dictated, to some extent, by stability considerations. Although a scrupulous matching of the ligands and substrates is needed to reach high selectivity while maintaining practical levels of activity and stability, catalysts of this type have powered various kinds of highly *Z*-selective transformations (Fig. 2B). This includes macrocyclization reactions as well as cross metatheses of allylic amides, enol ethers, and alkenyl- or allylboronates (*23*–*27*), in addition to polymerizations that are not discussed in this review.

The beautiful concept notwithstanding, a few additional aspects need to be taken into account. First, any postmetathetic isomerization must be kept to a minimum. Because *Z* alkenes are inherently more susceptible than their *E* counterparts to reenter the catalytic cycle when working with a *Z*-selective catalyst, they get preferentially depleted if the retro-path is facile. A careful control of the conditions and the reaction time is therefore necessary (in several cases, prolonged stirring resulted

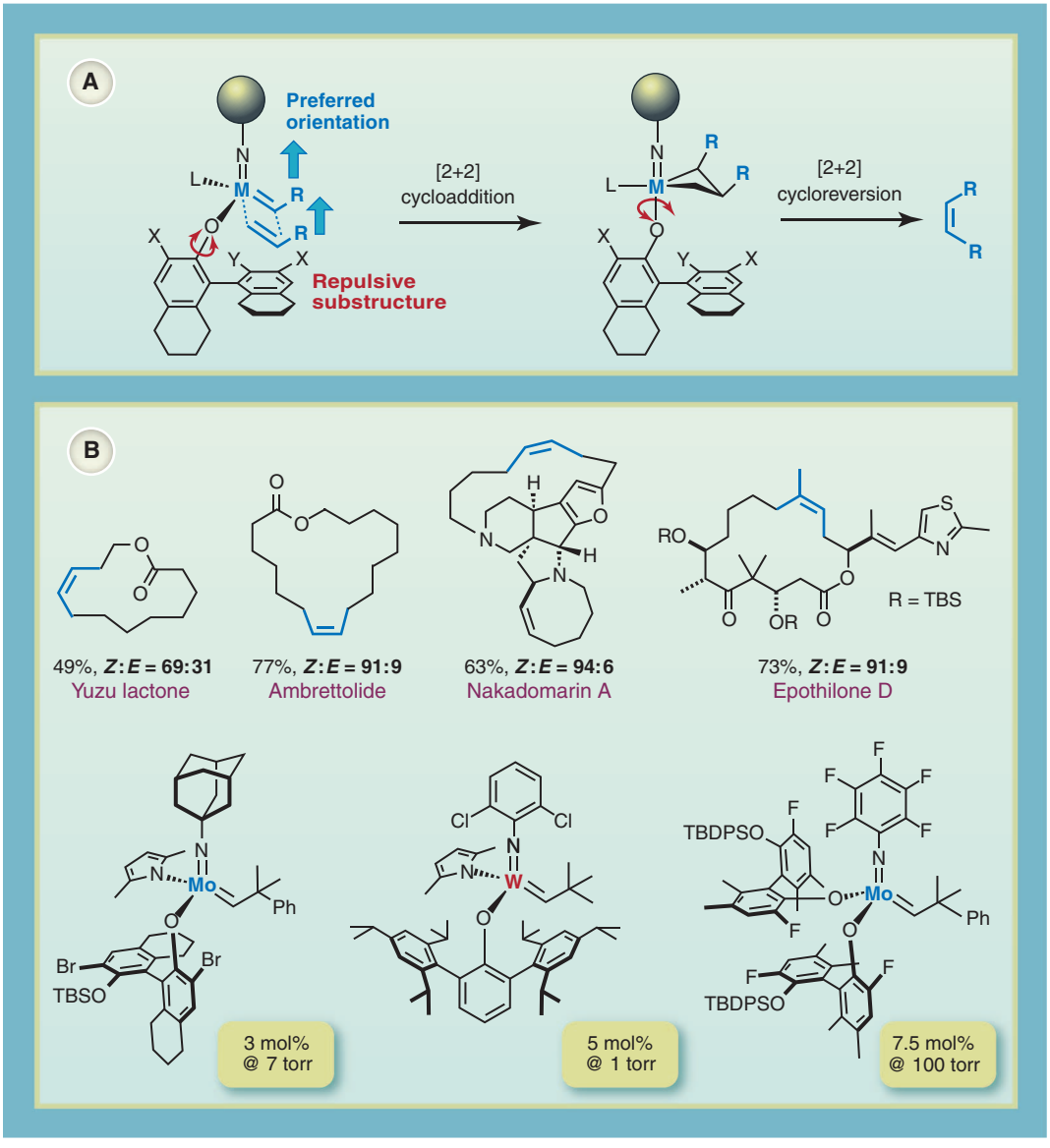

Fig. 2. *Z*-selective Mo and W catalysts (*23*–*26*). The *Z* selectivity observed with a new generation of Schrock alkylidene complexes is thought to derive from the differential in size of a (relatively) small imido- and a bulky aryloxide ligand, which translates into a metallacyclobutane intermediate orienting the substituents R toward the more open sector (**A**); representative examples are shown of *Z*-selective RCM reactions together with the optimal catalysts for each individual case (**B**). Abbreviations: TBS, *tert*-butyl-dimethylsilyl; TBDPS, *tert*-butyl-diphenylsilyl.

in substantial erosion of the selectivity). It is also likely that such secondary processes are favored whenever the product olefin is (even gently) strained. This may explain why the level of *Z* selectivity in RCM reactions seems to be correlated, to a certain extent, with ring size; for example, the yield and selectivity for the 13-membered yuzu lactone were much less favorable than those for the larger but otherwise closely related ambrettolide (Fig. 2B) (*26*).

The reactions are best performed under reduced pressure to remove the produced ethylene, which seriously competes with the substrate for the metal catalyst. Because the resulting methylidene complexes effectively promote secondary *Z*-alkene isomerization, their concentration must be kept as low as possible. This is particularly true for the molybdenum series, whereas tungsten methylidenes seem somewhat less damaging. As a rule of thumb, conformationally flexible substrates require molybdenum-based catalysts, whereas the less reactive (but more easily handled) tungsten analogs suffice when working with more biased starting materials (*26*).

These intricacies explain why a catalyst screening, as well as a careful optimization of the reaction conditions, is mandatory at the present stage of development. The four examples compiled in Fig. 2 are representative in that three substantially different catalysts had to be found for optimal results. Particularly noteworthy is the selective formation of tri-substituted alkenes (*28*), which are intrinsically more difficult to form with high levels of selectivity; once the double-bond geometry has been set, however, they benefit from being less prone to deleterious isomerization by secondary processes.

In parallel work, the ruthenium-based Grubbs-carbenes were also rendered *Z* selective. Complexes **9** and **10**, comprising a cyclometalated adamantyl residue and an equally chelating nitrato ligand, are currently the most effective variants (Fig. 3A) (*29*, *30*). The posited mechanism entails a "side-bound pathway," in which the incoming olefin approaches the metal center cis to the bulky NHC ligand (rather than trans to it, as is the case for the standard Grubbs catalysts) and trans to the chelating adamantyl group (*31*). The cyclometallated motif locks the orientation of the operative carbene unit and hence enforces formation of the crucial metallacyclobutene under the umbrella of the bulky aromatic ring. This environment ensures that the substituents (R) are preferentially oriented downward, which disfavors all possible transition states leading to *E* alkenes. In line with this rationale, catalyst **10,** bearing a bulkier *N*-2,6-diisopropylphenyl group on the NHC, performs better than its analog with a slightly smaller *N*-mesityl substituent (*29*, *30*). Appreciable *Z* selectivities and moderate to good yields were observed in homo- and cross metatheses (*32*), as well as in a number of more challenging macrocyclizations (Fig. 3A). Somewhat surprisingly, a resident ketone and an alcohol group in the substrate compromised the obtained *Z* selectivity for reasons that are not entirely clear. Again, static vacuum has to be applied, and the reactions need gentle warming.

An alternative design was pursued by Jensen and co-workers, who obtained a fairly *Z*-selective catalyst **11** simply upon exchange of one of the chloride ligands of the standard Grubbs-Hoveyda catalyst **5** (X is H) with a bulky 2,4,6-triphenylbenzenethiolate group (Fig. 3B) (*33*). The only applications so far, however, were homo-metathesis reactions of relatively simple terminal alkenes. Again, secondary processes seem to deplete the inherent *Z* selectivity of the catalyst, thus rendering the outcome dependent on reaction time and conversion. Much as in the above cases, the application of static vacuum was mandatory, and the presence of a free –OH group in a substrate halted the reaction. It remains to be seen how this readily prepared complex performs in more challenging cases. While this review was in press, the prototype of yet another ruthenium carbene catalyst was published, which owes its *Z* selectivity to a chelating disulfide ligand (*34*); although applications were limited to ring-opening/cross metathesis and ring-opening metathesis polymerizations, the basic design seems very flexible and hence potentially highly promising.

Can the *E* Alkene Be Selected?

At present, inherently *E*-selective olefin metathesis catalysts are basically unknown, and thermodynamic control remains the only viable handle. Alternatively, it is possible to obtain an *E* alkene in pure form upon depleting the *Z* isomer from a product mixture via selective ethenolysis; both the molybdenum- (*35*) and the ruthenium-based

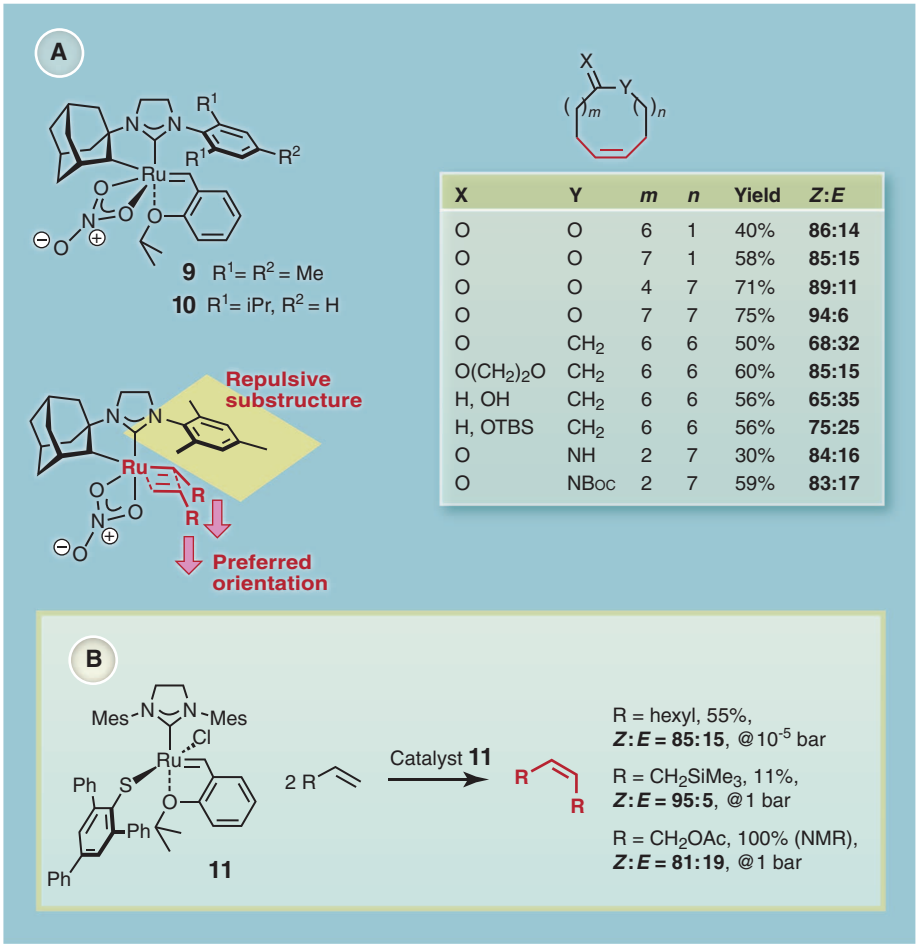

Fig. 3. *Z*-selective Ru catalysts. Grubbs-type ruthenium carbene complexes gain *Z* selectivity on cyclometalation, which locks the orientation of the carbene and ensures that the metallacyclobutadiene intermediate is formed under the umbrella of the *N*-aryl ring; the trajectory of the incoming substrate is thought to be cis rather than trans to the NHC ligand for stereoelectronic reasons (A) (*29*, *30*). Selected macrocyclizations with catalyst **9** indicate that the results are correlated, to some extent, with the ring size and substitution pattern (*30*). An alternative design principle relies on exchange of one of the chloride ligands of the standard catalyst **5** (X is H) by a bulky thiolato group (**B**) (*33*); the resulting complex **11** has so far been tested only in metathesis-type dimerization reactions of barely functionalized substrates; for yet another *Z*-selective ruthenium carbene complex with a chelating disulfide ligand, which was published while this review was in press, see (*34*). Abbreviations: Ac, acetyl; Boc, *tert*-butoxycarbonyl; iPr, isopropyl; Mes, 2,4,6-trimethylphenyl (mesityl); NMR, nuclear magnetic resonance; Ph, phenyl; TBS, *tert*-butyl-dimethylsilyl.

Z-selective catalysts (*30*) presented above were successfully used for this purpose. This approach may avoid delicate separations but does not allow escape from the thermodynamic trap. The literature records many examples in which the *E* alkene was needed but the *Z* isomer was preferentially or exclusively produced (*1*–*9*). A recently disclosed indirect solution relies on the stereoselective formation of cyclic alkenyl siloxanes by RCM (*36*, *37*). Proto-desilylation unveiled the corresponding *Z* alkenes, whereas halo-desilylation could be performed either with retention or with inversion of configuration; however, the outcome was not totally general but somewhat ring-size dependent. The resulting alkenyl halides can eventually be further functionalized into olefins of either configuration (*37*).

Selectivity from Alkynes

The arguably most general metathesis-based method toward either geometric isomers of a given disubstituted alkene relies on alkyne metathesis followed by semi-reduction (Fig. 4) (*38*). Application of Lindlar hydrogenation (or its synthetic equivalents) to the alkyne products opens a convenient entry into the *Z* series. Birch reduction constitutes the stereochemical complement, although this classical transformation is harsh and not overly attractive when working with elaborate compounds. The catalytic trans-hydrosilylation/desilylation (*39*) or the recently discovered direct catalytic trans-hydrogenation of alkynes (*40*) provide more attractive gateways to *E* alkenes. In concert with

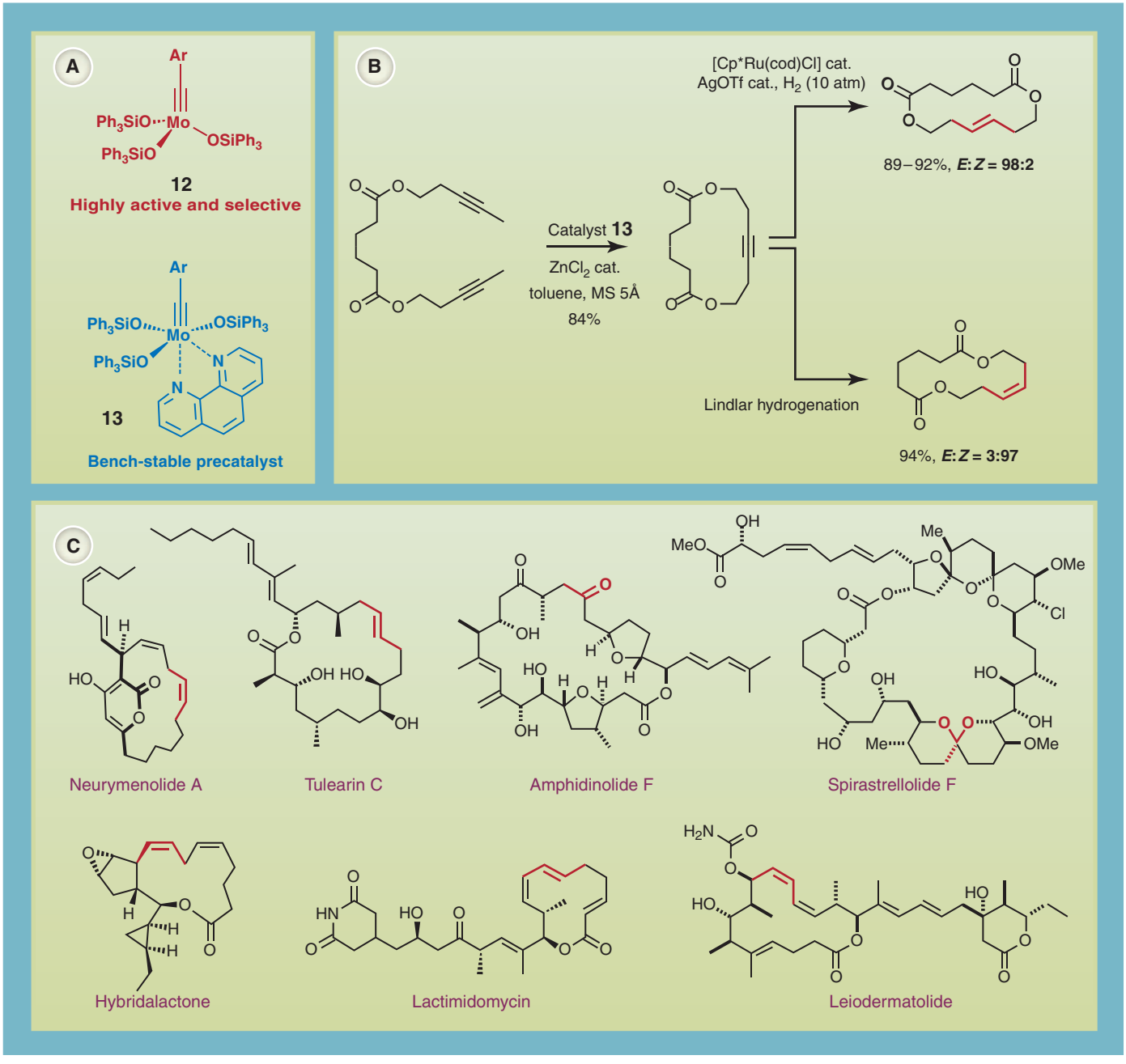

Fig. 4. A new generation of alkyne metathesis catalysts. These Mo alkylidyne complexes combine excellent activity, functional group tolerance, and user-friendliness (A) (*41*, *42*). Alkyne metathesis provides access to a host of stereodefined alkenes when the (cyclo)alkyne products initially formed are subjected to stereoselective semi-reduction (*38*). This method allows either double-bond configuration to be accessed with high selectivity (**B**) and proved successful even with structurally demanding and labile polyunsaturated targets (**C**). In the case of amphidinolide F (*48*) and spirastrellolide F (*49*), the originally formed cycloalkynes were elaborated into the color-coded ketone or spiroketal substructures by noble-metal–catalyzed transannular addition reactions. Abbreviations: Ar, aryl; cod, 1,5-cyclooctadiene; Cp*, pentamethylcyclopentadienyl; MS, molecular sieves; Ph, phenyl; Tf, trifluoromethanesulfonyl.

these methods, alkyne metathesis guarantees full control over a disubstituted double-bond geometry, as well as generally excellent levels of selectivity.

Alkyne metathesis had long suffered from the exceptional sensitivity of the available catalysts, which were therefore difficult to use. Recently, however, a new series of molybdenum alkylidynes bearing silanolates as ancillary ligands was introduced (*41*, *42*). Complexes such as **12** are rendered bench stable and therefore easy to handle on complexation with 1,10-phenanthroline; treatment of the resulting adduct **13** with $ZnCl_2$ or $MnCl_2$ in the presence of molecular sieves gently releases the active species. This simple protocol allows the remarkable activity and exquisite selectivity of **12** to be harnessed without any particular expertise in the handling of sensitive organometallic compounds (*41*, *42*). Many alkyne metathesis reactions performed with the aid of these catalysts proceed at ambient temperature and require only low loadings; representative examples are shown in Fig. 4.

This methodology has already proven effective in complex settings (*38*). Equally important is that catalysts such as **12** are rigorously alkynophilic and do not touch the π system of olefins of any kind, be they terminal, internal, or conjugated to a polarizing substituent. By virtue of this strict orthogonality, alkyne metathesis is particularly well suited for applications to polyunsaturated targets. Even conjugated or labile skipped dienes (polyenes) can be obtained in any possible stereochemical format, whether they are *Z*,*Z*-, *Z*,*E*-, *E*,*Z*-, or *E*,*E*-configured. The recent total syntheses of lactimidomycin (*43*, *44*) and the antimitotic agent leiodermatolide (*45*) provide pertinent illustrations (Fig. 4C). Suffice it to say that the stereoselective formation of compounds with two or more *Z*-configured double bonds in their molecular frame remains a nontrivial task if *Z*-selective alkene metathesis catalysts are to be used.

The price to pay has to do with the fact that alkynes are usually more "expensive" substrates than alkenes, as fewer of them are manufactured commercially and their synthesis often requires more than one step. This is particularly true for nonterminal acetylene derivatives that were the sole substrate class amenable to metathesis until very recently. The discovery that terminal alkynes can also be metathesized, at least in certain cases, may help alleviate this drawback to some extent (*46*, *47*). On the other hand, alkyne products need not be converted into (stereodefined) alkenes but offer rich opportunities for other postmetathetic transformations as well. Several total syntheses of targets that are structurally as demanding and highly functionalized as the marine macrolides amphidinolide F and spirastrellolide F highlight this notion (*48*, *49*). In these cases, platinum and gold catalysts were used to engage the metathesis products into transannular additions of protic nucleophiles across the precursor alkyne units.

Outlook

The already tremendous impact of metathesis on synthesis will likely further increase as new ways of gaining rigorous control over the double-bond geometry start to emerge. Although this is not the only issue in the metathesis arena that needs attention, it is certainly the most pressing one from the preparative viewpoint. Yet, synthetic chemistry is in a favorable position, as different and—to some extent—complementary approaches are about to mature that hold the promise of solving this important problem. Again, it is the awesome power of organometallic chemistry that pays the essential dividends.

Box 1. Glossary terms.

The term "**metathesis**" was originally coined to describe a mutual exchange process that converts one pair of alkenes (olefins) into a new pair with the help of a transition metal catalyst. The operative metal-alkylidene unit (**Schrock alkylidene**) consists of a double bond between a carbon-based ligand and a high-valent transition metal center (M). Although **alkene metathesis** is arguably the most important incarnation of this reactivity principle, other substrates are amenable to similar redistribution processes. This includes (internal) acetylene derivatives, which undergo surprisingly facile **alkyne metathesis** reactions on treatment with catalysts comprising formal carbon-metal triple bonds ("**metal alkylidynes**").

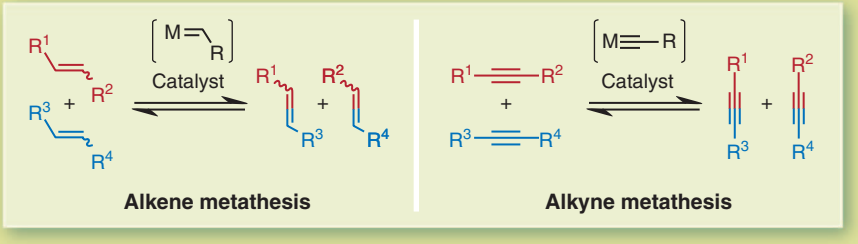

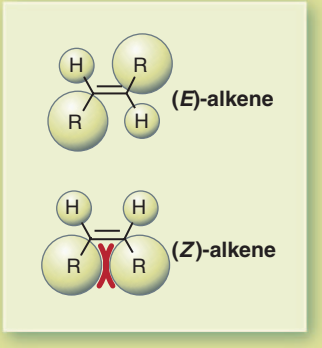

The substituents R in a given alkene can be oriented in different ways as outlined for a disubstituted case. For steric reasons, ***E* alkenes** (for *entgegen*, German for "opposite") are usually more stable than the corresponding ***Z* alkenes** (for *zusammen*, German for "together"), although subtle electronic factors can overlay or even override the steric bias. The energetic differences are case dependent and often too small to allow for selective alkene synthesis on purely thermodynamic grounds. Because the **stereochemistry** strongly determines the physical and chemical properties, as well as any biological activities, it is of utmost importance to gain rigorous control over this structural feature.

References and Notes

1. R. H. Grubbs, Ed., *Handbook of Metathesis* (Wiley-VCH, Weinheim, Germany, 2003), vols. 1 to 3.
2. R. R. Schrock, Multiple metal–carbon bonds for catalytic metathesis reactions (Nobel Lecture). *Angew. Chem. Int. Ed.* **45**, 3748–3759 (2006). doi: 10.1002/anie.200600085
3. R. H. Grubbs, Olefin-metathesis catalysts for the preparation of molecules and materials (Nobel Lecture). *Angew. Chem. Int. Ed.* **45**, 3760–3765 (2006). doi: 10.1002/anie.200600680
4. A. Fürstner, Olefin metathesis and beyond. *Angew. Chem. Int. Ed.* **39**, 3012–3043 (2000). doi: 10.1002/1521-3773(20000901)39:17<3012::AID-ANIE3012>3.0.CO;2-G
5. K. C. Nicolaou, P. G. Bulger, D. Sarlah, Metathesis reactions in total synthesis. *Angew. Chem. Int. Ed.* **44**, 4490–4527 (2005). doi: 10.1002/anie.200500369
6. S. J. Connon, S. Blechert, Recent developments in olefin cross-metathesis. *Angew. Chem. Int. Ed.* **42**, 1900–1923 (2003). doi: 10.1002/anie.200200556
7. A. H. Hoveyda, A. R. Zhugralin, The remarkable metal-catalysed olefin metathesis reaction. *Nature* **450**, 243–251 (2007). doi: 10.1038/nature06351; pmid: 17994091
8. J. Heppekausen, A. Fürstner, Rendering Schrock-type molybdenum alkylidene complexes air stable: User-friendly precatalysts for alkene metathesis. *Angew. Chem. Int. Ed.* **50**, 7829–7832 (2011). doi: 10.1002/anie.201102012
9. A. Fürstner, Metathesis in total synthesis. *Chem. Commun. (Camb.)* **47**, 6505–6511 (2011). doi: 10.1039/c1cc10464k; pmid: 21519622
10. G. C. Vougioukalakis, R. H. Grubbs, Ruthenium-based heterocyclic carbene-coordinated olefin metathesis catalysts. *Chem. Rev.* **110**, 1746–1787 (2010). doi: 10.1021/cr9002424; pmid: 20000700
11. R. R. Schrock, A. H. Hoveyda, Molybdenum and tungsten imido alkylidene complexes as efficient olefin-metathesis catalysts. *Angew. Chem. Int. Ed.* **42**, 4592–4633 (2003). doi: 10.1002/anie.200300576
12. C. Samojłowicz, M. Bieniek, K. Grela, Ruthenium-based olefin metathesis catalysts bearing *N*-heterocyclic carbene ligands. *Chem. Rev.* **109**, 3708–3742 (2009). doi: 10.1021/cr800524f; pmid: 19534492
13. M. Gatti *et al.*, Efficient ring-closing metathesis of alkenyl bromides: The importance of protecting the catalyst during the olefin approach. *J. Am. Chem. Soc.* **132**, 15179–15181 (2010). doi: 10.1021/ja108253f; pmid: 20936851
14. A. Fürstner *et al.*, Total synthesis of iejimalide A-D and assessment of the remarkable actin-depolymerizing capacity of these polyene macrolides. *J. Am. Chem. Soc.* **129**, 9150–9161 (2007). doi: 10.1021/ja072334v; pmid: 17602484

15. J. Gagnepain, E. Moulin, A. Fürstner, Gram-scale synthesis of iejimalide B. *Chem. Eur. J.* **17**, 6964–6972 (2011). doi: 10.1002/chem.201100178; pmid: 21557354
16. J. Wagner *et al*., Synthesis of macrolide analogues of sanglifehrin by RCM: Unique reactivity of a ruthenium carbene complex bearing an imidazol-2-ylidene ligand. Ring-closing metathesis. *J. Org. Chem.* **65**, 9255–9260 (2000). doi: 10.1021/jo001296u; pmid: 11149884
17. D. Gallenkamp, A. Fürstner, Stereoselective synthesis of *E*,*Z*-configured 1,3-dienes by ring-closing metathesis. Application to the total synthesis of lactimidomycin. *J. Am. Chem. Soc.* **133**, 9232–9235 (2011). doi: 10.1021/ja2031085; pmid: 21604689
18. C. W. Lee, R. H. Grubbs, Stereoselectivity of macrocyclic ring-closing olefin metathesis. *Org. Lett.* **2**, 2145–2147 (2000). doi: 10.1021/ol006059s; pmid: 10891252
19. A. Fürstner *et al*., Total syntheses of the phytotoxic lactones herbarumin I and II and a synthesis-based solution of the pinolidoxin puzzle. *J. Am. Chem. Soc.* **124**, 7061–7069 (2002). doi: 10.1021/ja020238i; pmid: 12059230
20. P. Jakubec, D. M. Cockfield, D. J. Dixon, Total synthesis of (-)-nakadomarin A. *J. Am. Chem. Soc.* **131**, 16632–16633 (2009). doi: 10.1021/ja908399s; pmid: 19883080
21. X. Wei *et al*., A highly convergent and efficient synthesis of a macrocyclic hepatitis C virus protease inhibitor BI 201302. *Org. Lett.* **15**, 1016–1019 (2013). doi: 10.1021/ol303498m; pmid: 23406520
22. H. J. Martin, T. Magauer, J. Mulzer, In pursuit of a competitive target: Total synthesis of the antibiotic kendomycin. *Angew. Chem. Int. Ed.* **49**, 5614–5626 (2010). doi: 10.1002/anie.201000227
23. A. J. Jiang, Y. Zhao, R. R. Schrock, A. H. Hoveyda, Highly *Z*-selective metathesis homocoupling of terminal olefins. *J. Am. Chem. Soc.* **131**, 16630–16631 (2009). doi: 10.1021/ja908098t; pmid: 19919135
24. S. J. Meek, R. V. O'Brien, J. Llaveria, R. R. Schrock, A. H. Hoveyda, Catalytic *Z*-selective olefin cross-metathesis for natural product synthesis. *Nature* **471**, 461–466 (2011). doi: 10.1038/nature09957; pmid: 21430774
25. M. Yu *et al*., Synthesis of macrocyclic natural products by catalyst-controlled stereoselective ring-closing metathesis. *Nature* **479**, 88–93 (2011). doi: 10.1038/nature10563; pmid: 22051677
26. C. Wang *et al*., Efficient and selective formation of macrocyclic disubstituted Z alkenes by ring-closing metathesis (RCM) reactions catalyzed by Mo- or W-based monoaryloxide pyrrolide (MAP) complexes: Applications to total syntheses of epilachnene, yuzu lactone, ambrettolide, epothilone C, and nakadomarin A. *Chem. Eur. J.* **19**, 2726–2740 (2013). doi: 10.1002/chem.201204045; pmid: 23345004
27. E. T. Kiesewetter *et al*., Synthesis of *Z*-(pinacolato)allylboron and *Z*-(pinacolato)alkenylboron compounds through stereoselective catalytic cross-metathesis. *J. Am. Chem. Soc.* **135**, 6026–6029 (2013). doi: 10.1021/ja403188t; pmid: 23586708
28. C. Wang, F. Haeffner, R. R. Schrock, A. H. Hoveyda, Molybdenum-based complexes with two aryloxides and a pentafluoroimido ligand: Catalysts for efficient *Z* -selective synthesis of a macrocyclic trisubstituted alkene by ring-closing metathesis. *Angew. Chem. Int. Ed.* **52**, 1939–1943 (2013). doi: 10.1002/anie.201209180
29. L. E. Rosebrugh, M. B. Herbert, V. M. Marx, B. K. Keitz, R. H. Grubbs, Highly active ruthenium metathesis catalysts exhibiting unprecedented activity and *Z*-selectivity. *J. Am. Chem. Soc.* **135**, 1276–1279 (2013). doi: 10.1021/ja311916m; pmid: 23317178
30. V. M. Marx, M. B. Herbert, B. K. Keitz, R. H. Grubbs, Stereoselective access to *Z* and *E* macrocycles by ruthenium-catalyzed *Z*-selective ring-closing metathesis and ethenolysis. *J. Am. Chem. Soc.* **135**, 94–97 (2013). doi: 10.1021/ja311241q; pmid: 23244210
31. P. Liu *et al*., Z-Selectivity in olefin metathesis with chelated Ru catalysts: Computational studies of mechanism and selectivity. *J. Am. Chem. Soc.* **134**, 1464–1467 (2012). doi: 10.1021/ja2108728; pmid: 22229694
32. B. K. Keitz, K. Endo, M. B. Herbert, R. H. Grubbs, *Z*-selective homodimerization of terminal olefins with a ruthenium metathesis catalyst. *J. Am. Chem. Soc.* **133**, 9686–9688 (2011). doi: 10.1021/ja203488e; pmid: 21649443
33. G. Occhipinti, F. R. Hansen, K. W. Törnroos, V. R. Jensen, Simple and highly *Z*-selective ruthenium-based olefin metathesis catalyst. *J. Am. Chem. Soc.* **135**, 3331–3334 (2013). doi: 10.1021/ja311505v; pmid: 23398276
34. R. K. M. Khan, S. Torker, A. H. Hoveyda, Readily accessible and easily modifiable Ru-based catalysts for efficient and Z-selective ring-opening metathesis polymerization and ring-opening/cross metathesis. *J. Am. Chem. Soc.* **135**, 10258–10261 (2013). doi: 10.1021/ja404208a
35. S. C. Marinescu, D. S. Levine, Y. Zhao, R. R. Schrock, A. H. Hoveyda, Isolation of pure disubstituted *E* olefins through Mo-catalyzed *Z*-selective ethenolysis of stereoisomeric mixtures. *J. Am. Chem. Soc.* **133**, 11512–11514 (2011). doi: 10.1021/ja205002v; pmid: 21718001
36. Y. Wang *et al*., Control of olefin geometry in macrocyclic ring-closing metathesis using a removable silyl group. *J. Am. Chem. Soc.* **133**, 9196–9199 (2011). doi: 10.1021/ja202012s; pmid: 21557625
37. Y. Wang *et al*., Selective access to trisubstituted macrocyclic *E*- and *Z*-alkenes from the ring-closing metathesis of vinylsiloxanes. *Org. Lett.* **15**, 1218–1221 (2013). doi: 10.1021/ol400134d; pmid: 23448432
38. A. Fürstner, Alkyne metathesis on the rise. *Angew. Chem. Int. Ed.* **52**, 2794–2819 (2013). doi: 10.1002/anie.201204513
39. B. M. Trost, Z. T. Ball, Markovnikov alkyne hydrosilylation catalyzed by ruthenium complexes. *J. Am. Chem. Soc.* **123**, 12726–12727 (2001). doi: 10.1021/ja0121033; pmid: 11741457
40. K. Radkowski, B. Sundararaju, A. Fürstner, A functional-group-tolerant catalytic *trans* hydrogenation of alkynes. *Angew. Chem. Int. Ed.* **52**, 355–360 (2013). doi: 10.1002/anie.201205946
41. J. Heppekausen, R. Stade, R. Goddard, A. Fürstner, Practical new silyloxy-based alkyne metathesis catalysts with optimized activity and selectivity profiles. *J. Am. Chem. Soc.* **132**, 11045–11057 (2010). doi: 10.1021/ja104800w; pmid: 20698671
42. J. Heppekausen *et al*., Optimized synthesis, structural investigations, ligand tuning and synthetic evaluation of silyloxy-based alkyne metathesis catalysts. *Chem. Eur. J.* **18**, 10281–10299 (2012). doi: 10.1002/chem.201200621; pmid: 22807024
43. K. Micoine, A. Fürstner, Concise total synthesis of the potent translation and cell migration inhibitor lactimidomycin. *J. Am. Chem. Soc.* **132**, 14064–14066 (2010). doi: 10.1021/ja107141p; pmid: 20831202
44. K. Micoine *et al*., Total syntheses and biological reassessment of lactimidomycin, isomigrastatin and congener glutarimide antibiotics. *Chem. Eur. J.* **19**, 7370–7383 (2013). doi: 10.1002/chem.201300393; pmid: 23595541
45. J. Willwacher, N. Kausch-Busies, A. Fürstner, Divergent total synthesis of the antimitotic agent leiodermatolide. *Angew. Chem. Int. Ed.* **51**, 12041–12046 (2012). doi: 10.1002/anie.201206670
46. B. Haberlag, M. Freytag, C. G. Daniliuc, P. G. Jones, M. Tamm, Efficient metathesis of terminal alkynes. *Angew. Chem. Int. Ed.* **51**, 13019–13022 (2012). doi: 10.1002/anie.201207772
47. P. Persich *et al*., Increasing the structural span of alkyne metathesis. *Chem. Eur. J.* 10.1002/chem.201302320 (2013).
48. G. Valot *et al*., Total synthesis of amphidinolide F. *Angew. Chem. Int. Ed.* **52**, 9534–9538 (2013). doi: 10.1002/anie.201301700; pmid: 23610047
49. S. Benson *et al*., Second-generation total synthesis of spirastrellolide F methyl ester: The alkyne route. *Angew. Chem. Int. Ed.* **50**, 8739–8744 (2011). doi: 10.1002/anie.201103270

Acknowledgments: I acknowledge support from the Max-Planck-Gesellschaft, Fonds der Chemischen Industrie, and SusChemSys (Ziel 2 Programm, NRW).

10.1126/science.1229713

Dynamically Reshaping Signaling Networks to Program Cell Fate via Genetic Controllers

Kate E. Galloway, Elisa Franco, Christina D. Smolke*

READ THE FULL ARTICLE ONLINE
http://dx.doi.org/10.1126/science.1235005

Cite this article as K. E. Galloway *et al.*, *Science* **341**, 1235005 (2013).
DOI: 10.1126/science.1235005

Introduction: Engineering of cell fate through synthetic gene circuits requires methods to precisely implement control around native decision-making pathways and offers the potential to direct developmental programs and redirect aberrantly activated cell processes. We set out to develop molecular network diverters, a class of genetic control systems, to activate or attenuate signaling through a mitogen-activated protein kinase (MAPK) pathway, the yeast mating pathway, to conditionally route cells to one of three distinct fates.

Methods: We used a combination of genetic elements—including pathway regulators, RNA-based transducers, and constitutive and pathway-responsive promoters—to build modular network diverters. We measured the impact of these genetic control systems on pathway activity by monitoring fluorescence from a transcriptional pathway reporter. Cell fate determination was measured through halo assays, in which mating-associated cell cycle arrest above a certain concentration of pheromone from wild-type cells results in a "halo" or cleared region around a disk saturated in pheromone. A phenomenological model of our system was built to elucidate design principles for dual diverters that integrate opposing functions while supporting independent routing to alternative fates.

Results: We identified titratable positive (Ste4) and negative (Msg5) regulators of pathway activity that result in divergent cell fate decisions when controlled from network diverters. A positive diverter, controlling Ste4 through a feedback architecture, routed cells to the mating fate, characterized by pathway activation in the absence of pheromone. A negative diverter, controlling Msg5 through a nonfeedback architecture, routed cells to the nonmating fate, characterized by pathway inhibition in the presence of pheromone. When integrated into a dual-diverter architecture, the opposing functions of these positive and negative diverters resulted in antagonism, which prevented independent routing to the alternative fates. However, a modified architecture that incorporated both constitutive and feedback regulation over the pathway regulators enabled conditional routing of cells to one of three fates (wild type, mating, or nonmating) in response to specified environmental signals.

Discussion: Our work identified design principles for networks that induce differentiation of cells in response to environmental signals and that enhance the robust performance of integrated mutually antagonistic genetic programs. For example, integrated negative regulators can buffer a system against noise amplification mediated through positive-feedback loops by providing a resistance to amplification. Negative feedback can play an important role by reducing population heterogeneity and mediating robust, long-term cell fate decisions. The dual-diverter configuration enables routing to alternative fates and minimizes impact on the opposing diverter by integrating differential regulatory strategies on functionally redundant genes. Molecular network diverters provide a foundation for robustly programming spatial and temporal control over cell fate.

FIGURES IN THE FULL ARTICLE

SUPPLEMENTARY MATERIALS

Materials and Methods
Supplementary Text
Figs. S1 to S14
Tables S1 to S17
References

RELATED ITEMS IN *SCIENCE*

C. A. Sarkar, Concentrating (on) natural signaling proteins for synthetic control of cell fate. *Science* **341**, 1349–1350 (2013).
DOI: 10.1126/science.1243994

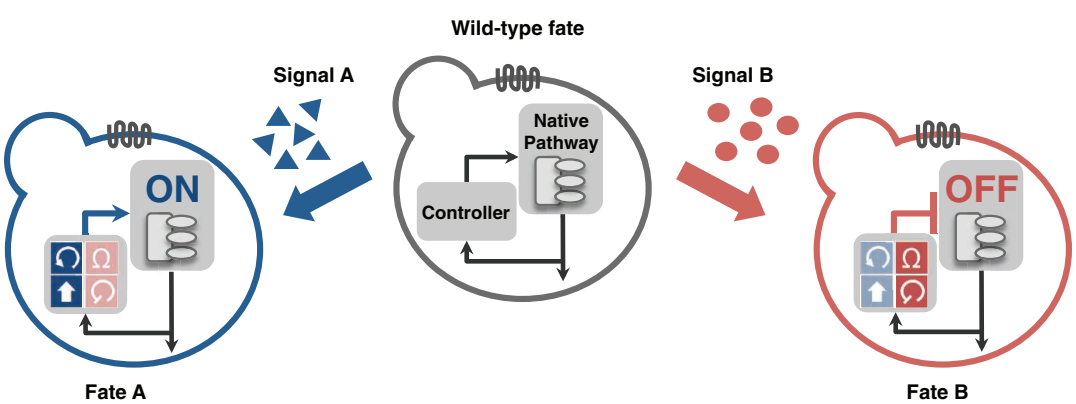

The molecular network diverter (controller) interfaces with a native signaling pathway to conditionally route cells to one of three fates in response to distinct environmental signals. Signal A (**left**) and signal B (**right**) trigger the positive and negative elements of the diverter via their cognate transducers to activate or inhibit, respectively, signaling through the yeast mating pathway.

The list of author affiliations is available in the full article online.
*Corresponding author. E-mail: christina.smolke@stanford.edu

Dynamically Reshaping Signaling Networks to Program Cell Fate via Genetic Controllers

Kate E. Galloway,[1] Elisa Franco,[2] Christina D. Smolke[3]*

Engineering of cell fate through synthetic gene circuits requires methods to precisely implement control around native decision-making pathways and offers the potential to direct cell processes. We demonstrate a class of genetic control systems, molecular network diverters, that interface with a native signaling pathway to route cells to divergent fates in response to environmental signals without modification of native genetic material. A method for identifying control points within natural networks is described that enables the construction of synthetic control systems that activate or attenuate native pathways to direct cell fate. We integrate opposing genetic programs by developing network architectures for reduced antagonism and demonstrate rational tuning of performance. Extension of these control strategies to mammalian systems should facilitate the engineering of complex cellular signaling systems.

Organisms orchestrate complex, coordinated tasks by dynamically programming the extracellular space with distributed molecular signals that are processed by individual cells into concerted responses (*1*–*3*). Programmed cells can harness sophisticated and complex biological processes to direct developmental programs and redirect aberrantly activated cell processes (*4*–*10*). The engineering of biological systems to regulate cell fate requires precise control over gene circuit performance (*11*, *12*) and the ability to interface with key decision-making pathways (*13*). Advances in synthetic biology may facilitate the design of sophisticated genetic circuits capable of sensing and actuating changes in native signaling networks (*14*).

Mitogen-activated protein kinase (MAPK) pathways are a class of signaling pathways that control such key cellular processes as differentiation, mitosis, and apoptosis (*1*). Many diseases, including one-third of human cancers, result from aberrant signaling through MAPK pathways (*15*, *16*). Conservation of the form and function of MAPK pathways has facilitated the translation of principles identified in yeast to higher eukaryotes (*17*, *18*). In the model organism *Saccharomyces cerevisiae*, pheromone stimulates cells to activate a three-tiered MAPK cascade that increases transcription of mating genes, induces cell cycle arrest, and initiates polarized cell growth. Synthetic circuits can be constructed with pathway-responsive promoters to form feedback control systems that directly prescribe dynamic pathway activation profiles (*19*, *20*). Chimeric protein scaffolds can also be used to route cells to alternative pathway responses (*21*). Although successful in modulating pathway activity or fate or both, these strategies primarily rely on genetic knockouts of endogenous genes, which can alter wild-type behavior and are difficult to implement in higher eukaryotes such as humans.

Interfacing native networks with purely synthetic exogenous circuits that route cell fate through precisely controlled ectopic expression of pathway regulators provides a less invasive scheme for directing cell fate. Such control systems require little or no manipulation of the host's native genetic material, preserve access to wild-type behaviors, and minimize difficulty in transfer to higher eukaryotes. Modulation of pathway components at key control points, or pathway regulators, can alter a network response and redirect cellular fate. Introducing feedback loops at these control points reshapes network topology, alters dynamic signaling profiles, and may enhance robustness of phenotypic selection (*22*, *23*). Synthetic RNA-based transducers can be used to link diverse environmental signals to exogenous control systems so as to reshape network topology conditionally and to redirect cell fate (*4*, *5*, *24*). These synthetic control systems, or molecular network diverters, are composed of a promoter, which acts as a modulator; a pathway regulator; and an RNA-based transducer (Fig. 1, A and B). The modulator and transducer determine the strength, mode, and signal responsiveness of a diverter. Molecular network diverters conditionally divert the native network and confer orthogonal control of cell fate within a genetically homogenous cell population through specified environmental signals. Orthogonal control through diverters provides an added degree of freedom in specifying cell fate, as it preserves existing mechanical, chemical, and biochemical channels. We set out to develop molecular network diverters to activate or attenuate signaling through a native MAPK pathway to conditionally redirect, or route, cells to one of three distinct fates.

Results

Identifying Control Points Within Natural Networks

To build molecular network diverters for the yeast mating pathway, we identified titratable positive and negative regulators of pathway activity that result in divergent cell fate decisions when ectopically expressed (Fig. 1C). We measured pathway activity by monitoring fluorescence from a transcriptional reporter combined with green fluorescent protein (*pFUS1-GFP*). Cell fate determination was measured through halo assays, where cells are plated around a filter disc saturated in pheromone. The disc creates a pheromone concentration gradient, and mating-associated cell cycle arrest above a certain concentration of pheromone from wild-type cells results in a "halo" or cleared region around the disc. We used an engineered galactose-inducible promoter system to titrate amounts of various pathway signaling proteins (*25*). The set of tested pathway proteins was selected for those that were more likely to dominate pathway activity and to exhibit minimal toxicity when overexpressed (*26*, *27*). The majority of examined proteins failed to alter pathway activation when overexpressed, which supported the hypothesis that, within native pathways, regulatory architectures filter out perturbations in the amounts of various components (*28*–*34*). Despite the endogenous control schemes, we identified two control points where ectopic overexpression of associated signaling proteins dominated pathway activity (Fig. 2, A and B, and fig. S1, A and B). Ste4 activated the mating pathway and induced cell cycle arrest in the absence of pheromone (fig. S2A), whereas overexpression of Msg5 reduced pathway activation and eliminated pheromone-induced cell cycle arrest (fig. S2B).

We examined the relations between pathway response and the predicted abundance of the regulator (Ste4 or Msg5). Amounts of each pathway regulator were varied by pairing the regulator with promoters and RNA-based transducers of various activities (Fig. 2, C, D, and E). By compiling pathway activity data, we determined the pathway response curve as a function of predicted Ste4 concentrations, calculated from the combined promoter and transducer activities (Fig. 2F, fig. S3, and supplementary text S1). By combining the pathway response curve with data on cell fate, we identified a narrow transitory range of ectopic Ste4 expression at which cell fate diverged from wild-type to an alternative "mating" fate. The "mating" fate is characterized by constitutive activation of the pathway and cell cycle arrest in the absence of pheromone, which results in undetectable cell growth outside the halo region. We also examined a positive-feedback architecture by replacing the constitutive promoter (*pC*) with

[1]Division of Chemistry and Chemical Engineering, 1200 East California Boulevard, MC 210-41, California Institute of Technology, Pasadena, CA 91125, USA. [2]Department of Mechanical Engineering, 900 University Avenue, University of California at Riverside, Riverside, CA 92521, USA. [3]Department of Bioengineering, 473 Via Ortega, MC 4201, Stanford University, Stanford, CA 94305, USA.

*Corresponding author. E-mail: csmolke@stanford.edu

the pathway-responsive promoter (*pFB*), which increased expression of the regulator in response to pathway activity. To analyze the quantitative effect of the various modes of expression (*pC*, *pFB*) on the pathway response to Ste4, we fit each response curve to a Hill function (table S1). The Hill function model indicates that the positive-feedback architecture shifted the concentration of Ste4 at which half-maximal pathway activation (EC_{50}) was achieved to predicted concentrations of Ste4 almost 1/10th those for the nonfeedback system ($EC_{50\text{-}Ste4,FB}$ = 0.02, $EC_{50\text{-}Ste4,C}$ = 0.21) (Fig. 2F). The results support the hypothesis that positive feedback increased the pathway sensitivity to Ste4 expression, which shifted the threshold of pathway response to lower amounts of Ste4 and sharpened the divergence of the wild-type and mating fates.

Using similar strategies, we generated pathway response curves as a function of predicted concentrations of the negative regulator, Msg5, under constitutive (*pC*) and feedback (*pFB*) expression. Quantification of the pathway response characteristics was performed by fitting the data to a Hill function (table S2). In contrast to the Ste4 system, the Msg5 systems demonstrated different efficacies ($V_{max\text{-}Msg5,C}$ = 0.86, $V_{max\text{-}Msg5,FB}$ = 0.53), which resulted in different maximal pathway attenuation for each expression mode (*pC* or *pFB*) (Fig. 2G). Constitutive expression of Msg5 resulted in a sharper decrease in pathway activity and greater maximal pathway attenuation compared with the negative-feedback architecture, which showed a more graded response that leveled out to higher values of pathway activity. For both modes of Msg5 expression, the pathway response curves combined with the phenotypic assays demonstrated a low and narrow range of ectopic Msg5 expression (<0.1) across which cell fate diverged from wild-type to an alternative "nonmating" fate. The "nonmating" fate is characterized by constitutive inhibition of the pathway and cell cycle arrest in the presence of pheromone, which resulted in cell growth into the halo region. The data indicate that Msg5 is a potent regulator of pathway activity.

Developing Positive and Negative Diverters Based on Identified Control Points

We constructed a positive diverter with a positive-feedback architecture to activate the pathway in the absence of pheromone in response to an environmental signal. By using the pathway-responsive promoter (*pFB*) and various tetracycline-responsive RNA-based transducers (*SXtc*) to control Ste4 expression, we constructed positive-feedback diverters of varying strength. Within the positive-feedback architecture (*pFB-Ste4-SXtc*), we identified transducers that demonstrated robust small-molecule pathway activation and routing of cells to the mating fate (Fig. 3A and fig. S1C). As transducer activity increased, and thus increased the strength of the positive-feedback diverter, cells exhibited increasing pathway activity. Positive-feedback diverters composed of tetracycline-responsive transducers S3tc and S4tc activated the mating pathway and induced switching to the mating fate in the presence of tetracycline while maintaining the wild-type fate in its absence, as measured by halo assays. We also constructed positive diverters without feedback (*pC-Ste4-SXtc*) with the same components as the positive-feedback diverters except with a constitutive promoter (*pC*) replacing the pathway-responsive promoter. As expected from the pathway response curves (Fig. 2F), the positive diverters without feedback, or booster diverters, exhibited weaker effects than the positive-feedback diverters (fig. S4). We built positive diverters with and without feedback (*pFB-Ste4-SXth* and *pC-Ste4-SXth*) with theophylline-responsive RNA-based transducers (*SXth*), which allowed similar control of cell fate with a different small-molecule input (fig. S5). Transducers responsive to different inputs with similar basal activities and dynamic ranges induced similar pathway activities and similarly routed cells to the mating fate, which indicated that fate routing is independent of the input signal identity. The data support the ability to rationally tune network diverters through the exchange of modular, well-defined parts.

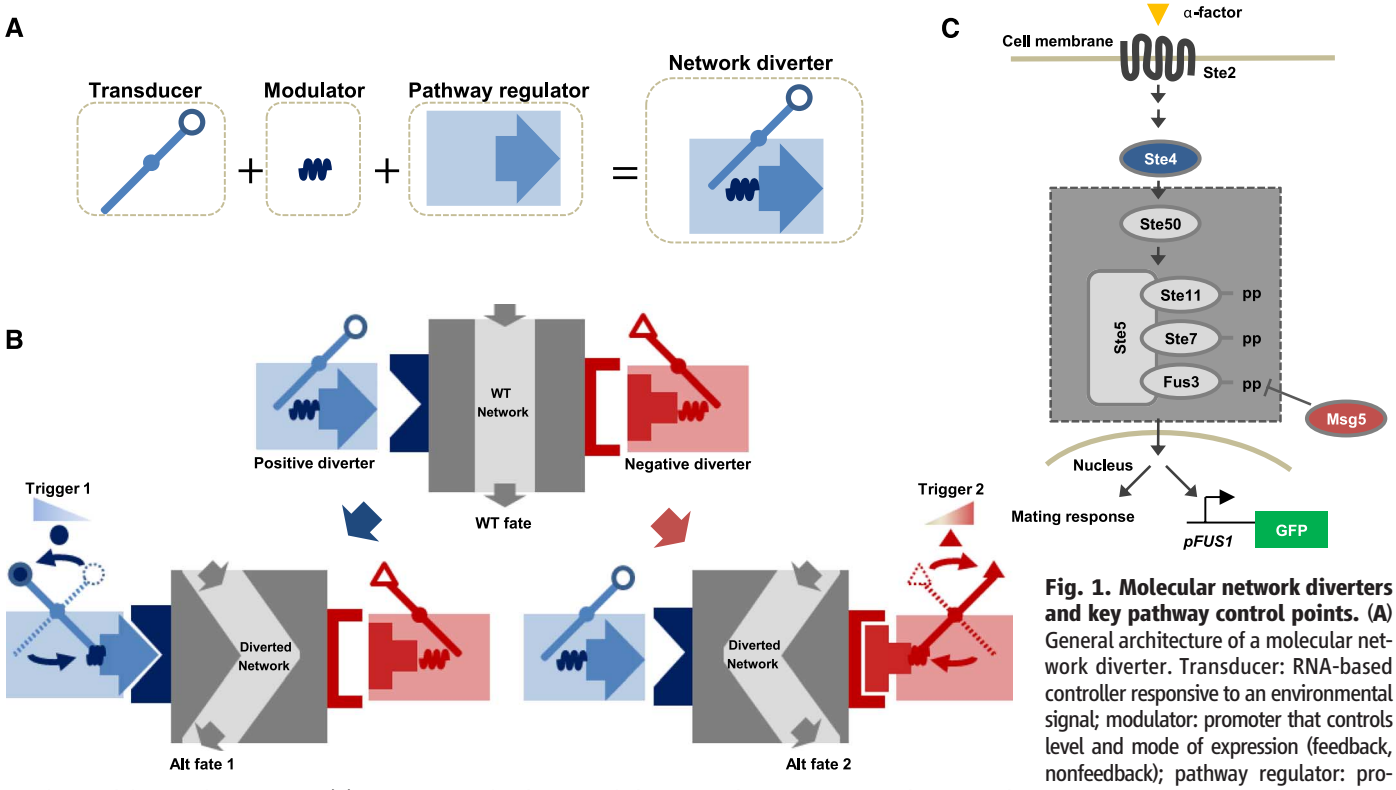

Fig. 1. Molecular network diverters and key pathway control points. (**A**) General architecture of a molecular network diverter. Transducer: RNA-based controller responsive to an environmental signal; modulator: promoter that controls level and mode of expression (feedback, nonfeedback); pathway regulator: protein that modulates pathway activity. (**B**) Diagram of molecular network diverters reshaping native signaling networks in response to environmental signals. WT, wild type. (**C**) Schematic of the yeast mating pathway. Pheromone (α-factor) binds to a transmembrane receptor (Ste2), where the signal is relayed through G proteins (Ste4), an adaptor protein (Ste50), and a scaffold-bound (Ste5-bound) three-tiered MAPK cascade. Phosphorylated Fus3 (dephosphorylated by Msg5) is translocated to the nucleus, which results in activation of mating genes. Pathway activity and mating response are monitored through a *pFUS1-GFP* reporter and pheromone-induced cell cycle arrest, respectively.

We constructed negative diverters to attenuate the pathway in the presence of pheromone in response to an environmental signal using similar design strategies. Because of the efficacy and potency of Msg5, negative diverters that maintained wild-type fate in the absence of input signal required stringent transducers (those with low basal activities) (*35*). We evaluated pathway attenuation and fate routing by negative diverters

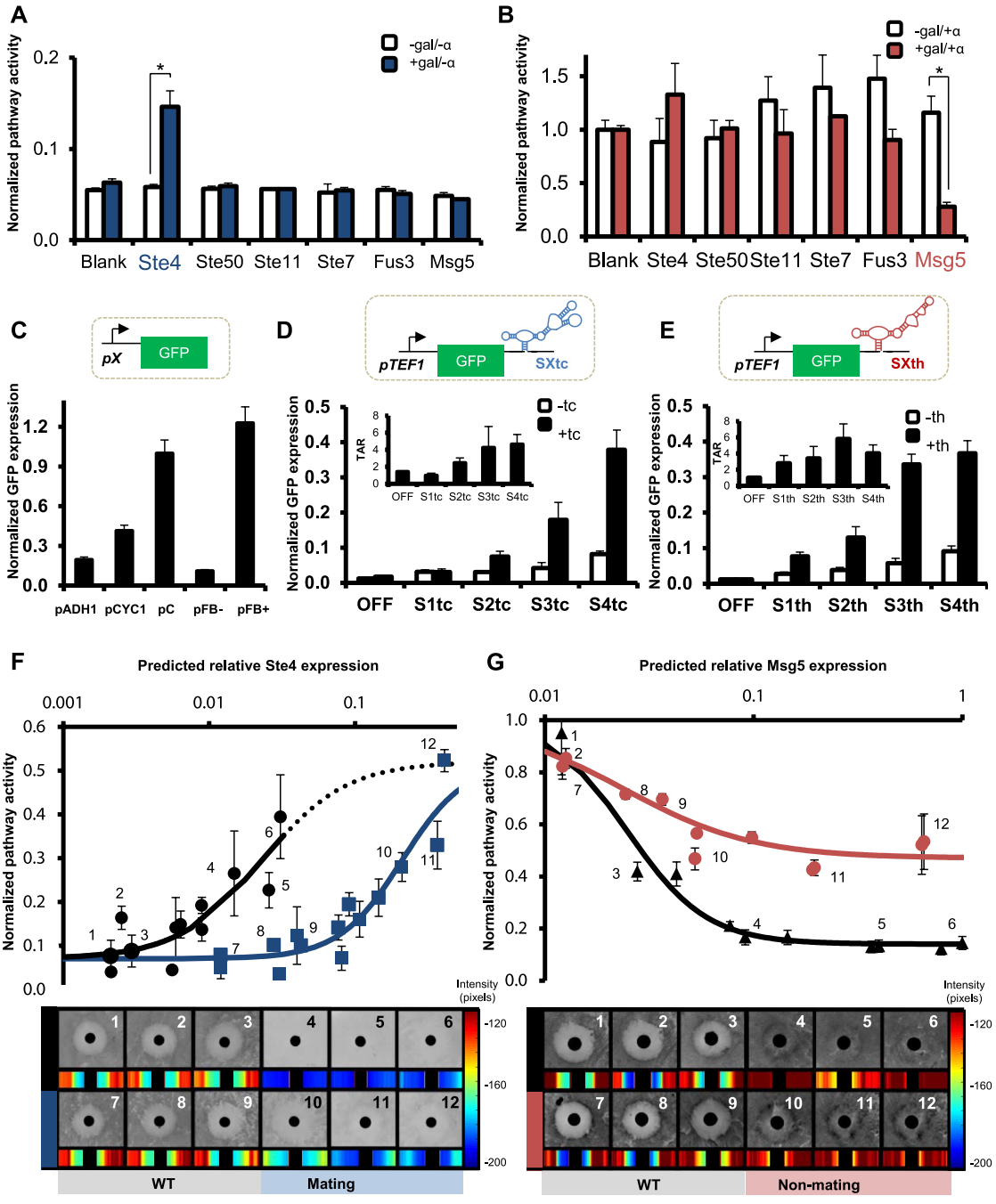

Fig. 2. A synthetic biology toolbox for constructing molecular network diverters. (**A**) Identification of activating regulators. Normalized pathway activity is reported as the geometric mean GFP value from cells overexpressing (+gal) or not overexpressing (-gal) the indicated proteins of the mating pathway. GFP values are normalized to that of the control (cells harboring a blank plasmid in the presence of saturating pheromone at the corresponding galactose concentration; gal: -gal, no galactose; +gal, 1% galactose; α: -α, no α mating factor; +α, 100 nM α mating factor). For $n = 3$, $^*P < 0.01$. (**B**) Identification of attenuating regulators. Normalized pathway activity from attenuating constructs is reported as described in (A) except that cells were assayed in the presence of saturating concentration of pheromone. (**C**) Relative promoter activities for modulating concentrations of pathway regulators. Three constitutive promoters (*pADH1*, *pCYC1*, and *pTEF1mutant7/pC*) and one mating-responsive promoter (*pFUS1/pFB*) were characterized. *pFB* activities were measured in the absence (pFB-) and presence (pFB+) of α-factor. Normalized GFP expression is reported as the geometric mean GFP value from cells harboring the specified construct normalized to that of the control (cells harboring the *pC* construct). (**D** and **E**) Activities of tetracycline-responsive (SXtc) (D) and theophylline-responsive (SXth) (E) RNA transducer sets (th: -th, no theophylline; +th, 5 mM theophylline; tc: -tc, no tetracycline; +tc, 1 mM tetracycline). Normalized GFP expression is reported as the geometric mean GFP value from cells harboring the specified construct normalized to that of the control (cells harboring the ON state control construct at the corresponding signal concentration). The TAR (transducer activation ratio) is reported as the ratio of normalized GFP expression for a given transducer in the presence and absence of signal. For $n \geq 3$, $P < 0.001$ for all noncontrol transducers. (**F**) Pathway response as a function of predicted Ste4 expression for constitutive and feedback architectures (circles: *pFB*; squares: *pC*). Predicted relative Ste4/Msg5 expression is reported as the calculated expression normalized to that of the control (construct pairing *pC* and ON RNA transducer). Normalized pathway activity from activating constructs is reported as the geometric mean GFP value from cells harboring the specified construct in the absence of pheromone at the indicated signal concentration normalized to that of the control (cells harboring a blank plasmid in the presence of saturating pheromone). Each data set is fit to a Hill function (line). Dash indicates extrapolated fit. Numbers indicate corresponding pathway activity and cell cycle arrest data for identical constructs. (**G**) Pathway response as a function of predicted Msg5 expression for constitutive and feedback architectures (triangles: *pC*; circles: *pFB*). Normalized pathway activity from attenuating constructs is reported as described in (F) except that cells are assayed in the presence of saturating pheromone. Values reported represent means ± SD for $n \geq 3$.

with the constitutive architecture and theophylline-responsive transducers (*pC-Msg5-SXth*) (Fig. 3B and fig. S1D). Pathway activity decreased with increasing transducer activity and maintenance of the wild-type halo in the absence of theophylline required stringent transducers (S1th, S2th) (Fig. 2E). The negative diverter without feedback, or resistance diverter, composed of theophylline-responsive transducer S2th reduced mating pathway activity and induced switching to the nonmating fate in the presence of theophylline while maintaining a slightly diminished wild-type fate in its absence. Fate routing was not observed with any single negative diverter constructed with the feedback architecture (*pFB-Msg5-SXth*), although cells harboring individual constructs within the negative-feedback set adopted either wild-type or nonmating fates (fig. S6). The Hill function model of the pathway response to negative feedback indicates that this architecture has reduced efficacy (Fig. 2G). The data indicate that the pathway is less sensitive to negative feedback (*36*). Thus, the transducers do not span the requisite expression range separating the wild-type and nonmating fates in this architecture. Reduced pathway sensitivity to changes in Msg5 concentrations would be expected to result in smaller changes in pathway activity, which could prevent fate routing.

Dual Diverter Highlights Need to Precisely Balance Opposing Activities

A dual diverter is a genetic control system that will support routing of an entire cell population to one of three cell fates in response to specified environmental signals. We designed a dual-diverter architecture that integrated positive and negative diverters optimized for independent cell fate routing to either the mating or nonmating fates. We paired several tetracycline-responsive positive-feedback diverters (*pFB-Ste4-SXtc*) with resistance diverters that incorporated a set of theophylline-responsive RNA transducers (*pC-Msg5-SXth*) to examine effects of pairing diverters encoding opposing functions. When opposing diverters that route signals through a native network are integrated, basal activity from the nontriggered diverter may antagonize routing from the triggered diverter (Fig. 4A), even if, independently, neither diverter affects cell fate in the absence of their cognate signal. Our results indicate that integrating the independently optimized positive-feedback and resistance diverters leads to antagonism, such that independent routing to the alternative fates cannot be achieved in cells harboring these opposing functions (fig. S7).

We developed a simple black-box model of our system to explore the pathway response to integration of multiple modules (i.e., individual regulator expression cassettes such as positive-feedback, booster, negative-feedback, and resistance modules) of varying strength set by transducer activity (Fig. 4B and table S3). We analyzed the dual-diverter architecture that integrated positive-feedback and resistance diverters by simulating pathway output for varying positive-feedback and resistance strengths in the absence and presence of pheromone (Fig. 4C). The model predicts that pathway activation across the range of positive-feedback strengths was significantly diminished even in the presence of a low-strength resistance diverter and completely inhibited for resistance strengths (amounts of Msg5) above $K_{M,Msg5}$ (the concentration of Msg5 at which half-maximal pathway attenuation was achieved). The modeling results suggest that, even at a resistance strength corresponding to the lowest basal transducer activity, the resistance module will inhibit pathway activation from the positive-feedback diverter.

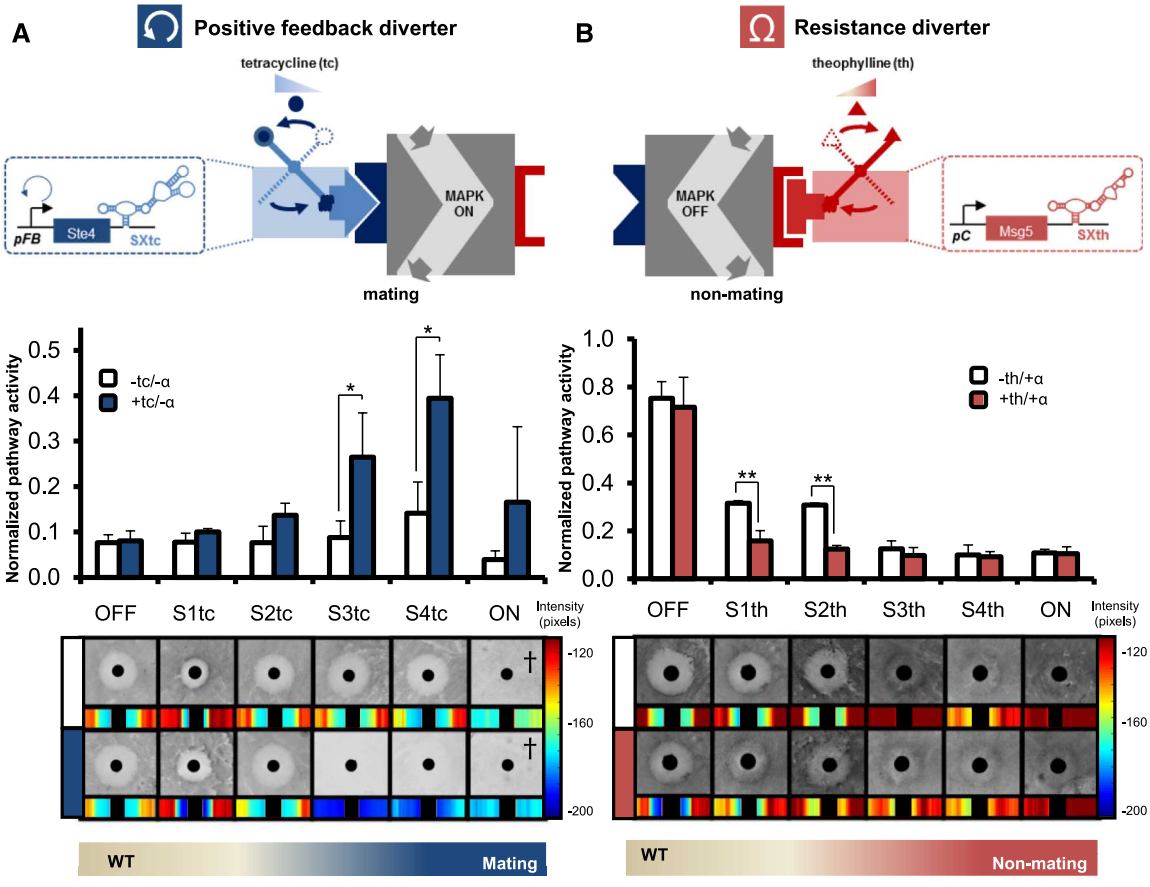

Fig. 3. Optimized design of independent positive and negative diverters. (**A**) A positive-feedback diverter supports robust pathway activation in the absence of pheromone (-α) and cell fate routing to the mating fate (tc: -tc, no tetracycline; +tc, 1 mM tetracycline). Normalized pathway activity from activating constructs is reported as described in Fig. 2F. Dagger: see fig. S3 and supplementary text S1. (**B**) A resistance diverter supports robust pathway attenuation in the presence of pheromone (+α) and cell fate routing to the nonmating fate (th: -th, no theophylline; +th, 5 mM theophylline). Normalized pathway activity from attenuating constructs is reported as described in Fig. 2G. For $n \geq 5$, $^{*}P < 0.05$, $^{**}P < 0.005$. Values reported represent means ± SD.

Conversely, positive-feedback strength limited the maximal attenuation from the resistance diverter, which led to reduced maximal attenuation as positive-feedback strength increased. These results indicate that the basal expression from the integrated opposing diverters may significantly antagonize the other diverter.

Given the limitations of performance for a dual diverter based on integrating the positive-feedback and resistance diverters, we examined alternative designs to limit antagonism and enhance the cell fate–routing functions. The modeling results indicate that strategies based on modifying the strength of the positive-feedback diverter for increased activity may limit the performance of the negative diverter (Fig. 4C). Thus, we used the model to examine the impact of adding a second positive module, or a booster module encoding constitutive expression of Ste4, to the positive-feedback diverter (Fig. 4D). The combination of the booster and positive-feedback modules enhanced system tolerance to Msg5 expression and allowed for pathway activation at amounts of Msg5 produced at basal strength (in the absence of cognate signal) of the resistance diverter. In the absence of its cognate signal, the basal strength of the booster module was predicted to have minimal effect on attenuation from the resistance diverter.

Based on the enhancement to the performance of the positive diverter achieved by combining two modules, we examined the impact of adding a second negative module, or a negative-feedback module, to the resistance diverter (Fig. 4E). Negative feedback was predicted to globally enhance attenuation and to make it robust to minor variations in Ste4 and Msg5 expression from the other modules. The addition of negative feedback to the negative diverter was predicted to have minimal impact on pathway activation

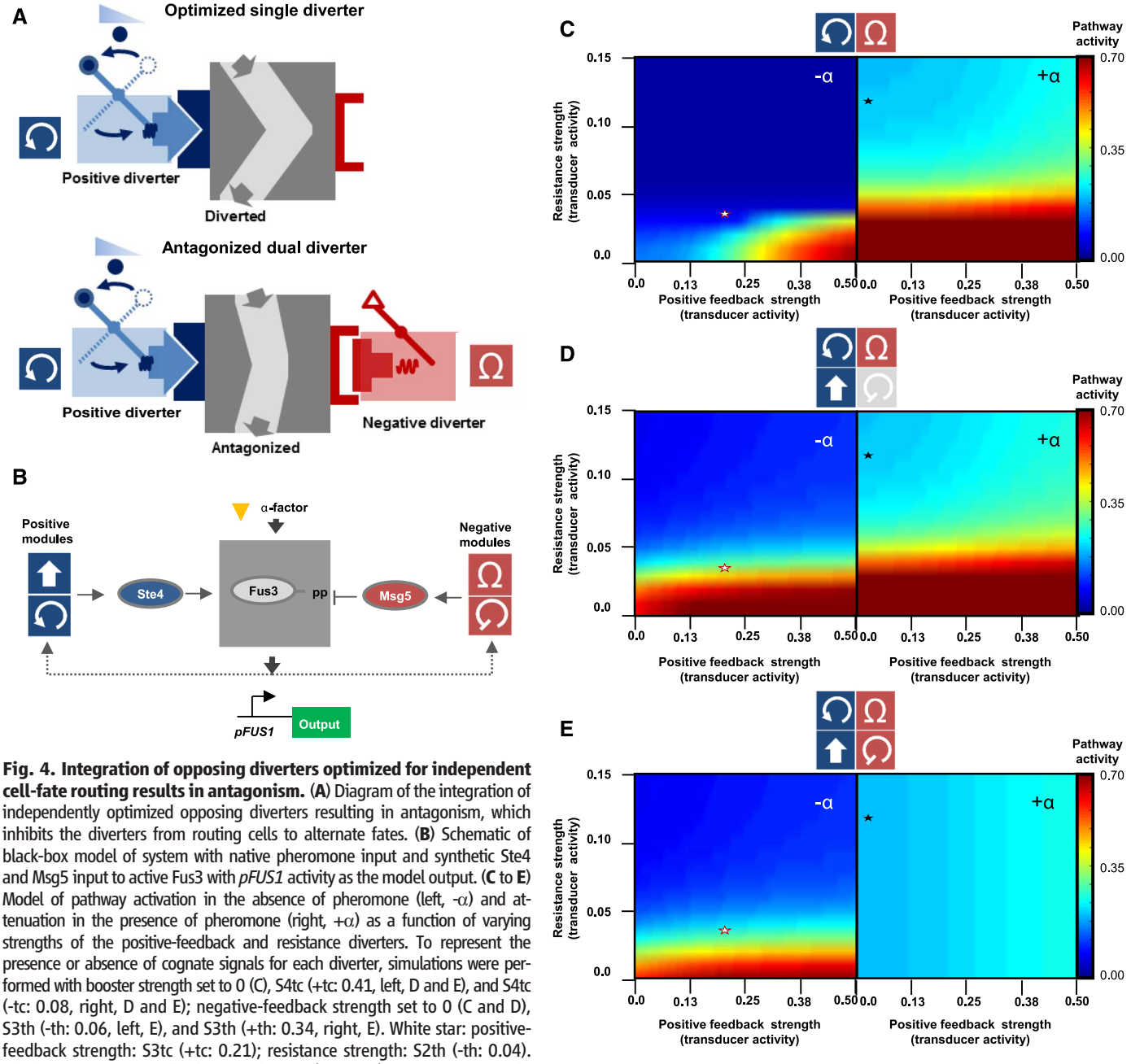

Fig. 4. Integration of opposing diverters optimized for independent cell-fate routing results in antagonism. (**A**) Diagram of the integration of independently optimized opposing diverters resulting in antagonism, which inhibits the diverters from routing cells to alternate fates. (**B**) Schematic of black-box model of system with native pheromone input and synthetic Ste4 and Msg5 input to active Fus3 with *pFUS1* activity as the model output. (**C** to **E**) Model of pathway activation in the absence of pheromone (left, -α) and attenuation in the presence of pheromone (right, +α) as a function of varying strengths of the positive-feedback and resistance diverters. To represent the presence or absence of cognate signals for each diverter, simulations were performed with booster strength set to 0 (C), S4tc (+tc: 0.41, left, D and E), and S4tc (-tc: 0.08, right, D and E); negative-feedback strength set to 0 (C and D), S3th (-th: 0.06, left, E), and S3th (+th: 0.34, right, E). White star: positive-feedback strength: S3tc (+tc: 0.21); resistance strength: S2th (-th: 0.04). Black star: positive-feedback strength: S3tc (-tc: 0.04); resistance strength: S2th (+th: 0.13).

through the positive diverter. Thus, the model predicts that restructuring the positive and negative diverters to include two differentially regulated modules of the same pathway regulator will enhance the function of the individual diverters, while minimizing the impact on the opposing diverter.

Genetic Strategies for Minimizing Pathway Antagonism

We developed and incorporated a number of strategies to reduce antagonism in the dual diverter and to allow for routing to multiple fates. We constructed an alternative RNA transducer architecture that minimized basal expression from the positive-feedback diverter in response to the cognate signal from the negative diverter to maximize pathway attenuation. The composite transducer S3tc—comprising S4tc (tetracycline-responsive "ON" switch) and S1OFFth (theophylline-responsive "OFF" switch)—was designed to reduce expression of Ste4 in response to theophylline and to increase Ste4 expression in response to tetracycline (Fig. 5A). When this composite transducer was implemented in the positive-feedback diverter, pathway activity was between those of S2tc and S4tc for basal and tetracycline-triggered activities. In the presence of theophylline, activity for S3tc was similar to S2tc basal activity (Fig. 5B). Thus, S3tc yielded a larger fold difference in pathway activity (8.0; $activity_{tc}$: $activity_{th}$) than did S2tc (3.8) or S4tc (2.5). Several integrated dual-diverter configurations that used the positive-feedback diverter incorporating S3tc (*pFB-Ste4-S3tc*) achieved strong pathway attenuation when paired with resistance diverters. As predicted from the model, all configurations displayed weak pathway activation (fig. S8), which suggested that basal expression of Msg5 from the resistance diverter prevented the requisite pathway activation to trigger positive feedback–induced amplification. Improved performance of a dual diverter may be achieved with the use of RNA transducers exhibiting even lower basal activities and larger dynamic ranges. However, computational models of RNA transducer activities indicate a trade-off between stringency and input sensitivity of these genetic devices (*37*). Given these constraints, the dual-diverter architecture is inherently biased to allow basal expression from the opposing diverters to promote antagonism, which cannot be mitigated solely by changing transducer or promoter activities.

We developed an alternate positive-diverter architecture to support increased pathway activation with minimal impact on the negative diverter (Fig. 5C). The modeling results indicate that strategies based on modifying the strength of the positive-feedback module for increased activity limit the performance of the negative diverter (Fig. 4C). Thus, we added a second module, or a booster module, encoding constitutive expression of Ste4 and a strong tetracycline-responsive RNA-based transducer (*pC-Ste4-S4tc*), to the positive-feedback diverter. The resulting enhanced positive diverter, or amplifying diverter, combined a positive-feedback module (*pFB-Ste4-S3tc*) and booster module (*pC-Ste4-S4tc*) to increase pathway activation while minimizing antagonism of the attenuating function of the negative diverter. As predicted by the model, this dual-diverter architecture restores pathway activation (Fig. 5E). However, this architecture did not allow for routing to the nonmating fate (fig. S9). The data indicate that amplification of pathway activation from the positive-feedback module in the amplifying diverter in the presence of high concentrations of pheromone overwhelmed attenuation from the resistance diverter.

To counteract amplification from the amplifying diverter at high concentrations of pheromone, we constructed an enhanced negative diverter by adding a negative-feedback module, linking a pathway-responsive promoter and a theophylline-responsive RNA-based transducer to Msg5 (*pFB-Msg5-SXth*) to the resistance diverter (Fig. 5D). The resulting attenuating diverter combined a negative-feedback module (*pFB-Msg5-S3th*) and resistance module (*pC-Msg5-S2th*) (Fig. 5D). As predicted by the model, the attenuating diverter had minimal impact on pathway activation through the amplifying diverter, which retained tetracycline-induced routing to the mating fate (Fig. 5E).

We observed that the robustness of pathway activation varied with the different dual-diverter architectures. Although effective in routing cells to the mating fate, the high basal pathway activity associated with the positive-feedback diverter provided little resolution between triggered and nontriggered populations (Fig. 5E and fig. S10A). Addition of the resistance diverter inhibited routing to the mating fate. By combining the positive-feedback and booster modules in the amplifying diverter, cells were routed to the mating fate in the presence of the resistance diverter. Addition of the negative-feedback module significantly increased resolution by reducing population heterogeneity (fig. S10B).

We probed the performance of the dual diverter constructed with amplifying and attenuating diverters under varying strengths of the resistance module by varying the transducer activity (*pC-Msg5-SXth*). The data demonstrated a strong correlation between resistance strength and pathway activity (Fig. 5F). Pathway activation diminished and attenuation increased with increasing resistance strength (fig. S11, A and B). Thus, resistance strength must be precisely tuned for the dual diverter to achieve routing to multiple alternative and divergent cell fates.

We used our model to analyze the impact of the resistance module on system robustness and output. Basal concentration of Msg5 from the resistance module acts as a buffer to pathway activity, by filtering out perturbations in Ste4 concentrations from the amplifying diverter (Fig. 5G). In the presence of the resistance module, the amplifying diverter maintains low pathway activity until Ste4 concentrations cross a threshold and pathway activity is amplified. We evaluated the buffer capacity of the system by identifying the Ste4 expression from the booster module that resulted in pathway activation (above basal pathway activity ~0.07) as a function of resistance strength (Fig. 5H). Buffer capacity increased for increasing resistance strength and was inversely related to pathway activation with an optimum for buffer capacity and pathway activation when resistance strength is set at 80% of $K_{M,Msg5}$. Our results suggest that there is a trade-off in tuning our system for both signal output and robustness.

Optimized Dual Diverter Routes Cells to Three Distinct Fates

Our optimized dual diverter integrated a number of strategies to minimize antagonism, including improved transducer architecture, amplifying and attenuating diverters, and a precisely tuned amount of resistance (Fig. 6, A and B). Although the dual diverter (booster: *pC-Ste4-S4tc*; positive feedback: *pFB-Ste4-S3tc;* resistance: *pC-Msg5-S2th;* negative feedback: *pFB-Msg5-S3th*) exhibited lower pathway activation than did the positive-feedback diverter alone or ON control (dual diverter without the negative-feedback module), the dual diverter exhibited a stronger fold pathway activation (7.2) than the positive-feedback diverter (1.6), approaching that of the ON control (10.9) (Fig. 6C). The dual-diverter attenuated pathway activity as well as the resistance diverter alone, and the pathway activity approached that of the OFF control (positive feedback: *pFB-Ste4-OFF*; resistance: *pC-Msg5-S3th*; negative feedback: *pFB-Msg5-S3th*) (Fig. 6E). The dual diverter routed cells to the mating fate as well as did the positive-feedback diverter (Fig. 6D). Additionally, the cells harboring the dual diverter maintained a more robust wild-type halo compared with those harboring the resistance diverter, while routing nearly as well to the nonmating fate. Finally, cell routing could be modulated through the concentration of environmental signals (fig. S11C). Although the ON control and dual diverter exhibited similar pathway attenuation, only the latter routed cells to the nonmating fate, which indicated that negative feedback is a critical element in regulating longer time-scale events, such as cell cycle arrest. Thus, the optimized dual diverter achieved conditional routing of genetically identical cells to diverse phenotypes in response to distinct molecular signals.

Beyond controlling transcriptional activation of the pathway and cell cycle arrest, the diverters also controlled mating. The positive-feedback diverter and the ON control allowed a tetracycline-induced increase in mating efficiency and increased basal mating efficiency (Fig. 6F). The resistance diverter and the OFF control exhibited a theophylline-triggered reduction in mating efficiency. The dual diverter increased mating efficiency by ~70% in response to tetracycline, similar to the effect of the positive-feedback diverter (~66%), and reduced mating efficiency to an amount similar to that from cells harboring the resistance diverter in the presence of theophylline. The mating data indicated that the dual diverter is

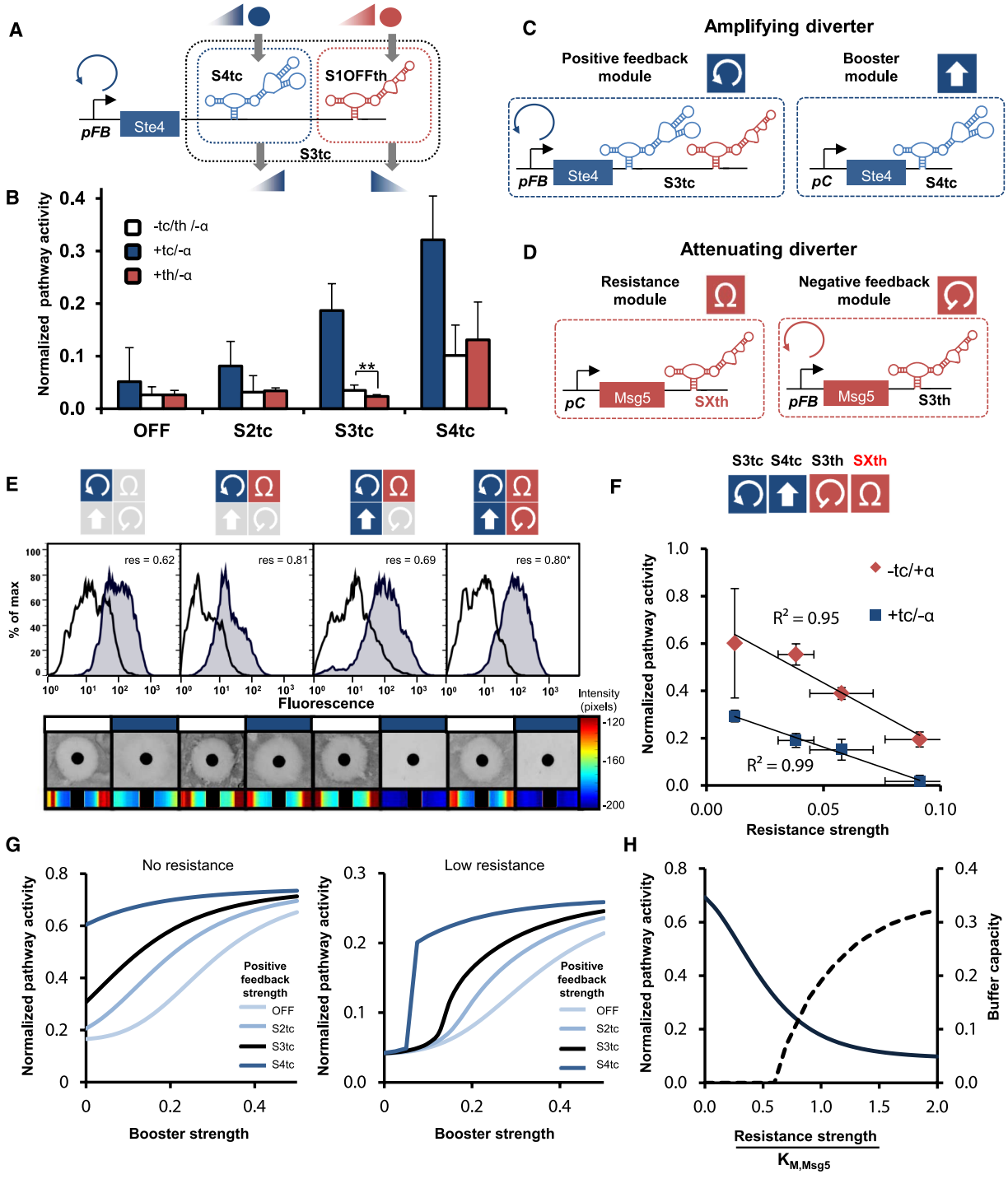

Fig. 5. Optimizing the dual-diverter architecture and components for the integration of opposing diverters. (**A**) Schematic of the composite RNA transducer S3tc designed to reduce expression of the linked regulator in response to theophylline and increase expression in response to tetracycline. (**B**) Pathway activity of cells with composite transducer S3tc in response to tetracycline or theophylline (tc: -tc, no tetracycline; +tc, 1 mM tetracycline; th: -th, no theophylline; +th, 20 mM theophylline; α: -α, no α mating factor; +α, 100 nM α mating factor). For $n = 6$, $^{**}P < 0.02$. (**C**) Schematic of the amplifying diverter comprising a positive-feedback module and a booster module. (**D**) Schematic of the attenuating diverter comprising a resistance module and a negative-feedback module. (**E**) Impact of resistance, booster, and negative-feedback modules on the resolution and variation in population-level pathway activation and routing to mating fate for cells harboring the positive-feedback module (white: 0 mM tetracycline; blue: 1 mM tetracycline). GFP histograms for triggered and nontriggered cell populations and routing to the mating fate are shown for cells harboring: (left) the positive-feedback module (*pFB-Ste4-S3tc*); (second from left) the positive-feedback and resistance (*pC-Msg5-S2th*) modules; (second from right) the positive-feedback, resistance, and booster (*pC-Ste4-S4tc*) modules; (right) the positive-feedback, resistance, booster, and negative-feedback (*pFB-Msg5-S3th*) modules. For $n = 3$, $^{*}P < 0.0005$. (**F**) Pathway activity of the dual diverter as a function of varying resistance strength. R^2 represented for linear fit of data. (**G**) Predicted pathway activation from the dual diverter as a function of booster strength in the absence (left) and presence (right) of low resistance. Lines represent predicted relations under the indicated positive-feedback strengths, as set by transducer activity. (**H**) Predicted pathway activation and buffer capacity from the dual diverter as a function of varying resistance strength relative to $K_{M,Msg5}$. Solid: pathway activity; dashed: buffer capacity. Values reported represent means ± SD for $n \geq 3$.

optimized to route cells to the divergent fates as effectively as each single diverter.

Discussion

Our studies describe a class of genetic control systems, molecular network diverters, that route cells to divergent fates in response to specified environmental signals. The system integrates complex positive and negative routing functions through stringent RNA-based transducers to limit antagonism, amplify activation, and induce attenuation, which allows genetically identical cells to be conditionally routed to one of three fates in response to specified environmental signals. We focused our analysis of the effects of the molecular network diverters on steady-state pathway activation, as measured by transcriptional activation of the pathway, and cell fate determination, as measured by cell cycle arrest and mating efficiency. Other properties of the network, including temporal response of pathway activation and pathway sensitivity to pheromone concentrations, can also be measured and analyzed for changes in the engineered systems and the relation of these network properties to fine-tuning cell fate decisions (*33*, *38*). Positive- or negative-feedback loops, as well as constitutive overexpression of signaling components, can tune MAPK pathways for prescribed temporal pathway activation responses (*19*). In addition, altering the

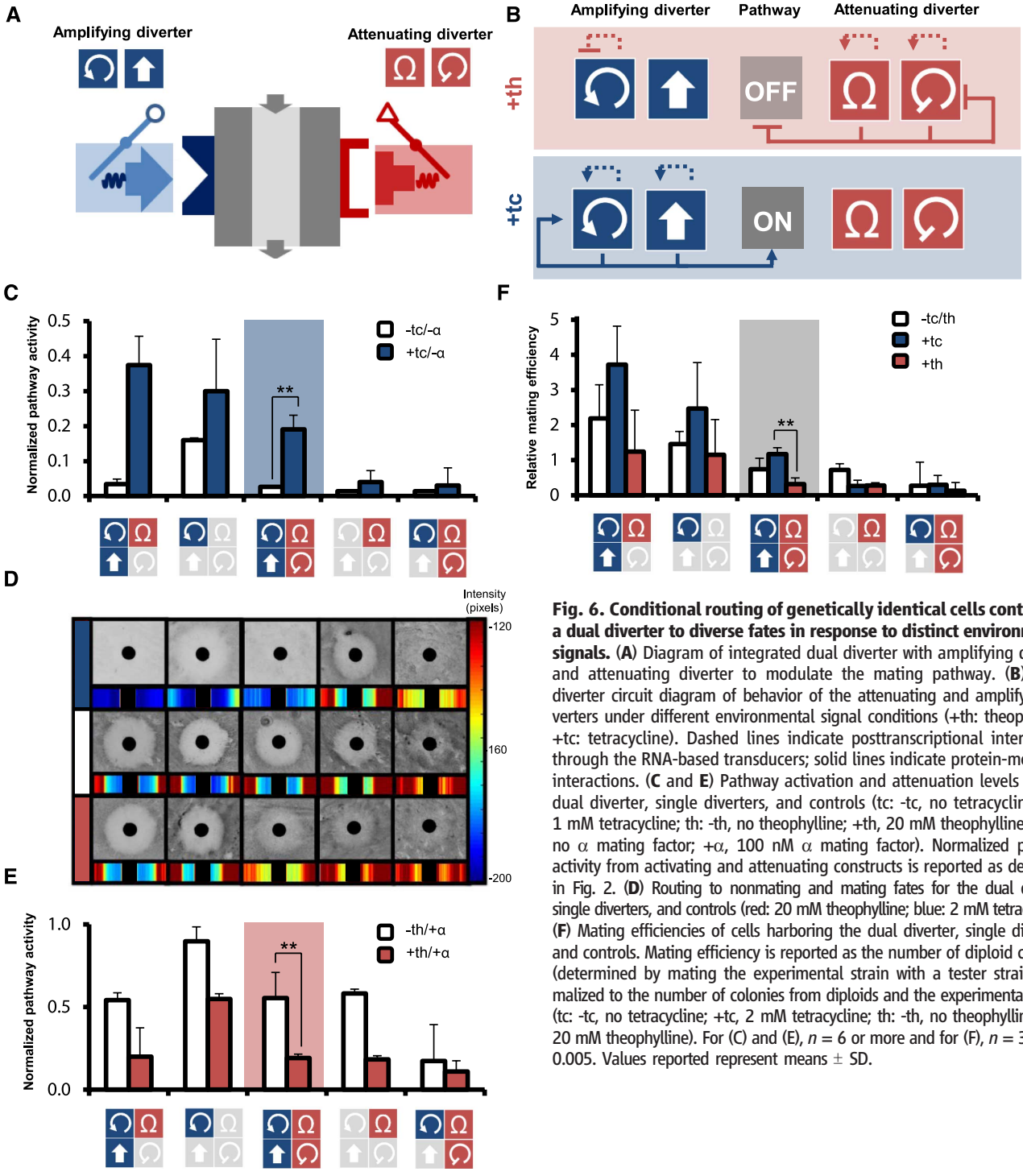

Fig. 6. Conditional routing of genetically identical cells containing a dual diverter to diverse fates in response to distinct environmental signals. (**A**) Diagram of integrated dual diverter with amplifying diverter and attenuating diverter to modulate the mating pathway. (**B**) Dual-diverter circuit diagram of behavior of the attenuating and amplifying diverters under different environmental signal conditions (+th: theophylline; +tc: tetracycline). Dashed lines indicate posttranscriptional interactions through the RNA-based transducers; solid lines indicate protein-mediated interactions. (**C** and **E**) Pathway activation and attenuation levels for the dual diverter, single diverters, and controls (tc: -tc, no tetracycline; +tc, 1 mM tetracycline; th: -th, no theophylline; +th, 20 mM theophylline; α: -α, no α mating factor; +α, 100 nM α mating factor). Normalized pathway activity from activating and attenuating constructs is reported as described in Fig. 2. (**D**) Routing to nonmating and mating fates for the dual diverter, single diverters, and controls (red: 20 mM theophylline; blue: 2 mM tetracycline). (**F**) Mating efficiencies of cells harboring the dual diverter, single diverters, and controls. Mating efficiency is reported as the number of diploid colonies (determined by mating the experimental strain with a tester strain) normalized to the number of colonies from diploids and the experimental strain. (tc: -tc, no tetracycline; +tc, 2 mM tetracycline; th: -th, no theophylline; +th, 20 mM theophylline). For (C) and (E), $n = 6$ or more and for (F), $n = 3$, $^{**}P < 0.005$. Values reported represent means ± SD.

relative amounts of pathway kinases can tune the sensitivity of the pathway response to pheromone concentrations (*33*). Thus, the molecular network diverters can be adapted to the regulation of other pathway signaling components to engineer a wider range of network properties.

The modular architecture of the diverters, availability of tuned RNA-based transducers, and incorporation of feedback allow for precise balancing of positive and negative regulator activities even in the presence of external pathway stimulation. Our work identified design principles for networks that induce differentiation of cells in response to environmental signals and that enhance the robust performance of integrated mutually antagonistic genetic programs. As an example, integrated negative regulators can act to buffer a system to noise amplification mediated through positive-feedback loops by providing a resistance to amplification. Additionally, pathway output can be tuned through resistance, which may be a key design consideration when adopting the network diverter architecture to new signaling pathways with different thresholds of pathway activity corresponding to alternative fates. Further, negative feedback can play an important role by reducing population heterogeneity and mediating robust, long-term cell fate decisions. The dual-diverter configuration enables routing to alternative fates and minimizes impact on the opposing diverter by integrating differential regulatory strategies on functionally redundant genes. Differential regulation of functionally redundant parts is observed in natural biological networks, such as those regulating bone formation, osteoblast differentiation, plant defense, and metabolism (*39*, *40*), and may represent a common strategy for amplifying and attenuating pathway responses to environmental signals.

Our studies focused on the development and elucidation of design principles for this class of genetic control systems in the model organism *S. cerevisiae*. Conservation of the form and function of MAPK pathways through higher eukaryotes highlights the possible applications of these controllers in mammalian systems. For example, a threefold overexpression of MPK-1 (homolog to yeast Msg5) can significantly reduce MAPK phosphorylation and block persistent pathway activation (*41*). In addition, overexpression of MPK-1 blocks apoptosis by inhibiting extracellular signal-regulated kinase and c-Jun N-terminal kinase signaling (*42*–*44*). As another example, overexpression of a neuroendocrine-associated phosphatase can suppress nerve growth factor–stimulated neuron differentiation in PC12 cells (*45*). However, differences in the regulation of these pathways in higher organisms compared with yeast may prohibit a direct translation of the strategies described here, and extension into higher organism may require further engineering optimization efforts.

Molecular network diverters provide a foundation for robustly programming spatial and temporal control over cell fate. The extension of similar control strategies to mammalian systems may facilitate construction of sophisticated genetic programs encoding complex cellular functions, such as patterning of cell fate, tissue homeostasis, and autonomous immune surveillance (*14*). The connection of synthetic circuits to downstream effector processes, like drug-delivery and apoptosis, requires reliable signal processing to target therapeutic effects. Strategies that enhance the robustness of signal processing in synthetic circuits will enable such smart therapeutics. Our ability to construct synthetic circuits that interface with native pathways, like molecular network diverters, will continue to expand as more pathway-responsive genetic elements and regulatory RNAs are identified. Advances in our capabilities to extract information from and direct responses in native pathways will facilitate the translation of synthetic biology tools to applications in medicine and biotechnology.

Materials and Methods

Plasmid and Strain Construction

Details are available in Materials and Methods in the supplementary materials available online.

Measuring Promoter and RNA Transducer Activities

Details are available in supplementary materials.

Measuring Mating Pathway Activity Through a Transcriptional Reporter

For the galactose titration studies, plasmids harboring the galactose-inducible promoter (*pGAL1*) controlling expression of various pathway regulators (*STE4*, *STE50*, *STE11*, *STE7*, *FUS3*, and *MSG5*) and appropriate controls were transformed into the reporter yeast strain CSY532. Cells were inoculated into the appropriate dropout medium, grown overnight at 30°C, and backwards diluted into fresh medium in the presence of varying concentrations of galactose (0, 0.25, 0.5, 1, 2 and 3%) to an optical density at 600 nm (OD_{600}) of <0.1. To identify negative pathway regulators, after growing cells for 3 hours at 30°C, we stimulated them with saturating pheromone levels [100 nM final concentration of α mating factor (Sigma-Aldrich, St. Louis, MO)] to activate the mating pathway. The pathway was not stimulated when evaluating the potential of positive regulators. After 6 hours of growth after back-dilution, GFP fluorescence levels from the *pFUS1-yEGFP3* reporter were evaluated by flow cytometry using a Cell Lab Quanta SC flow cytometer (Beckman Coulter, Fullerton, CA). GFP was exited from a 488-nm laser, and emission was measured from 520/40-nm bandpass filter with a photomultiplier tube setting of 5.0. Cells were gated for viability on the basis of side scatter and electronic volume. For each sample, the GFP values of 10,000 viable cells were measured. Cells were then gated for GFP levels above background. Flow cytometry data were analyzed using the FlowJo v.10 (Tree Star, Inc.) software package. Normalized pathway activity is calculated as the geometric mean GFP value of cells harboring the indicated construct normalized to that of cells harboring the blank plasmid control (not bearing a gene) stimulated with saturating α mating factor at the corresponding galactose concentration for three biological replicates. Error bars represent the standard deviation of at least three replicates.

The molecular network diverter plasmids and appropriate controls were transformed into the reporter yeast strain CSY840. Cells were inoculated into the appropriate dropout medium, grown overnight at 30°C, and backwards diluted into fresh medium in the presence or absence of the appropriate trigger molecule (theophylline or tetracycline) at the specified concentration to an OD_{600} of <0.1. For negative diverters, after growing cells for 3 hours at 30°C, we stimulated cells with saturating pheromone levels (100 nM final concentration α mating factor) to activate the mating pathway, whereas we tested positive diverters in the absence of pheromone. After 6 hours of growth after back-dilution, GFP fluorescence levels from the *pFUS1-yEGFP3* reporter were evaluated by flow cytometry using a Cell Lab Quanta SC flow cytometer as described above. For cells stimulated with tetracycline, GFP values were corrected by subtracting the calculated tetracycline autofluorescence. Tetracycline autofluorescence was calculated as the difference in GFP values between the 0 mM and 1 mM tetracycline samples for the wild-type control. GFP values for the wild-type control were not altered in the presence of theophylline. Normalized pathway activity is calculated as the geometric mean GFP value of cells harboring the indicated construct normalized to that of cells harboring the blank plasmid control stimulated with saturating α mating factor in the absence of either small molecule. Error bars represent the standard deviation of at least three replicates. *P* values were determined by a two-tailed *t* test of the compared data sets.

Measuring Mating Pathway Activity via Halo Assays

Mating associated cell-cycle arrest was evaluated with halo assays as previously described (*46*). Briefly, halo assays were performed on cultures harboring the indicated constructs grown overnight in the appropriate dropout medium, backwards diluted into fresh medium to an OD_{600} of <0.1, and grown to an OD_{600} between 0.2 and 0.4. Each replicate was plated at a volume of 300 µl on the appropriate dropout plates. For galactose-titration halo assays, cells were plated on noninducing, nonrepressing solid medium with varying concentrations of galactose (0, 0.25, 0.5, 1, 2, and 3%). For characterization of the molecular network diverters, we plated cells on solid dropout medium containing the indicated concentration of signal molecule (theophylline or tetracycline). After plating the cells, a gradient of α mating factor was established by saturating a filter disk (2-mm diameter) of Whatman paper with

9 µl of 0.1 mg/ml α mating factor and placing the disk on the center of the plate. Cells were grown for 18 hours at 30°C and imaged via epi-white illumination with a GelDoc XR+ System (Bio-Rad). Representative images are presented from experiments performed at least in triplicate.

Images from halo assays were analyzed using ImageJ (NIH, Bethesda, MD) software analysis to extract pixel intensity at each position along a horizontal slice of the halo image by using the rectangular tool. Standard slices were centered on the filter disc. Heat maps were generated using the "HeatMap" function from MATLAB (Mathworks, Natick, MA) for the halo assays at a standard window size. To ensure that the heat map captured the changes in growth and was standardized across all maps, we excluded high-intensity data (e.g., the filter disc) and fixed the range of intensities (pixels of 120 to 200).

Calculating Relative Regulator Expression

Details are available in supplementary materials.

Evaluating Selection of Mating-Resistant Population

Details are available in supplementary materials.

Determining Resolution and Variation in Positive-Diverter Networks

Details are available in supplementary materials.

Measuring Mating Efficiencies

Details are available in supplementary materials.

Modeling of Molecular Networks Diverter Interactions with the Mating Pathway

We built a simple phenomenological model to describe the dynamic behavior of key components of our pathway: Ste4, Fus3, Msg5, and Fus1 (output). The model consists of four deterministic ordinary differential equations (ODEs 1 to 4 below), and it builds on models previously proposed in the literature (*47*–*49*). A complete description of this signaling cascade would include additional phosphorylation intermediates and scaffold proteins (*19*). However, detailed mechanistic ODE models of the MAPK pathway in *Xenopus* show that the resulting input and output behavior of this multilayered signaling cascade is equivalent to a highly cooperative activation enzymatic process (*47*). Thus, we reduced the model to a four-component system, where the unmodeled phosphorylation and dephosphorylation kinetics between Ste4, Msg5, and Fus3 are qualitatively captured by Hill functions with high Hill coefficients.

Each synthetic regulatory element in our pathway is individually modeled. We used zero-order production rates to capture the effects of constitutive promoters and switches on the native pathway. These production rates are modulated according to the strength of the switch employed. We used Hill functions to model the pathway-responsive promoter (*pFUS1*/*pFB*), which generates the positive-feedback (Ste4 activation) and negative-feedback (Msg5 activation) loops.

The model was fit to normalized *pFUS1-GFP* steady-state data. We used the results of several experimental assays, testing the effects of each individual synthetic regulatory module on the native pathway output. The steady-state data sets simultaneously used in the fitting algorithm include the response of the pathway (i) at different concentrations of pheromone (α-factor), (ii) in the presence of *pC-Ste4*, (iii) in the presence of *pC-Msg5*, (iv) in the presence of *pFB-Ste4*, (v) in the presence of *pFB-Msg5* with a range of transducers for each (ii-v). Fits were generated using MATLAB "fmincon" routine, minimizing the squared error between the numerically generated steady-state of Fus1 and the normalized measured data. ODEs were integrated using a forward Euler method. Upper and lower bounds were chosen for each parameter to guarantee positivity and boundedness of the solutions.

The parameters resulting from our fit are in general agreement with expected relative values of reaction rates for promoter activity and for phosphorylation and dephosphorylation pathways (table S3). The Mgs5-mediated maximal dephosphorylation rate of Fus3 is high relative to other rates; the efficacy of Msg5 as a strong phosphatase for Fus3 is well known (*50*, *51*), but few experimental kinetic measurements are available in the literature (*52*). Our parameter for Msg5 dephosphorylation is consistent with previous work (*52*). The half-maximal concentration of Msg5 ($K_{M,Msg5}$) is low, in agreement with our experimental observations.

$$\frac{d}{dt}[Ste4] = \beta_{Ste4} - \delta_{Ste4}[Ste4] + k_{C,Ste4}SCtc + k_{FB,Ste4}SFtc\frac{[Fus1]^{n_{pf}}}{K_{M,Fus1,pf}^{n_{pf}} + [Fus1]^{n_{pf}}} \quad (1)$$

$$\frac{d}{dt}[Fus3] = \beta_{Fus3} + k_{Ste4}\frac{[Ste4]^m}{K_{M,Ste4}^m + [Ste4]^m} + k_\alpha\frac{[\alpha]^n}{K_{M,\alpha}^n + [\alpha]^n} - \delta_{Fus3}[Fus3] - k_{Msg5}[Fus3]\frac{[Msg5]^q}{K_{M,Msg5}^q + Msg5^q} \quad (2)$$

$$\frac{d}{dt}[Msg5] = \beta_{Msg5} - \delta_{Msg5}[Msg5] + k_{C,Msg5}SCth + k_{FB,Msg5}SFth\frac{[Fus1]^{n_{nf}}}{K_{M,MFus1,nf}^{n_{nf}} + [Fus1]^{n_{nf}}} \quad (3)$$

$$\frac{d}{dt}[Fus1] = \beta_{Fus1} - \delta_{Fus1}[Fus1] + k_{Fus3}\frac{[Fus3]^p}{K_{M,Fus3}^p + [Fus3]^p} \quad (4)$$

References and Notes

1. R. Seger, E. G. Krebs, The MAPK signaling cascade. *FASEB J.* **9**, 726–735 (1995). pmid: 7601337
2. K. L. Pierce, R. T. Premont, R. J. Lefkowitz, Seven-transmembrane receptors. *Nat. Rev. Mol. Cell Biol.* **3**, 639–650 (2002). doi: 10.1038/nrm908; pmid: 12209124
3. A. Negro, B. K. Brar, K. F. Lee, Essential roles of Her2/erbB2 in cardiac development and function. *Recent Prog. Horm. Res.* **59**, 1–12 (2004). doi: 10.1210/rp.59.1.1; pmid: 14749494
4. Y. Y. Chen, M. C. Jensen, C. D. Smolke, Genetic control of mammalian T-cell proliferation with synthetic RNA regulatory systems. *Proc. Natl. Acad. Sci. U.S.A.* **107**, 8531–8536 (2010). doi: 10.1073/pnas.1001721107; pmid: 20421500
5. S. J. Culler, K. G. Hoff, C. D. Smolke, Reprogramming cellular behavior with RNA controllers responsive to endogenous proteins. *Science* **330**, 1251–1255 (2010). doi: 10.1126/science.1192128; pmid: 21109673
6. J. C. Anderson, E. J. Clarke, A. P. Arkin, C. A. Voigt, Environmentally controlled invasion of cancer cells by engineered bacteria. *J. Mol. Biol.* **355**, 619–627 (2006). doi: 10.1016/j.jmb.2005.10.076; pmid: 16330045
7. C. Kemmer *et al.*, Self-sufficient control of urate homeostasis in mice by a synthetic circuit. *Nat. Biotechnol.* **28**, 355–360 (2010). doi: 10.1038/nbt.1617; pmid: 20351688
8. W. Weber, M. Daoud-El Baba, M. Fussenegger, Synthetic ecosystems based on airborne inter- and intrakingdom communication. *Proc. Natl. Acad. Sci. U.S.A.* **104**, 10435–10440 (2007). doi: 10.1073/pnas.0701382104; pmid: 17551014
9. H. Ye, M. Daoud-El Baba, R. W. Peng, M. Fussenegger, A synthetic optogenetic transcription device enhances blood-glucose homeostasis in mice. *Science* **332**, 1565–1568 (2011). doi: 10.1126/science.1203535; pmid: 21700876
10. Z. Xie, L. Wroblewska, L. Prochazka, R. Weiss, Y. Benenson, Multi-input RNAi-based logic circuit for identification of specific cancer cells. *Science* **333**, 1307–1311 (2011). doi: 10.1126/science.1205527; pmid: 21885784
11. J. M. Callura, D. J. Dwyer, F. J. Isaacs, C. R. Cantor J. J. Collins, Tracking, tuning, and terminating microbial physiology using synthetic riboregulators. *Proc. Natl. Acad. Sci. U.S.A.* **107**, 15898–15903 (2010). doi: 10.1073/pnas.1009747107; pmid: 20713708
12. T. L. Deans, C. R. Cantor, J. J. Collins, A tunable genetic switch based on RNAi and repressor proteins for regulating gene expression in mammalian cells. *Cell* **130**, 363–372 (2007). doi: 10.1016/j.cell.2007.05.045; pmid: 17662949
13. H. Kobayashi *et al.*, Programmable cells: Interfacing natural and engineered gene networks. *Proc. Natl. Acad. Sci. U.S.A.* **101**, 8414–8419 (2004). doi: 10.1073/pnas.0402940101; pmid: 15159530
14. Y. Y. Chen, K. E. Galloway, C. D. Smolke, Synthetic biology: Advancing biological frontiers by building synthetic systems. *Genome Biol.* **13**, 240 (2012). doi: 10.1186/gb-2012-13-2-240; pmid: 22348749
15. D. Hanahan, R. A. Weinberg, The hallmarks of cancer. *Cell* **100**, 57–70 (2000). doi: 10.1016/S0092-8674(00)81683-9; pmid: 10647931
16. F. McCormick, Signalling networks that cause cancer. *Trends Cell Biol.* **9**, M53–M56 (1999). doi: 10.1016/S0962-8924(99)01668-2; pmid: 10611683
17. H. G. Dohlman, J. W. Thorner, Regulation of G protein-initiated signal transduction in yeast: Paradigms and principles. *Annu. Rev. Biochem.* **70**, 703–754 (2001). doi: 10.1146/annurev.biochem.70.1.703; pmid: 11395421
18. E. A. Elion, Pheromone response, mating and cell biology. *Curr. Opin. Microbiol.* **3**, 573–581 (2000). doi: 10.1016/S1369-5274(00)00143-0; pmid: 11121776
19. C. J. Bashor, N. C. Helman, S. Yan, W. A. Lim, Using engineered scaffold interactions to reshape MAP kinase pathway signaling dynamics. *Science* **319**, 1539–1543 (2008). doi: 10.1126/science.1151153; pmid: 18339942

20. N. T. Ingolia, A. W. Murray, Positive-feedback loops as a flexible biological module. *Curr. Biol.* **17**, 668–677 (2007). doi: 10.1016/j.cub.2007.03.016; pmid: 17398098
21. S. H. Park, A. Zarrinpar, W. A. Lim, Rewiring MAP kinase pathways using alternative scaffold assembly mechanisms. *Science* **299**, 1061–1064 (2003). doi: 10.1126/science.1076979; pmid: 12511654
22. S. D. Santos, P. J. Verveer, P. I. Bastiaens, Growth factor-induced MAPK network topology shapes Erk response determining PC-12 cell fate. *Nat. Cell Biol.* **9**, 324–330 (2007). doi: 10.1038/ncb1543; pmid: 17310240
23. E. Franco, F. Blanchini, Structural properties of the MAPK pathway topologies in PC12 cells. *J. Math. Biol.* (2012). doi: 10.1007/s00285-012-0606-x
24. M. N. Win, C. D. Smolke, A modular and extensible RNA-based gene-regulatory platform for engineering cellular function. *Proc. Natl. Acad. Sci. U.S.A.* **104**, 14283–14288 (2007). doi: 10.1073/pnas.0703961104; pmid: 17709748
25. R. G. Palpant, R. Steimnitz, T. H. Bornemann, K. Hawkins, The Carter Center Mental Health Program: Addressing the public health crisis in the field of mental health through policy change and stigma reduction. *Prev. Chronic Dis.* **3**, A62 (2006). pmid: 16539803
26. M. Osterberg *et al*., Phenotypic effects of membrane protein overexpression in *Saccharomyces cerevisiae*. *Proc. Natl. Acad. Sci. U.S.A.* **103**, 11148–11153 (2006). doi: 10.1073/pnas.0604078103; pmid: 16847257
27. S. A. Chapman, A. R. Asthagiri, Quantitative effect of scaffold abundance on signal propagation. *Mol. Syst. Biol.* **5**, 313 (2009). doi: 10.1038/msb.2009.73; pmid: 19888208
28. H. B. Fraser, A. E. Hirsh, G. Giaever, J. Kumm, M. B. Eisen, Noise minimization in eukaryotic gene expression. *PLoS Biol.* **2**, e137 (2004). doi: 10.1371/journal.pbio.0020137; pmid: 15124029
29. J. Stelling, E. D. Gilles, F. J. Doyle 3rd, Robustness properties of circadian clock architectures. *Proc. Natl. Acad. Sci. U.S.A.* **101**, 13210–13215 (2004). doi: 10.1073/pnas.0401463101; pmid: 15340155
30. J. Stelling, U. Sauer, Z. Szallasi, F. J. Doyle 3rd, J. Doyle, Robustness of cellular functions. *Cell* **118**, 675–685 (2004). doi: 10.1016/j.cell.2004.09.008; pmid: 15369668
31. A. Eldar *et al*., Robustness of the BMP morphogen gradient in *Drosophila* embryonic patterning. *Nature* **419**, 304–308 (2002). doi: 10.1038/nature01061; pmid: 12239569
32. G. Stoll, M. Bischofberger, J. Rougemont, F. Naef, Stabilizing patterning in the *Drosophila* segment polarity network by selecting models in silico. *Biosystems* **102**, 3–10 (2010). doi: 10.1016/j.biosystems.2010.07.014; pmid: 20655356
33. E. C. O'Shaughnessy, S. Palani, J. J. Collins, C. A. Sarkar, Tunable signal processing in synthetic MAP kinase cascades. *Cell* **144**, 119–131 (2011). doi: 10.1016/j.cell.2010.12.014; pmid: 21215374
34. T. M. Thomson *et al*., Scaffold number in yeast signaling system sets tradeoff between system output and dynamic range. *Proc. Natl. Acad. Sci. U.S.A.* **108**, 20265–20270 (2011). doi: 10.1073/pnas.1004042108; pmid: 22114196
35. J. C. Liang, A. L. Chang, A. B. Kennedy, C. D. Smolke, A high-throughput, quantitative cell-based screen for efficient tailoring of RNA device activity. *Nucleic Acids Res.* **40**, e154 (2012). doi: 10.1093/nar/gks636; pmid: 22810204
36. A. Becskei, L. Serrano, Engineering stability in gene networks by autoregulation. *Nature* **405**, 590–593 (2000). doi: 10.1038/35014651; pmid: 10850721
37. C. L. Beisel, C. D. Smolke, Design principles for riboswitch function. *PLOS Comput. Biol.* **5**, e1000363 (2009). doi: 10.1371/journal.pcbi.1000363; pmid: 19381267
38. C. J. Marshall, Specificity of receptor tyrosine kinase signaling: Transient versus sustained extracellular signal-regulated kinase activation. *Cell* **80**, 179–185 (1995). doi: 10.1016/0092-8674(95)90401-8; pmid: 7834738
39. C. Banerjee *et al*., Differential regulation of the two principal Runx2/Cbfa1 N-terminal isoforms in response to bone morphogenetic protein-2 during development of the osteoblast phenotype. *Endocrinology* **142**, 4026–4039 (2001). doi: 10.1210/en.142.9.4026; pmid: 11517182
40. Y. Yuan *et al*., Alternative splicing and gene duplication differentially shaped the regulation of isochorismate synthase in *Populus* and *Arabidopsis*. *Proc. Natl. Acad. Sci. U.S.A.* **106**, 22020–22025 (2009). doi: 10.1073/pnas.0906869106; pmid: 19996170
41. U. S. Bhalla, P. T. Ram, R. Iyengar, MAP kinase phosphatase as a locus of flexibility in a mitogen-activated protein kinase signaling network. *Science* **297**, 1018–1023 (2002). doi: 10.1126/science.1068873; pmid: 12169734
42. W. Wu, T. Pew, M. Zou, D. Pang, S. D. Conzen, Glucocorticoid receptor-induced MAPK phosphatase-1 (MPK-1) expression inhibits paclitaxel-associated MAPK activation and contributes to breast cancer cell survival. *J. Biol. Chem.* **280**, 4117–4124 (2005). doi: 10.1074/jbc.M411200200; pmid: 15590693
43. W. Wu *et al*., Microarray analysis reveals glucocorticoid-regulated survival genes that are associated with inhibition of apoptosis in breast epithelial cells. *Cancer Res.* **64**, 1757–1764 (2004). doi: 10.1158/0008-5472.CAN-03-2546; pmid: 14996737
44. S. Srikanth, C. C. Franklin, R. C. Duke, R. S. Kraft, Human DU145 prostate cancer cells overexpressing mitogen-activated protein kinase phosphatase-1 are resistant to Fas ligand-induced mitochondrial perturbations and cellular apoptosis. *Mol. Cell. Biochem.* **199**, 169–178 (1999). doi: 10.1023/A:1006980326855; pmid: 10544965
45. J. Y. Wang, C. H. Lin, C. H. Yang, T. H. Tan, Y. R. Chen, Biochemical and biological characterization of a neuroendocrine-associated phosphatase. *J. Neurochem.* **98**, 89–101 (2006). doi: 10.1111/j.1471-4159.2006.03852.x; pmid: 16805799
46. G. F. Sprague Jr., Assay of yeast mating reaction. *Methods Enzymol.* **194**, 77–93 (1991). doi: 10.1016/0076-6879(91)94008-Z; pmid: 2005823
47. C. Y. Huang, J. E. Ferrell Jr., Ultrasensitivity in the mitogen-activated protein kinase cascade. *Proc. Natl. Acad. Sci. U.S.A.* **93**, 10078–10083 (1996). doi: 10.1073/pnas.93.19.10078; pmid: 8816754
48. D. Angeli, J. E. Ferrell Jr., E. D. Sontag, Detection of multistability, bifurcations, and hysteresis in a large class of biological positive-feedback systems. *Proc. Natl. Acad. Sci. U.S.A.* **101**, 1822–1827 (2004). doi: 10.1073/pnas.0308265100; pmid: 14766974
49. W. Kolch, M. Calder, D. Gilbert, When kinases meet mathematics: The systems biology of MAPK signalling. *FEBS Lett.* **579**, 1891–1895 (2005). doi: 10.1016/j.febslet.2005.02.002; pmid: 15763569
50. X. L. Zhan, R. J. Deschenes, K. L. Guan, Differential regulation of FUS3 MAP kinase by tyrosine-specific phosphatases PTP2/PTP3 and dual-specificity phosphatase MSG5 in *Saccharomyces cerevisiae*. *Genes Dev.* **11**, 1690–1702 (1997). doi: 10.1101/gad.11.13.1690; pmid: 9224718
51. J. Andersson, D. M. Simpson, M. Qi, Y. Wang, E. A. Elion, Differential input by Ste5 scaffold and Msg5 phosphatase route a MAPK cascade to multiple outcomes. *EMBO J.* **23**, 2564–2576 (2004). doi: 10.1038/sj.emboj.7600250; pmid: 15192700
52. B. Kofahl, E. Klipp, Modelling the dynamics of the yeast pheromone pathway. *Yeast* **21**, 831–850 (2004). doi: 10.1002/yea.1122; pmid: 15300679

Acknowledgments: We thank D. Endy, J. Michener, A. Chang, and Y.-H. Wang for comments on the manuscript; J. Liang for technical guidance with RNA transducers; and R. Yu and S. Chapman for discussions on mating assays. This work was supported by funds from the NIH (grant to C.D.S.), NSF (grant to C.D.S.), Defense Advanced Research Projects Agency (grant to C.D.S.), and the Bill and Melinda Gates Foundation (grant to C.D.S.). K.E.G. and C.D.S. designed the study and experiments; K.E.G. performed experiments; E.F. and K.E.G. designed and constructed the model; and C.D.S. and K.E.G. analyzed and discussed all results and wrote the manuscript.

Supplementary Materials

www.sciencemag.org/content/341/6152/1235005/suppl/DC1
Materials and Methods
Supplementary Text
Figs. S1 to S14
Tables S1 to S17
References (*53*–*60*)

9 January 2013; accepted 24 July 2013
Published online 15 August 2013;
10.1126/science.1235005

Protection Against Malaria by Intravenous Immunization with a Nonreplicating Sporozoite Vaccine

Robert A. Seder,[1]*† Lee-Jah Chang,[1]* Mary E. Enama,[1] Kathryn L. Zephir,[1] Uzma N. Sarwar,[1] Ingelise J. Gordon,[1] LaSonji A. Holman,[1] Eric R. James,[2] Peter F. Billingsley,[2] Anusha Gunasekera,[2] Adam Richman,[2] Sumana Chakravarty,[2] Anita Manoj,[2] Soundarapandian Velmurugan,[2] MingLin Li,[3] Adam J. Ruben,[2] Tao Li,[2] Abraham G. Eappen,[2] Richard E. Stafford,[2,3] Sarah H. Plummer,[1] Cynthia S. Hendel,[1] Laura Novik,[1] Pamela J. M. Costner,[1] Floreliz H. Mendoza,[1] Jamie G. Saunders,[1] Martha C. Nason,[4] Jason H. Richardson,[5] Jittawadee Murphy,[5] Silas A. Davidson,[5] Thomas L. Richie,[6] Martha Sedegah,[6] Awalludin Sutamihardja,[6] Gary A. Fahle,[7] Kirsten E. Lyke,[8] Matthew B. Laurens,[8,9] Mario Roederer,[1] Kavita Tewari,[1] Judith E. Epstein,[6] B. Kim Lee Sim,[2,3] Julie E. Ledgerwood,[1] Barney S. Graham,[1]‡ Stephen L. Hoffman,[2,3]‡ the VRC 312 Study Team§

Consistent, high-level, vaccine-induced protection against human malaria has only been achieved by inoculation of *Plasmodium falciparum* (Pf) sporozoites (SPZ) by mosquito bites. We report that the PfSPZ Vaccine—composed of attenuated, aseptic, purified, cryopreserved PfSPZ—was safe and well tolerated when administered four to six times intravenously (IV) to 40 adults. Zero of six subjects receiving five doses and three of nine subjects receiving four doses of 1.35×10^5 PfSPZ Vaccine and five of six nonvaccinated controls developed malaria after controlled human malaria infection ($P = 0.015$ in the five-dose group and $P = 0.028$ for overall, both versus controls). PfSPZ-specific antibody and T cell responses were dose-dependent. These data indicate that there is a dose-dependent immunological threshold for establishing high-level protection against malaria that can be achieved with IV administration of a vaccine that is safe and meets regulatory standards.

Malaria control interventions, including insecticide-impregnated bednets, insecticide spraying, and antimalarial drugs, have substantially reduced malaria morbidity and mortality (*1*). However, despite these measures there were in 2010 an estimated 220 million clinical cases and 0.66 to 1.24 million deaths caused by malaria (*1*, *2*). A highly effective vaccine will be ideal for preventing malaria in individuals and eliminating malaria in defined geographic areas. It would optimally target the parasite at asymptomatic, pre-erythrocytic stages (*3*, *4*). The World Health Organization malaria vaccine technology roadmap set a vaccine efficacy goal of 80% by 2025 (*5*). Heretofore, no injectable malaria vaccine candidate has consistently approached that level of efficacy.

RTS,S/AS01 is the most advanced subunit malaria vaccine, protecting ~50% of subjects against controlled human malaria infection (CHMI) 2 to 3 weeks after the last dose of vaccine and 22% at 5 months after last immunization (*6*). In a large-scale phase 3 efficacy trial in African infants 6 to 12 weeks of age, RTS,S/AS01 reduced the rates of clinical and severe malaria acquired over a 12-month period by 31.3 and 36.6%, respectively (*7*).

It has been known for 40 years that it is possible to achieve high-level, sustained, protective immunity against the pre-erythrocytic stages of the parasite through immunization by the bites of >1000 irradiated mosquitoes carrying *Plasmodium falciparum* (Pf) sporozoites (SPZ) (*8*–*11*). Advancing this technique beyond administration by mosquitoes required the capacity to manufacture aseptic, radiation-attenuated, metabolically active, purified, cryopreserved PfSPZ for an injectable vaccine that met regulatory standards (*12*). This was achieved (*13*, *14*), and the first clinical trial of the PfSPZ Vaccine, composed of Pf NF54 strain SPZ (*15*), was conducted in 80 adults (*14*), who received up to 6 doses of 1.35×10^5 PfSPZ Vaccine subcutaneously (SC) or intradermally (ID). The PfSPZ Vaccine was safe and well-tolerated but elicited low-level immune responses and minimal protection. We hypothesized that the limited efficacy was due to the inefficiency of ID and SC administration for sufficient presentation of PfSPZ antigens at critical inductive sites required to achieve a protective immunological threshold (*16*). Therefore, we immunized nonhuman primates (NHPs) with the PfSPZ Vaccine and showed that intravenous (IV), but not SC, administration of the PfSPZ Vaccine elicited potent and durable PfSPZ-specific T cell responses in peripheral blood and most notably in the liver (*14*), the likely site of immune protection (*17*). On the basis of these data, we hypothesized that IV administration of the PfSPZ Vaccine would be protective in humans (*14*) and conducted a phase 1 clinical trial in order to determine safety, immunogenicity, and protective efficacy against CHMI of IV immunization with the PfSPZ Vaccine (*18*).

Study Population

Fifty-seven subjects, composed of 40 vaccine recipients, 12 CHMI controls, and five back-up controls, enrolled from October 2011 to October 2012 (baseline characteristics are shown in table S1). Thirty-six of 40 (90%) subjects completed all scheduled vaccinations (Fig. 1 and fig. S1). Of these 36 subjects, two were immunized with 2×10^3 PfSPZ Vaccine per dose so as to assess safety only on schedules without CHMI, whereas at higher doses, CHMI was administered to 17 in July 2012 and to 15 in October 2012. Two subjects in the 1.35×10^5 PfSPZ Vaccine-per-dose group did not undergo CHMI because of an unrelated serious adverse event (SAE) and travel, respectively (Fig. 1).

Adverse Events

Vaccinations were well tolerated, and there were no breakthrough malaria infections before CHMI (Table 1). Thirty (75%) vaccine recipients had no local reactogenicity, nine (22.5%) had mild pain and tenderness or bruising, and one (2.5%) had moderate bruising at the injection site (Table 1 and table S2). Solicited systemic reactogenicity was none for 19 (47.5%), mild for 16 (40%), moderate for four (10%) and severe for one (2.5%) subject (Table 1 and table S3); the latter reported a headache after the third dose of 1.35×10^5 PfSPZ Vaccine.

Transient, asymptomatic increases in aspartate aminotransferase (AST) and/or alanine aminotransferase (ALT), assessed as possibly related to vaccination, were observed in 16 (40%) of vaccinees and were not dose-dependent (table S4 and figs. S2 and S3). Two SAEs occurred: One subject was diagnosed with colon cancer and did not participate in CHMI. After CHMI, one vaccine recipient developed anxiety and headache 14 days after completing chloroquine treatment and was hospitalized overnight for diagnostic

[1]Vaccine Research Center (VRC), National Institute of Allergy and Infectious Diseases, National Institutes of Health, Bethesda, MD 20852, USA. [2]Sanaria, Rockville, MD 20850, USA. [3]Protein Potential, Rockville, MD 20850, USA. [4]Biostatistics Research Branch, Division of Clinical Research, National Institute of Allergy and Infectious Diseases, National Institutes of Health, Bethesda, MD 20852, USA. [5]Entomology Branch, Walter Reed Army Institute of Research, Silver Spring, MD 20910, USA. [6]U.S. Military Malaria Vaccine Program, Naval Medical Research Center, Silver Spring, MD 20910, USA. [7]Department of Laboratory Medicine, National Institutes of Health, Bethesda, MD 20892, USA. [8]Center for Vaccine Development, University of Maryland School of Medicine, Baltimore, MD 21201, USA. [9]Howard Hughes Medical Institute, Baltimore, MD 21201, USA.

*These authors contributed equally to this work.
†To whom correspondence should be sent. E-mail: rseder@mail.nih.gov
‡These authors contributed equally to this work.
§The VRC 312 Study Team members are listed in the supplementary materials.

purposes. The symptoms, which were attributed to chloroquine, resolved within 1 month.

Vaccine Efficacy CHMI #1

In July 2012, subjects who received 7.5×10^3 and 3×10^4 PfSPZ Vaccine per dose underwent CHMI ~3 weeks after last immunization, and 16 of 17 developed parasitemia (Fig. 2). Among the nine subjects who had received four doses of 3×10^4 PfSPZ Vaccine, one did not develop parasitemia, whereas the other eight had a 1.4-day prolongation of time to parasitemia by thick blood smear (prepatent period) as compared with the six nonvaccinated controls ($P = 0.007$, Log-Rank) (Fig. 2 and table S5). This observation suggests a modest reduction in the numbers of liver stage parasites. The prepatent periods in the 7.5×10^3 PfSPZ Vaccine-per-dose group were not significantly different than those of controls (Fig. 2 and table S5).

Second Vaccine Efficacy CHMI

In October 2012, subjects who received 1.35×10^5 PfSPZ Vaccine per dose underwent CHMI ~3 weeks after last immunization along with six new controls. Five of six controls developed parasitemia. Three of nine subjects in the four-dose group and none of six in the five-dose group developed parasitemia ($P = 0.015$ for the five-dose group versus controls, Fisher's exact test) (Fig. 2 and table S5). All subjects who did not develop parasitemia detected with thick blood smear were negative as determined by means of quantitative polymerase chain reaction (PCR) at 28 days after CHMI. In the three vaccinated subjects that became infected, there was a modest delay in the time to positive PCR (table S5). Overall, 12 of 15 subjects immunized with 1.35×10^5 PfSPZ Vaccine per dose were protected ($P = 0.028$) (Fig. 2 and table S5).

Antibody Responses

Monoclonal antibodies against the major surface protein on SPZ, the circumsporozoite protein (CSP), prevent malaria by blocking SPZ invasion and development in hepatocytes (*19*). Furthermore, the RTS,S/AS01 malaria vaccine is thought to mediate protection primarily through the induction of high levels of antibodies against PfCSP (*20*). Antibodies mediate some protection in rodents immunized with irradiated SPZ (*21*). In human subjects immunized via irradiated PfSPZ-infected mosquito bites, PfCSP or PfSPZ antibody titers have been detected by means of enzyme-

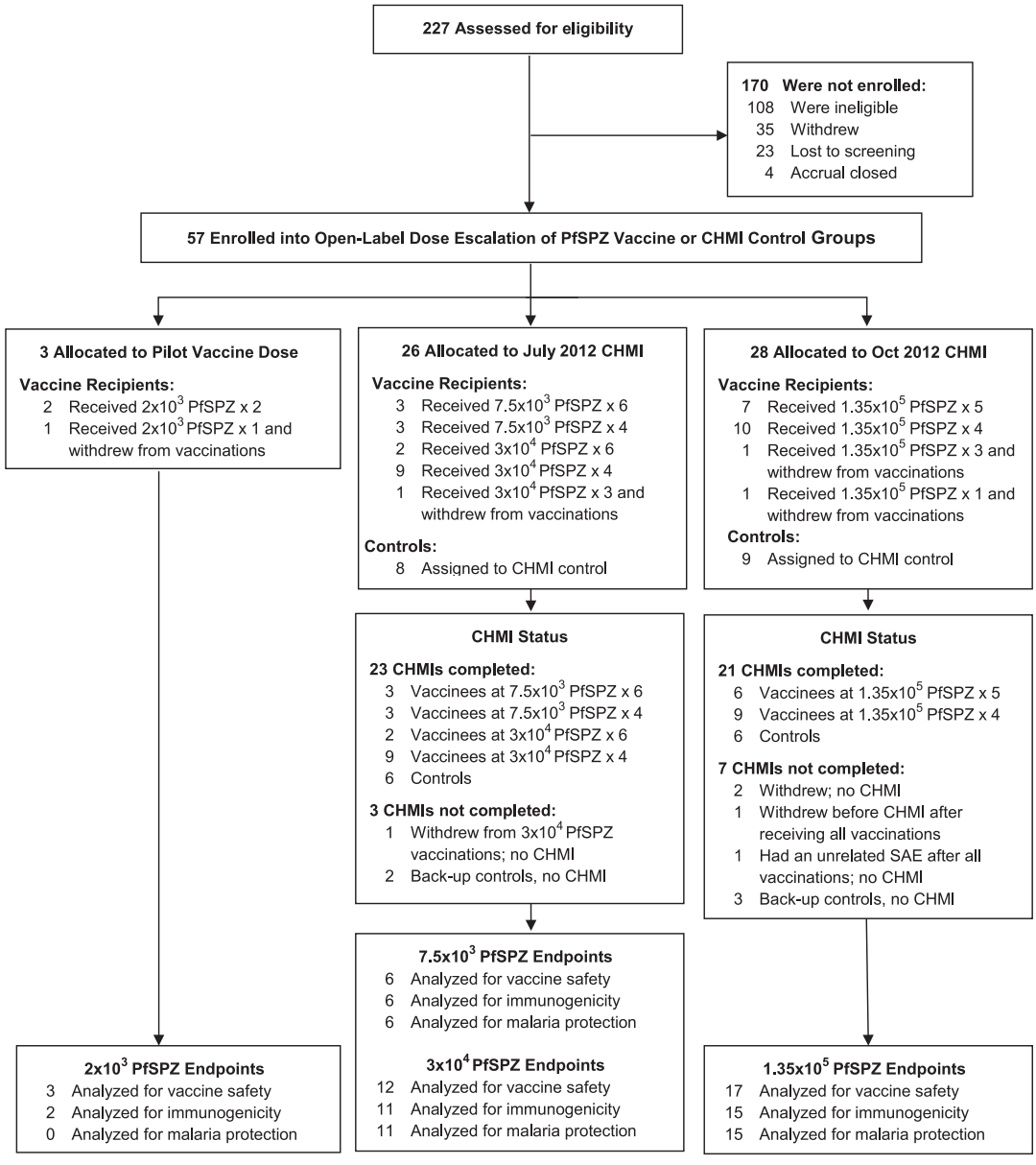

Fig. 1. Screening, enrollment, vaccinations, CHMI, and study endpoints analyses. SAE denotes serious adverse event.

linked immunosorbent assay (ELISA) or immunofluorescence assay (IFA), respectively (*22*). On the basis of these data, we assessed antibodies against PfCSP and the entire PfSPZ (IFA) as well as performed a functional assay using subject serum so as to assess inhibition of sporozoite invasion (ISI) in a hepatocyte line in vitro.

Two weeks after the final vaccination, there was a correlation between the total dosage of PfSPZ Vaccine administered and results of PfCSP ELISA, PfSPZ IFA, and PfSPZ ISI (Spearman $R = 0.77$, 0.83 and 0.84, respectively; $P < 0.001$) (Fig. 3, A to C). Among the nine subjects who received four doses of 1.35×10^5 PfSPZ Vaccine, antibodies for all three assays were numerically

Table 1. Frequency of solicited and unsolicited adverse events. Solicited reactogenicity was collected for 7 days after each vaccination. Each vaccine recipient is counted once at worst severity for any local and systemic parameter. Unsolicited AE percentages indicate the number of vaccine recipients with the given event (regardless of severity) divided by the total number who received PfSPZ Vaccine.

	≤7.5×10^3 PfSPZ per dose (n = 9 subjects)	3×10^4 PfSPZ per dose (n = 12 subjects)	1.35×10^5 PfSPZ per dose (n = 19 subjects)	All groups (n = 40 subjects)
	Number (%)			
Any local reactogenicity				
None	8 (88.9)	10 (83.3)	12 (63.2)	30 (75.0)
Mild	1 (11.1)	1 (8.3)	7 (36.8)	9 (22.5)
Moderate	0 (0)	1 (8.3)	0 (0)	1 (2.5)
Severe	0 (0)	0 (0)	0 (0)	0 (0)
Any systemic reactogenicity				
None	6 (66.7)	7 (58.3)	6 (31.6)	19 (47.5)
Mild	3 (33.3)	4 (33.3)	9 (47.4)	16 (40.0)
Moderate	0 (0)	1 (8.3)	3 (15.8)	4 (10)
Severe	0 (0)	0 (0)	1 (5.3)	1 (2.5)
Unsolicited adverse events*				
Number with one or more adverse event	8 (88.9)	11 (91.7)	17 (89.5)	36 (90)
ALT and/or AST increased	5 (55.6)	6 (50)	5 (26.3)	16 (40)
Upper respiratory tract infection	3 (33.3)	2 (16.7)	5 (26.3)	10 (25.0)
Anemia	2 (22.2)	1 (8.3)	3 (15.8)	6 (15.0)
Leukopenia	2 (22.2)	0 (0)	2 (10.5)	4 (10)
Neutropenia	0 (0)	0 (0)	4 (21.1)	4 (10)
Gastroenteritis	0 (0)	1 (8.3)	3 (15.8)	4 (10)
Eosinophilia	1 (11.1)	1 (8.3)	1 (5.3)	3 (7.5)
Lymphopenia	0 (0)	1 (8.3)	2 (10.5)	3 (7.5)
Thrombocytopenia	0 (0)	2 (16.7)	1 (5.3)	3 (7.5)
Leukocytosis	0 (0)	0 (0)	2 (10.5)	2 (5.0)
Abdominal pain	0 (0)	0 (0)	2 (10.5)	2 (5.0)
Diarrhea	0 (0)	0 (0)	2 (10.5)	2 (5.0)
Dyspepsia	0 (0)	0 (0)	2 (10.5)	2 (5.0)
Muscle strain	0 (0)	1 (8.3)	1 (5.3)	2 (5.0)
Dizziness	0 (0)	1 (8.3)	0 (0)	1 (2.5)
Pruritus	0 (0)	1 (8.3)	0 (0)	1 (2.5)

*MedDRA terms for which one or more AE was assessed as possibly related to vaccination are shown; adverse event terms for which no events were considered related are not shown. Frequency of any hepatic enzyme adverse event [alanine aminotransferase (ALT) increased, aspartate aminotransferase (AST) increase, or both] are counted together; more detail on these events is available in table S4.

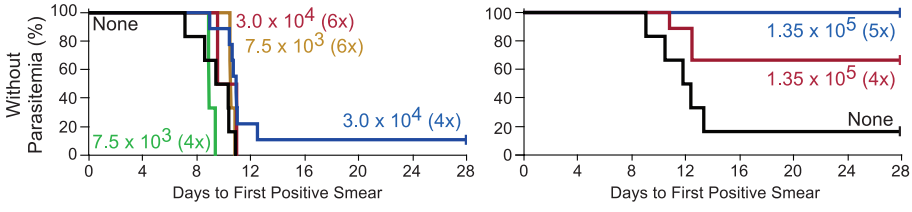

Vaccination Dose	# Inj.	CHMI Parasite*	# of Subjects	Parasite Free	Vaccine Efficacy
None		NF54	6	0	
7.5 x 10^3	4	NF54	3	0	0%
7.5 x 10^3	6	NF54	3	0	0%
3.0 x 10^4	4	NF54	9	1	11%
3.0 x 10^4	6	NF54	2	0	0%

Vaccination Dose	# Inj.	CHMI Parasite*	# of Subjects	Parasite Free	Vaccine Efficacy
None		3D7	6	1	
1.35 x 10^5	4	3D7	9	6	60%
1.35 x 10^5	5	3D7	6	6	100%

Fig. 2. Kaplan-Meier curves and protection table results. Kaplan-Meier curves are shown for the July and October CHMIs, indicating the frequency of subjects who remained without *Plasmodium falciparum* parasitemia after CHMI. CHMI Parasite* refers to the Pf parasite used to produce infected mosquitoes for CHMI (supplementary materials). Each dose group and regimen is labeled and listed in the tables. Vaccine efficacy (VE) against acquiring *P. falciparum* malaria is shown in the last column. For the groups receiving the 1.35×10^5 dose of PfSPZ Vaccine in the October CHMI, estimates of VE [defined as 1-Relative Risk (RR)], and (exact, unconditional) 95% confidence intervals (CIs) are as follows: five doses, 0/6 versus 5/6 estimated RR = 0; estimated VE = 100% [95% CI for VE (0.464, 1)]; four doses, 3/9 versus 5/6 estimated RR = 0.4; estimated VE = 60% [95% CI for VE (−0.127, 0.92)]; combined, 3/15 versus 5/6 estimated RR = 0.24; estimated VE = 76% [95% CI for VE (0.272, 0.955)].

higher in the six protected than the three non-protected subjects and significantly higher for the PfSPZ ISI ($P = 0.05$) (Fig. 3, A to C).

Antibodies to asexual or sexual erythrocytic stage parasites and antigens were undetectable, indicating that the irradiated PfSPZ were attenuated and did not develop beyond the early liver stage.

Cellular Immune Responses

Studies in mice and NHPs show that protective immunity induced with irradiated SPZ requires cellular immunity, and most preclinical data indicate that $CD8^+$ T cells and interferon-γ (IFN-γ) are critical mediators of protection (*21*, *23*–*25*). $CD4^+$ T cells, $CD3^+$ γδ T cells, and natural killer (NK) cells can also play a role in protection (*24*, *26*, *27*). Therefore, we used multiparameter flow cytometry to assess the frequency of PfSPZ-specific IFN-γ, interleukin-2 (IL-2), tumor necrosis factor (TNF), or perforin-producing $CD3^+CD4^+$, $CD3^+CD8^+$, and $CD3^+$ γδ T cells and NK cells from cryopreserved peripheral blood mononuclear cells (PBMCs) prior to immunization and 2 weeks after the final immunization (fig. S4). The memory phenotype of PfSPZ-specific cells was assessed on the basis of differential expression of the cell-surface markers, CD45RA and CCR7 (fig. S4, C and G).

PfSPZ-specific memory $CD3^+CD4^+$ T cells from a representative protected subject produced IFN-γ, IL-2, and TNF, whereas PfSPZ-specific memory $CD3^+CD8^+$ T cells produced IFN-γ but little TNF and no IL-2 (Fig. 3D). There was a dose-dependent increase in frequency of PfSPZ-specific $CD3^+CD4^+$ T cells ($P \leq 0.001$) and $CD3^+CD8^+$ T cells producing any combination of IFN-γ, IL-2, or TNF ($P = 0.01$) (Fig. 3E).

We assessed PfSPZ-specific, IFN-γ–producing T cells in subjects who received 1.35×10^5 PfSPZ Vaccine per injection because of the critical role of IFN-γ in mediating attenuated SPZ-induced protective immunity. For PfSPZ-specific $CD3^+CD4^+$ IFN-γ–producing T cells, there was no significant difference between protected and unprotected subjects (Fig. 4A). For PfSPZ-specific $CD3^+CD8^+$ IFN-γ–producing T cells, protected subjects who received four doses showed a trend toward higher and more consistent responses (Fig. 4A). Although all subjects who received five doses were protected, there was considerable variability in their responses. In terms of memory phenotype, PfSPZ-specific cytokine-producing $CD3^+CD4^+$ T cells were detected in central (T_{CM}) and effector (T_{EM}) memory subsets (Fig. 4B and figs. S4G and S5). In contrast, PfSPZ-specific $CD3^+CD8^+$ T cells were within effector (T_{EM}) and terminal effector (T_{TE}) memory subsets (Fig. 4B and fig. S4G).

We next characterized the quality of PfSPZ-specific T cell cytokine responses. Among PfSPZ-specific $CD3^+CD4^+$ T cells, there were three primary populations, comprising IFN-γ, IL-2, and TNF;

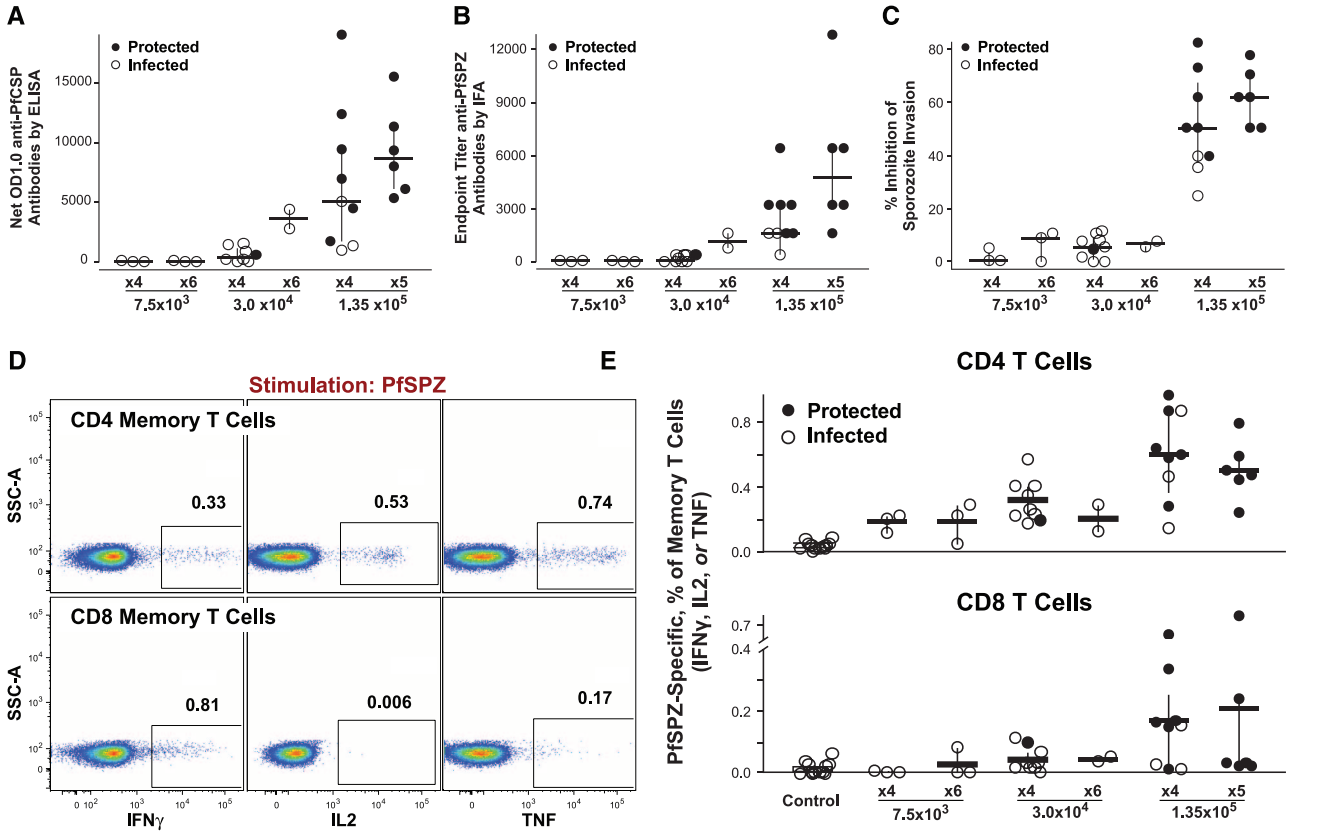

Fig. 3. Antibody, $CD3^+CD4^+$, and $CD3^+CD8^+$ T cell cytokine responses in all immunized participants. (**A** to **C**) Antibodies. Assessment of antibodies was performed from serum of all subjects before immunization and 2 weeks after the last dose of the PfSPZ Vaccine, which was ~1 week before CHMI. (A) Net OD 1.0 antibodies to PfCSP by means of ELISA was the serum dilution for each volunteer at which the optical density was 1.0 based on the difference between values in post- and preimmunization serum. (B) Endpoint titer antibodies to PfSPZ by means of IFA for each volunteer was the last serum dilution at which the IFA was positive. (C) Percent inhibition of sporozoite invasion was the percent reduction of the numbers of PfSPZ that invaded a human hepatocyte line in the presence of immune serum as compared with that in the presence of preimmunization serum from the same volunteer, both at a dilution of 1:5. (**D** and **E**) T cells. PBMCs were analyzed by means of multiparameter flow cytometry for PfSPZ-specific cytokine-producing (IFN-γ, IL-2, or TNF) memory $CD3^+CD4^+$ and $CD3^+CD8^+$ T cells from all subjects at week 2 after the final immunization with PfSPZ Vaccine after in vitro restimulation (fig. S4). The frequency of PfSPZ-specific memory $CD3^+CD4^+$ and $CD3^+CD8^+$ T cells was calculated as the fraction of cells making any cytokine in response to PfSPZ minus the response to 1% human serum albumin (diluent). (D) A representative dot plot showing PfSPZ-specific IFN-γ–, IL-2–, or TNF-producing memory $CD3^+CD4^+$ (top) and $CD3^+CD8^+$ (bottom) T cells from a volunteer who received five doses of 1.35×10^5 PfSPZ Vaccine and was protected. (E) The frequency of total PfSPZ-specific cytokine-producing (IFN-γ, IL-2, or TNF) memory $CD3^+CD4^+$ (top) and $CD3^+CD8^+$ (bottom) T cells from all subjects within each group. Data in all four graphs show a point for each subject. Horizontal bars denote the medians, and whiskers denote the interquartile ranges.

IL-2 and TNF; or TNF (Fig. 4C) and no differences between protected and unprotected subjects. In contrast, among protected subjects ~50 to 80% of the total PfSPZ-specific $CD3^+CD8^+$ T cells produced IFN-γ only, as compared with <30% in unprotected subjects (Fig. 4D). The PfSPZ-specific IFN-γ–producing $CD3^+CD8^+$ T cells uniformly expressed perforin, as did other effector lymphocytes populations, except for $CD3^+CD4^+$ T cells (fig. S4F).

$CD3^+$ γδ T cells from naïve humans respond to malaria antigens after in vitro stimulation (*28*). Accordingly, we also detected IFN-γ in $CD3^+$ γδ T cells from the majority of subjects before immunization in response to PfSPZ stimulation (fig. S4D). Although the proportion of $CD3^+$ γδ T cells producing IFN-γ in response to PfSPZ stimulation did not change after vaccination (fig. S4E), the overall frequency of $CD3^+$ γδ T cells increased in subjects who received 1.35×10^5 PfSPZ Vaccine per dose (Fig. 5).

Last, to assess cellular immunity with a method commonly reported for other malaria vaccine trials, we used enzyme-linked immunosorbent spot assays to enumerate the frequency of IFN-γ responses to PfSPZ and six Pf proteins. PfSPZ-specific responses ranged from 100 to 300 spot-forming cells (SFCs) per 10^6 PBMCs and were highest in the 1.35×10^5 PfSPZ Vaccine five-dose group (fig. S6A). Responses to stimulation with peptide pools spanning five individual Pf pre-erythrocytic stage antigens were low to undetectable (mostly <100 SFCs per 10^6 PBMCs) but generally higher than to one Pf blood-stage antigen included as a control (MSP1) (fig. S6B).

Discussion

The protection against infection we observed in all of the subjects who received the highest dosage

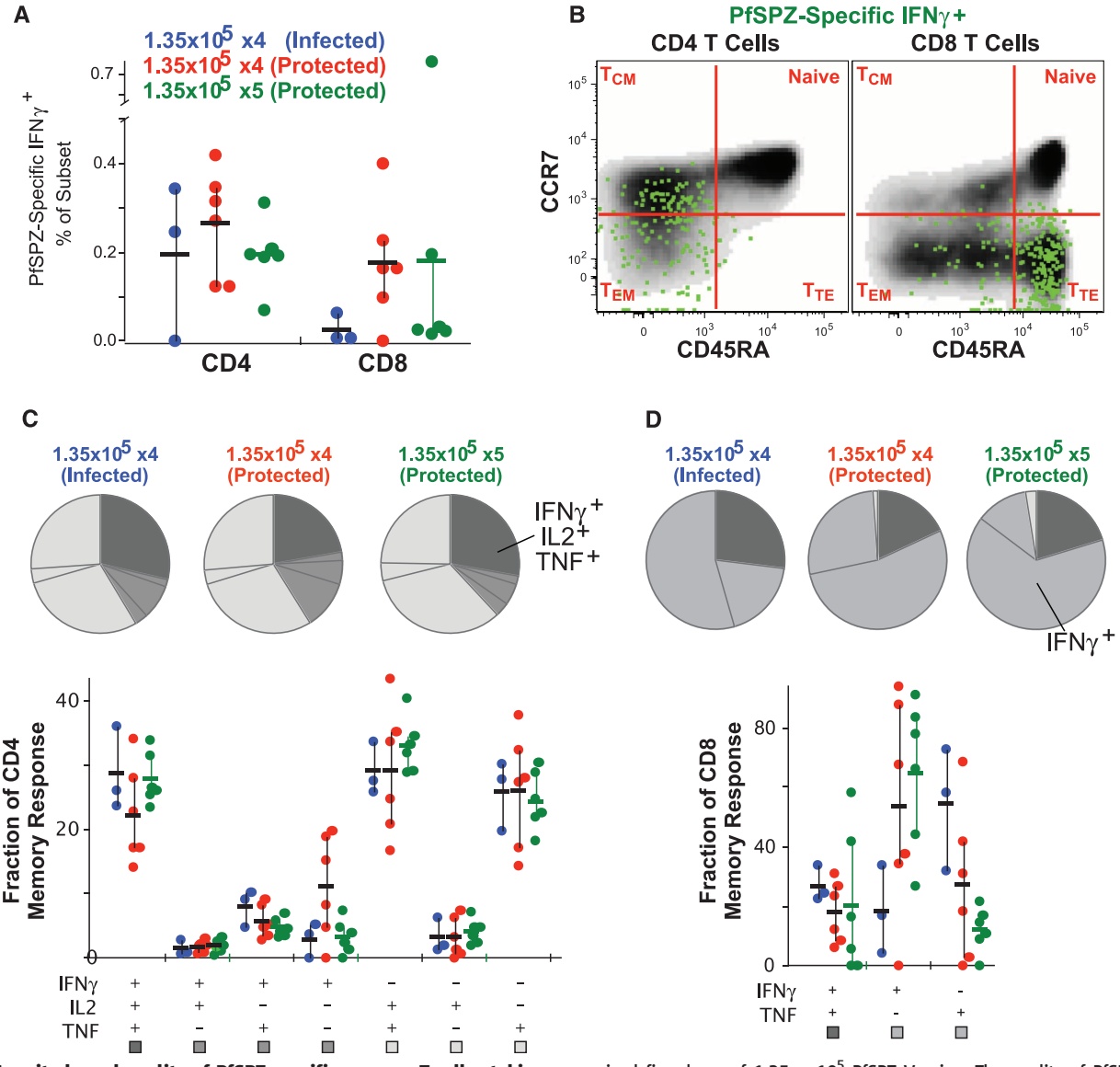

Fig. 4. Magnitude and quality of PfSPZ-specific memory T cell cytokine responses in participants immunized with 1.35×10^5 PfSPZ per dose. PBMCs were analyzed by means of multiparameter flow cytometry after in vitro stimulation with PfSPZ in all volunteers at week 2 after administration of final dose of 1.35×10^5 PfSPZ Vaccine (fig. S4). (**A**) The frequency of IFN-γ–producing memory $CD3^+CD4^+$ or $CD3^+CD8^+$ T cells in all protected and unprotected subjects who received 1.35×10^5 PfSPZ Vaccine either four or five times. (**B**) A representative dot plot showing the distribution of PfSPZ-specific IFN-γ–producing $CD3^+CD4$ and $CD3^+CD8^+$ T cells within T_{CM}, T_{EM}, and T_{TE} phenotype T cells as defined by expression of CCR7 and CD45RA from a volunteer who received five doses of 1.35×10^5 PfSPZ Vaccine. The quality of PfSPZ-specific memory (**C**) $CD3^+CD4^+$ and (**D**) $CD3^+CD8^+$ T cell response was determined by using Simulation Program with Integrated Circuit Emphasis (SPICE) analysis, defining distinct populations producing any combination of IFN-γ, IL-2, or TNF ($CD3^+CD4^+$) or any combination of IFN-γ or TNF ($CD3^+CD8^+$) at the single-cell level. The relative proportions of each of these populations from the three unprotected and six protected subjects who received four or five doses of 1.35×10^5 PfSPZ Vaccine is shown by pie charts or plotted as a percentage of the total cytokine response. In (A), (C), and (D), a point is shown for each subject. Horizontal bars denote the medians, and whiskers denote the interquartile ranges.

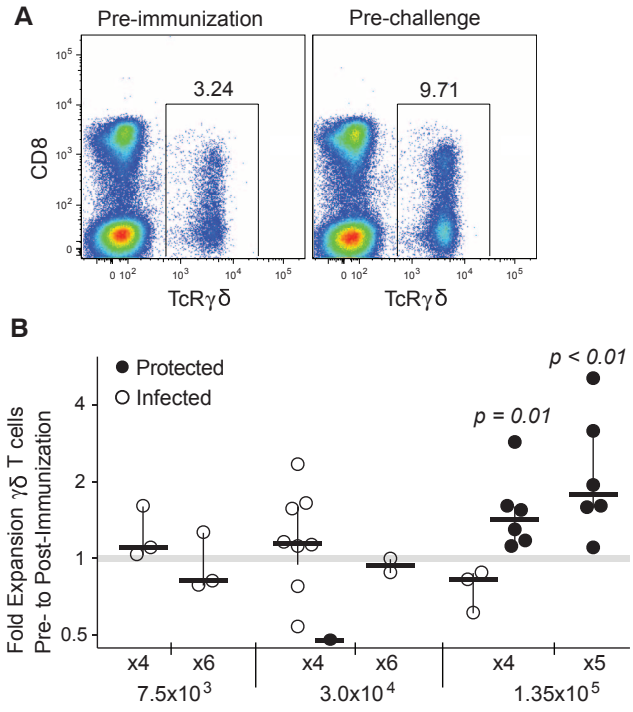

Fig. 5. Expansion of TCRγδ T cells after immunization with PfSPZ Vaccine. PBMCs were analyzed for frequency of TCR γδ T cells in all subjects immunized with PfSPZ Vaccine preimmunization and pre-CHMI, as shown in fig. S4. (**A**) A representative dot plot showing the frequency of TCR γδ T cells preimmunization and pre-CHMI from a volunteer immunized with five doses of 1.35×10^5 PfSPZ Vaccine. (**B**) The fold expansion in the total frequency of TCR γδ T cells after immunization with PfSPZ Vaccine is shown for subjects from all groups and distinguishes protected from nonprotected volunteers. In (B), a point is shown for each subject. Horizontal bars denote the medians, and whiskers denote the interquartile range.

of PfSPZ Vaccine has only been achieved previously through immunization with whole PfSPZ administered through mosquito bites (*11*, *29*). The dose threshold at which we observed the highest rate of protection is consistent with prior studies in which >90% protection was associated with exposure to >1000 irradiated PfSPZ-infected mosquitoes (*11*).

The five-dose group in which all vaccinees were protected differed in two potentially important ways from other groups. These subjects received the highest total number of PfSPZ Vaccine (6.75×10^5), and there was a 7-week interval between the fourth and fifth doses. We do not know whether the protection in all subjects who received five doses as compared with subjects who received four doses of 1.35×10^5 PfSPZ Vaccine was due to the total dosage of PfSPZ, the numbers of doses, or the increased interval between the fourth and fifth dose. Studies in NHPs show that extending the time between the fourth and fifth dose to ~8 weeks boosted the PfSPZ-specific $CD8^+$ T cell responses as compared with that of 4 weeks. Demonstrating that modifications in dose and schedule can achieve a protective immunological threshold in humans will guide future clinical trials designed to optimize the immunization regimen.

Two clinical trials of the PfSPZ Vaccine have established that IV administration of PfSPZ Vaccine induced superior immunogenicity and protective efficacy as compared with those of SC and ID administration (*14*). The findings are consistent with prior studies in NHP that show IV administration induced a higher frequency of liver resident $CD8^+$ T cells specific for PfSPZ and antibodies against PfSPZ (*14*). Although the IV route is routinely used for therapeutic interventions in humans, it has not previously been used for administration of preventive vaccines against infectious diseases. Accordingly, a series of clinical trials of the PfSPZ Vaccine administered with IV injection are now planned in Africa, Europe, and the United States to expand critical data on the vaccine for clinical development as a method to prevent malaria in travelers, military, and other high-risk groups and for mass immunization of populations to eliminate Pf malaria from geographically defined areas. The findings of the current study suggest that the protective immune threshold could potentially be achieved in humans with higher numbers of PfSPZ administered in fewer doses by a different schedule or by other routes, as has been done in mice (*14*). This could be facilitated with microneedle arrays or other novel devices.

The dose-dependent increase in the frequencies of PfSPZ-specific $CD3^+CD4^+$, $CD3^+CD8^+$, and $CD3^+$γδ T cells in the peripheral blood after immunization is consistent with studies of Pf infection and treatment (*28*). Because $CD3^+$γδ T cells and other IFN-γ–producing cells such as NK cells represent a higher proportion of lymphocytes in liver as compared with blood in humans (*30*), they could contribute to protection.

Although we detected PfSPZ-specific $CD3^+CD8^+$ T cells in 7 of 12 protected subjects at 1.35×10^5 PfSPZ Vaccine per dose, five protected subjects had low to undetectable responses. This finding is consistent with data obtained from NHP studies. We reported that some NHPs with a high frequency (~3%) of PfSPZ-specific $CD3^+CD8^+$ T cells in the liver had no detectable responses in blood after IV immunization with PfSPZ Vaccine (*14*). We speculate that as in mice (*21*, *23*, *24*) and NHPs (*25*), PfSPZ-specific $CD3^+CD8^+$ T cells are required for protection in most individuals and are primarily confined to the liver because of persistence of parasite antigens after vaccination and/or retained as tissue-resident memory cells (*31*).

There was a dose-dependent increase in PfSPZ-specific antibodies using three assays. Although antibodies may have contributed to protection, such responses may best be used to predict vaccine take and serve as a biomarker or nonmechanistic correlate of protection.

Vaccine efficacy against CHMI in this trial was considerably higher than that induced by subunit vaccines (*6*, *32*) and consistent with data generated by immunization with mosquito bites (*11*). However, the antibody and cellular immune responses induced by the PfSPZ Vaccine against the specific malaria antigens tested were substantially lower than those induced by experimental Pf subunit vaccines (*6*, *32*–*35*). It remains an open question whether protection results from the summation of multiple low-level antigen-specific responses or from robust responses to a small number of as-yet unidentified antigens from among the ~1000 proteins expressed by sporozoites (*36*). We show that there are multiple populations of lymphocytes responding to PfSPZ, providing a breadth of effector responses. Furthermore, we speculate that the PfSPZ Vaccine induces immunity to a broad spectrum of antigens among the ~1000 expressed by attenuated PfSPZ (*36*–*38*). The capacity to induce a cascade of multiple adaptive and innate effector cells and the breadth of antigenic specificity may explain the advantage of whole PfSPZ vaccines compared with existing subunit vaccines.

Demonstration of high-level protection through IV administration is a critical first step in the development of the PfSPZ Vaccine. Future studies will determine the duration of protection and degree of protection against heterologous strains of Pf, establish immune correlates of protection, and optimize approaches to deliver IV vaccine administration to achieve the coverage in mass administration campaigns needed to eliminate Pf malaria from defined areas.

References and Notes

1. World Health Organization, World Malaria Report: 2012 (2012); available at www.who.int/malaria/publications/world_malaria_report_2012/report/en/index.html.
2. C. J. Murray *et al.*, *Lancet* **379**, 413–431 (2012).
3. C. V. Plowe, P. Alonso, S. L. Hoffman, *J. Infect. Dis.* **200**, 1646–1649 (2009).
4. malERA Consultative Group on Vaccines, *PLoS Med.* **8**, e1000398 (2011).
5. Malaria Vaccine Technology Roadmap, 2006; available at www.malariavaccine.org/files/Malaria_Vaccine_TRM_Final.pdf.
6. K. E. Kester *et al.*, *J. Infect. Dis.* **200**, 337–346 (2009).
7. S. T. Agnandji *et al.*, *N. Engl. J. Med.* **367**, 2284–2295 (2012).
8. R. S. Nussenzweig, J. P. Vanderberg, H. Most, C. Orton, *Nature* **222**, 488–489 (1969).
9. D. F. Clyde, H. Most, V. C. McCarthy, J. P. Vanderberg, *Am. J. Med. Sci.* **266**, 169–177 (1973).
10. K. H. Rieckmann, P. E. Carson, R. L. Beaudoin, J. S. Cassells, K. W. Sell, *Trans. R. Soc. Trop. Med. Hyg.* **68**, 258–259 (1974).

11. S. L. Hoffman *et al*., *J. Infect. Dis.* **185**, 1155–1164 (2002).
12. T. C. Luke, S. L. Hoffman, *J. Exp. Biol.* **206**, 3803–3808 (2003).
13. S. L. Hoffman *et al*., *Hum. Vaccin.* **6**, 97–106 (2010).
14. J. E. Epstein *et al*., *Science* **334**, 475–480 (2011).
15. T. Ponnudurai, J. H. Meuwissen, A. D. Leeuwenberg, J. P. Verhave, A. H. Lensen, *Trans. R. Soc. Trop. Med. Hyg.* **76**, 242–250 (1982).
16. S. Chakravarty *et al*., *Nat. Med.* **13**, 1035–1041 (2007).
17. S. L. Hoffman, D. L. Doolan, *Nat. Med.* **6**, 1218–1219 (2000).
18. Materials and methods are available as supplementary materials on *Science* Online.
19. P. Potocnjak, N. Yoshida, R. S. Nussenzweig, V. Nussenzweig, *J. Exp. Med.* **151**, 1504–1513 (1980).
20. V. S. Moorthy, W. R. Ballou, *Malar. J.* **8**, 312 (2009).
21. L. Schofield *et al*., *Nature* **330**, 664–666 (1987).
22. J. E. Egan *et al*., *Am. J. Trop. Med. Hyg.* **49**, 166–173 (1993).
23. W. R. Weiss, M. Sedegah, R. L. Beaudoin, L. H. Miller, M. F. Good, *Proc. Natl. Acad. Sci. U.S.A.* **85**, 573–576 (1988).
24. D. L. Doolan, S. L. Hoffman, *J. Immunol.* **165**, 1453–1462 (2000).
25. W. R. Weiss, C. G. Jiang, *PLoS ONE* **7**, e31247 (2012).
26. W. R. Weiss, M. Sedegah, J. A. Berzofsky, S. L. Hoffman, *J. Immunol.* **151**, 2690–2698 (1993).
27. M. Tsuji *et al*., *Proc. Natl. Acad. Sci. U.S.A.* **91**, 345–349 (1994).
28. A. C. Teirlinck *et al*., *PLoS Pathog.* **7**, e1002389 (2011).
29. M. Roestenberg *et al*., *N. Engl. J. Med.* **361**, 468–477 (2009).
30. D. G. Doherty, C. O'Farrelly, *Immunol. Rev.* **174**, 5–20 (2000).
31. I. A. Cockburn *et al*., *PLoS Pathog.* **6**, e1000877 (2010).
32. I. Chuang *et al*., *PLoS ONE* **8**, e55571 (2013).
33. J. A. Stoute *et al*., *N. Engl. J. Med.* **336**, 86–91 (1997).
34. K. E. Kester *et al*., *J. Infect. Dis.* **183**, 640–647 (2001).
35. G. A. O'Hara *et al*., *J. Infect. Dis.* **205**, 772–781 (2012).
36. L. Florens *et al*., *Nature* **419**, 520–526 (2002).
37. A. Trieu *et al*., *Mol. Cell. Proteomics* **10**, M11.007948 (2011).
38. D. L. Doolan *et al*., *Proc. Natl. Acad. Sci. U.S.A.* **100**, 9952–9957 (2003).

Acknowledgments: The data presented in this manuscript are tabulated in the main figures and the supplementary materials. The clinical trial was funded and supported by the National Institute of Allergy and Infectious Diseases (NIAID) Intramural Research Program. Production and characterization of the vaccine were supported in part by NIAID Small Business Innovation Research grants 4R44AI055229-08, 3R44AI055229-06S1, and 5R44AI058499-05. Preclinical toxicology and biodistribution studies were supported in part by NIAID preclinical service contract N01-AI-40096. Molecular diagnosis was supported by the Howard Hughes Medical Institute. A materials transfer agreement will be required for the use of recombinant PfMSP-1 and PfEBA-175, HC-04 cells, and 2A10 monoclonal antibody. A number of patents on PfSPZ have been issued, allowed, or filed in the United States and internationally. The U.S. patents include S. L. Hoffman *et al*., U.S. Patent 7,229,627 (2007) (there is a divisional of this patent with claims directed to aseptic adult *Anopheles*-species mosquitoes and aseptic *Plasmodium*-species sporozoites, USSN 11/726,622); S. L. Hoffman *et al*., U.S. Patent Pub. US2005/0208078 (2005); and B. K. L. Sim, S. L. Hoffman, M. Li, R. E. Stafford, U.S. Patent Pub U.S. 2010/0183680 (2010). There is also a patent on HC-04 cells [J. Prachumsri *et al*., U.S. Patent 7015036 (2006)]. The findings and conclusions in this report are those of the authors and do not necessarily reflect the views of the funding agency or collaborators. The views expressed in this article are those of the author and do not necessarily reflect the official policy or position of the Department of the Navy, Department of the Army, Department of Defense, or the U.S. government. This work was supported by work unit number 6000.RADI.F.A0309. The study protocol was approved by the Naval Medical Research Center Institutional Review Board in compliance with all applicable federal regulations governing the protection of human subjects. J.E.E., T.L.R., J.H.R., J.M., and S.A.D. are military service members. This work was prepared as part of their official duties. Title 17 U.S.C. §101 defines a U.S. government work as a work prepared by a military service member or employee of the U.S. government as part of that person's official duties. The opinions or assertions contained herein are the private views of the authors and are not to be construed as official or as reflecting true views of the Departments of the Army, Navy, or Defense. The authors thank the vaccine trial participants for their contribution and commitment to vaccine research. We acknowledge the contributions of our NIH Clinical Center and NIAID colleagues, especially A. S. Fauci for thoughtful advice and review of the manuscript; J. Stein, J. Pierson, R. Eckes, P. Driscoll, L. Ediger, and the nursing staff of the 5NW, SCSU, 5SE-S, and 5SE-N units; our VRC colleagues, especially B. Flynn, A. Mittelman, M. Young, C. Artis, R. Hicks, and T. Abram; the EMMES Corporation; R. Thompson, F. Beams, M. Garley, A. Hoffman, and D. Dolberg of Sanaria for administrative, operations, and legal support and T. Luke for insight and inspiration; the NIAID Institutional Review Board; the NIAID Office of Communications and Government Relations; the NIH Clinical Center Investigational New Drug Pharmacy; and the NIH Clinical Center Patient Recruitment and Public Liaison Office. We appreciate the expert reviews of the Safety Monitoring Committee (A. Durbin, K. Kester, and A. Cross) and the assistance from the U.S. Military Malaria Vaccine Program, the Walter Reed Army Institute of Research Entomology Branch, and the Naval Medical Research Center, especially A. Reyes, Y. Alcorta, G. Banania, C. Fedders, M. Dowler, T. Savransky, D. Patel, C. Brando, and K. Kobylinski.

Supplementary Materials

www.sciencemag.org/content/341/6152/1359/suppl/DC1
Materials and Methods
Supplementary Text
Figs. S1 to S6
Tables S1 to S6
References (*39*–*51*)

11 June 2013; accepted 25 July 2013
Published online 8 August 2013;
10.1126/science.1241800

Linear Structures in the Core of the Coma Cluster of Galaxies

J. S. Sanders,[1,2]* A. C. Fabian,[2] E. Churazov,[3,4] A. A. Schekochihin,[5] A. Simionescu,[6,7,8] S. A. Walker,[2] N. Werner[6,7]

The hot x-ray–emitting plasma in galaxy clusters is predicted to have turbulent motion, which can contribute around 10% of the cluster's central energy density. We report deep Chandra X-ray Observatory observations of the Coma cluster core, showing the presence of quasi-linear high-density arms spanning 150 kiloparsecs, consisting of low-entropy material that was probably stripped from merging subclusters. Two appear to be connected with a subgroup of galaxies at a 650-kiloparsec radius that is merging into the cluster, implying coherence over several hundred million years. Such a long lifetime implies that strong isotropic turbulence and conduction are suppressed in the core, despite the unrelaxed state of the cluster. Magnetic fields are presumably responsible. The structures seen in Coma present insight into the past billion years of subcluster merger activity.

Galaxy clusters are the largest gravitationally bound structures and are dominated by dark matter. They are the latest structures to form in the cosmological hierarchical structure formation scenario. They grow through mergers and by the accretion of matter. Most of their baryonic matter consists of a hot plasma (the intracluster medium, or ICM), heated during cluster formation to temperatures of several 10^7 K and visible by its x-ray emission. Cluster major mergers, the mergers between clusters of similar mass, are the most energetic events in the local universe, injecting turbulence and motions contributing to the total ICM energy density by around 10% of the thermal value (*1*, *2*), increasing with radius.

The Coma cluster of galaxies is one of the best-studied nearby rich clusters. However, it is not dynamically relaxed. X-ray observations have shown the disturbed nature of its ICM (*3*, *4*). In particular, a group of galaxies associated with NGC 4839 to the southwest is merging with the main cluster. Unusually, the cluster has two central giant elliptical galaxies, NGC 4874 and NGC 4889, with a line-of-sight velocity difference of 700 km s^{-1} (*5*). The distribution of galaxy velocities within the cluster implies several different subgroups.

We examined the core of the Coma cluster (Fig. 1) with a 546-ks-deep set of Chandra observations (*6*). At the ~9 keV (10^8 K) temperature of the ICM in Coma, x-ray surface brightness variations are mainly due to density fluctuations. The most striking features are a set of high–surface-brightness "arms" (labeled A1 to A4). A1 is enhanced in surface brightness with respect

[1]Max-Planck-Institut für Extraterrestrische Physik, Giessenbachstrasse 1, 85748 Garching, Germany. [2]Institute of Astronomy, University of Cambridge, Madingley Road, Cambridge CB3 0HA, UK. [3]Max-Planck-Institut für Astrophysik, Karl-Schwarzschild-Strasse 1, 85748 Garching, Germany. [4]Space Research Institute (IKI), Profsoyuznaya 84/32, Moscow 117997, Russia. [5]Rudolf Peierls Centre for Theoretical Physics, University of Oxford, 1 Keble Road, Oxford OX1 3NP, UK. [6]Kavli Institute for Particle Astrophysics and Cosmology, Stanford University, 452 Lomita Mall, Stanford, CA 94305, USA. [7]Department of Physics, Stanford University, 382 Via Pueblo Mall, Stanford, CA 94305–4060, USA. [8]Institute of Space and Astronautical Science, Japan Aerospace Exploration Agency, 3-1-1 Yoshinodai, Chuo-ku, Sagamihara, Kanagawa 252-5210, Japan.

*Corresponding author. E-mail: jsanders@mpe.mpg.de

to the larger-scale emission by up to around 10%, although this can increase to 15 or 20% when different models of the underlying surface brightness are used. Unless we are viewing these features from a special direction, the most likely morphology of the arms is that they are roughly cylindrical and are as deep as they are wide on the sky. We estimate that they are enhanced in density by 35 to 40%, assuming that they lie in the plane of the sky at the midpoint of the cluster. The fractional density enhancement relative to their surroundings increases if the arms are significantly in front of or behind the cluster. In addition, if they are inclined along the line of sight, their surface brightness would be boosted by 1/sin θ, where θ is the angle between the arm and the line of sight. If this is the case, the density in the arms would be smaller than our estimates. Small values of θ will boost their chances of being detected, but their intrinsic lengths would be much larger than observed on the sky.

Around NGC 4889 and NGC 4874 are bright dense "halos" of gas, labeled in H1 and H2, respectively, in Fig. 1A. They are larger than the compact galactic mini-coronae (*7*), which we do not examine here. A more detailed view of the region between these galaxies is shown in Fig. 2. There is also a region of enhancement, labeled H3, around 100 kpc to the north, east, and south of NGC 4874. An edge to this region between NGC 4889 and NGC 4874 is apparent (labeled E). This may be a shock (the projected pressure jumps by 10%), but the data are insufficient to verify the expected temperature change.

Between this edge and NGC 4889 are 50-kpc-long filamentary features running in the northeast to southwest direction (marked as F1) and also radiating away from NGC 4874 to the northwest and west (labeled F2). These filamentary features are enhanced by approximately 5% in surface brightness and are not associated with detector features (fig. S1). The minimum length scale observed in the x-ray image is around the mean free path for electrons here (~7 kpc). These linear structures are likely to require magnetic fields in order to be stable.

Behind the galaxy GMP 2910 there is a remarkably straight 48-kpc-long soft x-ray tail (labeled T in Fig. 1A). The spectrum of this material is consistent with thermal material at a temperature of ~1 keV (fig. S2). This tail of presumably stripped gas was also seen by its Hα emission (*8*). A similar tail of stripped gas with x-ray emission was also seen in A3627 (*9*).

There is a gradient in emission-weighted projected temperature from the hot northwest side of the core to the cool southeast, previously seen using the Advanced Satellite for Cosmology and Astrophysics (*10*) and X-ray Multi-Mirror Mission (XMM-Newton) (*11*) (Fig. 3). The arms are cooler than their surroundings and the gaps between the arms. There is also a cooler region north and south of NGC 4874, along the direction of arm A3. Accounting for projection effects, the pressure enhancement of A1 and A3 relative to their surroundings is 18 ± 13 and 24 ± 11%, statistically, respectively. However, if the arms are not in the plane of the sky or if our geometrical assumptions are incorrect, the above pressure values will be reduced. Therefore, the arms are consistent with being in pressure equilibrium with their surroundings.

Arm A1 has a "specific entropy" 30% lower than its surroundings, assuming a cylindrical morphology in the plane of the sky. In a relaxed galaxy cluster, the lowest-entropy material lies at the bottom of the potential well. In Coma, the lowest-entropy x-ray–emitting material appears to lie in the arms, offset from the core itself. We estimate that arm A1 contains around 4×10^{10} solar masses of material.

To examine the connection of the observed structures to those on larger scales, we examined XMM-Newton observations of the fractional deviation in the surface brightness from the average at each radius (Fig. 4). Arms A1 and A2 are immediately apparent, and A3 and A4 are also visible. The strongest feature (labeled L1) is a bright arm of emission extending from the center toward NGC 4911 and then toward NGC 4921, seen previously using the Röntgen Satellite (ROSAT) (*12*) and XMM (*13*). NGC 4911 is probably part of a distinct high-velocity group merging with the main cluster (*5*). L1 may turn back toward the center of the cluster as L2, toward the central galaxy NGC 4889.

A2 appears to be the extension of L1 into the core. A1 may also be part of this structure, if L1 bifurcates, or it may be a separate feature. The whole L1 structure spans from 200 kpc radius in the center of the cluster out to radii of at least 650 kpc, or further if the feature is not in the plane of the sky. The central galaxy NGC 4889 itself may also be part of this large-scale structure.

The arms and other features in the core of Coma are likely to be the result of the gas stripped from subclusters merging with the cluster. The stripped gas retains memory of the temperature and entropy of the subcluster. The lower entropy of the arms relative to their surroundings supports the hypothesis that they are stripped material. The

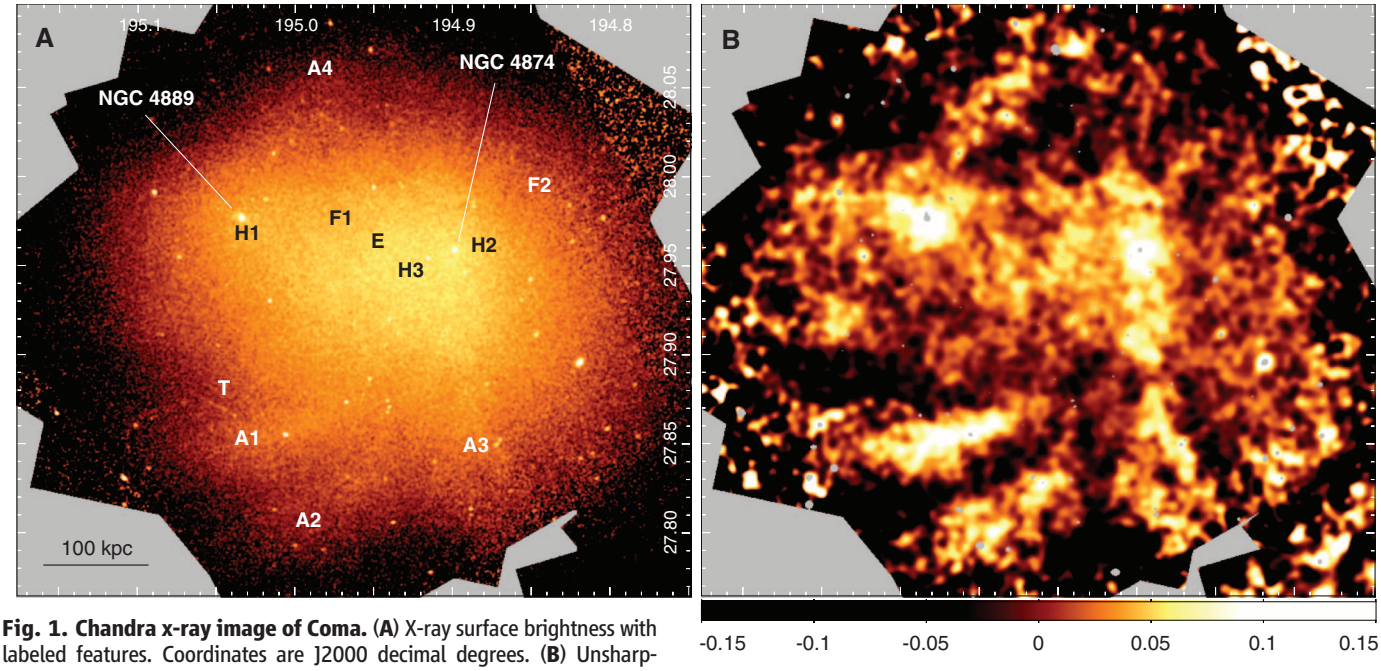

Fig. 1. Chandra x-ray image of Coma. (**A**) X-ray surface brightness with labeled features. Coordinates are J2000 decimal degrees. (**B**) Unsharp-masked image of the same region, enhancing features below ~30 kpc. The numerical values show the fractional surface brightness enhancement or suppression in smaller-scale features relative to larger-scale emission. Gray areas lie outside the data set or are excluded point sources.

tail of stripped material behind GMP 2910 (labeled T in Fig. 1A) demonstrates that stripping is occurring in Coma. Stripping is clearly seen in the Virgo Cluster, where a subcluster of galaxies associated with M86 is merging with the main cluster (*14*). It has been highlighted (*15*) that low-entropy gas associated with the merging group can give rise to density variations. However, there appear to be several arms in Coma not associated with the NGC 4911 group.

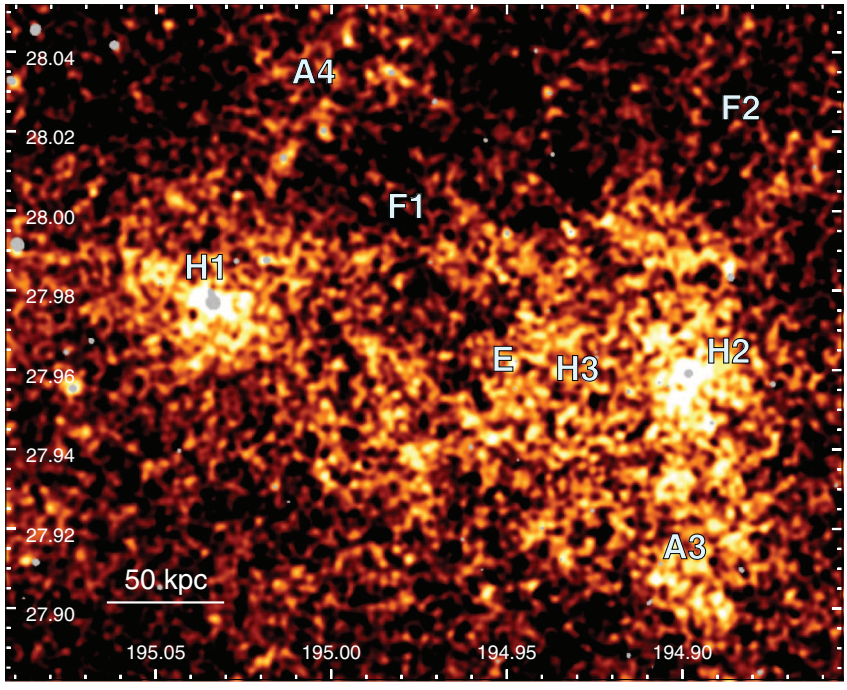

Fig. 2. Detailed view of the cluster center. A more detailed unsharp-masked image of the region around the two central galaxies.

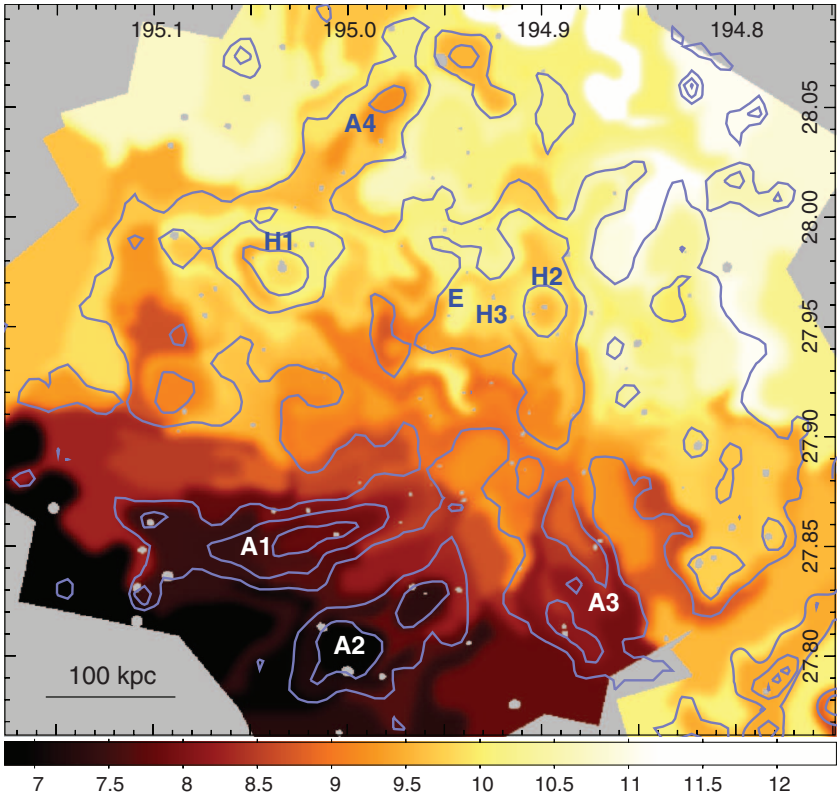

Fig. 3. Temperature map. Emission-weighted ICM temperature (in kilo–electron volts), calculated by spectral fitting. The contours show lines of constant surface brightness enhancement in an unsharp-masked map with levels of 0, 3.5, and 7%.

If arms A1, A2, and L1 are stripped material from the NGC 4911 subgroup merger, then such material can remain coherent over several hundred kiloparsecs. The arms are likely to be around 300 million years old (taking the projected radius of NGC 4911 and dividing by the sound speed). The linear morphology of the arms is suggestive of laminar flow, indicating a lack of strong turbulence and a relatively high effective viscosity. Measurements of surface brightness fluctuations also indicate few strong density variations (*15*). The arms, however, are massive and require time scales of ~70 million years to be accelerated by ram pressure to the sound speed and so do not instantaneously trace the ICM motion. Isotropic conduction with the surroundings must be suppressed, probably by magnetic fields. The time scale for conduction at the Spitzer level to equilibrate the temperature is around 8 million years, reducing if the length of the conduction zone is shorter than the arm width. This is much shorter than their 300 million year age, assuming that they are due to stripping from the NGC 4911 subgroup. Tangential motion of structures through a cluster can induce magnetic draping (*16*), where field lines are stretched, suppressing transport processes with the surroundings.

The NGC 4911 subgroup could have passed through the cluster core from the west to the east, leaving stripped material A1 and A2 in its wake. L1 is also cooler than its surroundings (*11*, *17*), implying that it has a different origin from the bulk cluster gas. Arm A3 points roughly in the direction of the NGC 4839 group, so it could be related to this merger. This supports the argument that the group has already passed through the cluster center (*18*), because the structure could not precede the galaxies in the group. However, it should be noted that A3 appears to end close to the edge of the Chandra field (Fig. 4) and does not continue any further toward NGC 4839. There is also a chain of cluster member galaxies along the direction of A3 (*5*), and a velocity substructure is detected nearby and also close to the inner part of A2 (*19*). The arm might be material stripped from galaxies in this chain. The origins of arm A4 are uncertain. Away from the core of the cluster there are some other velocity subgroups in that direction (*5*, *19*), but alternatively A4 could consist of material stripped from galaxies associated with an NGC 4889 subgroup, because the arm ends at that galaxy.

The cluster contains a well-studied giant radio halo (*20*). Such emission is exclusively found in merging clusters (*21*), but the source of the relativistic electrons required is still a matter of debate. The electrons could be accelerated by shocks or turbulence in the ICM, or they could be generated by relativistic proton collisions in the cluster. If we compare the observed x-ray structures with previous low-frequency radio maps (*22*), we do not see any features in common (fig. S3). Therefore, we do not observe emission from

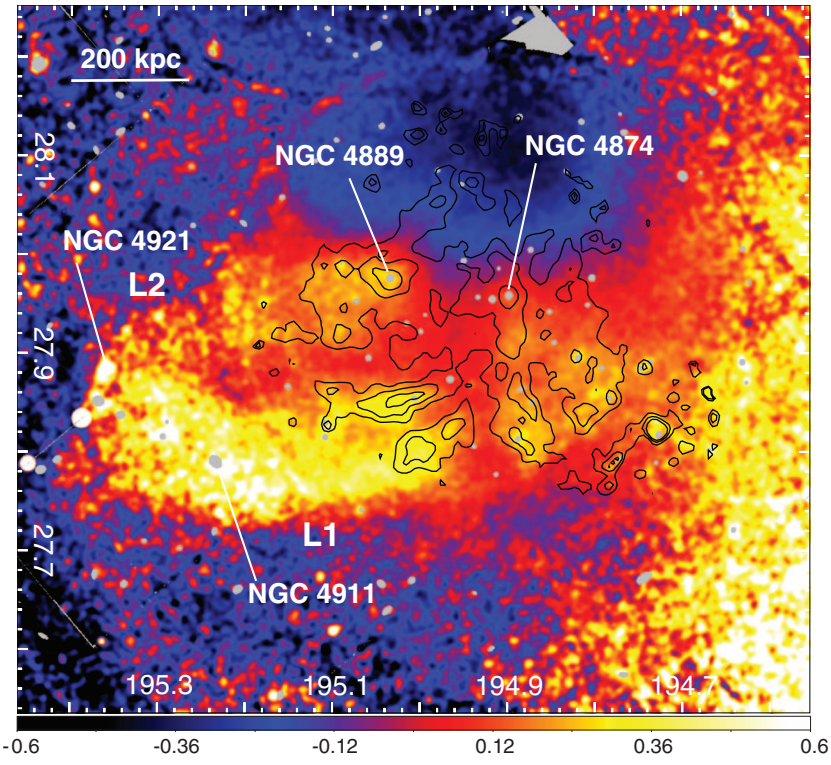

Fig. 4. Larger-scale x-ray distribution. XMM EPIC-MOS image of the fractional difference in surface brightness from the average at each radius. The two halves of the large-scale structure, L1 and L2, are labeled. The contours are as in Fig. 3.

electron acceleration processes, such as turbulence or shocks, associated with the arms. The outer edge of the L1 feature coincides with the edge of the radio emission and with a shock detected using Planck and XMM (*23*).

References and Notes

1. E. T. Lau, A. V. Kravtsov, D. Nagai, *Astrophys. J.* **705**, 1129–1138 (2009).
2. F. Vazza *et al.*, *Astron. Astrophys.* **504**, 33–43 (2009).
3. U. G. Briel, J. P. Henry, H. Boehringer, *Astron. Astrophys.* **259**, L31 (1992).
4. S. D. M. White, U. G. Briel, J. P. Henry, *Mon. Not. R. Astron. Soc.* **261**, L8 (1993).
5. C. Adami, A. Biviano, F. Durret, A. Mazure, *Astron. Astrophys.* **443**, 17–27 (2005).
6. Materials and methods are available as supplementary materials on *Science* Online.
7. A. Vikhlinin, M. Markevitch, W. Forman, C. Jones, *Astrophys. J.* **555**, L87–L90 (2001).
8. M. Yagi *et al.*, *Astrophys. J.* **660**, 1209–1214 (2007).
9. M. Sun, M. Donahue, G. M. Voit, *Astrophys. J.* **671**, 190–202 (2007).
10. R. H. Donnelly *et al.*, *Astrophys. J.* **513**, 690–694 (1999).
11. M. Arnaud *et al.*, *Astron. Astrophys.* **365**, L67–L73 (2001).
12. A. Vikhlinin, W. Forman, C. Jones, *Astrophys. J.* **474**, L7–L10 (1997).
13. D. M. Neumann, D. H. Lumb, G. W. Pratt, U. G. Briel, *Astron. Astrophys.* **400**, 811–821 (2003).
14. S. Randall *et al.*, *Astrophys. J.* **688**, 208–223 (2008).
15. E. Churazov *et al.*, *Mon. Not. R. Astron. Soc.* **421**, 1123–1135 (2012).
16. A. Vikhlinin, M. Markevitch, S. S. Murray, *Astrophys. J.* **549**, L47–L50 (2001).
17. A. Simionescu *et al.*, *Astrophys. J.*, http://arxiv.org/abs/1302.4140 (2013).
18. J. O. Burns, K. Roettiger, M. Ledlow, A. Klypin, *Astrophys. J.* **427**, L87 (1994).
19. C. Adami *et al.*, *Astron. Astrophys.* **507**, 1225–1241 (2009).
20. M. A. G. Willson, *Mon. Not. R. Astron. Soc.* **151**, 1 (1970).
21. R. Cassano *et al.*, *Astrophys. J.* **721**, L82–L85 (2010).
22. S. Brown, L. Rudnick, *Mon. Not. R. Astron. Soc.* **412**, 2–12 (2011).
23. Planck Collaboration, *Astron. Astrophys.* **554**, A140 (2013).

Acknowledgments: A.C.F. acknowledges the support of the Royal Society. We thank S. D. Brown for providing the 352-MHz radio map. Support for this work was provided by NASA through Chandra Award Number GO2-13145X issued by the Chandra X-ray Observatory Center, which is operated by the Smithsonian Astrophysical Observatory for and on behalf of NASA under contract NAS8-03060. The scientific results reported in this article are based on observations made by the Chandra X-ray Observatory and data obtained from the Chandra Data Archive, as well as observations obtained with XMM-Newton, a European Space Agency (ESA) science mission with instruments and contributions directly funded by ESA Member States and NASA. The data analyzed here can be found in the XMM-Newton Science Archive and Chandra Data Archive.

Supplementary Materials

www.sciencemag.org/content/341/6152/1365/suppl/DC1
Materials and Methods
Figs. S1 to S5
Tables S1 to S3
References (*24*–*34*)

26 March 2013; accepted 13 August 2013
10.1126/science.1238334

Control of Surface Charges by Radicals as a Principle of Antistatic Polymers Protecting Electronic Circuitry

H. Tarik Baytekin,* Bilge Baytekin,* Thomas M. Hermans,† Bartlomiej Kowalczyk, Bartosz A. Grzybowski‡

Even minute quantities of electric charge accumulating on polymer surfaces can cause shocks, explosions, and multibillion-dollar losses to electronic circuitry. This paper demonstrates that to remove static electricity, it is not at all necessary to "target" the charges themselves. Instead, the way to discharge a polymer is to remove radicals from its surface. These radicals colocalize with and stabilize the charges; when they are scavenged, the surfaces discharge rapidly. This radical-charge interplay allows for controlling static electricity by doping common polymers with small amounts of radical-scavenging molecules, including the familiar vitamin E. The effectiveness of this approach is demonstrated by rendering common polymers dust-mitigating and also by using them as coatings that prevent the failure of electronic circuitry.

Beyond kids' play at electrifying balloons and "static cling," (*1*) accumulation of static electricity on polymers is a serious technological problem responsible for shocks and explosions (*2*, *3*), as well as damage to satellites (*4*) and other electronic equipment measured in billions of dollars each year (*5*). Despite centuries of research (*6*, *7*), we still do not know why certain polymers charge more than others and, most important, how to design polymers that would resist static electricity and could potentially act as general-purpose antistatic coatings avoiding the limitations of currently used materials [e.g., moisture-sensitive ionic conductors, resins requiring high metal loading, and the like (*5*, *8*) (fig. S1)]. It has only been recently that works by us (*9*–*11*) and others (*12*–*14*) revealed that electrification of polymers due to physical contact leads to spatially heterogeneous transfer of charge and material, as well as the creation of

Department of Chemistry and Department of Chemical and Biological Engineering, Northwestern University, 2145 Sheridan Road, Evanston, IL 60208, USA.

*These authors contributed equally to this work.
†Present address: Institut de Science et d'Ingénierie Supramoléculaires (ISIS), 8 Allée Gaspard Monge, BP 7002867083, Strasbourg Cedex, France.
‡Corresponding author. E-mail: grzybor@northwestern.edu

mechanoradicals upon homolytic bond cleavage (*11*). Here, we show that when polymers are electrified—either upon contact with other materials (*15*) or during electrostatic discharge (*16*)—the charges and the radicals colocalize to the same nanoscopic regions. Remarkably, the presence of radicals stabilizes the charged species; conversely, the removal of radicals destabilizes charge domains and results in a rapid discharge of the electrified material. Capitalizing on this interplay between charges and radicals, we demonstrate that doping polymers with small amounts of free-radical scavengers prevents static charging. This finding is of considerable technological importance. Indeed, by using radical-scavenging additives as familiar as vitamin E, it is now possible to transform various common polymers into antistatic coatings such as those sought by the electronics industry to protect semiconductor devices from failure caused by the build-up of static electricity.

We electrified various types of polymers—including, but not limited to, acrylate-based adhesive Scotch tape, poly(dimethylsiloxane) (PDMS), and polystyrene (PS) (*17*)—either by contact-charging them against other materials or by exposing them to a corona discharge from an electrostatic gun. Subsequently, these charged surfaces were examined by several atomic force microscopy (AFM) modalities on a Bruker Dimension Icon system (Bruker Biosciences, Billerica, Massachusetts) (for images of surfaces before electrification, see fig. S2). Specifically, Kelvin force microscopy (KFM) was used to visualize surface charge distributions (*9*), and magnetic force microscopy (MFM) visualized the distribution of radicals (*11*, *18*). In addition, conventional AFM was used to visualize surface topography, and AFM phase and AFM PF-QNM modes [PeakForce Quantitative Nanomechanical Property Mapping (Bruker Biosciences)] (*10*) provided quantitative elastic property mapping of the surfaces at the nanoscopic level and allowed identification of regions where material was transferred (if electrification involved physical contact).

Figure 1, A to F, shows typical experimental AFM-phase, MFM, and KFM images of the same region of contact-charged polymer (in this case, Scotch tape) as well as the correlation maps (see the supplementary materials for equations) for different image pairs. In these maps, the peaks at (0,0) indicate that the two images being compared are highly correlated—or, colloquially put, can be superimposed. In other words, the regions where the material is transferred correspond faithfully to the regions that develop static charges [in the form of previously described (*9*) positive/negative charge "mosaics"] and to the regions that contain the radicals. These observations are congruent with a scenario in which contact electrification is due to the transfer of nanoscopic patches of material (*9*, *10*), which entails both heterolytic bond cleavage giving rise to charged species and homolytic bond cleavage giving rise to radicals (fig. S4) (*11*). The important finding is that all these phenomena are spatially colocalized.

Next, we consider whether charge-radical colocalization applies to polymers charged not only by contact but also by discharge. Charging by electrostatic/corona discharge from an electrostatic gun does not involve polymer transfer but produces charged species of both polarities (*19*), as well as radicals (*20*). The KFM analysis of the polymers electrified by corona discharge reveals charged regions [of a polarity dependent on gun squeezing or releasing (see Fig. 1G for negatively charged PDMS)], whereas MFM gives distinct signals due to radicals (Fig. 1H). Notably, these species are again colocalized, as evidenced by the correlation maps (Fig. 1I).

The colocalization of surface charges and radicals suggests a possible interplay between these species. To verify this, we performed a series of charging experiments with native polymers, as well as polymers doped with small amounts of chemical substances scavenging the radicals such as (±)-α-tocopherol (vitamin E), bis(1-octyloxy-2,2,6,6-tetramethyl-4-piperidyl) sebacate (HALS), or 2,2-diphenyl-1-picrylhydrazyl (DPPH) (*11*). Data in Fig. 2A illustrate that the presence of radical scavengers reduces the propensity of polymers to develop static electricity during contact charging. Moreover, the magnitude of charge decreases with increasing dopant concentration (Fig. 2B and fig. S6). We note that this effect cannot be attributed to the alterations in the mechanical properties of PDMS, which remain unchanged by this low level of doping (fig. S7). Furthermore, we demonstrated that the part of the dopant that affects radical scavenging also affects the charging. To show this, we synthesized 2,2-diphenyl-1-picryl hydrazine (DPPH-H) dopant that differs from the DPPH scavenger by only one hydrogen atom (*21*). Despite close structural similarity, this molecule is not able to scavenge radicals. Importantly, when the PDMS was doped with DPPH-H, its charging propensity was indistinguishable from pure PDMS (Fig. 2C). We emphasize that the same effects are observed upon corona discharge, where doped polymers accumulate only up to ~10% of the charge that is detected on the native/undoped polymers under the same discharge and subsequent measurement conditions.

The role of radicals is to stabilize the charges. This is evidenced by experiments illustrated in Fig. 2, D to G, where the spontaneous discharge in air of the contact- or corona-electrified polymers was monitored as a function of time. Irrespective of the method and polarity of charging, pure polymers discharge over the course of hours (Fig. 2, D and F), while the same polymers doped with radicals scavengers discharge within minutes (Fig. 2, E and G, and fig. S8). Most important, the discharge kinetics is related to the presence

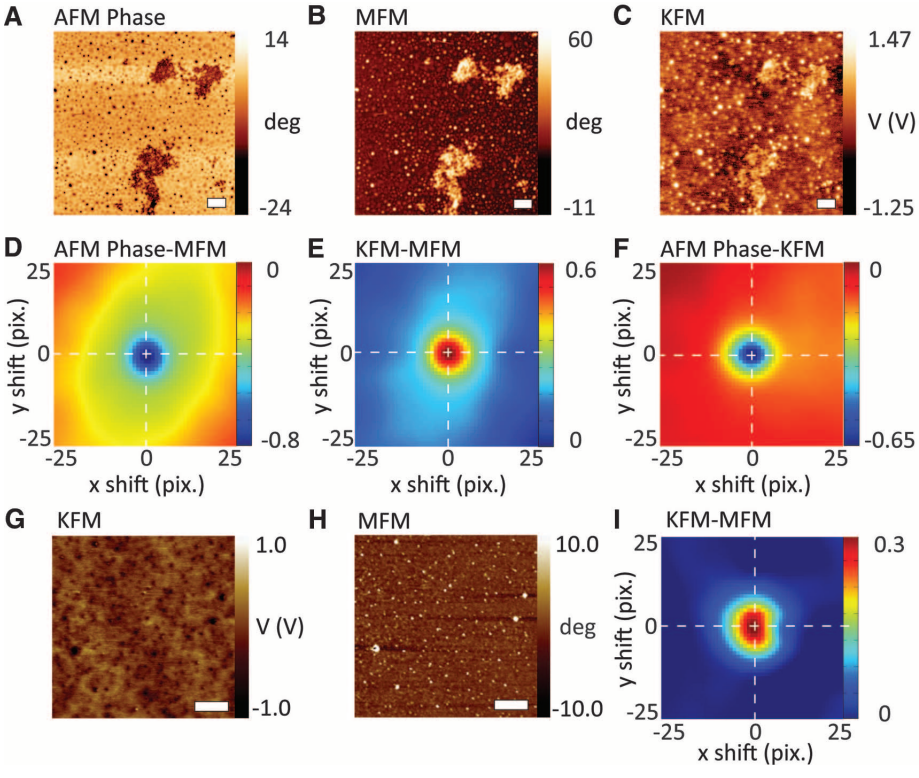

Fig. 1. Colocalization of charges and radicals on electrified surfaces. (**A** to **C**) On contact-charged surfaces, surface charges (by KFM) colocalize with radicals (by MFM) and correspond to regions of material transfer (by AFM-phase). See also figs. S3 and S5. (**D** to **F**) Cross-correlation maps between (D) AFM phase and MFM, (E) MFM and KFM, and (F) AFM phase and KFM. (**G** and **H**) KFM and MFM maps of the same regions of PDMS corona-charged (here, negatively) using an electrostatic gun. (**I**) The corresponding KFM/MFM correlation map. All scale bars, 1 μm. All maps shown in the figure are highly correlated with peak $|\gamma(x,y)|$ values as high as 0.7 and all P values << 0.01 (that is, >99% confidence intervals).

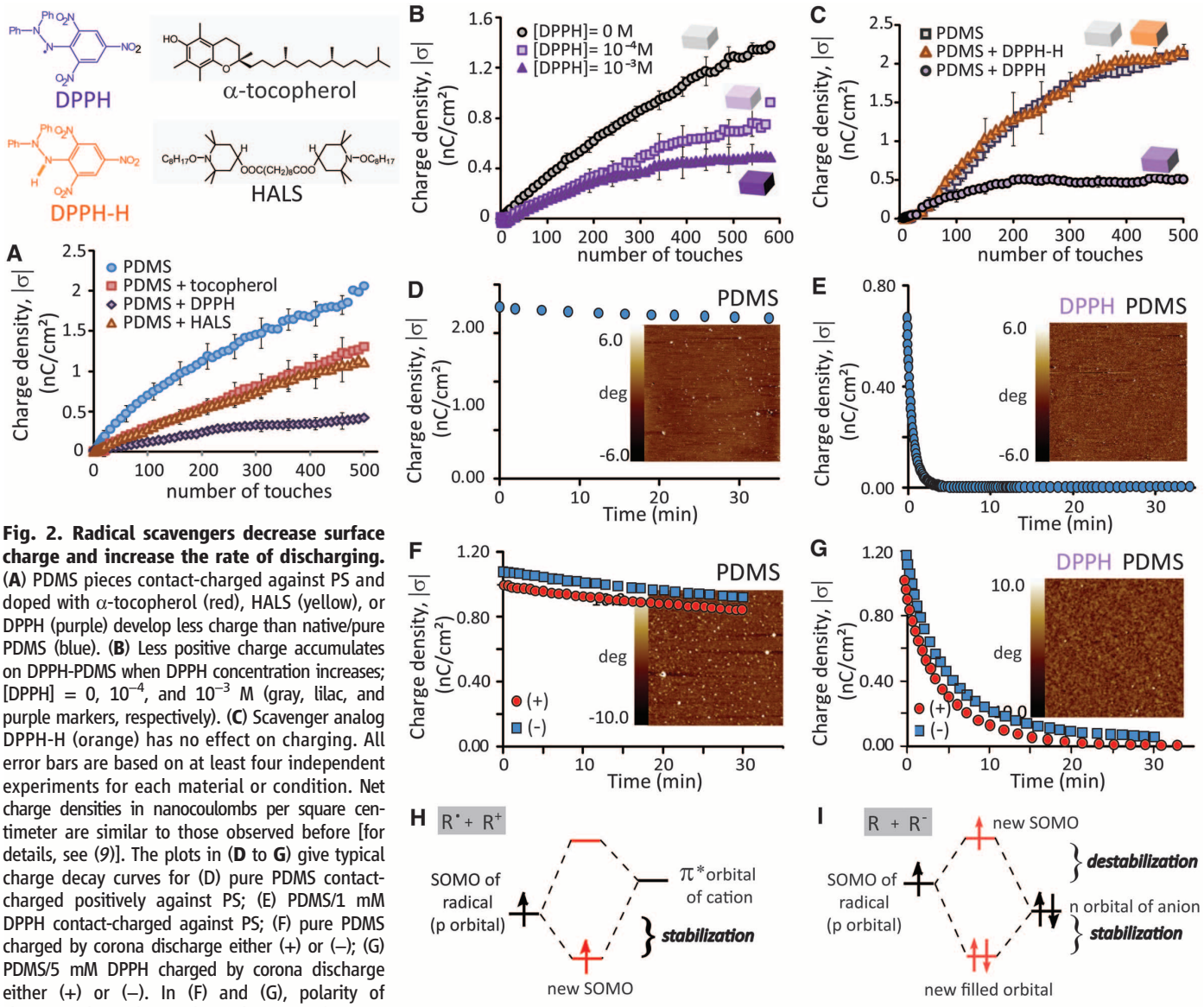

Fig. 2. Radical scavengers decrease surface charge and increase the rate of discharging. (**A**) PDMS pieces contact-charged against PS and doped with α-tocopherol (red), HALS (yellow), or DPPH (purple) develop less charge than native/pure PDMS (blue). (**B**) Less positive charge accumulates on DPPH-PDMS when DPPH concentration increases; [DPPH] = 0, 10^{-4}, and 10^{-3} M (gray, lilac, and purple markers, respectively). (**C**) Scavenger analog DPPH-H (orange) has no effect on charging. All error bars are based on at least four independent experiments for each material or condition. Net charge densities in nanocoulombs per square centimeter are similar to those observed before [for details, see (*9*)]. The plots in (**D** to **G**) give typical charge decay curves for (D) pure PDMS contact-charged positively against PS; (E) PDMS/1 mM DPPH contact-charged against PS; (F) pure PDMS charged by corona discharge either (+) or (–); (G) PDMS/5 mM DPPH charged by corona discharge either (+) or (–). In (F) and (G), polarity of charging depends on the polarity of the ions produced by the ion gun, but the rates of discharge do not (the *y* axes have the absolute values of surface charge density). The images in the insets give the corresponding MFM maps recorded after 24 hours. More radicals (white spots) are present on pure PDMS than on PDMS/DPPH. (**H** and **I**) Qualitative illustration of orbital interactions of (H) radicals and cations and (I) radicals and anions on contact-charged surfaces.

or absence of radicals. The MFM maps accompanying the discharge curves in Fig. 2, D to G and images in fig. S9 evidence that for slowly discharging, pure PDMS, the radicals are still present even after 24 hours. In contrast, for the rapidly discharging PDMS/DPPH, there are much fewer radicals left on the surface after the same time.

As we have shown previously, the radicals that form as a result of homolytic bond cleavage during electrification are mostly peroxy radicals, $ROO^{\bullet}$ (*11*), known for their relatively high stability due to resonance stabilization (*22*). We suggest that charge stabilization can be rationalized—at least qualitatively—on the basis of molecular orbital theory, whereby the singly occupied molecular orbitals (SOMO) of the radicalic species interact with the empty orbitals of cationic species (Fig. 2H) or with the filled orbitals of the anionic species (Fig. 2I and supplementary text, Section 4). When the radical scavengers are present, they either (i) trap and stabilize the radicals (e.g., as in vitamin E, which forms a tocopheroxy radical), thus lowering the energy of SOMO and preventing it from effective participation in electron sharing, or (ii) annihilate the radicals by reacting with them (e.g., DPPH reacts into DPPH-R, whereas HALS forms N-alkoxy derivatives). We note that alternative explanations based on the dopants' increasing conductivity of the polymers do not apply. First, surface resistivities that we measured for both undoped and doped polymers are on the order of 10^{16} ohms per square (Ω/sq), well above the 10^{10} to 10^{12} Ω/sq for antistatic materials (*8*). Second, there is no increased ability of the doped polymers to condense surface water (contact angles do not change perceptibly upon doping, e.g., 106.5° ± 1.3° for pure PDMS and 107.0° ± 0.8° for PDMS doped with 0.5×10^{-2} M DPPH). We also verified that all the trends we observed remained unchanged in a water free-atmosphere, under dry Ar.

The practical importance of the charge-radical interplay that we described above is in the ability to engineer antistatic materials by simply doping common insulating polymers with small amounts of radical scavengers. Figure 3A illustrates how PS beads shaken in a PS petri dish change from highly charging to virtually noncharging. Figure 3B shows another example where a piece of PDMS doped with DPPH and contact-charged against PS discharges and "de-dusts" from small shreds of paper within tens of minutes. For comparison, a native/undoped PDMS charged to the

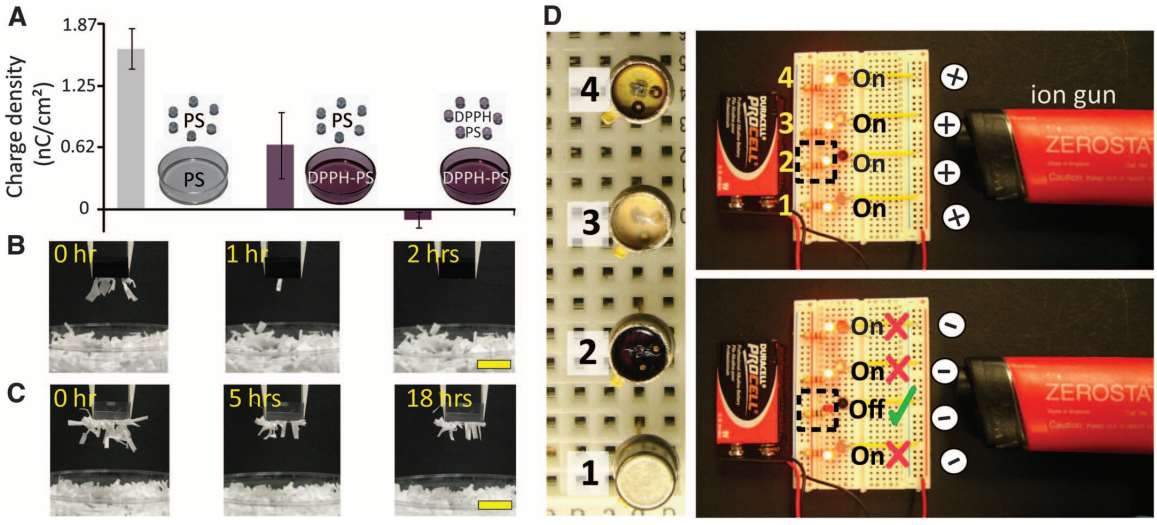

Fig. 3. Applications of antistatic polymers based on radical scavenging. (**A**) For PS beads contact-charged by shaking in PS petri dishes, the average density of charge decreases as one (middle) or both (right) of the contacting materials are doped with DPPH. Error bars correspond to standard deviations of the charges on 25 beads used in each experiment. See fig. S10 for analogous experiments with other materials. (**B**) PDMS block-doped with 1 mM of DPPH contact-charged against PS to 0.75 nC/cm^2 attracts much less small shreds and "de-dusts" completely within ~1 hour, compared with undoped PDMS piece in (C). (**C**) An equally shaped and charged PDMS piece holds paper shreds for more than a day. Scale bar, 1 cm. (**D**) An electronic circuit (for scheme, see fig. S11) in which only transistor #2 (with cap removed and with the gate covered with PS/DPPH) is undamaged (see fig. S11D) after exposure to electrostatic discharge from an ion gun.

same degree retains static electricity and paper shreds for more than a day (Fig. 3C).

Arguably, the most impactful application of the charge-radical regulation is illustrated in Fig. 3D. There, PS doped with DPPH is used to protect electronic components from failure due to electrostatic discharge, which is a ubiquitous problem in the microelectronics industry, damaging semiconductor-based devices (either upon direct contact or arcing) and resulting in losses currently measured in billions of dollars per year (*5*). The circuit shown comprises n-channel junction field-effect transistors (JFETs) (2N 4861A, Solitron Devices) connected serially to light-emitting diodes (LEDs). When exposed to consecutive positive/negative cycles of electrostatic/corona discharge from an electrostatic gun, the LEDs connected to undamaged transistors go cyclically "on" and "off." If, however, the accumulation of static electricity on the gate damages the transistor, its associated LED should always be "on" (*23*). In our circuit, we used four types of transistors: #1 was an intact JFET; #2 was a JFET with the metal shield removed but with the gate covered with a ~200- to 500-μm-thick layer of PS doped with 1.8% w/w DPPH; #3 had the shield removed, but the gate was covered with pure PS; and #4 had the shield removed with no polymer on the gate. As shown in Fig. 3D, the ion gun causes the damage of all transistors but #2, for which DPPH helps scavenge the radicals produced by corona discharge, thus destabilizing the accumulated charges and preventing the build-up of static electricity to damaging levels (see fig. S11 and, for additional experiments, fig. S12). Because similar effects are observed with other types of polymers and scavengers we studied—notably, the edible and biocompatible vitamin E—our results can herald a general, technically straightforward and environmentally "green" way of protecting electronics of various types from the untoward effects of static electricity.

References and Notes

1. T. Shinbrot, T. S. Komatsu, Q. Zhao, *Europhys. Lett.* **83**, 24004 (2008).
2. W. D. Greason, *IEEE Trans. Ind. Appl.* **IA-23**, 205–216 (1987).
3. N. Gibson, *J. Electrost.* **40-41**, 21–30 (1997).
4. S. T. Lai, *Spacecraft Charging: Progress in Astronautics and Aeronautics, Vol. 237* (American Institute of Aeronautics and Astronautics, Reston, VA, 2011).
5. M. Angelopoulos, *IBM J. Res. Develop.* **45**, 57–75 (2001).
6. A. Volta, *Philos. Trans. R. Soc. London* **90**, 403–431 (1800).
7. D. J. Lacks, *Angew. Chem. Int. Ed.* **51**, 6822–6823 (2012).
8. M. Tolinski, *Additives for Polyolefins: Getting the Most out of Polypropylene, Polyethylene and TPO* (Elsevier, Oxford, 2009), pp. 79–91.
9. H. T. Baytekin *et al.*, *Science* **333**, 308–312 (2011).
10. H. T. Baytekin, B. Baytekin, J. T. Incorvati, B. A. Grzybowski, *Angew. Chem. Int. Ed.* **51**, 4843–4847 (2012).
11. B. Baytekin, H. T. Baytekin, B. A. Grzybowski, *J. Am. Chem. Soc.* **134**, 7223–7226 (2012).
12. W. R. Salaneck, A. Paton, *J. Appl. Phys.* **47**, 144 (1976).
13. T. A. L. Burgo *et al.*, *Langmuir* **28**, 7407–7416 (2012).
14. M. Williams, *AIP Adv.* **2**, 010701 (2012).
15. J. Lowell, A. C. Rose-Innes, *Adv. Phys.* **29**, 947–1023 (1980).
16. L. B. Loeb, *Electrical Coronas* (Univ. of California, Berkeley, 1965).
17. Materials and methods are available as supplementary materials on *Science* Online.
18. M. Miyasaka, Y. Saito, H. Nishide, *Adv. Funct. Mater.* **13**, 113–117 (2003).
19. M. J. Waltman, P. Dwivedi, H. H. Hill Jr., W. C. Blanchard, R. G. Ewing, *Talanta* **77**, 249–255 (2008).
20. M. Kuzuya, J. Niwa, H. Ito, *Macromolecules* **26**, 1990–1995 (1993).
21. D. H. Solomon, J. D. Swift, *J. Polym. Sci. A* **3**, 3107–3116 (1965).
22. J. J. Orlando, G. S. Tyndall, *Chem. Soc. Rev.* **41**, 6294–6317 (2012).
23. S. H. Voldman, *ESD Failure Mechanisms and Models* (Wiley, Chichester, UK, 2009).

Acknowledgments: This work was supported by the Non-Equilibrium Energy Research Center (NERC), which is an Energy Frontier Research Center funded by the U.S. Department of Energy, Office of Science, Office of Basic Energy Sciences under award DE-SC0000989. T.M.H. acknowledges a grant from the Human Frontier Science Program. We thank T. Aytun for help in measuring transistor characteristics.

Supplementary Materials

www.sciencemag.org/content/341/6152/1368/suppl/DC1
Materials and Methods
Supplementary Text
Figs. S1 to S14
Reference (*24*)

3 June 2013; accepted 14 August 2013
10.1126/science.1241326

Glassy Dynamics in Condensed Isolated Polymer Chains

Martin Tress,[1] Emmanuel U. Mapesa,[1] Wilhelm Kossack,[1] Wycliffe K. Kipnusu,[1] Manfred Reiche,[2] Friedrich Kremer[1]*

In the course of miniaturization down to the nanometer scale, much remains unknown concerning how and to what extent the properties of materials are changed. To learn more about the dynamics of condensed isolated polymer chains, we used broadband dielectric spectroscopy and a capacitor with nanostructured electrodes separated by 35 nanometers. We measured the dynamic glass transition of poly(2-vinylpyridine) and found it to be bulk-like; only segments closer than 0.5 nanometer to the substrate were weakly slowed. Our approach paves the way for numerous experiments on the dynamics of isolated molecules.

Many applications in modern technology (e.g., photoresists, sensors for drug delivery, batteries, etc.) rely on materials that are subject to confinement and/or finite size effects. How and to what extent the properties of a material—especially a polymer—are changed

under such conditions is a topic of intense debate (*1*–*8*). The ultimate objective is isolated molecules and their properties in comparison to the bulk. Various techniques are available to deposit (*9*, *10*) and to manipulate (*11*) single low–molecular weight polymeric molecules on a surface and to characterize (*12*–*16*) their structure and conformation. In contrast, little is known about the dynamics in such systems as measured in a broad spectral range and at widely varying temperatures. Investigations have been limited to nanometer thin films of low molecular weight (*17*) and polymeric (*1*–*7*, *18*) layers. Here, we report an approach (*8*) that enables the study of both conformation and dynamics of isolated polymer coils by combining atomic force microscopy (AFM) and broadband dielectric spectroscopy (BDS).

Using nanostructured electrode arrangements (*19*) (Fig. 1, A to C), we assembled a capacitor with a separation of 35 nm and isolated polymer coils deposited on one of the electrodes (Fig. 1D and supplementary materials). As a model system, we used poly(2-vinylpyridine) (P2VP), which is known to establish attractive interactions with the native silica on the silicon electrodes. Consideration of the bulk density and the number-averaged molecular weight enables us to estimate the average volume of a single chain, $\hat{V}_{chain}$ (supplementary materials). A comparison with the coils shown in Fig. 1E (close-up and profile) reveals volumes close to $\hat{V}_{chain}$ (left profile, $V \approx 1.8\hat{V}_{chain}$; right profile, $V \approx 0.4\hat{V}_{chain}$). In view of the molecular weight distribution, this diversity of volumes is expected for single chains. The average coil volume corresponds to $0.9\hat{V}_{chain}$, hence on average, there is only one (isolated) P2VP polymer chain per nanodroplet. In the semi-isolated case, we detected volumes equal to $7.8\hat{V}_{chain}$ and $5.1\hat{V}_{chain}$ for two different molecular weights (Table 1).

In BDS measurements, the dynamic glass transition is associated with the so-called α-relaxation (*20*). Our measurements show that this relaxation process is still present in samples containing only isolated condensed polymer chains (Fig. 2). Because they, and similarly semi-isolated agglomerates consisting of ~5 to 10 chains, have a large surface-to-volume ratio, one would expect notable interactions with the supporting substrate, as is the case for thin polymer layers, for which the literature predicts and reports enhancement or reduction (*1*–*3*) of the glassy dynamics (depending on the type of polymer-substrate interaction). Such changes would result in a shift of the α-relaxation with respect to the bulk. Although similar scenarios have been reported (*1*–*3*), the results are contradictory. Several studies found no alteration of the glassy dynamics in thin polymer layers in the linear response regime (*4*–*7*). In our measurements, the maximum position of the α-relaxation in semi-isolated and isolated condensed polymer chains shows (i) a Vogel-Fulcher-Tammann (VFT) temperature dependence (see supplementary materials), which is the characteristic signature of the dynamic glass transition, and (ii) no deviations from the bulk within the experimental uncertainty (Fig. 3). A close look at the α-relaxation peak reveals a broadening in the case of polymer coils relative to the bulk; this is most pronounced in the case of isolated chains (Fig. 2). The dielectric loss spectra normalized with respect to the peak maximum show that this broadening happens almost exclusively on the low-frequency side (Fig. 3, inset). The observed broadening of the α-relaxation peak accounts for 12% of the total

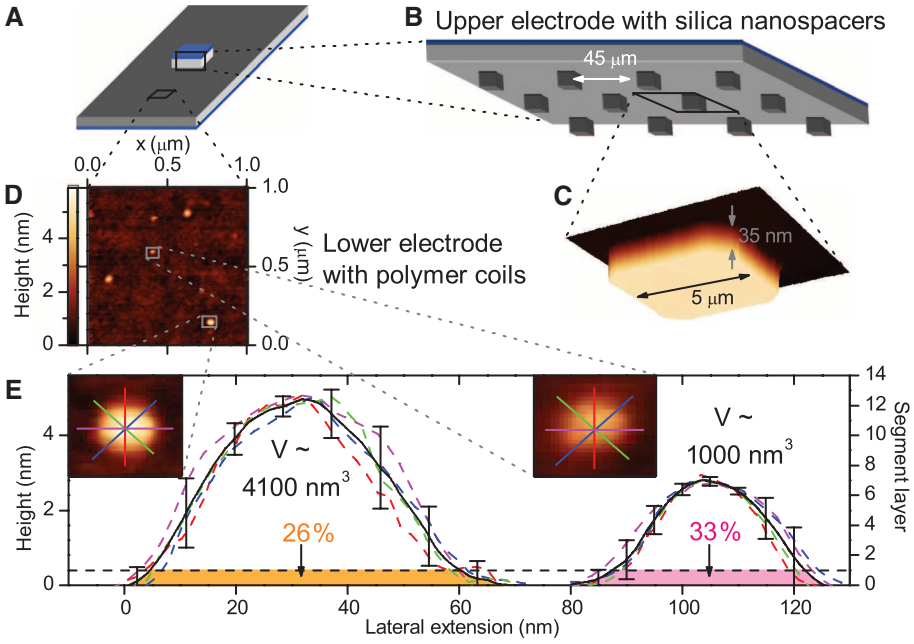

Fig. 1. Sample arrangement required to study condensed (semi-)isolated polymer coils by means of BDS and their topography. (**A**) Two highly doped, conductive silicon electrodes (measures for bottom and top electrode: 4×10 mm^2 and 1×1 mm^2, respectively) are assembled to build the sample capacitor. (**B**) The top electrode has an array of strongly insulating silica nanostructures as spacers on its lower side, which cover about 1% of the surface area. (**C**) Spacers of a height of 35 nm, as shown in this AFM image, were used to conduct measurements of condensed isolated P2VP chains. (**D**) AFM scans of the same sample studied by BDS were taken to analyze the volume of the polymer coils. (**E**) Averaged profiles of two coils from (D) (shown in the close-ups) demonstrate the variation in height, radius, and volume among the coils. The error bars correspond to the standard deviation of the four height profiles as indicated by the colored lines (which are the basis of the averaged profiles); this illustrates a high degree of symmetry within each coil. The percent values give the volume proportion of the layer of chain segments in direct contact with the solid substrate.

Table 1. Specification of the polymers used and mean coil volume analysis of the condensed polymer coils of the samples that have successfully been measured by BDS. The molecular weight and number-average molecular weight (M_W and M_n, respectively) as well as the polydispersity index (PDI) were determined by gel permeation chromatography.

Polymer property	Polymer 1 values	Polymer 2 values	
M_W (kg/mol)	1020	2250	
M_n (kg/mol)	766	1510	
PDI	1.33	1.49	
T_g (K) by DSC	371 (±1)	375 (±1)	
$\hat{V}_{chain}$ (nm^3)	1142	2251	
Chain distribution	Semi-isolated	Semi-isolated	Isolated
$\hat{V}_{coil}$ (nm^3) ± SE	8864 (±2500)	11,564 (±3500)	2033 (±500)
$\hat{V}_{coil}/\hat{V}_{chain}$ ± SE	7.8 (±2.2)	5.1 (±1.6)	0.9 (±0.2)
Coil density (μm^{-2})	37.5	10.0	4.0
Area analyzed (μm^2)	8	8	13.75
Number of analyzed coils	300	80	55

[1]Faculty of Physics and Earth Science, University of Leipzig, 04103 Leipzig, Germany. [2]Max Planck Institute of Microstructure Physics, 06120 Halle (Saale), Germany.

*Corresponding author. E-mail: kremer@physik.uni-leipzig.de

peak area, which is a measure of the number density of the fluctuating molecular dipoles. Therefore, only this proportion of the mobile segments no longer have bulk-like dynamics.

To connect this insight concerning the dynamics to the interfacial topology of the (semi-) isolated polymer coils, the height distribution of the volume is deduced from AFM images. Because two or three monomer segments constitute the structural unit underlying glassy dynamics (*21*), this volume is subdivided into layers, each with a thickness of ~0.4 nm, approximating the width of a P2VP chain (*16*). The most reasonable conjecture is that the segments closest to the solid substrate (Fig. 1E) account for the slower relaxation modes in the case of attractive interactions, as present in the investigated system. The volume fraction of the first layer of segments in direct contact with the solid substrate accounts for 25 to 30% and 15 to 20% of the total coil volume in the cases of isolated and semi-isolated chains, respectively. These proportions are considerably larger than the fraction of slower relaxation modes (~12%), indicating that not all segments that are in direct vicinity of the solid interface contribute to the detected slower dynamics.

Examination of the interactions at the P2VP-silica interface using infrared (IR) spectroscopy revealed that ~50% of the terminal hydroxyl (OH) groups of the silica surface interact with the pyridine ring of the P2VP segments (fig. S3 and supplementary materials). Because the size of a segment is similar to the distance between the OH groups (*22*), we conclude that only about half of the segments in the first layer at the interface are subject to hydrogen bonding. Hence, the amount of broadening found in the BDS data is in accord with the volume fraction of the first segment layer in the polymer coils. However, it remains unknown whether the interacting proportion of segments exhibits the detected slower dynamics, or whether they are completely immobilized and the slower relaxations have to be assigned to those segments neighboring the pinned ones. The latter scenario is suggested by other studies on the adsorption of polymer chains at solid interfaces (*23*).

A cooperative process such as the dynamic glass transition (*24*) can take place even in condensed isolated polymer chains because the length scale on which this fluctuation takes place—which typically corresponds to two or three polymer segments (*21*)—is much smaller than the extension of the coil as a whole (Fig. 3, lower left).

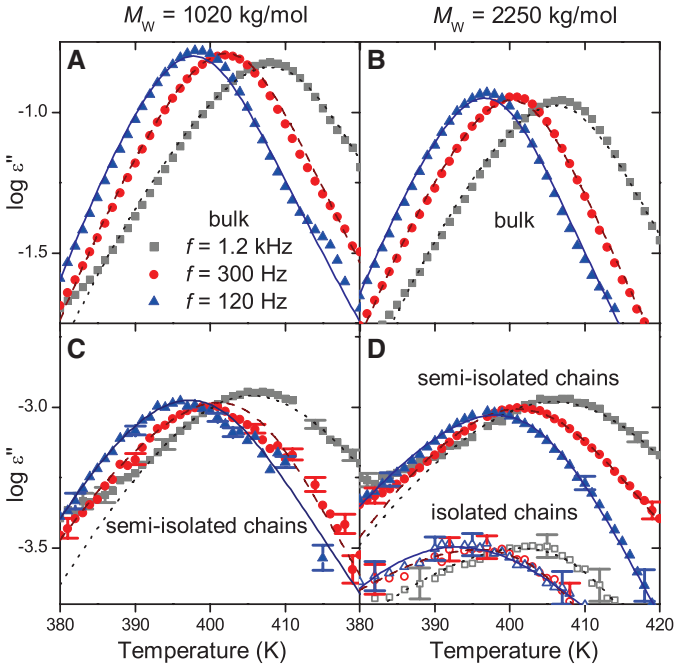

Fig. 2. Dielectric loss ε″ versus temperature for two different molecular weights (labeled at the top of each column) of P2VP bulk, condensed semi-isolated polymer coils and condensed isolated coils at different frequencies as indicated (same symbol shapes denote same frequencies in all panels). (**A** and **B**) In the bulk, the α-relaxation is clearly visible. (**C** and **D**) The same is true in the case of condensed semi-isolated (solid symbols) and even isolated [(D), open symbols)] P2VP polymer chains. The decrease in dielectric strength (signal intensity) in the semi-isolated and isolated coils is due to the much smaller filling fraction of the sample capacitor because ε″ is averaged over the whole capacitor volume. For clarity, a conductivity contribution intrinsic to P2VP was subtracted. In the bulk measurements, the experimental error is smaller than the symbol size; for the other measurements, the error bars correspond to the accuracy of the dielectric measurement system (3×10^{-5}). The dotted, dashed, and solid lines are Havriliak-Negami functions extended with a VFT temperature dependence of the relaxation time τ_{HN} fitted to the data (see supplementary materials).

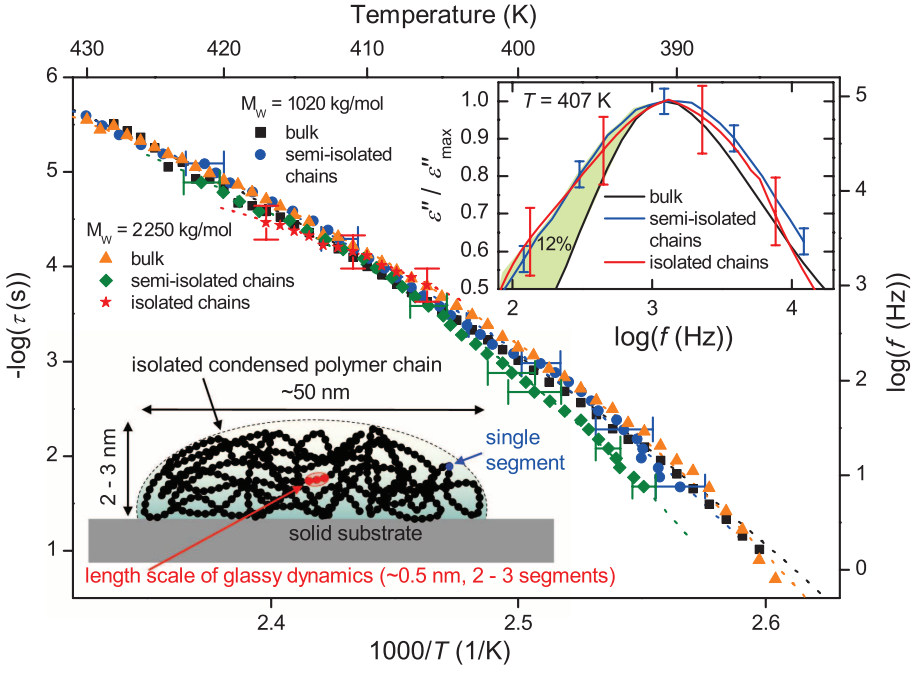

Fig. 3. Activation plot of the α-relaxation of condensed semi-isolated and isolated P2VP polymer coils and the respective bulk dynamics for two molecular weights as indicated. The dotted lines are VFT fits to the data; the error bars indicate the accuracy of the determination of the peak position of the α-relaxation. **Inset:** Dielectric loss spectra (recorded at 407 K) of bulk, semi-isolated chains, and isolated chains normalized by the respective maximum value; the latter two are broadened, especially on the low-frequency side, which corresponds to the occurrence of longer relaxation time modes. In the bulk measurements, the experimental uncertainty is smaller than the line width; for the other measurements, the error bars correspond to the accuracy of the dielectric measurement system (3×10^{-5}). The sketch at lower left illustrates the length scale intrinsic to glassy dynamics in comparison to the size of a single condensed polymer chain.

References and Notes

1. O. K. C. Tsui, T. P. Russell, C. J. Hawker, *Macromolecules* **34**, 5535–5539 (2001).
2. C. J. Ellison, S. D. Kim, D. B. Hall, J. M. Torkelson, *Eur. Phys. J. E* **8**, 155–166 (2002).
3. Y. Koh, G. McKenna, S. L. Simon, *J. Polym. Sci. B* **44**, 3518–3527 (2006).
4. M. Efremov, E. Olson, M. Zhang, Z. Zhang, L. Allen, *Macromolecules* **37**, 4607–4616 (2004).
5. E. U. Mapesa *et al*., *Eur. Phys. J. Spec. Top.* **189**, 173–180 (2010).
6. M. Tress *et al*., *Macromolecules* **43**, 9937–9944 (2010).
7. M. Erber *et al*., *Macromolecules* **43**, 7729–7733 (2010).
8. F. Kremer, E. U. Mapesa, M. Tress, M. Reiche, in *Recent Advances in Broadband Dielectric Spectroscopy*, Y. Kalmykov, Ed. (Springer, Dordrecht, Netherlands, 2013), pp. 163–178.
9. R. B. Salazar, A. Shovsky, H. Schönherr, G. J. Vancso, *Small* **2**, 1274–1282 (2006).
10. M. Jaschke, H.-J. Butt, *Langmuir* **11**, 1061–1064 (1995).
11. C. Acikgoz, M. A. Hempenius, G. Julius Vancso, J. Huskens, *Nanotechnology* **20**, 135304 (2009).
12. J. Kumaki, Y. Nishikawa, T. Hashimoto, *J. Am. Chem. Soc.* **118**, 3321–3322 (1996).
13. J. Kumaki, T. Hashimoto, *J. Am. Chem. Soc.* **125**, 4907–4917 (2003).
14. A. Kiriy, G. Gorodyska, S. Minko, M. Stamm, C. Tsitsilianis, *Macromolecules* **36**, 8704–8711 (2003).
15. M. E. McConney, S. Singamaneni, V. V. Tsukruk, *Pol. Rev.* **50**, 235–286 (2010).
16. Y. Roiter, S. Minko, *J. Am. Chem. Soc.* **127**, 15688–15689 (2005).
17. S. Capponi, S. Napolitano, M. Wübbenhorst, *Nat. Commun.* **3**, 1233 (2012).
18. E. V. Russell, N. E. Israeloff, L. E. Walther, H. Alvarez Gomariz, *Phys. Rev. Lett.* **81**, 1461–1464 (1998).
19. A. Serghei, F. Kremer, *Rev. Sci. Instrum.* **79**, 026101 (2008).
20. F. Kremer, A. Schönhals, Eds., *Broadband Dielectric Spectroscopy* (Springer, Berlin, 2003).
21. I. Bahar, B. Erman, F. Kremer, E. Fischer, *Macromolecules* **25**, 816–825 (1992).
22. C. Iacob *et al*., *Phys. Chem. Chem. Phys.* **12**, 13798–13803 (2010).
23. S. Napolitano, M. Wübbenhorst, *Nat. Commun.* **2**, 260 (2011).
24. G. Adam, J. Gibbs, *J. Chem. Phys.* **43**, 139 (1965).

Acknowledgments: We thank the Leibniz Institute of Polymer Research Dresden (IPF), especially P. Uhlamnn and A. Lederer, for conducting GPC measurements and A. Synytska for helpful discussions. Supported by the Graduate School BuildMoNa (M.T.), a Deutsche Forschungsgemeinschaft (DFG) grant within project SPP 1369 (E.U.M.), and DFG grant SFB TRR 102. A description of the sample preparation and the volume detection of the polymer coils, as well as details on the BDS and IR measurements, can be found in the supplementary materials. F.K. initiated and guided the project; M.R. was responsible for the fabrication of the nanostructured silicon wafers; M.T. and E.U.M. tested the suitability of the silicon wafers and developed the cleaning procedure; M.T. conducted the BDS experiments and AFM measurements, and analyzed the data; W.K.K. produced and filled the silica pores; W.K. performed and analyzed the IR measurements; and M.T., F.K., and E.U.M. wrote the manuscript.

Supplementary Materials

www.sciencemag.org/content/341/6152/1371/suppl/DC1
Materials and Methods
Supplementary Text
Figs. S1 to S3
References (*25*–*37*)

9 April 2013; accepted 14 August 2013
10.1126/science.1238950

Lewis Acidity of Organofluorophosphonium Salts: Hydrodefluorination by a Saturated Acceptor

Christopher B. Caputo, Lindsay J. Hounjet, Roman Dobrovetsky, Douglas W. Stephan*

Prototypical Lewis acids, such as boranes, derive their reactivity from electronic unsaturation. Here, we report the Lewis acidity and catalytic application of electronically saturated phosphorus-centered electrophilic acceptors. Organofluorophosphonium salts of the formula $[(C_6F_5)_{3-x}Ph_xPF][B(C_6F_5)_4]$ (x = 0 or 1; Ph, phenyl) are shown to form adducts with neutral Lewis bases and to react rapidly with fluoroalkanes to produce difluorophosphoranes. In the presence of hydrosilane, the cation $[(C_6F_5)_3PF]^+$ is shown to catalyze the hydrodefluorination of fluoroalkanes, affording alkanes and fluorosilane. The mechanism demonstrates the impressive fluoride ion affinity of this highly electron-deficient phosphonium center.

Phosphorus(III) Lewis bases are widely exploited as ligands in transition metal coordination and organometallic chemistry; however, the electrophilic nature of phosphorus centers has garnered lesser attention. P(III) phosphenium cations have been explored by Gudat, Burford, and Ragogna, among others (*1*, *2*). In recent computational work, phosphenium cations have been predicted to exhibit fluorophilicities comparable to those of known neutral Lewis acids, but substantially weaker than those of electrophilic cations such as $[Me_3Si]^+$ (Me, methyl) (*3*). Although P(V) Lewis acidity has been explored less (*4*), it is noteworthy that the P(V) centers in ylide reagents account for the classic Wittig reactions with ketones (*5*). Similarly, phosphonium cations have been used to facilitate additions to polar unsaturates (*6*) and Diels-Alder reactions (*7*). In related efforts, Hudnall *et al*. have also recently exploited the acceptor capabilities of phosphonium cations, in tandem with boranes, to develop a series of fluoride ion sensors (*8*). Whereas these findings reveal the Lewis acidity of P cations, the chemistry of highly electrophilic phosphonium salts remains unexplored. Targeting such systems, we reported nucleophilic attack of a phosphine donor at an electron-deficient organofluorophosphonium salt (*9*, *10*), leading to the phosphonium-difluorophosphorane product $[Ph_3P(1,4\text{-}C_6F_4)Ph_2PF_2][O_3SCF_3]$ (Ph, phenyl) (*9*). This behavior is reminiscent of the reactivity of $B(C_6F_5)_3$ (*11*), suggesting that $[(C_6F_5)Ph_2PF]^+$ and $B(C_6F_5)_3$ have similar Lewis acidity. Nonetheless, in contrast to the electrophilic nature of borane species, which is derived from the presence of a vacant p orbital, the Lewis acidity of organofluorophosphonium cations resides in the σ* acceptor orbital oriented opposite the fluoride substituent (*12*). Further, the trigonal planar, electronically unsaturated nature of borane Lewis acids make them reactive toward most donor molecules. In contrast, phosphonium cations are electronically saturated and contain a P center that is sterically shielded by a pseudo-tetrahedral arrangement of substituents. As a consequence, most phosphonium salts are unreactive toward electron donors. Herein, the incorporation of electrophilic substituents at P is shown to afford highly Lewis acidic phosphonium centers. As a demonstration of their particularly strong fluorophilicity, these organofluorophosphonium cations are shown to directly activate C–F bonds and to effect the catalytic hydrodefluorination (HDF) of fluoroalkanes.

The electron-deficient phosphines $(C_6F_5)_2PhP$ and $(C_6F_5)_3P$ are cleanly oxidized with XeF_2 to give difluorophosphoranes $(C_6F_5)_2PhPF_2$ (**1**) and $(C_6F_5)_3PF_2$ (**2**) in quantitative yields. These species exhibit triplet resonances in their $^{31}P\{^1H\}$ nuclear magnetic resonance (NMR) spectra at chemical shifts [δ/parts per million (ppm)] –54.8 and –48.0, respectively, with a one-bond coupling constant ($^1J_{PF}$) of ~695 Hz. In contrast to the more electron-rich difluorophosphorane $(C_6F_5)Ph_2PF_2$ (*13*), neither **1** nor **2** undergoes fluoride ion abstraction by the Lewis acids $B(C_6F_5)_3$ or Me_3SiOTf (OTf, trifluoromethanesulfonate) (*9*, *10*), leading to our inference that the targeted fluorophosphonium cations should exhibit comparatively stronger Lewis acidity. Nevertheless, **1** and **2** both undergo fluoride ion abstraction by $Al(C_6F_5)_3{\cdot}C_7H_8$ (*14*) or $[Et_3Si][B(C_6F_5)_4]{\cdot}2C_7H_8$ (Et, ethyl) (*15*, *16*) to generate the corresponding fluorophosphonium salts $[(C_6F_5)_2PhPF]X$ {X = $[F(Al(C_6F_5)_3)_2]$, **3**; $[B(C_6F_5)_4]$, **4**} and $[(C_6F_5)_3PF]X$ {X = $[F(Al(C_6F_5)_3)_2]$, **5**; $[B(C_6F_5)_4]$, **6**}, respectively (Fig. 1). Products **5** and **6** were easily identified by distinctive doublet resonances in their $^{31}P\{^1H\}$ NMR spectra at δ 77.7 ($^1J_{PF}$ = 1042 Hz) and 67.8 ($^1J_{PF}$ = 1062 Hz) and in their ^{19}F NMR spectra at δ –121.9 (doublet of pentets, $^1J_{PF}$ = 1042 Hz) and –120.5 (doublet of septets, $^1J_{PF}$ = 1062 Hz), respectively. The x-ray structure of **3** (Fig. 2A) clearly reveals the tetrahedral geometry of the

Department of Chemistry, University of Toronto, 80 St. George Street, Toronto, Ontario M5S 3H6, Canada.

*Corresponding author. E-mail: dstephan@chem.utoronto.ca

fluorophosphonium cation, with its P–F bond length of 1.533(2) Å. The anion contains an approximately linear Al(1)–F–Al(2) angle of 171.84(11)°, with Al(1)–F and Al(2)–F bond lengths of 1.788(2) and 1.780(2) Å, respectively. The cation and anion pack in the solid state such that the P–F(2) bond is oriented along the Al(1)–F–Al(2) vector with an F(2)···Al(1) interatomic separation of 3.677(2) Å, well within the sum of the van der Waals radii of these nuclei (3.98 Å). This interesting feature may be suggestive of π-stacking interactions between arenes of the cation and anion and/or of a weak dative F(2)→Al(1) attraction, consistent with the well-known hypervalency of Al.

Recognizing that **5** and **6** should incorporate the most electron-deficient P centers, efforts were made to gauge their Lewis acidity. Treatment of **6** with excess *N*,*N*-dimethylformamide (DMF) in CD_2Cl_2 solution gave rise to a new high-field doublet in the $^{31}P\{^1H\}$ NMR spectrum at δ –46.7 with $^1J_{PF}$ = 705 Hz. The ^{19}F NMR spectrum of this sample shows a downfield shift of the corresponding P–F signal to δ –3.6. These data demonstrate DMF coordination to the cation of **6**, affording the salt $[(Me_2NC(O)H)(C_6F_5)_3PF][B(C_6F_5)_4]$ (**7**). Although **7** is generated in the presence of excess DMF, it was not isolable. Nonetheless, coordination of DMF demonstrates the Lewis acidity (*7*) of the phosphonium cation and stands in contrast to simple alkyl- or aryl-phosphonium species. Efforts to employ more conventional Lewis acidity tests were also undertaken. Addition of crotonaldehyde to **6** as prescribed by Childs' method (*17*) resulted in a mixture of unidentified products. In contrast, following the Gutmann protocol (*18*), the combination of **6** and Et_3PO was monitored by ^{31}P NMR spectroscopy. Adding 1 equivalent of Et_3PO to a CD_2Cl_2 solution of **6** at ambient temperature generated the adduct $[(Et_3PO)(C_6F_5)_3PF][B(C_6F_5)_4]$ (**8**) (Fig. 1), as evidenced by two new doublet-of-doublet signals in the $^{31}P\{^1H\}$ NMR spectrum at δ_P –51.3 ($^1J_{PF}$ = 674 Hz, $^2J_{PP}$ = 66 Hz) and 91.1 ($^2J_{PP}$ = 66 Hz, $^3J_{PF}$ = 7 Hz). The latter resonance was attributed to the coordinated Et_3PO unit and is shifted downfield from that of free Et_3PO (δ_P 50.7). This shift (Δ = 40.4 ppm) is considerably larger than that observed when $B(C_6F_5)_3$ and Et_3PO are combined (Δ = 26.6 ppm), suggesting that the cation of **6** is ~1.5 times more Lewis acidic than $B(C_6F_5)_3$ on the Gutmann scale. To further probe the Lewis acidic nature of **5** and **6**, the geometry of the cation was optimized at the wB97XD/def2-TZVPP level of theory (see supplementary materials). The lowest unoccupied molecular orbital (LUMO) of **5** and **6** is concentrated on the P center (Fig. 2B). The major component occupies space opposite the P–F bond and is sheltered by the arene rings. Smaller components of the LUMO reside at the ortho and para positions of these groups and at the P-bound F atom.

Another demonstration of the Lewis acidity of **6** is derived from its reaction with Ph_3CF. Combining **6** with Ph_3CF (*19*) in a 1:1 ratio in CD_2Cl_2 results in an instantaneous coloration of the reagents to produce a yellow-orange solution. The resulting ^1H NMR spectrum shows conversion of Ph_3CF to $[Ph_3C][B(C_6F_5)_4]$, whereas ^{19}F and $^{31}P\{^1H\}$ NMR spectra demonstrate the formation of **2** (see supplementary materials). Reactions of **6** with fluoroalkanes are not limited to systems that generate stable carbocations. Indeed, **6** was also shown to react immediately with 1-fluoropentane, producing **2**, as confirmed by x-ray analysis of crystals isolated from the reaction mixture (*13*). The reactive *n*-pentyl cation generated by this process gave rise to unidentifiable side products arising from its reaction with $[B(C_6F_5)_4]^-$, as has been observed previously (*20*). In a similar fashion, the addition of excess α,α,α-trifluorotoluene to solid **6** showed a more gradual conversion to **2**, along with slower degradation of the $[B(C_6F_5)_4]^-$ anion, as noted above.

The aforementioned reactivity was subsequently exploited for HDF reactions using the phosphonium salt **6** as a catalyst. Fluoroalkanes were combined with Et_3SiH in the presence of 1 mole percent (mol %) of **6** (Table 1) at room temperature. In this fashion, 1-fluoroadmantane, 1-fluoropentane, fluorocyclohexane, and α,α,α-trifluorotoluene are catalytically converted to the corresponding hydrocarbons within 3 hours, whereas 1,4-*bis*(difluoromethyl)benzene required 24 hours, as evidenced by disappearance of the C–F resonances and appearance of the Et_3SiF signal in the ^{19}F NMR spectra (see supplementary materials). In some cases, additional substituent redistribution affords small amounts of Et_2SiF_2 and Et_4Si, similar to that previously observed (*21*). Interestingly, octafluorotoluene could be converted exclusively to pentafluorotoluene ($C_6F_5CH_3$) and related products (*22*), demonstrating selective activation of the $C(sp^3)$–F groups, and retention of $C(sp^2)$–F groups. The substrates 1-bromo-3,5-*bis*(trifluoromethyl)benzene and 1,3,5-*tris*(trifluoromethyl)benzene also undergo

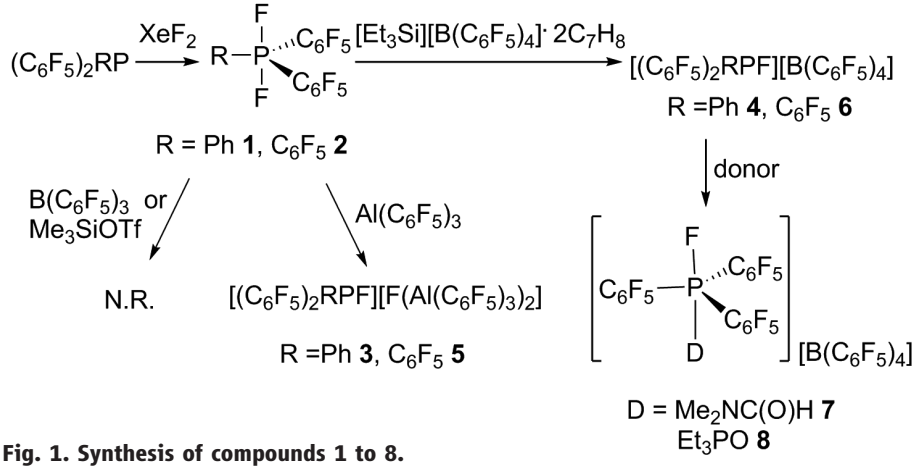

Fig. 1. Synthesis of compounds 1 to 8.

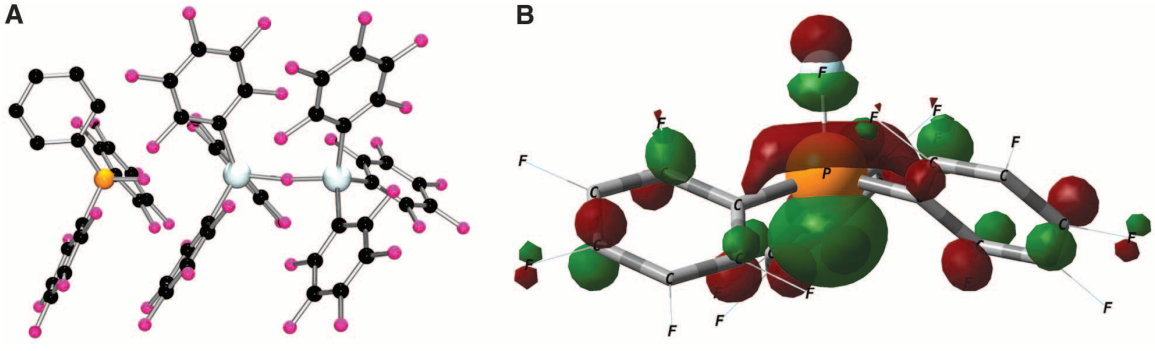

Fig. 2. Crystallography and electronic structure of fluorophosphonium salts. (**A**) Persistence of Vision Raytracer depiction of **3**. C, black; Al, blue-gray; F, pink; P, orange. All hydrogen atoms are omitted for clarity. (**B**) Graphical presentation of the LUMO of $[(C_6F_5)_3PF]^+$ calculated at the wB97XD/def2-TZVPP level of theory (surface iso-value = 0.05).

HDF in this manner, although higher catalyst loadings (5 mol %) were required, an observation that is consistent with the greater number of C–F bonds present in these substrates. Nevertheless, using 10 mol % of **6** resulted in complete defluorination of these substrates after 24 hours. Previous reports have described C–F bond cleavage and catalytic HDF of fluoroalkanes by conventional, main-group Lewis acids such as $B(C_6F_5)_3$ (*23*), silylium (*20*), carbenium (*24*), and alumenium cations (*25*), though not by phosphonium salts.

We probed the mechanism of the HDF reaction. Combining $HSiEt_3$ and **6** resulted in no reaction, even on standing for several weeks as evidenced by $^{31}P\{^1H\}$ and ^{19}F NMR spectra. This observation is contrary to a mechanism involving hydride abstraction from silane by **6**, generating silylium cation, a known HDF catalyst (*26*). In sharp contrast, reactions of fluoroalkanes with the Lewis acidic phosphonium ion **6** lead to immediate C–F bond activation to produce intermediate difluorophosphorane **2** and a carbocation. In the catalytic process, the carbocation is quenched by the hydridosilane to afford an alkane and a transient silylium ion, which abstracts fluoride from phosphorane **2** to regenerate active catalyst **6** (Fig. 3). Further support for this proposition was obtained by a direct-competition experiment. Adding 1 equivalent of $[Et_3Si][B(C_6F_5)_4]\cdot 2C_7H_8$ to a 1:1 mixture of **2** and $C_6F_5CF_3$ in C_6H_5Br led to the immediate precipitation of **6** with no spectroscopic evidence for C–F bond activation after 10 min (see supplementary materials). This observation demonstrates that the fluoride ion in **2** is more labile than the alkyl C–F bond, supporting the proposition that catalyst **6** is regenerated by fluoride ion abstraction from **2**.

Additional support for this mechanism was acquired computationally at the wB97XD/def2-TZVPP level of theory (gas phase) (*27*, *28*). We considered two conceivable reaction pathways and found hydride abstraction from Me_3SiH by $[(C_6F_5)_3PF]^+$ (+30.2 kcal·mol^{-1}) to be much more endothermic than fluoride abstraction from *t*BuF (+12.1 kcal·mol^{-1}; *t*, tert). In either case, regeneration of catalyst **6** with production of alkane and fluorosilane is substantially exothermic, with a change in enthalpy ΔH value of –44.9 kcal·mol^{-1}. These computed energies support a reaction mechanism whereby the cation of **6** catalyzes HDF by directly activating the C–F bond of the fluoroalkane (see supplementary materials).

The ability of **6** to activate strong C–F bonds (bond energy = ~490 kJ/mol) (*29*) and effect HDF catalysis results from the fluorophilicity of the organofluorophosphonium cation. Such reactivity is potentially important, as chlorofluorocarbons, hydrofluorocarbons, and perfluorocarbons (*30*) are persistent greenhouse gases. Indeed, transition metal reagents and catalysts have been developed to effect stoichiometric cleavage of C–F bonds and to bring about HDF catalysis (*31*, *32*). Metal-free strategies to HDF catalysis have also been pursued, exploiting highly Lewis acidic, electronically unsaturated species, including silicon cations (R_3Si^+), carbocations, alumenium ions (R_2Al^+), organoaluminum species, and $B(C_6F_5)_3$ (*33*). Though the silylium catalysts show greater activity (*20*), the present development of electron-deficient organofluorophosphonium salts exploits electron-withdrawing substituents to generate enhanced Lewis acidity derived from a σ* orbital of an electronically saturated species. The result-

Table 1. Catalytic hydrodefluorination of fluoroalkanes. R, alkyl; TON, turnover number.

$$R\text{-}F + Et_3SiH \xrightarrow{\mathbf{6}} R\text{-}H + Et_3SiF$$

Substrate	Cat. (mol %)*	t (h)	%Si–F†	%C–F‡	TON
Adamantyl-F	1	1	84	100	100
$C_5H_{11}F$	1	2	88	100	100
$C_6H_{11}F$	1	1	>95	100	100
$PhCF_3$	1	3	>95	>99	33
$1,4\text{-}C_6H_4(CF_2H)_2$	1	24	81	87	3.6
$C_6F_5CF_3$	1	24	71	98	4.1
$3,5\text{-}C_6H_3Br(CF_3)_2$	5	24	67	91	0.76
	10		77	>98	0.41
$1,3,5\text{-}C_6H_3(CF_3)_3$	5	24	49	69	0.58
	10		73	>99	0.41

*Relative to fluoroalkane substrate. †Calculated from the proportion of C–F bonds originally present relative to Si–F bonds formed. ‡Calculated from the proportion of C–F bonds consumed after time *t* (in hours). Conversions were determined by ^{19}F NMR spectroscopy using fluorobenzene as an internal standard.

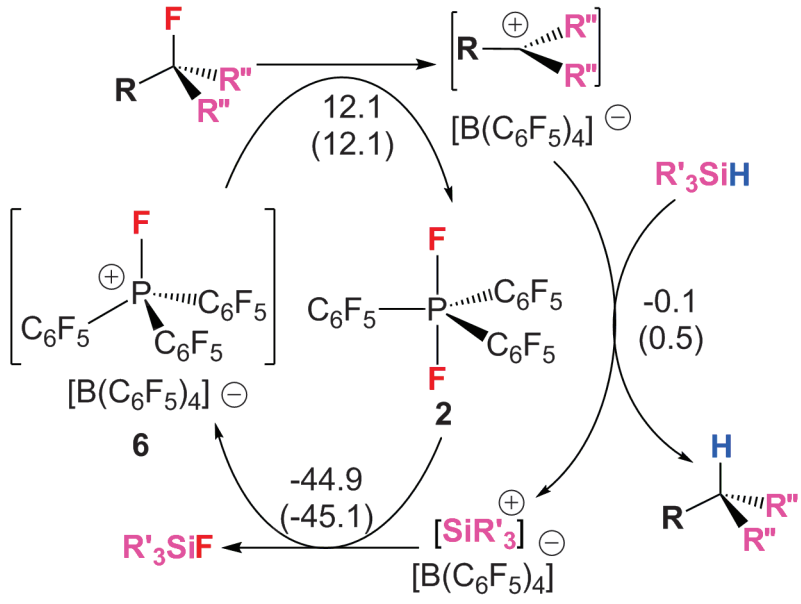

Fig. 3. Proposed reaction mechanism for phosphonium-catalyzed HDF reactions. Energies are calculated at the wB97XD/def2-TZVPP level of theory. Energy values are given in units of kilocalories per mol relative to the energy of the $[(C_6F_5)_3PF]^+$, Me_3SiH, and *t*BuF compounds; Gibbs free energies are given in parentheses.

ing electrophilic P cation coordinates donors and activates C(sp^3)–F bonds of fluoroalkanes in both stoichiometric and catalytic reactions. The mechanism for this HDF catalysis illustrates the highly fluorophilic nature of these stable and readily accessible cations.

References and Notes

1. D. Gudat, *Acc. Chem. Res.* **43**, 1307–1316 (2010).
2. N. Burford, P. J. Ragogna, *ACS Symp. Ser.* **917**, 280–292 (2005).
3. J. M. Slattery, S. Hussein, *Dalton Trans.* **41**, 1808–1815 (2012).
4. T. Werner, *Adv. Synth. Catal.* **351**, 1469–1481 (2009).
5. G. Wittig, U. Schöllkopf, *Chem. Ber.* **87**, 1318–1330 (1954).
6. O. Sereda, S. Tabassum, R. Wilhelm, *Top. Curr. Chem.* **291**, 349–393 (2010).
7. M. Terada, M. Kouchi, *Tetrahedron* **62**, 401–409 (2006).
8. T. W. Hudnall, Y. M. Kim, M. W. P. Bebbington, D. Bourissou, F. P. Gabbaï, *J. Am. Chem. Soc.* **130**, 10890–10891 (2008).
9. L. J. Hounjet, C. B. Caputo, D. W. Stephan, *Dalton Trans.* **42**, 2629–2635 (2013).
10. L. J. Hounjet, C. B. Caputo, D. W. Stephan, *Angew. Chem. Int. Ed.* **51**, 4714–4717 (2012).
11. G. C. Welch, R. R. San Juan, J. D. Masuda, D. W. Stephan, *Science* **314**, 1124–1126 (2006).
12. K. C. K. Swamy, N. S. Kumar, *Acc. Chem. Res.* **39**, 324–333 (2006).
13. G. M. Sheldrick, *Acta Crystallogr. B* **31**, 1776–1778 (1975).
14. G. S. Hair, A. H. Cowley, R. A. Jones, B. G. McBurnett, A. Voigt, *J. Am. Chem. Soc.* **121**, 4922–4923 (1999).
15. J. B. Lambert, S. Zhang, S. M. Ciro, *Organometallics* **13**, 2430–2443 (1994).
16. M. Nava, C. A. Reed, *Organometallics* **30**, 4798–4800 (2011).
17. R. F. Childs, D. L. Mulholland, A. Nixon, *Can. J. Chem.* **60**, 801–808 (1982).
18. V. Gutmann, *Coord. Chem. Rev.* **18**, 225–255 (1976).
19. F. J. Weigert, *J. Org. Chem.* **45**, 3476–3483 (1980).
20. C. Douvris, O. V. Ozerov, *Science* **321**, 1188–1190 (2008).
21. V. J. Scott, R. Celenligil-Cetin, O. V. Ozerov, *J. Am. Chem. Soc.* **127**, 2852–2853 (2005).
22. M. I. Bruce, *J. Chem. Soc. A* **1968**, 1459–1464 (1968).
23. C. B. Caputo, D. W. Stephan, *Organometallics* **31**, 27–30 (2012).
24. M. Alcarazo, C. Gomez, S. Holle, R. Goddard, *Angew. Chem. Int. Ed.* **49**, 5788–5791 (2010).
25. W. Gu, M. R. Haneline, C. Douvris, O. V. Ozerov, *J. Am. Chem. Soc.* **131**, 11203–11212 (2009).
26. C. Douvris, C. M. Nagaraja, C.-H. Chen, B. M. Foxman, O. V. Ozerov, *J. Am. Chem. Soc.* **132**, 4946–4953 (2010).
27. J.-D. Chai, M. Head-Gordon, *Phys. Chem. Chem. Phys.* **10**, 6615–6620 (2008).
28. S. Grimme, *J. Comput. Chem.* **27**, 1787–1799 (2006).
29. M. F. Kuehnel, D. Lentz, T. Braun, *Angew. Chem. Int. Ed.* **52**, 3328–3348 (2013).
30. K. P. Shine, W. T. Sturges, *Science* **315**, 1804–1805 (2007).
31. A. Nova, R. Mas-Balleste, A. Lledos, *Organometallics* **31**, 1245–1256 (2012).
32. T. Stahl, H. F. T. Klare, M. J. Oestreich, *J. Am. Chem. Soc.* **135**, 1248–1251 (2013).
33. T. Stahl, H. Klare, M. Oestreich, *ACS Catal.* **2013**, 1578–1587 (2013).

Acknowledgments: D.W.S. gratefully acknowledges the financial support of the Natural Sciences and Engineering Research Council (NSERC) of Canada and the award of a Canada Research Chair. C.B.C. is grateful for the support of an NSERC-CGS-D Scholarship. Metrical parameters for the solid-state structure of compound **3** are available free of charge from the Cambridge Crystallographic Data Centre under reference number CCDC-951501.

Supplementary Materials

www.sciencemag.org/content/341/6152/1374/suppl/DC1
Materials and Methods
Supplementary Text
Figs. S1 to S16
References

11 June 2013; accepted 9 August 2013
10.1126/science.1241764

Deep-Focus Earthquake Analogs Recorded at High Pressure and Temperature in the Laboratory

Alexandre Schubnel,[1]* Fabrice Brunet,[2] Nadège Hilairet,[3]† Julien Gasc,[3] Yanbin Wang,[3] Harry W. Green II[4]

Phase transformations of metastable olivine might trigger deep-focus earthquakes (400 to 700 kilometers) in cold subducting lithosphere. To explore the feasibility of this mechanism, we performed laboratory deformation experiments on germanium olivine (Mg_2GeO_4) under differential stress at high pressure (P = 2 to 5 gigapascals) and within a narrow temperature range (T = 1000 to 1250 kelvin). We found that fractures nucleate at the onset of the olivine-to-spinel transition. These fractures propagate dynamically (at a nonnegligible fraction of the shear wave velocity) so that intense acoustic emissions are generated. Similar to deep-focus earthquakes, these acoustic emissions arise from pure shear sources and obey the Gutenberg-Richter law without following Omori's law. Microstructural observations prove that dynamic weakening likely involves superplasticity of the nanocrystalline spinel reaction product at seismic strain rates.

The origin of deep-focus earthquakes fundamentally differs from that of shallow (<100 km) earthquakes (*1*), for which theories of rock fracture rely on the properties of coalescing cracks and friction (*2*–*4*). As pressure and temperature increase with depth, intracrystalline plasticity dominates the deformation regime so that rocks yield by creep or flow rather than by brittle fracturing (*4*). Polymorphic phase transitions in olivine have provided an attractive alternative mechanism for deep-focus earthquakes (*5*, *6*). For instance, transformation of olivine to its high-pressure polymorphs could induce faulting in polycrystalline Mg_2GeO_4 olivine (*7*, *8*). This was further confirmed on silicate olivine, $(Mg,Fe)_2SiO_4$, during the olivine-wadsleyite transition (*9*). Additional experiments demonstrated that the mechanism produced acoustic emissions (AEs) (*10*).

In total, we performed eight experiments on both powdered and sintered Ge-olivine samples in the stability field of the spinel polymorph, at confining pressures from 2 to 5 GPa and temperatures between 973 and 1573 K (fig. S2). Sintered samples consisted of fully densified "rocks" of isostatically hot pressed polycrystalline Mg_2GeO_4 (Ge-olivine) containing minor amounts of Ge-pyroxene (<5 vol %) (*11*). We used the germanate analog of Mg_2SiO_4 olivine because transformation into its denser polymorph can be reached at pressures routinely achievable in the deformation apparatus. Stress, transformation progress, and strain were measured in situ by using x-ray powder diffraction (XRD) and radiographic imaging, respectively. AEs were recorded continuously on six channels. Description of the set-up is given in the supplementary materials (fig. S1) (*12*).

Differential stress, strain, and acoustic activity for sample D1247 evolved as a function of time (Fig. 1). The sample was first pressurized to 4 GPa at room temperature then deformed at a constant temperature of 973 K with a strain rate

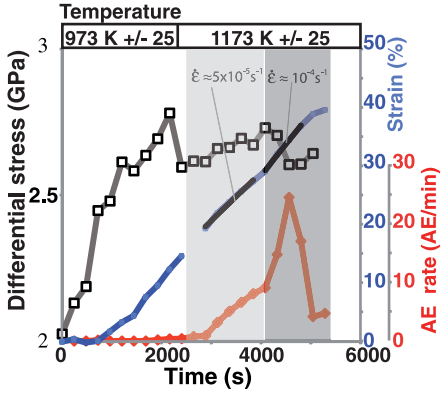

Fig. 1. Stress, strain and acoustic emission. Evolution of temperature, differential stress, strain, and AE rate during experiment D1247 performed at 4 GPa effective mean stress.

[1]Laboratoire de Géologie, CNRS UMR 8538, Ecole Normale Supérieure, 75005 Paris, France. [2]Institut des Sciences de la Terre, CNRS, Université de Grenoble 1, 73370 Grenoble, France. [3]GeoSoilEnviroCARS, University of Chicago, Argonne, IL 60439, USA. [4]Department of Earth Sciences, University of California at Riverside, CA 92507, USA.

*Corresponding author. E-mail: aschubnel@geologie.ens.fr
†Present address: Unité Matériaux et Transformations, CNRS UMR 8207, Université Lille 1, 59655 Villeneuve d'Ascq, France.

of $5 \pm 1 \times 10^{-5}$ s^{-1}. Differential stress built up to 2.75 GPa [discussion of uncertainties of stress measurement in synchrotron experiments can be found in (*12*, *13*)] at 10% strain, followed by temperature ramping to 1173 K, which induced some softening. No spinel was detected in XRD patterns, and no AE was observed up to this point. Beyond 20% strain, however, AEs were triggered; their release rate peaked at time (t) ~ 4200 s, coinciding with an abrupt increase in strain rate, to $1 \pm 0.1 \times 10^{-4}$ s^{-1}, a stress drop of ≈100 MPa and a large burst of intense AEs. The sources of these AEs were located inside the sample (fig. S3) (*12*). XRD data collected toward the end of the experiment revealed the presence of a small amount (<5%) of spinel.

Complete AE waveform catalogs were built for two experiments (D1247 and D1253), at 4 and 5 GPa confining pressure, respectively. In total, more than 500 AEs were recorded. Waveforms, amplitude, and length of the AEs varied considerably (Fig. 2A), lasting from 10 μs to 4 ms. Generally, the recorded acoustic signals are a combination of the source, resonance of the sensors, and that of mechanical set-up, so that the duration of the AEs is not directly representative of that of the source but scales with the AE amplitude. Here, the longest AE events displayed amplitudes exceeding the voltage saturation limit of our recording system (5 V). These amplitudes are larger than those observed during cold compression of quartz at high pressure (*14*) and are comparable with those observed during brittle failure of centimeter-sized samples of pure glass (*15*). The frequency of relative moment magnitudes (M_{AE}) for two AE catalogs follows a power law distribution (Fig. 2B), generally referred to as the Gutenberg-Richter (GR) law, that is systematically observed both in the field (*1*, *16*) and in the laboratory (*17*). In consequence, there was a range of source sizes in our experiments—the upper limit being the length of the sample (3 mm)—which opens the possibility that the phenomenon could be scaled to much larger dimensions. Here, the power law exponent (or b-value) is on the order of 0.5 to 0.6—lower than 1, as often observed in the case of deep-focus earthquakes (*1*). The absence of long and sustained "aftershock" sequences (Omori-type sequence) after large AEs in our experiments also seems to correspond to a peculiarity of deep-focus earthquakes; for instance, the largest deep earthquake ever recorded [moment magnitude (M_w) 8.3 Sea of Okhotsk earthquake on 24 May 2013, 610 km depth] was followed by only a few aftershocks until now in the immediate vicinity of the rupture plane.

With six recording sensor "stations" and using first-motion relative amplitudes (fig. S3), we performed moment tensor inversions (*12*) for 44 events with $1 < M_{AE} < 2$ (Fig. 3). Like deep-focus earthquakes, which invariably show the absence of volumetric component associated with the earthquake source (*1*), all 44 events exhibit a negligible isotropic component; no volumetric strain is associated with the source. AEs are more than 95% in shear ($k < 0.05$), some showing positive or negative compensated linear vector dipole (CLVD) component, which might be due to geometric complexities during source propagation (fig. S4). Some deep-focus earthquakes have also been reported as being up to 50% CLVD (*1*).

Sample D1253 is crosscut by a set of conjugate macroscopic faults (Fig. 4A) and displays

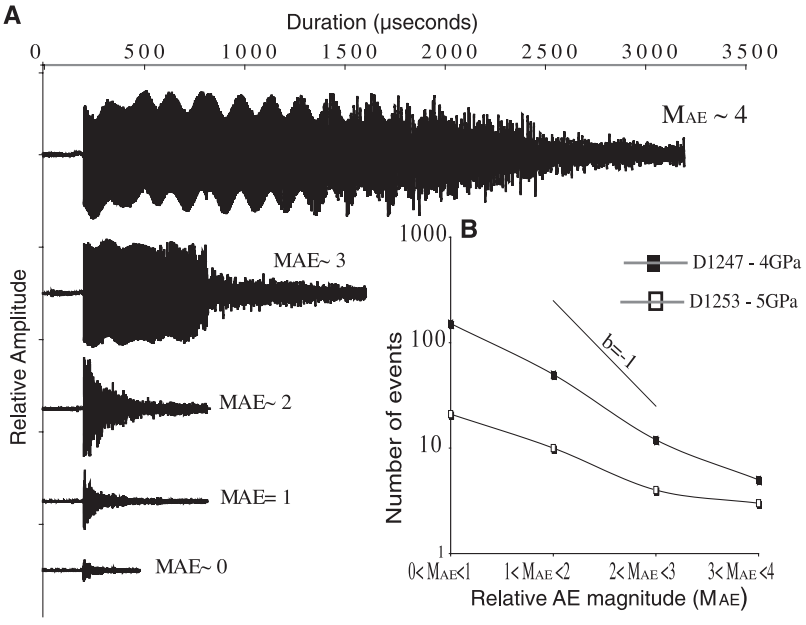

Fig. 2. AE magnitude catalog and GR distribution. (**A**) Amplitude and duration of 5 AEs of relative magnitude equal to ≈0, ≈1, ≈2, ≈3 and ≈4, respectively, from bottom to top. The reference event M_{AE} = 1 is shown. (**B**) Statistical distribution of the relative magnitudes within four magnitude bins ($0 < M_{AE} < 1$, $1 < M_{AE} < 2$, $2 < M_{AE} < 3$, and $3 < M_{AE} < 4$) and for experiments D1247 (4 GPa) and D1253 (5 GPa). The moment magnitude completeness of each catalog is $M_{AE} > 0$. A slope of 1 for the b value is displayed for reference.

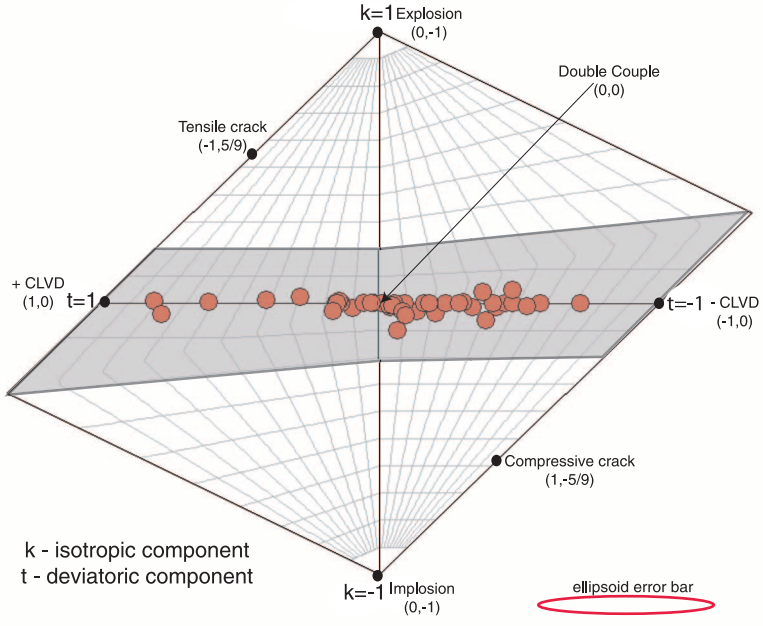

Fig. 3. AE moment tensor inversion. Moment tensor inversions displayed within a T-K plot ($1 < M_{AE} < 2$). The variables t and k represent the decomposition of the moment into a deviatoric (shear) and an isotropic (volumetric) component, respectively (*12*, *30*). The ellipsoid of error indicates that the uncertainty on the ratio between isotropic and deviatoric components is low.

typical barreling of the sides, as expected for a specimen deformed within the ductile regime. A close-up view of the fracture (Fig. 4B) reveals a pyroxene grain intensely sheared during fracture propagation. Using the grain as a marker, the total displacement across the fault is ≈30 μm. Transmission electron microscopy (TEM) examination of a focused ion beam foil (Fig. 4C) demonstrates that the fault is ~100 nm thick (Fig. 4D). The fault "gouge" consists of nanocrystalline spinel (Fig. 4E), the largest crystals measuring only 20 to 40 nm. No amorphous material was observed. On both sides of the fracture, high dislocation density indicates intense deformation. Selected area electron diffraction patterns collected on both sides of the fault plane demonstrated that the fracture walls consist of several large olivine grains, indicating that the fault has cut through multiple grains. These microstructural observations confirm our AE moment tensor inversion. Indeed, the faults being so narrow, the volumetric contraction induced by the solid-phase transformation ($\Delta V \approx 7\%$) is negligible when compared with the shear across the fault. In such a way, AEs in our experiment have shear sources, yet their propagation does involve a—negligible—volumetric contraction.

For a rupture to radiate acoustic waves during propagation, it must travel at a velocity that is a nonnegligible fraction (>10%) of the shear wave velocity *cs*, which for Ge-olivine in these conditions is ~5 km/s. Assuming a rupture propagation velocity of 0.2 *cs* only (*18*) and considering the millimeter size of our specimens, the source duration of the largest AEs must be on the order of a few microseconds only. The offsets of the largest fault observed within the specimen being of ~10 μm, and assuming only 10% of that slip as "coseismic," the minimum bound for the sliding velocity is on the order of ~1 m/s (for a crack-like rupture), which is comparable with slip velocities typically inferred during earthquakes (*19*). Considering that the fault extends over ~1 mm, the stress drop $\Delta\sigma = C\mu D/L$ [where μ is the shear modulus (~100 GPa), C is a geometric constant on the order of 1, D is the coseismic slip, and L is the fault length] (*20*) inferred on this large fault is on the order of 100 MPa. This is consistent with the stress drop observed in our stress-strain record. It corresponds to maximum values inferred by seismologic studies of deep (*18*, *20*) and intermediate (*21*) earthquakes up to date. A large number of smaller faults could be observed (fig. S4) for which the ratio of slip versus fault length may indicate smaller stress drops. If some of these complex systems of parallel and conjugate faults were propagating contemporaneously—meaning that if the source consisted of not a singular fault plane but several segments propagating together—these could possibly be at the origin of the large CLVD components observed.

No evidence of melting or amorphous material (*19*) was found at any scale, implying that the phase transformation must have been essentially instantaneous during fault propagation. Because of high normal stress, this observation not only implies that little frictional heating occurred (dynamic friction coefficient of ≈0.1 at most) (supplementary text) but also that dynamic weakening occurred during fracture propagation in the absence of fluids or melt.

In these experiments, AEs were observed only after a certain level of axial strain (10 to 20%). High dislocation density within Ge-olivine grains promotes spinel nucleation at dislocation pile-ups or tangles. Stress concentrations due to volumetric contraction are likely also playing an important role (*6*), as well as reaction-driven latent heat release. Our observations suggest that instabilities are triggered when nucleation is the dominant control mechanism (relatively cold conditions and large pressure overstepping) so that the grain size of the (spinel) reaction product is on the nanometer scale (Fig. 4D). Superplastic flow is commonly observed in ultrafine-grained materials (*22*), and a crude extrapolation of superplastic flow laws in olivine (*23*) shows that under these conditions (high stresses and extremely fine grains), grain boundary sliding can accommodate strain rates as high as 10^3 to 10^4 s^{-1} (supplementary text). These are compatible with seismic strain rates, implying that the dynamic weakening mechanism is superplastic flow. The paradox between the observation of extreme dynamic weakening and partial stress drops, also true in brittle materials (*24*), implies extremely fast fault strength recovery. Superplastic flow may only be active at the rupture tip and within the breakdown zone, where the stress concentrations are high enough. Last, the paucity of aftershocks may be explained by the fact that rupture nucleation and propagation are intrinsically linked to the phase transformation, which is irreversible.

In all eight experiments, the temperature range (fig. S2A) at which we observed AEs was narrow (1000 to 1250 K) over a wide range of confining pressure conditions (2 to 5 GPa), which extends former experimental observations (*7*, *8*) to higher pressures, suggesting that transformational faulting is controlled by spinel nucleation kinetics and therefore by absolute temperature rather than homologous temperature (ratio of absolute temperature to melting temperature). The direct implication is that deep-focus seismicity depth range and rate should, at least in part, correlate with

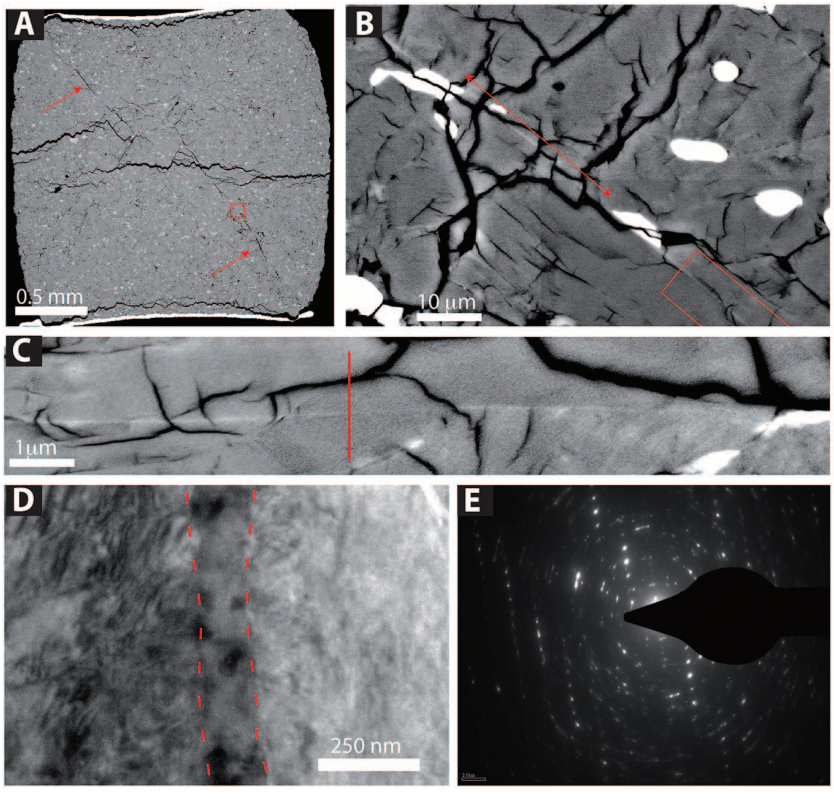

Fig. 4. Microstructure of the transformed fault zone. Electron micrographs of sample D1253, which failed at 5 GPa. (**A**) Full view of the sample (σ_1 is vertical). Horizontal fractures are likely to have been caused during decompression. The red box corresponds to the location of (B). (**B**) High-magnification view of one of the fracture planes. The white grains are Ge-enstatite ($MgGeO_3$), and the gray grains are Ge-olivine, the grain size of which are <10 and 150 μm, respectively. The red box corresponds to the location of (C). (**C**) A narrow band of light gray material highlights the fault. The red line indicates the location of the FIB section (D). (**D**) Close-up TEM view of the fault zone. Dashed lines highlight the main fault, only 100 nm thick. The gouge consists of fully crystalline nanometric material. The fracture walls are intensely deformed. (**E**) Electron diffraction patterns of the gouge and adjacent wall rock display bright olivine spots and numerous spinel spots emanating from the gouge itself.

the subducted lithosphere temperature, and thus its age.

Although in our experiments the absolute stress value remains high (fig. S2B) compared with stresses expected within the cold core of subducted slabs (*25*), the observed stress drops are broadly consistent with those calculated for deep earthquakes (*1*, *18*, *20*, *21*). Constant differential stress conditions at failure over a wide range of confinement (2 to 5 GPa) strongly suggest that transformational faulting is largely independent of normal stress and thus involves nonfrictional processes. We suggest that rupture nucleation is controlled by dislocation density and spinel nucleation kinetics, whereas propagation is controlled by superplastic flow. High-stress and high–dislocation density conditions can be met in a cold subducting slab full of metastable olivine (*26*–*28*) owing to stress concentrations at the micro- and mesoscopic scales because of buckling, folding, and/or inherited fractures (*29*). This is particularly true in the Tonga-Kermadec region, for instance (*28*, *29*), for which the largest catalog of deep-focus earthquakes is available (*1*).

References and Notes

1. C. Frohlich, *Deep Earthquakes* (Cambridge Univ. Press, Cambridge, 2006).
2. J. D. Byerlee, *Pure Appl. Geophys.* **116**, 586–602 (1978).
3. C. Marone, *Annu. Rev. Earth Planet. Sci.* **26**, 643–696 (1998).
4. M. S. Paterson, T.-f. Wong, *Experimental Rock Deformation—The Brittle Field*. (Springer–Verlag, Berlin, Heidelberg, 2005).
5. D. T. Griggs, D. W. Baker, *The Origin of Deep-Focus Earthquakes*, H. Mark, S. Fernbach, Eds. (Interscience, New York, 1969), pp. 23–42.
6. S. Kirby, *J. Geophys. Res.* **92**, 13789–13800 (1987).
7. H. W. Green II, P. C. Burnley, *Nature* **341**, 733–737 (1989).
8. P. C. Burnley, H. W. Green II, D. Prior, *J. Geophys. Res.* **96**, (B1), 425–443 (1991).
9. H. W. Green II, T. E. Young, D. Walker, C. H. Scholz, *Nature* **348**, 720–722 (1990).
10. H. W. Green II, C. H. Scholz, T. N. Tingle, T. E. Young, T. A. Koczinski, *Geophys. Res. Lett.* **19**, 789–792 (1992).
11. E. M. Riggs, H. W. Green II, *J. Geophys. Res.* **110**, B03202 (2005).
12. Materials and methods are available as supplementary materials on *Science* Online.
13. N. Hilairet, Y. Wang, T. Sanegira, S. Merckel, S. Mei, *J. Geophys. Res.* **117**, B01203 (2012).
14. J. Gasc *et al.*, *Phys. Earth Planet. Inter.* **189**, 121–133 (2011).
15. A. Ougier-Simonin, J. Fortin, A. Schubnel, Y. Guéguen, F. Bouyer, *Int. J. Eng. Sci.* **49**, 105–121 (2011).
16. B. Gutenberg, C. F. Richter, *Nature* **176**, 795–795 (1955).
17. C. H. Scholz, *Bull. Seismol. Soc. Am.* **58**, 399–415 (1968).
18. H. Kanamori, D. L. Anderson, T. H. Heaton, *Science* **279**, 839–842 (1998).
19. G. Di Toro *et al.*, *Nature* **471**, 494–498 (2011).
20. M. Antolik, D. Dreger, B. Romanowicz, *J. Geophys. Res.* **104**, 863–894 (1999).
21. G. A. Prieto, G. C. Beroza, S. A. Barett, G. A. López, M. Florez, *Tectonophysics* **570–571**, 42–56 (2012).
22. A. M. Boullier, Y. Guéguen, *Contrib. Mineral. Petrol.* **50**, 93–104 (1975).
23. T. Hiraga, T. Miyazaki, M. Tasaka, H. Yoshida, *Nature* **468**, 1091–1094 (2010).
24. F. X. Passelègue, A. Schubnel, S. Nielsen, H. S. Bhat, R. Madariaga, *Science* **340**, 1208–1211 (2013).
25. C. R. Bina, S. Stein, F. C. Marton, E. M. Van Ark, *Phys. Earth Planet. Inter.* **127**, 51–66 (2001).
26. T. Iidaka, D. Suetsugu, *Nature* **356**, 593–595 (1992).
27. H. Kawakatsu, S. Yoshioka, *Earth Planet. Sci. Lett.* **303**, 1–10 (2011).
28. D. A. Wiens, J. J. McGuire, P. J. Shore, *Nature* **364**, 790–793 (1993).
29. R. Myhill, *Geophys. J. Int.* **192**, 837–853 (2012).
30. J. A. Hudson, R. G. Pearce, R. M. Rogers, *J. Geophys. Res.* **94**, 765–774 (1989).

Acknowledgments: We thank A. Addad, D. Deldicque, I. Estève, E. Larue, and Y. Pinquier for technical support and three reviewers for their constructive remarks, which helped to improve this work. This work was funded through Institut National des Sciences de l'Univers (project "Deep Quakes") and L'Agence Nationale de la Recherche (project "DELF"). GeoSoilEnviroCARS is supported by the National Science Foundation–Earth Sciences (EAR-1128799) and U.S. Department of Energy–Geosciences (DE-FG02-94ER14466). Use of the Advanced Proton Source was supported by the U.S. Department of Energy, Office of Science, Office of Basic Energy Sciences, under contract DE-AC02-06CH11357. Part of the AE technical development was made possible by the National Science Foundation grant EAR-0968456 (Y.W.). Data are available in the supplementary materials.

Supplementary Materials

www.sciencemag.org/content/341/6152/1377/suppl/DC1
Materials and Methods
Supplementary Text
Figs. S1 to S4
Data Files S1 and S2
References (*31*–*50*)
Movies S1 and S2

7 May 2013; accepted 9 August 2013
10.1126/science.1240206

Energy Release of the 2013 M_w 8.3 Sea of Okhotsk Earthquake and Deep Slab Stress Heterogeneity

Lingling Ye,[1] Thorne Lay,[1]* Hiroo Kanamori,[2] Keith D. Koper[3]

Earth's deepest earthquakes occur in subducting oceanic lithosphere, where temperatures are lower than in ambient mantle. On 24 May 2013, a magnitude 8.3 earthquake ruptured a 180-kilometer-long fault within the subducting Pacific plate about 609 kilometers below the Sea of Okhotsk. Global seismic *P* wave recordings indicate a radiated seismic energy of ~1.5×10^{17} joules. A rupture velocity of ~4.0 to 4.5 kilometers/second is determined by back-projection of short-period *P* waves, and the fault width is constrained to give static stress drop estimates (~12 to 15 megapascals) compatible with theoretical radiation efficiency for crack models. A nearby aftershock had a stress drop one to two orders of magnitude higher, indicating large stress heterogeneity in the deep slab, and plausibly within the rupture process of the great event.

The occurrence of earthquakes in the depth range from 400 to 720 km (the mantle transition zone) has long been enigmatic, given the immense pressure exerted by the overlying rock mass on any fault surface. Seismic radiation from deep earthquakes indicates that they likely involve shear faulting basically indistinguishable from shallow earthquakes despite the extreme pressure conditions. Deep earthquakes only initiate in relatively low-temperature regions of subducted oceanic lithosphere. Very high deviatoric stresses may be present in the core of the subducted slab, and some mechanism must exist to offset the inhibiting effects of pressure to allow shear faulting to initiate (*1*). For the depth range from 50 to 400 km, it is generally believed that release of water by mineral dehydration reactions or production of other fluid phases reduces the effective normal stress on surfaces and enables fluid-assisted frictional sliding. It is not clear whether such mechanisms can account for transition-zone earthquakes, the largest of which tend to occur below a 600-km depth. Much research has focused on processes such as abrupt phase transitions (*2*) that may be able to nucleate rupture under tremendous confining stress. Once deep fault slip initiates and becomes substantial, frictional heating can lead to melting of the fault surface, abetting runaway rupture expansion for large deep earthquakes (*3*).

On 24 May 2013 the largest deep earthquake yet recorded occurred near a depth of 609 km [05:44:49 UTC, 54.874°N, 153.281°E (*4*)] in the Pacific plate subducting along the Kuril-Kamchatka subduction zone (Fig. 1). The event locates under the Sea of Okhotsk. Globally recorded long-period seismic waves indicate that the overall earthquake process appears to involve shear faulting with a seismic moment of ~4.1×10^{21} N·m [moment magnitude (M_w) = 8.3] (*4*, *5*). The event is slightly larger than the 637-km-deep Bolivia earthquake of 9 June 1994 that had a seismic moment of ~3×10^{21} N·m (M_w = 8.3) (*6*, *7*).

Both great events have similar faulting geometries with very shallow-dipping normal fault mechanisms and only minor deviations from shear double-couple solutions. The 1994 Bolivia

[1]Department of Earth and Planetary Sciences, University of California Santa Cruz, Santa Cruz, CA 95064, USA. [2]Seismological Laboratory, California Institute of Technology, Pasadena, CA 91125, USA. [3]Department of Geology and Geophysics, University of Utah, Salt Lake City, UT 84112, USA.

*Corresponding author. E-mail: tlay@ucsc.edu

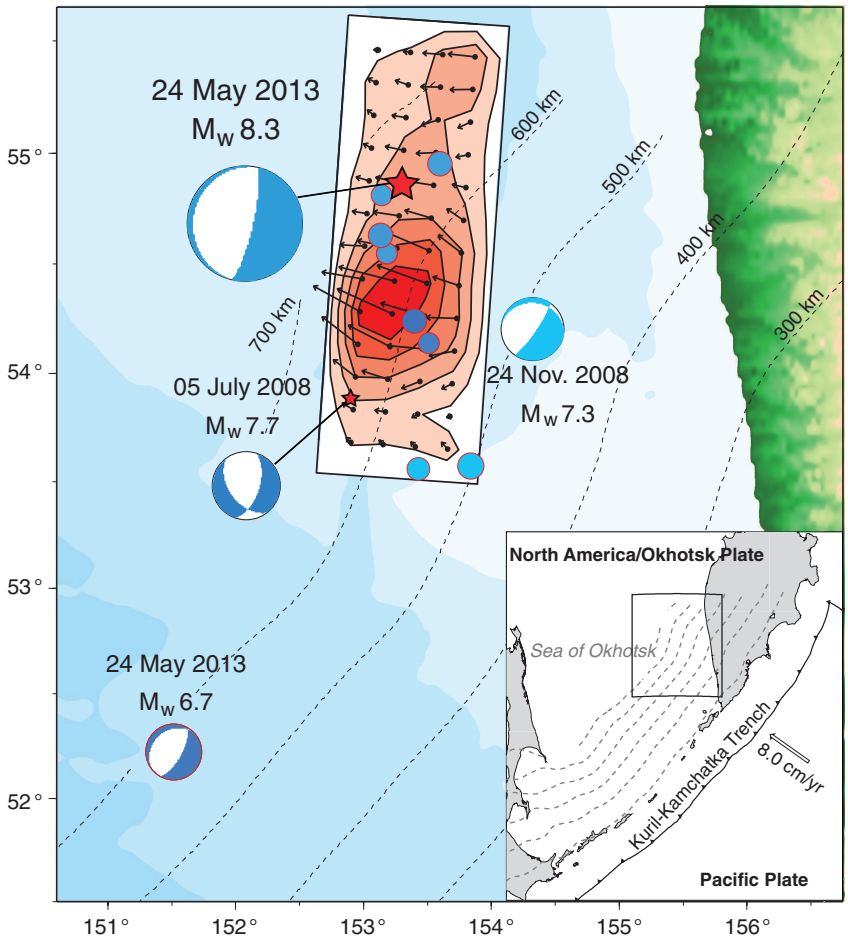

Fig. 1. Tectonic setting of the 2013 M_w 8.3 deep Sea of Okhotsk slab earthquake. (**Inset**) The plate configuration, with the Pacific plate underthrusting the North American/Sea of Okhotsk plate along the Kuril-Kamchatka subduction zone at a convergence velocity of ~8.0 cm/year. Dashed lines are depth contours for the subducted oceanic slab beneath the Sea of Okhotsk. The main map shows best-double couple faulting mechanisms from global centroid-moment tensor inversions for recent large earthquakes in the deep slab, with blue indicating events below 600 km depth and cyan indicating events around 500 km deep. Focal mechanisms are at the event epicenter unless offset with a tie line. Small circles are locations of aftershocks of the 24 May 2013 event with magnitudes from 4.1 to 4.4. The contoured plot indicates the slip distribution of the preferred rupture model for the mainshock, with the large red star being the hypocenter at a depth of 608.9 km. The arrows indicate the magnitude and the direction of slip of the upper side of the fault, with the fault dipping 10° toward the west. The peak slip is 9.9 m, and the colors indicate about 2.2-m slip contour increments.

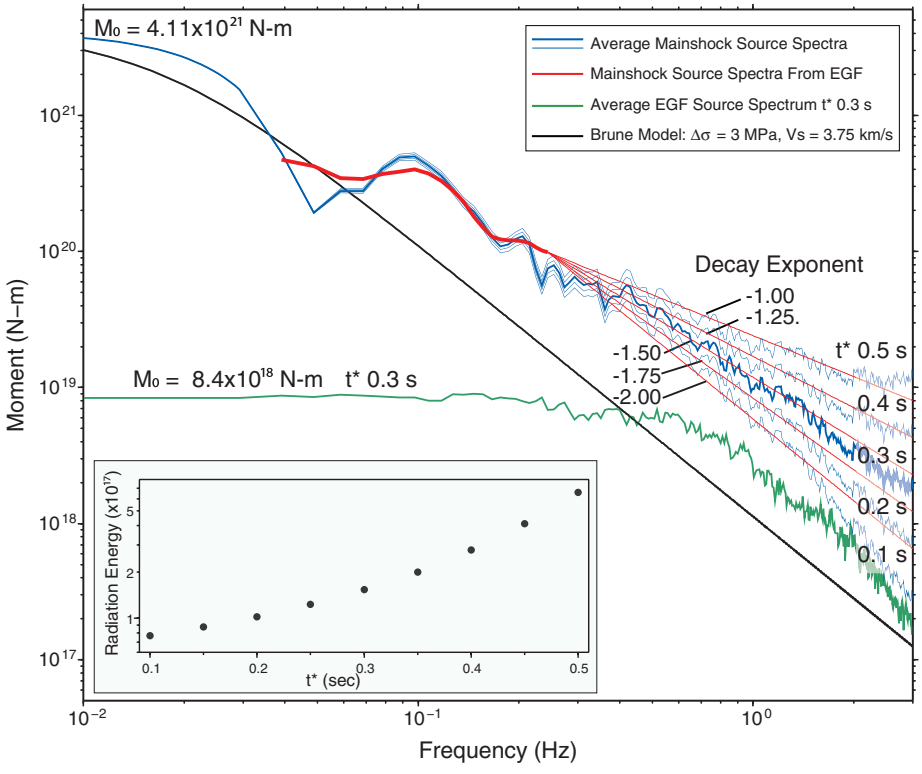

Fig. 2. Source spectra estimates for the 2013 M_w 8.3 Sea of Okhotsk mainshock and M_w 6.7 aftershock. The mainshock spectrum is estimated by two methods. The blue curves are estimates based on the spectrum of the source time function from finite-fault inversion for frequencies less than 0.05 Hz and from averaging many teleseismic *P* wave spectra with propagation and radiation pattern corrections from 0.05 to 3.0 Hz. Results are shown for different attenuation parameters of t^* = 0.1 to 0.5 s. The red curve is an estimate of the mainshock source spectrum from 284 spectral ratios of the mainshock and the aftershock (EGF) spectra at the same station for the frequency band 0.03 to 0.25 Hz. The extrapolated spectra to 3 Hz assume source spectrum decay exponents from −1.0 to −2.0. The green curve is the average source spectrum for the M_w 6.7 event based on the first method, using an assumed t^* = 0.3 s. (**Inset**) The dependence of estimates of E_R on the assumed value of t^* for the mainshock signals, given by averaging energy estimates from individual path-corrected *P* wave spectra.

earthquake was interpreted as having a relatively slow rupture velocity, V_r ~ 1 to 2 km/s, with an ~40-s rupture duration and a spatially compact rupture zone with a scale of about 40 km by 60 km (*6*–*11*), leading to large stress drop estimates of around 110 to 150 MPa (*7*, *11*).

In the first 4 days after the 2013 earthquake, nine aftershocks were detected, eight having small magnitudes of 4.1 to 4.4 at depths from 487 to 627 km, and an M_w = 6.7 event struck 9 hours after the mainshock [14:56:31, 52.222°N, 151.515°E, 623 km deep (*4*)] about 200 km to the southwest (Fig. 1). Six nearby aftershocks with depths of around 600 km define a north-south trend about 90 km long, preferentially extending southward from the mainshock hypocenter. The trend is generally compatible with rupture along either of the two nodal planes of the mainshock focal mechanism but slightly favors the shallow plane. Aftershock occurrence for large deep earthquakes is highly variable (*12*), and the large depth range for the 2013 aftershocks suggests that some are triggered away from the mainshock rupture zone. The 2013 event was preceded by nearby large earthquakes in 2008 (M_w = 7.3 and 7.7, Fig. 1), the larger of which was ~100 km along strike to the south.

Two of the most fundamental seismological properties of a large earthquake are the source spectrum and the radiated seismic energy. We analyzed extensive global seismic recordings of *P* waves for the 2013 event to estimate both. Source spectrum estimates obtained from two distinct approaches provide estimates of the radiated seismic energy (Fig. 2). The radiated energy estimates depend on attenuation corrections. The attenuation corrections are parameterized by t^*, the ratio of total *P* wave travel time to average attenuation quality factor, $Q(f)$, along each path as a function of frequency, f. The precise $Q(f)$ on each path is not known in detail and is expected to vary strongly because of upper mantle heterogeneity in attenuation structure beneath the seismic stations. For deep focus earthquakes, the t^* values are expected to be on average ~0.5 s at 0.1 Hz for teleseismic *P* waves (half of the t^* value for a shallow source) and about 0.25 to 0.5 s at 1.0 Hz, with t^* likely decreasing as frequency increases above 1.0 Hz. Lacking knowledge of specific path or even best average attenuation parameters, we show spectral estimates for a range of constant t^* values from 0.1 to 0.5 s, with a value of 0.3 s deemed to be a reasonable value. The uncertainty in t^* affects the high-frequency spectral levels, which are very important for radiated seismic energy estimates. We averaged the energy values obtained from 102 stations by integrating the energy spectrum from the *P*-wave ground-motion velocities (*13*–*16*) after correcting for faulting geometry and propagation effects. Use of t^* = 0.3 s for each station and frequencies up to 3 Hz gives radiated energy of $E_R = 1.5 \times 10^{17}$ J, with a range of reasonable estimates being given by results for t^* = 0.2 s ($E_R = 1.0 \times 10^{17}$ J) to 0.4 s ($E_R = 2.8 \times 10^{17}$ J). For t^* = 0.3 s, the moment-scaled energy is $E_R/M_0 = 3.7 \times 10^{-5}$.

To confirm the source spectrum estimate, we used *P*-wave observations of the nearby M_w 6.7 aftershock at the same stations as for the mainshock to explicitly cancel out the unknown path effects. The large aftershock is remarkably short duration, with impulsive *P* wave motions that have average pulse widths of about 1.8 s. The average source spectrum for the aftershock found assuming t^* = 0.3 s for 22 stations has a very flat spectrum up to ~0.5 Hz (Fig. 2), indicating that this event can serve as an impulse response, or empirical Green's function (EGF), up to near that frequency. For t^* = 0.3 s, E_R is 2.36×10^{15} J for the EGF from log averaging of the 22 individual station energies, and E_R/M_0 is 2.8×10^{-4} using our finite-fault inversion estimates of the seismic moment $M_0 = 8.4 \times 10^{18}$ N·m.

We computed mainshock/EGF spectral ratios for 284 broadband *P*-wave observations (fig. S1), correcting for differences in radiation pattern, geometric spreading, and multiplying by the EGF M_0. The ratios are in close agreement with the averages of mainshock *P* spectra over the corresponding passband (Fig. 2). This ensures that uncertainties in t^* do not bias the average spectrum estimate in this passband.

Extrapolations of the spectral ratios from 0.25 to 3.0 Hz are made for various assumed mainshock spectral decay slopes with frequency exponents varying from –1 to –2. For reference, a shallow interplate earthquake source spectrum for a moment equal to that of the mainshock has a decay exponent of –2, a stress parameter of 3 MPa, and source velocity of 3.75 km/s. The deep earthquake spectral amplitudes are enriched in high frequency relative to the reference model, in part because of higher source velocity and in part because of higher stress drop. The precise spectral decay slope expected near 1 Hz is not known, because it depends on the detailed space-time history of slip on the fault, but values around –1.5 to –2 are consistent with assuming t^* values around 0.3 s. We conclude that $E_R \sim 1.5 \times 10^{17}$ J, with about a factor of 2 uncertainty. This is about three times as large as for the 1994 Bolivia event [$E_R \sim 5.2 \times 10^{16}$ J (*3*, *17*)].

The spatial extent of the 2013 Sea of Okhotsk deep earthquake faulting is critical for estimating additional properties of the source, such as slip pattern and static stress drop. Back-projection of teleseismic short-period *P* waves was used to estimate V_r and the source rupture dimensions (Fig. 3). The data are from large continental seismic networks in Europe and North America that recorded coherent broadband waveforms (fig. S4). For both array geometries, the back-projections indicate asymmetric bilateral extent of short-period radiation extending 50 to 60 km to the north of the hypocenter and about 120 km to the south, along the trend of the deep after-

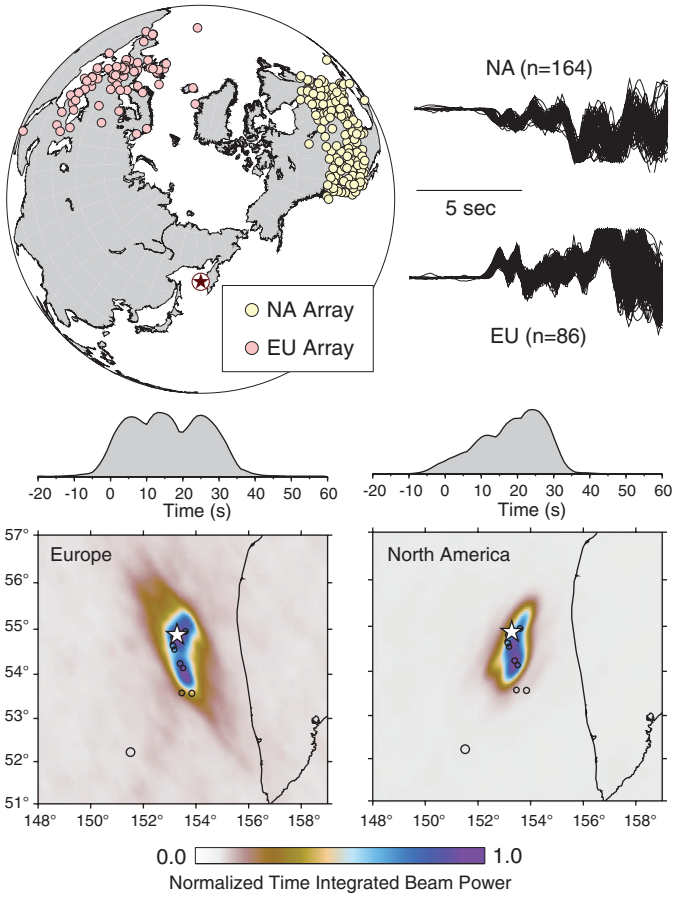

Fig. 3. Constraints on rupture velocity from *P* wave back-projection. Teleseismic *P* waves in the frequency band from 0.5 to 2.0 Hz from large networks of stations in North America (NA) and Europe (EU) were used to image the space-time history of coherent high-frequency seismic radiation from the 2013 M_w 8.3 Sea of Okhotsk earthquake. The time-integrated power stacked on a grid around the source are shown here relative to the mainshock epicenter (white stars). The darker blue colors indicate coherent energy release with an asymmetric spread of source radiation in the north-south direction being resolved by the images from both networks. movie S1 shows the time-varying images throughout the rupture process.

shocks, with a source time duration of about 30 s. Animations of the back-projections show the space time evolution of the short-period radiation (movie S1).

If we adopt the V_r estimate of 4.0 km/s obtained from the back-projections as a constraint on the finite-fault inversions, we find rupture models with average slip of 1.9 to 2.3 m and an average static stress drop of 4 to 5 MPa for rupture areas that have a radius of about 74 to 82 km (figs. S2 and S3) for the two fault plane choices. For these estimates, only subfaults with moment at least 15% of the peak subfault moment were retained to diminish sensitivity to poorly resolved low-slip areas of the model (*18*).

A problem with these solutions is that they can give large (>1) estimates of calculated radiation efficiency, η_R, which is the ratio of E_R to the available potential energy, ΔW_0:

$$\eta_R = E_R/\Delta W_0 = 2\mu E_R/(\Delta\sigma_s M_0)$$

where $\Delta\sigma_s$ is the static stress drop and μ is the rigidity.

Radiation efficiency has been calculated as a function of V_r for mode II, mode III, and energy-based (mode E) crack models (Fig. 4) (*19*–*23*). For higher V_r, there is less energy dissipation near the crack tip, so the radiation efficiency approaches 1 as V_r approaches the limiting speed (the Rayleigh velocity for mode II and the shear velocity for mode III and mode E). For the 2013 Sea of Okhotsk event, $V_r < 2.5$ km/s is required for the circularly expanding rupture models to have large enough calculated stress drop to lower the seismic efficiency to intersect the predictions of crack theory (Fig. 4). Such a low V_r cannot account for the faulting dimensions indicated by the back-projections for the 2013 Sea of Okhotsk event. In order to obtain radiation efficiency consistent with the crack models, the width of the ruptures for high V_r must be constrained, essentially increasing the static stress drop by imposing rectangular rather than circular fault expansion.

For $V_r = 4.0$ km/s, $\Delta\sigma_s = 15$ MPa is needed to give $\eta_R = 0.6$ for a mode III rupture (Fig. 4). For a 180-km rupture length, imposing a fault width of 60 km yields an effective rupture area that gives the required stress drop. For V_r = 5 km/s, the fault width is increased to 68 km and gives $\Delta\sigma_s = 12$ MPa and $\eta_R = 0.75$ (Fig. 4). These models are now physically acceptable, and the slip distribution for the shallow-dipping plane for $V_r = 4$ km/s has average slip of 4.4 m (Fig. 1 and fig. S9a). Good fits to observed *P* waveforms are obtained (fig. S10). The slip distribution has asymmetric bilateral extent of 60 km north northeast and 120 km south southwest. Large slip is concentrated between 30 and 90 km south of the hypocenter, with the area of significant slip being 9675 km^2. We have some preference for the shallow-dipping plane, but very similar results are found for the steeply dipping plane (fig. S9b); the narrow rectangular faults give similar waveforms at most stations for the along-strike rupture.

Although there are limitations in the precision of the back-projection constraints and the theoretical crack-model efficiency is calculated for very simple models, the basic model with $V_r \sim 4.0$ km/s and $\Delta\sigma_s \sim 15$ MPa appears to be a valid representation of the overall source rupture. The V_r and rupture area are both about a factor of 4 larger than for the 1994 Bolivia event, and $\Delta\sigma_s$ is about an order of magnitude lower. The $\Delta\sigma_s \sim 15$ MPa estimate is comparable to values for shallow intraplate earthquakes (*13*, *24*, *25*), and the fault dimensions are similar to those for the shallow trench-slope intraplate normal faulting event in the Kuril Islands of 13 January 2007 ($M_w = 8.1$) (*26*). The fault geometry is compatible with rerupture of such an outer rise normal fault surface within the plate, rotated by the dip of the deep slab. However, the $M_w = 6.7$ aftershock has an unusually short rupture duration and finite-fault inversions for variable assumed rupture velocities for that event give $\Delta\sigma_s$ estimates in the range 157 to 5856 MPa (fig. S12). Independent constraints on the aftershock fault area or rupture velocity are not available, but there is no question that it has a localized stress drop greatly exceeding the average stress drop for the 8.3 mainshock and substantially lower radiation efficiency suggestive of a more dissipative source process. It is plausible that within the mainshock rupture zone there were corresponding very high stress drop slip patches that cannot be resolved. The envelope of teleseismic *P*-wave ground accelerations for the mainshock follows the source-time function shape (fig. S13), so a very heterogeneous stress distribution on the fault does appear likely (*27*–*29*), and the average parameters do not represent the total degree of slip and stress heterogeneity.

The 2013 mainshock rupture extends along the slab strike, with slip likely confined to the low temperature core of the slab. The subducted plate is older and colder than the slab where the 1994 Bolivia earthquake occurred, and this difference in thermal state may have fundamentally affected how rupture expanded for the two events (*30*). The Sea of Okhotsk event is similar to a shallow intraplate earthquake, with a large aspect ratio fault area defined by the brittle core of the slab. For the Bolivia event, the brittle core volume is smaller, and surrounding ductile or plastic material with a finite strength may dominate. Faulting for the Bolivia event involved a rupture with a very dissipative source process that deposited a large amount of energy into the rupture zone, likely leading to melting. This behavior may be akin to that of a shear band. The Sea of Okhotsk mainshock rupture appears to have been less dissipative, and little or no melting may have occurred, although seismology cannot directly constrain the amount of melting.

The stress drops found for the 2013 mainshock and large aftershock suggest preexisting zones with strong and weak regions, likely inherited from shallow faulting of the slab. The warm plate in Bolivia may have more strong, less-brittle patches than weak-brittle patches, whereas the cold plate in the Sea of Okhotsk has more weak-brittle patches than strong, less-brittle patches. Strong patches may be distributed only sparsely in the Sea of Okhotsk slab, with one rupturing in the aftershock, and may act to stop rupture propagation on weak patches. The difference in the distribution of strong, less-brittle and weak-brittle patches caused by the difference in the thermal state is likely responsible

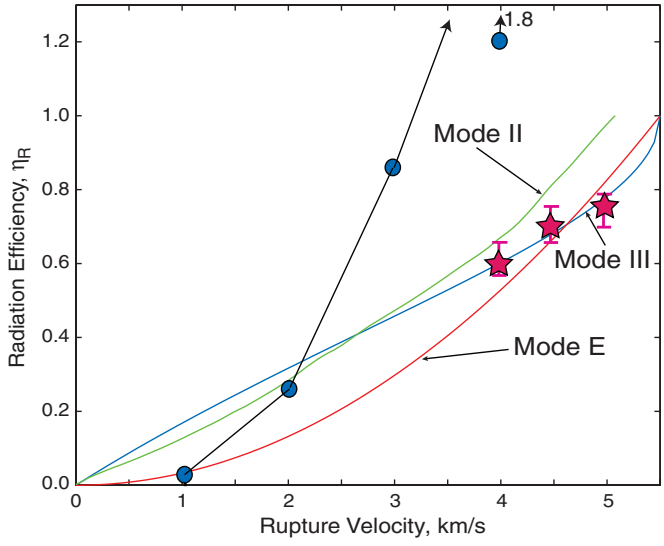

Fig. 4. Model constraints from consideration of radiation efficiency for crack models with varying rupture speed. Reference curves for mode II and mode III cracks and an energy-based model (mode E) have η_R values that approach 1 as the rupture speeds approach their limiting velocities (~5.1 km/s for mode II, ~5.5 km/s for mode III and mode E at a depth of 610 km) (*16*, *23*). The blue circles indicate calculated radiation efficiencies for rupture models (fig. S2) with varying V_r and fault dimensions scaling proportional to V_r. These models are only compatible with the crack theory for $V_r \sim 1.5$ to 2.0 km/s, but this is inconsistent with the rupture extent indicated by back-projection in Fig. 3, which favors V_r of 4.0 to 5.0 km/s. By constraining the width of the slip models, we find high-V_r models consistent with the theoretical radiation efficiency, with preferred models giving the red stars. The solution shown in Fig. 1 is the 15-MPa stress drop model for $V_r = 4.0$ km/s. The pink bars indicate variation in estimates for different thresholds (0.1 to 0.2, with stars for 0.15) used to remove poorly resolved low slip regions of the fault models.

for the drastically different source characteristics of the Bolivian and the Sea of Okhotsk events.

References and Notes

1. H. W. Green II, H. Houston, *Annu. Rev. Earth Planet. Sci.* **23**, 169–213 (1995).
2. H. W. Green II, P. C. Burnley, *Nature* **341**, 733–737 (1989).
3. H. Kanamori, D. L. Anderson, T. H. Heaton, *Science* **279**, 839–842 (1998).
4. U.S. Geological Survey, http://earthquake.usgs.gov/earthquakes/eventpage/usb000h4jh#summary.
5. Global Centroid Moment Tensor Project, www.globalcmt.org/CMTsearch.html.
6. P. G. Silver *et al.*, *Science* **268**, 69–73 (1995).
7. M. Kikuchi, H. Kanamori, *Geophys. Res. Lett.* **21**, 2341–2344 (1994).
8. S. L. Beck, P. Silver, T. C. Wallace, D. James, *Geophys. Res. Lett.* **22**, 2257–2260 (1995).
9. P. F. Ihmlé, *J. Geophys. Res.* **103**, 17,919 (1998).
10. W.-P. Chen, *Geophys. Res. Lett.* **22**, 2261–2264 (1995).
11. M. Antolik, D. Dreger, B. Romanowicz, *Geophys. Res. Lett.* **23**, 1589–1592 (1996).
12. D. A. Wiens, J. J. McGuire, *Geophys. Res. Lett.* **22**, 2245–2248 (1995).
13. A. Venkataraman, H. Kanamori, *J. Geophys. Res.* **109**, B05302 (2004).
14. L. Rivera, H. Kanamori, *Geophys. J. Int.* **162**, 148–155 (2005).
15. H. Kanamori, L. Rivera, *AGU Geophys. Monogr.* **170**, 3–13 (2006).
16. A. V. Newman, E. A. Okal, *J. Geophys. Res.* **103**, 26885 (1998).
17. N. W. Winslow, L. J. Ruff, *Phys. Earth Planet. Inter.* **115**, 181–190 (1999).
18. H. Noda, N. Lapusta, H. Kanamori, *Geophys. J. Int.* **193**, 1691–1712 (2013).
19. L. B. Freund, *J. Elast.* **2**, 341–349 (1972).
20. A. F. Fossum, L. B. Freund, *J. Geophys. Res.* **80**, 3343–3347 (1975).
21. B. V. Kostrov, *J. Appl. Math. Mech. Engl. Transl.* **30**, 1241–1248 (1966).
22. N. F. Mott, *Engineering* **165**, 16 (1948).
23. H. Kanamori, E. Brodsky, *Rep. Prog. Phys.* **67**, 1429–1496 (2004).
24. B. P. Allmann, P. M. Shearer, *J. Geophys. Res.* **114**, B01310 (2009).
25. J. A. Convers, A. V. Newman, *J. Geophys. Res.* **116**, B08304 (2011).
26. T. Lay *et al.*, *J. Geophys. Res.* **114**, B11308 (2009).
27. H. Houston, H. M. Benz, J. E. Vidale, *J. Geophys. Res.* **103**, 29895 (1998).
28. W.-Y. Chung, H. Kanamori, *Phys. Earth Planet. Inter.* **23**, 134–159 (1980).
29. L.-R. Wu, W.-P. Chen, *Bull. Seismol. Soc. Am.* **91**, 102–111 (2001).
30. R. Tibi, G. Bock, D. A. Wiens, *J. Geophys. Res.* **108**, 2091 (2003).

Acknowledgments: We thank E. Brodsky for helpful discussions and three anonymous reviewers for their thoughtful comments. The Incorporated Research Institutions for Seismology (IRIS) data management center provided the seismic recordings. This work was supported in part by NSF under grant EAR-1245717 (T.L.). All data used are available from the IRIS data center at www.iris.edu.

Supplementary Materials

www.sciencemag.org/content/341/6152/1380/suppl/DC1
Materials and Methods
Figs. S1 to S13
References
Movie S1

17 June 2013; accepted 7 August 2013
10.1126/science.1242032

Nonlegumes Respond to Rhizobial Nod Factors by Suppressing the Innate Immune Response

Yan Liang,[1] Yangrong Cao,[1] Kiwamu Tanaka,[1] Sandra Thibivilliers,[1]* Jinrong Wan,[2] Jeongmin Choi,[1] Chang ho Kang,[3] Jing Qiu,[4] Gary Stacey[1]†

Virtually since the discovery of nitrogen-fixing *Rhizobium*-legume symbioses, researchers have dreamed of transferring this capability into nonlegume crop species (for example, corn). In general, nonlegumes were assumed to lack the ability to respond to the rhizobial lipo-chitin Nod factors, which are the essential signal molecules that trigger legume nodulation. However, our data indicate that *Arabidopsis thaliana* plants, as well as other nonlegumes, recognize the rhizobial Nod factor via a mechanism that results in strong suppression of microbe-associated molecular pattern (MAMP)–triggered immunity. The mechanism of action leads to reduced levels of pattern-recognition receptors on the plasma membrane involved in MAMP recognition.

A general theory for the development of commensal and mutualistic symbioses is that they evolved from pathogenic relationships (*1*). Although the *Rhizobium*-legume symbiosis is beneficial and benign, the plant initially responds with a pathogen defense response that is quickly suppressed (*2*, *3*). The lipo-chitin nodulation factors (known as Nod factors) are substituted acylate chitin oligomers of three to five *N*-acetylglucosamine residues and are the key signaling molecules for the establishment of *Rhizobium*-legume symbioses. These factors induce plant responses that lead to the development of the nodule, which becomes the intracellular home of the invading symbiont (*4*, *5*). Nod factors function at nanomolar levels (*6*, *7*), but on only specific, compatible legume hosts. Extension of nitrogen-fixing symbioses beyond these already compatible legume hosts could help reduce dependence on applied fertilizers (*8*).

Plant innate immunity can be triggered by the recognition of microbe-associated molecular patterns (MAMPs) (*9*). The best-studied MAMP is bacterial flagellin (flg22, a conserved 22–amino acid peptide from flagellin), which is recognized by the FLAGELLIN-SENSING 2 (FLS2) receptor located on the plasma membrane (*10*). Perception of flg22 activates a signaling cascade of defense responses, including calcium influx (*11*), reactive oxygen species (ROS) production (*12*), activation of mitogen-activated protein (MAP) kinases (*13*), gene expression (*14*), callose deposition (*15*), and bacterial growth restriction (*10*). Together, these responses are called MAMP-triggered immunity.

To study the intersection between symbiosis and pathogenesis, we added both flg22 and purified Nod factor from *Bradyrhizobium japonicum*, the soybean symbiont, to soybean leaves (see supplementary materials and methods). The flg22-triggered ROS production was reduced 25% in the presence of Nod factor (Fig. 1A). Chitin is also a strong MAMP but only when the oligomers have more than six *N*-acetylglucosamine residues. Nod factor is composed of shorter oligomers (three to five residues). We tested the chitin oligomers containing one to eight residues for their ability to suppress flg22-triggered ROS production. Chitotetraose (C4) and chitopentaose (C5) reduced flg22-triggered ROS production, but not as efficiently as Nod factor (fig. S1). Chitin oligomers C6 through C8 did not affect flg22-triggered ROS production (fig. S1). These results are similar to some symbiotic responses in which simple chitooligomers can suffice but only at higher concentration than the Nod factor (*16*, *17*). Treatment with Nod factor or chitotetraose alone did not induce ROS production (Fig. 1A). Pretreatment of plants with Nod factor or chitotetraose enhanced the suppressive effect of flg22-triggered ROS production (Fig. 1B). For example, flg22-induced ROS production was reduced 60% with 30 min of chitotetraose pretreatment (Fig. 1B).

The suppressive effects of Nod factor or chitotetraose addition were also seen when chitooctaose, a potent MAMP, was used to induce ROS production (fig. S2). During nodulation, application of Nod factors at picomolar to nanomolar concentrations elicits a variety of symbiotic responses (for instance, root hair deformation). The lowest concentration of Nod factor required to reduce flg22-triggered ROS production was 1 nM (Fig. 1C). One of the downstream signals after flg22 treatment in *Arabidopsis* is MAP kinase phosphorylation, which can be detected immuno-

[1]Divisions of Plant Science and Biochemistry, National Center for Soybean Biotechnology, Christopher S. Bond Life Sciences Center, University of Missouri, Columbia, MO 65211, USA. [2]Division of Plant Science, 46 Agriculture Building, University of Missouri, Columbia, MO 65211, USA. [3]Plant Molecular Biology and Biotechnology Research Center, Gyeongsang National University, Building 6-421, Jinjudaero 501, JinJu, Gyeongsangnam-do, 660-701, South Korea. [4]Department of Statistics, 134I Middlebush Hall, University of Missouri, Columbia, MO 65211, USA.

*Present address: Department of Microbiology and Plant Biology, University of Oklahoma, Norman, OK 73019, USA.
†Corresponding author. E-mail: staceyg@missouri.edu

logically with the use of an anti-phospho-p44/p42 MAP kinase antibody. Similarly, soybean phosphorylates MAP kinase after flg22 elicitation. We observed that Nod factor or chitotetraose pretreatment of soybean leaves reduced flg22-induced MAP kinase activation (Fig. 1D). Nod factor or chitotetraose alone did not induce MAP kinase activation (Fig. 1D).

We also tested the ability of Nod factor and chitotetraose to suppress flg22-triggered immunity in *Arabidopsis*, which is not a legume and has been the subject of much research on plant immunity, including the mechanisms of MAMP-triggered immunity. A 1-hour pretreatment of *Arabidopsis* leaves with Nod factor or chitotetraose significantly reduced flg22-induced ROS production (Fig. 2A and fig. S3) and MAP kinase phosphorylation (fig. S4). The suppressive effect of Nod factor is weaker and slower in *Arabidopsis* than in soybean.

Application of Nod factor and chitotetraose to *Arabidopsis* also interfered with other responses to flg22, such as callose deposition (Fig. 2B and fig. S5) and changes in gene expression (fig. S6). In *Arabidopsis*, flg22-triggered immunity inhibits growth of the bacterial pathogen *Pseudomonas syringae*. However, treatment with Nod factor or chitotetraose suppressed this inhibition, resulting in more extensive pathogen colonization (Fig. 2C). One of the earliest flg22 responses upstream of ROS production is the transient increase of cytosolic Ca^{2+} concentration due to calcium influx. In the presence of either Nod factor or chitotetraose, flg22-triggered calcium influx was significantly reduced in both *Arabidopsis* seedlings (Fig. 2D) and roots (fig. S7). Thus, *Arabidopsis*, although not a legume, can recognize Nod factor in a way that results in suppression of flg22-triggered immunity, similar to what is seen in soybean treated with Nod factor.

Calcium influx is induced within minutes after flg22 treatment and acts immediately downstream of flg22 perception. The inhibitory effect of Nod factor and chitotetraose on flg22-triggered calcium influx suggested a mechanism that may involve FLS2, the receptor of flagellin. The levels of FLS2 at the plasma membrane are regulated, in part, by ubiquitination and 26*S* proteasome degradation induced by flg22 recognition (*18*). We used Western blot analysis with anti-FLS2 antibody to examine whether Nod factor could directly affect FLS2 protein levels. FLS2 protein levels were significantly reduced 1 hour after Nod factor treatment (Fig. 3A), whereas the transcript level was unaltered (fig. S8). Addition of MG132, an inhibitor of proteasome-mediated degradation, blocked the effect of Nod factor on FLS2 protein levels (Fig. 3A).

The leucine-rich repeat receptor kinase BAK1 is required to recruit specific E3 ligases to FLS2 for the attenuation of flg22 responses in *Arabidopsis* (*18*). Nod factor–induced FLS2 degradation was absent in the *bak1-4 Arabidopsis* mutant (Fig. 3B), indicating that Nod factor action on FLS2 is dependent on BAK1. The addition of Nod factor did not affect BAK1 protein levels (fig. S9). We observed that fluorescence on the plasma membrane derived from a green fluorescent protein (GFP)–tagged FLS2 construct in wild-type *Arabidopsis* was also reduced within 1 hour of

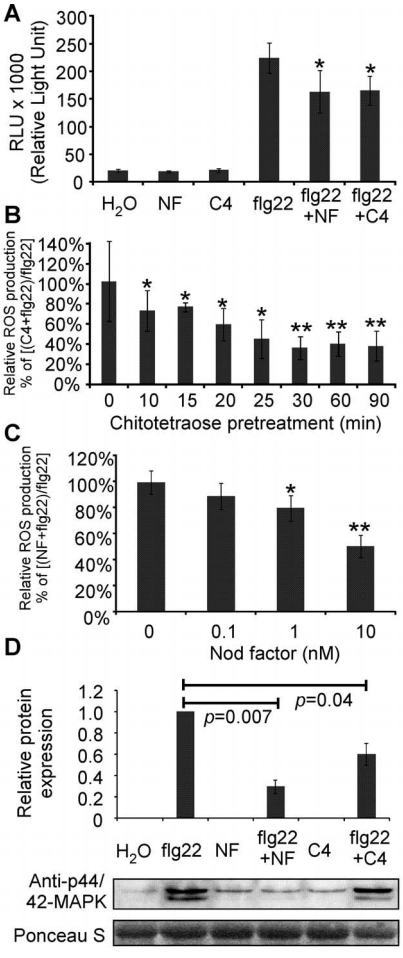

Fig. 1. Nod factor (NF) and chitotetraose (C4) treatment reduces flg22-triggered immunity in soybean leaves. (**A**) Nod factor and chitotetraose reduced flg22-triggered ROS production. Leaf discs were treated with H_2O, Nod factor (100 nM), chitotetraose (10 μM), and flg22 (100 nM) with or without the addition of Nod factor or chitotetraose. (**B**) Pretreatment enhanced the suppressive effect of C4 on flg22-triggered ROS production. (**C**) Nod factor (1 nM) reduced flg22-triggered ROS production. Leaf discs were pretreated with different concentrations of Nod factor for 30 min before flg22 (100 nM) treatment. (A to C) The data are shown as means ± SD (error bars; $n = 6$ leaf discs). Asterisks indicate significant differences from flg22 treatment (**$P \leq 0.01$, *$P \leq 0.05$). All experiments were repeated twice with similar results. (**D**) Nod factor and chitotetraose reduced flg22-induced MAP kinase (MAPK) phosphorylation. Lower panels shows representative Western blot; upper panel shows quantification of normalized protein levels to flg22 treatment. Data are means ± SE (error bars) from three independent biological repeats.

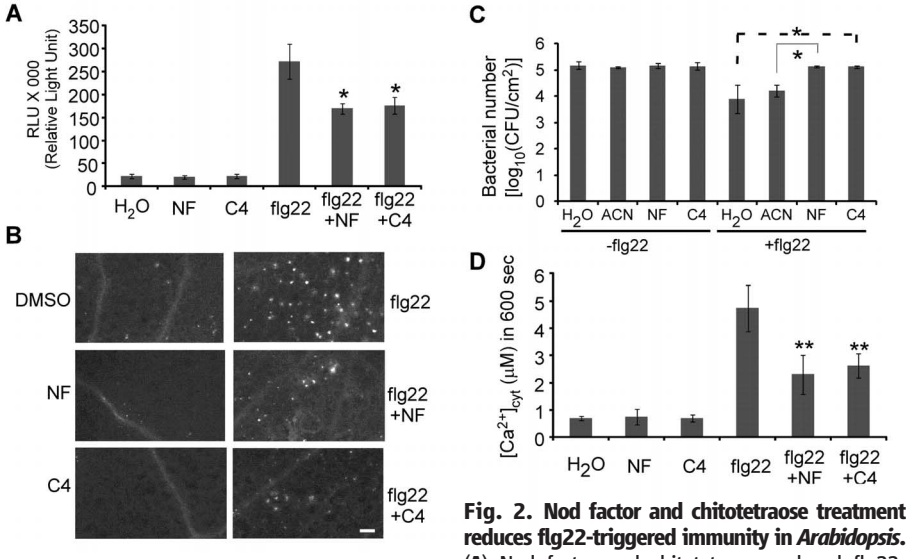

Fig. 2. Nod factor and chitotetraose treatment reduces flg22-triggered immunity in *Arabidopsis*. (**A**) Nod factor and chitotetraose reduced flg22-triggered ROS production in *Arabidopsis* leaves. (**B**) Nod factor and chitotetraose reduced flg22-triggered callose deposition. Representative images are shown here, and the quantification data are shown in fig. S5. Scale bar, 1 mm. DMSO, dimethyl sulfoxide. (**C**) Nod factor and chitotetraose reduced flg22-triggered bacterial growth restriction. Five-week-old *Arabidopsis* plants were infiltrated with the indicated treatment before *Pseudomonas syringae* pv. tomato DC3000 inoculation at a concentration of 10^5 colony-forming units (CFU)/ml. Bacterial growth was determined 3 days after inoculation. The data are shown as means ± SD (error bars) from three replicates (*$P \leq 0.05$). (**D**) Nod factor and chitotetraose reduced flg22-triggered calcium influx in *Arabidopsis* seedlings. Leaf disc (A) or 6-day-old seedlings (D) were pretreated with H_2O, Nod factor (100 nM), and chitotetraose (10 μM) for 1 hour before flg22 (10 nM) treatment. Data are means ± SD (error bars; $n = 6$ leaf discs; **$P \leq 0.01$, *$P \leq 0.05$). All experiments were repeated twice with similar results.

Nod factor treatment (Fig. 3C). Thus, the response in *Arabidopsis* to Nod factor treatment includes the reduced level of FLS2 from the plasma membrane, a process that requires ubiquitin-dependent protein degradation.

Arabidopsis also responds to MAMPs other than flg22, including the peptide elf26 (fig. S10), chitin, and pep1 (an endogenous peptide from *Arabidopsis* that induces defense responses), as well as the crude extract of rhizobia. Similar to the results obtained with flg22, ROS production elicited by elf26, pep1, chitin, and crude rhizobial extract was significantly reduced in the presence of Nod factor or chitotetraose (figs. S11 and S12). The *B. japonicum* Nod factor used in our studies was purified from bacterial cultures. However, chemically synthesized Nod factors also reduced flg22-triggered calcium influx in *Arabidopsis* (fig. S13). EFR (the receptor of elf26) protein levels were significantly reduced after Nod factor treatment, and the protein degradation was inhibited by the addition of MG132 (fig. S14).

We tested two other nonlegume plant species (tomato and corn) for their ability to recognize and respond to Nod factor. Both Nod factor and chitotetroase could suppress flg22-induced ROS production in tomato (fig. S15), and chitooctaose-triggered ROS production in corn (fig. S16). Thus, the mechanism of Nod factor recognition and action that legumes have so effectively used is conserved in the nonlegumes *Arabidopsis*, tomato (a dicot), and corn (a monocot).

Mutations of Nod factor receptors have been identified in various legumes (*19*–*21*) and include soybean *nod49* (*nfr1*) and *nod139* (*nfr5*) mutants (*22*, *23*). We found that, although soybean mutants in Nod factor receptor 1 (NFR1) or NFR5 were unable to induce symbiotic functions (e.g., gene expression) in response to Nod factor addition, these mutants retained the ability to suppress MAMP-triggered immunity upon addition of Nod factor (fig. S17). The soybean NFRs are closely related to the chitin receptor LYK1/CERK1 in *Arabidopsis* and rice (*24*, *25*). These receptors are all characterized by the presence of one or more lysin motifs (LysMs) in their extracellular domain. In *Arabidopsis*, five LysM receptor kinases (*LYKs*), including LYK1/CERK1, have been identified. Therefore, we tested mutants in each of these *LYK* genes for their ability to recognize Nod factor and suppress flg22-triggered ROS production. Plants defective in the LYK3 protein failed to suppress flg22-triggered ROS production upon Nod factor

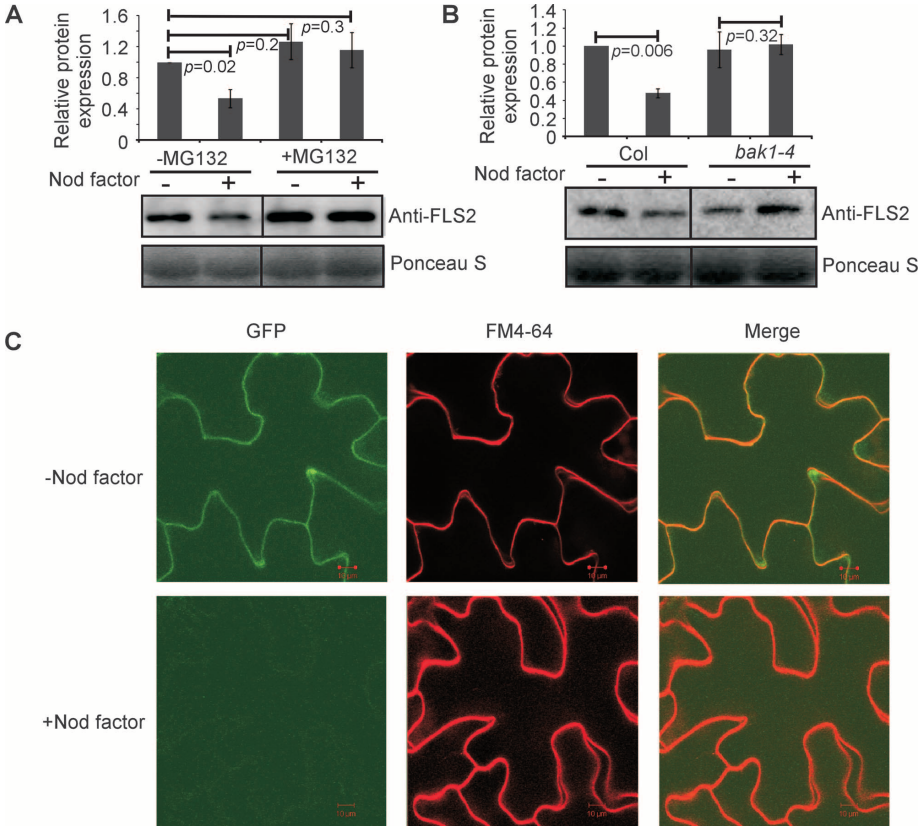

Fig. 3. Nod factor induces FLS2 protein degradation in *Arabidopsis*. (**A**) Nod factor induces FLS2 protein degradation, and the protein degradation was inhibited by the addition of MG132. Ten-day-old seedlings were treated with or without MG132 (50 μM) for 1 hour before Nod factor (100 nM) treatment. Total protein was extracted 1 hour after Nod factor treatment. (**B**) Nod factor–induced FLS2 protein degradation was absent in *bak1-4* mutants. Immunoblot analysis was performed with the anti-FLS2 antibody. Ponceau S staining was used for protein loading control. (A and B) Lower panels show representative Western blot; upper panels show quantification of normalized FLS2 levels to the control. The data are shown as means ± SE (error bars) from three independent biological repeats. (**C**) Nod factor addition results in the reduced level of FLS2:GFP from the plasma membrane. Five-day-old *FLS2::FLS2:GFP* seedlings were treated with or without Nod factor (100 nM). Images were taken from cotyledon 1 hour after Nod factor treatment. Costaining with FM4-64 (10 μM) highlights the plasma membrane. Scale bars, 10 μm.

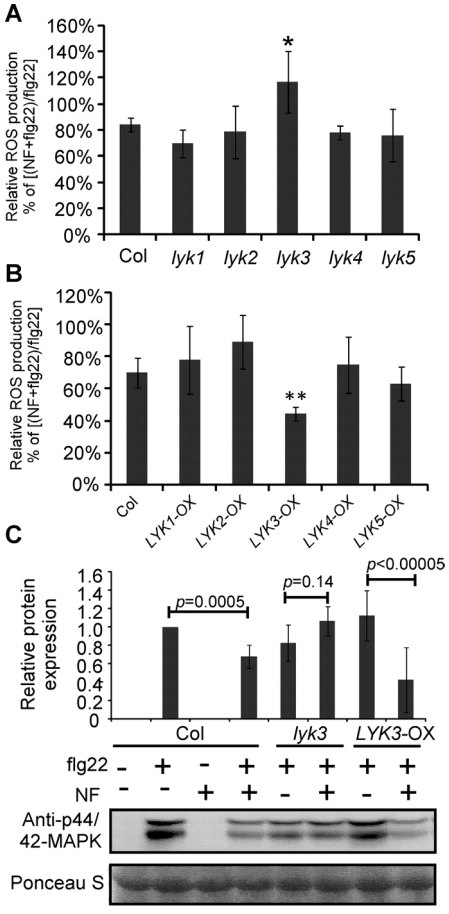

Fig. 4. *AtLYK3* is required for Nod factor suppression of flg22-triggered immunity. (**A**) *lyk3* mutants are defective in Nod factor suppression of flg22-triggered ROS production. (**B**) Transgenic plants ectopically overexpressing *LYK3* (*LYK3*-OX) are hypersensitive to Nod factor suppression of flg22-triggered ROS production. Leaf discs in (A) and (B) were pretreated with H_2O or Nod factor (100 nM) for 1 hour before flg22 (10 nM) treatment. The relative ROS production was calculated as a percentage of the value of flg22 plus Nod factor divided by the value of flg22. The data are shown as means ± SD (error bars; $n = 6$ leaf discs). Asterisks indicate significant difference from the wild type (**$P \leq 0.01$, *$P \leq 0.05$). All experiments were repeated twice with similar results. (**C**) *lyk3* mutants and *LYK3*-OX transgenic plants exhibited altered response to Nod factor suppression of flg22-triggered MAP kinase phosphorylation. Lower panels show representative Western blot; upper panel shows quantification of normalized protein levels to flg22 treatment. The data are shown as means ± SE (error bars) from four independent biological repeats.

addition (Fig. 4A), whereas ectopic overexpression of *LYK3* enhanced Nod factor–induced suppression of ROS production (Fig. 4B). Similarly, mutation or overexpression of LYK3 also altered the suppressive effect of Nod factor on flg22-triggered MAP kinase phosphorylation (Fig. 4C). The other four *lyk* mutants did not show altered responses to Nod factor treatment. Therefore, our results suggest that LYK3 is required in *Arabidopsis* for Nod factor–induced suppression of MAMP-triggered immunity.

The lysin motif was first characterized in bacterial proteins involved in remodeling of bacterial peptidoglycan (*26*). Similar proteins were also shown to recognize lipo-chitin signals produced by mycorrhizal fungal symbionts (*27*). Collectively, these findings led to the suggestion that chitin recognition is an ancient plant trait that probably evolved from mycorrhizal recognition, whose symbiosis has been documented more than 400 million years ago (*28*), or perhaps from fungal pathogen-plant interaction, whose origin has not been dated. However, *Arabidopsis* is not infected by either rhizobia or mycorrhizae (*29*). Hence, the mechanism of Nod factor recognition in this plant must be independent of these symbiotic pathways. If Nod factor suppression of MAMP-triggered immunity is universal in plants, then it may predate the mycorrhizal symbiosis and could represent the beginning of recognition mechanisms for this interesting molecule.

References and Notes

1. T. Nakagawa *et al.*, *Plant J.* **65**, 169–180 (2011).
2. F. El Yahyaoui *et al.*, *Plant Physiol.* **136**, 3159–3176 (2004).
3. H. Kouchi *et al.*, *DNA Res.* **11**, 263–274 (2004).
4. S. R. Long, *Plant Cell* **8**, 1885–1898 (1996).
5. R. Geurts, T. Bisseling, *Plant Cell* **14** (suppl.), S239–S249 (2002).
6. J. Dénarié, J. Cullimore, *Cell* **74**, 951–954 (1993).
7. A. Broghammer *et al.*, *Proc. Natl. Acad. Sci. U.S.A.* **109**, 13859–13864 (2012).
8. P. H. Beatty, A. G. Good, *Science* **333**, 416–417 (2011).
9. J. L. Dangl, J. D. Jones, *Nature* **411**, 826–833 (2001).
10. C. Zipfel *et al.*, *Nature* **428**, 764–767 (2004).
11. S. Ranf, L. Eschen-Lippold, P. Pecher, J. Lee, D. Scheel, *Plant J.* **68**, 100–113 (2011).
12. M. A. Torres, J. L. Dangl, *Curr. Opin. Plant Biol.* **8**, 397–403 (2005).
13. T. Asai *et al.*, *Nature* **415**, 977–983 (2002).
14. C. Denoux *et al.*, *Mol. Plant* **1**, 423–445 (2008).
15. N. K. Clay, A. M. Adio, C. Denoux, G. Jander, F. M. Ausubel, *Science* **323**, 95–101 (2009).
16. E. Minami *et al.*, *Mol. Plant Microbe Interact.* **9**, 574–583 (1996).
17. S. A. Walker, V. Viprey, J. A. Downie, *Proc. Natl. Acad. Sci. U.S.A.* **97**, 13413–13418 (2000).
18. D. Lu *et al.*, *Science* **332**, 1439–1442 (2011).
19. E. Limpens *et al.*, *Science* **302**, 630–633 (2003).
20. E. B. Madsen *et al.*, *Nature* **425**, 637–640 (2003).
21. S. Radutoiu *et al.*, *Nature* **425**, 585–592 (2003).
22. A. Indrasumunar *et al.*, *Plant Cell Physiol.* **51**, 201–214 (2010).
23. A. Indrasumunar *et al.*, *Plant J.* **65**, 39–50 (2011).
24. H. Kaku *et al.*, *Proc. Natl. Acad. Sci. U.S.A.* **103**, 11086–11091 (2006).
25. J. Wan *et al.*, *Plant Cell* **20**, 471–481 (2008).
26. A. Miya *et al.*, *Proc. Natl. Acad. Sci. U.S.A.* **104**, 19613–19618 (2007).
27. C. Béliveau, C. Potvin, J. Trudel, A. Asselin, G. Bellemare, *J. Bacteriol.* **173**, 5619–5623 (1991).
28. R. Op den Camp *et al.*, *Science* **331**, 909–912 (2011).
29. W. Remy, T. N. Taylor, H. Hass, H. Kerp, *Proc. Natl. Acad. Sci. U.S.A.* **91**, 11841–11843 (1994).

Acknowledgments: We thank A. Bent for providing the anti-FLS2 antibody and *EFR::EFR:HA* transgenic seeds, M. R. Knight for aequorin transgenic seeds, S. Robatzek for *FLS2::FLS2:GFP* transgenic seeds, Novozymes (Bagsvaerd, Denmark) for the purified Nod factor, and S. Peck for critical comments to improve the manuscript. This work was supported by the Division of Chemical Sciences, Geosciences, and Biosciences, Office of Basic Energy Sciences of the U.S. Department of Energy through grant DE-FG02-08ER15309 and by the Next-Generation BioGreen 21 Program Systems and Synthetic Agrobiotech Center, Rural Development Administration, Republic of Korea (grant PJ009068 to G.S). Additional support was provided by Novozymes.

Supplementary Materials

www.sciencemag.org/content/341/6152/1384/suppl/DC1
Materials and Methods
Figs. S1 to S17
References (*30*–*36*)

3 July 2013; accepted 26 August 2013
Published online 5 September 2013;
10.1126/science.1242736

Structure of the CCR5 Chemokine Receptor–HIV Entry Inhibitor Maraviroc Complex

Qiuxiang Tan,[1]* Ya Zhu,[1]* Jian Li,[1] Zhuxi Chen,[2] Gye Won Han,[3] Irina Kufareva,[4] Tingting Li,[1] Limin Ma,[1] Gustavo Fenalti,[3] Jing Li,[1] Wenru Zhang,[1] Xin Xie,[1] Huaiyu Yang,[2] Hualiang Jiang,[2] Vadim Cherezov,[3] Hong Liu,[1] Raymond C. Stevens,[1,3,5] Qiang Zhao,[1] Beili Wu[1]†

The CCR5 chemokine receptor acts as a co-receptor for HIV-1 viral entry. Here we report the 2.7 angstrom–resolution crystal structure of human CCR5 bound to the marketed HIV drug maraviroc. The structure reveals a ligand-binding site that is distinct from the proposed major recognition sites for chemokines and the viral glycoprotein gp120, providing insights into the mechanism of allosteric inhibition of chemokine signaling and viral entry. A comparison between CCR5 and CXCR4 crystal structures, along with models of co-receptor–gp120-V3 complexes, suggests that different charge distributions and steric hindrances caused by residue substitutions may be major determinants of HIV-1 co-receptor selectivity. These high-resolution insights into CCR5 can enable structure-based drug discovery for the treatment of HIV-1 infection.

Chemokine receptors and their peptidic ligands, chemokines, are the main organizers of leukocyte trafficking and are validated therapeutic targets owing to their involvement in many physiopathological disorders (*1*, *2*). The chemokine receptor CCR5 binds and responds to four endogenous chemokine agonists: RANTES, macrophage inflammatory protein–1α (MIP-1α), MIP-1β, and monocyte chemotactic protein–2 (MCP-2) (*3*). CCR5 and another chemokine receptor, CXCR4, are required for human immunodeficiency virus type 1 (HIV-1) infectivity, acting as co-receptors of the viral envelope glycoprotein gp120 (*4*). The structure of CXCR4 has been determined (*5*), but the details of chemokine recognition and viral infectivity are poorly understood. HIV can infect a variety of CD4-expressing immune cells and evolves inside the infected organism to encompass a wider range of susceptible cells by changing its co-receptor specificity, a phenomenon related to HIV tropism. HIV-1 strains using the co-receptor CCR5 are termed R5, and the strains using CXCR4 are termed X4, and those using either co-receptor are R5X4 (*6*). Intense research into the development of inhibitors capable of blocking HIV entry by targeting the co-receptor CCR5 has led to approval of the allosteric CCR5 inhibitor maraviroc for treatment of HIV-1 infection (*7*–*11*).

Structural studies were carried out using an engineered human CCR5 construct, purified and crystallized in complex with maraviroc (figs. S1 and S2) (*12*). The crystal structure of the CCR5-maraviroc complex was determined at 2.7 Å resolution with two complexes per asymmetric unit (ASU) (Fig. 1, figs. S3 and S4, and table S1). Molecule A will be used for discussion purposes.

The overall CCR5 fold shares a similar architecture with previously solved class A G protein–coupled receptor (GPCR) structures, containing seven transmembrane (7TM) α helices (I to VII) connected by three extracellular loops (ECL1-3) and three intracellular loops (ICL1-3) (Fig. 1A).

[1]CAS Key Laboratory of Receptor Research, Shanghai Institute of Materia Medica, Chinese Academy of Sciences, 555 Zuchongzhi Road, Pudong, Shanghai, China 201203. [2]Drug Discovery and Design Center, Shanghai Institute of Materia Medica, Chinese Academy of Sciences, 555 Zuchongzhi Road, Pudong, Shanghai, China 201203. [3]Department of Integrative Structural and Computational Biology, The Scripps Research Institute, 10550 North Torrey Pines Road, La Jolla, CA 92037, USA. [4]University of California, San Diego, Skaggs School of Pharmacy and Pharmaceutical Sciences, La Jolla, CA 92093,USA. [5]iHuman Institute, ShanghaiTech University, Shanghai, China 201203.

*These authors contributed equally to this work.
†Corresponding author. E-mail: beiliwu@simm.ac.cn

CCR5 is structurally similar to the chemokine receptor CXCR4 [Cα root mean square deviation within the 7TM bundle between CCR5-maraviroc and CXCR4-IT1t is 1.8 Å (sequence identity = 34%)]. The largest loop in CCR5, ECL2, forms a β-hairpin structure; the conformations of the N-terminal segment (residues 19 to 26) and ECLs are constrained by two disulfide bonds, one linking Cys-101$^{3.25}$ (*13*) with Cys-178 of ECL2, and another one connecting Cys-20 at the N terminus with Cys-269$^{7.25}$ (Fig. 1, B and C). Despite the overall similarity, CCR5 and CXCR4 structures differ substantially in a number of regions. In the CXCR4 crystal structures, the C terminus after helix VII adopted an extended disordered conformation (*5*), whereas in CCR5, a short α helix VIII is observed. This difference could be explained by the presence of an α-helical sequence motif F(RK)xx(FL)xxx(LF) in CCR5's helix VIII, whereas in CXCR4 this motif is partially modified (FKxxAxxxL) (*5*, *14*). However, it cannot be excluded that this difference might also be due to different crystal-packing interactions. Helix IV in CCR5 is tilted by about 15° with respect to the corresponding helix in CXCR4; its intracellular portion is 1.5 turns shorter than in CXCR4 and forms a classical α helix, in contrast with a distorted π helix in CXCR4. ICL2, which is unstructured in CXCR4, contains a two-turn α helix in CCR5 running parallel to the membrane (Fig. 1D). Phe-135 and Ala-136 in the α helix of ICL2 form a hydrophobic cluster with Leu-128$^{3.53}$ and Ala-129$^{3.54}$ at the intracellular end of helix III to stabilize the conformation of ICL2.

In the CCR5-maraviroc structure, the ligand occupies the bottom of a pocket defined by residues from helices I, II, III, V, VI, and VII (Fig. 2A and fig. S5). The nitrogen of the tropane group is likely protonated and engaged in a salt-bridge interaction with Glu-283$^{7.39}$. The carboxamide nitrogen forms a hydrogen bond with Tyr-251$^{6.51}$. The length of the carbon chain between the above-mentioned two nitrogens was reported to be critical for the anti-HIV infection activity of the inhibitors (*15*), which correlates with the spatial locations of Glu-283$^{7.39}$ and Tyr-251$^{6.51}$. The amine moiety of the triazole group hydrogen bonds with Tyr-37$^{1.39}$ and with a water molecule. Another two hydrogen bonds are formed by one of the fluorines in the cyclohexane ring with Thr-195$^{5.39}$ and Thr-259$^{6.59}$. In addition, the phenyl group reaches deep into the pocket to form hydrophobic interactions with five aromatic residues: Tyr-108$^{3.32}$, Phe-109$^{3.33}$, Phe-112$^{3.36}$, Trp-248$^{6.48}$, and Tyr-251$^{6.51}$. The triazole, tropane, and cyclohexane groups also fit into small subpockets and make hydrophobic contacts with CCR5. The above interactions are supported by previous mutagenesis studies (Fig. 2B) (*11*, *16*).

Compared to the CXCR4–IT1t structure, the binding site for maraviroc in CCR5 is deeper and occupies a larger area of the pocket, making no contacts with the ECLs (Fig. 3, A, B, D, and E). In CCR5, the extracellular end of helix VII shifts away from the central axis of the receptor by ~3 Å compared with CXCR4, leading to a corresponding shift of CCR5's N-terminal fragment connected to helix VII by the disulfide bond Cys-20–Cys-269$^{7.25}$. Also in CXCR4, Asp-97$^{2.63}$ and Arg-183 in ECL2 form a salt bridge, which is absent in CCR5 because of substitutions to Tyr-89$^{2.63}$ and His-175, resulting in a 6 Å shift at the β-hairpin tip of ECL2 of CXCR4 toward the ligand-binding pocket compared with CCR5. Consequently, the entrance to the CXCR4 ligand-binding pocket is partially covered by its N terminus and ECL2, whereas the CCR5 ligand binding pocket is more open.

Maraviroc has been characterized as an inverse agonist of CCR5 (*17*), suggesting that maraviroc stabilizes CCR5 in an inactive conformation. The major evidence for an inactive state of the CCR5-maraviroc structure is the conformation of the highly conserved class A GPCR residues Trp-248$^{6.48}$ and Tyr-244$^{6.44}$, which are involved in relaying ligand-stabilized conformational changes in the binding pocket into conformational changes in the cytoplasmic domain. In the CCR5-maraviroc structure, these residues are in conformations similar to those observed in other inactive structures and distinct from their active-state conformations (*18*, *19*). Moreover, the phenyl group of maraviroc forms a hydrophobic interaction with Trp-248$^{6.48}$, preventing its activation-related motion. The inactive state of the CCR5-maraviroc structure is also manifested by the close packing of helix VI with other helices of the 7TM bundle at the intracellular side of receptor that precludes G-protein binding. The inactive conformation of helix VI can be stabilized by an "ionic lock" formed by a salt-bridge interaction between the conserved Arg$^{3.50}$ in helix III and Asp/Glu$^{6.30}$ at the intracellular end of helix VI (*20*, *21*). Although wild-type CCR5 lacks any acidic residue at position 6.30, the thermostabilizing mutation Ala-233$^{6.33}$Asp makes a salt-bridge contact with Arg$^{3.50}$, potentially locking the receptor in an inactive conformation (fig. S2).

Mutagenesis and biochemical studies suggest that maraviroc and some other small-molecule CCR5 inhibitors are allosteric modulators (*9*–*11*, *16*, *17*). The N-terminal region of CCR5, together with ECL2, have been identified as the major binding determinants for its chemokine ligands (*22*). In the so-called two-site model, this region is viewed as a chemokine recognition site (site 1), which interacts with the chemokine core (*16*). Several residues in the 7TM region were found to be important for CCR5 activation upon binding to the chemokine ligand, such as Tyr-37$^{1.39}$ and Trp-248$^{6.48}$ (*11*), which are involved in maraviroc binding. This region is considered as an activation site (site 2), which interacts with the flexible N terminus of the chemokine (*23*). In the CCR5 structure, maraviroc is buried in a cavity within the 7TM domain, which is distinct from site 1 of chemokine recognition, but potentially overlaps with site 2. Thus, the CCR5-maraviroc structure indicates that maraviroc most likely inhibits chemokine function by blocking receptor activation through interactions with site 2, which explains the allosteric inhibition of chemokine signaling by maraviroc. It has also been reported that CCR5's N terminus and ECL2 play an important role in gp120 binding and HIV-1 infection (*11*, *24*, *25*), suggesting that maraviroc interferes with the effects of gp120 binding in a similar allosteric fashion. The above conclusion does not rule out the possibility that maraviroc

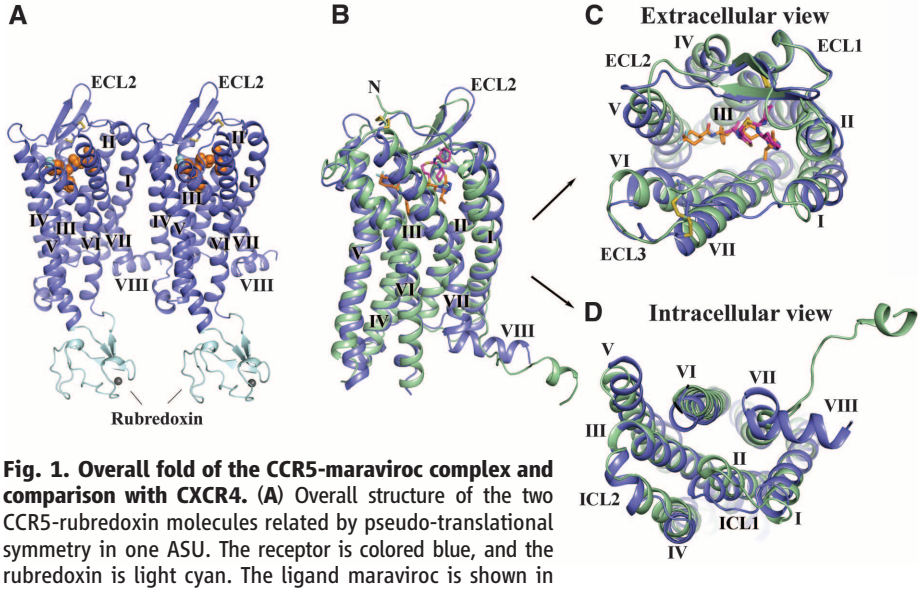

Fig. 1. Overall fold of the CCR5-maraviroc complex and comparison with CXCR4. (**A**) Overall structure of the two CCR5-rubredoxin molecules related by pseudo-translational symmetry in one ASU. The receptor is colored blue, and the rubredoxin is light cyan. The ligand maraviroc is shown in orange sphere representation. The disulfide bonds are shown as yellow sticks. Zinc ions are shown as gray spheres. (**B** to **D**) Structure comparison between CCR5 (blue) and CXCR4 (PDB ID: 3ODU, green). The ligands are shown in stick representation. maraviroc in CCR5 and IT1t in CXCR4 have orange and magenta carbons, respectively. (C) Top view of the extracellular side of CCR5 and CXCR4; (D) bottom view of the intracellular side of CCR5 and CXCR4.

may reduce chemokine and gp120 binding in an allosteric inverse agonism manner by stabilizing CCR5 in an inactive conformation. Thus, maraviroc may alter chemokine signaling and gp120 binding by allosterically blocking agonist recognition and/or inhibiting receptor activation.

The third variable region, V3 loop, of gp120 forms a β-hairpin structure and has been identified as the major determinant of cellular tropism and co-receptor specificity (*24*, *26*, *27*). The stem region of the V3 loop has been reported to be responsible for gp120 binding to the co-receptor's N terminus, whereas the V3 crown interacts with the co-receptor's ECL2 and residues inside the ligand-binding pocket (*24*, *25*, *28*). Sequence analysis of the V3 region shows that it is more positively charged in the X4-tropic viruses than in the R5-tropic viruses (*29*, *30*). Several acidic residues in CXCR4—Asp-97$^{2.63}$, Asp-171$^{4.60}$, Asp-187 (ECL2), Asp-193$^{5.32}$, and Asp-262$^{6.58}$—are key for ligand binding in the CXCR4 structures (*5*) and have been reported to be critical for HIV-1 infectivity (*28*). In CCR5, these acidic residues are substituted by uncharged residues Tyr-89$^{2.63}$, Gly-163$^{4.60}$, Ser-179, Gln-188$^{5.32}$, and Asn-258$^{6.58}$, respectively. Additionally, the N terminus of CXCR4 contains nine acidic residues, whereas CCR5 only has three (Fig. 3, C and F, and fig. S6A). These differences may correlate with the different charge distribution in the V3 loops of X4- and R5-tropic viruses. It was reported that the binding of gp120 to CCR5 was sensitive to mutations of some uncharged residues of CCR5, such as Trp-86$^{2.60}$, Trp-94, Tyr-108$^{3.32}$, Trp-248$^{6.48}$, and Tyr-251$^{6.51}$ (*11*), providing additional evidence for the importance of the net

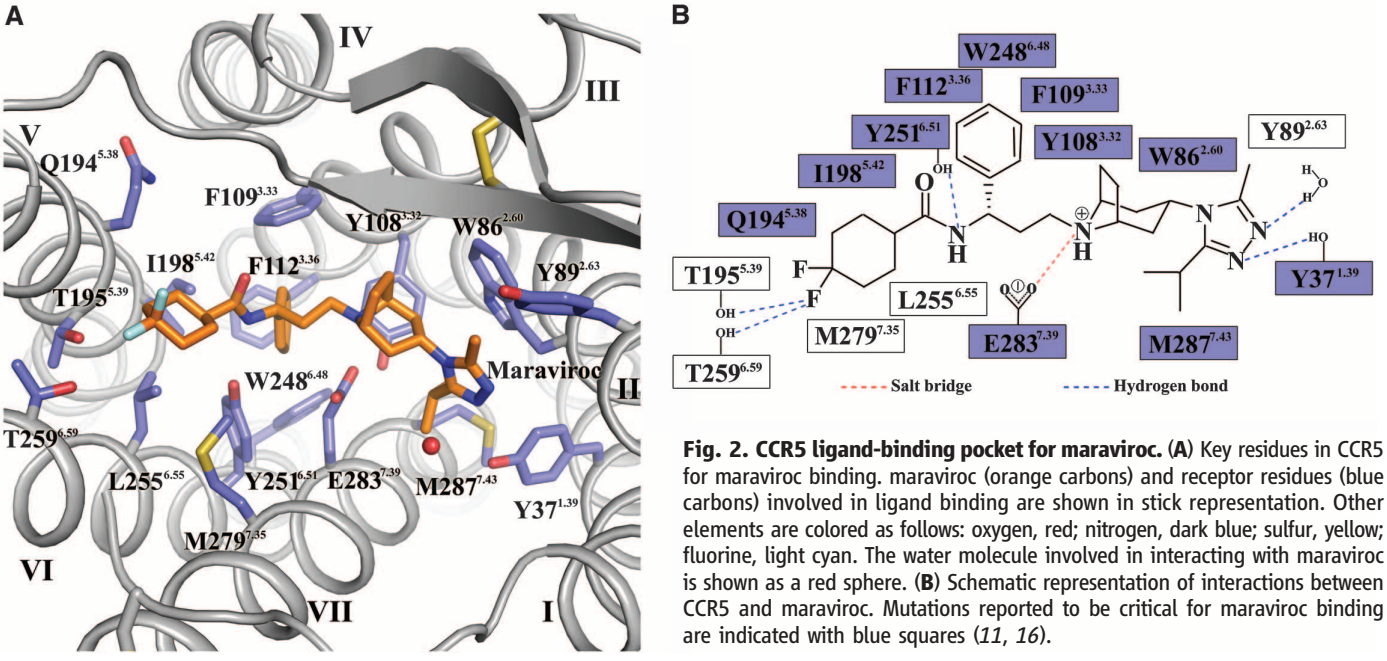

Fig. 2. CCR5 ligand-binding pocket for maraviroc. (**A**) Key residues in CCR5 for maraviroc binding. maraviroc (orange carbons) and receptor residues (blue carbons) involved in ligand binding are shown in stick representation. Other elements are colored as follows: oxygen, red; nitrogen, dark blue; sulfur, yellow; fluorine, light cyan. The water molecule involved in interacting with maraviroc is shown as a red sphere. (**B**) Schematic representation of interactions between CCR5 and maraviroc. Mutations reported to be critical for maraviroc binding are indicated with blue squares (*11*, *16*).

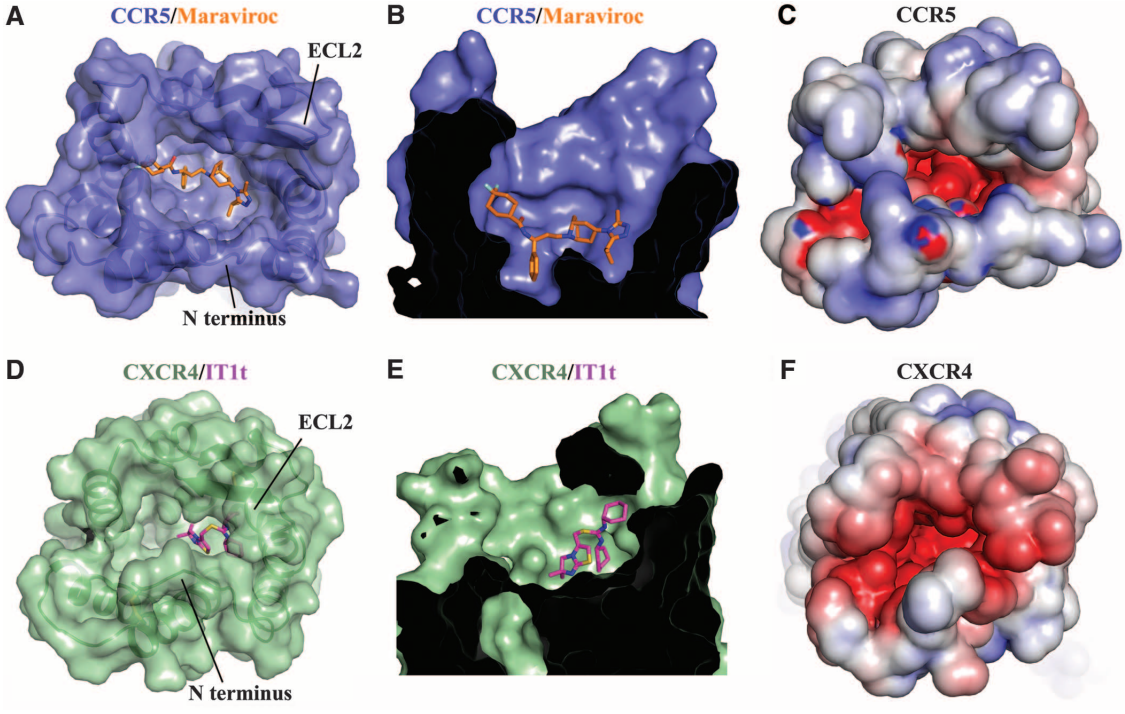

Fig. 3. Comparison of the ligand-binding pockets between CCR5-maraviroc and CXCR4-IT1t. (**A** and **D**) Top views of the ligand-binding pockets in CCR5 [(A), blue] and CXCR4 [(D), green], showing a more open ligand-binding pocket in CCR5. The receptors are shown in both cartoon and molecular surface representations. The ligands are shown in stick representation. maraviroc in CCR5 and IT1t in CXCR4 have orange and magenta carbons, respectively. (**B** and **E**) Side views of the ligand binding pockets in CCR5 (B) and CXCR4 (E), showing that maraviroc binds deeper in CCR5 than IT1t in CXCR4. (**C** and **F**) Top views of the ligand-binding pockets in CCR5 (C) and CXCR4 (F). Both CCR5 and CXCR4 surfaces are colored according to their electrostatic potential from red (negative) to blue (positive), showing different charge distribution within the ligand-binding pockets of these two receptors.

charge in the V3 loop for co-receptor selectivity. These residues form a cluster within the CCR5 ligand-binding pocket, which composes a potential binding site for gp120 (fig. S7).

To further understand the mechanism of co-receptor selectivity, we have built models of CCR5–R5-V3 and CXCR4–X4-V3 complexes based on the CCR5 structure and previous studies (*5*, *25*, *30*) (fig. S6B). The models suggest that the different charge distributions in the co-receptor ligand binding pockets and steric hindrances caused by residue substitutions may be major determinants of HIV-1 co-receptor selectivity (fig. S8) (*12*). These models initiate our understanding of HIV-1 tropism in a structural perspective; however, additional structures of the co-receptors in an apo state or complemented with the same or similar allosteric or orthosteric ligands, and complexes between the co-receptors and gp120-CD4, are needed to fully understand the mechanisms of HIV-1 tropism.

References and Notes

1. M. Baggiolini, *Nature* **392**, 565–568 (1998).
2. C. Gerard, B. J. Rollins, *Nat. Immunol.* **2**, 108–115 (2001).
3. C. Blanpain *et al.*, *Blood* **94**, 1899–1905 (1999).
4. E. A. Berger, P. M. Murphy, J. M. Farber, *Annu. Rev. Immunol.* **17**, 657–700 (1999).
5. B. Wu *et al.*, *Science* **330**, 1066–1071 (2010).
6. E. Coakley, C. J. Petropoulos, J. M. Whitcomb, *Curr. Opin. Infect. Dis.* **18**, 9–15 (2005).
7. A. Palani, J. R. Tagat, *J. Med. Chem.* **49**, 2851–2857 (2006).
8. *Aids Alert* **22**, 103 (2007).
9. C. Watson, S. Jenkinson, W. Kazmierski, T. Kenakin, *Mol. Pharmacol.* **67**, 1268–1282 (2005).
10. V. M. Muniz-Medina *et al.*, *Mol. Pharmacol.* **75**, 490–501 (2009).
11. J. Garcia-Perez *et al.*, *J. Biol. Chem.* **286**, 33409–33421 (2011).
12. Materials, methods, and discussion are available as supplementary materials on *Science* Online.
13. In Ballesteros-Weinstein numbering, a single most-conserved residue among the class A GPCRs is designated x.50, where x is the transmembrane helix number. All other residues on the helix are numbered relative to this conserved position.
14. Single-letter abbreviations for the amino acid residues are as follows: A, Ala; C, Cys; D, Asp; E, Glu; F, Phe; G, Gly; H, His; I, Ile; K, Lys; L, Leu; M, Met; N, Asn; P, Pro; Q, Gln; R, Arg; S, Ser; T, Thr; V, Val; W, Trp; Y, Tyr; and x, any amino acid.
15. S. Imamura *et al.*, *J. Med. Chem.* **49**, 2784–2793 (2006).
16. D. J. Scholten *et al.*, *Br. J. Pharmacol.* **165**, 1617–1643 (2012).
17. J. Garcia-Perez *et al.*, *J. Biol. Chem.* **286**, 4978–4990 (2011).
18. S. G. Rasmussen *et al.*, *Nature* **477**, 549–555 (2011).
19. V. Katritch, V. Cherezov, R. C. Stevens, *Annu. Rev. Pharmacol. Toxicol.* **53**, 531–556 (2013).
20. E. Y. Chien *et al.*, *Science* **330**, 1091–1095 (2010).
21. K. Palczewski *et al.*, *Science* **289**, 739–745 (2000).
22. L. Duma, D. Häussinger, M. Rogowski, P. Lusso, S. Grzesiek, *J. Mol. Biol.* **365**, 1063–1075 (2007).
23. C. Blanpain *et al.*, *J. Biol. Chem.* **278**, 5179–5187 (2003).
24. C. C. Huang *et al.*, *Science* **317**, 1930–1934 (2007).
25. M. J. Biscone *et al.*, *Virology* **351**, 226–236 (2006).
26. R. F. Speck *et al.*, *J. Virol.* **71**, 7136–7139 (1997).
27. R. L. Stanfield, M. K. Gorny, S. Zolla-Pazner, I. A. Wilson, *J. Virol.* **80**, 6093–6105 (2006).
28. A. Brelot, N. Heveker, M. Montes, M. Alizon, *J. Biol. Chem.* **275**, 23736–23744 (2000).
29. T. Cardozo *et al.*, *AIDS Res. Hum. Retroviruses* **23**, 415–426 (2007).
30. S. H. Xiang, B. Pacheco, D. Bowder, W. Yuan, J. Sodroski, *Virology* **438**, 5–13 (2013).

Acknowledgments: We thank I. Wilson, V. Katritch, and T. Handel for careful review and scientific feedback on the manuscript; A. Walker for assistance with manuscript preparation; C. Wang and D. Wacker for help on collection of x-ray diffraction data; and E. Kellenberger for providing the CCR5 model. Atomic coordinates and structure facors have been deposited in the Protein Data Bank with identification code 4MBS. This work was supported by "National Basic Research Program of China" grants 2012CB518000 and 2012CB910400; NIH grant R01 AI100604; National Science Foundation of China grants 31270766, 81161120425, and 81025017; and Shanghai Science and Technology Committee grants 11JC1414800 and 12PJ1410500. Additionally, V.C. and R.C.S. acknowledge support from NIH grant U54 GM094618 (Target GPCR-28); I.K. acknowledges support from U01 GM094612, U54 GM094618, and R01 GM071872. The data presented in this paper are tabulated in the main paper and in the supplementary materials.

Supplementary Materials

www.sciencemag.org/content/341/6152/1387/suppl/DC1
Materials and Methods
Supplementary Text
Figs. S1 to S8
Table S1
References (*31*–*40*)

4 June 2013; accepted 23 August 2013
Published online 12 September 2013;
10.1126/science.1241475

Pivotal Roles of cGAS-cGAMP Signaling in Antiviral Defense and Immune Adjuvant Effects

Xiao-Dong Li,[1]* Jiaxi Wu,[1]* Daxing Gao,[1] Hua Wang,[1] Lijun Sun,[1,2]† Zhijian J. Chen[1,2]†

Invasion of microbial DNA into the cytoplasm of animal cells triggers a cascade of host immune reactions that help clear the infection; however, self DNA in the cytoplasm can cause autoimmune diseases. Biochemical approaches led to the identification of cyclic guanosine monophosphate–adenosine monophosphate (cGAMP) synthase (cGAS) as a cytosolic DNA sensor that triggers innate immune responses. Here, we show that cells from cGAS-deficient (*cGas*$^{-/-}$) mice, including fibroblasts, macrophages, and dendritic cells, failed to produce type I interferons and other cytokines in response to DNA transfection or DNA virus infection. *cGas*$^{-/-}$ mice were more susceptible to lethal infection with herpes simplex virus 1 (HSV1) than wild-type mice. We also show that cGAMP is an adjuvant that boosts antigen-specific T cell activation and antibody production in mice.

The detection of foreign DNA invasion is a fundamental mechanism of host defense. In mammalian cells, the presence of foreign or self DNA in the cytoplasm is a danger signal that triggers the host innate immune responses (*1*). Through biochemical studies, we have recently identified cyclic guanosine monophosphate–adenosine monophosphate (cGAMP) synthase (cGAS) as an innate immune sensor of cytosolic DNA that triggers the production of type I interferons and other inflammatory cytokines (*2*, *3*). cGAS binds to DNA independently of its sequence; this binding activates cGAS to catalyze the synthesis of a specific cGAMP isomer, which contains both 2′-5′ and 3′-5′ phosphodiester linkages (*4*–*7*). This molecule, termed 2′3′cGAMP, functions as a second messenger that binds and activates the adaptor protein STING (*3*, *7*). STING then activates the protein kinases IκB kinase (IKK) and TANK-binding kinase 1 (TBK1), which in turn activate the transcription factors nuclear factor–κB (NF-κB) and interferon regulatory factor 3 (IRF3) to induce interferons and cytokines (*8*).

To investigate the function of cGAS in vivo, we generated a *cGas* knockout mouse strain, in which the first exon is spliced into a LacZ cassette, thus abrogating the expression of the endogenous locus (fig. S1, A and B) (*9*). The *cGas*$^{-/-}$ mice were born at the Mendelian ratio, and did not display any overt developmental abnormality (fig. S1, C and D). Quantitative reverse transcription polymerase chain reaction (qPCR) analyses of RNA from lung fibroblasts and bone marrow–derived macrophages (BMDMs) confirmed that the *cGas*$^{-/-}$ cells were defective in producing cGas RNA, whereas *cGas*$^{+/-}$ cells produced intermediate levels of cGas RNA (fig. S1, E and F).

We obtained lung fibroblasts from wild-type (WT), *cGas*$^{+/-}$, and *cGas*$^{-/-}$ mice as well as the goldenticket (gt/gt) mouse, which has a point mutation that results in the loss of expression of STING (*10*). Transfection of different types of DNA, including herring testis DNA (HT-DNA), *Escherichia coli* DNA, and interferon stimulatory DNA (ISD) [a 45-base-pair double-stranded DNA] (*11*), into the lung fibroblasts from WT and *cGas*$^{+/-}$ mice led to robust production of interferon-β (IFN-β) protein, as measured by enzyme-linked immunosorbent assay (ELISA) (Fig. 1A). In contrast, the *cGas*$^{-/-}$ and *Sting*$^{gt/gt}$

[1]Department of Molecular Biology, University of Texas Southwestern Medical Center, Dallas, TX 75390–9148, USA. [2]Howard Hughes Medical Institute, University of Texas Southwestern Medical Center, Dallas, TX 75390–9148, USA.

*These authors contributed equally to this work.
†Corresponding author. E-mail: Zhijian.Chen@UTSouthwestern.edu (Z.J.C.); Lijun.Sun@UTSouthwestern.edu (L.S.)

cells failed to produce any detectable level of IFN-β. Poly[I:C], a double-stranded RNA analog known to induce IFN-β through the RIG-I–like receptor (RLR) pathway (*12*), induced IFN-β normally in the absence of cGAS or STING. Interestingly, poly[dA:dT], which was previously shown to induce type I interferons through the RNA polymerase III–RIG-I–MAVS pathway (*13*, *14*), induced IFN-β normally in the *cGas*$^{-/-}$ and *Sting*$^{gt/gt}$ cells. qPCR analyses further confirmed that cGAS is essential for IFN-β RNA induction by different types of synthetic or bacterial DNA, except poly[dA:dT] (fig. S2A). Time-course experiments showed that IFN-β induction by ISD was completely abolished in *cGas*$^{-/-}$ lung fibroblasts even at early time points (2 to 8 hours) after the DNA transfection (fig. S2, B and C), indicating that cGAS is indispensable for IFN-β induction by cytosolic DNA.

To measure cGAMP production in WT and *cGas*$^{-/-}$ cells, we performed a bioassay that measures the cGAMP activity in cytoplasmic extracts from ISD-transfected cells. The extracts were heated at 95°C to denature most proteins, which were removed by centrifugation. The supernatants that might contain cGAMP were delivered to the human monocytic cell line THP1, which had been permeabilized with the bacterial toxin perfringolysin-O (PFO). Dimerization of IRF3, a hallmark of its activation, was then measured by native gel electrophoresis (fig. S2D). This assay showed that the extracts of ISD-transfected lung fibroblasts from WT but not *cGas*$^{-/-}$ mice contained the cGAMP activity, demonstrating that cGAS has a nonredundant role in catalyzing cGAMP synthesis in these cells in response to cytosolic DNA.

We next infected the lung fibroblasts with the DNA viruses herpes simplex virus 1 (HSV1), vaccinia virus (VACV) and a mutant strain of HSV1 called d109, which has a deletion of viral proteins such as ICP0 that is known to antagonize immune responses (*15*). IFN-β induction by each of these viruses was largely abolished in *cGas*$^{-/-}$ and *Sting*$^{gt/gt}$ cells, and partially inhibited in *cGas*$^{+/-}$ cells (Fig. 1B). In contrast, IFN-β induction by Sendai virus, an RNA virus known to activate the RIG-I pathway, was not affected by the deficiency in cGas or Sting. Delivery of cGAMP into the cytoplasm rescued IFN-β induction in *cGas*$^{-/-}$ cells but not *Sting*$^{gt/gt}$ cells (Fig. 1B). Similarly, induction of the chemokine CXCL10 by the DNA viruses was dependent on cGas and Sting (fig. S2E). Measurement of IRF3 dimerization showed that *cGas*$^{-/-}$ cells failed to activate IRF3 in response to transfection of HT-DNA or infection by WT HSV1 or the HSV1 strain 7134, which also lacks the interferon antagonist ICP0 (Fig. 1C) (*16*). The cGas deficiency did not impair IRF3 activation by Sendai virus. Thus, cGAS is required for IRF3 activation and cytokine induction by DNA viruses but not RNA viruses in mouse lung fibroblasts.

BMDMs from *cGas*$^{-/-}$ and *Sting*$^{gt/gt}$ mice were defective in producing IFN-β in response to transfection with HT-DNA or ISD (Fig. 1D). Similarly, IFN-β induction by VACV and the HSV1 strains d109 and 7134 was largely abolished in *cGas*$^{-/-}$ and *Sting*$^{gt/gt}$ BMDMs. However, IFN-β induction by WT HSV1 was severely but not completely blocked in either *cGas*$^{-/-}$ or *Sting*$^{gt/gt}$ BMDMs, suggesting that these cells possess another pathway that could partially compensate for the loss of the cGAS-STING pathway to detect WT HSV1 infection. The loss of cGAS or STING in BMDMs did not affect IFN-β induction by Sendai virus. Kinetic experiments showed that IFN-β induction by ISD and HSV1-d109 was abolished in *cGas*$^{-/-}$ BMDMs throughout the time course of stimulation (fig. S3, A and B). Similarly to IFN-β, the induction of TNFα by HT-DNA or ISD was abolished in *cGas*$^{-/-}$ or *Sting*$^{gt/gt}$ BMDMs (fig. S3C). qPCR analyses showed that the induction of IFN-β, interleukin-6 (IL6), and CXCL10 RNA by transfection of HT-DNA or ISD or infection with HSV1-d109 was completely dependent on cGas and Sting (fig. S3, D to F). In contrast, the RNA levels of these cytokines induced by poly[I:C] or Sendai virus were not affected by the deficiency in cGas or Sting.

We obtained conventional dendritic cells (cDC) and plasmacytoid DCs (pDC) by culturing bone marrow in conditioned media containing granulocyte-macrophage colony-stimulating factor (GM-CSF) and Flt3 ligand (Flt3L), respectively. The GM-CSF DCs, which contain largely cDC, from the *cGas*$^{-/-}$ and *Sting*$^{gt/gt}$ mice failed to induce IFN-α or IFN-β in response to transfection of HT-DNA or ISD (Fig. 2, A and B). The loss of cGAS or STING in GM-CSF DCs abolished

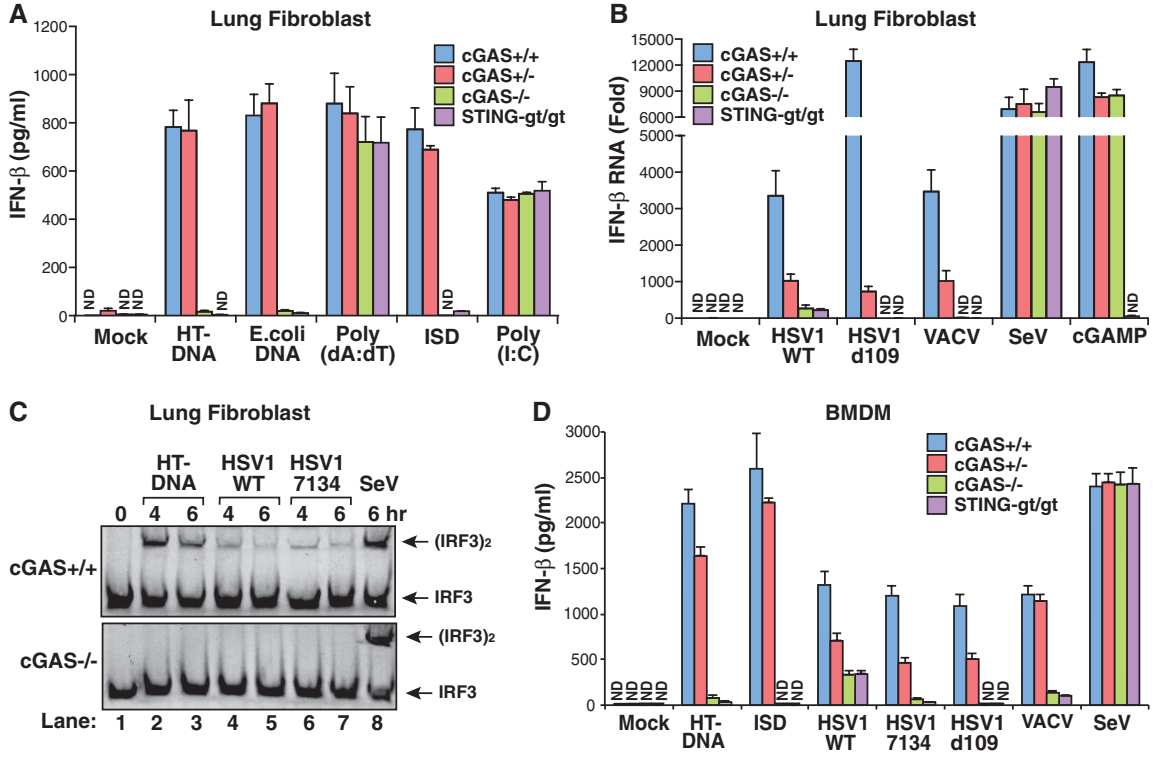

Fig. 1. cGAS is essential for IRF3 activation and IFN-β induction by DNA transfection and DNA virus infection in fibroblasts and macrophages. (**A**) Mouse lung fibroblasts were transfected with different forms of DNA or poly[I:C] (2 μg/ml) for 24 hours, followed by measurement of IFN-β protein by ELISA. Unless indicated otherwise, lipofectamine 2000 was used in all transfection experiments. (**B**) Lung fibroblasts were infected with the indicated viruses or stimulated with 2′3′cGAMP (200 nM) for 9 hours, followed by measurement of IFN-β RNA by qPCR. (**C**) Lung fibroblasts were transfected with HT-DNA or infected with HSV1 or Sendai virus for the indicated times. Cell extracts were analyzed for IRF3 dimerization by native gel electrophoresis. (**D**) BMDMs were transfected with HT-DNA or ISD or infected with the indicated virus for 20 hours, and then IFN-β levels were measured by ELISA. For the qPCR results in this and other figures, the error bars represent SDs of triplicate measurements. Unless otherwise indicated, the error bars of ELISA assays in this and other figures represent variation ranges of duplicate measurements. ND, not detected.

IFN-β induction by HSV1-d109 and VACV and partially inhibited IFN-β induction by WT HSV1. In contrast, the deficiency in cGAS or STING did not impair IFN-α or IFN-β induction by Sendai virus. qPCR experiments further confirmed that cGAS and STING were essential for the induction of IFN-β, IL6, and CXCL10 RNA by transfection with HT-DNA or ISD or infection with HSV1-d109, whereas the induction of these cytokines by poly[I:C] or Sendai virus was independent of cGAS or STING (fig. S4, A to C).

pDCs are known to express TLR9 that is responsible for the induction of type I interferons by synthetic CpG DNA containing phosphorothioate bonds (*17*). When the CpG DNA was used to stimulate Flt3L DCs, which contain largely pDCs, in the presence or absence of liposome (lipofectamine 2000), it induced robust production of IFN-α and IFN-β even in the *cGas*$^{-/-}$ and *Sting*$^{gt/gt}$ cells (Fig. 2C and fig. S4D). In contrast, other forms of DNA, including ISD, poly[dA:dT], and genomic DNA from *E. coli* and *Vibrio cholerae*, induced IFN-α in Flt3L DCs only in the presence of liposome, and this induction by each DNA was abolished in the absence of cGAS or STING. The strong dependency of IFN-α induction by poly[dA:dT] on cGAS and STING in pDCs suggests that the cGAS-STING pathway, but not the Pol-III–RIG-I pathway, plays a major role in sensing the DNA in these cells. The Flt3L DCs from the *cGas*$^{-/-}$ and *Sting*$^{gt/gt}$ mice induced IFN-α and IFN-β in response to infection by Sendai virus but not HSV1 (Fig. 2D and fig. S4D). Together, these results demonstrate that cGAS is responsible for detecting natural DNA (e.g., bacterial DNA) and DNA virus infections in dendritic cells.

To determine the role of cGAS in immune defense against DNA viruses in vivo, we infected WT and *cGas*$^{-/-}$ mice with HSV1 via the intravenous route (Fig. 3). ELISA analyses showed that the sera of WT mice contained elevated levels of IFN-α and IFN-β, which peaked at 8 and 4 hours, respectively, after HSV1 infection [1×10^7 plaque-forming units (pfu) per mouse]. The levels of IFN-α and IFN-β were severely attenuated in the *cGas*$^{-/-}$ mice infected with the same infectious dose of HSV1 (Fig. 3, A and B). In an independent experiment in which the mice were monitored for their survival after infection with HSV1 at the infectious dose of 1×10^6 pfu per mouse, four out of the five *cGas*$^{-/-}$ mice developed ataxia and paralysis 3 days after the virus infection and died a few hours after these symptoms appeared (Fig. 3C). The fifth *cGas*$^{-/-}$ mouse died on day 4 after infection. Three out of five WT mice developed these symptoms on day 6 and died shortly afterward. When the brains of WT and *cGas*$^{-/-}$ mice were extracted to measure viral titers on day 3 after infection, high levels of HSV1 were detected in all five *cGas*$^{-/-}$ mice, whereas none of the WT mice had detectable levels of HSV1 in the brain (Fig. 3D). Similar survival curves were observed and similar viral titers in the brains were detected in independent experiments where the infectious dose of HSV1 was increased to 1×10^7 pfu per mouse (fig. S5, A and B). The susceptibility of *cGas*$^{-/-}$ mice to HSV1 infection was similar to that of *Sting*$^{gt/gt}$ mice, which also had marked reduction of IFN-α and IFN-β in the sera, and these mice died within 3 to 4 days after HSV1 infection (fig. S5, C to E) (*18*).

Our results that cGAS is essential for the induction of type I interferons by cytosolic DNA in multiple cell types, including antigen-presenting cells, suggest that the cGAS product, 2′3′cGAMP, may be used to substitute for the immune stimulatory effect of DNA, including the adjuvant effect of DNA vaccines (*19*). To explore the potential adjuvant effect of 2′3′cGAMP, we injected the model protein antigen ovalbumin (OVA) in the absence or presence of 2′3′cGAMP into WT

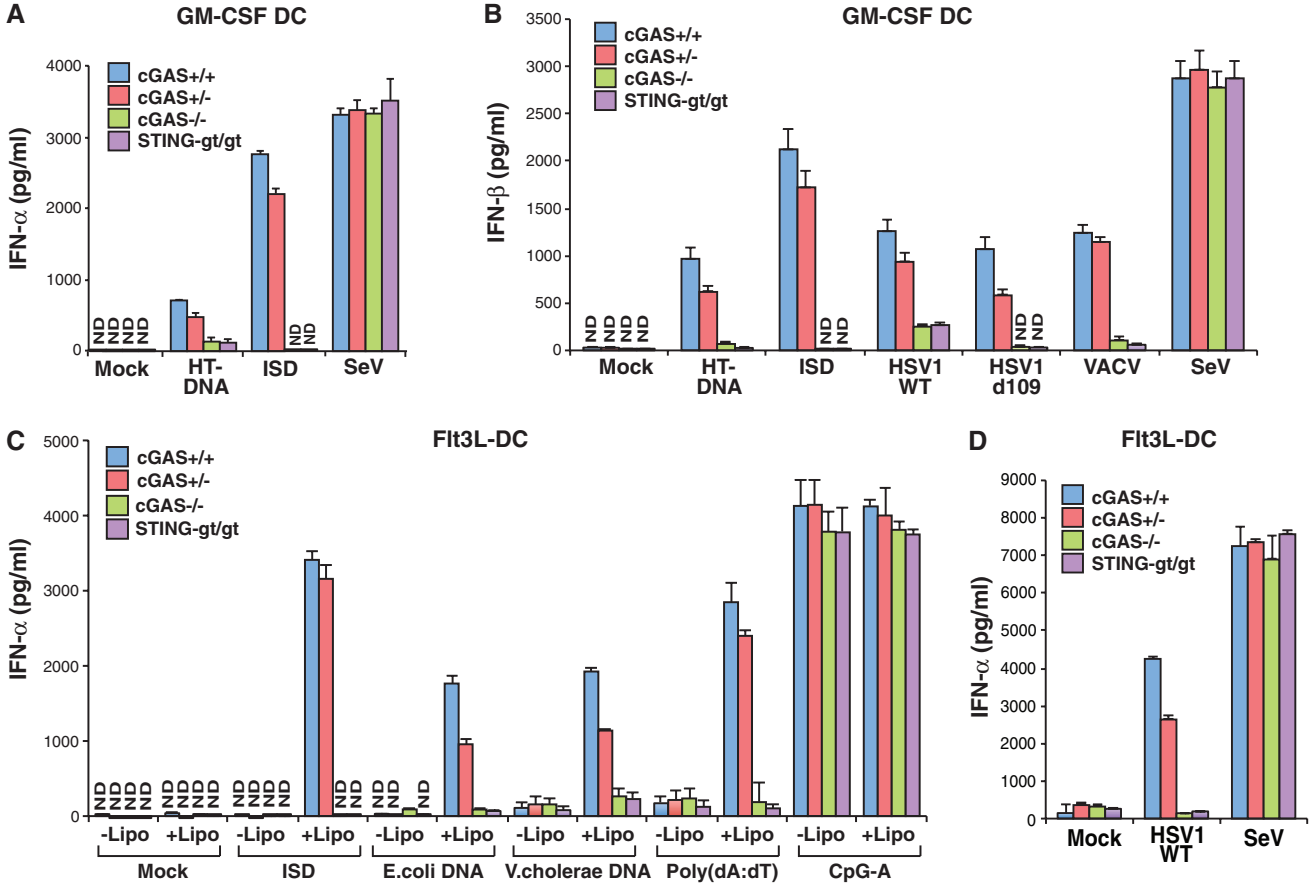

Fig. 2. cGAS is essential for type I interferon induction by DNA transfection and DNA virus infection in dendritic cells. (**A**) GM-CSF–induced DCs were transfected with HT-DNA or ISD or infected with Sendai virus for 20 hours, followed by measurement of IFN-α by ELISA. (**B**) GM-CSF DCs were transfected with the indicated DNA or viruses for 20 hours, and then IFN-β was measured by ELISA. (**C** and **D**) Flt3L-induced dendritic cells (Flt3L-DCs) were incubated with the indicated DNA for 16 hours in the absence or presence of lipofectamine 2000 (C), or infected with HSV1 or Sendai virus (D) for 16 hours, followed by measurement of IFN-α by ELISA. Lipo, lipofectamine 2000.

or *Sting*$^{gt/gt}$ mice via the intramuscular route. The mice were boosted once on day 10 with the same antigen formulation. ELISA analyses showed that 2′3′cGAMP strongly enhanced the production of OVA-specific antibodies on day 17 in the WT mice but not the *Sting*$^{gt/gt}$ mice (Fig. 4A). This adjuvant effect of 2′3′cGAMP was also reduced in type I interferon receptor–deficient mice (*Ifnar*$^{-/-}$) (fig. S6). To investigate the effect of 2′3′cGAMP on T cell activation, splenic leukocytes isolated from the WT mice, which had been immunized with OVA or OVA + 2′3′cGAMP for 7 days, were cultured with an OVA peptide known to stimulate CD4 T cells through the major histocompatibility complex (MHC) class II molecule I-A^b or another OVA peptide that stimulates CD8 T cells through the MHC class I molecule H-2K^b. Both CD4 and CD8 T cells from the mice immunized with OVA + 2′3′cGAMP, but not OVA alone, produced elevated levels of IFN-γ and IL-2 after stimulation with the cognate peptides (Fig. 4, B and C). Flow cytometry analysis using a tetramer composed of an OVA peptide in complex with H-2K^b showed a marked increase in the percentage of the tetramer-positive CD8 T cells in the mice immunized with OVA + 2′3′cGAMP, indicating that 2′3′cGAMP stimulated the expansion of CD8 T cells bearing the OVA-specific T cell receptor (Fig. 4D). Taken together, these results indicate that 2′3′cGAMP functions as an immune adjuvant to stimulate antigen-specific T cell and B cell responses.

Here, we provide genetic evidence that cGAS is essential for the induction of type I interferons and other inflammatory cytokines by DNA transfection and DNA virus infection. With the exception of poly[dA:dT] and CpG DNA, most DNA molecules, especially those found in nature (e.g, bacterial and viral DNA), stimulate type I interferons exclusively through the cGAS-cGAMP-STING pathway. In multiple cell types, including fibroblasts, macrophages, and dendritic cells, the induction of type I interferons by vaccinia viruses and several strains of HSV1 is completely dependent on cGAS and STING. Notably, however, IFN-β induction by WT HSV1 is severely but not completely abolished in BMDMs and GM-CSF DCs from *cGas*$^{-/-}$ or *Sting*$^{gt/gt}$ mice. It is possible that other putative DNA sensors, such as IFI16 or DDX41, may be involved in this residual induction of IFN-β by WT HSV1 (*20*, *21*). However, the roles of these other putative DNA sensors in vivo have yet to be investigated through genetic experiments. In the case of cGAS, the phenotypes

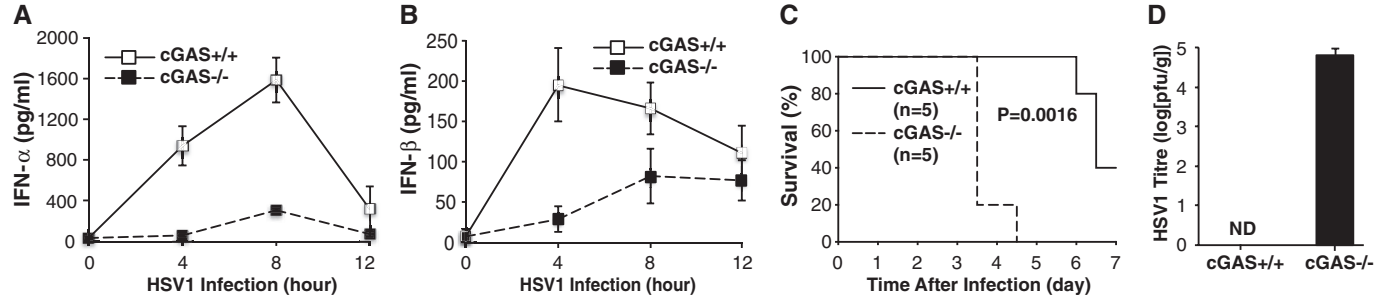

Fig. 3. cGAS is essential for immune defense against HSV1 infection in vivo. (**A** and **B**) WT and *cGas*$^{-/-}$ mice (n = 5 each) were infected intravenously with HSV1 at 1 × 10^7 pfu per mouse, and then sera were collected at different time points as indicated. The levels of IFN-α and IFN-β were measured by ELISA. Error bars, mean ± SD. (**C**) WT and *cGas*$^{-/-}$ mice (n = 5 each) were infected intravenously with HSV1 at 1 × 10^6 pfu per mouse. The survival of each mouse was monitored for 7 days. (**D**) Brains of the HSV1-infected mice were excised on day 3 to prepare homogenates, which were used to measure viral titers by the plaque assay. The viral titer was recorded as pfu per gram of brain (pfu/g). The experiments shown in (C) and (D) were repeated in an independent set of experiments, except that the HSV1 infectious dose was increased to 1 × 10^7 pfu per mouse (fig. S5, A and B).

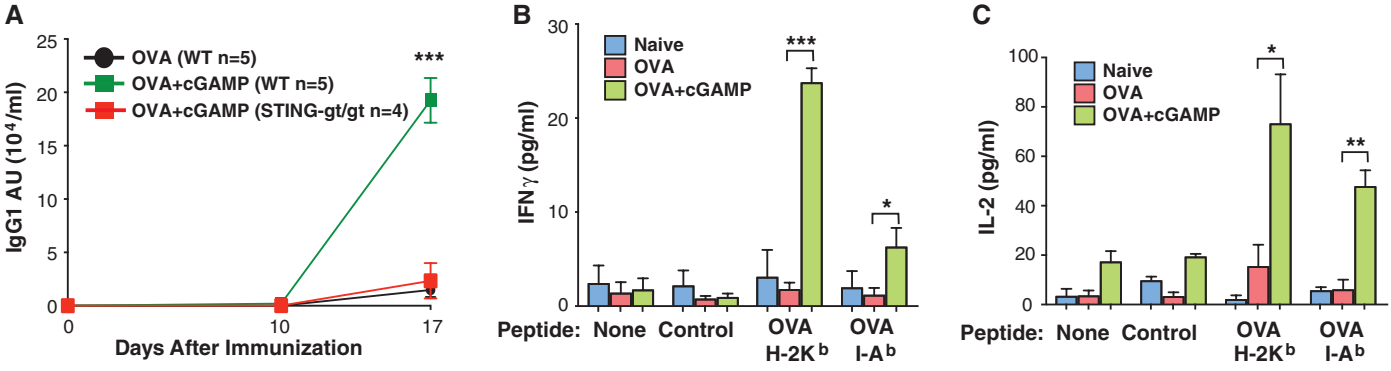

Fig. 4. cGAMP is an adjuvant that stimulates T cell activation and antibody production in a STING-dependent manner. (**A**) WT and *Sting*$^{gt/gt}$ mice were injected intramuscularly with OVA alone or OVA + 2′3′cGAMP on day 1 and day 10. Sera were collected at the indicated time points to measure OVA-specific immunoglobulin G1 (IgG1) by ELISA. Error bar, mean ± SEM. Data are representative of three independent experiments, each with four or five mice per group as indicated. AU, absorbance units at OD450. (**B** and **C**) WT mice were immunized with OVA or OVA + 2′3′cGAMP as above. Spleen leukocytes were collected on day 7 and stimulated with OVA peptides known to complex with MHC class I (H-2K^b) or class II (I-A^b). Secretion of IFN-γ (B) and IL-2 (C) by T cells was measured by ELISA. *P < 0.05, ** P < 0.01, and ***P < 0.001; Student's t test. (**D**) Similar to (B), except that fluorescence-activated cell sorting analysis was performed to measure the percentage of CD8 T cells bearing the T cell receptor specific for an OVA-H-2K^b tetramer. *P < 0.05, Student's t test. Data shown in (B) to (D) are representative of two independent experiments, each with three mice per group.

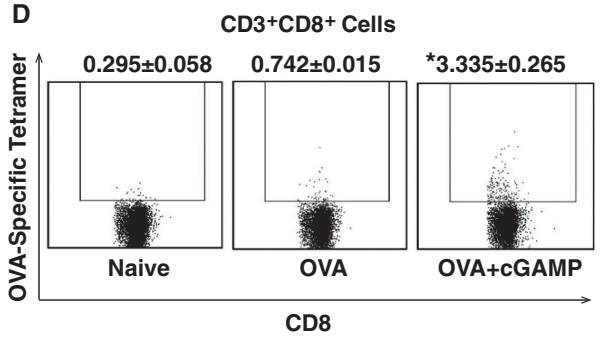

of *cGas*$^{-/-}$ mice are strikingly similar to those of *Sting*$^{-/-}$ mice [this study and (*18*)]. These results, together with our biochemical data showing that cGAS is a cytosolic enzyme activated by its binding to generic DNA (*2*, *3*), formally demonstrate that cGAS is a nonredundant and general cytosolic DNA sensor that activates STING.

We present evidence that 2′3′cGAMP is an effective adjuvant that boosts the production of antigen-specific antibodies and T cell responses in mice. Although the bacterial second messengers cyclic di-GMP and cyclic di-AMP are being developed as potential vaccine adjuvants (*22*), 2′3′cGAMP is a much more potent ligand of STING than any of the bacterial cyclic dinucleotides (*7*). Thus, 2′3′cGAMP may be developed as an adjuvant for next-generation vaccines to prevent or treat human diseases, including infectious diseases and cancer.

References and Notes

1. L. A. O'Neill, *Science* **339**, 763–764 (2013).
2. L. Sun, J. Wu, F. Du, X. Chen, Z. J. Chen, *Science* **339**, 786–791 (2013).
3. J. Wu *et al.*, *Science* **339**, 826–830 (2013).
4. A. Ablasser *et al.*, *Nature* **498**, 380–384 (2013).
5. E. J. Diner *et al.*, *Cell Rep* **3**, 1355–1361 (2013).
6. P. Gao *et al.*, *Cell* **153**, 1094–1107 (2013).
7. X. Zhang *et al.*, *Mol. Cell* **51**, 226–235 (2013).
8. H. Ishikawa, G. N. Barber, *Cell. Mol. Life Sci.* **68**, 1157–1165 (2011).
9. *cGas*$^{-/-}$ mice were generated by in vitro fertilization using sperm harboring a targeted insertion at the *cGas/Mb21d1* locus. For details, see materials and methods in the supplementary materials.
10. J. D. Sauer *et al.*, *Infect. Immun.* **79**, 688–694 (2011).
11. D. B. Stetson, R. Medzhitov, *Immunity* **24**, 93–103 (2006).
12. M. Yoneyama *et al.*, *Nat. Immunol.* **5**, 730–737 (2004).
13. A. Ablasser *et al.*, *Nat. Immunol.* **10**, 1065–1072 (2009).
14. Y. H. Chiu, J. B. Macmillan, Z. J. Chen, *Cell* **138**, 576–591 (2009).
15. L. A. Samaniego, L. Neiderhiser, N. A. DeLuca, *J. Virol.* **72**, 3307–3320 (1998).
16. G. T. Melroe, N. A. DeLuca, D. M. Knipe, *J. Virol.* **78**, 8411–8420 (2004).
17. O. Takeuchi, S. Akira, *Cell* **140**, 805–820 (2010).
18. H. Ishikawa, Z. Ma, G. N. Barber, *Nature* **461**, 788–792 (2009).
19. C. J. Desmet, K. J. Ishii, *Nat. Rev. Immunol.* **12**, 479–491 (2012).
20. Z. Zhang *et al.*, *Nat. Immunol.* **12**, 959–965 (2011).
21. L. Unterholzner *et al.*, *Nat. Immunol.* **11**, 997–1004 (2010).
22. W. Chen, R. Kuolee, H. Yan, *Vaccine* **28**, 3080–3085 (2010).

Acknowledgments: We thank R. Hammer and the transgenic core facility at University of Texas Southwestern Medical Center for performing in vitro fertilization, S. Murray for technical assistance in HSV1 infection in mice, and N. DeLuca and D. Knipe for providing HSV1 strains d109 and 7134, respectively. This work was supported by grants from NIH (AI-093967) and the Cancer Prevention and Research Institute of Texas (RP110430). H.W. was supported by an NIH postdoctoral training grant (5T32AI070116). Z.J.C. is an investigator of Howard Hughes Medical Institute. The University of Texas has filed a patent on using cGAMP and its derivatives as vaccine adjuvants (U.S. patents 61/829,251 and 61/739.072; pharmaceutical targeting of a mammalian cyclic di-nucleotide signaling pathway). Materials including the *cGas*$^{-/-}$ mice may be requested upon signing a materials transfer agreement. The data presented in this manuscript are tabulated in the main paper and the supplementary materials.

Supplementary Materials

www.sciencemag.org/content/341/6152/1390/suppl/DC1
Materials and Methods
Figs. S1 to S6
References (*23*–*25*)

31 July 2013; accepted 16 August 2013
Published online 29 August 2013;
10.1126/science.1244040

Constitutive μ-Opioid Receptor Activity Leads to Long-Term Endogenous Analgesia and Dependence

G. Corder,[1] S. Doolen,[1] R. R. Donahue,[1] M. K. Winter,[2] B. L. Jutras,[3] Y. He,[4] X. Hu,[4] J. S. Wieskopf,[5] J. S. Mogil,[5] D. R. Storm,[6] Z. J. Wang,[4] K. E. McCarson,[2] B. K. Taylor[1]*

Opioid receptor antagonists increase hyperalgesia in humans and animals, which indicates that endogenous activation of opioid receptors provides relief from acute pain; however, the mechanisms of long-term opioid inhibition of pathological pain have remained elusive. We found that tissue injury produced μ-opioid receptor (MOR) constitutive activity (MOR_{CA}) that repressed spinal nociceptive signaling for months. Pharmacological blockade during the posthyperalgesia state with MOR inverse agonists reinstated central pain sensitization and precipitated hallmarks of opioid withdrawal (including adenosine 3′,5′-monophosphate overshoot and hyperalgesia) that required *N*-methyl-D-aspartate receptor activation of adenylyl cyclase type 1. Thus, MOR_{CA} initiates both analgesic signaling and a compensatory opponent process that generates endogenous opioid dependence. Tonic MOR_{CA} suppression of withdrawal hyperalgesia may prevent the transition from acute to chronic pain.

Chronic pain is determined by facilitatory mechanisms such as long-term potentiation (LTP) of synaptic strength in dorsal horn neurons (*1*–*3*). Whereas exogenously applied opiates prevent (*4*, *5*) and/or erase (*6*) spinal LTP, and spinal enkephalin release exerts inhibitory control of acute pain intensity soon after tissue injury (*7*, *8*), it remains unclear how the endogenous opioid system might persistently repress pathological pain. Opiates provide powerful pain relief, but repeated administration leads to the development of compensatory neuroadaptations underlying opiate tolerance and dependence (*9*), including the selective up-regulation of calcium-sensitive adenylyl cyclase (AC) isoforms (*10*, *11*). Cessation of opiates leads to cellular and behavioral symptoms of withdrawal (*12*–*16*). An intriguing hypothesis of drug addiction suggests that chronic opiates increase μ-opioid receptor (MOR) constitutive activity (MOR_{CA}) to preserve physical and psychological dependence (*17*–*21*), which is enhanced by enkephalins (*22*). Whether MORs adopt constitutive signaling states in other disease syndromes, such as chronic pain, is unknown. We tested the hypothesis that tissue injury increases MOR_{CA} in the spinal cord. With sufficient time after injury, enhanced basal MOR signaling should produce endogenous cellular and physical dependence in the CNS.

We first discovered that spinal opioid signaling promotes the intrinsic recovery of acute inflammatory pain and orchestrates long-lasting antinociception. In mice, a unilateral intraplantar injection of complete Freund's adjuvant (CFA) produced mechanical hyperalgesia that resolved within 10 days (Fig. 1A). Subcutaneous chronic minipump infusion of naltrexone hydrochloride (NTX), a nonselective opioid receptor antagonist, prolonged hyperalgesia throughout the 14-day infusion period in CFA-injured mice ($F_{3,17} = 25.4$, $P < 0.0001$) (Fig. 1B), although it had no effect in sham-injured mice. When the NTX pump was removed, hyperalgesia rapidly declined. NTX did not alter the induction phase of CFA-induced hyperalgesia (fig. S1, A and B, and supplementary text S1); however, when delivered 21 days after CFA injection (CFA-21d mice) in the complete absence of pain, systemic NTX reinstated hyperalgesia ($F_{1,21} = 41$, $P < 0.0001$) (Fig. 1C) in a dose-dependent manner with no effect in sham-injured mice (Fig. 1D). By contrast, systemic injection of naltrexone methobromide (NMB), an opioid receptor antagonist that does not cross the blood-brain barrier, failed to alter mechanical thresholds at either the ipsilateral or contralateral paws (both $P > 0.05$) (Fig. 1E). Intrathecal administration of either NTX or NMB precipitated robust hyperalgesia in CFA-treated mice after 21 days at both the injured ipsilateral paw ($P < 0.05$) (Fig. 1F) and uninjured contralateral paw ($P < 0.05$) (Fig. 1F), with no effect in sham-injured mice (Fig. 1G). NTX also induced heat hyperalgesia ($P < 0.05$) (Fig. 1H), as well as spontaneous pain in males ($P < 0.05$) (Fig. 1I) and females (fig. S3). Intrathecal NTX reinstated hyperalgesia in a model of postsurgical pain ($P < 0.05$)

[1]Department of Physiology, University of Kentucky, Lexington, KY 40536, USA. [2]Department of Pharmacology, Toxicology and Therapeutics, University of Kansas Medical Center, Kansas City, KS 66160, USA. [3]Department of Microbiology, Immunology and Molecular Genetics, University of Kentucky, Lexington, KY 40536, USA. [4]Department of Biopharmaceutical Sciences, University of Illinois, Chicago, IL 60612, USA. [5]Department of Psychology and Alan Edwards Centre for Research on Pain, McGill University, Montreal, Quebec H3A 1B1, Canada. [6]Department of Pharmacology, School of Medicine, University of Washington, Seattle, WA 98195, USA.

*Corresponding author. E-mail: brad.taylor@uky.edu

(Fig. 1J) (*23*), in several other models of inflammatory and neuropathic pain, and in multiple mouse strains.

Whether signaling with MOR and heterotrimeric GTP-binding protein (G protein) can be maintained for sufficient duration to oppose chronic pain is unknown. First, we found that disruption of $G\alpha_{i/o}$ signaling with intrathecal injection of pertussis toxin precipitated hyperalgesia in CFA-21d mice but not sham-injured mice ($P < 0.05$) (Fig. 1K). Second, we assessed guanosine-5′-*O*-(3-[^{35}S]thio)triphosphate ([^{35}S]GTP-γ-S) binding in fresh spinal cord slices (Fig. 1, L and M). In control slices, the MOR-selective agonist [D-Ala^2, *N*-methyl-Phe^4, Gly-ol^5]-enkephalin (DAMGO) elicited a stimulation of [^{35}S]GTP-γ-S binding with a maximum physiological effect (E_{max}) and median effective concentration (EC_{50}) of 58.02 ± 0.67% and 0.24 ± 0.01 μM, respectively (Fig. 1M). E_{max} was potentiated in CFA-21d slices not only in the ipsilateral dorsal horns (79.85 ± 7.35%, $P < 0.05$ compared with sham-injured) (Fig. 1M) but also in the contralateral dorsal horns (74.05 ± 4.13%, $P < 0.05$ compared with sham-injured)

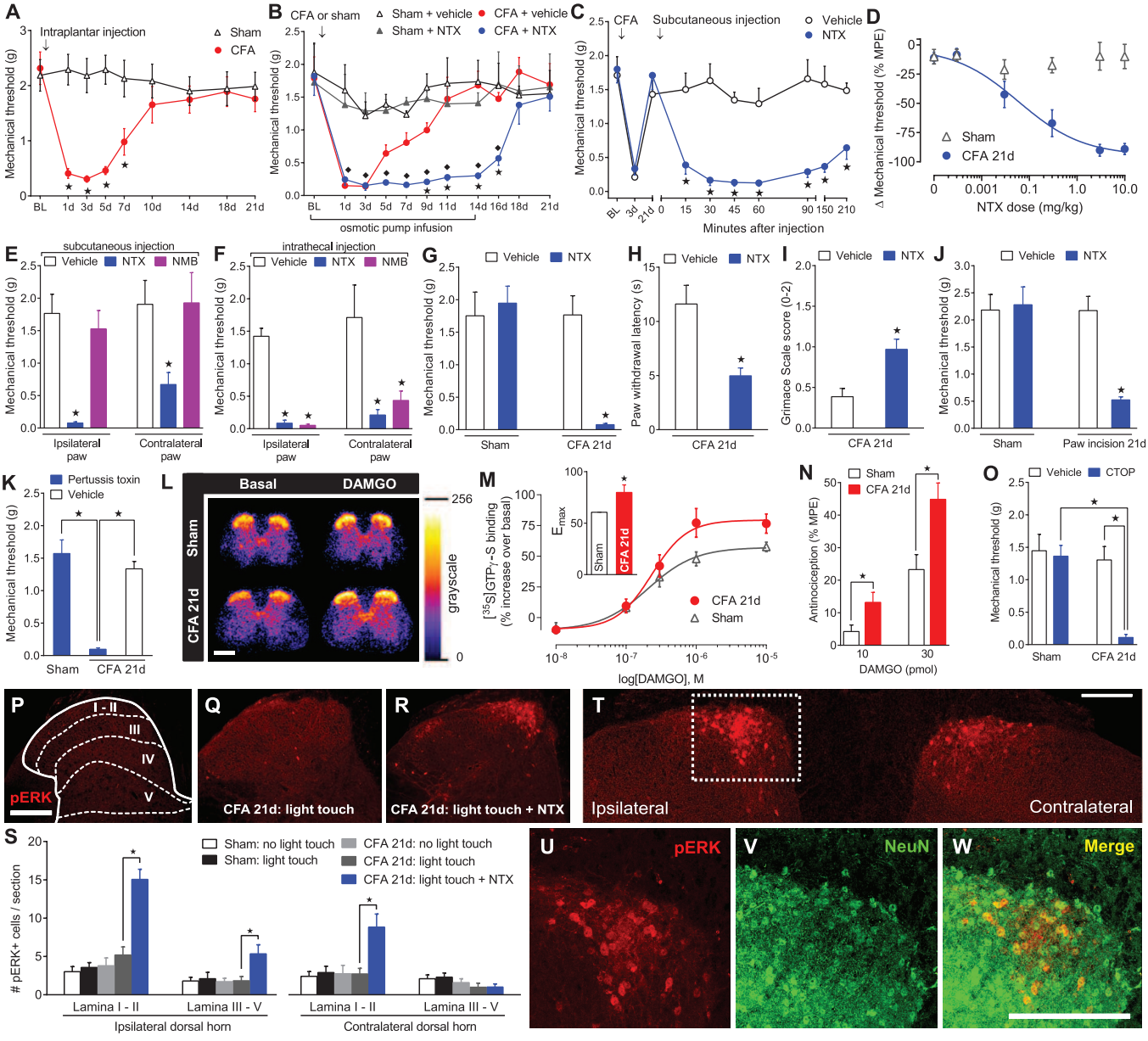

Fig. 1. Injury-induced pain sensitization is tonically opposed by spinal MOR–G-protein signaling. (**A**) Progression of mechanical hyperalgesia after intraplantar CFA (5 μl) injection ($n = 10$). (**B**) Resolution of hyperalgesia during and 14 days after infusion of NTX (10 mg/kg of body weight per day, subcutaneously) in sham-injured and CFA-injected mice ($n = 5$ to 6). ★$P <$ 0.05 compared with CFA+saline, ◆$P < 0.05$ compared with Sham+NTX. (**C**) Time course of reinstatement of hyperalgesia after subcutaneous NTX (3 mg/kg) in CFA-21d mice ($n = 6$ to 13). (**D**) Dose-response effects of NTX on hyperalgesia ($n = 6$ per dose). MPE: maximal possible effect. (**E** and **F**) Effect on hyperalgesia of (E) subcutaneous or (F) intrathecal NTX (3 mg/kg or 1 μg) or NMB (3 mg/kg or 0.3 μg) ($n = 5$ to 10). (**G** to **J**) Effect of intrathecal NTX (1 μg) on reinstatement of (G) mechanical hyperalgesia in sham-injured and CFA-injected mice ($n = 5$ to 8), (H) heat hyperalgesia ($n = 5$ to 10), (I) spontaneous pain ($n = 4$ to 8), and (J) postoperative pain ($n = 6$ to 11). (**K**) Effect of intrathecal pertussis toxin (0.5 μg) on hyperalgesia ($n = 6$). (**L**) Representative radiograms and (**M**) dose-response effects of DAMGO-stimulated [^{35}S]GTP-γ-S binding in lumbar spinal cord; (inset) binding E_{max} ($n = 7$ to 9). (**N**) Effect of DAMGO administered intrathecally on hotplate latency ($n = 8$). (**O**) Effect of intrathecal CTOP (100 ng) on hyperalgesia ($n = 6$ to 7). (**P** to **R**) Representative images and (**S**) dorsal horn laminar quantification (I and II and III to V) of light touch-evoked pERK after intrathecal NTX (1 μg) ($n = 5$ to 7). (**T**) Confocal image of pERK+ cells. (**U** to **W**) From boxed region in (T): Co-localization of pERK with the biomarker NeuN. All scale bars, 200 μm. ★$P < 0.05$ for all panels. All data shown as means ± SEM. See fig. S1 for full time-course data for (E) to (J) and (O).

(fig. S4), with no change in the EC_{50}. Third, the antinociceptive effects of intrathecal DAMGO were potentiated in CFA-21d mice ($P < 0.05$) (Fig. 1N), which reflected increases in receptor number, receptor affinity, or descending modulatory circuits. Fourth, intrathecal injection of Phe-Cys-Tyr-Trp-Orn-Thr-Pen-Thr-NH_2 (CTOP), a MOR-selective antagonist, reinstated hyperalgesia in CFA-21d mice but not sham-injured mice ($P < 0.05$) (Fig. 1M).

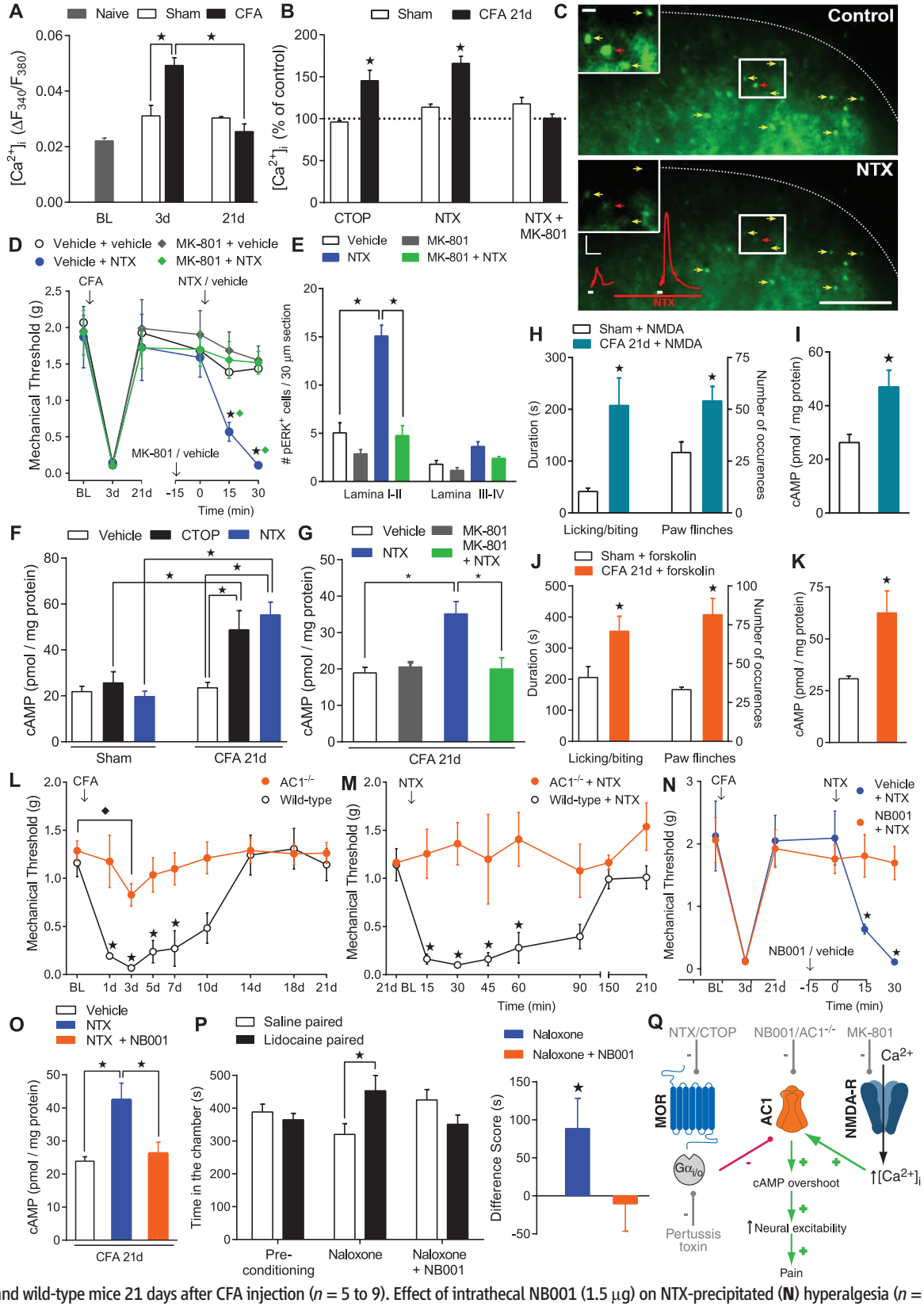

Fig. 2. Pain reinstatement requires potentiated NMDAR activation of calcium-sensitive AC 1. (**A**) Time course of glutamate-evoked (0.3 mM) $[Ca^{2+}]_i$ in spinal cord slices from sham-injured and CFA-injected mice ($n = 4$ to 7 mice) shown as the ratio of change in fluorescence intensity at 340 nm and 380 nm ($\Delta F_{340}/F_{380}$). Naïve BL, baseline. (**B**) Effect of CTOP (1 μM), NTX (10 μM), or NTX+MK-801 (100 μM) on $[Ca^{2+}]_i$. Values are relative to predrug control responses ($n = 3$ to 5 mice). (**C**) Representative fluorescence intensity at 380 nm, image of dorsal horn neurons from a CFA-21d slice responding to glutamate before (top) and after NTX (10 μM) (bottom) (yellow arrows). Decrease in fluorescence intensity corresponds to increase in $[Ca^{2+}]_i$. The red traces illustrate the rise in $[Ca^{2+}]_i$ for the indicated cell (red arrow). (Insets) Areas in white boxes. Scale bars: 0.02 for $\Delta F/F$ (vertical) and 3 min (horizontal), and 100 μm and 10 μm (inset). Effect of intrathecal MK-801 (1 μg) on NTX-precipitated (1 μg) (**D**) hyperalgesia and (**E**) touch-evoked dorsal horn pERK expression ($n = 5$ to 10). (**F**) Spinal cord cAMP levels after intrathecal vehicle ($n = 14$ to 18), CTOP (100 ng; $n = 6$), or NTX (1 μg; $n = 6$ to 10). (**G**) Effect of intrathecal MK-801 (1 μg) on NTX-precipitated spinal cAMP overshoot ($n = 5$). (**H** to **K**) Effect of intrathecal NMDA (3 pmol; $n = 5$ to 7) or forskolin (1.5 μg; $n = 6$) on (H and J) spontaneous nocifensive behaviors and (I and K) spinal cAMP levels. (**L**) Progression of mechanical hyperalgesia and (**M**) effect of intrathecal NTX in $AC1^{-/-}$ and wild-type mice 21 days after CFA injection ($n = 5$ to 9). Effect of intrathecal NB001 (1.5 μg) on NTX-precipitated (**N**) hyperalgesia ($n = 4$ to 7), (**O**) spinal cAMP levels ($n = 6$ to 9), and (**P**) affective pain ($n = 6$ to 12). (**Q**) Schematic of cellular pathways involved in endogenous opioid withdrawal and pain reinstatement. ★, ◆, *$P < 0.05$.

We next asked whether central sensitization (increased responsiveness of CNS nociceptive neurons to normal or subthreshold afferent input) silently persists in the posthyperalgesia state under the control of endogenous MOR inhibition. Tested 21 days after CFA injection, an innocuous light touching of the injured hindpaw did not increase the dorsal horn expression of phosphorylated extracellular signal–regulated kinase (pERK) (Fig. 1, Q and S). However, intrathecal NTX increased touch-evoked pERK in lamina I and II ($P < 0.05$) (Fig. 1, R and S, and fig. S4) and III to V ($P < 0.05$) (Fig. 1, R and S). NTX also increased pERK at the contralateral dorsal horn (opiates $P < 0.05$) (Fig. 1, S and T). Confocal microscopy revealed that pERK was expressed in neurons (Fig. 1, U to W, and fig. S5) but not in microglia or astrocytes (fig. S5).

We next tested the hypothesis that *N*-methyl-D-aspartate receptor (NMDAR)–Ca^{2+}-dependent mechanisms of central sensitization (*1*, *24*) continue to operate after the resolution of inflammatory pain. Using live-cell Fura-2 ratiometric analysis in adult spinal cord slices (*25*), we found that glutamate-evoked intracellular calcium (Ca^{2+}) in lamina II neurons was potentiated 3 days after CFA injection and then resolved by day 21 ($F_{3,17} = 15$, $P < 0.0001$) (Fig. 2A). This potentiation coincides with the temporal onset and resolution of inflammatory hyperalgesia. Perfusion of either CTOP or NTX increased the peak amplitude of glutamate-evoked intracellular Ca^{2+} in CFA-21d slices but not sham-injured slices [lamina II: $P < 0.05$

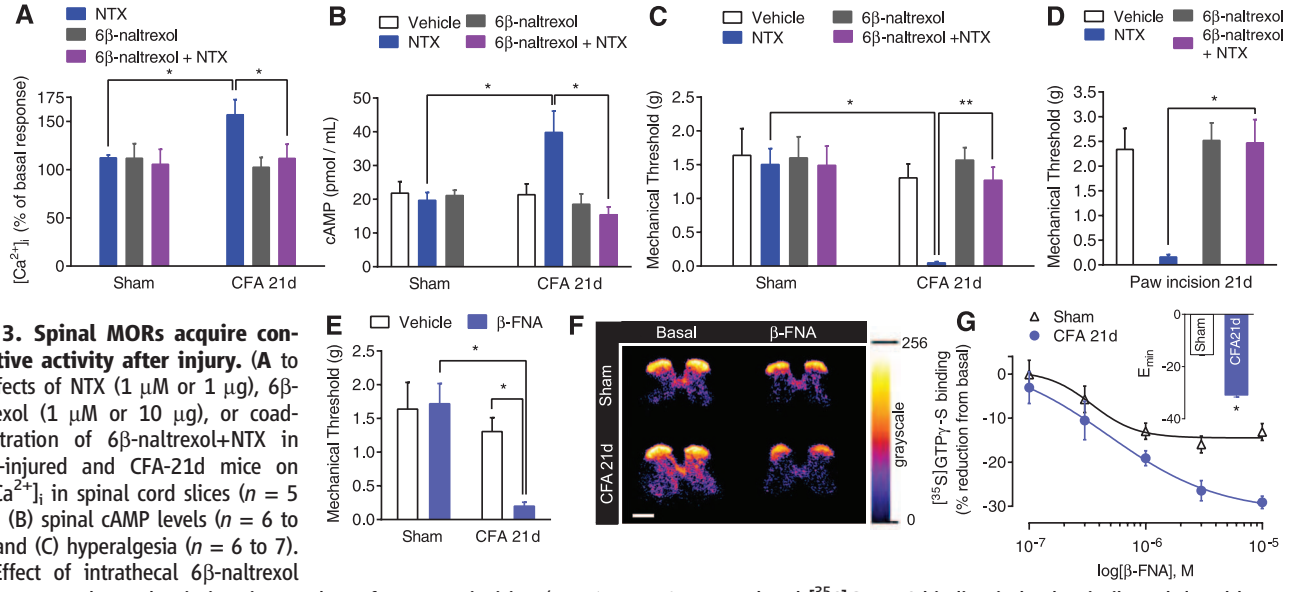

Fig. 3. Spinal MORs acquire constitutive activity after injury. (**A** to **C**) Effects of NTX (1 μM or 1 μg), 6β-naltrexol (1 μM or 10 μg), or coadministration of 6β-naltrexol+NTX in sham-injured and CFA-21d mice on (A) $[Ca^{2+}]_i$ in spinal cord slices (n = 5 to 6), (B) spinal cAMP levels (n = 6 to 11), and (C) hyperalgesia (n = 6 to 7). (**D**) Effect of intrathecal 6β-naltrexol and/or NTX on hyperalgesia in mice 21 days after a paw incision (n = 6 to 7). (**E**) Effect of intrathecal β-funaltrexamine (β-FNA, 2.5 μg) on hyperalgesia (n = 6 to 7). (**F**) Representative radiograms and (**G**) dose-response effects of β-FNA on basal [^{35}S]GTP-γ-S binding in lumbar ipsilateral dorsal horn; (inset) binding E_{max} (n = 7 to 9). *$P < 0.05$. All data are shown as means ± SEM. See fig. S9 for full time-course data of (C) to (E).

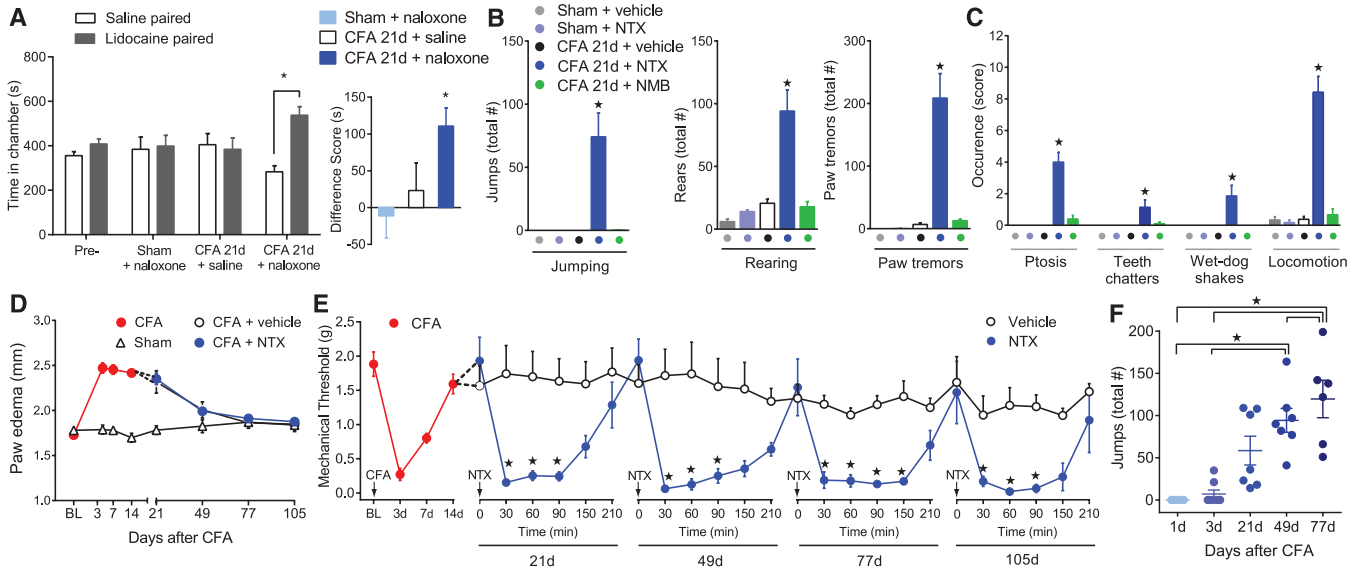

Fig. 4. Prolonged endogenous MOR signaling generates psychological and physical dependence. (**A**) Behavioral signs of psychological withdrawal (aversion associated with spontaneous pain) were reflected by place preference for intrathecal lidocaine upon naloxone administration. (Left) Intragroup chamber analysis for intrathecal saline (5 μl) or lidocaine (0.04%) in sham-injured and CFA-21d mice treated with intraperitoneal saline or naloxone (3 mg/kg). (Right) Intergroup difference score analysis illustrating time spent in intrathecal lidocaine-paired chambers (n = 6 per group). (**B** and **C**) Behavioral signs of physical withdrawal, recorded for 60 min after injection of NTX (3 mg/kg), NMB (3 mg/kg), or vehicle (n = 6 to 7). (**D**) Progression of paw edema and (**E**) effects of repeated subcutaneous vehicle or NTX (3 mg/kg) on hyperalgesia over 105 days after CFA (n = 7 per group). (**F**) Effect of repeated NTX (3 mg/kg) on the number of precipitated escape jumps over 77 days after CFA (n = 8). *, ★$P < 0.05$. All data shown as means ± SEM.

(Fig. 2, B and C, and fig. S6); lamina I: $P < 0.05$ (fig. S7)] or CFA-injured slices after 24 hours (fig. S1C). The activity-dependent NMDAR blocker, MK-801, prevented the NTX-mediated rise in intracellular calcium concentration $[Ca^{2+}]_i$ ($F_{1,16} = 4.6$, $P < 0.05$) (Fig. 2C), hyperalgesia ($F_{3,22} = 6.5$, $P < 0.005$) (Fig. 2D) and dorsal horn pERK levels ($P < 0.05$) (Fig. 2E, ipsilateral and fig. S8, contralateral).

Opioids produce their acute actions in part through inhibition of ACs, whereas chronic opiate exposure produces a homeostatic up-regulation of ACs (*9*, *14*). In this opioid-dependent state, receptor antagonists produce cellular withdrawal, characterized by an adenosine 3′,5′-cyclic monophosphate (cAMP) overshoot response. To determine whether similar homeostatic mechanisms operate in the setting of tonic opioid receptor signaling after injury, we sampled intracellular cAMP content from ex vivo lumbar spinal tissue. Basal spinal cAMP levels were comparable in sham-injured and CFA-21d mice, suggestive of a return to baseline AC function (Fig. 2F and supplementary text S2). In CFA-21d mice, however, intrathecal CTOP or NTX increased cAMP levels in CFA-21d mice ($P < 0.05$) (Fig. 2F), indicative of AC superactivation. Because the Ca^{2+}-stimulated isoforms of ACs are activated by NMDARs (*26*), we hypothesized that NMDAR signaling contributes to this cAMP overshoot. Intrathecal MK-801 abolished the NTX-precipitated increases in cAMP ($P < 0.05$ compared with NTX group) (Fig. 2G). Moreover, direct activation of spinal NMDARs and ACs by intrathecal NMDA or forskolin, respectively, increased nocifensive behaviors ($P < 0.05$) (Fig. 2, H and J) and spinal cAMP levels ($P < 0.05$) (Fig. 2, I and K) in CFA-21d mice as compared with sham-injured mice, which suggests latent up-regulation, but not occlusion, of NMDAR–AC pathways.

Adenylyl cyclase type 1 (AC1) in the brain is intricately linked to morphine dependence (*27*, *28*) and chronic pain (*29*), whereas in the spinal cord, it contributes to activity-dependent LTP (*30*). Baseline mechanical thresholds were similar in wild-type and AC1 knockout mice ($AC1^{-/-}$) (*29*) (Fig. 2L). However, AC1 gene deletion reduced inflammatory hyperalgesia (3 days later versus baseline: $P < 0.05$, *t* test; $F_{1,11} = 31.5$, $P < 0.0005$, Genotype × Time) (Fig. 2L), without affecting edema (fig. S9). At day 21 after CFA treatment, NTX reinstatement was lost in $AC1^{-/-}$ mice ($F_{1,7} = 20.3$, $P < 0.005$) (Fig. 2M). Furthermore, intrathecal NB001, a selective AC1 inhibitor (*30*), prevented NTX-based reinstatement of hyperalgesia ($F_{1,9} = 6.6$, $P < 0.05$) (Fig. 2N), as well as cAMP overshoot and spontaneous pain ($P < 0.05$) (Fig. 2, O and P). These data suggest that withdrawal from tonic MOR signaling increases pronociceptive neural excitability consequent to AC1 superactivation (Fig. 2Q).

Tonic MOR signaling arises from either continuous agonist stimulation or constitutive (agonist-independent) activity (*31*–*34*). MOR_{CA} develops with chronic morphine administration and leads to physical and affective signs of opiate dependence and addiction (*17*, *19*–*22*). To determine the existence and physiologic significance of MOR_{CA} in pathological pain processing, we used the neutral antagonist 6β-naltrexol, a structural analog of NTX (*35*). Intrathecal 6β-naltrexol alone did not change Ca^{2+} levels in sham-injured or CFA-21d spinal slices (Fig. 3A) and failed to precipitate a cAMP overshoot (Fig. 3B) or hyperalgesia (Fig. 3C). 6β-Naltrexol abolished the ability of NTX to produce Ca^{2+} mobilization ($P < 0.05$) (Fig. 3A), cAMP overshoot ($P < 0.05$) (Fig. 3B), and hyperalgesia in CFA-21d mice ($P < 0.05$) (Fig. 3C). 6β-Naltrexol also abolished NTX-induced reinstatement of mechanical hyperalgesia in a postoperative pain model (*23*) (Fig. 3D). These data suggest that NTX acts as an inverse agonist to inactivate MOR_{CA} in multiple models of inflammatory pain (supplementary text S3 and S4) (*36*, *37*).

Intrathecal administration of an alternative μ-selective inverse agonist, β-funaltrexamine (β-FNA) (*38*), reinstated hyperalgesia in CFA-21d, but not sham-injured, mice ($P < 0.05$) (Fig. 3E). Because MOR_{CA} results in elevated basal G protein cycling (*19*, *38*), we determined whether β-FNA could promote the MOR-inactive state and, thereby, decrease spontaneous basal GDP/GTP-γ-S exchange. β-FNA reduced basal [^{35}S]GTP-γ-S binding in a concentration-dependent manner in dorsal horn sections from CFA-21d mice and, to a significantly lesser degree, sham-injured mice, in both ipsilateral and contralateral dorsal horns (Fig. 3, F and G, and fig. S11).

Pain comprises sensory (hyperalgesia) and affective (aversiveness) components; the latter can be identified by changes in the rewarding property of analgesics and associated motivational behavior. In a conditioned place preference paradigm (*39*–*41*), the negative reinforcing capacity of intrathecal lidocaine (motivation to seek pain relief) demonstrates the presence of aversive pain 1 day after CFA injection (*40*). This aversive component was absent at 21 days (Fig. 4A, CFA-21d+saline group). CFA-21d, but not sham-injured, mice responded to systemic naloxone by spending more time in the chamber paired with intrathecal lidocaine (538 ± 39 s) than with intrathecal saline (283 ± 28 s, $P < 0.001$) (Fig. 4A). Systemic NTX, but not saline or NMB, precipitated numerous escape and somato-motor behaviors analogous to classical morphine withdrawal (*42*, *43*) in CFA-21d mice, with no effect in sham-injured mice (Fig. 4, B and C).

To determine whether pain sensitization and endogenous opioid physical dependence persist beyond tissue healing, we gave periodic injections of NTX during and after the course of inflammatory edema, which subsided within 77 days after CFA injection (Fig. 4D). NTX, but not saline, reinstated hyperalgesia for at least 105 days after CFA treatment (21 days: $F_{1,80} = 8.5$, $P < 0.05$; 49 days: $F_{1,72} = 59$, $P < 0.0001$; 77 days: $F_{1,72} = 76$, $P < 0.0001$; 105 days: $F_{1,64} = 33$, $P < 0.0001$) (Fig. 4E). This was true 200 days after CFA injection (fig. S12 and supplementary text S5), and after a single intrathecal injection 105 days after CFA injection, without prior exposure of the animal to the testing environment, of NTX or CTOP (fig. S12). NTX-precipitated escape-jump frequency increased with time after the injury ($F_{4,29} = 14$, $P < 0.0001$) (Fig. 4F), which suggested that intensifying opioidergic and compensatory neuroadaptations create a physical and psychological dependence that greatly outlasts acute pain and tissue injury (supplementary text S6).

These data indicate that blockade of MOR_{CA} unmasks a silent AC1 central sensitization pathway that persists beyond the resolution of pain and inflammation, reflective of hyperalgesic priming (*44*). The presence of contralateral spinal MOR_{CA} and neural sensitization illustrates the spread of this pathology to areas of the CNS beyond those directly innervated by the injured tissue. Thus, MOR_{CA} might tonically repress widespread hyperalgesia (supplementary text S7). If true, then loss of MOR_{CA} antinociception (e.g., during stress) could lead to the emergence of rampant chronic pain (*45*, *46*).

We have identified an injury-induced MOR_{CA} that promotes both endogenous analgesia and dependence. Our data suggest that long-term MOR_{CA} inhibition of AC1-mediated central sensitization drives a counteradaptive, homeostatic increase in pronociceptive AC1 signaling cascades (*29*, *47*) and thereby paradoxically promotes the maintenance of latent central sensitization. Thus, injury produces a long-lasting dependence on MOR_{CA} that tonically prevents withdrawal hyperalgesia, consistent with proposed mechanisms of dependence to opiate drugs such as morphine (*27*, *48*). We contend that loss of MOR_{CA}, and the ensuing reinstatement of pain, reflects a process of spinal cellular withdrawal (NMDA-mediated AC1 superactivation) to enhance pronociceptive synaptic strength (supplementary text S8) (*49*, *50*), as observed after NMDA-R–dependent spinal LTP at C-fiber synapses during withdrawal from exogenous opiates (*12*). Indeed, stress (*46*) or injury (*51*) escalates opposing inhibitory and excitatory influences on nociceptive processing, as a pathological consequence of increased endogenous opioid tone. This raises the prospect that opposing homeostatic interactions between MOR_{CA} analgesia and latent NMDA-R–AC1 pain sensitization create a lasting susceptibility to develop chronic pain.

References and Notes

1. A. Latremoliere, C. J. Woolf, *J. Pain* **10**, 895–926 (2009).
2. H. Ikeda *et al.*, *Science* **312**, 1659–1662 (2006).
3. R. Ruscheweyh, O. Wilder-Smith, R. Drdla, X. G. Liu, J. Sandkühler, *Mol. Pain* **7**, 20 (2011).
4. G. W. Terman, C. L. Eastman, C. Chavkin, *J. Neurophysiol.* **85**, 485–494 (2001).
5. J. Benrath, C. Brechtel, E. Martin, J. Sandkühler, *Anesthesiology* **100**, 1545–1551 (2004).
6. R. Drdla-Schutting, J. Benrath, G. Wunderbaldinger, J. Sandkühler, *Science* **335**, 235–238 (2012).
7. A. I. Basbaum, H. L. Fields, *Annu. Rev. Neurosci.* **7**, 309–338 (1984).
8. M. H. Ossipov, G. O. Dussor, F. Porreca, *J. Clin. Invest.* **120**, 3779–3787 (2010).
9. M. J. Christie, *Br. J. Pharmacol.* **154**, 384–396 (2008).
10. T. Avidor-Reiss, I. Nevo, D. Saya, M. Bayewitch, Z. Vogel, *J. Biol. Chem.* **272**, 5040–5047 (1997).

11. S. B. Lane-Ladd *et al.*, *J. Neurosci.* **17**, 7890–7901 (1997).
12. R. Drdla, M. Gassner, E. Gingl, J. Sandkühler, *Science* **325**, 207–210 (2009).
13. C. Heinl, R. Drdla-Schutting, D. N. Xanthos, J. Sandkühler, *J. Neurosci.* **31**, 16748–16756 (2011).
14. E. J. Nestler, G. K. Aghajanian, *Science* **278**, 58–63 (1997).
15. J. A. Kauer, R. C. Malenka, *Nat. Rev. Neurosci.* **8**, 844–858 (2007).
16. M. S. Angst, J. D. Clark, *Anesthesiology* **104**, 570–587 (2006).
17. Z. Wang, E. J. Bilsky, F. Porreca, W. Sadée, *Life Sci.* **54**, PL339–PL350 (1994).
18. J. G. Liu, P. L. Prather, *Mol. Pharmacol.* **60**, 53–62 (2001).
19. D. Wang *et al.*, *J. Pharmacol. Exp. Ther.* **308**, 512–520 (2004).
20. J. R. Shoblock, N. T. Maidment, *Neuropsychopharmacology* **31**, 171–177 (2006).
21. F. J. Meye, R. van Zessen, M. P. Smidt, R. A. Adan, G. M. Ramakers, *J. Neurosci.* **32**, 16120–16128 (2012).
22. J. R. Shoblock, N. T. Maidment, *Neuroscience* **149**, 642–649 (2007).
23. E. M. Pogatzki, S. N. Raja, *Anesthesiology* **99**, 1023–1027 (2003).
24. C. Luo, P. H. Seeburg, R. Sprengel, R. Kuner, *Pain* **140**, 358–367 (2008).
25. S. Doolen, C. B. Blake, B. N. Smith, B. K. Taylor, *Mol. Pain* **8**, 56 (2012).
26. D. M. Chetkovich, J. D. Sweatt, *J. Neurochem.* **61**, 1933–1942 (1993).
27. V. Zachariou *et al.*, *Biol. Psychiatry* **63**, 1013–1021 (2008).
28. M. S. Mazei-Robison, E. J. Nestler, *Cold Spring Harbor Perspect. Med.* **2**, a012070 (2012).
29. F. Wei *et al.*, *Neuron* **36**, 713–726 (2002).
30. H. Wang *et al.*, *Sci. Transl. Med.* **3**, 65ra3 (2011).
31. T. Kenakin, *FASEB J.* **15**, 598–611 (2001).
32. T. Kenakin, *Trends Pharmacol. Sci.* **25**, 186–192 (2004).
33. T. Costa, A. Herz, *Proc. Natl. Acad. Sci. U.S.A.* **86**, 7321–7325 (1989).
34. R. Seifert, K. Wenzel-Seifert, *Naunyn Schmiedebergs Arch. Pharmacol.* **366**, 381–416 (2002).
35. K. M. Raehal *et al.*, *J. Pharmacol. Exp. Ther.* **313**, 1150–1162 (2005).
36. W. Sadée, D. Wang, E. J. Bilsky, *Life Sci.* **76**, 1427–1437 (2005).
37. H. Lam *et al.*, *Mol. Pain* **7**, 24 (2011).
38. J. G. Liu, M. B. Ruckle, P. L. Prather, *J. Biol. Chem.* **276**, 37779–37786 (2001).
39. T. King *et al.*, *Nat. Neurosci.* **12**, 1364–1366 (2009).
40. Y. He, X. Tian, X. Hu, F. Porreca, Z. J. Wang, *J. Pain* **13**, 598–607 (2012).
41. K. J. Sufka, *Pain* **58**, 355–366 (1994).
42. G. F. Koob, R. Maldonado, L. Stinus, *Trends Neurosci.* **15**, 186–191 (1992).
43. B. Kest *et al.*, *Neuroscience* **115**, 463–469 (2002).
44. M. N. Asiedu *et al.*, *J. Neurosci.* **31**, 6646–6653 (2011).
45. M. De Felice *et al.*, *Brain* **133**, 2475–2488 (2010).
46. C. Rivat *et al.*, *Neuropsychopharmacology* **32**, 2217–2228 (2007).
47. M. Zhuo, *Drug Discov. Today* **17**, 573–582 (2012).
48. S. Li *et al.*, *Mol. Pharmacol.* **70**, 1742–1749 (2006).
49. H. C. Lu *et al.*, *Nat. Neurosci.* **6**, 939–947 (2003).
50. H. Xu *et al.*, *J. Neurosci.* **28**, 7445–7453 (2008).
51. C. Rivat *et al.*, *Anesthesiology* **96**, 381–391 (2002).

Acknowledgments: The authors thank H. L. Fields, A. I. Basbaum, L. Hough, J. C. Marvizon, E. Bilsky, W. Sadee, G. Scherrer, K. Westlund High, M. Werner, J. Dahl, and B. Solway for critical discussions and J. Grasch, L. Martin, and R. Griggs for technical assistance and blinding. This work was supported by NIH grants F31DA032496 (G.C.), HD02528 (M.K.W. and K.E.M.), R01NS45954 (B.K.T.), and 5K02DA19656 (B.K.T.). Author contributions: G.C. and B.K.T. formulated the hypotheses, designed, analyzed and coordinated all experiments. G.C. performed surgeries, behavioral pharmacology, histology, and fluorescence imaging and analyzed the data. G.C. and B.L.J. carried out the biochemical studies and G.C. analyzed the data. S.D. and G.C. carried out Ca^{2+} imagining experiments and analyzed the data. M.K.W., K.E.M., G.C., and B.K.T. designed the [^{35}S]GTP-γ-S binding studies; M.K.W. collected the data; and G.C., K.E.M., and B.K.T. analyzed the data. D.R.S. supplied the $AC1^{-/-}$ breeders. Z.J.W., G.C., and B.K.T. designed the conditioned place preference experiments, and Y.H. and X.H. conducted experiments and analyzed the data. J.S.M., J.S.W., G.C., and B.K.T. designed the Mouse Grimace Scale experiments, and J.W. conducted the experiments. R.R.D. conducted the plantar incision studies. G.C. and B.K.T. wrote the manuscript.

Supplementary Materials

www.sciencemag.org/content/341/6152/1394/suppl/DC1
Materials and Methods
Supplementary Text
Figs. S1 to S13
References (*52*–*80*)

19 April 2013; accepted 20 August 2013
10.1126/science.1239403

Human LilrB2 Is a β-Amyloid Receptor and Its Murine Homolog PirB Regulates Synaptic Plasticity in an Alzheimer's Model

Taeho Kim,[1]* George S. Vidal,[1] Maja Djurisic,[1] Christopher M. William,[2] Michael E. Birnbaum,[3] K. Christopher Garcia,[3] Bradley T. Hyman,[2] Carla J. Shatz[1]*

Soluble β-amyloid (Aβ) oligomers impair synaptic plasticity and cause synaptic loss associated with Alzheimer's disease (AD). We report that murine PirB (paired immunoglobulin-like receptor B) and its human ortholog LilrB2 (leukocyte immunoglobulin-like receptor B2), present in human brain, are receptors for Aβ oligomers, with nanomolar affinity. The first two extracellular immunoglobulin (Ig) domains of PirB and LilrB2 mediate this interaction, leading to enhanced cofilin signaling, also seen in human AD brains. In mice, the deleterious effect of Aβ oligomers on hippocampal long-term potentiation required PirB, and in a transgenic model of AD, PirB not only contributed to memory deficits present in adult mice, but also mediated loss of synaptic plasticity in juvenile visual cortex. These findings imply that LilrB2 contributes to human AD neuropathology and suggest therapeutic uses of blocking LilrB2 function.

Soluble oligomeric species of β-amyloid (Aβ) are thought to be key mediators of cognitive dysfunction in Alzheimer's disease (AD) (*1*, *2*). Transgenic mice expressing elevated levels of human Aβ experience memory loss and synaptic regression (*3*–*6*). Aβ production is thought to be activity-dependent (*7*, *8*), and even in wild-type mice, addition of soluble Aβ oligomers to hippocampal slices or cultures induces loss of long-term potentiation (LTP), increases long-term depression (LTD), and decreases dendritic spine density (*9*–*11*). Aβ oligomers may exert some of their adverse effects on synaptic plasticity and memory by binding to receptors, thereby perturbing or engaging downstream signaling. At least two Aβ receptors, cellular prion protein (PrP^C) and ephrin type B receptor 2 (EphB2), have been identified, and downstream signaling from both alters *N*-methyl-D-aspartate (NMDA) receptor function in response to Aβ (*6*, *12*, *13*). Aβ oligomers are also known to engage other signaling pathways, including the actin-severing protein cofilin and protein phosphatases PP2A and PP2B/calcineurin, thereby mediating spine loss and synaptic defects (*9*, *14*); however, signaling upstream of these pathways is not well understood.

[1]Departments of Biology and Neurobiology and Bio-X, James H. Clark Center, Stanford University, Stanford, CA 94305, USA. [2]Neuropathology Service, Massachusetts General Hospital, Charlestown, MA 02129, USA. [3]Howard Hughes Medical Institute, Department of Molecular and Cellular Physiology, and Department of Structural Biology, Stanford University School of Medicine, Stanford, CA 94305, USA.

*Corresponding author. E-mail: cshatz@stanford.edu (C.J.S.); tkim808@stanford.edu (T.K.)

Recently, a very early loss of activity-dependent plasticity was discovered in vivo in APP/PS1 transgenic mice, an AD model in which mutant alleles of both amyloid precursor protein (APPswe) and presenilin 1 (PSEN1ΔE9) are expressed (*15*, *16*): Ocular dominance plasticity (ODP) during the critical period of development in visual cortex [postnatal day 22 (P22) to P32] is defective (*17*). This observation directly contrasts with mice lacking PirB (paired immunoglobulin-like receptor B), in which ODP is enhanced during the critical period and in adults (*18*). PirB, a receptor originally thought to function exclusively in the immune system (*19*), is now also known to be expressed by neurons, present in neuronal growth cones, and associated with synapses (*18*, *20*). Thus, it is possible that Aβ acts through PirB to diminish ODP in APP/PS1 mice.

To determine whether PirB can act as a receptor for soluble Aβ oligomers, we prepared biotinylated synthetic human $Aβ_{1-42}$ (Aβ42) peptides either without (mono-Aβ42) or with oligomerization (oligo-Aβ42; consists primarily of high-*n* oligomers) (Fig. 1, A and B, and fig. S1A) (*12*, *21*, *22*). We then measured binding of Aβ42 peptides to human embryonic kidney (HEK) 293 cells that expressed mouse PirB (PirB-IRES-EGFP) or control vector (IRES-EGFP). Relative to monomeric Aβ42, oligomerized Aβ42 peptides bound to PirB-expressing cells about 6 times as much (Fig. 1, A to D). Oligo-Aβ42 was consistently associated with PirB protein, as seen both by coimmunostaining (Fig. 1E, arrowheads) and by coimmunoprecipitation (fig. S1, B and C), indicating a direct interaction with PirB. This assay also confirms previously reported Nogo-66 binding to PirB (fig. S2) (*20*). In contrast, binding of Aβ42 oligomers was not evident in heterologous cells expressing mouse

PirA1, mouse PirA4, or an isoform of rat PirB (*23*); all of these receptors are closely related to mouse PirB (Fig. 1, F and G, and fig. S3). This finding indicates that Aβ42 oligomers bind selectively to PirB. Oligo-Aβ42 binding to PirB expressed in HEK293 cells was saturable, with an apparent dissociation constant (K_d) of 180 nM monomer equivalent of total Aβ42 peptide (Fig. 1, H to J) (*24*). An alkaline phosphatase assay gave a similar binding affinity (K_d = 160 nM; fig. S4). In contrast, mono-Aβ42 exhibited no apparent binding affinity to PirB (Fig. 1, H to J).

Aβ42 oligomer binding to cultured cortical neurons from PirB$^{-/-}$ mice was diminished by about 50% relative to wild-type neurons, indicating that binding is PirB-dependent. The estimated K_d for Aβ42 oligomers and neuronal PirB is 110 nM (Fig. 1K), similar to that observed for PirB-expressing HEK293 cells (Fig. 1, I and J). We note that this binding is not completely abolished in the absence of PirB (Fig. 1K), which suggests that additional binding sites for Aβ oligomers exist (*6*, *12*, *25*). Together, these results suggest that PirB is a high-affinity receptor for Aβ oligomers.

The human homolog of murine PirB is leukocyte immunoglobulin (Ig)–like receptor B, which comprises five family members, LilrB1 to LilrB5 (*19*, *20*). To identify which of these orthologs functions analogously to PirB as a receptor for Aβ oligomers, we examined the three most related LilrB receptors, LilrB1, 2, and 3 (*19*, *20*, *26*, *27*), as well as a moderately related human killer immune receptor (Kir) (Fig. 2A). Aβ42 oligomers robustly bound to LilrB2-expressing heterologous cells, but not to LilrB1-, LilrB3-, or Kir (3DL1)–expressing cells (Fig. 2B and fig. S5A). Binding was saturable, with an apparent K_d of 206 nM (Fig. 2, C and D; also fig. S5, B and C: K_d = 250 nM). LilrB2 displayed minimal binding to mono-Aβ42 (Fig. 2, C and D), which suggests selective binding with Aβ42 oligomers. LilrB2 proteins were detected in human brain specimens from

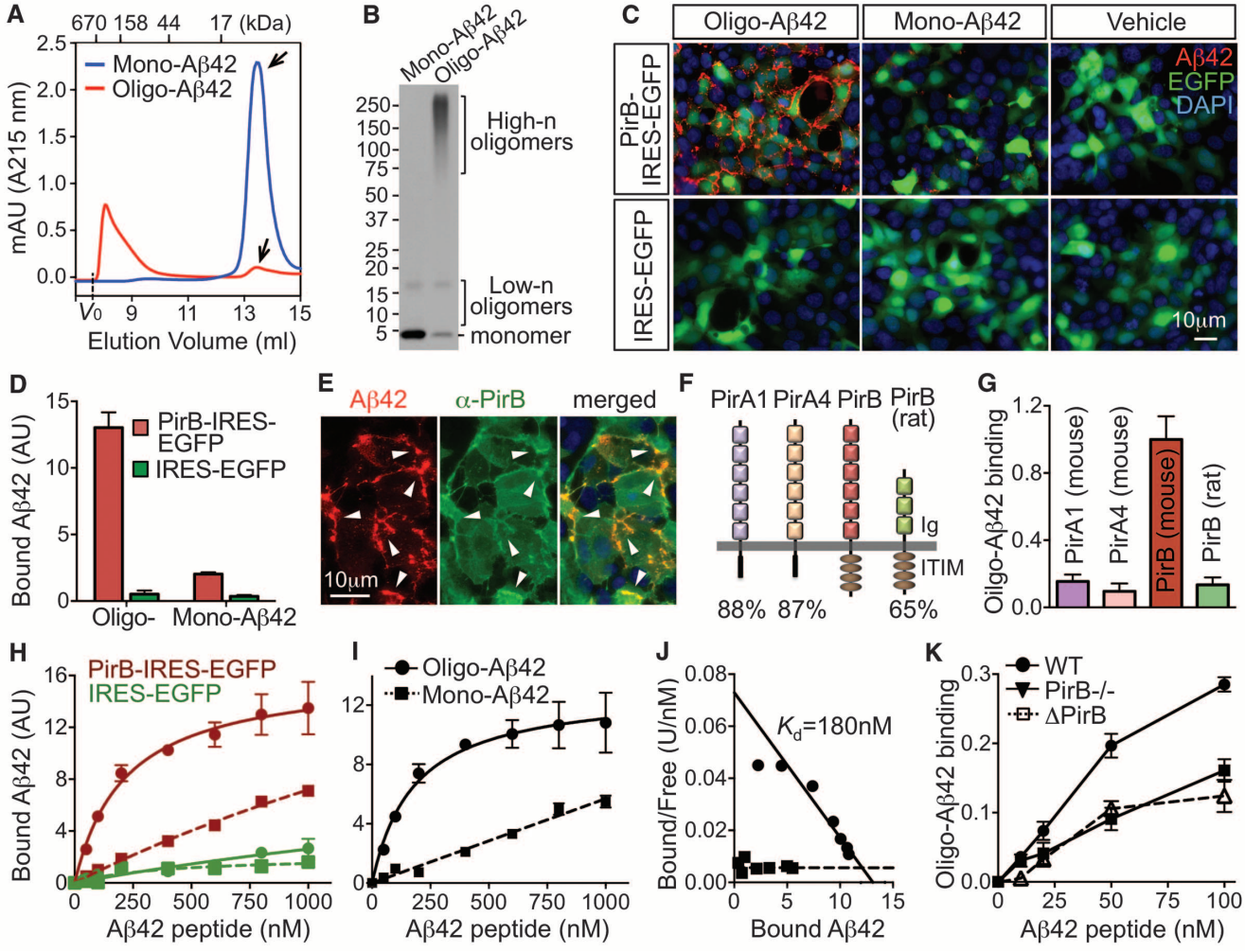

Fig. 1. PirB is a receptor for oligomeric Aβ. (**A**) Monomeric (mono) or oligomerized (oligo) synthetic human Aβ42 peptides (fig. S1A) (*21*, *22*) were analyzed by size exclusion column chromatography. Arrows indicate monomeric form; V_0, void volume; absorbance at 215 nm is in arbitrary units. (**B**) The same peptides were analyzed by Western blotting with antibody to Aβ (4G8; detects Aβ17-24). (**C**) PirB-IRES-EGFP–transfected (top) or control IRES-EGFP–transfected (bottom) HEK293 cells (green) were treated with mono- or oligo-Aβ42 (100 nM total peptide, monomer equivalent), and bound Aβ42 (red) was visualized. See also fig. S1. DAPI, 4′,6-diamidino-2-phenylindole. (**D**) Quantification of Aβ42 binding represented in (C). AU denotes average signal per pixel (*22*); data are means ± SEM (PirB-IRES-EGFP, n = 5; IRES-EGFP, n = 4). (**E**) PirB-expressing cells were treated with oligo-Aβ42 (100 nM) and immunostained for Aβ and PirB. Colocalization is observed particularly at cell membrane (i.e., arrowheads). (**F**) Schematic of mouse PirB, the highly related mouse PirA1 and PirA4, and a rat PirB isoform (*23*). Amino acid sequence similarities to mouse PirB (% score, ClustalW) are indicated at bottom. Ig, immunoglobulin domain; ITIM, immunoreceptor tyrosine-based inhibitory motif. (**G**) Relative oligo-Aβ42 (200 nM) binding to HEK293 cells expressing mouse PirB, PirA1, or PirA4 or rat PirB; see also fig. S3. Data are means ± SEM (n = 4 or 5). (**H**) Dose-dependent binding of mono- or oligo-Aβ42 (squares and circles, respectively) to HEK293 cells expressing IRES-EGFP (green) or PirB-IRES-EGFP (red), assessed as a function of Aβ42 total concentration. (**I**) Binding curve of mono- or oligo-Aβ42 to PirB. Data (PirB-IRES-EGFP minus IRES-EGFP) are from (H) (*22*). (**J**) Scatchard plots of data from (I). Data are means ± SEM (n = 4). Calculated K_d = 180 ± 52 nM; see also fig. S4. (**K**) Binding of oligo-Aβ42 to cultured cortical neurons (21 days in vitro) is diminished ~50% by deletion of PirB (PirB$^{-/-}$), as assessed by alkaline phosphatase assay. Data are means ± SEM (n = 6). Estimated K_d for neuronal PirB [dashed line: ΔPirB = wild type (WT) minus PirB$^{-/-}$] is 110 nM.

both AD patients and non-AD adults (table S1), with no significant difference in levels (Fig. 2, E and F); however, downstream signaling was altered in AD (see below). These results suggest that LilrB2 is available as a receptor for Aβ oligomers in human brain. LilrB2 has also been identified as a human ortholog of PirB for other recently discovered nonimmune ligands: In vitro, PirB and LilrB2 act as functional receptors to inhibit axonal outgrowth on Nogo, myelin-associated glycoprotein, and oligodendrocyte myelin glycoprotein substrates (*20*); in the hematopoetic system, angiopoietin-like proteins can also bind to PirB and LilrB2 to support stem cell and leukemia development (*26*). These observations imply that mouse PirB may have diverse functions well beyond inhibitory signaling in the innate immune system and that LilrB2 may execute these roles in humans, particularly in the nervous system.

To determine the domains of PirB or LilrB2 responsible for Aβ oligomer binding, we made full-length or deletion mutants of PirB and LilrB2 (Fig. 2G). Because Aβ oligomers appear to bind preferentially to dimeric PirB in heterologous cells (fig. S6A), soluble dimeric forms of PirB or LilrB2 extracellular domain were constructed using human IgG1-Fc (fig. S6B). In vitro binding to Aβ42 oligomers revealed that the two most N-terminal Ig domains (D1D2) of PirB and of LilrB2 are critical, whereas the PirB-D5D6 and LilrB2-D3D4 domains have minimal affinity (Fig. 2, G and H, and fig. S6C) (*28*). In this assay, PirB-Fc, LilrB2-Fc, and PirB(D1D2)-Fc proteins pulled down high-*n* Aβ42 oligomers (Fig. 2H), recapitulating coimmunoprecipitation results (fig. S1B). PirB(D5D6)-Fc was used as a negative control and the oligomeric status of bound Aβ42 was confirmed using the oligomer-specific antibody OMAB (*29*) (Fig. 2H and fig. S6D). These results suggest that PirB and LilrB2 are potent receptors for Aβ42 oligomers, and that their D1D2 domains are sufficient to mediate binding.

If PirB or LilrB2 mediates deleterious effects of Aβ on synaptic function, then deletion of PirB should mitigate them in cellular or animal models of AD. A cellular mechanism proposed to underlie memory impairment in AD is loss of hippocampal LTP resulting from the presence of soluble Aβ oligomers (*2*, *12*). To assess a direct contribution of PirB to this cellular correlate of AD pathology, we examined the effects of acute Aβ42 oligomer addition in wild-type and PirB$^{-/-}$ hippocampal slices; LTP at Schaffer collateral-CA1 synapses was measured (Fig. 3, A to D). Because PirB has high affinity for Aβ oligomers ($K_d \approx 110$ to 180 nM; Fig. 1 and fig. S4), slices were treated with 200 nM total peptide of oligomerized Aβ42 or with vehicle control, and field

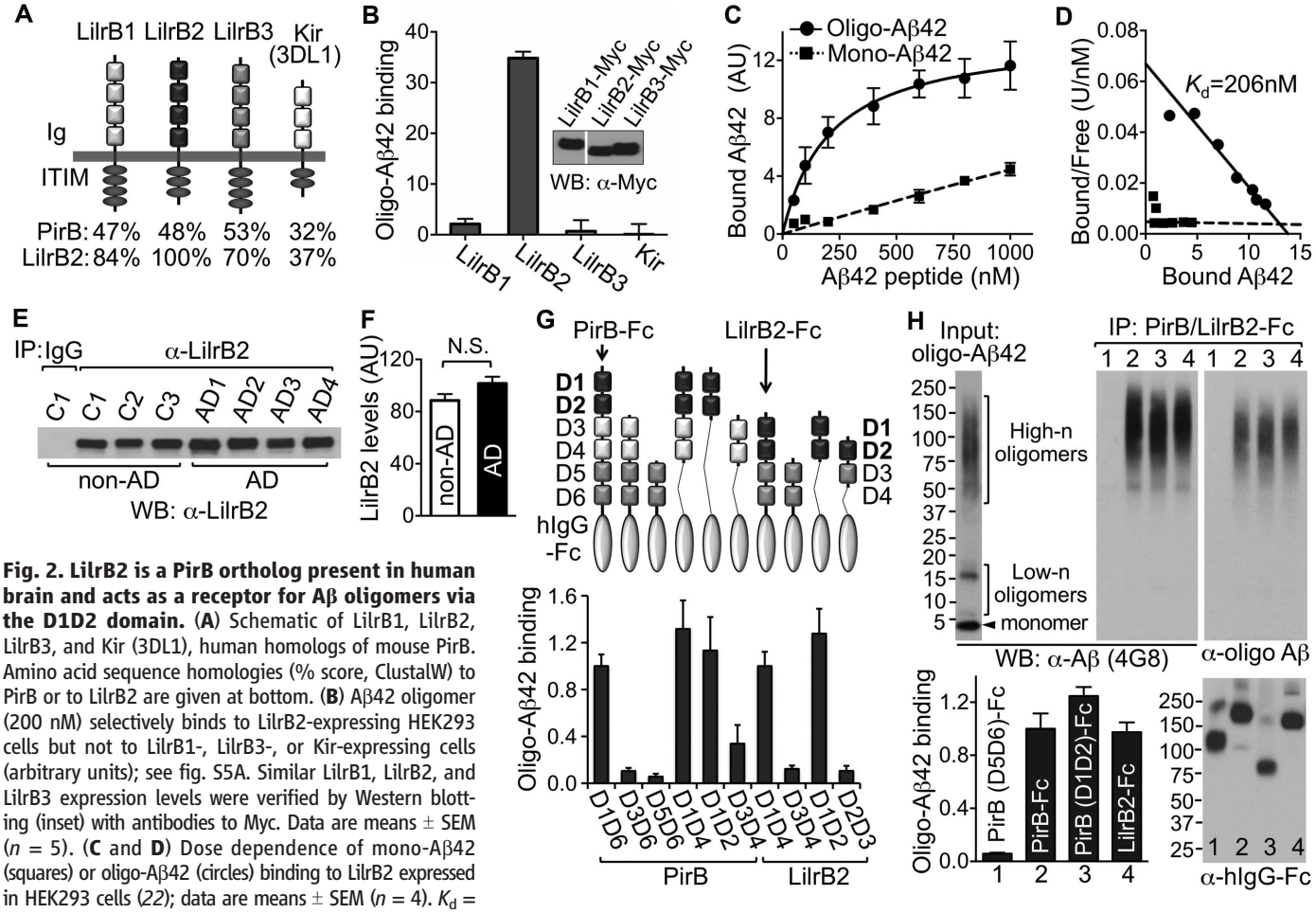

Fig. 2. LilrB2 is a PirB ortholog present in human brain and acts as a receptor for Aβ oligomers via the D1D2 domain. (**A**) Schematic of LilrB1, LilrB2, LilrB3, and Kir (3DL1), human homologs of mouse PirB. Amino acid sequence homologies (% score, ClustalW) to PirB or to LilrB2 are given at bottom. (**B**) Aβ42 oligomer (200 nM) selectively binds to LilrB2-expressing HEK293 cells but not to LilrB1-, LilrB3-, or Kir-expressing cells (arbitrary units); see fig. S5A. Similar LilrB1, LilrB2, and LilrB3 expression levels were verified by Western blotting (inset) with antibodies to Myc. Data are means ± SEM (n = 5). (**C** and **D**) Dose dependence of mono-Aβ42 (squares) or oligo-Aβ42 (circles) binding to LilrB2 expressed in HEK293 cells (*22*); data are means ± SEM (n = 4). K_d = 206 ± 65 nM; see also fig. S5, B and C. (**E**) LilrB2 is expressed in frontal lobe of specimens from three adult humans (non-AD; C1 to C3) and from four Alzheimer's patients (AD1 to AD4) (table S1). Protein extracts from fresh frozen frontal lobe were immunoprecipitated with control IgG or LilrB2-specific antibodies followed by Western blot analysis. (**F**) Quantitation of LilrB2 protein levels shown in (E). Data are means ± SEM. (**G**) Deletion of the D1D2 domain abrogates binding of Aβ42 oligomers to PirB and LilrB2. Top: Schematic of PirB and LilrB2 ectodomain constructs: full-length or truncated Ig domains fused to human IgG-Fc (hIgG-Fc). Bottom: Bar graphs of average band intensities ± SEM from experiments such as that shown in fig. S6C (n = 3). Note that sequence analysis using pairwise alignment indicates that the D1D2 domain of LilrB2 aligns closely with the D1D2 domain of PirB (*28*). (**H**) PirB-Fc or LilrB2-Fc binds predominantly to high-*n* oligomeric forms of Aβ42. Oligomerized Aβ42 (input; also contains low-*n* oligomers and monomeric Aβ42) was subjected to immunoprecipitation with full-length or truncated soluble PirB- or LilrB2-Fc proteins followed by Western blot analysis. Aβ oligomer binding domain–deficient PirB (D5D6)-Fc treatment was used as negative control (lane 1). Top right: Western blot with antibodies to Aβ specific for oligomeric forms (OMAB; see fig. S6D); Bottom left: quantification of Aβ42 binding. Data are normalized average band intensities ± SEM (n = 3).

excitatory postsynaptic potentials (fEPSPs) after theta burst stimulation (TBS) were recorded. Consistent with previous reports (*12*, *30*), Aβ42 oligomers abolished LTP in hippocampal slices from wild-type mice (vehicle, 134 ± 4% of baseline; Aβ42 oligomer, 94 ± 7% of baseline; Fig. 3, A and C). In marked contrast, in PirB$^{-/-}$ slices, LTP remained intact even in the presence of Aβ42 oligomers (135 ± 5% of baseline; Fig. 3, B and C); these effects were significantly different between wild-type and PirB$^{-/-}$ slices (Fig. 3D). Application of vehicle control in PirB$^{-/-}$ slices did not alter the magnitude of LTP, which was similar to wild-type mice (125 ± 4% of baseline; Fig. 3, B and C), consistent with previous observations of hippocampal LTP in PirB$^{-/-}$ mice (*31*). These experiments demonstrate that the deleterious effects of Aβ oligomers on hippocampal LTP depend on PirB.

To assess whether PirB contributes in vivo to cognitive deficits, we crossed APP/PS1 transgenic (Tg) mice with PirB$^{-/-}$ mice to generate APP/PS1 littermates with (PirB$^{+/-}$ Tg) or without (PirB$^{-/-}$ Tg) PirB. First, recognition memory was examined using two tests: novel object recognition and novel place recognition (*6*, *32*). As expected (*32*), impaired behaviors were observed in both tests in 9-month-old PirB$^{+/-}$ Tg mice; however, these learning and memory defects were not evident in mice lacking PirB (PirB$^{-/-}$ Tg) (Fig. 3, E and F). Together, these observations demonstrate that PirB contributes not only to Aβ-mediated loss of hippocampal LTP but also to defects in recognition memory that characterize older APP/PS1 mice and are symptoms of synaptic pathology in AD.

One of the earliest manifestations of pathology detected in APP/PS1 mice is impaired ODP (*17*). We evaluated ODP during the developmental critical period (P22 to P32) by measuring the ability of one eye to expand its functional representation within visual cortex after removal of the other eye (Fig. 3G). ODP was significantly diminished in APP/PS1 mice (PirB$^{+/-}$ Tg) (18%; Fig. 3, H and I) (*17*). When we deleted PirB, the mice (PirB$^{-/-}$ Tg) showed no loss in ODP. In fact, PirB$^{-/-}$ Tg mice had ODP similar to that of PirB$^{-/-}$ mice and greater than that of PirB$^{+/-}$ mice (Fig. 3, H and I), consistent with previous observations (*18*) and with the fact that PirB binds other ligands known to limit ODP in addition to Aβ (i.e., MHCI; Nogo; fig. S2 and S10) (*18*, *20*, *33*).

Cellular mechanisms associated with ODP in visual cortex of juvenile APP/PS1 mice were also examined. LTD of synaptic responses in cortical layer 2/3 induced by low-frequency stimulation

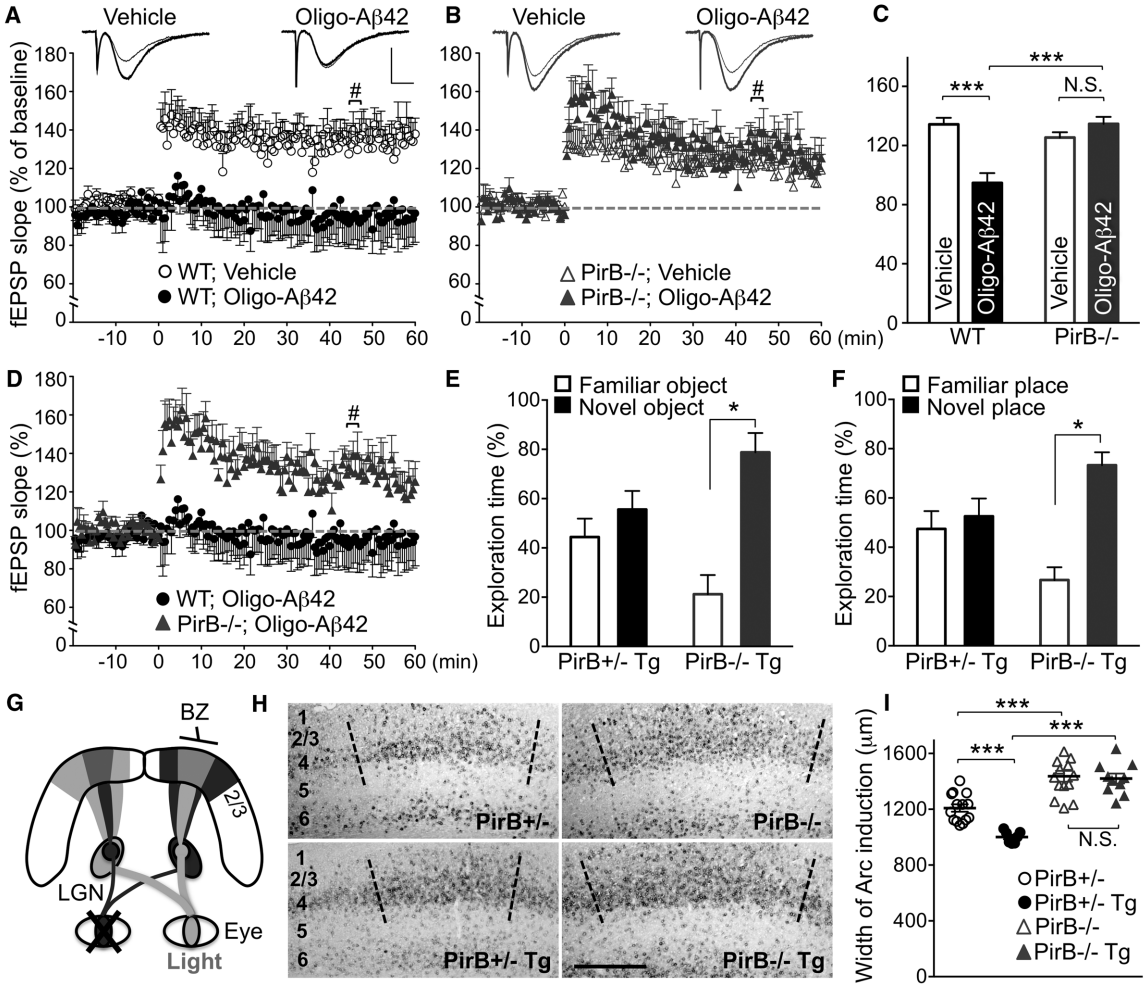

Fig. 3. PirB deletion rescues synaptic plasticity and behavioral deficits in AD models. (**A**) Acute application of oligo-Aβ42 inhibits LTP in WT hippocampal slices. fEPSPs were recorded from stratum radiatum in the CA1 region of hippocampal slices from 4- to 5-month-old WT mice with or without addition of oligo-Aβ42 (200 nM total peptide). Top panels show example fEPSP traces immediately before (light traces) and 45 min after (heavy traces) TBS; each is an average of five individual consecutive traces. Calibration bar = 0.5 mV/5 ms. The slope of the fEPSP after TBS, relative to baseline, is plotted as a function of time in the lower panel. Vehicle, n = 7 animals, 9 slices; Aβ42 oligomer, n = 6, 9 slices. (**B**) Aβ42 oligomer does not block LTP in PirB$^{-/-}$ slices. Vehicle, n = 5 animals, 8 slices; Aβ42 oligomer, n = 4, 6 slices. (**C**) Histograms of fEPSP slope measured 45 min after TBS. Each is a 2-min average of recordings taken from all slices of a given condition at time marked # in (A) and (B); all data are means ± SEM, ***P < 0.0001, t test. (**D**) Comparison of Aβ42 oligomer effects on hippocampal LTP from WT and PirB$^{-/-}$ mice; replotted from (A) and (B). (**E**) Novel object recognition memory of 9-month-old mice was evaluated by measuring percent of time mice spent exploring a novel versus a familiar object during a 10-min test session. (**F**) Novel place recognition memory (9-month-old) reflects percent time mice spent exploring familiar objects whose locations were or were not changed. Values are means ± SEM, *P < 0.05, paired t test. PirB$^{+/-}$; APP/PS1 (PirB$^{+/-}$ Tg, n = 6), PirB$^{-/-}$; APP/PS1 (PirB$^{-/-}$ Tg, n = 5). (**G**) Schematic of mouse visual system showing connections from eyes to lateral geniculate nucleus (LGN) to visual cortex. Cortical binocular zone (BZ) receives inputs from both eyes via the LGN. (**H**) In situ hybridization for Arc mRNA (digoxigenin-labeled antisense riboprobe) in visual cortex BZ of PirB;APP/PS1 littermates. At P22, one eye was removed; 10 days later (P32), induction of mRNA for the immediate early gene Arc at P32 was used to monitor width of territory receiving functional input from the open (ipsilateral) eye. Note that high Arc mRNA expression in layer 2/3 neurons within dashed lines, denoting domain of Arc induction in visual cortex. Scale bar, 500 μm. (**I**) Quantification of expansion in width of Arc mRNA signal in L2/3 visual cortex shown in (H). Data are means ± SEM; ***P < 0.001, t test; PirB$^{+/-}$ (n = 14 animals), PirB$^{+/-}$ Tg (n = 7), PirB$^{-/-}$ (n = 14), PirB$^{-/-}$ Tg (n = 10).

of layer 4 (fig. S7A) shares mechanisms with those that cause weakening of deprived-eye visually driven responses after monocular deprivation (*34*, *35*). The magnitude of LTD at L4 to L2/3 synapses in APP/PS1 mice is almost 3-fold greater than in nontransgenic littermates (fig. S7, B and C). This excessive LTD in PirB$^{+/-}$ Tg slices is not evident in PirB$^{-/-}$ Tg slices (fig. S7, B to D). Collectively, these data show that PirB function is associated not only with synaptic and cognitive alterations induced in adult mice by Aβ but also with loss of plasticity during early development in visual cortex of APP/PS1 mice.

Next, to identify signaling mechanisms engaged by the association of oligomeric Aβ with either PirB or LilrB2, we compared downstream signaling pathways in APP/PS1 mice with or without PirB. From an unbiased proteomic screen, we identified the actin-depolymerizing factor cofilin, as well as the serine-threonine phosphatases PP2A and PP2B/calcineurin, as potential PirB interactors. These candidates have already been implicated in Aβ-dependent synaptic loss and are engaged after induction of hippocampal LTD or LTP (*9*, *14*, *36*–*38*). In forebrains of APP/PS1 (PirB$^{+/-}$ Tg) mice, interactions of PirB with cofilin (Fig. 4A), as well as with protein phosphatases PP2A, B, or C (fig. S8), were increased relative to nontransgenic littermates. In contrast, other PirB signaling pathways, including tyrosine phosphorylation of PirB and its association with SHP-2 (*18*, *39*, *40*), were not significantly changed (Fig. 4A, lanes 1 and 2), nor were the levels of Aβ oligomers, including previously reported Aβ*56 (*41*) (56-kD high-*n* oligomers) (fig. S9; lanes 2 and 4). Together, these results suggest that the elevated interactions between PirB and cofilin or protein phosphatases in APP/PS1 mice are most likely to be caused by Aβ-PirB interactions.

PP2A and PP2B/calcineurin can activate cofilin by dephosphorylation at the Ser^3 residue (*42*, *43*), and the resulting actin filament disassembly appears to be crucial for Aβ oligomer–induced spine loss (*9*). Indeed, levels of cofilin phosphorylation at Ser^3 normalized to total cofilin levels were reduced about 40% in juvenile (P30) APP/PS1 forebrains (Fig. 4, B and D), as well as in adult (P200) hippocampal synaptosomes (Fig. 4, C and E), which were fully restored to normal levels by knocking out PirB (Fig. 4, B to E). Cofilin activity could be decreased by LIM kinase (LIMK) 1/2, an upstream kinase that phosphorylates cofilin at Ser^3; no evident change was detected in LIMK1/2 activity in APP/PS1 mice with or without PirB (Fig. 4, B to E), implying that PirB and LIMK signaling may regulate cofilin independently. Addition of Aβ42 oligomers to cultures of cortical neurons also consistently triggers cofilin activation (25% reduction in cofilin phosphorylation in wild-type neurons after 1 hour of treatment), as well as the loss of the postsynaptic protein PSD-95 (23% reduction after 24 hours of treatment) (Fig. 4, F and G). These changes did not occur in cortical neuron cultures from PirB$^{-/-}$ mice. Levels of cofilin phosphorylation in human Alzheimer's brains were reduced by about 38% relative to those in non-AD control brains (Fig. 4, H and I). In AD brains, elevated Tau phosphorylation was also observed (Fig. 4H), consistent with AD diagnosis (table S1). Thus, the PirB receptor may act directly to link Aβ-induced synaptotoxicity and cofilin or protein phosphatase pathways (*9*): Aβ oligomer–PirB binding would recruit cofilin-signaling modules to facilitate actin depolymerization, resulting in synaptic loss (indicated by reduction of PSD-95), ultimately leading to altered synaptic plasticity and cognitive deficits in APP/PS1

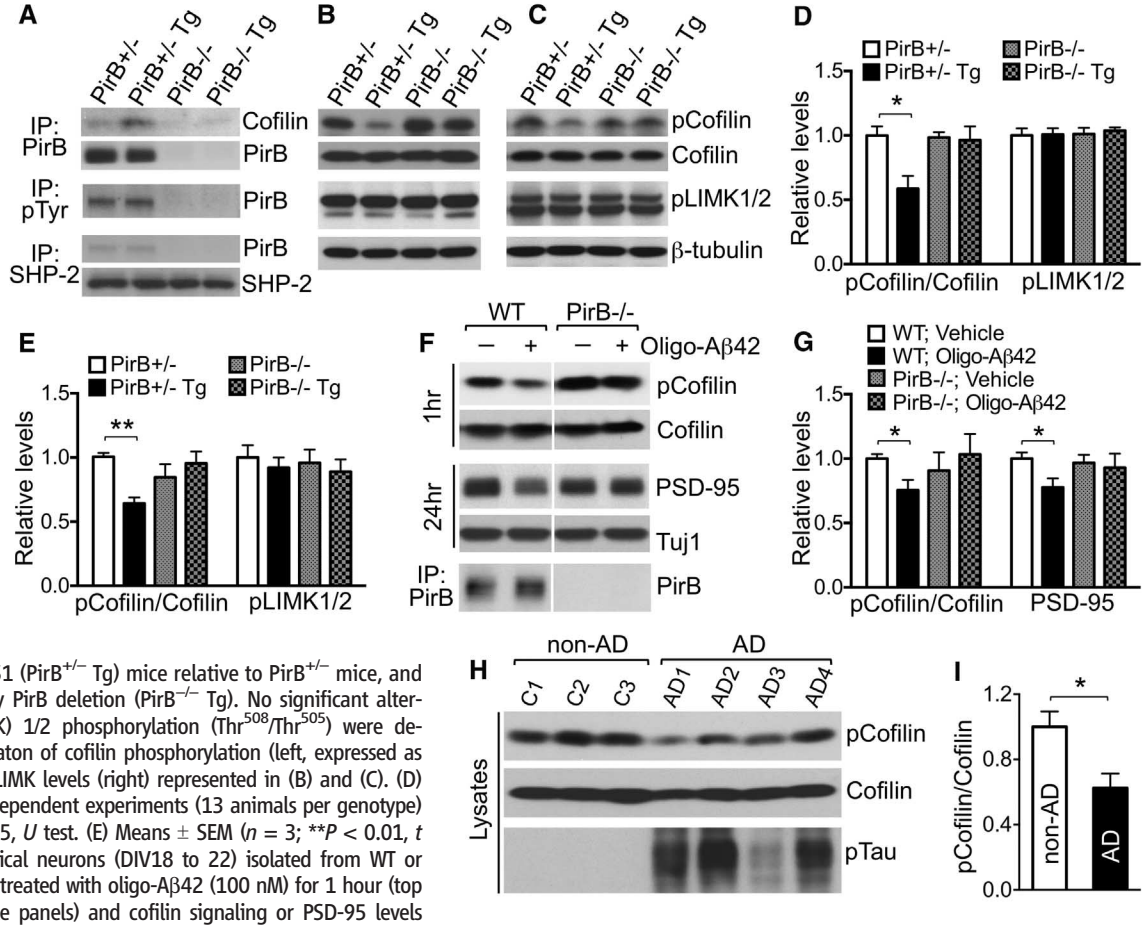

Fig. 4. Cofilin is recruited and activated by PirB in an Aβ-dependent manner in vivo and in vitro and is altered in human AD frontal cortex. (**A**) PirB interacts with cofilin in vivo in PirB$^{+/-}$ Tg mice (P30, forebrain), assessed by immunoprecipitation for PirB. Other known PirB-proximal signaling and interactions such as tyrosine phosphorylation of PirB and SHP-2 recruitment to PirB are not altered in PirB$^{+/-}$ relative to PirB$^{+/-}$ Tg mice. Representative data are shown ($n > 2$). (**B** and **C**) Cofilin phosphorylation is reduced in both (B) juvenile (P30, forebrain) and (C) adult (P200, hippocampal synaptosomes) PirB$^{+/-}$; APP/PS1 (PirB$^{+/-}$ Tg) mice relative to PirB$^{+/-}$ mice, and this reduction is rescued by PirB deletion (PirB$^{-/-}$ Tg). No significant alterations in LIM kinase (LIMK) 1/2 phosphorylation (Thr^{508}/Thr^{505}) were detected. (**D** and **E**) Quantificaton of cofilin phosphorylation (left, expressed as pCofilin/total cofilin) and pLIMK levels (right) represented in (B) and (C). (D) Means ± SEM from four independent experiments (13 animals per genotype) (*22*) shown in (B). *$P < 0.05$, *U* test. (E) Means ± SEM ($n = 3$; **$P < 0.01$, *t* test) shown in (C). (**F**) Cortical neurons (DIV18 to 22) isolated from WT or PirB$^{-/-}$ embryos (E16) were treated with oligo-Aβ42 (100 nM) for 1 hour (top panels) or 24 hours (middle panels) and cofilin signaling or PSD-95 levels were analyzed by Western blotting. Anti-Tuj1 (βIII-tubulin) antibodies detect neuronal tubulin. Bottom panels: Expression of PirB in these neurons detected by PirB immunoprecipitation. (**G**) Summary of cofilin phosphorylation (left; *$P < 0.05$, *U* test, $n = 7$) or PSD-95 levels (right; *$P < 0.05$, *U* test, $n = 6$) represented in (F). (**H**) Increased cofilin activity and Tau phosphorylation (Ser^{396}) in human frontal cortex specimens from Alzheimer's patients (AD1 to AD4) relative to non-AD adults (C1 to C3) (table S1), assessed by Western blot analysis. (**I**) Summary of cofilin phosphorylation cases represented in (H). Means ± SEM, *$P < 0.05$, *t* test.

mice (fig. S10). In the cerebral cortex of Alzheimer's patients, LilrB2 could engage similar cofilin-mediated downstream mechanisms.

Our results show that murine PirB and its human ortholog LilrB2 act as receptors for oligomeric forms of Aβ42. Mice lacking PirB are immune to the damaging effects of Aβ in hippocampal LTP and recognition memory, as well as to alterations in cofilin signaling and PSD-95 synaptic loss. We suggest that interactions between Aβ oligomers and PirB generate not only synaptotoxicity in mouse models of AD but also early defects in developmental plasticity present in visual cortex (*17*). The demonstration here that $PirB^{-/-}$ but not wild-type hippocampal slices are resistant to the acute effects of Aβ oligomers on LTP and that Aβ oligomers can alter cofilin signaling in wild-type but not $PirB^{-/-}$ cortical neurons in vitro, also argues that the rescue of AD phenotypes in $PirB^{-/-}$ Tg mice is via direct abrogation of PirB action, rather than indirect compensation or parallel signaling pathways. We also identify LilrB2 in human brain as an Aβ receptor that may contribute to synaptic loss and cognitive impairment in AD progression. Our results show that via PirB, Aβ oligomers can engage signaling pathways for neuronal actin organization that lead to synapse elimination. Therapies that selectively block LilrB2 function may be promising for treatment of AD even in the prodromal stage.

References and Notes

1. M. Sheng, B. L. Sabatini, T. C. Südhof, *Cold Spring Harb. Perspect. Biol.* **4**, a005777 (2012).
2. J. J. Palop, L. Mucke, *Nat. Neurosci.* **13**, 812–818 (2010).
3. M. Faizi *et al.*, *Brain Behav* **2**, 142–154 (2012).
4. C. Perez-Cruz *et al.*, *J. Neurosci.* **31**, 3926–3934 (2011).
5. S. Knafo *et al.*, *Cereb. Cortex* **19**, 586–592 (2009).
6. M. Cissé *et al.*, *Nature* **469**, 47–52 (2011).
7. F. Kamenetz *et al.*, *Neuron* **37**, 925–937 (2003).
8. J. Wu *et al.*, *Cell* **147**, 615–628 (2011).
9. G. M. Shankar *et al.*, *J. Neurosci.* **27**, 2866–2875 (2007).
10. G. M. Shankar *et al.*, *Nat. Med.* **14**, 837–842 (2008).
11. H. Hsieh *et al.*, *Neuron* **52**, 831–843 (2006).
12. J. Laurén, D. A. Gimbel, H. B. Nygaard, J. W. Gilbert, S. M. Strittmatter, *Nature* **457**, 1128–1132 (2009).
13. J. W. Um *et al.*, *Nat. Neurosci.* **15**, 1227–1235 (2012).
14. X. Wang *et al.*, *J. Alzheimers Dis.* **30**, 665–673 (2012).
15. J. L. Jankowsky *et al.*, *Hum. Mol. Genet.* **13**, 159–170 (2004).
16. M. Garcia-Alloza *et al.*, *Neurobiol. Dis.* **24**, 516–524 (2006).
17. C. M. William *et al.*, *J. Neurosci.* **32**, 8004–8011 (2012).
18. J. Syken, T. Grandpre, P. O. Kanold, C. J. Shatz, *Science* **313**, 1795–1800 (2006).
19. T. Takai, *Immunology* **115**, 433–440 (2005).
20. J. K. Atwal *et al.*, *Science* **322**, 967–970 (2008).
21. On the basis of size exclusion column chromatography (Fig. 1A) and Western blot analyses (Fig. 1B), as well as previous studies (*7*), the average degree of polymerization (DP) of oligomerized Aβ42 is estimated to be 60 (DPn ≈ 270 kD/4.5 kD). The mono-Aβ42 preparation consists almost exclusively of monomeric peptides with a small fraction (<5%) of low-*n* oligomers (dimer, trimer, or tetramer; Fig. 1, A and B).
22. See supplementary materials on *Science* Online.
23. H. D. VanGuilder Starkey *et al.*, *J. Mol. Neurosci.* **48**, 111–126 (2012).
24. K_d is calculated using concentration of monomer equivalent for total Aβ42 peptides (fig. S1A). Because the K_d of mono-Aβ42 is minimal (Fig. 1J), it is likely that the K_d for PirB and high-*n* Aβ42 oligomers is much lower than 180 nM. If the high-*n* species of Aβ42 responsible for binding have a DPn of ~60 (*21*) and consist of ~30% of total Aβ42 peptides (fig. S1A, and Fig. 1, A and B) (*22*), the corrected K_d would be ~1 nM.
25. T.-I. Kam *et al.*, *J. Clin. Invest.* **123**, 2791–2802 (2013).
26. J. Zheng *et al.*, *Nature* **485**, 656–660 (2012).
27. G. Ma *et al.*, *Immunity* **34**, 385–395 (2011).
28. The closest human homolog for murine PirB among the five members of the human leukocyte immunoglobulin (Ig)–like receptor B (LilrB) family has been considered to be LilrB3 based on overall amino acid sequence homology (Fig. 2A) (*27*). However, domain sequence analysis indicates that the D1D2 domain of LilrB2 aligns with the D1D2 domain of PirB, where Aβ oligomer binding occurs, whereas the D1D2 domain of LilrB3 aligns more closely with the D3D4 domain of PirB, which suggests that conservation present in the D1D2 domains, as well as tertiary structure surrounding Aβ binding site, is important for this binding.
29. M. Lindhagen-Persson, K. Brännström, M. Vestling, M. Steinitz, A. Olofsson, *PLoS ONE* **5**, e13928 (2010).
30. H. W. Kessels, L. N. Nguyen, S. Nabavi, R. Malinow, *Nature* **466**, E3–E4, discussion E4–E5 (2010).
31. S. J. Raiker *et al.*, *J. Neurosci.* **30**, 12432–12445 (2010).
32. P. L. McClean, V. Parthsarathy, E. Faivre, C. Hölscher, *J. Neurosci.* **31**, 6587–6594 (2011).
33. A. W. McGee, Y. Yang, Q. S. Fischer, N. W. Daw, S. M. Strittmatter, *Science* **309**, 2222–2226 (2005).
34. G. B. Smith, A. J. Heynen, M. F. Bear, *Philos. Trans. R. Soc. London Ser. B* **364**, 357–367 (2009).
35. R. A. Crozier, Y. Wang, C. H. Liu, M. F. Bear, *Proc. Natl. Acad. Sci. U.S.A.* **104**, 1383–1388 (2007).
36. S. Li *et al.*, *Neuron* **62**, 788–801 (2009).
37. H. Y. Wu *et al.*, *J. Neurosci.* **30**, 2636–2649 (2010).
38. M. B. Rust *et al.*, *EMBO J.* **29**, 1889–1902 (2010).
39. J. D. Adelson *et al.*, *Neuron* **73**, 1100–1107 (2012).
40. Y. Fujita, S. Endo, T. Takai, T. Yamashita, *EMBO J.* **30**, 1389–1401 (2011).
41. S. Lesné *et al.*, *Nature* **440**, 352–357 (2006).
42. P. J. Meberg, S. Ono, L. S. Minamide, M. Takahashi, J. R. Bamburg, *Cell Motil. Cytoskeleton* **39**, 172–190 (1998).
43. N. V. Oleinik, N. I. Krupenko, S. A. Krupenko, *Oncogene* **29**, 6233–6244 (2010).

Acknowledgments: We thank the Human Brain and Spinal Fluid Resource Center for providing human brain specimens; P. Kemper, C. Chechelski, and N. Sotelo-Kury for assistance with mouse husbandry; M. Stern for technical assistance; and C. Cepko (Harvard) for providing the pCAGIG vector. We also thank M. Frosch (MGH/Harvard) and M. Shamloo (Stanford Behavioral and Functional Neuroscience Laboratory, NIH grant NS069375) for helpful suggestions and advice. Supported by NIH grant EY02858 (C.J.S.), the G. Harold and Leila Y. Mathers Charitable Foundation (C.J.S.), the Ellison Medical Foundation (C.J.S.), NIH grant 5T32EY020485 (T.K.), a Regina Casper Stanford Graduate Fellowship (G.S.V.), NIH grant K08NS069811 (C.M.W.), NIH grant 5R01AG041507 (B.T.H.), an Alzheimer Disease Research Center pilot grant (NIH grant 5P50AG005134 to C.M.W.), NSF predoctoral fellowship (M.E.B.), and HHMI (K.C.G.). B.T.H. is on the Scientific Advisory Board of Neurophage and is a consultant and collaborator with Takeda Pharmaceutical Company, Bristol Meyer Squibb, Acumen, AZTherapeutics, Siemens, Sanofi, Neotope, and Fidelity Biosciences, none of which were involved in this study. C.J.S. and T.K. are inventors on a patent application assigned to the Board of Trustees of the Leland Stanford Junior University on methods and compositions for inhibiting the effects of β-amyloid oligomers (U.S. provisional application no. 61/777,835).

Supplementary Materials

www.sciencemag.org/content/341/6152/1399/suppl/DC1
Materials and Methods
Figs. S1 to S10
Table S1
References (*44*–*52*)

18 June 2013; accepted 29 July 2013
10.1126/science.1242077

An Epidermal MicroRNA Regulates Neuronal Migration Through Control of the Cellular Glycosylation State

Mikael Egebjerg Pedersen,[1] Goda Snieckute,[1] Konstantinos Kagias,[1] Camilla Nehammer,[1] Hinke A.B. Multhaupt,[2] John R. Couchman,[2] Roger Pocock[1]*

An appropriate balance in glycosylation of proteoglycans is crucial for their ability to regulate animal development. Here, we report that the *Caenorhabditis elegans* microRNA *mir-79*, an ortholog of mammalian *miR-9*, controls sugar-chain homeostasis by targeting two proteins in the proteoglycan biosynthetic pathway: a chondroitin synthase (SQV-5; squashed vulva-5) and a uridine 5′-diphosphate–sugar transporter (SQV-7). Loss of *mir-79* causes neurodevelopmental defects through SQV-5 and SQV-7 dysregulation in the epidermis. This results in a partial shutdown of heparan sulfate biosynthesis that impinges on a LON-2/glypican pathway and disrupts neuronal migration. Our results identify a regulatory axis controlled by a conserved microRNA that maintains proteoglycan homeostasis in cells.

Animal development requires the differentiation and assembly of distinct cell types into specific tissues and organs. During these processes, cells are guided by interactions with the extracellular matrix (ECM), which contains a variety of signaling molecules, including proteoglycans (*1*). Proteoglycans are made up of core proteins, such as syndecans, glypicans, and perlecans, that are decorated with varying numbers of long, unbranched glycosaminoglycan (GAG) chains. GAG chains vary in type and length and may be modified by sulfation and epimerization. Differential glycosylation and modification produce diverse interfaces for ligand-receptor interactions (*2*, *3*). These structural parameters must be regulated to permit the coordination of specific and context-dependent intercellular signaling events (*4*, *5*). The biosynthetic pathways that assemble and modify GAG chains on core proteins are highly conserved, and their disruption can cause developmental defects and lead to disease in many systems (*4*, *6*, *7*). GAG biosynthesis requires the transport of nucleotide sugars [uridine 5′-diphosphate

[1]Biotech Research and Innovation Centre, University of Copenhagen, Ole Maaløes Vej 5, Copenhagen, Denmark. [2]Department of Biomedical Sciences, University of Copenhagen, Denmark.
*Corresponding author. E-mail: roger.pocock@bric.ku.dk

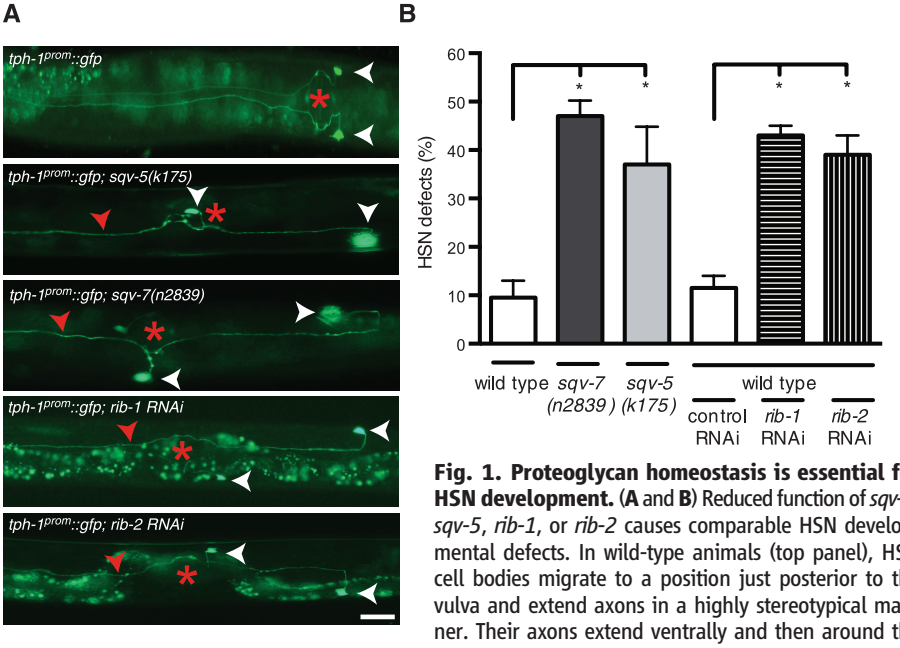

Fig. 1. Proteoglycan homeostasis is essential for HSN development. (**A** and **B**) Reduced function of *sqv-7*, *sqv-5*, *rib-1*, or *rib-2* causes comparable HSN developmental defects. In wild-type animals (top panel), HSN cell bodies migrate to a position just posterior to the vulva and extend axons in a highly stereotypical manner. Their axons extend ventrally and then around the vulva before entering the ventral nerve cord, where each axon is separated by the hypodermal ridge. Hypomorphic alleles of *sqv-5(k175)* and *sqv-7(n2839)* (middle panels) as well as RNAi against *rib-1* or *rib-2* (bottom panels) cause similar HSN developmental defects. HSN cell bodies do not migrate to their correct position, and their axons are misguided. Vulval position is marked with a red asterisk, cell bodies with white arrowheads, and misguided axons by red arrowheads. Ventral view, anterior to the left. Scale bar: 20 μm. $n > 50$, $^{*}P < 0.05$. Error bars represent means ± SEM.

(UDP)–sugars] from the cytoplasm to the Golgi apparatus (fig. S1). Generation of GAG chains commences with the addition of four specific UDP-sugars, which are added to defined attachment sites on core proteins to form a common core tetrasaccharide linkage region (fig. S1) (*8*). At this point, there is a bifurcation in the biosynthetic pathway where specific synthases and glycosyltransferases extend either chondroitin or heparan sulfate chains onto the core tetrasaccharide intermediate (fig. S1) (*8*). The supply of UDP-sugars and the relative expression levels of the respective biosynthetic enzymes inform the balance of heparan sulfate and chondroitin substitution, as exemplified by defects caused by disruption of the respective biosynthetic enzymes or UDP-sugar transporters (*6*, *7*, *9*–*11*).

We used *Caenorhabditis elegans* to study the biological requirements of proteoglycan homeostasis for neuronal development. The hermaphrodite-specific neurons (HSNs) migrate a long distance during embryogenesis. During larval development, the HSN axons navigate a precisely defined path (*12*, *13*). These complex neurodevelopmental decisions are regulated by multiple conserved molecular pathways and the external environment (*12*–*15*). As posttranslational modification of heparan sulfate proteoglycans is important for HSN development (*14*), we used this paradigm to test the effect of disrupting UDP-sugar supply

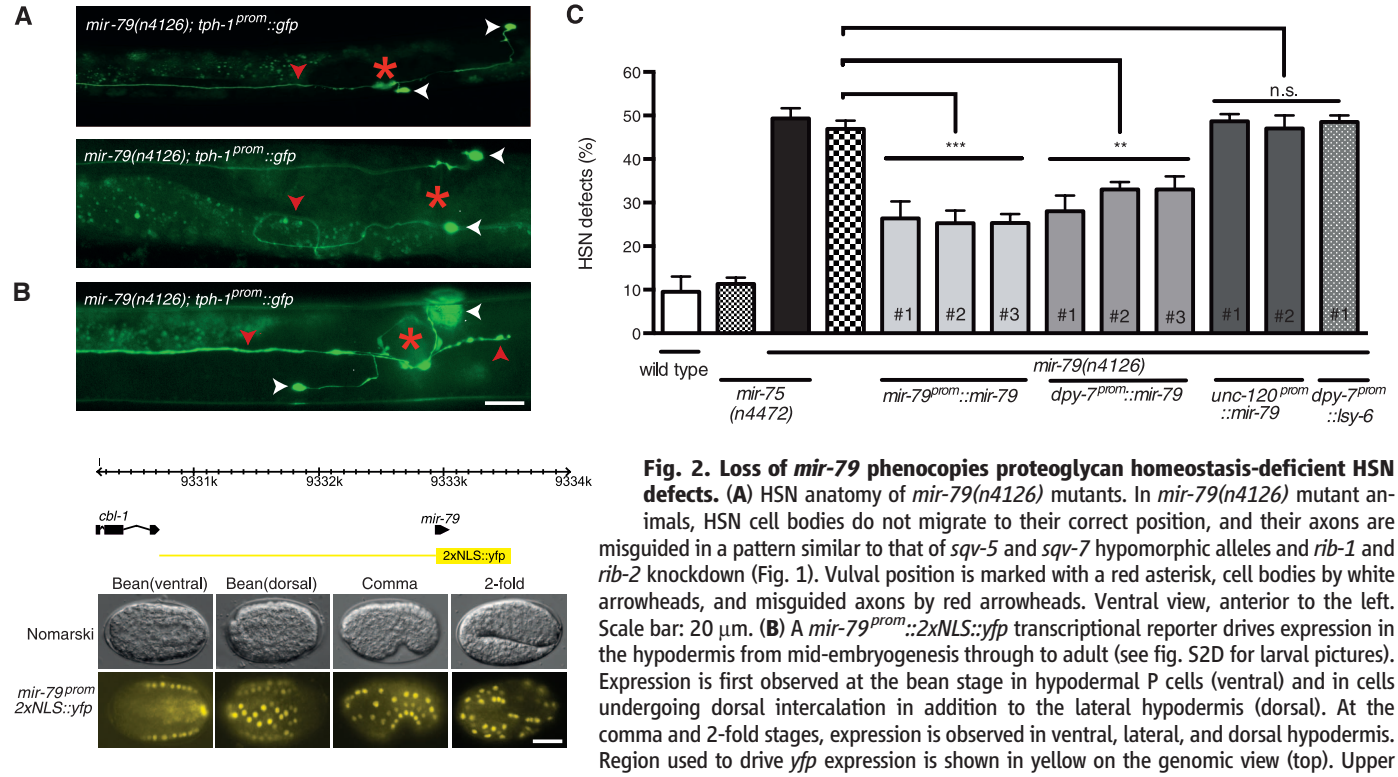

Fig. 2. Loss of *mir-79* phenocopies proteoglycan homeostasis-deficient HSN defects. (**A**) HSN anatomy of *mir-79(n4126)* mutants. In *mir-79(n4126)* mutant animals, HSN cell bodies do not migrate to their correct position, and their axons are misguided in a pattern similar to that of *sqv-5* and *sqv-7* hypomorphic alleles and *rib-1* and *rib-2* knockdown (Fig. 1). Vulval position is marked with a red asterisk, cell bodies by white arrowheads, and misguided axons by red arrowheads. Ventral view, anterior to the left. Scale bar: 20 μm. (**B**) A *mir-79*^{prom}*::2xNLS::yfp* transcriptional reporter drives expression in the hypodermis from mid-embryogenesis through to adult (see fig. S2D for larval pictures). Expression is first observed at the bean stage in hypodermal P cells (ventral) and in cells undergoing dorsal intercalation in addition to the lateral hypodermis (dorsal). At the comma and 2-fold stages, expression is observed in ventral, lateral, and dorsal hypodermis. Region used to drive *yfp* expression is shown in yellow on the genomic view (top). Upper panels are Nomarski micrographs and bottom panels are fluorescence images of the same embryos. Anterior to the left. Scale bar: 10 μm. (**C**) *mir-75(4472)* mutant animals do not exhibit defects in HSN development, and the *mir-75(n4472); mir-79(n4126)* double knockout does not show an additive effect when compared to the *mir-79(n4126)* mutant. Driving *mir-79* expression using either its own or a heterologous hypodermal promoter (*dpy-7*) rescues *mir-79(n4126)*-induced HSN developmental defects. Driving *mir-79* expression using a heterologous muscle promoter (*unc-120*) does not rescue *mir-79(n4126)*–induced HSN developmental defects. Driving expression of an unrelated miRNA (*lsy-6*) in the hypodermis does not rescue the *mir-79(n4126)*–induced HSN developmental defects. $n > 50$, $^{**}P < 0.01$, $^{***}P < 0.001$; n.s., not significant. # refers to independent transgenic lines. Error bars represent means ± SEM.

or reducing chondroitin and heparan sulfate synthesis (Fig. 1). We tested the effect of disrupting proteoglycan homeostasis on HSN development using hypomorphic alleles of *sqv-7* (squashed vulva), a UDP-sugar transporter required for GAG biosynthesis and the chondroitin synthase *sqv-5* (Fig. 1, A and B) (*16*–*18*). In addition, we performed RNA-mediated interference (RNAi) to knock down the heparan sulfate glycosyltransferases *rib-1* and *rib-2* (related to mammalian RIB-affecting EXT gene family) (Fig. 1, A and B). We analyzed HSN development using a transgenic strain in which the HSN cell bodies and axons are marked with green fluorescent protein (*gfp*). We found that similar defects in HSN development could be caused by any of three avenues: (i) reduction of UDP-sugar supply, (ii) disruption of chondroitin synthesis, or (iii) reduction of heparan sulfate synthesis (Fig. 1, A and B). These data suggest that regulatory mechanisms exist to maintain the correct balance of UDP-sugars supplied to the Golgi and to maintain the correct amounts of chondroitin and heparan sulfate biosynthetic enzymes.

We hypothesized that the regulatory mechanisms required to maintain proteoglycan homeostasis would need to be rapid and reversible owing to the demands of the changing molecular and cellular landscape during development. Thus, microRNAs (miRNAs) would be excellent candidate regulators of the proteoglycan biosynthetic pathway. We analyzed the 3′–untranslated regions (3′UTRs) of the *sqv-5*, *sqv-7*, *rib-1*, and *rib-2* genes and found that only two conserved miRNA families are predicted to target these genes—the *mir-79* and *mir-124* families (table S1). We therefore examined knockout alleles of *mir-75*, *mir-79*, and *mir-124* for defects in HSN development. We found that only loss of *mir-79* caused defects in HSN cell migration and axon guidance (Fig. 2 and fig. S2A). The defects observed were similar to those caused by disruption of proteoglycan homeostasis. *mir-79* is predicted to target both *sqv-5* and *sqv-7*, suggesting that the *mir-79* HSN phenotype is caused by dysregulation of these proteoglycan biosynthetic pathway genes.

mir-79 is highly expressed during embryogenesis and the L2/L3 larval stages (*19*) (fig. S2). The temporal pattern of *mir*-79 expression coincides with the developmental timing of the HSN migration and axon guidance events (*12*). To identify the tissue(s) in which *mir*-79 functions to regulate HSN development, we monitored the spatial and temporal expression pattern of *mir-79* using the full intergenic sequence, upstream of the *mir-79* hairpin, to drive nuclear-localized expression of the gene encoding yellow fluorescent protein (*yfp*). We found that expression of the *mir-79^{prom}::2xNLS::yfp* reporter was first detected in embryonic hypodermal (epidermal) tissue at 330 min after fertilization and continued to be expressed in the hypodermis through larval development (Fig. 2B and fig. S2D).

Although vertebrate *miR-9* family members are predominantly expressed in the nervous system (*20*), we did not detect expression of the *mir-79* reporter in the *C. elegans* nervous system. Nonetheless, we found that expression of the *mir-79* hairpin under the control of either its own promoter or a heterologous hypodermal-specific promoter partially rescued HSN migration defects of *mir-79* mutant animals (Fig. 2C). *mir-79* expression in muscle or expression of an unrelated miRNA (*lsy-6*) in the hypodermis could not rescue HSN migration defects (Fig. 2C). We did not observe any defects in hypodermal patterning or specification in the *mir-79* mutant (fig. S3), suggesting that the HSN phenotypes observed are likely caused by a signaling rather than a structural defect. Taken together, these results indicate that *mir-79* functions in the hypodermis to control HSN development.

Because the majority of miRNAs are known to inhibit translation, we hypothesized that the putative *mir-79* targets, *sqv-5* and *sqv-7*, would be up-regulated in the *mir-79* mutant background, possibly in the hypodermis. We therefore examined whether the abundance of *sqv-5* and *sqv-7* mRNAs was increased in *mir-79* mutant animals using quantitative polymerase chain reaction analysis of total RNAs from embryos (Fig. 3A).

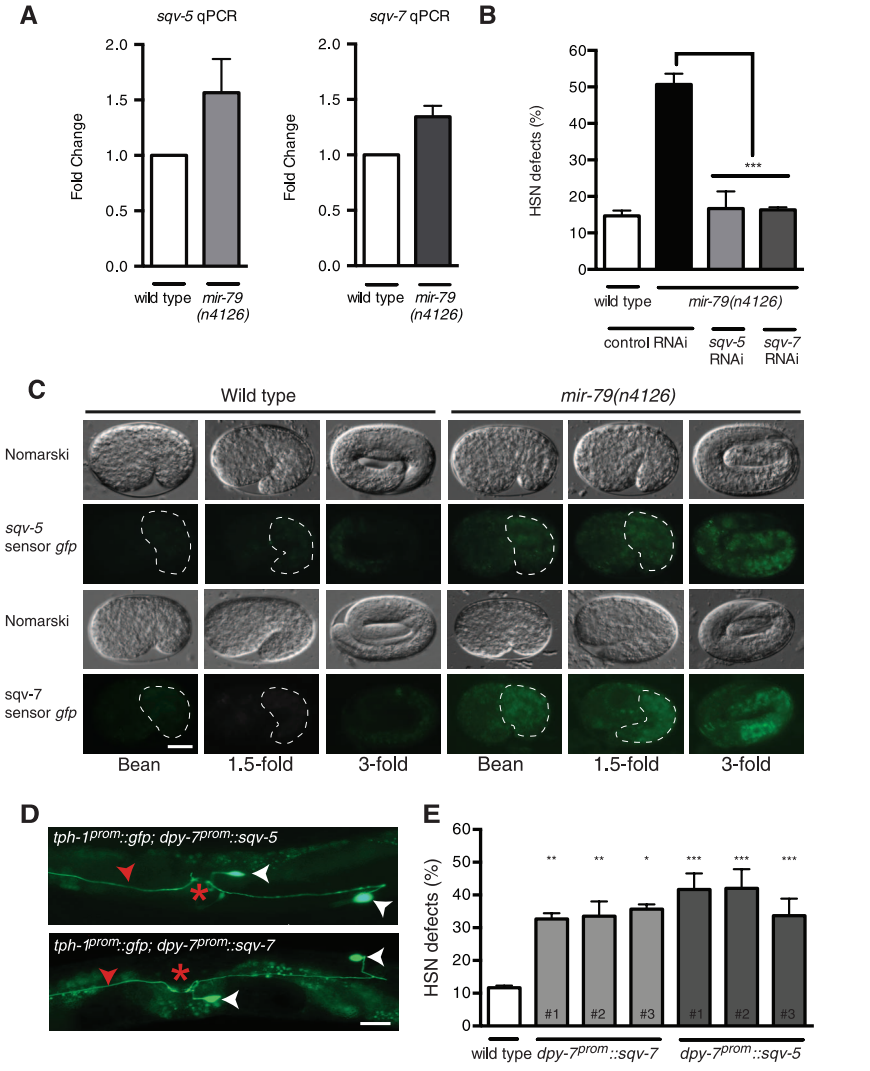

Fig. 3. *mir-79*–induced HSN defects are caused by dysregulated *sqv-5* and *sqv-7*. (**A**) *sqv-5* and *sqv-7* mRNA is up-regulated in *mir-79*–null embryos. Measurements were taken in triplicate. (**B**) Knockdown of *sqv-5* or *sqv-7* using RNAi fully suppresses *mir-79(n4126)* HSN developmental defects. $n > 100$, $^{***}P < 0.001$. (**C**) Expression of *sqv-5* and *sqv-7* translational *gfp* reporter transgenes under the control of their respective endogenous 3′UTRs. *mir-79(n4126)* mutant animals exhibit increased expression of the fluorescent fusion proteins at three stages of embryonic development. In fluorescent images of bean and 1.5-fold–stage embryos, the field of HSN migration is marked (white dashed line). Scoring of fluorescence intensity of 1.5-fold embryos is detailed in fig. S4. Upper panels are Nomarski micrographs and bottom panels are fluorescence images of the same embryos. Anterior to the left. Scale bar: 10 μm. (**D** and **E**) Overexpression of *sqv-5* or *sqv-7* in the hypodermis phenocopies the HSN developmental defects of *mir-79(n4126)* mutant animals. The penetrance of HSN developmental defects were similar to those observed with loss of *mir-79*, as were the severity of phenotypes. Vulval position is marked with a red asterisk, cell bodies with white arrowheads, and misguided axons by red arrowheads. Ventral view, anterior to the left. Scale bar: 20 μm. $n > 50$, $^{*}P < 0.05$, $^{**}P < 0.01$, $^{***}P < 0.001$. # refers to independent transgenic lines. All error bars represent means ± SEM.

We found that *sqv-5* and *sqv-7* mRNA abundance is up-regulated in *mir-79* mutant animals by 1.6-fold and 1.3-fold, respectively (Fig. 3A). These modest changes in mRNA abundance may indicate that up-regulation in the hypodermis is not easily detectable in the context of the whole organism or that *mir-79* does not act to degrade these target mRNAs. To study the effect of *mir-79* on SQV-5 and SQV-7 proteins, we constructed translational *gfp* reporter strains that express fluorescent fusion proteins upstream of the respective endogenous 3′UTRs. These integrated expression lines exhibit weak expression in wild-type embryos (Fig. 3C). When these same reporters were crossed into the *mir-79* mutant, we observed that

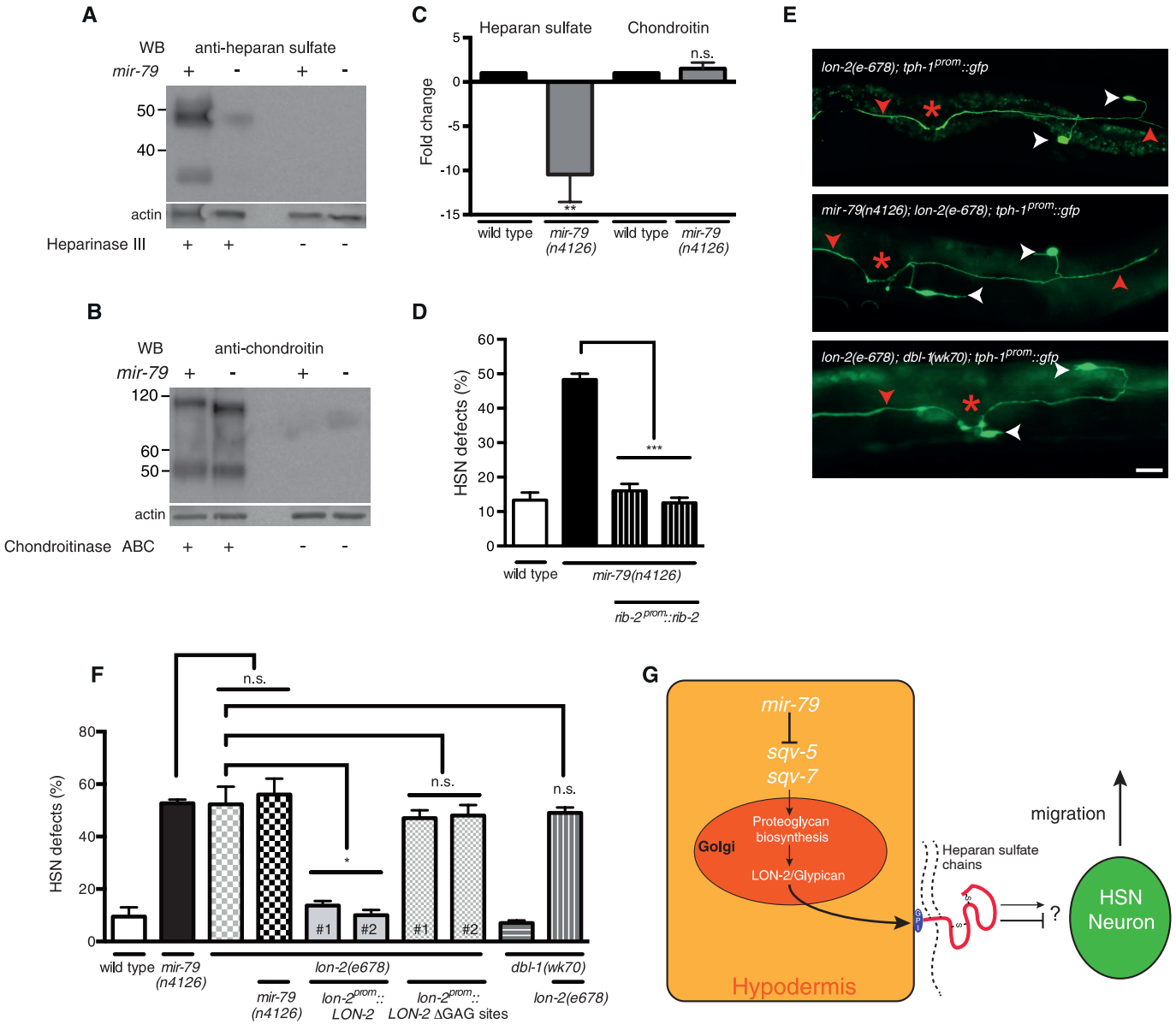

Fig. 4. Heparan-sulfated LON-2/glypican acts downstream of *mir-79* to direct neuronal guidance. (**A** to **C**) Intact proteoglycans were isolated from N2 or *mir-79(n4126)* embryos and treated with heparinase III or chondroitinase ABC. Western blot analysis was performed using monoclonal antibodies specific for heparan sulfate (A) or chondroitin (B). Antibodies only detect heparan sulfate or chondroitin stubs that are revealed after enzymatic digestion. Actin was used to normalize expression. Three Western blots from independent samples were performed, the mean values of which are depicted in (C), and representative examples are shown in (A) and (B). Data are presented as wild-type set to one-fold. Error bars represent SE. $^{**}P < 0.01$. (**D**) Driving *rib-2* expression under the control of its own promoter rescues *mir-79(n4126)*–induced HSN developmental defects. $n > 50$, $^{***}P < 0.001$. # refers to independent transgenic lines. (**E**) HSN anatomy of *lon-2(e678)*, *mir-79(n4126); lon-2(e678)* and *lon-2(e678); dbl-1(wk70)* mutant animals. Vulval position is marked with a red asterisk, cell bodies by white arrowheads, and misguided axons by red arrowheads. Ventral view, anterior to the left. Scale bar: 20 μm. (**F**) Scoring of HSN developmental defects in *mir-79(n4126)*, *lon-2(e678)*, *mir-79(n4126); lon-2(e678)*, *dbl-1(wk70)*, and *lon-2(e678); dbl-1(wk70)* mutant animals. $n > 50$. The *mir-79(n4126); lon-2(e678)* double-mutant HSN phenotype is not significantly different from either single mutant. In addition, the *lon-2(e678); dbl-1(wk70)* double-mutant HSN phenotype is not significantly different from the *lon-2(e678)* single mutant. $n > 70$. Rescue scoring of HSN developmental defects in *lon-2(e678)* mutant animals shows that wild-type LON-2 protein (*lon-2^{prom}::LON-2*) fully rescues the mutant phenotype, whereas mutant LON-2 protein, with the mutated GAG attachment sites (*lon-2^{prom}::LON-2*ΔGAG sites), is unable to rescue. $n > 30$. The mutated LON-2 protein does rescue the Lon phenotype (data not shown). $^{*}P < 0.05$; n.s., not significant. All error bars represent means ± SEM. (**G**) *mir-79* is expressed in the hypodermis, where it regulates the expression of two proteoglycan biosynthesis pathway genes (*sqv-5* and *sqv-7*). Correct control of this pathway during embryogenesis enables faithful heparan sulfate substitution of LON-2/glypican, which directs HSN neuronal development through an as-yet unknown mechanism.

the expression of both SQV-5 and SQV-7 fusion proteins was increased at three stages of embryonic development that we examined (bean, 1.5-fold, and 3-fold stages) (Fig. 3C and fig. S4). These embryonic stages coincide with the time at which HSN neuronal migration occurs (*12*). These data suggest that overexpression of *sqv-5* and *sqv-7* in *mir-79* mutant animals causes HSN developmental defects.

We used two approaches to confirm whether overexpression of *sqv-5* and *sqv-7* causes the HSN developmental defects in the *mir-79* mutant. First, we used RNAi to knock down the expression of *sqv-5* and *sqv-7* in the *mir-79* mutant and evaluated suppression of the HSN migration phenotype (Fig. 3B). RNAi knockdown of either *sqv-5* or *sqv-7* fully suppressed the *mir-79* HSN migration phenotype to background levels (Fig. 3B). As the *mir-79* HSN migration defect is fully suppressed by RNAi knockdown of either *sqv-5* or *sqv-7*, we next hypothesized that overexpression of these proteins in the hypodermis (the site of *mir-79* action) would phenocopy the *mir-79* phenotype in wild-type animals. We found that hypodermal overexpression of *sqv-5* or *sqv-7* causes quantitatively and qualitatively HSN migration defects similar to those of the *mir-79* mutant (Fig. 3, D and E). Taken together, these data suggest that the correct balance of expression of GAG biosynthesis pathway genes is required for HSN development in *C. elegans*.

To assess the possible direct regulation of *sqv-5* and *sqv-7* expression by *mir-79* in vivo, we used a heterologous 3′UTR sensor assay, which had been previously used to measure the activity of the *let-7* miRNA (*21*). We generated one transgene on which we expressed two reporters in the pharynx: one green fluorescent protein (*gfp*) "sensor" reporter with the 3′UTR of either *sqv-5* or *sqv-7* and another with a red fluorescent protein (*mCherry*) reporter under the control of the *unc-54* 3′UTR, which does not contain any *mir-79* binding sites. On a second transgene, we also expressed *mir-79* in the pharynx. As expected, we found that expression of *mir-79* robustly down-regulated *gfp* expression (controlled through *sqv-5* or *sqv-7* 3′UTR sequence) but not *mCherry* expression (fig. S5). These data suggest that *mir-79* can directly interact with the *sqv-5* and *sqv-7* 3′UTRs to down-regulate their expression. *mir-79* regulation of the *sqv-5* and *sqv-7* 3′UTRs was lost when the *mir-79* target sites were mutated (fig. S5). We found that the *Drosophila* and human orthologs of SQV-5—CG9220 and CHSY1, respectively—are also predicted targets of *miR-9* (fig. S6) and, in the case of CHSY1, this relationship is also suggested by PAR-CLIP data (*22*).

To analyze the impact of imbalance in the proteoglycan biosynthetic pathway on the glycosylation of core proteins, we isolated intact proteoglycans from wild-type and *mir-79* mutant animals (Fig. 4, A to C). Proteoglycans were treated with heparinase III or chondroitinase ABC, which cleave heparan sulfate and chondroitin chains, respectively. Removal of the chains result in "stub" oligosaccharides, which are recognized by antibodies against heparan sulfate and chondroitin (*23*, *24*). Western blot analysis using heparan sulfate– and chondroitin-specific antibodies showed that in *mir-79* mutant animals, the expression level of heparan sulfated proteoglycans is reduced by a factor of 10, whereas the level of proteoglycans with chondroitin chains is unaffected (Fig. 4, A to C). Overexpression of *rib-2*, one of the two glycosyltransferases required for heparan sulfate synthesis in *C. elegans* (*25*), provided sufficient heparan sulfate to rescue *mir-79*–induced HSN defects (Fig. 4D). Taken together, our biochemical and genetic analyses suggest that the neurodevelopmental defects observed in the *mir-*79 mutant are caused by defects in the biosynthesis of heparan sulfate proteoglycan in the hypodermis.

There are four canonical heparan sulfate proteoglycan core proteins in the *C. elegans* genome: *lon-2*/glypican, *gpn-1*/glypican, *sdn-1*/syndecan, and *unc-52*/perlecan (*2*). We focused on *lon-2* and its role in HSN migration, as it is expressed in the hypodermis (*26*), where *mir-79* functions, and *lon-2*–null mutant animals exhibit HSN phenotypes similar to those of *mir-79* mutant animals (Fig. 4E). We asked whether the *mir-79* HSN defects are caused by defective LON-2 signaling by performing genetic double-mutant analysis. Null mutations of *mir-79* and *lon-2* exhibit similar penetrance of HSN developmental defects (Fig. 4F). If *mir-79* functions in a pathway parallel to that of *lon-2* rather in the same pathway, we would expect the phenotype of the double mutant to be additive. However, we found that the penetrance of HSN defects of *mir-79; lon-2* double-mutant animals was not significantly different from either single mutant, suggesting that *mir-79* and *lon-2* act in the same pathway to regulate HSN development (Fig. 4F). The three GAG attachment sites on the LON-2 core protein are unnecessary for LON-2 regulation of body length (*27*). Our work would imply that these GAG attachment sites are crucial for the regulation of HSN migration owing to the requirement of LON-2 heparan sulfate chains. Indeed, we found that LON-2 cannot direct HSN development without intact GAG attachment sites (Fig. 4F). To regulate body length in *C. elegans*, *lon-2* acts to repress the *dbl-1*/TGFβ (transforming growth factor–β) pathway through the core protein and independently of GAG attachment (*26*, *27*). This suggests that the HSN developmental defects of *lon-2* mutant animals are also independent of the *dbl-1* pathway. Indeed, *lon-2*; *dbl-1* double mutant animals exhibit the *lon-2* mutant HSN phenotype, indicating that LON-2/glypican regulates HSN neuronal development through a pathway independent of the *dbl-1*/TGFβ pathway that governs body length (Fig. 4F).

We have identified a regulatory axis through which the highly conserved *mir-79* gene controls a specific neurodevelopmental event (HSN cell migration and axon guidance) in *C. elegans* (Fig. 4G). *mir-79* regulates this event non–cell-autonomously by controlling hypodermal expression of two components of the GAG biosynthetic pathway, *sqv-5* and *sqv-7*, which encode a chondroitin synthase and UDP-sugar transporter, respectively. Aberrant expression of these proteins in the *mir-79* deletion mutant reduces heparan sulfate biosynthesis and disrupts LON-2/glypican signaling. Our results imply that proteoglycan biosynthesis is tightly regulated to shape cell-surface glycosylation architecture required to direct neuronal migration—a control we have shown to be mediated by a microRNA.

References and Notes

1. J. R. Couchman, *Annu. Rev. Cell Dev. Biol.* **26**, 89–114 (2010).
2. H. E. Bülow, O. Hobert, *Annu. Rev. Cell Dev. Biol.* **22**, 375–407 (2006).
3. M. Forsberg *et al.*, *J. Biol. Chem.* **287**, 10853–10862 (2012).
4. H. E. Bülow, O. Hobert, *Neuron* **41**, 723–736 (2004).
5. H. E. Bülow *et al.*, *Curr. Biol.* **18**, 1978–1985 (2008).
6. Y. Bellaiche, I. The, N. Perrimon, *Nature* **394**, 85–88 (1998).
7. J. Tian *et al.*, *Am. J. Hum. Genet.* **87**, 768–778 (2010).
8. L. Kjellén, U. Lindahl, *Annu. Rev. Biochem.* **60**, 443–475 (1991).
9. E. M. Selva *et al.*, *Nat. Cell Biol.* **3**, 809–815 (2001).
10. S. Mizuguchi *et al.*, *Nature* **423**, 443–448 (2003).
11. K. Lidholt *et al.*, *Proc. Natl. Acad. Sci. U.S.A.* **89**, 2267–2271 (1992).
12. C. Desai, G. Garriga, S. L. McIntire, H. R. Horvitz, *Nature* **336**, 638–646 (1988).
13. C. E. Adler, R. D. Fetter, C. I. Bargmann, *Nat. Neurosci.* **9**, 511–518 (2006).
14. T. Kinnunen *et al.*, *Proc. Natl. Acad. Sci. U.S.A.* **102**, 1507–1512 (2005).
15. R. Pocock, O. Hobert, *Nat. Neurosci.* **11**, 894–900 (2008).
16. T. Herman, E. Hartwieg, H. R. Horvitz, *Proc. Natl. Acad. Sci. U.S.A.* **96**, 968–973 (1999).
17. P. Berninsone, H. Y. Hwang, I. Zemtseva, H. R. Horvitz, C. B. Hirschberg, *Proc. Natl. Acad. Sci. U.S.A.* **98**, 3738–3743 (2001).
18. H.-Y. Hwang, S. K. Olson, J. D. Esko, H. R. Horvitz, *Nature* **423**, 439–443 (2003).
19. M. Kato, A. de Lencastre, Z. Pincus, F. J. Slack, *Genome Biol.* **10**, R54 (2009).
20. A. X. Sun, G. R. Crabtree, A. S. Yoo, *Curr. Opin. Cell Biol.* **25**, 215–221 (2013).
21. N. J. Lehrbach *et al.*, *Nat. Struct. Mol. Biol.* **16**, 1016–1020 (2009).
22. M. Hafner *et al.*, *Cell* **141**, 129–141 (2010).
23. J. R. Couchman, B. Caterson, J. E. Christner, J. R. Baker, *Prog. Clin. Biol. Res.* **151**, 31–46 (1984).
24. G. David, X. M. Bai, B. Van der Schueren, J. J. Cassiman, H. Van den Berghe, *J. Cell Biol.* **119**, 961–975 (1992).
25. H. Kitagawa *et al.*, *J. Biol. Chem.* **276**, 4834–4838 (2001).
26. T. L. Gumienny *et al.*, *Curr. Biol.* **17**, 159–164 (2007).
27. S. Taneja-Bageshwar, T. L. Gumienny, *Dev. Biol.* **371**, 66–76 (2012).

Acknowledgments: We thank O. Hobert, H. Buelow, P. Brodersen, and A. Lund for comments on the manuscript and T. Gumienny for *lon-2* strains and reagents. Some strains used in this study were provided by the *Caenorhabditis* Genetics Center, which is funded by NIH Office of Research Infrastructure Programs (P40 OD010440). This work was supported by grants from the European Research Council (ERC Starting Grant no. 260807 to R.P.), the Lundbeck Foundation (Project nos. R118-A11481 to R.P. and R44-A4407 to J.R.C.), the Danish National Research Foundation, and the Novo Nordisk Foundation (to J.R.C.).

Supplementary Materials

www.sciencemag.org/content/341/6152/1404/suppl/DC1
Materials and Methods
Figs. S1 to S6
Tables S1 and S2
References (*28*–*33*)

28 June 2013; accepted 19 August 2013
10.1126/science.1242528

Introducing the new BD FACSAria™ Fusion

Integrated cell sorting and biosafety.

The fusion of safety, performance, and sorting.

BD

Helping all people live healthy lives

The BD FACSAria™ Fusion cell sorter is built on the solid foundation of patented technologies, exceptional multicolor performance and ease-of-use that was first brought to the world of sorting by the launch of the BD FACSAria™ cell sorter in 2003.

Now this sorting know-how is combined with best-in-class biosafety expertise to create the BD FACSAria Fusion, a fully integrated advanced cell sorter and biosafety solution for research laboratories.

The BD FACSAria Fusion has been verified to meet personnel and product protection standards for a Class II Type A2 biosafety cabinet, the National Sanitation Foundation International Standard 49, the European Standard 12469, and the Australian Standard AS 2252.2–2009.

Choose up to six laser wavelengths and 20 detector positions to measure up to 18 colors simultaneously.

Learn more at **bdbiosciences.com/go/fusion.**

BD Biosciences
2350 Qume Drive
San Jose, CA 95131
bdbiosciences.com

LightCycler®

Super capabilities are now within your reach

Rely on Roche´s long-standing expertise in providing qPCR instruments that enable research breakthroughs. The new LightCycler® 96 System delivers data in line with all current scientific and technology standards.

- Fast precision thermal cycling
- Innovative optics for high accuracy
- Smart, intuitive user interface
- Powerful data analysis software

Become a publication superhero with the new LightCycler® 96 Real-Time PCR System from Roche.

Find out more on www.lightcycler96.com

For life science research only.
Not for use in diagnostic procedures.

Roche Diagnostics GmbH
Sandhofer Straße 116
68305 Mannheim, Germany

Roche

eppendorf

New accessory:
Eppendorf
ThermoTop®

Multiple Talents

Eppendorf ThermoMixer™ and Eppendorf ThermoStat™

The new generation of Eppendorf Temperature Control and Mixing Instruments offer you more than what meets the eye.

Not only do they provide the versatility and accurate temperature control you come to expect, they now also offer you superior mixing performance, outstanding ergonomic operation and a unique ThermoTop.

> ^{2D}Mix-Control: perfect mixing results in all vessel formats
> Eppendorf QuickRelease™: ergonomic block exchange in just 2 seconds
> Intuitive operation: pre-optimized program and temperature keys
> Eppendorf ThermoTop prevents condensate formation for more accurate results.

www.eppendorf.com/thermomixer-c

How do you engage?

AAAS Early Career Award for Public Engagement with Science

Nominations are open **now through October 15** for the **AAAS Early Career Award for Public Engagement with Science.** With this award, AAAS recognizes early-career scientists and engineers who demonstrate excellence in their contribution to public engagement with science activities. The award recipient will receive a monetary prize of $5,000, a commemorative plaque, and complimentary registration and reimbursement of travel expenses to the 2014 AAAS Annual Meeting in Chicago.

For eligibility information and instructions on submitting nominations, visit **www.aaas.org/go/PESaward**.

Deadline October 15

AAAS
ADVANCING SCIENCE, SERVING SOCIETY

ISOLATION MOUNTS

The Vibralevel DSM Dual Stiffness Isolation Mount is a new concept in vibration isolation for moving load applications. Providing the optimal combination of damping and vibration isolation, the Vibralevel DSM is a cost-effective alternative to active vibration isolation systems. Designed primarily for applications where a moving load is supported on vibration isolation mounts, the Vibralevel DSM virtually eliminates platform tilt by activating the "stiff" mode when a load undergoes an aggressive move. On a signal from the machine controller, it transitions from a softer vibration isolation system to a stiffer support platform within 500 ms. Upon receipt of a signal such as "servo-in-position" when the move is complete, the system reverts to "soft" mode, providing the vibration isolation required for accurate placement or inspection. The Vibralevel DSM is ideal for applications involving both shifting loads and the need for pinpoint positioning applications and is well suited to die bonders, systems with robotic arms, and pick-and-place machines.

Kinetic Systems
For info: 617-522-8700 | www.kineticsystems.com

FLUORESCENCE SPECTROSCOPY SYSTEM

The Aqualog, the only simultaneous absorbance and fluorescence system that measures CDOM (colored dissolved organic matter) in water, is 100 times faster than previous fluorescence methods, and now offers both lower absorbance and fluorescence excitation wavelengths down to 200 nm, and extended emission coverage up to 800 nm. To support the new ozone-producing lamp, a deozonating scrubbing filter has been included. Sample Queue software has also been added for automatic, continuous data collection of excitation emission matrices for up to 1,000 samples without interruption. The software is compatible with multi-position sample changers and flow-through cells. An enhanced Solo software package from Eigenvector Inc. enables rapid import to multivariate modeling and provides rapid, automated generation of component identification and quantification tables. The Solo Parallel Factor Analysis has been upgraded with split-half validation analysis and an improved Rayleigh and Raman scattering masking toolkit.

Horiba Scientific
For info: 732-494-8660 | www.aqualog.com

ADVANCED CHARGED AEROSOL DETECTOR

The Dionex Corona Veo is an advanced charged aerosol detector (CAD) for liquid chromatography (LC) engineered to increase the effectiveness of CAD technology with expanded low-flow capability and additional sensitivity compared to its previous detectors. A new FocusJet concentric nebulization system was developed specifically for the Corona Veo detector to enhance performance, especially for the detection of semi-volatile compounds. Compared with its past systems, the new aerosol flow path is improved for a wider range of usable LC mobile phase compositions and can accommodate a broader range of separation chemistries and column technologies. The Corona Veo detector is designed to make the universal detection benefits of CAD accessible with the speed and resolution of UHPLC at sub-nanogram sensitivity levels. The detector works with non-volatile and many semi-volatile compounds, from large to small molecules. The Corona Veo detector can be used to evaluate relative analyte concentrations, even when standards are not available.

Thermo Fisher Scientific
For info: 800-874-3723 | www.thermoscientific.com/Veo

PROTEIN INTERACTION BIOSENSORS

The new samX platform is designed for real-time, label-free biomolecular interaction assays, and includes advanced acoustic wave biosensor technology. Based on SAW's Surface Acoustic Wave technology, the biosensors measure changes in mass and viscoelasticity at the chip surface based on changes in the high-frequency acoustic oscillations running across the chip surface. This innovative approach is complementary to other biophysical techniques, such as surface plasmon resonance and quartz crystal microbalance for measuring protein interactions, and can also be used for samples and applications that are difficult to analyze by these other methods, thus providing additional information and insights. The samX platform is ideally suited to the study of native membrane proteins and protein complexes such as the 7TM G-protein coupled receptors, either as membrane fragments or within liposome or vesicle particles. Such complexes can be very challenging to analyze by traditional biosensor platforms.

SAW Instruments
For info: +49-22-88128-760 | www.saw-instruments.com

CELL PROLIFERATION/VALIDATION ASSAYS

A new range of 96-well format 3D Spheroid Cell Proliferation/Viability Assays provide a new tool to allow cell-based assays to be carried out in 3-D. The new assay provides a useful tool for modeling tumor response in vitro. The kit utilizes a 3D Culture Qualified 96 Well Spheroid Formation Plate alongside a specialized Spheroid Formation Extracellular Matrix to drive aggregation and/or spheroid formation of cells. Upon completion of spheroid formation, the spheroid may be treated with pharmacological agents to evaluate tumor viability after drug treatment. Tumor spheroid expansion is visualized microscopically and can be quantitated through image analysis software for real-time and label-free evaluation. At the conclusion of the assay, cell viability may be assessed by fluorescence using Resazurin. The assay offers an in vitro, standardized, three-dimensional, high-content format for inducing multicellular tumor spheroid formation and quantitating cell viability within the spheroids in response to pharmacological treatment.

AMS Biotechnology
For info: +44-(0)-1235-828200 | www.amsbio.com

Electronically submit your new product description or product literature information! Go to **www.sciencemag.org/products/newproducts.dtl** for more information.

Newly offered instrumentation, apparatus, and laboratory materials of interest to researchers in all disciplines in academic, industrial, and governmental organizations are featured in this space. Emphasis is given to purpose, chief characteristics, and availability of products and materials. Endorsement by *Science* or AAAS of any products or materials mentioned is not implied. Additional information may be obtained from the manufacturer or supplier.

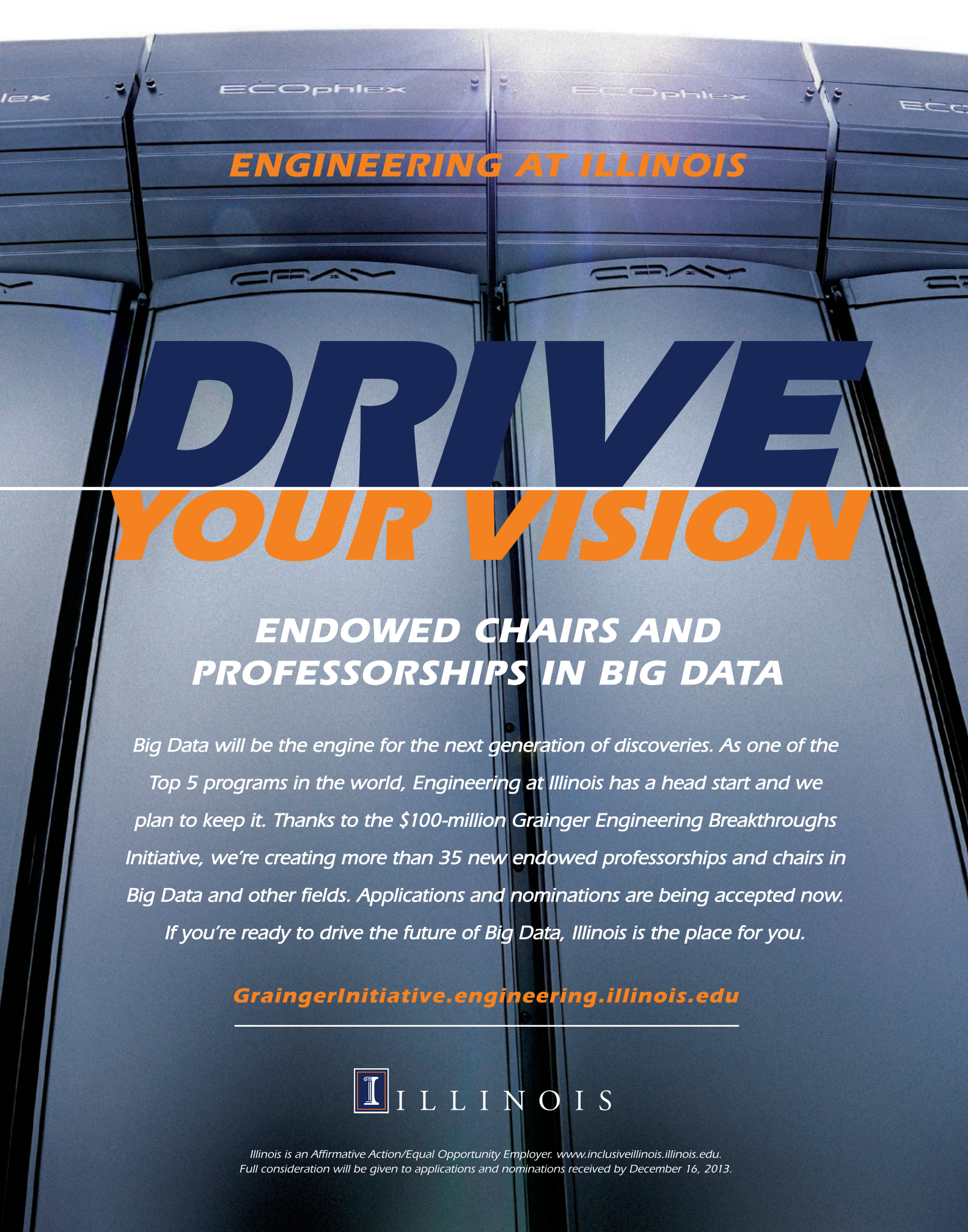

ENGINEERING AT ILLINOIS

DRIVE YOUR VISION

ENDOWED CHAIRS AND PROFESSORSHIPS IN BIG DATA

Big Data will be the engine for the next generation of discoveries. As one of the Top 5 programs in the world, Engineering at Illinois has a head start and we plan to keep it. Thanks to the $100-million Grainger Engineering Breakthroughs Initiative, we're creating more than 35 new endowed professorships and chairs in Big Data and other fields. Applications and nominations are being accepted now. If you're ready to drive the future of Big Data, Illinois is the place for you.

GraingerInitiative.engineering.illinois.edu

ILLINOIS

Illinois is an Affirmative Action/Equal Opportunity Employer. www.inclusiveillinois.illinois.edu.
Full consideration will be given to applications and nominations received by December 16, 2013.

POSITIONS OPEN

DEVELOPMENTAL CELL BIOLOGY & MARINE BIOLOGY
Department of Biological Sciences
Humboldt State University

Humboldt State University's (HSU) Department of Biological Sciences invites applications for two **TENURE-TRACK FACULTY POSITIONS** in Developmental Cell Biology and Marine Biology starting August 2014. Candidates should be committed to teaching excellence and to building a strong research program with undergraduate and graduate students.

Marine Biology (**Job #7586**): Expertise in Ecology and field studies focused on Marine Biology with strong quantitative skills. Instructional assignments may include: Marine Biology, Intertidal Ecology, Invertebrate Zoology or a course in the candidate's area of expertise.

Developmental Cell Biology (**Job #7587**): Expertise in Developmental Biology/Cell Biology ideally with skills in Stem Cell Biology or Developmental Immunology. Instructional assignments may include: Developmental Biology, Cell Biology, Genetics, Genetics Lab, Stem Cell Biology, Cell Biology or a course in candidate's area of expertise. For more info, please visit **website: http://apptrkr.com/388508.** First review of applications is November 1, 2013 for #7587 Developmental Cell Biology position and December 2, 2013 for #7586 Marine Biology position. Positions are open until filled. *HSU is an Equal Opportunity/Title IX/ADA Employer.*

COMPUTATIONAL BIOLOGIST

The Biochemistry and Molecular Biology (BCMB) program at the College of Wooster seeks to fill a tenure-track position, starting in August 2014. Primary responsibilities will be to develop a computational biology course, contribute to introductory and intermediate courses in the BCMB major, participate in the College's First-Year interdisciplinary program, and mentor undergraduates in our nationally recognized senior research program. Research expertise in any area of computational biology (biomodeling, genomics, neuroscience, pharmacology, etc.) is appropriate. Ph.D. required; postdoctoral research and/or teaching experience preferred. Send curriculum vitae, undergraduate and graduate transcripts, statement of teaching philosophy, description of research program, and three letters of reference to **e-mail: bsnyder@wooster.edu.** Address questions regarding the position to William Morgan (**e-mail: wmorgan@wooster.edu**), Chair of BCMB. Review of applications will begin October 1, 2013 and continue until the position is filled. *Wooster seeks to ensure diversity by its policy of employing persons without regard to age, sex, color, race, creed, religion, national origin, disability, veteran status, sexual orientation, or political affiliation. The College of Wooster is an Equal Opportunity/Affirmative Action Employer.*

POSTDOCTORAL POSITION

Postdoctoral position is available to work on aspects of lipid metabolism in relation to diabetes and atherosclerosis. Candidate should have strong background in molecular biological and lipid analytical skills. Familiarity with mitochondrial techniques and or mass spectrometry or organic synthesis would be a plus. To apply, submit curriculum vitae, a brief statement of your qualifications, research interest and future career plans as well as names and contact information of three references to **e-mail: spartha@ucf.edu.**

University of Central Florida is an Equal Opportunity/Affirmative Action Employer and encourages applicants from minorities, women, and other underrepresented groups. Search materials are available for public review as provided by Florida statute.

The Department of Earth and Planetary Sciences at the University of California Santa Cruz (UCSC), has an opening for a tenure-track **ASSISTANT PROFESSOR** in Planetary Sciences. Application closing date is October 21, 2013; please refer to **position #JPF00057-4** in all correspondence. Apply at **website: http://apptrkr.com/383850.** For more information, please **e-mail: epsjobs@ucsc.edu.** *UCSC is an Affirmative Action/Equal Employment Opportunity Employer.*

POSITIONS OPEN

ASSISTANT PROFESSOR of Biology (Wildlife Ecology)

The Biology Department at Missouri State University anticipates an August 2014 opening for a tenure-track Assistant Professor in Wildlife Ecology. Requirements include a Ph.D. in wildlife biology or related area with knowledge of disease ecology or epidemiology, peer-reviewed publications in wildlife ecology, and excellent communication skills. Duties include teaching courses in wildlife management, mammalogy or ornithology, and specialty; graduate and undergraduate advisement; and externally funded research. A letter of application (including a commitment to working with diverse student populations), curriculum vitae, names, and contact information for three references, a statement of teaching experience and interests, and copies of all university transcripts should be submitted online at **website: https://jobs.missouristate.edu.** Employment will require a criminal background check at University expense. Application review begins on 6 November 2013 and continues until position is filled. Starting date is 11 August 2014. Direct queries to **e-mail: briangreene@missouristate.edu.** *Equal Opportunity/Affirmative Action.*

UNIL | Université de Lausanne

Faculty of Biology and Medicine

| le savoir vivant |

THE FACULTY OF BIOLOGY AND MEDICINE OF THE UNIVERSITY OF LAUSANNE (UNIL), SWITZERLAND, AND THE LUDWIG CENTRE AT UNIL INVITE APPLICATIONS FOR THE POSITION OF

ASSISTANT PROFESSOR
TENURE TRACK TOWARDS ASSOCIATE PROFESSOR
IN SYSTEMS IMMUNOLOGY PROTEOMICS AND BIOINFORMATICS

The Ludwig Centre (http://www.unil.ch/licr) and the Department of Oncology at UNIL, together with the Federal Institute of Technology of Lausanne (EPFL), have selected Immune Engineering as an area of high priority for cancer research. The three institutions are jointly building a world-class environment in tumor immunology and immune engineering, as part of the new Swiss Cancer Centre.

We are seeking outstanding candidates with strong experience in bioinformatics, molecular modelling, integrative biostatistics of proteomics and genomics, and systems immunology. The successful candidate will use this knowledge to apply mass spectrometry and genomics approaches to identify and quantify MHC-associated peptides expressed by tumors, with the ultimate goal to develop fundamental knowledge in tumor antigen processing and presentation and in molecular systems immunology, as well as to support a clinical programme of personalized cancer vaccines. The candidate will benefit from a generous start-up package, a particularly rich research and translational clinical environment in cancer and immunology, a dual appointment at the Swiss Institute for Bioinformatics (SIB), and an array of state-of-the-art core facilities and laboratories within the Ludwig Cancer Centre and EPFL. Strong candidates with an interest in developing immune therapeutics based on genomic and proteomic data sets will be given the highest priority.

We envision the following profile for the successful candidate :

- PhD degree in bioinformatics and systems immunology.
- An outstanding research track record and ability to write competitive grant applications.
- A strong interest and strong expertise in, but not limited to, the immunopeptidome, integrating mass-spectrometry and MHC-associated peptide data to develop personalized vaccines against cancer.
- The drive to develop a highly successful and competitive independent research programme.
- Engagement in collaborations with translational research groups and clinicians in the multidisciplinary immunotherapy programme of the Cancer Centre as well as labs, groups and cores at UNIL, SIB and EPFL.

The job description is available on the Web at the address http://www.unil.ch/fbm/page64812.html.
Further information may be obtained from Prof. Mermod (Nicolas.Mermod@unil.ch), chairman of the search committee.

The applications, in English, will include the curriculum vitae, the list of publications with a copy of the five most significant ones, a brief statement of the research programme and teaching experience, as well as three references (names and contact information). They should be submitted by December 31st, 2013 as a single pdf file to www.unil.ch/iafbm/application.

Seeking to promote an equitable representation of men and women among its staff, the University encourages applications from women.

ÉCOLE POLYTECHNIQUE
FÉDÉRALE DE LAUSANNE

Bioengineering Faculty Positions in Immunoengineering

at Ecole polytechnique fédérale de Lausanne (EPFL)

The Institute of Bioengineering at EPFL is soliciting applications for **tenure-track assistant professors** in the broad area of **immunoengineering**, an emerging field at the interface of immunology and bioengineering. Appointments at other ranks will be exceptionally considered as well.

Bioengineering at EPFL is well integrated between the School of Engineering and the School of Life Sciences. Close interactions with the new Wyss Center for Bio- and Neuro-Engineering, University of Lausanne, the Canton of Vaud University Hospital (CHUV), and the Ludwig Institute for Cancer Research are possible, and encouraged.

The open faculty position is offered in a rich environment for both basic and translational science, of both theoretical and experimental research. The search is open in terms of research area within the broad domain of immunoengineering, including (but not limited to) systems and computational immunology, microfluidic and high-throughput technology, systems physiology, cell and tissue engineering, and materials and biomolecular engineering in vaccines and immunotherapeutics.

The EPFL is a dynamic science and engineering university fostering excellence and diversity. It is consistently ranked among the top research institutions in Europe, and offers a rich international environment with English as the common language. Research is supported by numerous outstanding core facilities including imaging, proteomics, bioinformatics, transgenomics, flow cytometry, microfabrication, and electron microscopy.

Successful candidates are expected to initiate independent, creative research programs and participate in undergraduate and graduate-level teaching. Internationally competitive salaries, start-up resources and benefits are offered.

Applications should include a curriculum vitae with a list of publications, a concise statement of research and teaching interests, and the names and addresses (including e-mail) of at least five referees. Applications should be uploaded (as PDF files) to the recruitment web site:
http://immunoeng-search.epfl.ch

Formal evaluation of candidates will begin on **30 November 2013** and continue until the position is filled.

Enquiries may be sent to:
Prof. Melody A. Swartz
Search Committee Chair
e-mail: immunoeng-search@epfl.ch

For additional information on the EPFL and the Institute of Bioengineering, please consult: www.epfl.ch, sti.epfl.ch, sv.epfl.ch and bioengineering.epfl.ch.

EPFL is committed to increasing the diversity of its faculty, and strongly encourages women to apply.

TM

Positions in Molecular or Biophysical Neuroscience
Department of Biochemistry
School of Molecular and Cellular Biology
University of Illinois at Urbana-Champaign

The School of Molecular and Cellular Biology (http://mcb.illinois.edu/) at the University of Illinois at Urbana-Champaign seeks outstanding applicants for two tenure-track Assistant Professor positions in the Department of Biochemistry in the area of **Molecular and Biophysical Neuroscience**.

We are interested in candidates conducting mechanistic research in any area of molecular neuroscience, including, but not limited to: biochemical or biophysical studies of neurotransmitter receptors and other membrane channels, transporters or receptors; axonal transport and protein trafficking/synaptic vesicle biology; biochemical studies of neurodegenerative diseases; molecular basis of memory; role of oxidative stress in neuronal function/dysfunction; and the biochemical basis for transcription, translation, RNA splicing, and/or epigenetic mechanisms in neural development.

Candidates must hold a Ph.D., M.D. or equivalent degree, have a strong track record of creativity and productivity, and strong potential for future independent research. The target starting date is August 16, 2014. Successful candidates will be located in the Department of Biochemistry and will be expected to conduct independent research, participate in our B.S. and Ph.D. programs, and teach effectively at the undergraduate and graduate levels. These positions offer excellent laboratory facilities, relocation and start-up funds, as well opportunities to work with outstanding graduate students. Our faculty strengths in membrane biophysics, structural biology, and gene regulation offer a strong infrastructure and provide opportunities for collaborative research.

The Urbana-Champaign campus offers state-of-the-art research facilities and programs that include the Beckman Institute, Institute of Genomic Biology, Roy J. Carver Biotechnology Center, Abbott/UIUC Center for Nutrition, Learning and Memory, and multiple student training grants, as well as facilities for NMR spectroscopy, X-ray crystallography, proteomics, metabolomics, high-throughput screening, flow cytometry, imaging (including fMRI), and transgenic mice. UIUC is a member of the Life Sciences Collaborative Access Team at Argonne National Lab, which provides routine access to synchrotron facilities for X-ray data collection. The campus has strong cross-departmental graduate programs in neuroscience, biophysics and quantitative biology and chemical biology, as well as superb computational resources at the National Center for Supercomputing Applications and the NIH Resource for Macromolecular Modeling and Bioinformatics.

Urbana-Champaign offers the residential advantages of a medium-sized university city, excellent cultural opportunities, and a high quality of life. In 2010, the University of Illinois at Urbana-Champaign received top rankings by Harvard University's Collaborative on Academic Careers in Higher Education for its pre-tenure practices in balancing work and home (http://www.insidehighered.com/news/2010/11/15/coache).

To ensure full consideration, create your candidate profile through **https://jobs.illinois.edu** and upload your application cover letter, curriculum vitae, concise summary of past research accomplishments, statement of future research plans and contact information for three professional references by **December 15, 2013**. Referees will be contacted electronically upon submission of the application. Although early applications are appreciated and interviews may be conducted before the closing date, hiring decisions will not be made until after the closing date. Questions can be addressed to the School of Molecular and Cellular Biology, 217-333-3166.

Illinois is an Affirmative Action/Equal Opportunity Employer and actively seeks individuals with diverse backgrounds, experiences, and ideas who embrace and value diversity and inclusivity (www.inclusiveillinois.illinois.edu).

NANYANG TECHNOLOGICAL UNIVERSITY

RISE TO THE OPPORTUNITY

with the fastest-rising university in the world's Top 50. **NTU.**

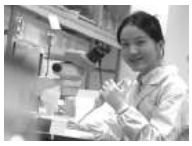

Faculty Positions at School of Chemical and Biomedical Engineering (SCBE)

Nanyang Technological University (NTU) in Singapore is ranked 47th in the QS World University Rankings 2012. SCBE at NTU invites applications for Assistant, Associate or Full Professors. For more information, visit www.scbe.ntu.edu.sg/About_Us/Pages/Open_Positions.aspx

Research Areas

Chemical and Biomolecular Engineering Division

- Process systems engineering
- Product and process design
- Pharmaceutical engineering
- Food engineering
- Separation technology
- Colloid and interface science
- Synthetic Biology

Bioengineering Division

- Therapeutic and diagnostic devices
- Biomechanics
- Bio-imaging and biosignal processing
- Biofluidics
- Neuro bioengineering
- Nature inspired bioengineering
- Mechanobiology of cell-cell and cell-matrix interactions

Application Details

Guidelines: www.ntu.edu.sg/ohr/Career/SubmitApplications/Pages/Faculty.aspx

Email: scbe_recruit@ntu.edu.sg

www.ntu.edu.sg

University of Nebraska Lincoln

Assistant Professor Cropping Systems Disease Management Specialist

The Department of Plant Pathology at the University of Nebraska-Lincoln invites applications for a 12-month tenure-track faculty position at the Assistant Professor level. This position is 60% research and 40% extension and is located at the West Central Research and Extension Center in North Platte, Nebraska. Tenure home will be the Department of Plant Pathology.

We are seeking candidates interested in research establishing an integrated research/extension program emphasizing fungal pathogens on multiple field crops, e.g. corn, soybean, wheat and grasses. There is an expectation to work with soilborne fungal pathogens and address root and above ground plant health in cropping systems, and disease management in limited water use cropping systems. Responsibilities include serving as a member of an interactive extension plant pathology team and working with an interdisciplinary cropping systems team in the west central region and across Nebraska. The candidate will work with other faculty to develop grant proposals and publish research and extension results. The candidate will be expected to obtain grant funds to maintain active programs in research and extension.

A Ph.D. in plant pathology or closely related field is required as well as a demonstrated research record consisting of publications in peer-reviewed journals, the ability to attract grant funds, and good verbal and written communication skills. Relevant postdoctoral experience and extension experience is preferred. To apply, go to **http://employment.unl.edu**. Search for requisition **#F_130180**. Click on "Apply to this job." Complete the application and attach a letter of interest, curriculum vitae, and a 2-3 page description of research and extension interests/activities (other). In addition, arrange to have 3 letters of recommendation sent to: **Search Committee Chair, Department of Plant Pathology, Rm. 406 Plant Science Hall, University of Nebraska-Lincoln, Lincoln, NE 68583-0722**. Review of applications will commence on **November 4, 2013** and will continue until the position is filled or the search is closed. Salary will be commensurate with qualifications and experience. Contact **Dr. James Steadman** at **402-472-2858** or **jsteadman1@unl.edu** with any questions.

The University of Nebraska is committed to a pluralistic campus community through Affirmative Action, Equal Opportunity, work-life balance, and dual careers.

Assistant Professor

Department of Cell Biology and Anatomy

The Department of Cell Biology and Anatomy of The Chicago Medical School, Rosalind Franklin University of Medicine and Science, invites applications for a tenure-track Assistant Professor faculty position. The successful applicant is expected to establish a strong, extramurally funded research program, and to contribute to medical and graduate teaching. Candidates are particularly encouraged who are applying cellular and molecular approaches to the study of fundamental mechanisms of human disease. Clinical populations and physician collaborators are available through affiliations with Advocate Lutheran General Hospital and the Lovell Federal Health Care Center (a veterans administration hospital), and other sites in the Chicago area. Available core resources include confocal, live-cell and electron microscopy facilities, as well as structural biology and proteomics centers. Current areas of research in the Department include the neurobiology of learning and memory, community structure of neural networks, molecular cell biology of muscle development, cellular trafficking and extracellular matrix, RNA biology, RNA processing in human disease, organization of gene expression, and molecular defects underlying muscular dystrophies. Information on the Department may be found at: http://www.rosalindfranklin.edu/cms/biology.aspx.

To apply, visit **http://rosalindfranklin.peopleadmin.com/postings/6243**. Applicants must submit a CV, a cover letter containing the names of three references, and a statement of current and future research plans. Review of applications will begin immediately and will continue until the position is filled.

Rosalind Franklin University of Medicine and Science is an Equal Opportunity/Affirmative Action Employer.

University of Miami

Faculty Searches in Biology

Neuroscience: Outstanding applicants engaged in answering fundamental questions in systems level neuroscience by combining optical approaches with molecular genetics are encouraged to apply. To promote synergy with other laboratories, the successful candidate will be housed in the new Neuroscience Annex that brings together faculty from diverse departments at the University of Miami including Biology, Psychology, and the Miami Project to Cure Paralysis. Inquiries should be directed to the Search Chair at **neuroscience@bio.miami.edu**.

Systems Biology: Outstanding applicants engaged in answering fundamental questions in evolution using both computational and experimental approaches are encouraged to apply. Applications from biologists with the desire to interact with a group of interdisciplinary scientists in Complexity Science are attractive. Inquiries should be directed to the Search Chair at **evolsysbio@bio.miami.edu**.

To be eligible for these tenure-track appointments at the Assistant/Associate Professor level, successful candidates must hold a PhD, have postdoctoral experience, are expected to develop vigorous, externally funded research programs and to teach at both the undergraduate and graduate levels. More information about the Department and University can be found at **http://www.as.miami.edu/biology/**. Applicants should submit a cover letter describing interactions they foresee with existing university research programs, a curriculum vita, two representative publications, a research statement, a teaching statement and the names of at least three references online to **http://www.as.miami.edu/sciencecluster/**.

Application materials must be received by **November 15, 2013**.

The University of Miami is an Affirmative Action, Equal Opportunity Employer committed to expanding the diversity of its faculty. Women, persons with disabilities, and members of other underrepresented groups are encouraged to apply.

University of Illinois at Urbana-Champaign
College of Liberal Arts and Sciences
School of Molecular and Cellular Biology
Department of Cell and Developmental Biology
Assistant Professor

The School of Molecular and Cellular Biology (http://mcb.illinois.edu/) and the Department at Cell and Developmental Biology at the University of Illinois at Urbana-Champaign seeks outstanding applicants for a full-time tenure track Assistant Professor position in any area of Developmental, Regeneration, or Stem Cell Biology.

Candidates must have a Ph.D., M.D., or equivalent degree, a strong track record during their graduate and postdoctoral career, and a compelling vision for their future, independent research direction. The target starting date is August 16, 2014. The successful candidate will be located in the Department of Cell and Developmental Biology and will be expected to conduct independent research, perform academic duties associated with our BS and PhD programs, and have the ability to teach effectively at both undergraduate and graduate levels. Salary is competitive and commensurate with experience. This position offers excellent laboratory facilities, relocation start-up funds, and the opportunity to work with outstanding colleagues and graduate students.

The Urbana-Champaign campus offers a wide range of state-of-the-art research support facilities that include the Roy J. Carver Biotechnology Center, the W. M. Keck Center for Comparative and Functional Genomics, as well as facilities for proteomics, metabolomics, high-throughput screening, immunology, flow cytometry, microscopy, and transgenic mice. The campus has strong programs in biophysics, bioengineering, biological physics, and chemical biology, and superb computational resources are available at the National Center for Supercomputing Applications and the NIH Resource for Macromolecular Modeling and Bioinformatics.

Urbana-Champaign offers the residential advantages of a medium-sized university city, excellent cultural opportunities, and a high quality of life. In 2010, the University of Illinois at Urbana-Champaign received top rankings by Harvard University's Collaborative on Academic Careers in Higher Education for its pre-tenure practices in balancing work and home. (http://www.insidehighered.com/news/2010/11/15/coache)

To ensure full consideration, create your candidate profile through **https://jobs.illinois.edu** and submit your application cover letter, curriculum vitae, a concise summary of past research accomplishments, a statement of future research plans and contact information for three professional references by **December 15, 2013**. Referees will be contacted electronically upon the submission of the application. Although early applications are appreciated and interviews may be conducted before the closing date, no hire will be made until after the closing date.

Questions can be addressed to the School of Molecular and Cellular Biology, 217-333-3166.

Illinois is an Affirmative Action /Equal Opportunity Employer and welcomes individuals with diverse backgrounds, experiences, and ideas who embrace and value diversity and inclusivity. (www.inclusiveillinois.illinois.edu).

University of Illinois at Urbana-Champaign
College of Liberal Arts and Sciences
School of Molecular and Cellular Biology
Department of Molecular and Integrative Physiology
Assistant Professors

The School of Molecular and Cellular Biology (http://mcb.illinois.edu/) at the University of Illinois at Urbana-Champaign seeks outstanding applicants for two tenure track Assistant Professor positions in the following areas:

Metabolic Regulation and Cancer: We are interested in candidates with innovative research programs using mammalian model systems to explore molecular, cellular and systemic mechanisms underlying normal homeostatic metabolic balance and their pathophysiological dysregulation in human diseases ranging from diabetes, obesity and the metabolic syndrome to cancer. Candidates with novel ideas on how cellular signaling networks could be targeted therapeutically in the context of metabolic diseases and cancer are encouraged to apply. Successful candidates would provide synergy with campus research thrusts in endocrinology, metabolism, and cancer.

Molecular and Cellular Neuroscience: We are interested in candidates with research interests in the following topics: (i) ion channel function, regulation, and localization within neurons; (ii) molecular basis of sensory transduction; (iii) molecular basis of synaptic plasticity; (iv) molecular basis of neurodegenerative diseases, such as Alzheimer's and Parkinson; (v) neuro-endocrine interactions; and (vi) neural regulation of metabolism and ingestive behavior. Successful candidates will have opportunity to participate in the multi-disciplinary Neuroscience Program, the Abbott/UIUC Center for Nutrition, Learning and Memory, and the NSF IGERT that combines both biology and engineering.

Candidates must hold a Ph.D., M.D., or equivalent degree, and have a strong track record during their graduate and postdoctoral career and a compelling vision for their future, independent research direction. The target starting date is August 16, 2014. The successful candidate will be located in the Department of Molecular and Integrative Physiology and will be expected to conduct independent research, perform academic duties associated with our BS and PhD programs, and have the ability to teach effectively at both the undergraduate and graduate levels. Salary is competitive and commensurate with experience. These positions offer excellent laboratory facilities, relocation start-up funds, and the opportunity to work with outstanding colleagues and graduate students.

The Urbana-Champaign campus offers a wide range of state-of-the-art research facilities that include the Beckman Institute, Institute of Genomic Biology, Roy J. Carver Biotechnology Center, the W. M. Keck Center for Comparative and Functional Genomics, as well as facilities for proteomics, metabolomics, high-throughput screening, flow cytometry, microscopy, and transgenic mice. The campus has strong programs in bioengineering, biological physics, and chemical biology, and superb computational resources are available at the National Center for Supercomputing Applications and the NIH Resource for Macromolecular Modeling and Bioinformatics.

Urbana-Champaign offers the residential advantages of a medium-sized university city, excellent cultural opportunities, and a high quality of life. In 2010, the University of Illinois at Urbana- Champaign received top rankings by Harvard University's Collaborative on Academic Careers in Higher Education for its pre-tenure practices in balancing work and home. (http://www.insidehighered.com/news/2010/11/15/coache).

To ensure full consideration, create your candidate profile through **https://jobs.illinois.edu** and upload your application cover letter, curriculum vitae, a concise summary of past research accomplishments, a statement of future research plans and contact information for three professional references by **December 15, 2013**. Referees will be contacted electronically upon the submission of the application. Although early applications are appreciated and interviews may be conducted before the closing date, no hire will be made until after the closing date. Questions can be addressed to the School of Molecular and Cellular Biology, 217-333-3166.

Illinois is an Affirmative Action /Equal Opportunity Employer and welcomes individuals with diverse backgrounds, experiences, and ideas who embrace and value diversity and inclusivity (www.inclusiveillinois.illinois.edu).

PENNSTATE HERSHEY Children's Hospital

Director, Pediatric Molecular Oncology Program
Penn State Hershey Children's Hospital
Pennsylvania State University College of Medicine

The Division of Pediatric Hematology/Oncology at the Penn State Hershey Children's Hospital is recruiting a director for the newly established Pediatric Molecular Oncology Program. This Program is supported by a $20 M endowment from the Four Diamonds Fund of the PSU College of Medicine, part of a $50 M endowment supporting the Four Diamonds Pediatric Cancer Research Program. The mission of the Pediatric Molecular Oncology Program is to understand tumor development at a molecular level and to develop genetic and proteomics analysis of pediatric cancers to individualize selection of therapy. This will include support for basic and translational research studies and/or clinical trials. Rank is at the Associate to Full Professor level commensurate with the applicant's experience and accomplishments. Successful applicants will have an M.D./Ph.D., Ph.D., or M.D. degree with an established track record in cancer research and demonstrated ability to obtain extramural funding (R01-type award). The Division of Pediatric Hematology/Oncology has 11 full-time Pediatric Hematologists/Oncologists and 6 Ph.D. faculty. Over 100 new oncology patients are seen annually, and there are programs in pediatric stem cell transplantation, neuro-oncology, survivorship, hemophilia, and sickle cell disease. The division has an accredited Pediatric Heme/Onc fellowship program and is an active member of COG and POETIC. The Four Diamonds Pediatric Cancer Research Program includes NIH-funded basic science and translational research in transcriptional and epigenetic changes in leukemia and solid tumors. Research is supported by the Penn State Cancer Institute, the Penn State Hershey Institute for Personalized Medicine, an NIH-funded CTSA, and Pediatric Clinical Trials Office. Basic core, translational, and clinical facilities provide an excellent environment for research.

Please submit a current CV and letter of interest to: **Barbara Miller, M.D. (bmiller3@psu.edu), Chief, Division of Pediatric Hematology/Oncology, Penn State Children's Hospital, the Pennsylvania State University College of Medicine, Box 850, MC H085, Hershey, Pennsylvania 17033**. Applications are accepted until position filled.

Penn State Milton S. Hershey Medical Center and the College of Medicine are Equal Opportunity/Affirmative Action Employers and encourage applications from women and members of minority groups.

KAROLINSKA INSTITUTET ANNO 1810 Karolinska Institutet

Senior Research Fellow in Neuroscience

A position as Senior Researcher/ Associate Professor in Neuroscience is open for application at The Strategic Research Program in Neuroscience at Karolinska Institutet (StratNeuro) in Stockholm, Sweden. The position is secured financially for five years, and is aimed to recruit and support an excellent researcher who has passed the level of Assistant Professor.

Duties
The successful candidate should have a strong track record in basic or clinical neuroscience within the theme of the program, i.e., "Cognitive and Motor Functions in Health and Disease during the Lifespan". The candidate is expected to have an independent line of research and to have a plan how this can be further developed within the StratNeuro program. The program has a special interest to support researchers who can bridge the gap between basic and clinical neuroscience.

Entry requirements
Experience of a multidisciplinary approach to study the nervous system is a merit, as well as student supervision.

Bases of assessment
In the assessment of the applicant's qualifications, the following criteria will be used: (1) scientific competence; (2) international experience and collaborative skills; (3) teaching and supervision of graduate and postgraduate levels.

Last application date: 2013-11-01
Link to ad: ki.se/jobs

Biology Full-Time Tenure Track Faculty Position in Parasitology

The Boston College Biology Department seeks outstanding candidates for a tenure-track faculty position at the level of **ASSISTANT PROFESSOR** or **ASSOCIATE PROFESSOR**. Boston College provides competitive start-up funds and research space, with the expectation that the successful candidate will establish, or bring to the university, a vigorous, externally-funded research program. The successful applicant will have access to well-equipped animal facilities, core laboratories with state of the art instrumentation for fluorescence microscopy and flow cytometry, and substantial computational resources.

We seek someone with a research program in parasitology, ideally with an emphasis on immunology or systems biology. Special consideration will be given to candidates whose research program meshes with current faculty interests: see http://www.bc.edu/biology for profiles of current faculty research programs. In addition, the successful candidate will be expected to train graduate students and participate in the undergraduate teaching mission of the Biology Department. This appointment will begin on or after July 1, 2014.

Applicants should submit their cover letter, curriculum vitae, a statement of present and future research plans, and arrange to have three letters of reference submitted separately. All application materials can be submitted through Interfolio at: **http://apply.interfolio.com/22634**. Applications received before **October 1, 2013** will be given full consideration, but review of applications will continue until the position is filled.

Boston College is an Affirmative Action/Equal Opportunity Employer. To learn more about how BC supports diversity and inclusion throughout the university please visit the Office for Institutional Diversity at http://www.bc.edu/offices/diversity.

UNIVERSITY OF NEVADA •Reno

Department of Biology
University of Nevada, Reno
Neurobiology Faculty Position

The Department of Biology seeks at least one **NEUROBIOLOGIST** at the assistant professor level, tenure-track. We seek candidates in the broad area of neuroscience, with particular interests in integrative approaches, from cellular levels to plasticity, neural systems, neurophysiology, genetics and behavior. Competitive startup funds include support from funded NIH INBRE and COBRE career development grants, and excellent facilities. Our faculty members maintain nationally recognized, extramurally funded research programs, train PhD students, and participate in undergraduate teaching. The Department of Biology is home to 26 faculty members that teach biology and neuroscience courses, mentor 50 graduate students, with an average of $4 million/yr in extramural awards. Faculty members in the Department of Biology have close ties to the University of Nevada School of Medicine and over $60 million of NIH funds have recently been targeted for biomedical research development on campus. Reno is located in the Sierra Nevada mountains near Lake Tahoe, and was recently rated one of the best small cities in the US for outdoor recreation and overall quality of life.

Go to **http://jobs.unr.edu** to submit application materials, including an application letter, CV, research plans, teaching interests, and contact information for three references. Applications received by **October 16, 2013** will receive full consideration.

Equal Employment Opportunity/Affirmative Action.
Women and underrepresented groups are encouraged to apply.

Tenure-track positions in Systems Biology and Wildlife Biology

The Department of Biology at the University of North Dakota invites applications for two positions at the level of Assistant Professor.

Systems Biology: The position is integral to our new undergraduate major in Molecular and Integrative Biology. The individual will have the opportunity to collaborate with existing North Dakota faculty in ongoing development of research, including environmental epigenetics and genomics. The individual will combine transcriptomic, metabolomic, and/or proteomic analysis with computational modeling exploring the role of gene regulatory networks or protein interactions in organismal function. The specific organism(s) or model system used is of less importance than the integrative nature of the analytical approaches and the candidate's ability to teach both general biology courses and a Systems Biology course. A Ph.D. and postdoctoral experience are required. Review of applications will begin **October 15, 2013** and continue until the position is filled.

Wildlife Biology: The position is integral to our undergraduate major in Fisheries and Wildlife Biology and will also strengthen the department's teaching and research missions in ecology and evolutionary biology. We seek an individual with expertise in field-based, hypothesis-driven research involving the ecology of mammals. Specific interests may include but are not limited to human dimensions of wildlife biology, plant-herbivore interactions, disease ecology, and behavioral ecology. The successful candidate will benefit from our location in the northern plains (including three University-owned field stations in the region) and opportunities to engage with state and regional resource management agencies and conservation organizations. Course offerings will depend on the candidate's specific expertise, but may include courses such as Ecology of Mammals, Conservation Biology, or wildlife-related courses focused on human dimensions. A Ph.D. is required for this position and postdoctoral experience preferred. Review of applications will begin **October 21, 2013**, and continue until the position is filled.

Both positions: Teaching duties will not exceed two courses per year during the first several years.

How to apply: Send, in the following order, a cover letter, CV, statements of teaching and research interests, three representative reprints, and the names and contact information for at least three references as a single pdf file to **Dr. Diane Darland** at **diane.darland@und.edu** (Systems Biology) or **Dr. Robert Newman** at **robert.newman@und.edu** (Wildlife Biology). Address for mail contact is **University of North Dakota, Department of Biology, 10 Cornell St., Stop 9019, Grand Forks, ND 58202-9019**. The positions will begin 16 August, 2014. For additional details on these positions: **www.und.edu/dept/biology/jobs.htm**.

The University of North Dakota is an Equal Opportunity/Affirmative Action Employer and we strongly encourage applications from women and underrepresented groups. Veteran's preference does not apply to this position.

University of Pittsburgh School of Medicine Department of Otolaryngology

Faculty Position in Auditory Neuroscience

To expand its **Auditory Neuroscience Group (http://www.audres.pitt.edu)**, the Department of Otolaryngology at the University of Pittsburgh School of Medicine seeks applications for a **tenure-track faculty position**. To complement our existing strength, we are especially interested in investigators addressing fundamental questions about the structural and functional properties of the mammalian central auditory system using ***in vivo*** **physiological and/or behavioral/psychophysical approaches**.

Outstanding investigators at any rank will be considered. Candidates must have a Ph.D., M.D. or equivalent degrees. Faculties in the Auditory Neuroscience Group have secondary appointments in basic science departments and are expected to participate in neuroscience graduate training programs.

The University of Pittsburgh offers a highly dynamic research/academic environment that provides ample opportunities for collaborations on the basic science or translational level.

To ensure full consideration, **applications should be received by November 21st, 2013**, however the review process will continue until the position is filled. Applicants should submit a CV, a 2-3 page summary of past accomplishments and research plans, and the names of three references to **ausearch@pitt.edu**

The University of Pittsburgh is an Affirmative Action, Equal Opportunity Employer.

TENURED/TENURE TRACK FACULTY POSITION

THE DEPARTMENT OF CHEMISTRY AND BIOCHEMISTRY AT THE UNIVERSITY OF MARYLAND, BALTIMORE COUNTY (UMBC) invites applications for a full-time, tenured/ tenure-track faculty position at the Assistant or Associate Professor level. Applicants are expected to establish a vigorous, externally funded, research program in any sub-discipline of an area *broadly defined as analytical chemistry* (e.g., bio-analytical, materials, energy, etc.). The successful applicant should have a PhD and postdoctoral experience and will be expected to teach at both the undergraduate and graduate (PhD and MS) levels, with particular emphasis on analytical and instrumental chemistry courses. Applications from women, minorities, individuals with disabilities and other traditionally under-represented groups in the sciences are especially encouraged. The appointment will commence August 2014. The Department (www.umbc.edu/chem) is a highly cross-disciplinary and interactive group of faculty, post-doctoral fellows, and students engaged in cutting edge research, working in state-of-the-art laboratory facilities in a recently renovated building. UMBC is strategically situated on a suburban campus in the intellectually and culturally vibrant Baltimore-Washington corridor, providing unique opportunities afforded by its diversity, intermediate size and world-class infrastructure. Applicants should submit curriculum vitae, description of research plans, and statement of teaching philosophy as well as arrange for three letters of recommendation to be sent to:

Chair, Faculty Search Committee
Department of Chemistry and Biochemistry
University of Maryland, Baltimore County
1000 Hilltop Circle
Baltimore, MD 21250

Electronic submissions can also be made to **chemsearch@umbc.edu**. Review of applications will begin **November 15, 2013** and continue until the position is filled.

UMBC is an Equal Opportunity/Affirmative Action Employer.

Two Tenure-track Assistant Professor Positions Department of Biochemistry and Biophysics

University of California San Francisco

The Department of Biochemistry and Biophysics resides at the newly constructed Mission Bay Campus near to the San Francisco Bay waterfront and Embarcadero. Our department is a supportive and dynamic group with an established track record of mentoring and promoting the career development of young scientists. Research within the department spans a broad range of interests from protein structure to cell biology, systems biology, developmental biology and neuroscience. We have defined two broad areas of interest that span most of modern cellular, molecular and systems biology.

1) We seek individuals applying quantitative approaches characteristic of systems biology and/or structural biology to solve outstanding questions in any field of modern biology.
2) We seek individuals approaching questions in modern biology that range from cell to organism in scope. Individuals working in areas of cell biology, developmental biology and neuroscience with an emphasis on highly quantitative experimental approaches are encouraged to apply.

Individuals who have attained the level of PhD, MD or equivalent may apply. Our evaluation process emphasizes the selection of individuals who have made significant contributions to their field of research and who are able to clearly articulate both their past accomplishments and a vision of their future research program. A 1-2 page research statement should succinctly address two questions. (1) What have been your most significant scientific contributions to date? (2) What will be the significance of your future research program?

Please submit your CV, 1 page cover letter, 1-2 page research statement, and three letters of reference to https://bch-facultysearch.ucsf.edu by December 1, 2013. Successful candidates will be invited to interview at UCSF during the months of January and February, 2014.

UCSF seeks candidates whose experience, teaching, research, or community service has prepared them to contribute to our commitment to diversity and excellence. UCSF is an Affirmative Action/Equal Opportunity Employer. The University undertakes affirmative action to assure equal employment opportunity for underutilized minorities and women, for person with disabilities, and for covered veterans.